Development of antibacterial Polyhydroxyalkanoates for their use in nerve tissue engineering

Paxinou, A.

Development of antibacterial Polyhydroxyalkanoates for their use in nerve tissue engineering

Alexandra Paxinou

A thesis submitted in partial fulfilment of the requirements of the University of Westminster for the degree of Doctor of Philosophy

March 2020

Authors' declaration

I hereby declare that the present research work has been performed in accordance with the guidelines and regulation of the University of Westminster. This PhD thesis is original, except when cited by relevant references. This submission project, as a whole or part is not substantially same as any previous or current research, either in published or unpublished form, for a degree, diploma or similar qualification in any university or similar institution. Until the outcome of the current application of the University of Westminster is known, the work will not be submitted for such qualifications to another University or similar institution. Any views expressed in this work are those of the Author and in no way represent that of the University of Westminster.

Signed: Alexandra Paxinou Date: March 2020

ACKNOWLEDGEMENTS

I would like to thank Professor Ipsita Roy, my supervisor, for giving me the opportunity to accomplish this project in her lab. An incredible experience with a lot of learning on the way. Her support and guidance were invaluable for pursuing my PhD studies.

Huge thanks is due to my external supervisor Dr. Jochen Salber at Ruhr University, Bochum who so tirelessly offered his wisdom and for giving up so many h answering my questions and advising me during this thesis. The project would not have been possible without him. Thank you.

I offer my sincerest gratitude to my current director of studies, Professor Brendon Noble for his trust and encouragement, as well as my second supervisor at Westminster university Dr. Saki Raheem for his support and motivation.

Special thanks are also due to HyMedPoly Project consortium for the financial support and all our collaborators for their excellent cooperation and invaluable expertise. I am also particularly grateful to Dr. Pooja Basnett for her guidance and constant motivation and Dr. Rinat Nigmatullin for valuable advises, support and guidance.

Thanks also to all the colleagues in the microbiology department for medical microbiology at Ruhr-University Bochum for their help in the antibacterial studies.

Many thanks to Professor Costa Gallioti at ICEHT/FORTH, for suppling the graphene oxide and George Paterakis for all the assistance with Raman and XRD spectroscopy. My gratitude also to Dr. Lambrini Sygellou, for the XPS analysis.

I would also like to express my gratitude to Professor Aldo R. Boccaccini and Dr. Agata Lapa for suppling the cerium doped phosphate fibres.

Great thanks to Professor John Haycock for allowing me to perform part of the neuronal cell studies in his lab and to Dr. Caroline Tailor at the Kroto Research Institute for her assistance with NG-10815 neuronal cell studies and moral support.

I would like to thank the technical staff from University of Westminster. Big thanks to Neville for his continued support during the fermentation experiments and Kim that always resolved, any problem that arose.

I am very grateful to the UCL's technical staff, Dr. George Gergiou and Dr. Graham Palmer for their assistance with various techniques as well as Dr. Nicola Mordan for her help with various imaging techniques.

Thanks, are also due in no small measure to all members of the lab, both past and present for their friendship, support and time spent together. Thank you, Pooja, Rinat, Elena, Sheila, Isabel, Barbara and Patricia for all your support during my journey.

I would like to thank my family: my dad, my brother and sister for their love, understanding and encouragement.

Finally, I would like to wholeheartedly thank Panagiotis for his unconditional support, encouragement and patience without him none of this would have been possible. Thank you for believing in me.

ABSTRACT

The fabrication of nerve conduits (NGCs) with the appropriate features for a successful nerve regeneration is not always possible/fulfilled. The currently available implants partially meet the requirements of such medical devices. Despite the evolution of the polymer field and hydrogels, not much research has been conducted to exploit all possible bioplastics for their use in nerve tissue engineering. The drawbacks of current's NGCs are promoting alternative materials. In this perspective, this study utilized Polyhydroxyalkanoates (PHAs), linear bio-polyesters derived from bacterial fermentation process with biocompatible and biodegradable properties. PHAs are divided into two categories, according on the number of carbon atoms in a monomer unit: short chain length (scl) and medium chain length (mcl). Depending on the type of PHA the physicochemical properties differ. The use of these bio-polyesters is gaining high interest in a vast range of biomedical applications. Additionally, previous studies have shown that PHAs are highly promising candidates for their use in nerve tissue engineering.

In this study, the main objective was to develop a NGC, based on PHAs enriched with inorganic and organic compounds (garlic powder, cerium doped phosphate fibres and graphene oxide) in order to impart antibacterial properties to the final design. Production of scl and mcl-PHAs, P(3HB) and P(3HO-co-3HD), achieved via bacterial fermentation. Blends of these two biopolymers in different ratios, 80/20, 75/25, 25/75 and 20/80, were fabricated and characterized for their physicochemical and biocompatibility properties and future use as potential base materials for nerve tissue engineering. The addition of different amounts of organic and inorganic compounds resulted in the fabrication of novel composites. These composites were fully characterized for their physicochemical and biological properties. The antibacterial activity of these composites was evaluated using a range of tests and bacterial strains whereas their cytocompatibility was investigated using L929 murine fibroblasts and NG108-15 neuronal cells. The promising composite films were then translated to nerve conduits via fabrication by dip moulding process. The fabricated tubes were used for further NGCs development to insert guidance channels, formed by aligned electrospun PHA fibres. Alternatively, NGCs with aligned geometrical characteristic were

developed by rolling films of PHA composites with phosphate fibres into tubular structures.

Two groups of NGCs prototypes were fabricated using the 75/25 blend of PHAs as the polymer matrix. Three different percentages of cerium doped phosphate fibres (37 wt%, 74 wt% and 90 wt%) and graphene oxide (0.5 wt%, 2 wt% and 5 wt%) were incorporated in the polymer blend. These composites have shown to possess sufficient antibacterial activity against both Gram-negative and Gram-positive bacteria without introducing cytotoxic effect to the L929 murine fibroblasts and the NG108-15 neuronal cells.

In summary, the mechanical, antibacterial and cytocompatibility properties of the developed composites from natural bio-polyesters; showed that they are excellent candidates for their use in nerve tissue engineering and the fabrication of novel bioresorbable and antibacterial NGCs.

Table of Contents

Chapter 1 ..... **1**

1 Introduction **2**
1.1 Bacterial infection and antibiotic resistance **2**
1.2 Polymers as antibacterial materials **5**
1.3 Discovery of Polyhydroxyalkanoates (PHAs) **9**
1.3.1 Classification and properties of PHAs 11
1.3.2 Biodegradability of PHAs 14
1.3.3 Biocompatibility of PHAs 15
1.4 Biomedical applications of PHAs **17**
1.4.1 PHAs as drug delivery systems 17
1.4.2 PHAs as tissue engineering scaffolds 19
1.4.3 Injuries of peripheral nervous system 22
1.4.4 Therapeutic strategies of peripheral nerve injuries 25
1.4.5 PHAs as biomaterials for nerve conduits 28
1.5 Novel antibacterial agents **29**
1.5.1 Natural antimicrobial compounds 29
1.5.2 Inorganic compounds (metal ions, phosphate glass and graphene-based materials) 37
1.5.3 Aims and objectives 44

Chapter 2 ..... **46**

2 Materials and methods **47**
2.1 Materials **47**
2.1.1 Bacterial strains 47
2.1.2 Cell lines and cell culture materials 47
2.1.3 Organic and Inorganic compounds 48
2.2 Media composition **48**
2.3 PHA production **50**
2.3.1 P(3HB) production 50
2.3.2 P(3HO-co-3HD) production 50
2.4 Experimental Methods **50**
2.4.1 Production of P(3HB) by *Bacillus subtilis* OK2 in 10 L bioreactor 50
2.4.2 Production of P(3HO-co-3HD) by *Pseudomonas mendocina* CH50 in 20 L bioreactor 51
2.5 Extraction of PHAs from biomass **51**
2.5.1 Soxhlet extraction 51
2.5.2 Solvent dispersion method 52
2.6 PHA characterization **52**
2.6.1 Fourier Transform Infrared Spectroscopy (FTIR) 52
2.6.2 Gas chromatography Mass Spectrometry (GC-MS) 53
2.6.3 Nuclear Magnetic Resonance (NMR) 53
2.6.4 Differential scanning calorimetry 53
2.6.5 Tensile Testing 54

2.6.6 Surface Wettability of the films 54
2.6.7 Gel Permeation Chromatography (GPC) 54
2.6.8 Scanning electron microscopy (SEM) 55
2.6.9 X-ray diffraction (XRD) 55
2.6.10 Raman spectroscopy 55
2.6.11 X-ray photoelectron spectroscopy (XPS) 56
2.7 Temporal profiling of PHAs production during fermentation process 56
2.7.1 Optical density mesurements 56
2.7.2 pH monitoring 56
2.7.3 Glucose estimation 57
2.7.4 Nitrogen estimation 57
2.7.5 Polymer estimation during the fermentation process 57
2.7.6 Reagents 57
2.8 Film preparation by solvent casting 59
2.9 Composite film prearation 59
2.10 Processability of PHAs for nerve conduit development 60
2.10.1 Single lumen PHAs conduits via dip moulding 60
2.10.2 Nerve conduits with aligned PGFs fibres 60
2.10.3 Manufacture of aligned PHA microfibers by electrospinning 61
2.11 Antibacterial evaluation 62
2.11.1 Agar well diffusion method using allicin and garlic powder 62
2.11.2 Broth dilution method: estimation of MIC and MBC 62
2.11.3 Prevention of biofilm formation 63
2.11.4 PHAs loaded with Garlic powder, Ce-doped PGFs and graphene oxide assessed for their antibacterial properties 63
2.11.5 Disc diffusion assay 63
2.11.6 Evaluation of free planktonic cells and adhered cells on the PHA composites 64
2.11.7 *In vitro* antibacterial evaluation of Graphene oxide composites 64
2.12 Cell Culture 65
2.12.1 L929 murine fibroblasts cell culture 65
2.12.2 NG108-15 neuronal cell culture 65
2.13 Statistical analysis 67

Chapter 3 68

3 Production and characterisation of P(3HB) and P(3HO-co-3HD) 69
3.1 Introduction 69
3.2 PHA production 70
3.2.1 P(3HB) production by *B. subtilis* OK2 using glucose as the carbon source 70
3.2.2 P(3HO-co-3HD) production by *P. mendocina* using glucose as the carbon source 72
3.3 PHA Characterization 73
3.3.1 Attenuated Total Reflectance Fourier Transform Infrared Spectroscopy (ATR/FTIR) of P(3HB) and P(3HO-co-3HD) 73

3.3.2 Gas Chromatography-Mass Spectrometry (GC-MS) of P(3HB) and P(3HO-co-3HD) 75
3.3.3 Nuclear Magnetic Resonance (NMR) of P(3HB) and P(3HO-co-3HD) 77
3.3.4 Thermal analysis – Differential Scanning Calorimetry (DSC) of P(3HB) and P(3HO-co-3HD) 80
3.3.5 Mechanical properties 83
3.4 Discussion 84

Chapter 4 89

4 Development of novel P(3HO-co-3HD)/P(3HB) blends, their chemical and biological characterisation 90
4.1 Introduction 90
4.2 Results 92
4.2.1 Fabrication of films made of P(3HO-co-3HD)/P(3HB) blends 92
4.2.2 Attenuated Total Reflectance Fourier Transform Infrared Spectroscopy (ATR/FTIR) of the new PHA blends 93
4.2.3 Thermal characterisation of the new PHA blends 95
4.2.4 Mechanical characterisation of the new PHA blends 97
4.2.5 The water contact angle of the new PHA blends 99
4.2.6 Scanning Electron Microscopy of the new PHA blends 100
4.2.7 XRD analysis of the new PHA blends 102
4.2.8 Cell Viability Studies on new PHA blends 103
4.2.9 Cell Viability Studies on the new PHA blends using NG108-15 neuronal cells 106
4.3 Discussion 107

Chapter 5 111

5 Development of PHAs composites containing garlic powder 112
5.1 Introduction 112
5.2 Results 113
5.2.1 Development of PHAs films and blends containing garlic powder 113
5.2.2 ATR/FTIR of PHAs films and blends containing garlic powder 115
5.2.3 Thermal characterisation of PHAs films and blends containing garlic powder 118
5.2.4 Mechanical characterisation of PHAs films and blends containing garlic powder 120
5.2.5 Water contact angle tests of PHAs films and blends containing garlic powder 122
5.2.6 Scanning Electron Microscopy of the PHAs films and blends containing garlic powder 125
5.2.7 Antibacterial evaluation of garlic powder and films containing garlic powder 128
5.2.8 *In vitro* Cytocompatibility of films and blends containing garlic powder 144

5.3 Discussion 149

Chapter 6 158

6 Development of PHA- based composites containing cerium doped phosphate fibres 159

6.1 Introduction 159

6.2 Results 161

6.2.1 Development of PHA composites containing cerium-doped phosphate glass fibres 161

6.2.2 Attenuated Total Reflectance Fourier Transform Infrared Spectroscopy (ATR/FTIR) of PHA/PGF composites 163

6.2.3 Thermal characterisation of PHA/PGF composites 164

6.2.4 SEM analysis of PHA/PGF composites 166

6.2.5 XRD analysis of the PHA/PGF composites 168

6.2.6 *In vitro* antibacterial evaluation of PHA/PGF composites 169

6.2.7 *In vitro* cytocompatibility of PHA/PGF composites 175

6.3 Discussion 181

Chapter 7 187

7 Development of PHAs composites containing graphene oxide 188

7.1 Introduction 188

7.2 Results 191

7.2.1 Production of PHA/GO composites 191

7.2.2 Attenuated Total Reflectance Fourier Transform Infrared Spectroscopy (ATR/FTIR) of PHA/GO composites 193

7.2.3 Thermal characterisation of PHA/GO composites 196

7.2.4 Mechanical characterisation of PHA/GO composites 200

7.2.5 The water contact angle of the PHA/GO nanocomposites 202

7.2.6 Scanning Electron Microscopy of PHA/GO composites 208

7.2.7 XRD of PHA/GO composites 210

7.2.8 Raman of PHA/GO composites 213

7.2.9 XPS of PHA/GO composites 217

7.2.10 *In vitro* antibacterial evaluation of Graphene oxide composites 220

7.2.11 Indirect and direct cytocompatibility tests 228

7.2.12 Neurite outgrowth assessment on NG108-15 cells cultured on 75/25 blend and composite surfaces 240

7.3 Discussion 242

Chapter 8 252

8 Development of hollow P(3HO-co-3HD)/P(3HB) blend tubes and composites and incorporation of electro-spun PHA fibres 253

8.1 Introduction 253

8.2 Results 256

8.2.1 Tube formation by dip moulding technique using a 75/25 P(3HO-co-3HD)/P(3HB) polymer blend mixture 256

8.2.2 Development of P(3HO-co-HD)/P(3HB) blend tubes and PGFs composites 266
8.2.3 Development of electrospun fibres of PHA blends 268
8.3 Incorporation of the electrospun fibres in the hollow PHA/GO composite tubes 275
8.4 Discussion 276

Chapter 9 282

9 Conclusions and future perspectives 283
9.1 Conclusions 283
9.2 Future perspectives 289

References 291

Appendix 322

Table of Figures

Figure 1.1:::Antibiotic discovery timeline (adapted from Lewis, 2012). 2

Figure 1.2: Estimation of antimicrobial drug resistance linked mortality rate and its economic impact by 2050 (adapted from O'Neill, 2015). 4

Figure 1.3: Trend of development of antimicrobial agents and emergence of drug-resistant bacteria (adapted from Saga & Yamaguchi 2009).....4

Figure 1.4: Schematic representation of antibacterial polymers based on the working principles of the macromolecular systems: A) polymeric biocides, (B) biocidal polymers and (C) biocide-releasing polymers, (adapted from Barzic, et al., 2015; Alarfaj et al., 2016).....6

Figure 1.5: General structure of polyhydroxyalkanoates. R1/R2= alkyl groups C1–C13, x=1–4, n= 100–30 000 (adapted from Keshavarz and Roy, 2010). 9

Figure 1.6: Main causes of nerve injuries. 23

Figure 1.7: Structure of typical neuron. 24

Figure 1.8: Treatments for nerve regeneration.....27

Figure 1.9: Examples for nerve conduit designs (adapted from Arslantunali *et al*., 2014). 28

Figure 1.10: Structures of common antimicrobial plant chemicals (adapted from Cowan, 1999). 32

Figure 1.11: Generation of allicin from alliin (adapted from Marchese et al, 2016). 33

Figure 1.12: Various mechanisms of antimicrobial activity of the metal nanoparticles (adapted from Dizaj *et al.*, 2014). 39

Figure 1.13: Schematic illustration of the antibacterial applications of graphene-based nanomaterials (adapted from Ji et al., 2016). 44

Figure 2.1: Process of manufacturing 3D scaffold using blend PHA and Ce-PGFs by rolling the composite mat to a tubular structure (adapted from (Kim *et al.*, 2015)).....60

Figure 2.2: Electrospinning setup used for fabrication of aligned 75/25 P(3HB)/P(3HO-co-3HD) electrospun fibres (A) Syringe pump, (B) blunt needle connected to an electrode, (C) electrically grounded cylindrical collector, (D) electric motor, (E) voltage generator (Bochum Germany).....61

Figure 3.1: Temporal profiling of *B. subtilis* OK2 using glucose as the source of carbon. 70

Figure 3.2: Extracted and purified P(3HB) produced by *B. subtilis* OK2 using glucose as the source of carbon.....71

Figure 3.3: Temporal profiling of *P. mendocina* CH50 using glucose as the carbon source.....72

Figure 3.4: Extracted and purified P(3HO-co-3HD) produced by *P. mendocina* CH50 using glucose as the source of carbon. 73

Figure 3.5: ATR/FTIR spectrum of P(3HB) produced by *B. subtilis* OK2 using glucose as the carbon source.....74

Figure 3.6: ATR/FTIR spectrum of P(3HO-co-3HD) produced by *P. mendocina* CH50 using glucose as the carbon source. 74

Figure 3.7:GC-MS analysis of the polymer produced by *B. subtilis* OK2 using glucose as the carbon source.....76

Figure 3.8: GC-MS analysis of the polymer produced by *P. mendocina* CH50 using glucose as the carbon source. 77

Figure 3.9: ^{1}H NMR spectrum of P(3HB). 78

Figure 3.10: ^{13}C NMR spectrum of P(3HB). 78

Figure 3.11: ^{1}H NMR spectrum of P(3HO-co-3HD).....79

Figure 3.12: ^{13}C NMR spectrum of P(3HO-co-3HD). 80

Figure 3.13: DSC Thermogram of P(3HB) derived from *B. subtilis* OK2. 81

Figure 3.14: DSC Thermogram of P(3HO-co-3HD) derived from *P. mendocina* CH50. 82

Figure 4.1: Films prepared by solvent casting technique; (1) neat P(3HB), (2) neat P(3HO-co-3HD); Blends (3) 80/20, (4) 75/25, (5) 25/75, (6) 20/80 (w/w) P(3HO-co-3HD)/P(3HB). 92

Figure 4.2: ATR-FTIR spectra of P(3HO-co-3HD)/P(3HB) films showing the characteristic peaks of P(3HO-co-3HD) and P(3HB). The FTIR spectra of the **----** P(3HO-co-3HD), **----** 80/20 P(3HO-co-3HD)/P(3HB), **----** 75/25 P(3HO-co-3HD)/P(3HB), **----** 25/75 P(3HO-co-3HD)/P(3HB), **----** 20/80 P(3HO-co-3HD)/P(3HB) and **----** P(3HB).....93

Figure 4.3: DSC thermograms of the (A): **----** P(3HO-co-3HD), **----** 80/20 P(3HO-co-3HD)/P(3HB), **----** 75/25 P(3HO-co-3HD)/P(3HB) AND (B): **----** 25/75 P(3HO-co-3HD)/P(3HB), **----** 20/80 P(3HO-co-3HD)/P(3HB) and **----** P(3HB). Dotted lines: representative thermograms of the first heating scan of the materials. Solid lines: thermograms of the second heating run. 96

Figure 4.4: Static WCA values of the neat P(3HB) and P(3HO-co-3HD) films and their blends (n=3; error bars=±SD). 100

Figure 4.5: SEM images of (a) P(3HB), (b) P(3HO-co-3HD) (c), (d) 80/20 P(3HO-co-3HD)/P(3HB), (e), (f) 75/25 P(3HO-co-3HD)/P(3HB), (g), (h) 25/75

P(3HO-co-3HD)/P(3HB) and (i), (j) 20/80 P(3HO-co-3HD)/P(3HB) with high and low magnification. 101

Figure 4.6: XRD spectra of: **----** P(3HO-co-3HD), **----** 80/20 P(3HO-co-3HD)/P(3HB), **----** 75/25 P(3HO-co-3HD)/P(3HB), **----** P(3HB), **----** 25/75 P(3HO-co-3HD)/P(3HB) and **----** 20/80 P(3HO-co-3HD)/P(3HB). 103

Figure 4.7: Cell viability (% TCPS) of L929 cells seeded on P(3HO-co-3HD), P(3HB) and P(3HO-co-3HD)/P(3HB) blends, PE and TCPS (positive control). (Mean± SEM, n = 9 independent experiments). Statistical significance determination is represented as *p ≤ 0.05, **p ≤ 0.01, and ***p ≤ 0.001 for cells on TCPS vs. all materials. 105

Figure 4.8: Cytotoxicity of L929 cells seeded on P(3HO-co-3HD), P(3HB) and P(3HO-co-3HD)/P(3HB) blends, PE and TCPS (positive control). (Mean± SEM, n = 9 independent experiments). 105

Figure 4.9: Cell viability of NG108-15 cells seeded on P(3HO-co-3HD), P(3HB) and P(3HO-co-3HD)/P(3HB) blends, PE and TCPS (positive control). Mean± SEM, n = 9 independent experiments). Statistical significance determination is represented as *p ≤ 0.05, **p ≤ 0.01, and ***p ≤ 0.001 for cells on TCPS vs. all materials. 106

Figure 4.10: Cytotoxicity of NG108-15 cells seeded on P(3HO-co-3HD), P(3HB) and P(3HO-co-3HD)/P(3HB) blends, PE and TCPS (positive control). (Mean± SEM, n = 9 independent experiments). 107

Figure 5.1: Composites of P(3HB) and P(3HO-co-3HD) containing different concentrations of garlic powder. (A) P(3HB)/ 23 wt% GP, (B) P(3HB)/ 45 wt% GP, C) P(3HB)/ 90 wt% GP, (D) P(3HO-co-3HD)/ 23 wt% GP, (E) P(3HO-co-3HD)/ 45 wt% GP and (F) P(3HO-co-3HD)/ 90 wt% GP. 114

Figure 5.2: ATR-FTIR spectrum of the: ---- P(3HB), ---- GP, ---- P(3HB)/23 wt%GP, ---- P(3HB)/45 wt%GP P(3HB), ---- P(3HB)/90 wt%GP. 115

Figure 5.3: ATR-FTIR spectrum of the: ---- P(3HO-co-3HD), ---- GP, ---- P(3HO-co-3HD)/23 wt%GP, ---- P(3HO-co-3HD)/45 wt%GP P(3HB), ---- P(3HO-co-3HD)/90 wt%GP. 116

Figure 5.4: ATR-FTIR spectrum of the: ---- 75/25 P(3HO-co-3HD)/P(3HB), ---- GP and 75/25 P(3HO-co-3HD)/P(3HB) blends containing: ---- 23 wt%GP, ---- 45 wt%GP P(3HB) and ---- 90 wt%GP. 117

Figure 5.5: Static water contact angle measurements for P(3HB)/GP composites and control (Mean± SEM, n = 3 independent experiments, p statistical significance values (*p ≤ 0.05, **p ≤ 0.01, and ***p ≤ 0.001) were determined for air vs. respective glass side samples and neat matrix vs composites for both air and glass side). 123

Figure 5.6: Static water contact angle measurements for P(3HO-co-3HD)/GP composites and control Mean± SEM, n = 3 independent experiments, p

statistical significance values (*p ≤ 0.05, **p ≤ 0.01, and ***p ≤ 0.001) were determined for air vs. respective glass side samples and neat matrix vs composites for both air and glass side). 124

Figure 5.7: Static water contact angle measurements for 75/25/P(3HO-co-3HD)/ P(3HB)/GP composites and control Mean± SEM, n = 3 independent experiments, p statistical significance values (*p ≤ 0.05, **p ≤ 0.01, and ***p ≤ 0.001) were determined for air vs. respective glass side samples and neat matrix vs composites for both air and glass side). 125

Figure 5.8: SEM images of (a) neat P(3HB), (b) neat P(3HO-co-3HD), (c) P(3HB)/23 wt% GP, (d) P(3HO-co-3HD)/23 wt% GP, (e) P(3HB)/45 wt% GP, (f) P(3HO-co-3HD)/45 wt% GP, (g) P(3HB)/90 wt% GP and (h) P(3HO-co-3HD)/90 wt% GP. 126

Figure 5.9: SEM images of (a), (b) neat 75/25 P(3HO-co-3HD)/P(3HB), (c), (d) 75/25 P(3HO-co-3HD)/P(3HB)/23 wt% GP (e), (f) 75/25 P(3HO-co-3HD)/P(3HB)/45 wt% GP (g), (h) 75/25 P(3HO-co-3HD)/P(3HB)/90 wt% GP of × 100 and × 1000 magnification. 127

Figure 5.10: Antibacterial activity of Garlic Powder (left) and Allicin (right) against *S. aureus* (ATCC® 29213™) for different concentrations: (a) 3 mg, (b) 5 mg, (c) 7 mg and (d) positive control (antibiotic disc containing 1 µg of oxaccilin). 128

Figure 5.11: Antibacterial activity of Garlic Powder (left) and Allicin (right) against *E. coli* (ATCC® 25922™) for different concentrations: (a) 3 mg, (b) 5 mg, (c) 7 mg and (d) positive control (antibiotic disc containing 300 µg of streptomycin) 129

Figure 5.12: (A) Schematic demonstration of negative (NC) and positive (PC) controls and different concentrations of garlic powder solutions in the representative wells of the 96 well plate. Visual growth of (B) *Staphylococcus aureus* (ATCC® 29213™) (C) S*taphylococcus epidermidis* (ATCC® 12228™), (D) Methicillin-resistant *S. aureus* (MRSA), (E) Methicillin-resistant *S. epidermidis* (MRSE), (F) *Escherichia coli* (ATCC® 25922™), (G) *Pseudomonas aeruginosa* (ATCC® 27853™) using different concentrations of garlic powder. 130

Figure 5.13: The optical density (600 nm) of the supernatants from (A) *Staphylococcus aureus* (ATCC® 29213™) (B) *Staphylococcus epidermidis* (ATCC® 12228™) (C) Methicillin-resistant *S. aureus* (MRSA), (D) Methicillin-resistant *S. epidermidis* (MRSE), (E) *Escherichia coli* (ATCC® 25922™), (F) *Pseudomonas aeruginosa* (ATCC® 27853™) after treatment with different concentrations of garlic powder solutions for 24h..... 131

Figure 5.14: Absorbance of the stained biofilm formed in the 96 well plates after incubation with the different substrates (from left to right) of : NC, PC, 70, 35, 18, 9, 4.4, 2.2 mg/ml of garlic powder. 132

Figure 5.15: Biofilm-forming capacity of (A) *Staphylococcus aureus* (ATCC® 29213™), (B) *Staphylococcus epidermidis* (ATCC® 12228™), (C) Methicillin-resistant *S. aureus* (MRSA), (D) Methicillin-resistant *S. epidermidis* (MRSE), (E) *Escherichia coli* (ATCC® 25922™) and (F) *Pseudomonas aeruginosa* (ATCC® 27853™). 133

Figure 5.16: Schematic demonstration of samples and controls used for the disc diffusion tests. 134

Figure 5.17: Antibacterial activity of P(3HB) films incorporated with different concentrations of Garlic Powder (a) 23 wt%, (b) 45 wt%, (c) 90 wt% and (d) positive control against (A) *Staphylococcus aureus* (ATCC® 29213™), (B) *Staphylococcus epidermidis* (ATCC® 12228™), (C) Methicillin-resistant *S. aureus* (MRSA), (D) Methicillin-resistant *S. epidermidis* (MRSE), (E) *Escherichia coli* (ATCC® 25922™), and (F) *Pseudomonas aeruginosa* (ATCC® 27853™) using the agar disc diffusion method. 135

Figure 5.18: In vitro antibacterial inhibition zones of different P(3HB) composites against different bacterial strains. 136

Figure 5.19: Antibacterial activity of P(3HO-co-3HD) films incorporated with different concentrations of Garlic Powder (a) 23 wt%, (b) 45 wt%, (c) 90 wt% and (d) positive control against (A) *Staphylococcus aureus* (ATCC® 29213™), (B) *Staphylococcus epidermidis* (ATCC® 12228™), (C) Methicillin-resistant *S. aureus* (MRSA), (D) Methicillin-resistant *S. epidermidis* (MRSE), (E) *Escherichia coli* (ATCC® 25922™) and (F) *Pseudomonas aeruginosa* (ATCC® 27853™) using the agar disc diffusion method. 137

Figure 5.20: In vitro antibacterial inhibition zones of different P(3HO-co-3HD) composites against different bacterial strains. 138

Figure 5.21: Antibacterial activity of blend films incorporated with different concentrations of GP (a) 23 wt%, (b) 45 wt%, (c) 90 wt% and (d) positive control against (A) *Staphylococcus aureus* (ATCC® 29213™), (B) *Staphylococcus epidermidis* (ATCC® 12228™), (C) Methicillin-resistant *S. aureus* (MRSA), (D) Methicillin-resistant *S. epidermidis* (MRSE), (E) *Escherichia coli* (ATCC® 25922™) and (F) *Pseudomonas aeruginosa* (ATCC® 27853™) using the agar disc diffusion method. 139

Figure 5.22: Dependence of concentration of Garlic powder incorporated into P(3HB) matrix against *S. aureus* (ATCC® 29213™) and *E. coli* (ATCC® 25922™) 141

Figure 5.23: Dependence of the concentration of GP incorporated into P(3HO-co-3HD) matrix against *S. aureus* (ATCC® 29213™) and *E. coli* (ATCC® 25922™) 141

Figure 5.24: 96 well plate containing bacterial suspension and the polymer disc loaded with the antibacterial agent. 142

Figure 5.25: Loss of the adhered bacteria on the P(3HB), P(3HO-co-3HD) and 75/25 P(3HO-co-3HD)/ P(3HB) blend films incorporated with different concentrations of Garlic Powder: 23 wt%, 45 wt% and 90 wt% against (A) *Staphylococcus aureus* (ATCC® 29213™), (B) *Staphylococcus epidermidis* (ATCC® 12228™), (C) Methicillin-resistant *S. aureus* MRSA, (D) Methicillin-resistant *S. epidermidis* (MRSE) and (E) *Escherichia coli* (ATCC® 25922™). 143

Figure 5.26: Indirect cytocompatibility evaluation of the (A) P(3HB), (B) P(3HO-co-3HD) and (C) 75/25 P(3HO-co-3HD)/ P(3HB) composites containing different loadings of GP with respect to L929 cells (Mean± SEM, n = 9 independent experiments). Statistical significance determination is represented as *p ≤ 0.05, **p ≤ 0.01, and ***p ≤ 0.001 for cells on TCPS vs. all materials, and non-modified polymer blend vs. GP composites 146

Figure 5.27: Direct cytocompatibility evaluation of the (A) P(3HB), (B) P(3HO-co-3HD) and (C) 75/25 P(3HO-co-3HD)/ P(3HB) composites containing different loadings of GP with respect to L929 cells (Mean± SEM, n = 9 independent experiments). Statistical significance determination is represented as *p ≤ 0.05, **p ≤ 0.01, and ***p ≤ 0.001 for cells on TCPS vs. all materials, and non-modified polymer blend vs. GP composites. 147

Figure 7.1: Composites of P(3HB) and P(3HO-co-3HD) containing different concentrations of graphene oxide. (A) P(3HB)/0.5 wt% GO, (B) P(3HB)/2 wt% GO, (C) P(3HB)/5 wt% GO, (D) P(3HO-co-3HD)/0.5 wt% GO, (E) P (3HO-co- 3HD)/2 wt% GO and (F) P(3HO-co-3HD)/5 wt% GO.....192

Figure 7.2: Composites of (75/25) P(3HO-co-3HD)/P(3HB) blend, containing different concentrations of graphene oxide. (A) 75/25 blend /0.5 wt% GO, (B) 75/25 blend /2 wt% GO and (C) 75/25 blend /5 wt% GO.....192

Figure 7.3: ATR/FTIR spectra of: --- GO , ---P(3HB) and P(3HB) composites containing :---0.5 wt%, ---2 wt% and ---5 wt% GO.....194

Figure 7.4: ATR/FTIR spectra of: --- GO , ---P(3HO-co-3HD) and P(3HO-co-3HD) composites containing :---0.5 wt%, ---2 wt% and ---5 wt% GO. 195

Figure 7.5: ATR/FTIR spectra of: --- GO, ---75/25 P(3HO-co-3HD)/P(3HB) and 75/25 P(3HO-co-3HD)/P(3HB) composites containing :---0.5 %, ---2 % and ---5 wt% GO.....196

Figure 7.6: Air and glass sides of solvent casted film. 202

Figure 7.7: WCA (sessile drop) of neat P(3HB) and P(3HB)/GO composite films (GO contents: 0.5, 2 and 5wt%) (n=3). (p statistical significance values (*p ≤ 0.05, **p ≤ 0.01, and ***p ≤ 0.001) were determined for air vs. respective glass side samples and neat matrix vs composites for both air and glass side). 203

Figure 7.8: Static water contact angle measurements for the neat P(3HO-co-3HD) film and its GO composites (n=3). (p statistical significance values (*p ≤ 0.05, **p ≤ 0.01, and ***p ≤ 0.001) were determined for air vs. respective glass side samples and neat matrix vs composites for both air and glass side). 205

Figure 7.9: Static water contact angle measurements for the neat blend film and its GO composites (n=3). (p statistical significance values (*p ≤ 0.05, **p ≤ 0.01 and ***p ≤ 0.001) were determined for air vs. respective glass side samples and neat matrix vs composites for both air and glass side).....207

Figure 7.10: SEM images of (a) neat P(3HB), (b) neat P(3HO-co-3HD), (c) P(3HB)/0.5 wt% GO, (d) P(3HO-co-3HD)/0.5 wt% GO, (e) P(3HB)/2 wt% GO, (f) P(3HO-co-3HD)/2 wt% GO, (g) P(3HB)/5 wt% GO and (h) P(3HO-co-3HD)/5 wt% GO.....208

Figure 7.11: SEM images of: (a), (b) neat 75/25P(3HO-co-3HD)/P(3HB) (c), (d) 75/25 blend containing 0.5 wt%GO, (e), (f) 75/25 blend containing 2 wt%GO and (g), (h) 75/25 blend containing 5 wt%GO (low and high magnification x100 and x1000).....209

Figure 7.12: XRD patterns of GO and P(3HB)/GO composites with 0.5 wt%, 2 wt% 210

Figure 7.13: XRD patterns of GO and P(3HO-co-3HD)/GO composites with 0.5 wt%, 2 wt% and 5 wt% GO.....211

Figure 7.14: XRD patterns of GO and 75/25 of P(3HO-co-3HD)/ P(3HB) /GO composites with 0.5 wt%, 2 wt% and 5 wt% GO. 212

Figure 7.15: Raman spectra of GO and P(3HB)/GO composites with 0.5 wt%, 2 wt% 213

Figure 7.16: Raman spectra of GO and of P(3HO-co-3HD)/GO composites with 0.5 wt%, 2 wt% and 5 wt% GO.....215

Figure 7.17: Raman spectra of GO and of P(3HO-co-3HD)/ P(3HB) /GO composites with 0.5%, 2% and 5%wt GO. 216

Figure 7.18: Deconvoluted C1s XPS spectra of samples: P(3HB) neat, P(3HO-co-3HD) neat, 75/25 neat, P(3HB)/5 wt% GO, P(3HO-co-3HD)/5 wt% GO, 75/25 /5 wt% GO. 218

Figure 7.19: Recovered colonies after incubation with *S. aureus* (ATCC® 29213™): (a) P(3HB)/0.5 wt% GO (b) P(3HB)/2 wt% GO and (c) P(3HB)/5 wt% GO. 221

Figure 7.20: 7(A) Antibacterial activity against free planktonic bacterial cells and (B) loss of adhered bacteria of P(3HB)/0.5 wt% GO, P(3HB)/2 wt% GO and P(3HB)/5 wt% GO against *S. aureus* (ATCC® 29213™). 222

Figure 7.21: (A) Antibacterial activity against free planktonic bacterial cells and (B) loss of adhered bacteria of P(3HO-co-3HD)/0.5 wt% GO, P(3HO-co-3HD)/2 wt% GO and P(3HO-co-3HD)/5 wt% GO against *S. aureus* (ATCC® 29213™).....223

Figure 7.22: (A) Antibacterial activity against free planktonic bacterial cells and (B) loss of adhered bacteria of 75/25 P(3HO-co-3HD)P(3HB)/0.5 wt% GO, 75/25 P(3HO-co-3HD)P(3HB)/2 wt% GO and 75/25 P(3HO-co-3HD)P(3HB)/5 wt% GO against *S. aureus* (ATCC® 29213™). 224

Figure 7.23: (A) Antibacterial activity against free planktonic bacterial cells and (B) loss of adhered bacteria of P(3HB)/0.5 wt% GO, P(3HB)/2 wt% GO and P(3HB)/5 wt% GO against *E. coli* (ATCC® 25922™).....225

Figure 7.24: (A) Antibacterial activity against free planktonic bacterial cells and (B) loss of adhered bacteria of P(3HO-co-3HD)/0.5 wt% GO, P(3HO-co-3HD)/2 wt% GO and P(3HO-co-3HD)/5 wt% GO against *E. coli* (ATCC® 25922™).....226

Figure 7.25: (A) Antibacterial activity against free planktonic bacterial cells and (B) loss of adhered bacteria of 75/25 P(3HO-co-3HD)P(3HB)/0.5 wt% GO, 75/25 P(3HO-co-3HD)P(3HB)/2 wt% GO and 75/25 P(3HO-co-3HD)P(3HB)/5 wt% GO against *E. coli* (ATCC® 25922™). 227

Figure 7.26: Cell viability (% TCPS) of L929 cells seeded on (A) P(3HB), (B) P(3HO co-3HD) and (C) 75/25 P(3HO-co-3HD)/ P(3HB) composites containing different loadings of graphene oxide (Mean± SEM, n = 9 independent experiments). Statistical significance determination is represented as *p ≤ 0.05, **p ≤ 0.01, and ***p ≤ 0.001 for cells on TCPS vs. all materials, and non-modified polymer blend vs. GO composites 229

Figure 7.27: Fluorescence micrographs of L929 cells stained with Ethidium homodimer-III (red) and Calcein AM (green) after 24 h in culture with the aliquots of the respective samples (indirect test). 230

Figure 7.28: Direct cytocompatibility evaluation of the (A) P(3HB), (B) P(3HO-co-3HD) and (C) 75/25 P(3HO-co-3HD)/P(3HB) composites containing different loadings of graphene oxide with respect to L929 cells (Mean± SEM, n = 9 independent experiments). Statistical significance determination is represented as *p ≤ 0.05, **p ≤ 0.01, and ***p ≤ 0.001 for cells on TCPS vs. all materials, and non-modified polymer blend vs. GO composites. 231

Figure 7.29: Fluorescence micrographs of L929 cells stained with Ethidium homodimer-III (red) and Calcein AM (green) after 3 days in culture on the respective samples (direct test). 233

Figure 7.30: Indirect cytocompatibility evaluation of the (A) P(3HB), (B) P(3HO-co-3HD) and (C) 75/25 P(3HO-co-3HD)/ P(3HB) composites containing different loadings of graphene oxide with respect to NG108-15 neuronal cell line (Mean± SEM, n = 9 independent experiments). Statistical significance

determination is represented as *p ≤ 0.05, **p ≤ 0.01, and ***p ≤ 0.001 for cells on TCPS vs. all materials, and non-modified polymer blend vs. GO composites 235

Figure 7.31: Fluorescence micrographs of NG108-15 neuronal cells stained with Ethidium homodimer-III (red) and Calcein AM (green) after 24 h in culture with the aliquots on the respective samples (indirect test). 236

Figure 7.32: Fluorescence micrographs of NG108-15 neuronal cells stained with Ethidium homodimer-III (red) and Calcein AM (green) after 7 days in culture on the respective samples (direct test). 237

Figure 7.33: Number of live cells from live/dead analysis of neuronal cells on P(3HB), P(3HO-co-3HD) and 75/25 P(3HO-co-3HD)/ P(3HB) composites containing different loadings of graphene oxide for time periods of (A) 1 day (B) 3 days and (C) 7 days using TCPS as control (Mean± SEM, n = 9 independent experiments). Statistical significance determination is represented as *p ≤ 0.05, **p ≤ 0.01, and ***p ≤ 0.001 for cells on TCPS vs. all materials, and non-modified polymer blend vs. GO composites (direct test). 238

Figure 7.34: Micrographs of NG108-15 neuronal analogue cells immune-cytochemically- labelled for beta-III tubulin after 7 days culture on PHA blend composites. 240

Figure 7.35: Percentage of NG108-15 neuronal cells expressing neurites (left) and average length o neurites(right) (mean ± SEM, n = 9 independent experiments). Statistical significance determination is represented as *p ≤ 0.05, **p ≤ 0.01, and ***p ≤ 0.001 for cells on TCPS vs. all materials, and non-modified polymer blend vs. GO composites. 241

Figure 8.1: A range of designs for effective NGCs. 254

Figure 8.2: Manufacturing of tubes by dip-moulding. A) Dip-moulding apparatus, B) dried hollow tubes of 75/25 P(3HO-co-3HD)/P(3HB) blend and C) 75/25 blend/0.5 wt% GO. 256

Figure 8.3: DSC thermograms of the: (A) **----** 75/25 P(3HO-co-3HD)/P(3HB) neat tube, 75/25 P(3HO-co-3HD)/P(3HB) tube composites with (B) **----** 0.5 wt%,(C) **----** 2 wt% and (D) **----** 5 wt% GO content. 258

Figure 8.4: SEM micrographs of the (75/25) P(3HO-co-3HD)/P(3HB) tubes: (a) and (b) intralaminar and (c) and (d) cross section views 261

Figure 8.5: SEM micrographs of (75/25) blends of P(3HO-co-3HD) and P(3HB) containing (a), (d), (g) 0.5 wt% GO, (b), (e), (h) 2 wt% GO and (c), (f), (i) 5 wt% GO. 262

Figure 8.6: Direct cytocompatibility evaluation of NG108-15 cells seeded on 3D PHA composites containing different graphene oxide loadings (mean ± SEM, n = 9 independent experiments). Statistical significance determination is

represented as *p ≤ 0.05, **p ≤ 0.01, and ***p ≤ 0.001 for cells on TCPS vs. all materials, non-modified polymer blend vs. GO composites and between GO composites.....263

Figure 8.7: Micrographs of brightfield and fluorescence microscopy images: (a), (b) 75/25 blend tube, (c), (d) 75/25 0.5 wt% GO tube, (e), (f) 75/25 2 wt% GO tube and (g), (h) 75/25 5 wt% GO tube. 265

Figure 8.8: Process of manufacturing 3D scaffold using blend PHA and Ce-PGFs by rolling the composite mat to a tubular structure (adapted from (Kim et al., 2015)).....266

Figure 8.9: PHA composite mat with aligned PGFs fibres blend rolled into a NGC. 266

Figure 8.10: SEM micrographs of the (75/25) P(3HO-co-3HD)/P(3HB)/PGFs composite tubes of (a), (b), (c) 37 wt% PGFs (d), (e), (f) 74 wt% PGFs and (g), (h), (i) 90 wt% PGFs.....268

Figure 8.11: Micrographs of the developed PHA fibres using: (a)-(c): condition 1, (d)-(f): condition 2, (g)-(i): condition 3, (j)-(l): condition 4, (m)-(o): condition 5 and (p)-(r): condition 6 271

Figure 8.12: Direct cytocompatibility evaluation of electrospun75/25 P(3HB)/P(3HO-co-3HD) with respect toNG108-15 cell line for a time period of 7 days.....274

Figure 8.13: Threading electrospun fibres into the hollow tubes. The transparent tube is the control neat tube of 75/25 P(3HO-co-3HD)/P(3HB) and the black tube is the tube containing 5 wt% GO. 275

List of Tables

Table 1.1: Mechanical and thermal properties of neat P(3HO) and P(3HB) films (adapted from (Basnett et al., 2013; Rai *et al.*, 2011). 12

Table 1.2: A summary of polyhydroxyalkanoates used for animal testing and measuring in vivo responses of tissues (adapted from (Valappil *et al.*, 2006). 16

Table 1.3: Classification of nerve injury. 25

Table 1.4: Commercially available nerve conduits. 28

Table 1.5: Main groups of antimicrobial compounds from plants (adapted from Cowan, 1999). 31

Table 1.6: Antimicrobial activity of allicin and its combinations (adapted from (Marchese *et al.*, 2016) 35

Table 2.1: Media composition for scl-PHA production. 48

Table 2.2: Mineral Salt Medium (MSM) composition – second stage Rai *et al.*, 2011. 49

Table 2.3: Composition for the production stage. 49

Table 2.4: Composition of Trace element solution (TES). Basnett *et al.*, 2014. 49

Table 2.5: Dinitrosalicylic acid (DNS) reagent: 58

Table 2.6: Alkaline hypochlorite reagent: 58

Table 2.7: Phenol-nitroprusside buffer: 58

Table 3.1: Thermal properties of P(3HO-co-3HD) and P(3HB) polymers as determined by DSC. 82

Table 3.2: Mechanical properties of P(3HB) and P(3HO-co-3HD) polymers. 83

Table 4.1: Assignments of the peaks in the FTIR spectra of the controls and blends of P(3HO-co-3HD)/P(3HB). 94

Table 4.2: Thermal properties of P(3HO-co-3HD), P(3HB) and their blends obtained from the second heating cycle. 97

Table 4.3: Summary of the mechanical properties of P(3HO-co-3HD) produced by P. mendocina CH50 and P(3HB) produced by B. subtilis OK2 and their blends. 98

Table 5.1: Thermal properties of P(3HB) and P(3HB) containing different amounts of garlic powder. 118

Table 5.2: Thermal properties of P(3HO-co-3HD) and P(3HO-co-3HD) containing different amounts of garlic powder. 119

Table 5.3: Thermal properties of 75/25 blends of P(3HO-co-3HD) and P(3HB) containing garlic powder. 119

Table 5.4: Mechanical properties of P(3HB) and P(3HB) containing garlic powder (GP). 120

Table 5.5: Mechanical properties of P(3HO-co-3HD) and P(3HO-co-3HD) containing garlic powder (GP). 121

Table 5.6: Mechanical properties of 75/25 P(3HO-co-3HD)/ P(3HB) blends and blends containing garlic powder (GP). 122

Table 5.7: Inhibition zone of Garlic Powder and Allicin against *S. aureus* (ATCC® 29213™) 129

Table 5.8: MIC and MBC values of selected bacterial strains. 132

Table 5.9: Inhibition zones of P(3HB)/GP composite samples against different bacterial strains. 136

Table 5.10: Inhibition zones of P(3HO-co-3HD)/GP samples against different bacterial strains. 138

Table 5.11: Inhibition zones of blends containing GP samples against different bacterial strains. 140

Table 7.1: Thermal properties of P(3HB), P(3HO-co-3HD) and 75/25 composite which contain different amounts of graphene oxide. 197

Table 7.2: Normalized values of ΔH_m of P(3HB), P(3HO-co-3HD), and 75/25 blend containing different amounts of graphene oxide. 198

Table 7.3: Mechanical properties of PHA/GO composites. 200

Table 7.4: WCA values of the neat P(3HB) and its GO composites. 204

Table 7.5: Water contact angle values of the neat P(3HO-co-3HD) film and its GO composites. 206

Table 7.6: Water contact angle values of neat 75/25 P(3HO-co-3HD)/P(3HB) film and its GO composites. 207

Table 7.7: D and G band position and ratio of I_D/I_G for different composites containing GO. 214

Table 7.8: Assignment of C1s and O1s XPS peaks. 219

Table 7.9: Percentage of atomic oxygen and carbon in the carbon samples. 219

Table 7.10: Percentages of sp2, sp3, epoxides-hydroxides (C-O-C, C-O(H)), carbonyl and carboxyl groups as derived from C1s XPS spectrum deconvolution. 220

Table 8.1: Summary of the dimensions of the tube manufactured by the dip moulding technique. 257

Table 8.2: Thermal properties of 75/25 P(3HO-co-3HD)/P(3HB) and GO composite tubes. 258

Table 8.3: Normalized and observed values of ΔHm of P(3HB), P(3HO-co-3HD) and 75/25 P(3HO-co-3HD)/P(3HB) blend containing different amounts of graphene oxide.....259

Table 8.4: Mechanical properties of 75/25 tubes of P(3HO-co-3HD) and P(3HB) containing graphene oxide. 260

Table 8.5: Summary of the dimensions of the tubes manufactured by rolling a composite mat. 267

Table 8.6: Different conditions to develop electrospun PHA fibres formed from 15 wt% solution of 75/25 P(3HB)/P(3HO-co-3HD) blend. 269

Table 8.7: Average diameter of the developed electrospun fibres under different conditions of electrospinning. 271

List of Abbreviations

2D	Two-dimensional
3D	Three-dimensional
75/25	75/25 Poly(3-Hydroxyoctanoate-3-Hydroxydecanoate)/ Poly(3-hydroxybutyrate)
ATR-FTIR	Attenuated Total Reflectance Fourier-Transform Infrared Spectroscopy
Ce-PGFs	Cerium doped phosphate glass fibres
CFU	Colony Forming Units
CNS	Central Nervous System
Dcw	Dry cell weight
DMEM	Dulbecco's Modified Eagle's Medium
DOT	Dissolved oxygen tension
DSC	Differential Scanning Calorimetry
E	Elastic Modulus
EC	*Escherichia coli* (ATCC® 25922™)
FDA	Food and Drug Administration
GBMs	Graphene Based Materials
GC	Gas Chromatography
GC-MS	Gas Chromatography Mass Spectrometry
GO	Graphene Oxide
GP	Garlic Powder
HAI	Hospital Acquired Infections
HB	Poly(3-hydroxybutyrate)
HOHD	Poly(3-Hydroxyoctanoate-3-Hydroxydecanoate)
MBC	Minimum Bactericidal Concentration

McI-PHAs	medium chain length Polyhydroxyalkanoates
MIC	Minimum Inhibitory Concentration
MRSA	*Methicillin-resistant Staphylococcus aureus*
MRSE	*Methicillin-resistant Staphylococcus epidermidis*
MSM	Mineral Salt Media
NMR	Nuclear Magnetic Resonance
P(3HB)	Poly(3-hydroxybutyrate)
P(3HO-*co*-3HD)	Poly(3-Hydroxyoctanoate-3-Hydroxydecanoate)
PA	*Pseudomonas aeruginosa* (ATCC® 27853™)
PE	Polyethylene
PGFs	Phosphate glass fibres
PNS	Peripheral nervous system
SA	*Staphylococcus aureus* (ATCC® 29213™)
ScI-PHAs	short chain length Polyhydroxyalkanoates
SE	*Staphylococcus epidermidis* (ATCC® 12228™)
TCPS	Tissue culture polystyrene
T_g	Glass transition temperature
T_m	Melting temperature
ZDEC	Polyurethane film containing 0.1% zinc diethyldithiocarbamate
ε_b	Elongation at break

Chapter 1

Introduction

1 Introduction

1.1 Bacterial infection and antibiotic resistance

Bacteria constitute the earliest form of life on Earth. Hence, they are an integral part of our environment (air, soil, water, plants and animals) but also of our bodies. Bacteria are able to survive and grow on any surfaces and skin is one of them. The human body can be described as a vessel, which contains bacteria inside but also outside of it. Bacteria can exist inside the human body in a delicate cooperative balance (Ahmed, 2011). When this balance is disrupted, bacterial stop being beneficial for the human organism and cause infections that could lead to mortality.

Ancient Egyptians, Chinese and Greeks used moulds and plants to treat bacterial infections. Until the 20th century, infections that are now treatable – such as pneumonia and diarrhea, were the major killers in the early developed world. Scientists began to investigate antibacterial chemicals towards the late 19th century as shown in Figure 1.1. Penicillin was the first commercialized antibiotic, discovered in 1928 by Alexander Fleming (Ventola, 2015).

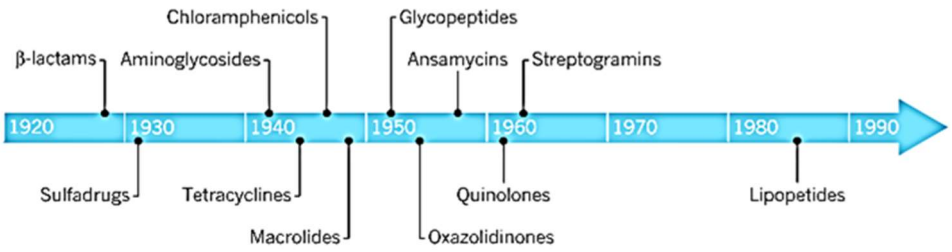

Figure 1.1::Antibiotic discovery timeline (adapted from Lewis, 2012).

According to the European Centre for Disease Prevention and Control (ECDC) and National Health System UK (NHS), antibiotics are used for the prevention and treatment of bacterial infections, that they may either kill or inhibit the growth of bacteria. Unfortunately, many of the bacteria that cause these infections are becoming resistant to existing antibiotics. The genes coding for antibiotic resistance in one species of bacteria can be transferred to other bacterial species

through exchange of genetic material. Additionally, mutations of the bacteria genes also impact the bacterial resistance to antibiotics, similarly to horizontal gene transfer (Martinez and Baquero, 2000; Piddock, 2006; Papkou *et al.*, 2020). As a result, the antibiotics become ineffective and infections persist in the body, increasing the risk of being contagious and resulting in mortality. Microorganisms, that develop antimicrobial resistance, are sometimes referred as “superbugs”. Some resistant bacteria namely are Methicillin-resistant *Staphylococcus aureus* (MRSA), Vancomycin-resistant Enterococcus (VRE) Carbapenem-resistant *Acinetobacter baumannii* (CRAB) and Multi-drug resistant *Pseudomonas aeruginosa* (van Duin and Paterson, 2016).

Antimicrobial resistance develops through several different mechanisms and can be classified as, (a) intrinsic resistance or (b) acquired resistance. Intrinsic resistance includes efflux pumps that pump out/decrease the concentration of the drug from the cell and decrease permeability of the cell wall/membrane leading to limited diffusion of antibacterial agents (Ahmed, 2011). In addition, the limitation of the antibacterial agents to diffuse their limited interaction, within the biofilm matrix is considered as intrinsic resistance. The biofilm matrix is composed of polysaccharides (such as glycocalyx, a polysaccharide that surrounds the cell membrane of bacteria), proteins and extracellular DNA.

The formation of the biofilm allows bacteria to attach even to inert materials such as rocks (Stewart *et al.*, 1998). Attachment is achieved by microbial aggregation, the bacterial cells merge forming the first colony which is attached to the surface *via* van der Waals forces. If the colony remains attached to the surface more bacteria will adhere or anchor themselves to the surface or to the earlier colonists (Anderson, 1989). Acquired resistance is developed from the alteration of target proteins, which allow bacteria to bypass the antibiotic effect and the enzymatic inactivation or degradation of the antibacterial agent before it reaches its target (Mcdermott *et al.*, 2003).

Antimicrobial resistant (AMR) infections is expected in future to cost at least 50,000 lives each year across Europe and the US alone, with many more hundreds of thousands dying in other parts of the world (Figure 1.2) and is predicted to further increase in future (Lewis, 2013; Laxminarayan *et al.*, 2014).

In addition, infections caused by antibiotic-resistant bacteria, lead to poor health conditions that require, prolonged hospitalization and expensive antibiotics, which have an impact on the world population and its economic output.

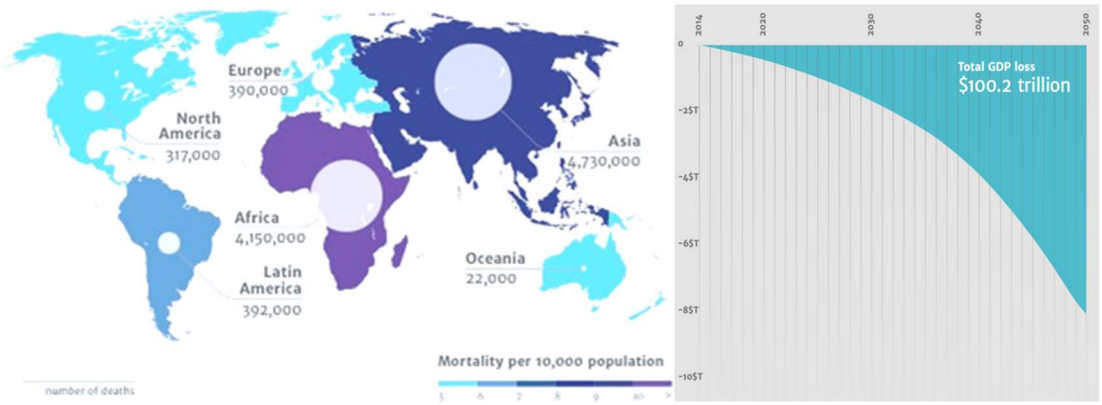

Figure 1.2: Estimation of antimicrobial drug resistance linked mortality rate and its economic impact by 2050 (adapted from O'Neill, 2015).

AMR is a result of the extensive use of antibiotics and the rise of the bacterial resistance to them. Figure 1.3 describes the interaction of the antibacterial agents and the resistance of bacteria through time.

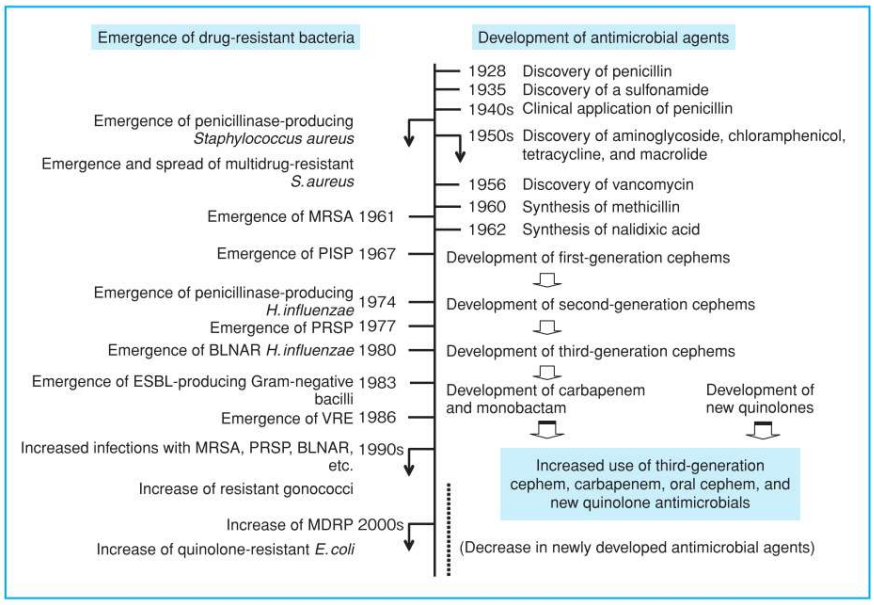

Figure 1.3*:* Trend of development of antimicrobial agents and emergence of drug-resistant bacteria (adapted from Saga & Yamaguchi 2009).

The most worrying aspect, however, is the limited options that exist to combat resistant bacteria. There are only a few new effective drugs. Global action is therefore essential to enhance multi-sectoral efforts against the antimicrobial resistance.

This rise of drug resistant strains has captured the interest of world-class pharmaceutical communities, academics and even the governments, as documented in the UK Five Year Antimicrobial Resistance Strategy (2013-2018) (O'Neill, 2015). By not having effective antibiotics, implies to high levels of danger for medical procedures such as organ transplantation, cancer chemotherapy, diabetes management. Especially, immune–compromised patients are more vulnerable with the rise of antibiotic resistance (Dettenkofer and Spencer, 2007). Furthermore, infections are the most common complication, which leads to implant failure.

It is obvious that, the use of antibiotic can save people's lives by treating their infections. However, the ability of bacteria to acquire resistance to antibacterial agents, necessitate the development of novel antibacterial agents. In this context procedures such as effective level of hygiene, sanitation, sterilization and disinfection are followed in order to prevent the spread of infections (Ahmed, 2011; O'Neill, 2015) are vital. If the preventative measures are not successful, bacteria can attach on the surface host and start colonization via biofilm formation.

Both scientific and health care communities are trying to develop alternative ways to fight antibacterial resistance. In this context, enormous efforts have been made to develop antibacterial materials (El-Refaie Kenawy *et al.*, 2007).

1.2 Polymers as antibacterial materials

Polymers with antibacterial activity have gained a lot of attention from the scientific community and industry as promising alternatives to combat MDR (Santos *et al.*, 2016). Polymers with antibacterial activity can have a variety of advantages including non-toxicity, chemical stability, and long-term activity (Santos *et al.*, 2016; Xue *et al.*, 2015).

The development of such polymers is accomplished by introducing conventional antibacterial agents and functional groups into polymers, which will enhance their effectiveness, reduce their toxicity, and extend the life span of these antimicrobial agents (Kenawy *et al.*, 2007).

These antimicrobial polymers have the ability to kill or inhibit bacteria by acting as a source of sterilizing ions or molecules (Ahmed *et al.*, 2008). Antimicrobial polymers can be classified into three categories; (i) biocidal polymers (polymers with intrinsic antimicrobial activity); (ii) polymeric biocides (based on polymer backbones with biocide molecules attached); and (iii) biocide-releasing polymers (polymers loaded with biocide molecules) (Barzic *et al.*, 2015; Alarfaj *et al.*, 2016), as shown in Figure 1.4.

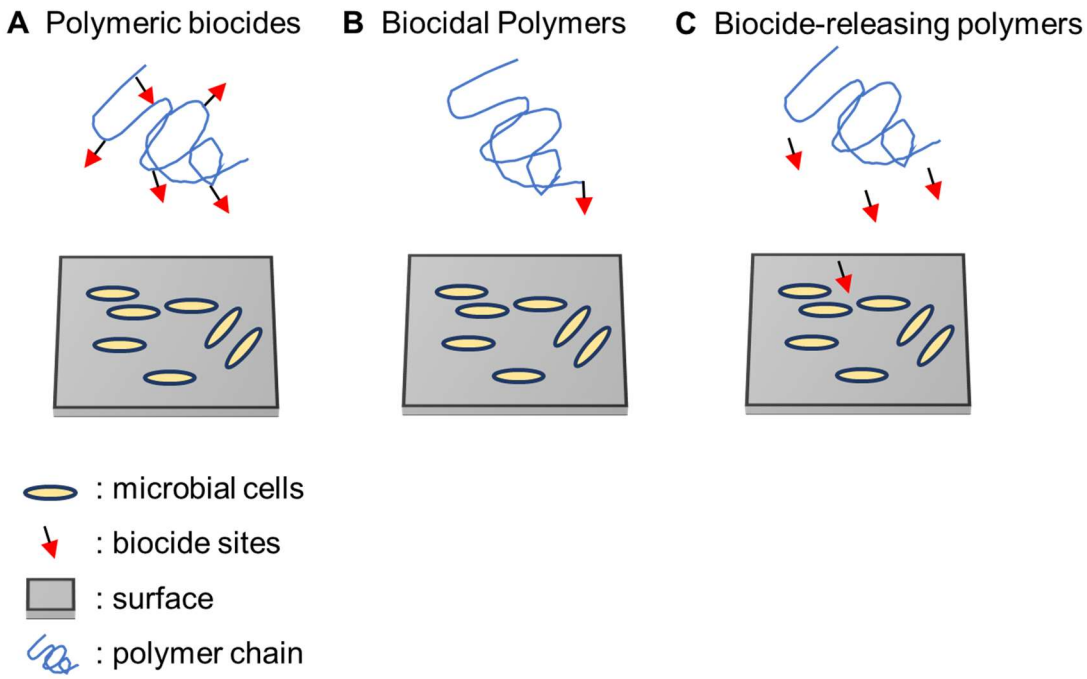

Figure 1.4: Schematic representation of antibacterial polymers based on the working principles of the macromolecular systems: (A) polymeric biocides, (B) biocidal polymers and (C) biocide-releasing polymers, (adapted from Barzic, *et al.*, 2015; Alarfaj *et al.*, 2016).

Polymeric biocides: are prepared by attaching a biocidal group to a polymer. Usually these materials have a lower efficacy to fight bacteria than the free biocide molecules, due to the steric hindrance created by the polymer backbone (Barzic *et al.*, 2015; Alarfaj *et al.*, 2016).

Biocidal polymers: are prepared through polymerizing monomers with biocidal agents as functional groups and are expected to be similar to these small-molecule counterparts (Chen *et al.*, 2016; Alarfaj *et al.*, 2016).

These polymers contain polycation - based intrinsic antibacterial activity. Polycations are capable of killing bacteria due to their negative net charge, attributed to membrane proteins and their phospholipids on the outer membrane of Gram-negative bacteria. In this way, polycations are attracted and are able to disrupt the outer membrane of the cells resulting in their death (Barzic *et al.*, 2015).

The most commonly used cationic groups in polymers are quaternary ammonium, quaternary phosphonium, guanidinium tertiary sulfonium. In some cases, the attached biocidal group is efficient only as repeating units while in some others the antibacterial activity is expressed by only one group (Siedenbiedel and Tiller, 2012).

Biocide-releasing polymers: involves entrapped biocides within the polymers that are released by diffusion and during the degradation of the (Rosenberg *et al.*, 2008). These techniques can be used to entrap the antibacterial agent inside the polymer matrix, protect and release the agent at a closer distance from the bacterial cell, consisting this approach as highly effective (Santos *et al.*, 2016).

Petroleum based plastics (such as polyglycolic acid (PGA), poly-L-lactic acid (PLLA) and poly (D-lactic acid) (PDLA)), are the most used polymers for medical applications. In general, polymeric materials attract significant interest in medical field due to their wide range of physical and chemical properties (Gironi and Piemonte, 2011).

The main biomedical applications of polymers are suture materials, tissue adhesives, surgical meshes, orthopaedic implants, vascular stents, ophthalmology, dentistry and neurosurgery.

Despite their versatile properties and their widespread use in medical applications, petroleum-based polymers can cause many problems when placed *in vivo*. For example, the use of poly(vinyl chloride) requires the addition of stabilizers and plasticizers, a combination that could cause toxicity. In addition, poly(methyl methacrylate) (PMMA) produced by in situ radical polymerization could damage the tissue due to the exothermic reaction of polymerization after *in vivo* implantation. Moreover, the poor biocompatibility of synthetic polymers

and the high likelihood of inflammation, for various reasons, make them unattractive for use in biomedical applications (Gironi and Piemonte, 2011).
Their main disadvantage is the general lack of biocompatibility because of the release of acidic products upon their degradation, which is often associated with inflammatory reactions (Gironi and Piemonte, 2011). In addition, these polymers are degraded by bulk erosion, leading to instability of the polymer scaffold when substantial degradation occurs.

To overcome the problems associated with these synthetic polymers, researchers have worked for the last two decades to develop a new range materials, based on natural polymers (Zinn *et al.*, 2001). These natural polymers can provide a sustainable platform to partially replace, or if possible completely replace, the use of cost-effective petroleum polymers and as well, a positive environment impact (Zhu *et al.*, 2016).

Desired features for new medical polymers include:

- The polymer should not evoke a sustained inflammatory or toxic response upon implantation in the body.
- The polymer should be stable in long-term applications.
- The degradation time of the polymer should match the healing or regeneration process.
- The polymer must have the appropriate mechanical properties for the indicated application as well as, a variants of these properties, during the degradation, in order to be compatible with the healing or the regeneration process (Nair and Laurencin, 2007).
- The degradation products must be non-toxic, capable of being metabolized and excreted from the body.
- The polymer must be permeable and processable for the intended application (Yoruc Binnaz Hazar and Sener Cem, 2012).

Natural polymers with the above characteristics are considered as promising candidates for biomedical applications (Lloyd, 2002). Most natural polymers are biocompatible, non-toxic, biodegradable, safe without side effects and hence suitable for the development of materials for biomedical applications. In addition,

most natural polymers possess some inherent advantages such as bioactivity, i.e. the ability to exhibit receptor-binding ligands in cells, susceptibility to cell-triggered proteolytic degradation and natural remodelling, which enhance their exceptional place in biomedical applications (Nair and Laurencin, 2007).

1.3 Discovery of Polyhydroxyalkanoates (PHAs)

Amongst other natural polymers, Polyhydroxyalkanoates (PHAs), have attracted great attention due to their biocompatibility and tunable biodegradability. Their general structure is shown in Figure 1.5. The French microbiologist, Lemoigne, first discovered PHAs in the late 1920s. Later, it was found that other microorganisms, besides *Bacillus megaterium* could also produce the homopolymer 3-hydroxybutyric acid (P(3HB)) polyester. Some of these, are soil bacteria and blue green algae. PHAs are formed intracellularly as an energy source and as a carbon storage compound.

The polymer accumulates in granules within the bacterial cells from which it can be extracted using organic solvents such as chloroform (Pouton and Akhtar, 1996). P(3HB) is the most well-known and commonly used biopolyester as it was the first to be discovered. Since then, numerous studies have been carried out in order to explore the desired conditions that are required to maximize the yield of the polymer and to identify the processes that facilitate production of polymers with different structures.

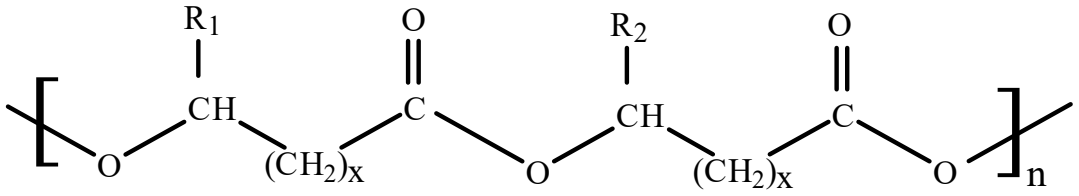

Figure 1.5: General structure of polyhydroxyalkanoates. R1/R2= alkyl groups C1–C13, x=1–4, n= 100–30 000 (adapted from Keshavarz and Roy, 2010).

The PHAs sector was developed in late 1973, but the interest in these biopolymers remained almost exclusively in their physiological significance as microbiological substances without considering their potential use as materials. Their potential application as a material was recognized in the first half of the

1960s, when the first patents were made on the production of P(3HB) by bacterial fermentations (Baptist, 1960), its recovery from biomass, plasticizing (Baptist, 1965) and the use as absorbable dies (Grace & Co., 1963).

Petrochemical plastics, on the other hand, were manufactured easier and at a much lower cost which prevented the development of the natural plastics industry. In 1976, the Imperial Chemical Industries (ICI) industry in England began to consider profitable production of P(3HB) via bacterial fermentation from carbohydrate raw materials (Senior, 1984).
It turned out that not only P(3HB) could be produced from renewable sources but that the properties of the polymer produced were similar to those of polypropylene (King, 1982). Other features of P(3HB), such as biodegradability, biocompatibility, piezoelectric properties and ability to be used as a source of optically active molecules (Howell, 1982), were recognized early in the process and kept the interest of ICI for P(3HB) when the crisis of oil had begun to pass. After P(3HB) discovery, in 1974 Wallen and Rohwedder reported the synthesis of 3-hydroxy-valerate (3HV) and 3-hydroxyhexanoate (3HHx) (Wallen and Rohwedder, 1974). This was the first report of a copolymeric PHA.
The significance of the existence of different PHAs of homopolymer P(3HB) was immediately recognized, and thus ICI proceeded to the production of P(3HB) copolymers with various other monomers, i.e. 3HV monomers, from various substrates, including carbohydrates such as glucose, and organic acids such as propionic acid (Holmes, Wright and Collins, 1982).

The interest for copolymers, and in particular for P(3HBV), is due to their lower melting points, less crystallinity, ductility, hardness, and better processability (Luzier, 1992). Also, the change in the percentage of 3HV in the copolymer P(3HBV) results in its thermo-mechanical properties being varied according to the composition. Copolymers P(3HBV) with 0-24 mol% 3HV were produced from the bacterium *Ralstonia eutropha* and sold under the trademark BIOPOL® by Monsanto. Monsanto acquired the BIOPOL® product in April 1996 from ZenecaBio, a company that emerged from ICI's partial segregation in June 1993. Its production capacity is around 800 tonnes annually (Braunegg, Lefebvre and Genser, 1998).

Over time, several companies developed the production of PHB, PHBV, PHBH and P(3HB-4HB) polymers such as Metabolix, Telles, P & G, Meredianus USA, Biotec, Biomer Inc., BASF in Germany, Polyferm Canada, Asahi, Mitsubishi, Kaneka Corp. in Japan, Novamont in Italy and others (Reddy *et al.*, 2003). In addition, it was reported by Witholt and Kessler (Witholt and Kessler, 1999), that *Pseudomonas oleovorans* can produce copolymers containing 3-hydroxyoctanoate (3HO) and 3HHx units when n-octane was used as a carbon source. The discovery of different copolymers offers a variety of PHAs that have potential in different applications.

Until now more than 300 different species of PHA producing microorganisms have been identified (Lee, 1996) and more than 150 different monomer units of PHAs have been discovered (Steinbüchel, 2001; Nigmatullin *et al.*, 2015).

1.3.1 Classification and properties of PHAs

PHAs are normally produced by bacteria under conditions of excess of carbon source and limitation of other nutrients such as oxygen, nitrogen, sulphur, magnesium and phosphate (Rai *et al.*, 2011). PHAs can be produced by both Gram-negative and Gram-positive bacterial strains (Amache *et al.*, 2013) and are accumulated in the form of grains of diameter between 0.2-0.5 μm in the cell cytoplasm.
The number and size of the grains per cell differs depending on the microorganism (Byrom, 1994). These natural polyesters (PHAs) can be classified depending on the number of carbon atoms in their monomer units. Short chain length PHAs (scl-PHAs) consist of monomers units with 3–5 carbon atoms. They are highly crystalline polymers.

While medium-chain length PHAs (mcl-PHAs), built of monomers with 6–14 carbon atoms, are semi-crystalline polymers with lower crystallinity (Misra *et al.*, 2006). Scl-PHAs like P(3HB) and P(HV) are brittle thermoplastics with high melting temperature (T_m), high tensile strength and low elongation at break. In contrast, mcl-PHAs are elastomeric polymers with low crystallinity, high elongation at break, low tensile strength and low melting temperature (T_m) (Table 1.1).

As other polymers, PHAs are classified as homopolymers and heteropolymers when polymers consist of one type of hydroxyalkanoate unit such as P(3HB) or, more than one type of hydroxylalkanoate unit such as poly(3-hydroxybutyrate-co-3-hydroxyvalerate), P(3HB-co-3HV) (Rai *et al.*, 2011). Also, all PHAs are characterized as piezoelectric, non-toxic, biocompatible, optically active materials.

Table 1.1: Mechanical and thermal properties of neat P(3HO) and P(3HB) films (adapted from (Basnett *et al.*, 2013; Rai *et al.,* 2011).

Samples	**Young's Modulus (MPa) E**	**Tensile strength (MPa)**	**Elongation at Break (%)**	**T_m (^oC)**	**T_g (^oC)**	**T_c (^oC)**
P(3HO)	5-7	1.8-9.6	204-1300	39-50	30.1	–
P(3HB)	3500	40	6	170-175	10.0	109.5
P(3HB-co-3HV)	700-2900	20-25	50	137-170		
P(3HB-co-4HB)	-	26	444	152		
P(4HB)	230	36	1000	53		
P(3HHx-co-3HO)	8	9	380	61		
P(3HB-co-3HHx)	-	20	850	52		
Polypropylene	1700	38	400	170		

PHB is the most widely studied polyesters from the PHAs family. Its molecular weight ranges from 2 to 4 × 10^3 kDa with a polydispersity of about 2, the glass transition temperature as measured by calorimetric analysis is 4°C and the melting temperature is 180°C (Rajan *et al.,* 2018). The densities of crystalline and amorphous PHB are 1.26 and 1.18 g/cm^3 respectively (Doi, 1990). PHB has mechanical properties similar to those of isotactic polypropylene such as the Young modulus (3.5 GPa) and tensile strength (43 MPa).

The most notable difference between the two materials is the elongation at break which for PHB is 5 % while for PP is 400 %. As result, PHB is characterized by greater rigidity and brittleness compared to polypropylene. Several studies have been carried out to understand the reasons for the brittle nature of PHB and to improve its physical properties. It was observed that the brittleness of PHB develops during storage, after its initial crystallization after melting. This second crystallization results in the reorganization of amorphous phase into the crystals leading to the decrease of amorphous phase fraction.

Two main drawbacks that prevent the commercial use of P(3HB). P(3HB) decomposes at 200°C, near the melting point, and becomes brittle after a period of several days when stored under ambient conditions. The physical and thermal properties of PHA copolymers can be regulated by altering their molecular structure and copolymer composition.

For 3HB copolymers, the introduction of other monomers improves mechanical properties (Holmes, 1988). The combination and composition of PHA copolymers defines the physical properties of the polymers such as the degree of crystallinity, the melting and glass transition temperatures as well as their mechanical properties (Sudesh, Abe and Doi, 2000). The structures and properties of the copolymers with various 3HB and 3HV compositions, have been extensively investigated.

P(3HB-co-3HV) exhibit approximately identical degrees of crystallinity to their homopolymers (50-70 %). The copolymer, however, becomes stiffer and more flexible when the percentage of 3HV increases, its ductility is also increasing. In addition, reducing the melting point by increasing 3HV content, allows the heat treatment of the copolymer without thermal degradation.
In the P(3HB-co-3HHx) copolymer when the proportion of the 3HHx fraction is increased from 0 to 25 % the melting temperature decreases from 177 to 52°C, the glass transition temperature decreases from 4 to -4°C and the tensile strength from 43 to 20 MPa.

On the contrary, elongation to break point is increased from 5 % to 850 %. So, these materials become more tough with the increase in (R) -3HHx fraction (Doi *et al.*, 1995). Similarly, the melting point decreases from 178 to 130°C for the copolymers of P(3HB-co-4HB). The glass transition temperature is reduced

from 4 to -48°C when the fraction of 4HB in the copolymer is increased from 0 to 100%.

The tensile strength reduced from 43 to 26 MPa and the elongation at breakage increased from 4 to 444 % when the 4HB fraction is increased from 0 to 16 % (Saito *et al.*, 1996; Saito and Doi, 1994). It was calculated that the tensile strength of P(4HB) homopolymer can reach 1GP thus copolymers P(3HB-co-4HB) cover a wide range of properties (Saito and Doi, 1994).

Moreover it was found that the genetically recombinant *Pseudomonas* sp bacterium is capable of synthesizing random copolymers consisting of 3HB and mcl-3HA groups consisting of 6-12 carbon atoms using glucose as a substrate (Kato *et al.*, 1996). In the P(3HB-co-3HA) copolymer, the 3HB fraction was 94%, but also contained 3 % 3HD and 3 % 3HDD.

The tensile strength of such copolymer was 17 MPa, while the elongation to breakage was increased to 680 % with the percentage of mcl-PHAs being only 6 %. This indicates that copolymers from 3HB and mcl-PHAs achieve the greatest enhancement in terms of the fragility of P(3HB). Also, the mechanical properties of this polymer appear to be similar to those of low density polyethylene (Kato *et al.*, 1996; Matsusaki *et al.*, 2000).

It is concluded from the above that PHA copolymers have a wide range of properties depending on the chemical structure of the monomeric units and their compositions. Their properties can also be modified depending on the processing they undergo. Currently, P(3HB-co-3HV) is the only copolymer produced in large quantities. More cost-effective production techniques and other PHAs should be developed, for the direct application of these biodegradable esters.

1.3.2 Biodegradability of PHAs

PHAs have boosted interest because their production comes from renewable sources and they are also environmentally friendly as they are fully biodegradable. Due to their biological origin, PHAs are highly biodegradable polyesters in various environments such as soil and water. Several studies have been conducted in order to obtain the hydrolytic and enzymatic degradation processes of PHAs.

The most important factors affecting the biodegradability of PHA polymers are as follows:

1. The crystallinity of the polymer. The degradation of a polyester is slower in its crystalline domains compared with the amorphous (Numata, Abe and Iwata, 2009).
2. Molecular weight of the polymer. Polymers with lower molecular weights are degraded more rapidly than those with higher molecular weights (Manavitehrani *et al.*, 2016).

Studies have shown that scl-PHAs possess have slower degradation rate than mcl due to their high crystallinity. In this context, an effective strategy to achieve the desired properties for different biomedical applications would be to develop blends of different types of PHAs (Amache *et al.*, 2013, Basnett *et al.*, 2013).

The use of blends will provide a range of mechanical and thermal properties but also could assist tailoring of the biocompatibility and biodegradability. Therefore, PHAs could be developed to obtain the favorable properties to meet any requirements for biomedical application. Moreover, due to their versatile features, they could be used as antibacterial polymers for a range of uses.

The development of a PHAs-based antibacterial polymer requires functionalization of the polymer structure. This functionalization could be an additive of metal ions/inorganic compounds, small molecules or a natural antibacterial agent. The addition of these agents will confer antibacterial properties on the biodegradable polymer.

1.3.3 Biocompatibility of PHAs

Biocompatible materials for medical applications are the components that perform with an appropriate host response in specific situations. In this context, PHAs are suitable candidates for biomedical applications as their biosynthesis excludes the use of catalysts and initiators, which usually could be the cause of toxicity issues (Pouton and Akhtar, 1996).

It is noteworthy that R-3-hydroxybutyric acid, which is a physiological blood component at concentrations between 0.3 and 1.3 mM, results from the

degradation of PHB. This indicates that the biomedical use of PHAs will not trigger an immune response of the human body (Muhammadi *et al.*, 2015).

Table 1.2: A summary of polyhydroxyalkanoates used for animal testing and measuring in vivo responses of tissues (adapted from (Valappil *et al*., 2006)**.**

PHA	Application	Animal model
P(3HB)	Sutures	Rat
	Conduits	Rat
	Carrier scaffold	Rat
	Stents	Rabbit
	Soft tissue repair	Rat
	Dura mater substitute	Pig
	Bone tissue scaffold	Cat
	Nerve repair	Calves, human trial
	Pericardial patch	Sheep
	Artery augmentation	Sheep
P(4HB)	Blood vessels	Sheep
	Artery augmentation	Sheep
	Heart valves	Sheep
	Vascular graft	Sheep
	Nerve guides	Rat
P(3HB-co-3HV)	Sutures	Rat
	Implant patches	Dog
	Bone tissue engineering	Rabbit, rat
	Urological stent	Dog
P(3HB-co-4HB)	Wound dressing	Rats
	Pericardial patch	Dog
	Vascular graft	Dog
	Nerve guides	Rat
P(3HB-co-3HHx)	Artificial esophagus	Dog
P(3HHx-co-3HO)	Heart valves	Sheep
	Vascular grafts	Sheep, rat

Several i*n vitro* studies have shown that tissue culture cells appeared to be favoured to proliferate on PHA films. *In vitro* tests using animal models to subject implants, have verified the safe use of PHAs for different applications as shown in Table 1.2.

In order to treat jaw-bone defects Kostopoulus and Karring used a rat model to subject P(3HB-co-3HV) membranes. After a period of six month, the P(3HB-co-3HV) membranes assisted the bone fill (Kostopoulos and Karring, 1994). The Nonwoven P(3HB) sheet has been used for nerve repair in cats and has successfully bridged a 3 mm nerve-gap (Hazari, 1999). Another nerve repair reported that P(3HB) polymer was used as the starting material. This time the conduit of PHA was able to bridge a 10 mm gap in a rat sciatic nerve (Mosahebi *et al.*, 2002).

More recently Basnett *et al.*, tested a range of films of different compositions of P(3HO)/P(3HB) blends. Human microvascular endothelial cells (HMEC-1) were used to test and prove the biocompatibility of the produced films. They prepared three different blends; P(3HO)/P(3HB) 20:80, 80:20 and 50:50, and found that the highest cell viability was detected for the blend with the highest amount of P(3HB) and that no cytotoxic products were released from these films (Basnett *et al.*, 2013).

1.4 Biomedical applications of PHAs

1.4.1 PHAs as drug delivery systems

Traditionally pharmacotherapy, administered either intravenously or via an extravascular route such as oral, nasal, sublingual or rectal, is not always as effective as desired, due to the ineffectiveness of the drug to maintain the therapeutic drug concentrations within the desired target window. Hence, alternative solutions are being investigated to overcome this major problem. Biodegradable polymers are explored as a solution for their use as drug delivery systems.

These polymers are the carriers of the drug and target the area of interest increasing the therapeutic benefit, while minimizing side effects. The most well studied polymers which performed sustained drug release over a 30 days period, are homo and copolymers of lactate and glycolate (Pouton and Akhtar, 1996).

Nevertheless, the lack of controlled release from these delivery systems has led to the investigation of other polymers as candidates for drug delivery devices.

In the early 1990s PHAs were considered as drug delivery carriers due to their remarkable biocompatibility and biodegradability (C.W. Pouton, S. Akhtar). 50-100 μm PHB microspheres, prepared by the solvent evaporation technique, were loaded with rifampicin to be used as chemo embolizing agent. The results showed that upon completion of a 24-hour period, the drug had almost released its 90 % and could still be adjusted by changing the combination of the particle size and the drug loading (Kassab *et al.,* 1999). Moreover, Sendil and co-workers noted a similar behaviour when they tested encapsulated P(HB-co-HV) with tetracycline (an antibiotic known to be effective against many of the periodontal disease-related microorganisms) without signs of degradation (Sendil *et al.,* 1999). For the treatment of chronic osteomyelitis, poly(3HB-co-22 mol%-3-HV) rods were supplemented with Sulbactam-cefoperazone antibiotic.

The rods were subjected into a rabbit's tibia which previously was infected by *S. aureus*. The results of this study showed that the infection had receded after 15 days and gone completely by the 30th day (Yagmurlu *et al.*, 1999). In another study, Francis *et al*., encapsulated tetracycline and gentamicin in P(3HB) microspheres, achieving slow control release, starting with burst release of the drug and followed by its sustained release (Francis *et al*., 2011).

In addition, the rapid release of rifampicin and tetracycline from P(3HB) microspheres, showed a direct correlation between the degree of crystallinity and the kinetic release (Zinn *et al.*, 2001). The study compared the release between PHB and PLA microspheres containing lomustine (an anticancer agent). Results showed that the release in the case of PHB was much faster (24 h) than the PLA microspheres (7 days) (Shrivastav, Kim and Kim, 2013).

PHB microspheres encapsulated with rubomycin (an antitumor drug) have demonstrated sufficient release that inhibits the proliferative activity of Ehrlich's carcinoma in mice (Shishatskaya *et al.*, 2008). In addition, P(3HB) microspheres were analysed for controlled release of the antitumor drug 2′,3′-diacyl-5-fluoro-2′-deoxyuridine.

The results showed that the PHB microspheres demonstrated low toxicity and good biocompatibility with mice and rats, whereas controlled release increased the therapeutic efficacy of the antimetabolic. A prolonged release system of PHB

nanoparticles containing PI3K inhibitor (TGX221) was developed from Lu *et al.* to block the proliferation of cancer cells (Lu *et al.*, 2011). As a result, TGX221 was gradually released expanding its half-life, leading to higher drug efficiency.

1.4.2 PHAs as tissue engineering scaffolds

Tissue engineering is a multi-disciplinary field where the principles of engineering and the life sciences are combined towards the development of biological products in order to restore, maintain or improve tissue function or a whole organ (Langer and J. Vacanti, 1993). Degeneration of the human tissue is attributed to diseases, injuries and trauma. To replace or regenerate damaged tissue, standard treatments require tissue transplantation from one area to another by the same patient (autograft) or a donation from another individual (allograft) (O'Brien, 2011a). Due to the disadvantages of these approaches, researchers are looking for alternative solutions.

The main procedure is the use of biomaterials-based scaffolds to promote cell attachment and proliferation, infusion of isolated cells or cell substitutes and implantation of polymeric scaffolds seeded with the required cell type depending on the application (Langer and JP Vacanti, 1993). Tissue engineering scaffolds fill the tissue void, providing structural support for the engineered tissue. Basic considerations of using scaffolding in tissue engineering include biocompatibility, biodegradability, mechanical properties, scaffolding architecture and manufacturing technology (O'Brien, 2011b). Some important requirements of materials for their use as tissue engineering scaffolds are:

- The ability of sterilization and surgical flexibility
- The absence of carcinogenicity and toxicity
- The competency of cell attachment and proliferation
- And the incorporation of bioactive molecules such as growth factors and genetic materials (Knight and Evans, 2004a).

In this context, PHAs were thoroughly investigated, as they are of great interest for their use in biomedical applications. Their prominent mechanical properties can be modified based on the nature of the application either by using different

types of copolymers or by producing blends of PHAs and composites with organic and inorganic additives (Basnett *et al.*, 2013).

In addition, the desired scaffold structure can be fabricated using a variety of techniques, allowing the production of suitable design where various surface treatments of the PHAs allow the attachment of bioactive agents (Knight and Evans, 2004b). In this context, PHAs have been used for several medical applications, such as: wound dressing, artificial skin, stents and nerve conduits.

Mcl-PHA scaffolds were developed based on P(3HO) homopolymer for soft tissue engineering use (Rai *et al.*, 2011). In this study, this polymer supported attachment and proliferation of human adult low calcium temperature keratinocytes (HaCaT) cells, demonstrating suitability for wound dressing applications. To enhance the fragility and bioactivity of PHB, researchers have been trying to incorporate bioactive fillers to form more suitable composites for tissue engineering applications.

The first attempt was carried out by Doyle *et al.* in 1991, describe that PHB based materials produce a suitable bone tissue adaptation response with no evidence of undesirable chronic inflammatory response after implantation periods up to 12 months. The bone formed in a short period of time around the material, and became highly organized, with up to 80 % of the implant surface, lying in direct apposition to the new bone.

The particulate hydroxyapatite (HA) supplemented into a PHB matrix, yielded a bioactive and biodegradable composite for applications in hard tissue replacement and regeneration. The study showed that within a short time, a layer of bonelike apatite was generated on the HA/PHB composite after exposure to simulated body fluid; phosphate-buffered saline at 37^{o}C for periods up to four months, demonstrating high in vitro bioactivity of the composite (Doyle *et al.*, 1991).

Since then, PHAs scaffolds in combination with a range of materials such as calcium phosphate, collagen and porous composites containing bioactive glass, have been investigated for bone tissue engineering.

Luklinska *et al.*, demonstrated the ability of poly(3HB)/hydroxyapatite composites to form an interface with the injured bone by creating interconnected structure followed by dense bone formation after six months of implantation in rabbits (Luklinska *et al.*, 1997).

Misra *et al.*, reported the development of PHB foams having 85 % porosity combining bioactive glass (BG) particles of 45S5 Bioglass® grade in the polymer matrix. The PHB/BG composite foams were evaluated for their bioactivity, biocompatibility and degradation behaviour using MG-63 osteoblast cells and showed no immune response. The nanocomposites have confirmed that are highly bioactive after measuring the formation of hydroxyapatite on material surfaces upon immersion in simulated body fluid (SBF) (Misra *et al.*, 2010).

In another study, Rivard *et al.*, compared the proliferation rate of fibroblast on P(3HB-co-3HV) with collagen sponges observing similar behaviours. Moreover, during a 5 days culture period of P(3HB-co-3HV) composite, it preserved its integrity while the collagen foams were significantly decreased. It was also noted that in the case of poly(3HB-co-3HV) foams, the total protein production was twice than on collagen foams (Rivard *et al.*, 1996). PHAs were first reported as an implant material for microspheres, tubes and pallets based on the utilization of poly-3-hydroxyoctanoate-co-3-hydroxyhex-anoate (PHOHHx) and were tested in mice as a model animal. The polyester proved to be completely non-immunogenic (Williams *et al.*, 1999).

Similarly, in experiments conducted by Lobler *et al.*, using PHB patches on the gastrointestinal tract of dogs, no inflammatory response or fibrosis was observed (Lobler M, *et al.*, 2003). Sutures of PHB and PHBV were compared with silk and catgut sutures to test animals intramuscularly. The tested PHA sutures showed to provide the necessary strength, during the healing process of the muscle-fascial wounds. PHB and PHBV sutures implanted intramuscularly for a time period of up to 1 year, did not cause any inflammation and acute vascular reaction at the site of implantation.

The tissue reaction in the polymeric implants was similar non-absorbable (silk) sutures and was less pronounced than the reaction in the catgut, resulting in a high macrophagal stage with a large number of macrophages present (Shishatskaya EI, Volova TG, Puzyr AP, Mogilnaya OA, 2004).

Basnett *et al.*, describe the development of P(3HO)/P(3HB) blends for biomedical applications. The addition of P(3HB) polymer led to a significant improvement in mechanical values such as, tensile strength and Young's modulus compared to neat P(3HO). In addition, protein absorption, cell viability, and degradation rate were remarkably higher in the case of blend films comparing to the neat P(3HO)

polymer. Hence, these materials were considered optimal candidates for various medical applications (Basnett *et al.*, 2013).

1.4.3 Injuries of peripheral nervous system

One of the essential aspects in tissue engineering is nerve reconstruction. The regeneration of the nervous system is a difficult and challenging field in neurosurgery (Zhang *et al.*, 2019). The nervous system is divided into the central nervous system (CNS) which includes the brain, the spinal cord and the peripheral nervous system (PNS). Unlike the CNS, for which there is still no effective treatment if damaged, the peripheral nervous system is possible to repair a nerve injury (Arslantunali *et al.*, 2014).

The causes of a nerve injury could be either accidental (e.g. fall, crush injuries, twist, cut, war, etc.) or a disease (such as diabetes, chronic liver/or kidney disease, Amyotrophic lateral sclerosis (ALS), etc.) (D. Grinsell and Keating, 2014). Only in United States there are twenty million people suffering from nerve injuries associated to trauma or medical disorders resulted in approximately $150 billion annual cost (Grinsell & Keating, 2014; Taylor *et al.*, 2008). Where in Europe there are more than 300000 cases of peripheral nerve injuries (PNI) per year (Belkas, Shoichet and Midha, 2004). Consequently, approximately 2.8 % of trauma patients in the United States and Europe require surgical intervention (Noble *et al.*, 1998).

Peripheral nerve lesions impair not only the patient's quality of life but can be devastating for the society (Clin, 2015). Patients suffering from PNI are affected from decrease or loss of their function at the peak of their employment productivity, impacting healthcare costs, reduced employer output and loss of income (Pateman *et al.*, 2015). Compared with other tissues in the body, peripheral nerve regeneration is slow and usually incomplete.

However, despite technological development; treatment of peripheral nerve injury remains major problems in trauma centres and the most challenging problem in reconstructive surgery (Sabongi, Fernandes and Dos Gomes Santos, 2015).

The PNS has an inherent ability to self-heal injuries, when these defects are less than a few millimetres, but it is not always feasible (Bozkurt *et al.*, 2007). Misdirection and inappropriate regeneration, such as the backward growth of axons due to lack of guidance, are some of the limitations of self-regenerating injured nerves (Thomas 1989, Huang *et al.,* 2005).

The main causes of nerve injuries are shown in Figure 1.6. According to National Institute of Diabetes and Digestive and Kidney Diseases (NIDDK) diabetes is one of the main causes of nerve injuries. Annually, up to 70 % of people with diabetes exhibits nerve injuries. Patients with type 1 and type 2 diabetes are a vulnerable group of the population in nerve defects. In UK, diabetes is the most common cause of peripheral neuropathy (NHS Choices, 2012).

Diabetic neuropathy is a result of damaged blood vessels due to the high levels of glucose in the bloodstream (Fradkin and Rodgers, 2013). In addition to diabetes other disease or disorders, including vitamin B12 deficiency, autoimmune diseases such as multiple sclerosis, kidney disorders, cancers and infections like shingles, HIV and Lyme disease, can cause peripheral nerve disease. Drug side effects and exposure to toxic substances from environmental or industrial origin are categorizes along with excessive alcohol consumption as causes of peripheral neuropathy. Finally, the most common cause of nerve injuries is the physical injury resulted from compression or nerves trauma (NHS Choices, 2012; NINDS, 2014).

Figure 1.6: Main causes of nerve injuries.

The nerve can be described as a “telephone wiring” system that transmits electrochemical nerve impulses from the brain and spinal cord to peripheral organs. Anatomically, the nerve fascicles consist of a cell body containing the nucleus and cytoplasm, the dendrites which carry the electrical impulses to the cell and a long axon that carrying impulses away from the cell.

The basic structure of a nerve is called cell body or soma. As illustrated in Figure 1.7, nerve is like a cord containing bundles of axons. The axon is surrounded by a connective tissue layer called endoneurium. The groups of the bundled axons are called fascicles and they are wrapped in a layer of connective tissue called perineurium. The entire nerve surrounded by connective tissue is called epinerium.

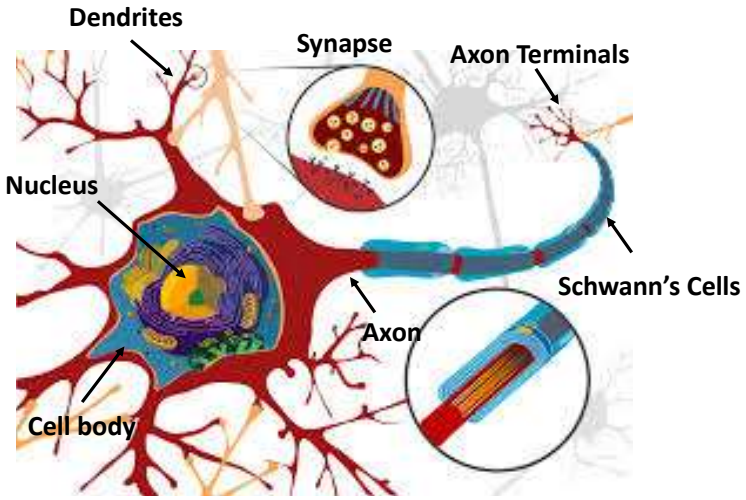

Figure 1.7: Structure of typical neuron.

The classification of nerve injuries has been established by Seddon in 1943. It described three basic types of peripheral nerve injury, and later in 1951, Sunderland expanded Seddon's classification to five degrees. According to Seddon’s classification, the injuries that can occur into a peripheral nerve are neurapraxia, axonotomesis, and neurotomesis (Evans, 2001). In Table 1.3 the correlation of the two different classifications is shown.

Table 1.3: Classification of nerve injury.

Type of injury Sunderland classification	Type of injury Seddon classification	Major structure involved
I	Neuropraxia	Myelin
II	Axonotmesis	Myelin, Axons
III	Neurotmesis	Myelin, Axons, Endoneurium, Perinerium, Epinerium
IV		
V		

During neurapraxia the patient experience a blunt trauma or stretching where there is no loss of continuity, in the case of axonotmesis the nerve is damaged but not severed, where at the same time a partial deficit occurs. Finally, in neurotmesis the nerve is severely injured.

1.4.4 Therapeutic strategies of peripheral nerve injuries

The nerve fibres of the transacted nerve are spontaneously regenerated to the extent that is limited by the size of the nerve gap, neuroma, and scar tissue formation. For injuries with a gap greater than 5 mm, self-healing ability is not feasible. In this case, the traditional treatment for the coaptation of the nerves achieved via tensionless end to end suturing of the two severed nerves. In more extreme conditions, the most common therapy is the use of allografts, vascularized nerve grafts and non-vessel nerve grafts (Arslantunali *et al.*, 2014; Muheremu and Ao, 2015).

Such treatment is considered as gold standard PNI. Despite the progress in microsurgical techniques and the early diagnosis, primary rehabilitation is not sufficient to reconstruct damaged nerves and successfully complete functional recovery. Current treatments can hardly be improved further (Muheremu and Ao, 2015).

The use of autologous grafting is not ideal as it is associated with various disadvantages along with the need for multiple surgeries, since the origin of this

segment is the patient's own body, sacrificing another motor or sensor nerve from another part to repair the damaged one.
This technique indicates a high risk of inability to repair the injured nerve but also the possibility of transferring morbidity to the donor site. In addition, the probability of a mismatch in dimension, between the donor segment and the injured region, as well as the limiting number of donors providing suitable grafts for harvesting make these treatments unreliable.

All of the above techniques are associated with high risk complications for the patient and reduce the regenerative capacity of an injured nerve. Moreover, the efficiency of regeneration is related to the extent and severity of the injury, as well as the biological factors and the patient's age.

Taking into account that less than half of patients recovering from nerve surgery, regain full motor and/or sensory function and the fact that current surgical treatments for such injuries remain similar to those described by Sunderland more than 60 years ago, researchers have focused on an alternative solution that seeks to simplify the surgical procedure and improve the recovery (Grinsell and Keating, 2014).

The use of nerve conduits minimizes the problems associated with lacerated tissues, namely, suturing with correct alignment, scar tissue formation, adhesion and mismatching of nerve fascicles. Tissue-engineered nerve conduits could be used to bridge a large gap between two damaged nerve stumps. In addition, the use of biodegradable nerve conduits, provides mechanical stability, chemical stimulation confining axonal sprouting, delivery of therapeutic cell types and nerve regeneration (Evans, 2001).

The complication of the first nerve conduit made from non-resorbable silicone tubes caused by its durability, which required a second operation to remove the conduit from the patients. In recent decades, many efforts have been made to improve nerve conduits. In this context, a variety of materials have been investigated as candidates for the development of nerve conduits.

However, so far there are only five available US Food and Drug Administration (FDA) approved nerve guidance. Most of them are bioresorbable with

degradation times ranging from 3 months to 4 years. Their trade names are Neurotube, Neurolac, NeuroGen, NeuromatrixNeuroflex and Salubridge. These components are made of PGA, PLCL, type I collagen (NeuroGen, Neuromatrix, Neuroflex) and PVA hydrogel accordingly (Alberti *et al.*, 2016). Poor biocompatibility, excessive swelling and inadequate degradation profile are complications which led the Neurolac conduits to be discontinued (Nectow *et al.*, 2012).

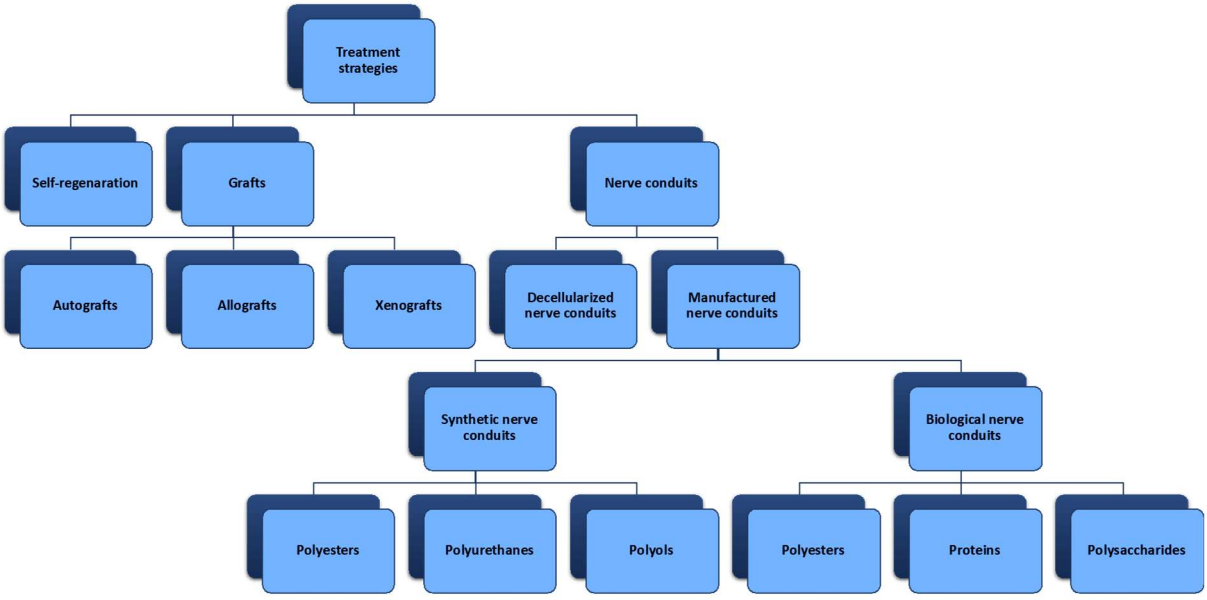

Figure 1.8: Treatments for nerve regeneration.

There are specific requirements that a 3D tubular structure must meet to be an ideal nerve conduit. The conduit material must be (Nectow *et al.*, 2012; Kehoe *et al.*, 2012):

- Biocompatible, preventing any inflammatory reaction.
- Biodegradable but should maintain stability during regeneration.
- Flexible in order to avoid compression of the regenerating nerves.
- Semi permeable to allow the passage of oxygen, nutrients and metabolites through pores in the conduit wall.

There are different approaches to designing a nerve structure. Figure 1.9 presents the different designs of nerve conduits.

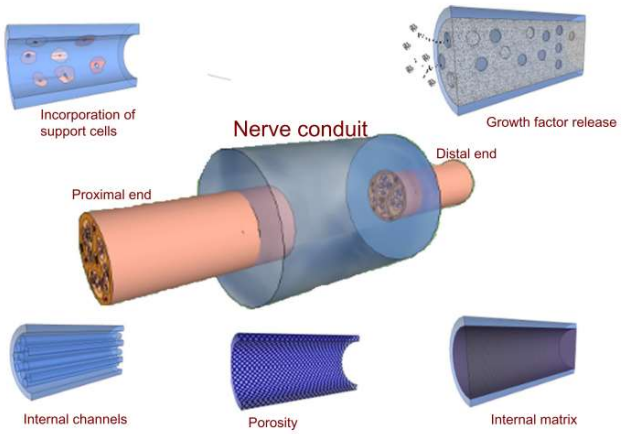

Figure 1.9: Examples for nerve conduit designs (adapted from Arslantunali *et al.*, 2014).

1.4.5 PHAs as biomaterials for nerve conduits

A variety of materials have been used over the years as implants, such as NGCs, for the reconstruction of transacted nerves. The materials used to develop such conduits (available on the market) are synthetic and natural polymers. Some of them are summarized in Table1.4 (Chrz, Derbisz and Suszy, 2018).

Table 1.4: Commercially available nerve conduits.

Material of nerve conduit:	Product name:
Collagen	Neuroflex™
	NeuroMatrix™
	NeuraGen®
	Revolnerv®
PCL	Neurolac®
PGA	Neurotube®
Chitosan	Reaxon® Nerve Guide
PVA	SaluTunnel™
SIS (material based on the submucosa of swine small intenstine)	AxoGuard™ Nerve Connector

In order to develop such structures, the polymer used as starting materials should be easy processable and meet the requirements outlined above with respect to the neuronal cells. Nerve regeneration studies using P(3HB), have already shown that PHAs are suitable biopolymers for such use (Arslantunali *et al.*, 2014).

In this context recently, Lizarraga- Valderrama *et al.* developed P(3HO)/P(3HB blends of various compositions. Films of 25:75, 50:50, and 75:25 blends of P(3HO)/P(3HB) were developed and tested with NG108-15 neuronal cells for their biocompatibility. Despite the fact that the both 25:75 and 75:25 blends of P(3HO)/P(3HB) had the required mechanical properties to develop a nerve conduit, the 25:75 P(3HO)/P(3HB) blend showed the highest biocompatibility among all the films, supporting effectively the neuronal growth (Lizarraga-Valderrama *et al.*, 2015).

The regeneration process and the time of the nerve to be repaired, depends upon the presence of hematoma, devitalized tissue and bacterial infection. In this light, the past two decades there has been an increase in the number of studies aiming at the development of biomaterials with antibacterial properties.

1.5 Novel antibacterial agents

1.5.1 Natural antimicrobial compounds

While the spectacular history, interest and importance of natural products can never be ignored, the recent Nobel Prize in Medicine for the discovery of artemisinin by Chinese scientists serves to emphasize their interest and significance in medicine and society (Su and Miller, 2016).

Some examples of the use of plants for healing in ancient times are the Chinese book “Pen T’Sao,” written in 2500 B.C., mention three plants still in use today, such as cinnamon, ginseng and jimson weed. Moreover, Vedas, a collection of ancient religious texts written in India (1500-1000 BCE), refer to treatments with herbs from India that are still used today such as clove, pepper and nutmeg. In addition, Hippocrates, “Father of Modern Medicine” in ancient Greece cited more than 300 medical plants and classified their use. The ancient Greek, Dioscorides “father of pharmacognosy,” wrote “De Materia Medica”, a catalog of plants

describing the curative properties of plants (Petrovska, 2012). The introduction of antibiotics in the 1950s overshadowed the use of plants as antibacterial agents.

Despite the development of new antibiotics, the resistance of microorganisms has increased. Understanding that the efficacy of antibiotics is limited in combination with consumer awareness for misuse, leads to the investigation of other antibacterial sources (Cowan, 1999). Recently, studies on the therapeutic treatment of plants, have increased (Nascimento *et al*, 2000). Substances responsible for protecting plants from insects and microorganisms, are also amenable to either odor, flavor or plant pigments. The active substances that cause the antibacterial features in plants can be divided into many categories (Table 1.5).

Thyme and tarragon are both active against bacteria and fungi, consisting of caffeic acid, representative of the phenolic group. In addition, catechol and pyrogallol phenols, containing two and three hydroxyl groups respectively, possess higher antibacterial activity and increased hydroxyl groups appear to increase toxicity to microorganisms (Cowan, 1999).

Flavanol, flavones and flavonoids are phenolic substances containing carbonyl group. Their mechanism of action is attributed to their ability to engage with both the extra cellular matrix and the bacterial cell walls. Quinones and tannins are also two other groups that are classified into phenol compounds. Quinones have two ketone substitutions in their aromatic rings and can cause inactivation of cellular protein, consisting them potential antibacterial agents. Tannins can be produced either by the polymerization of quinone units or by flavane precipitated into woody plant tissues (Cowan, 1999).

Another group derived from plants that are active against bacteria are essential oils. Essential oils are compounds based on an isoprene structure, and they are responsible for the fragrance of plants. These structures are called terpenes and when they contain other elements such as oxygen, they are called terpenoids. Both terpenoids and terpenes have been reported to exhibit antibacterial activity against bacterial, protozoa and fungi (Cowan, 1999).

Table 1.5: Main groups of antimicrobial compounds from plants (adapted from Cowan, 1999).

Class	Subclass	Example(s)	Mechanism
Phenolics	Simple phenols	Catechol	Substrate deprivation
		Epicatechin	Membrane disruption
	Phenolic acids	Cinnamic acid	
	Quinones	Hypericin	Bind to adhesins, complex with cell wall, inactivate enzymes
	Flavonoids	Chrysin	Bind to adhesins
	Flavones		Complex with cell wall
		Abyssinone	Inactivate enzymes
			Inhibit HIV reverse transcriptase
	Flavonols	Totarol	?
	Tannins	Ellagitannin	Bind to proteins
			Bind to adhesins
			Enzyme inhibition
			Substrate deprivation
			Complex with cell wall
			Membrane disruption
			Metal ion complexation
	Coumarins	Warfarin	Interaction with eucaryotic DNA (antiviral activity)
Terpenoids, essential oils		Capsaicin	Membrane disruption
Alkaloids		Berberine	Intercalate into cell wall and/or DNA
		Piperine	
Lectins and polypeptides		Mannose-specific agglutinin	Block viral fusion or adsorption
		Fabatin	Form disulfide bridges
Polyacetylenes		8S-Heptadeca-2(Z),9(Z)-diene-4,6-diyne-1,8-diol	?

Alkaloids are another antibacterial group derived from plants as shown in Figure 1.10. Morphine, codeine and heroin, are heterocyclic nitrogen compounds also known as alkaloids. Diterpenoid alkaloids are known to exhibit bactericidal activity. The mechanism of action of this category is attributed to the intercalation of alkaloids with the DNA.

Another group of plants that produce antibacterial compounds are disulphide-containing peptides. For example, thionins, peptides derived from wheat, found to be active against Gram-negative and Gram-positive bacteria. The mechanism of their action is attributed to the permeability of the cell membrane, via ion channels or due to the restriction of bacterial adhesion (Cowan, 1999; Kim *et al.*, 2009).

According to Savoia, there are two categories of mechanisms that plants derivatives can be classified into (Savoia, 2012). The first category of inhibitors is mostly active against Gram-positive microorganisms such as *Staphylococcus aureus* and less active against Gram-negative bacteria which possess the efflux system. Secondly, the biofilm inhibitors are highly important due to the major need to fight the biofilm formation which no longer can be treated with the conventional antibiotics.

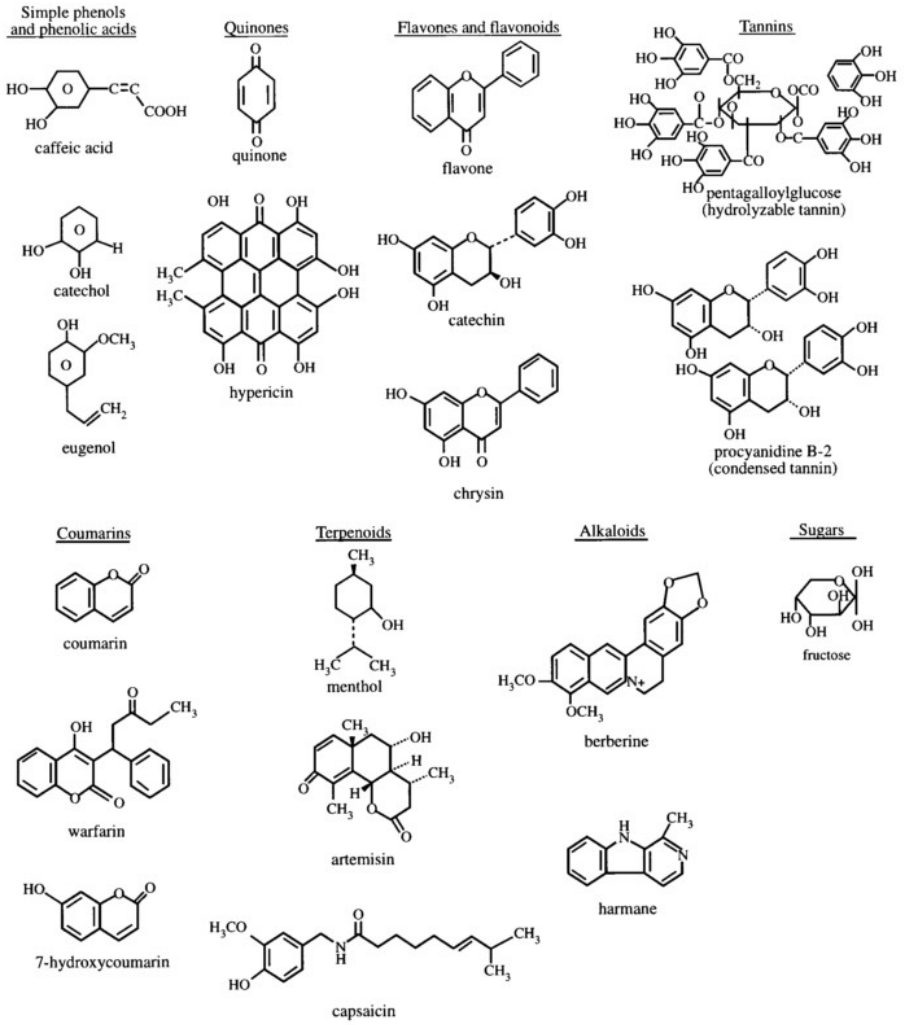

Figure 1.10: Structures of common antimicrobial plant chemicals (adapted from Cowan, 1999).

Biofilm formation occurs when planktonic cells (free cells) start colonization developing communities which cause chronic infections and are unable to be treated with antibiotics unlike the acute infections caused by the planktonic cells (Bryers, 2008). Artini *et al*, studied the inhibition of biofilm formation by natural compounds derived from plants.

They investigated four compounds originated from *Krameria, Aesculus hippocastanum*, *Macleya cordata* and *Chelidonium majus*. These compounds have alkaloids and flavonoids which, as previously mentioned, are two of the main antibacterial groups of plants. They found, that compounds derived from *Aesculus hippocastanum* and *Macleya cordata* exhibit inhibition against the biofilm formation preventing the process of the planktonic cells from being transformed into biofilm (Artini *et al*, 2012). Finally, QS inhibitors are responsible for interrupting the cell-to-cell communication and preventing the formation of

virulence and biofilms. There are three key points where inhibition can occur against: 1) the signal generator (LuxI homologue), 2) the signal molecule (AHL) and 3) the signal receptor (LuxR homologue). There are many plants that exhibit QS inhibition, including garlic. The examination of garlic extract proved to be extremely effective against the signal generator (Rasmussen and Givskov, 2006).

Garlic or else *Allium sativum* has been used since ancient times to treat coronary thrombosis, atherosclerosis and asserted to have antibacterial properties. The antibacterial activity of garlic is due to a compound called allicin (diallyl thiosulfinate) (Ankri and Mirelman, 1999). This organosulfur compound is produced by the action of the enzyme alliinase, as shown in Figure 1.11.
In an undamaged plant, the enzyme (allinase) and the amino acid (alliin) are stored in deferent compartments (Feldberg *et al*, 1988). When a wound in the garlic tissue, occurs then an enzyme converts alliin to allicin.

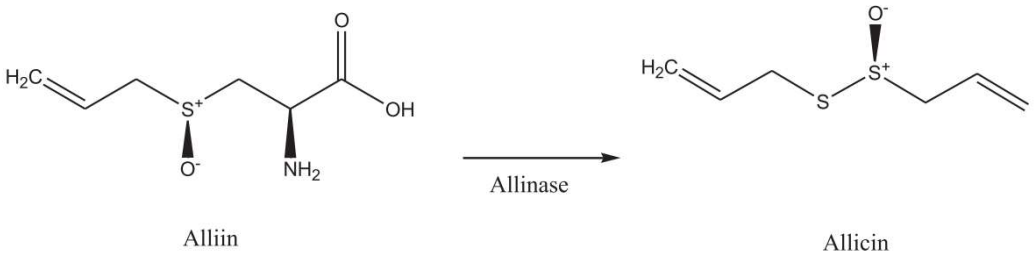

Figure 1.11: Generation of allicin from alliin (adapted from Marchese *et al*, 2016).

Cavallito and Bailey were the first to report that the active substance that makes garlic antibacterial was allicin (Cavallito and Bailey, 1944). Since then, garlic has been shown to have antibacterial activity against a plethora of microorganisms (*Escherichia, Salmonella, Staphylococcus, Streptococcus, Klebsiella, Proteus, Bacillus, and Clostridium*) but also viruses, fungi and protozoa (Nostro, 2006; Ankri and Mirelman, 1999). In addition, it has been reported to prevent the formation of *Staphylococcus* enterotoxins.
The main mechanism of action of allicin is attributed to its ability to inhibit thiol-containing enzymes when thiosulfinates react with thiol groups (Nostro, 2006), (Ankri and Mirelman, 1999). Several studies have been conducted to investigate the antibacterial activity of garlic. Amongst them, Bakri and Douglas studied the inhibition effects of the garlic extract against oral pathogens.

The evaluation of the tests showed that the garlic extract exhibit antibacterial activity against oral bacteria especially Gram-negative species (Bakri and Douglas, 2005). Wu *et al*, studied the antibiofilm and antibacterial effect of allicin and garlic extracts against *Staphylococcus epidermidis*.
They found that garlic extract had a higher antibacterial effect than allicin. Their findings show that garlic extracts with either water or alcohol exhibit antibacterial activity at lower concentrations than pure allicin.

They indicated that garlic extracts, have other compounds such as ajoene (also sulfuric component), known as quorum quencher and help with the biofilm inhibition (Wu *et al*, 2015). Garlic was amongst several plants, investigated by Woods-Panzaru *et al*, for their antibacterial activity. They found that only the aqueous garlic glove extract inhibited the growth of nine bacterial, compared to the extracts of onion (*Allium cepa*), Yarrow leaf (*Achillea millefolium*), Meadow sweet leaf (*Filipendula ulmaria*), Confrey leaf (*Symphytum officinale*), Ragwort (*Senecio jacobaea*) and Dandelion leaf and roots (*Taraxacum officinale*) (Woods-Panzaru *et al*, 2009). More recently, Marchese *et al*, (Marchese *et al*, 2016) conducted a comprehensive review of the antibacterial and antifungal activity of allicin.
The study refers to extensive investigations which have been conducted in recent years, to determine the bioavailability of allicin, originated from fresh and supplements of garlic. Moreover, various scientific studies have been carried out, in order to establish the antibacterial and antifungal activity of allicin. The Table 1.6 conclude the antimicrobial activity of allicin and its combinations (Marchese *et al*., 2016).

Table 1.6: Antimicrobial activity of allicin and its combinations (adapted from (Marchese *et al*, 2016).

Type of study	Bacteria & fungi	Conclusions
In vitro study of combination: - raw garlic extract and commercial garlic tablets - garlic+amoxycillin - garlic+clarithromycin - garlic+metronidazole - garlic+omeprazole to inhibit *H. pylori* causing gastric infection	*H. pylori* clinical isolates	The combination of garlic and omeprazole, studied with killing curves, showed a synergic effect which was concentration dependent. No synergistic or antagonist effect was found for garlic combinations with antibiotics.
In vivo study treatment with allicin to eradicate *H. pylori* gastric infection	*H. pylori*	Treatment with allicin on positive patients was not able to eliminate infection.
In vivo effectiveness of allicin, ascorbic acid and beta carotene to eradicate *H. pylori g*astric infection	*H. pylori*	Treatment on *H. pylori* positive patients with allicin seemed to be potentially effective for this bacteria eradication while ascorbic acid, beta carotene was found to be ineffective.
In vitro activity of three thiosulfinates from oil-macerated garlic extract against both Gram-positive and Gram- negative bacteria	*B. cereus, B. subtilis, S. pombe,* *S. aureus, K. pneumoniae, E. coli,* *M. luteus, P. aeruginosa,* *X. maltophilia, S. cerevisiae*	Allicin showed an antimicrobial activity comparable or superior to those the other compounds isolated and tested.
In vitro activity of allicin against common pathogens causing medical device related infections	*S. epidermidis,* *S. epidermidis ATCC 35984*	Allicin showed similar activity against MSSE and MRSE [minimum inhibitory concentration (MIC)90=8 mg l (-1)]. Subinhibitory concentrations (sub-MIC) of allicin diminished biofilm formation in the five strains analysed.
In vitro activity of aqueous extract of allicin from garlic in alternative to mupirocin to reduce nasal carriage and spread and to treat skin infections	MRSA clinical isolates	The great majority (88%) of the strains studied showed MICs value of 16 µg/ml, while all strains were inhibited at 32 µg/ml. 88% of MRSA had MBC of 128 µg/ml, and complete elimination was obtained at 256 µg/ml. 82% of these strains were intermediate or resistant to mupirocin.
In vitro activity of allicin alone and in combination with cefazolin/oxacillin/cefoperazone	*S. aureus* *S. epidermidis* *P. aeruginosa*	Allicin alone did not have good antibacterial activity (MIC_{90}>512 microg/ml) but it facilitated antibacterial activityof all three beta- lactams tested at subinhibitory concentrations.
In vitro activity of allicin + cefoperazone / tobramycin /ciprofloxacin	*P. aeruginosa*	The results of this study confirmed that allicin can promote the bactericidal activity of certain antibiotics.
In vitro activity of allicin and polymyxin B	*S. cerevisiae, C. albicans,* *A. niger* *A. fumigatus*	Allicin amplified the fungicidal activity of polymyxin B.
In vitro antifungal activity of allicin and amphotericin B	*C. albicans* *clinical isolates*	All strains were susceptible to amphotericin B and were inhibited by allicin (MIC_{50} ranged from 0.188 to 0.75 µg/ml; MIC_{90} ranged from 64 to 128 µg/ml); the combination of amphotericin B & allicin showed synergy
In vitro antifungal activity of allicin/ amphotericin B/ flucytosine and combinations of the three	*C. albicans*	The viability of C. albicans after treatment with allicin alone or with a single antifungal compound in addition was more than 40%, but the viability of groups treated with combinations of more than two drugs was less than 32%.

In vitro activity of allicin	*S. aureus* (MSSA and MRSA)	Allicin was active against *S. aureus* with MICs ranged from 32 to 64 µg/ml and decreased in a dose-dependent manner the production of α- toxin by *S. aureus*.
In vitro activity on effect of allicin and aqueous garlic extract on the haemolytic activity of streptolysin O	Group A streptococci	Allicin neutralized streptolysin O in a dose- and time-dependent manner (15 min of incubation with 35 microg of allicin totally inhibited the haemolytic activity of streptolysin O).
In vitro activity of aqueous and gel formulation of allicin to be used as preventive strategies to reduce the risk of premature rupture of membranes	*S. agalactiae* from vaginal swabs	MICs and MBCs of allicin liquid were 35 to 95 mg/L and 75 to 315 mg/L, respectively. Allicin gel produced an average zone size of 23±6 mm compared with 21±6 mm for allicin in water.
In vivo activity of allicin + vancomycin on prevention of biofilm formation and related prosthetic joint infections	*S. epidermidis* biofilm producer	The lowest number of viable bacterial counts of *S. epidermidis* recovered from the biofilm was in the rabbits treated with allicin + vancomycin and the biofilm formation was significantly reduced or undetectable by SEM in rabbits receiving allicin or allicin + vancomycin.
In vitro activity of allicin/vancomycin/chlorhexidine digluconate and mixed solution to prevent implant infection of reticular polypropylene mesh used for hernia repair	*S. aureus* ATCC 25923	Chlorhexidine was more effective than vancomycin, and allicin lost its effectiveness after 24 h. No bacteria adhered to the surface of the DualMesh Plus or the meshes soaked with vancomycin, chlorhexidine and allicin-chlorhexidine. On the contrary, saline and allicin allowed adherence of high loads of bacteria.
In vivo activity of allicin/vancomycin/chlorhexidine digluconate and mixed solution to prevent implant infection of reticular polypropylene mesh used for hernia repair	*S. aureus* ATCC 25923	Allicin interferes with the inflammatory processes and with the macrophage response promoting the survival of bacteria in the host tissue, whereas the pre-treatment of the medical devices with a low concentration of chlorhexidine gives an antibacterial protection to the mesh.
In vitro activity of allicin on prevention of biofilm formation and related infections	*P. aeruginosa* biofilm producer	Allicin was able to inhibit early bacterial adhesion, reduce extracellular polysaccharide substance secretion, and down-regulate virulence factors' production.
In vitro activity of fresh garlic extracts on prevention of biofilm formation and related infections	*C. albicans* biofilm producer	Fresh garlic extract was able to affect the different stages of C. albicansbiofilm.
In vitro activity of aqueous extract of garlic against oral pathogens	*S. mutans, F. nucleatum S. sanguis, S.parasanguis, S. mitis, S. crista, S. oralis, S. intermedius, S. constellatus S. anginosus, A. naeslundii, E. faecalis, S. gordoni, S. aureus A. actinomycetemcomitans P. intermedia, P. nigrescens, P. gingivalis, L.buccalis C.albicans*	The garlic extract inhibited the growth of all strain tested.
In vitro activity of allicin against oral pathogens	*A.actinomycetemcomitans*	Allicin was active against *A. actinomycetemcomitans*
In vitro activity of allicin	*B. cepacia*	The MICs and MBCs values of allicin ranged from 8 to 62 µg/ml and from 31 to 62 µg/ml, respectively.

1.5.2 Inorganic compounds (metal ions, phosphate glass and graphene-based materials)

1.5.2.1 Metal ions

During the last decades, great attention has been paid to the use of inorganic compounds for biomedical applications. Inorganic compounds are described as potential antibacterial agents.

Metal ions have been extensively used as inorganic compounds for different aspects. Metal complexes are important in the living systems because they can easily lose electrons and become positively charged ions allowing themselves to become soluble in biological fluids. In this way they can also bind to biological molecules such as proteins and DNA (which is reach in electrons) (Orvig and Abrams, 1999).

Moreover, 3 % of our body consists of metals. Metals such as silver, copper, zinc and iron pare involved in many chemical reactions, necessary for life, by incorporating into catalytic proteins (Holm *et al.*, 1996). For instance, hemoglobin, which is responsible for the transport and storage of oxygen in the body, contains an iron complex.

The use of metallic elements is beneficial not only as antibacterial agents but also as neurological, anticancer, antimicrobial, antiviral, anti-inflammatory, cardiovascular and as insulin-mimetic agents (Sekhon and Gandhi, 2006). Therefore, their use is increasing because of their ability to help cure many diseases.

Inorganic compounds have been used for thousands of years; copper was used in Egypt about 3000 BC to sterilize the water. Iron was used in Egypt around 1500 BC for many therapies, while zinc was found to help wound healing (Orvig and Abrams, 1999).

Nowadays, Inorganic compounds can be used to improve the antibacterial activity of organic drugs/agents. The use of metal complexes has been shown to increase the therapeutic index of the organic compound complexed with metal centers (Obaleye *et al.*, 2012). An example of this is an organometallic compound called Ferroquine, developed by Biot *et al* (Biot *et al.,*2000).

Ferroquine, a drug efficient against malaria, is prepared via incorporation a ferrocenyl group in the chloroquine side chain. Selenium and tellurium complexes containing Sulfonamides, were developed by Rudzinski *et al.*, and found to be

active against bacterial species (Rudzinski *et al.*,1982). Moreover, sulpha diazine complexes, were synthesized by Ajibade and Kolawole. It was reported that the Fe (III) complex was more active against pathogenic bacteria (Ajibade and Kolawole ,2008). Recently, Tella and Obaleye synthesized sulphadimidine metal complexes, with high antibacterial activity against *E. coli, K. pneumonia* and *S. aureus (*Tella and Obaleye, 2009).

There are several studies on metal particles that exhibit antibacterial activity against pathogenic bacteria. It has been reported that metal ions such as copper, cobalt, zinc and nickel, which form low molecular weight complexes, are used to increase the activity of antibiotics. In most cases, the metal complexes showed higher antibacterial activity than the free ligand and disturb the respiratory process (Dizaj *et al.*, 2014).

Two parameters are considered to be responsible for the effectiveness of the metal ions activity: the starting material used for the nanoparticles preparation and the size of nanoparticles (Dizaj *et al.*, 2014). Metallic nanoparticles such as silver (Ag), silicon (Si), copper (Cu), zinc oxide (ZnO), gold (Au), calcium oxide (CaO) and magnesium oxide (MgO) are described to exhibit antimicrobial activity. Amongst them, silver and copper are the most widely used in healthcare and industrial application. These two metals have been shown to exhibit effective antibacterial activity at very low concentrations (Dizaj *et al.*, 2014).

Silver has low toxicity to mammalian cells and has been proven to have antimicrobial activity against bacteria, viruses and other eukaryotic microorganisms. Silver nanoparticles are able to bind to the bacterial surface and alter the membrane function that disrupts bacterial growth (Bobbarala, 2012). Their ability to anchor to the bacterial cell membrane, results in secondary effects such as the generation of oxygen species (ROS) and damage the DNA.
In addition, when silver nanoparticles come in contact with the cell surface, free radicals are formed which disrupt the cell membrane and cause cell death (Palza, 2015).

In the case of copper the main mechanism that induces antibacterial activity, results from the release of ions from copper nanoparticles, forming complex

copper peptides, allowing their penetration into the cell membrane (Palza, 2015). The various mechanisms of metal ion action are shown in Figure 1.12.

The mechanisms of action of these nanometals are not completely clear but they can be classified as: (a) oxidative stress due to oxygen generation species (ROS) triggered by the metal reduction potential and (b) donor - atom selectivity where the metals are bound to donor ligands, such as O, N and S (Dizaj *et al.*, 2014). Oxidative stress can damage the proteins, lipids and DNA when the cell's antioxidant capacity is exceeded. Where in the second case, the strong and selective interactions result in cellular dysfunction due to the replacement of the original metals, present in biomolecules with the external metal ions (Lemire *et al.*, 2013).

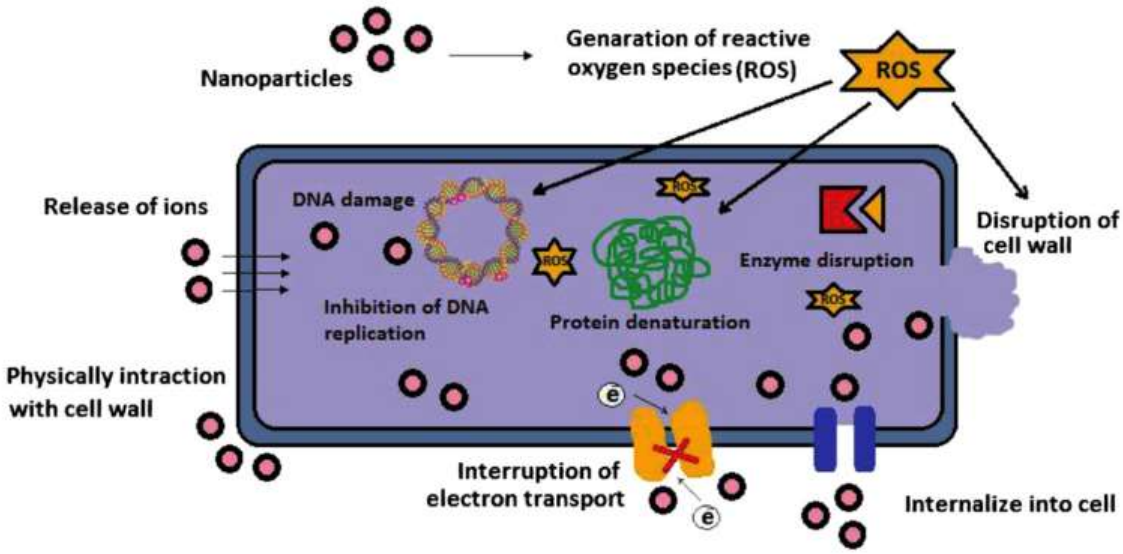

Figure 1.12: Various mechanisms of antimicrobial activity of the metal nanoparticles (adapted from Dizaj et *al*., 2014).

The incorporation of metallic nanoparticles into polymeric matrixes, extends their use and applications of antibacterial metal ions. The addition of metal particles can be achieved either via (chemo)sorption on the polymer surface or by incorporation into a polymer matrix. In this context, a great deal of research has been done and is continuing with promising results for the use of hybrid nanocomposites metal particles as antibacterial materials.

1.5.2.2 Phosphate glass

Phosphate-glasses are a class of glasses formed by P_2O_5 substrate (Islam *et al.,* 2017). Compared to silicone-glasses, phosphate-glasses are less rigid due to the presence of oxygen in the tetrahedral phosphate which reduces the network connectivity (Abou Neel *et al*., 2009).

Phosphate-glasses have been used as substrates for orthopaedic engineering, utilizing them as hard tissue substitutes (Bitar *et al.,* 2008). In addition, phosphate-based fibres (PGFs) are very good candidates for tissue engineering such as muscle, ligaments and nerve regeneration, having proven to possess excellent cytocompatibility and mechanical properties (Sharmin *et al.*, 2014). One of the drawbacks of PGFS when tested in relation to muscle cells, was the rapid dissolution of the fibres.

To further enhance the use of the phosphate-glasses, metal oxides were added which resulted in less cross-linking, due to the introduction of more terminal oxygen atoms, and thus reduced the chemical instability of P_2O_5 (Bae and Weinberg, 1991). Doping the fibres with Fe_2O_3 decreased the dissolution rate and improved the cell adhesion (Knowles, 2003).

As some of the metal ions such as silver and copper are known for their antibacterial activity and due to the problem of bacterial resistance to antibiotics, these metals were incorporated into PGFs to adjust the dissolution rate and confer antibacterial activity (Mulligan, Wilson and Knowles, 2003). Silver modified PGFs, were more effective against *Streptococcus sanguis* in tests using a Constant Depth Film Fermenter (CDFF), which mimicked the oral environment. They also showed limited antibacterial activity compared to the same ions incorporated in phosphate glasses as they produce rapid ion conducting glasses (Latia and Vancea 2003; Das *et al,* 2003).

Gilchrist *et al.*, (Gilchrist, Healy and Drake, 1991) incorporated silver released glass into the catheter line. As urine passes through the catheter device, it dissolves and releases the antibacterial ions that kill bacteria in the urine bag. In another case, Gilchrist *et al.*, conducted *in vivo* studies of tubular phosphate-based glasses for their use in nerve regeneration. The results were very promising and comparable to the control specimen (Gilchrist *et al.*, 1998).

The use of this nerve conduit allowed the alignment of the nerves, preventing the formation of scar tissue between the ends of the nerves and misdirecting the nerves to other tissues from the target sites. Another advantage of the PGFs is that they can be used as a reinforcement phase in a polymer matrix.

The high emergence of the development of degradable composites and their use in biomedical applications, allows the exploration and production of fully degradable composites. The advantages of this embodiment are the tailoring of the mechanical properties and control of the dissolution rate of the sophisticated composite as well as the addition of antibacterial properties if the metallic dopant exhibits any (Ahmed, Ren and Booth, 2019). Cerium oxide (CeO_2) nanoparticles are already used in biomedical industry due to their strong antioxidant properties. In addition, (CeO_2) has been reported to have antibacterial activity against both Gram-positive and Gram-negative bacterial strains that are more susceptible against *E. coli* bacteria (Farias, Dos Santos and Sampaio, 2018).

In another study, Shah *et al.*, showed that coating the polymer surface with CeO nanoparticles, exert antibacterial properties on the final composite when tested against *E. coli* (Shah *et al.*, 2012).

1.5.2.3 Graphene based materials

Another group of inorganic materials, recently investigated for their antibacterial activity, are graphene-based materials (GBMs). Graphene is a 2D material with exceptional physical and mechanical properties, suitable for a variety of applications. Its unique electronic, optical, thermal and mechanical properties allow its diverse applications in nanoelectronics, catalysis, sensors, composite materials, supercapacitors, optoelectronics and energy technology.

Some of the advantages of graphene-based materials used for biomedical applications are the improvement of mechanical and electrical properties of biomaterial and the increment of the cell attachment and growth on the biomedical surface (Pinto *et al.*, 2013).

Graphene based materials can reduce bacterial viability as concentration and the contact time with GBMs increase. In addition, there are studies reporting that smaller sized GBMs are more likely to interact with bacterial cells and cause their viability. These materials can be either hydrophobic or hydrophilic.

In the case of hydrophilic materials such as graphene oxide and reduced graphene oxide, they are able to penetrate the cell membrane resulting in cytoplasmatic, perinuclear or nuclear accumulation (Wang *et al.*, 2011).

Unlike hydrophilic materials, hydrophobic species such as graphite and graphene, are unable to interact and penetrate the cell membrane due to electrostatic and hydrodynamic interactions. Although, hydrophobic materials cannot enter the cell, they are found to cause cell deformation, intercellular stress and destabilize the cytoskeleton leading to apoptosis (Hu *et al.*, 2010). In both cases, GBMs has been shown to produce reactive oxygen species (ROS) that generate oxidative stress, leading to cell death similarly to metal ions. In particular, Liu *et al.* have tested different types of graphene-based materials against *E. coli*. They observed that the antibacterial activity of graphite (Gt), graphite oxide (GtO), graphene oxide (GO), and reduced graphene oxide (rGO) increased in the order of GtO > Gt > rGO > GO (Liu *et al.*, 2011). The study also showed that increased incubation time and GBMs concentration, led to a higher decrease in cell viability.

From these early studies, it has been shown that graphene-based materials can potentially induce cytotoxicity in a dose and time dependent manner (Wang *et al.*, 2011). Concerning the biocompatibility of these inorganic compound, *in vivo* and *in vitro* studies have shown that in most cases there is no death of animals, but there are some reports linking GBMs to inflammation.

The results depend on the physical-chemical properties of the GBMs, the concentration and exposure time. The biocompatibility of GBMs improved when they were introduced into a polymer matrix (Dubey *et al.*, 2015). In this sight, graphene-based polymer composites have attracted much attention. The incorporation of GBMs in polymer matrixes improved the properties of these nanocomposites.

Due to the unique properties of GBMs, nanocomposites have shown enhanced mechanical, thermal and electrical properties. This makes GBMs promising candidates as nanofillers compared to conventional ones (Kuilla *et al.*, 2010).

A review by Ji *et al.*, summarizes recent advances related to the antibacterial activity of graphene-based materials. Graphene-based nanocomposites are classified as: a) Graphene–metal nanocomposites, b) Graphene–metal oxide

nanocomposites, c) Graphene–polymer nanocomposites and d) Graphene-based multicomponent nanocomposites. In addition to the already mentioned ability of GBMs to permeate the cell membrane due to their sharp edges, it has been shown that their antibacterial activity is also caused by the extraction of lipid molecules. Moreover, their ability to trap microorganisms is an additional mechanism for killing bacterial cells.

By trapping the bacteria, they isolate them from their environment, inhibiting their proliferation. Large GO sheets exhibits higher antibacterial activity compared to smaller ones due to their ability to completely cover the bacterial surface (Liu *et al.*, 2012). All GBMs antibacterial mechanisms of action are illustrated in Figure 1.13.

In summary, all reports concluded that the activity of GBMs depends on the starting material, the fabrication method, the concentration, exposure time and the size/thickness of the nanomaterial.

As previously mentioned, silver and copper ions are widely used antibacterial agents, but their tendency to aggregate when they come in contact with bacterial cells, minimize their active surface area, thus weakening their activity. Thus, many efforts have been made to combine nanometals with GBMs (Moraes *et al,* 2020).

Silver nanoparticles - graphene complexes were developed using a number of reductants, some of which are hydrazine monohydrate (Li *et al.*, 2016), glucose (Shao *et al.*, 2015), starch (Han *et al.,* 2013) and plant extracts (Sedki *et al.*, 2015). A variety of hybrid nanocomposites has been developed with either silver or copper ions combined with GBMs. These composites exhibited higher stability and antibacterial activity than the neat metal ions due to the controlling release of GBMs (Ji *et al.*, 2016).

The limitation of solubility of graphene due to the strong interactions between graphene sheets, can be overcome when interacting with a polymer matrix. In this perception, a series of graphene-polymer nanocomposites have been investigated.

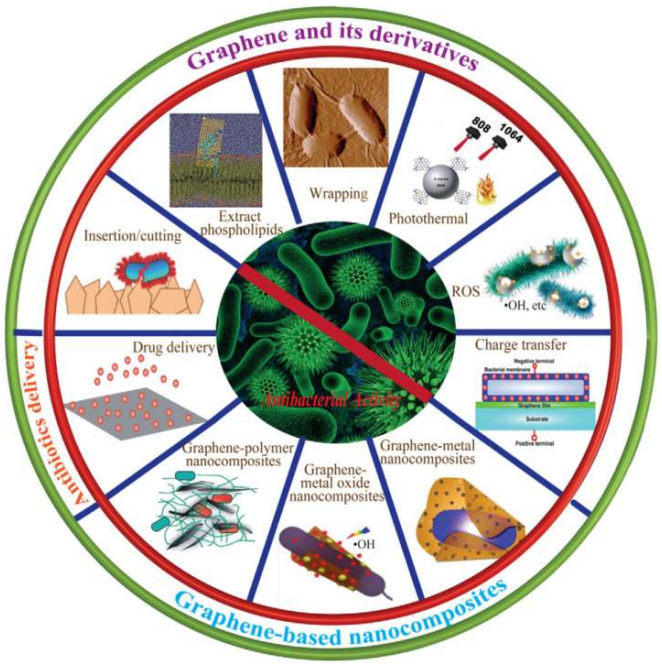

Figure 1.13: Schematic illustration of the antibacterial applications of graphene-based nanomaterials (adapted from Ji *et al.*, 2016).

A variety of polymers have been used as matrixes to interact with graphene-based materials. Some of them are nylon, polycarbonate, polyacrylamide, poly (methyl methacrylate) (PMMA), polystyrene (PS) and polyhydroxyalkanoates. The interaction between the polymer and the GBMs occurs by covalent or non-covalent bonds between matrix and filler (Potts *et al.*, 2011).

Barrett *et al.*, studied the properties of polyhydroxyalkanoate elastomers after the addition of thermally reduced graphene. They found that the intercalation of graphene in the polymer matrix increased the electrical conductivity, the Young's modulus and the melting temperature of the polymer (Barrett, Abdala and Srienc, 2014).

1.5.3 Aims and objectives

The main objective of this study was to investigate and obtain novel PHAs-based antibacterial biomaterials for their use in nerve tissue engineering and their potential for a new PHA-based nerve conduit. These novel composites would possess the required physicochemical properties to support their usage as NGCs. Additionally, they would be bioresorbable, so no post-surgery procedure would be required, and would have antibacterial properties against both

Gram-negative and Gram-positive bacterial strains in order to prevent bacterial infection and potential failure of the nerve regeneration due to infections.

To achieve this, the following specific objectives have been fulfilled:

1. Production and characterization of short chain and medium chain length PHA, P(3HB) and P(3HO-co-3HD) using *Bacillus subtilis* OK2 and *Pseudomonas mendocina* CH50.
2. Development of PHA blends films combining the scl and mcl-PHA in different ratios (80/20, 75/25, 25/75 and 20/80).
3. Addition of antibacterial compounds into the PHA polymer matrices and characterization.
4. Investigation of the physicochemical and biological properties (antibacterial and cytocompatibility) of the developed hybrids containing the antibacterial compounds.
5. Development of nerve conduits (3D structure) containing the antibacterial compounds.
6. Production and characterization of electro spun fibres made from P(3HB) and P(3HO-co-3HD) in 75/25 composition.
7. Incorporation of the PHA fibres in the hollow NGCs and determination of their biocompatibility with respect to NG108-15 neuronal cells.

Chapter 2

Materials and methods

2 Materials and methods

2.1 Materials

All the chemicals and reagents used in this study were purchased from Sigma-Aldrich (Dorset, UK) and VWR International (Leicestershire, UK). Cell culture media, antibiotic discs and other reagents were purchased from Sigma-Aldrich, Thermo Fisher Scientific (Waltham, USA). HPLC grade water was used for all experiments. Media preparation for bacterial use was done using general purpose reagents.

For all the analytical studies, analytical grade reagents were used. Chromatography grade reagents were used for Gel permeation chromatography (GPC) and Gas chromatography-mass spectroscopy (GC-MS) and HPLC grade water were used for these experiments.

2.1.1 Bacterial strains

The bacterial strains, Gram-positive bacteria, *Bacillus subtillis* OK2 and Gram-negative bacteria, *Pseudomonas mendocina* CH50 were used to produce scl-PHAs and mcl-PHAs, respectively. Both strains were obtained from the culture collection of Professor Roy's Laboratory, University of Westminster, UK. For the antibacterial evaluation, Gram-negative, *Escherichia coli* ATCC® 25922™, *Pseudomonas aeruginosa* ATCC® 27853™ and Gram-positive, *Staphylococous aureus* ATCC® 29213™, *Staphylococous epidermidis* ATCC® 12228™ and two clinical isolates of Methicillin resistant *Staphylococous aureus and* Methicillin resistant *Staphylococous epidermidis* where provided from University of Bochum, Germany where the secomend placement took place. Bacterial strains were stored on agar plates in the fridge at 4°C and as glycerol stocks in the freezer at -80°C.

2.1.2 Cell lines and cell culture materials

Both L929 murine fibroblasts and NG108-15 neuronal cells where purchased from the European Collection of Authenticated Cell Cultures (ECACC). Cell culture materials where purchased from Sigma Aldrich (Dusseldorf, Germany), Live/Dead was purchased from Promocell (Heidelberg, Germany), viability/Cytotoxicity Kit was purchased from Promega (Dusseldorf, Germany).

2.1.3 Organic and Inorganic compounds

Allicin supplement (AllicinMax) was purchased from Allicin International Ltd, (East Sussex, UK) were a second source of organosulfur compounds was derived from dehydrated garlic powder.

All the used moieties of inorganic origin were provided by the following collaborators. The graphene oxide (GO) powder was provided by the Foundation for Research and Technology - Hellas/Institute of Chemical Engineering Sciences, Patra where the cerium doped phosphate fibres (Ce-PGFs) provided by The Institute of Biomaterials, University of Erlangen-Nuremberg, (91058 Erlangen, Germany).

2.2 Media composition

The media components used for the production of the P(3HB) from *Bacillus subtilis* OK2 was a modification of Kannan and Rehacek medium and are shown in Table 2.1.

Table 2.1: Media composition for scl-PHA production.

Chemicals	Concentration (g/L)
Yeast Extract	**2.5**
Ammonium sulphate	**5.0**
Potassium chloride	**3.0**
Glucose	**35.0**

For the production of the P(3HO-co-3HD) from *Pseudomonas mendocina* CH50, two stages of culture media were required, second stage and production stage. The composition of the media used in this two-stage culture is shown in Table 2.2 and 2.3. The constituents of the trace element solution are shown in Table 2.4.

Table 2.2: Mineral Salt Medium (MSM) composition – second stage Rai *et al*., 2011.

Chemicals	Concentration (g/L)
Ammonium sulphate	**0.45**
Potassium dihydrogen phosphate	**2.38**
Sodium hydrogen phosphate	**3.42**
Magnesium sulphate	**0.40**
Trace element solution	**1 ml**

Table 2.3: Composition for the production stage.

Chemicals	Composition (g/L)
Ammonium sulphate	**0.50**
Potassium dihydrogen phosphate	**2.65**
Sodium hydrogen phosphate	**3.80**
Magnesium sulphate	**0.40**
Trace element solution	**1 ml**

Table 2.4: Composition of Trace element solution (TES). Basnett *et al*., 2014.

Constituent	Concentration (g/L)
$CoCl_2$	**0.22**
$CaCl_2$	**7.80**
$FeCl_3$	**9.70**
$NiCl_3$	**0.12**
$CrCl_3 \cdot 6H_2O$	**0.11**
$CuSO_4 \cdot 5H_2O$	**0.16**

2.3 PHA production

2.3.1 P(3HB) production

Cultivation of *B. subtilis* OK2 was carried out in sterile nutrient broth media, (10% of the final volume), inoculating the nutrient broth with a single colony of the bacterial strain taken from the agar plate. The culture in mid-log phase was then used for inoculating the PHA production media (modified Kannan and Rehacek medium, Table 2.1). PHA production was conducted in a batch mode in a 10 L bioreactor for a period of 48 h. The concentration of glucose was 35 g/L, air flow of 1 vvm, agitation speed of 200 rpm and at a temperature of 30^{o}C. The cells were then harvested, centrifuged and washed with distilled water and homogenised for 10 min using the T25 basic homogeniser (IKA Labortechnik). The obtained biomass was lyophilised and PHAs were extracted from the lyophilised cells.

2.3.2 P(3HO-co-3HD) production

P. mendocina CH50 was first cultivated in sterile nutrient broth (1% of the final volume of production media) and then seeded a in two-stage media, second stage mineral salt (MSM) media and production stage MSM media respectively, using glucose as the sole carbon source. First, the culture in in mid-log phase was used for inoculating the PHA MSM second stage media (composition shown in Table 2.2) and trace element (composition shown in Table 2.4) and grown at 30°C, 200 rpm for 24 h. Then, this culture was monitored by measuring optical density (OD) at 450 nm and further used to inoculate the sterile production stage medium and grown for 48 h at 30°C at 200 rpm.

2.4 Experimental Methods

2.4.1 Production of P(3HB) by *Bacillus subtilis* OK2 in 10 L bioreactor

P(3HB) production was conducted in the 10 L bioreactor. This vessel is equipped with 2 Rushton turbine impellers, pH and DOT (Dissolved oxygen tension) controllers. The vessel was sterilised with distilled water at 121ºC for 30 min. The glucose and media salts were sterilized separately and added to the bioreactor under sterile conditions.

The bioreactor was inoculated with seed culture as described previously in section 2.3.1. The stirrer speed was at 200 rpm and the air flow was set at 1 vvm. The pH of the media were adjusted to 6.8 and the fermentation process lasted for 48 h, at 30ºC, 200 rpm. Then the obtained culture was harvested, centrifuged, washed with distilled water and homogenised for 10 min. The obtained biomass was freeze-dried and used later in for the polymer extraction using Soxhlet apparatus (as described in section 2.5.1).

2.4.2 Production of P(3HO-co-3HD) by *Pseudomonas mendocina* CH50 in 20 L bioreactor

The mcl production using *Pseudomonas medocina* CH50 was carried out in a 20 L stainless steel bioreactor. The tank was sterilized with distilled water at 121ºC for 30 min. The vessel is equipped with 2 turbine impellers, temperature controllers, pH and Dissolved oxygen tension (DOT) sensors. Glucose, magnesium sulphate and MSM salts were sterilized separately and added to the bioreactor aseptically. The trace elements solution was added to the bioreactor, before the inoculum, after its filtration using 0.22 µm filters. The bioreactor was inoculated with 10 % of second stage seed inoculum. Steering speed was set at 200 rpm and the airflow at 1 vvm. pH was adjusted to 7 prior to the fermentation. Bacteria were grown for 48 h, at 30°C, 200 rpm. Then the obtained culture was harvested, centrifuged, washed with distilled water and homogenised for 10 min. The obtained biomass was freeze-dried and used later for polymer extraction using the Soxhlet apparatus.

2.5 Extraction of PHAs from biomass

2.5.1 Soxhlet extraction

After the completion of the fermentation process, the culture was centrifuged at 4600 rpm for 30 min to form a pellet. The supernatant was discarded, and the cell pellets were dried and lyophilised for 48 h. The dried biomass was crushed and weighed before their placement into the cellulose thimble (Whatman 28 mm × 100 mm) obtained from GE Healthcare Life Sciences.

The thimble containing the biomass was then placed into the Soxhlet extractor. The extractor was located between a condenser and a round bottom flask which was contained, in the first extraction, methanol and boiling stones and was heated

at 90°C for 24 h. In this first stage, organic substances soluble in methanol were removed from the biomass. Thereafter the methanol waste was discarded and replaced with chloroform in order to extract the polymer from the biomass. After 24 h at 80°C a chloroform solution containing the dissolved polymers is obtained and concentrated in a Büchi Rotavapor (R-215). Once the viscosity of the solution increases, the polymer is precipitated using ice-cold methanol under stirring conditions and dried at room temperature. Polymer yield was calculated as a percentage of dry cell weight, using the formula:

Polymer yield (% dcw) = (polymer weight/biomass) × 100

2.5.2 Solvent dispersion method

Estimation of the polymer yield was carried out via chloroform/sodium hypochlorite dispersion method (Hahn *et al*., 1993). The lyophilised biomass was crushed into fine powder and placed in the conical flasks. Per 0.3 g of biomass, 5 mL of 80 % sodium hypochlorite solution in distilled water and 22.5 mL of chloroform were added into the biomass and mixed well. The lyophilised cells were incubated in the solvent mixture, for 2 h, at 30°C, in the orbital shaker (140 rpm). After incubation the suspension was centrifuged at 3900 rpm for 20 min. As a result, phase separation of three separate layers was formed. The first two layers contained the aqueous phase of sodium hypochlorite and the cell debris were discarded. The last layer containing the polymer dissolved in chloroform was collected, filtered and precipitated in ice-cold methanol.

2.6 PHA characterization

2.6.1 Fourier Transform Infrared Spectroscopy (FTIR)

As preliminary identification of the kind of PHA produced, FTIR analysis was conducted using the Perkin-Elmer Spectrum. A sample of 5 mg was used for the investigation. The spectral resolution was set at 4 cm^{-1} with spectral range of 4000 to 400 cm^{-1}; window material, CsI: 10 scans.

2.6.2 Gas chromatography Mass Spectrometry (GC-MS)

GC-MS analysis was performed with methanolysed polymer samples. The methanolysis of the samples was carried in a reflux tube. 20 mg of the polymer was added with 20 µL of methyl benzoate. Then 2 mL of as prepared 15 % of sulphuric acid solution in methanol was added into the reaction mixture. Methanolysis was carried out under reflux conditions for 4 h in the case of scl-PHAs and 16 h in the case of mcl-PHAs. The incubation tubes were cooled down on ice and then 2 ml of HPLC grade water and were added to the mixture and vortexed. The two layers obtained were separated and the bottom layer containing the dissolved polymer was collected and dried using a mixture of 10 mg sodium bicarbonate and 10 mg sodium sulphate. After filtration, the final mixture was used for GC-MS analysis.

A Varian GS/MS system consisting Chrompack CP-3800 gas chromatograph and Saturn 200 MS/MS block was used for the GC-MS analysis. The injection volume of the prepared sample was 1 ml/min using helium as the carrier gas. The injector temperature was 225°C and the column temperature was increased from 40 to 240°C at 18°C/min and held at the final temperature for 10 min.

2.6.3 Nuclear Magnetic Resonance (NMR)

Structural characterisation of the polymer was carried out using ^{13}C and ^{1}H NMR. 20 mg of polymer were dissolved in 1 ml of deuterated chloroform ($CDCl_3$). The chemical shifts were referenced against the residual solvent signals, 7.26 ppm and 77.0 ppm for ^{1}H and ^{13}C respectively. The analysis of NMR spectra was completed using the MestRec software package. The NMR analysis was carried out at the Department of Chemistry, University College London, UK.

2.6.4 Differential scanning calorimetry

The thermal analysis of the samples was studied using DSC 214 Polyma (Netzsch, Germany) equipped with Intracooler IC70 cooling system, which provides measurements from -70°C. Sample mass of 5 mg were exposed to cooling and heating ramps to allow the calculation of the melting temperature (T_m) and glass transition temperature (T_g). The encapsulated samples in the aluminium crucibles were heated at a rate of 10°C per min from -70 to 170°C (mcl-PHAs) or 200°C (scl-PHAs) and kept at these temperatures for 2 min to remove the thermal history of the samples. This process was performed twice.

The thermograms of the second cycle were used for analysis using Proteus 7.0 software.

2.6.5 Tensile Testing

Tensile testing was conducted using the Instron 5940 testing system. Polymer strips were cut out from films previously made by the solvent casting technique with a pre-defined size of 5 mm wide and 35 mm long. The thickness and the width of the specimens were measured at different points, with a Vernier calliper and the lowest value was considered as the parameters for the cross-sectional area. The gauge length of the sample holder was set at 23 mm and the samples were subjected to a stretching process, until break. The deformation rate was set at 5 mm per minute and the stress-strain curve was used to calculate the Young's modulus (E), elongation at break (ε_b) and ultimate tensile strength (UTS). The average values of 5 specimens were used for the calculations. Analysis of the data was completed using the BlueHill 3 software.

2.6.6 Surface Wettability of the films

In order to evaluate the hydrophobicity/hydrophilicity of the PHA films and composites static contact angle study was carried out using a Theta Lite optical tensiometer (Biololin Scientific, Manchester, UK) controlled with One Attension software. An amount of 200 µL of deionized water was dropped on the surface of the films using a gas-tight micro-syringe. The contact angle of the droplet on the surface of the specimen was recorded with a total number of 10 images, captured with a frame interval of one second. All experiments were carried out in triplicates and the mean value was calculated.

2.6.7 Gel Permeation Chromatography (GPC)

The molecular weight of the produced polymers described by the number average molecular weight, (M_n) and weight average molecular weight, (M_w) were determined by using Gel Permeation Chromatography analysis (GPC). The eluent used for the preparation of the samples was chloroform. 2 mg/mL of polymer was injected into the GPC system at a flow rate of 1 mL/min. Prior to this, the PLgel 5 µm MIXED-C (300 × 7.5 mm) column was calibrated using the narrow molecular weight polystyrene standards from 162 Da to 15.000 kDa. Data analysis was carried out using "Agilent GPC/SEC" software.

2.6.8 Scanning electron microscopy (SEM)

Surface morphology of the PHA films and tubular structures were investigated using SEM. Aluminium stubs were used to fix the samples and coated with gold, using a EMITECH-K550 gold spluttering device for 2 mins, before viewing them under the SEM. In order to record different magnification of the images corresponding to the surface topography, a Philips XL30-SEM was used. The acceleration voltage of the SEM was 10 kV at 10 cm working distance. The SEM images were taken with an acceleration voltage of 15 kV (maximum) in order to avoid incineration of the polymer due to the beam heat.

The analysis of the samples was carried out at the Department of Biomaterials and Tissue engineering, Eastman Dental Institute, University College London, UK.

2.6.9 X-ray diffraction (XRD)

X-ray diffraction (XRD) analysis was performed on neat PHA films and composites. Samples were analysed on a Brüker D8 Advance diffractometer in flat plate geometry, equipped with Cu K_a, radiation and Ni filter. Data was collected from 5 to 100° (angle) with a primary beam slit size of 0.6 mm.

The XRD measurements were carried out at the Foundation for Research and Technology - Hellas/Institute of Chemical Engineering Sciences, Patra, Greece and the data analysis was carried out at University of Westminster.

2.6.10 Raman spectroscopy

Spectra were taken with at 785 nm laser using a MicroRaman (InVia Reflex, Rensihaw, UK) set-up. The laser power was kept below 1.5 mW on the sample to avoid laser-induced local heating, while an Olympus MPLN100x objective (NA = 0.90) was used to focus the beam on the samples.

The Raman measurements were carried out at the Foundation for Research and Technology - Hellas/Institute of Chemical Engineering Sciences, Patra, Greece and the data analysis was carried out at University of Westminster.

2.6.11 X-ray photoelectron spectroscopy (XPS)

The photoemission experiments were carried out in an ultra-high vacuum system (UHV) equipped with a dual anode Mg/Al X-Ray gun. Unmonochromatized AlKα line at 1486.6 eV and an analyser pass energy of 97 eV, giving a full width at half maximum (FWHM) of 1.7 eV for the $Ag3d_{5/2}$ peak, were used in all XPS measurements. The XPS core level spectra were analysed using a fitting routine, which can decompose each spectrum into individual mixed Gaussian-Lorentzian peaks after a Shirley background subtraction. The samples were pressed into pellets. The calibration of the analyser's kinetic energy scale was done according to ASTM-E 902-88. Wide Scans were recorded for all samples, while the core level peaks that were recorded in detail and presented here were: O1s, and C1s. Errors in quantitative data are found in the range of ~10 %, (peak areas) while the accuracy for BEs assignments is ~0.1 eV.

The XPS measurements and analysis was carried out at the Foundation for Research and Technology - Hellas/Institute of Chemical Engineering Sciences, Patra, Greece by Dr. Lambrini Sygelou.

2.7 Temporal profiling of PHAs production during fermentation process

In order to monitor the fermentation progress samples were taken in 3-h intervals and were analysed in order to evaluate the optical density, pH, dissolved oxygen tension glucose and nitrogen concentration, biomass and polymer yield.

2.7.1 Optical density mesurements

In order to verify the bacterial growth optical density of the culture was measured. A spectrophotometer using media as a blank (Single Beam Spectrophotometer, SB038, Cadex Inc.) was used at 450 nm for *Pseudomonas mendocina* CH50 where for *Bacillus subtilis* OK2 was set at 600 nm.

2.7.2 pH monitoring

The samples from the fermentation process were centrifuged at 13,200 rpm for 10 min. The supernatant was used to measure the pH using a Seven Compact pH meter (Mettler Toledo Ltd., Leicester). After the centrifugation at 13,200 rpm

for 10 min (Heraeus Pico 17 Centrifuge, Thermofisher Scientific, MA, US) the obtained pellet was dried and used for the biomass estimation.

2.7.3 Glucose estimation

Dinitrosalicylic acid (DNS) assay (Miller, 1959) was performed in order to estimate the glucose concentration. 2-hydroxy-3,5-dinitrobenzoic acid (3,5-dinitrosalicylic acid) is reacting with reducing sugars to 3-amino-5-nitrosalicylic acid, which gives brown colour product in the presence of reducing sugar. 1mL of diluted supernatant was incubated with 1 mL of the DNS reagent (section 2.7.6) in the water bath at 90°C for 10 min. 330 µL of 40 % sodium potassium tartrate solution was added to the reaction test tubes to prevent colour disappearance. The absorbance was read at 575 nm. Distilled water was used as a negative control. Glucose concentration was calculated from the calibration curve. DNS composition is shown in Table 2.5.

2.7.4 Nitrogen estimation

Phenol-hypochlorite method (Rai *et al.,* 2011) was used in order to estimate nitrogen concentration in the ammonia form. 250 µL of diluted sample as incubated with 100 µL of nitroprusside reagent and 150 µL of alkaline reagent protected from light for 45 min. The absorbance was read at 635 nm. Ammonium sulphate was used as a positive control. Distilled water was used as a negative control. Nitrogen concentration was calculated from the calibration curve prepared for ammonium sulphate. Both Alkaline hypochlorite and phenol-nitroprusside buffer are described in Table 2.6 and Table 2.7 accordingly.

2.7.5 Polymer estimation during the fermentation process

Polymer yield was estimated by extraction of the dried biomass by using chloroform/sodium hypochlorite dispersion method as described in the section 2.5.2.

2.7.6 Reagents

In order to estimate the glucose concentration Dinitrosalicylic acid (DNS) assay (Miller,1959) was performed as described in paragraph 2.7.3. The DNS reagents are shown in Table 2.5.

Table 2.5: Dinitrosalicylic acid (DNS) reagent:

Chemical compound Amount (g/L)	Chemical compound Amount (g/L)
Sodium sulphite	**0.5**
NaOH	**10.0**
Phenol	**2.0**
Dinitrosalicylic acid	**10.0**

Table 2.6 demonstrates the quantities of chloroform and sodium hypochlorite for the estimation of the polymer yield throughout the fermentation process.

Table 2.6: Alkaline hypochlorite reagent:

Chemical compound Amount (g/L)	Chemical compound Amount (mL/100mL)
NaOCl	**2.5**
1M NaOH	**40.0**

The estimation of nitrogen concentration throughout the fermentation process was measured in correlation to the ammonium sulphate concentration as described in section 2.7.4. The constituents of the phenol nitroprusside buffer are shown in Table 2.7.

Table 2.7: Phenol-nitroprusside buffer:

Chemical compound Amount (g/L)	Chemical compound Amount (g/L)
$C_6H_7NaO_7$	**3.0**
$Na_3PO_4.12H_2O$	**3.0**
$C_{10}H_{16}N_2O_8$	**0.3**
EDTA	**6.0**
Na_2 [Fe(CN)5NO].$2H_2O$	**0.02**

2.8 Film preparation by solvent casting

P(3HB), P(3HO-co-3HD) and six different blends of P(3HO-co-3HD)/P(3HB) were prepared using the solvent casting method. The PHAs were dissolved in chloroform in order to obtain a total polymer concentration of 4 wt%. The P(3HO-co-3HD)/P(3HB) blends were prepared in ratios of 90/10, 80/20, 75/25, 10/90, 20/80 and 25/75 by dissolving the required amounts of polymers in 10 mL of chloroform. A total amount 0.5 g of polymers were dissolved in chloroform and left under stirring for 24 h. After polymer dissolution, the solutions were casted in glass petri dishes that were 6 cm in diameter and dried at room temperature in the Stuart S160 incubator (Bibby Scientific Limited, Staffordshire, UK).

2.9 Composite film prearation

Polymer solutions of neat P(3HB), P(3HO-co-3HD) and 75/25 P(3HO-co-3HD)/P(3HB) blend, with a polymer concentration of 4 wt% were loaded with three different concentrations of garlic powder (23, 45 and 90 wt%), phosphate glass fibres (37, 74 and 90 wt%) and graphene oxide (0.5, 2 and 5 wt%).

For the garlic powder composites the different concentrations of garlic were stirred with the respective polymers in 10 ml of chloroform until a homogenous solution was obtained and then poured into the glass petri dishes.

The Ce-PGFs composites were prepared by the dissolution of the 75/25 P(3HO-co-3HD)/P(3HB) blend in 10 ml of chloroform. The homogenous solution was then poured into a glass petri dish. Once the polymer blend solution reached a certain viscosity, Ce-doped PGFs were added into the polymer in an aligned manner.

In the case of the GO composites the polymers were dissolved in chloroform and the different amounts of GO were simultaneously dispersed into the same solvent and sonicated for 30 min. Both solutions were then mixed and stirred constantly for 24 h. Before the solvent casting, the solution containing the polymer and the filler were sonicated for a further 45 min to ensure the optimal dispersion of GO.

2.10 Processability of PHAs for nerve conduit development

2.10.1 Single lumen PHAs conduits via dip moulding

GO composite solutions (0.5, 2 and 5 wt% of GO) fabricated using 75/25 P(3HO-co-3HD)/P(3HB) as the polymer host were selected for tube development. Nerve conduits were produced using the dip moulding method where dip conditions, i.e. concentration of the solution, number of dips, drying conditions had been optimised. Using the dip moulding technique, the dip coater PTL-MMB02 Millimeter Grade Desktop Programmable Dip Coater (1-200 mm/min) was used to obtain tubes using different the 75/25 P(3HO-co-3HD)/P(3HB) blend in order to obtain specific properties. The initial portions of the polymers were dissolved in a liquid mixture of chloroform:1,1,2,2-tetrachloroethane (70:30) wt/wt%. Mandrels with 1.8 mm diameter and 4 cm long were used to accomplish the tube formation. A set of 5 cycles was repeated four times. Each set consisted of 5 cycles with 55 sec of drying time between of each cycle. The travelling speed of the needles was 200 mm/min and the drying time between each cycle was 40 min. After the formation of the tubes they remained on the needles of the mandrels for 10 days at room temperature.

2.10.2 Nerve conduits with aligned PGFs fibres

Three different loadings of 34, 70 and 90 wt% of phosphate glass fibres were embedded into the solvent casted blend of 75/25 P(3HO-co-3HD)/P(3HB) (as described in section 2.9). After drying the composite films were rolled into a tubular structure and the edges of the film were glued with a small amount of P(3HO-co-3HD) as shown in Figure 2.1.

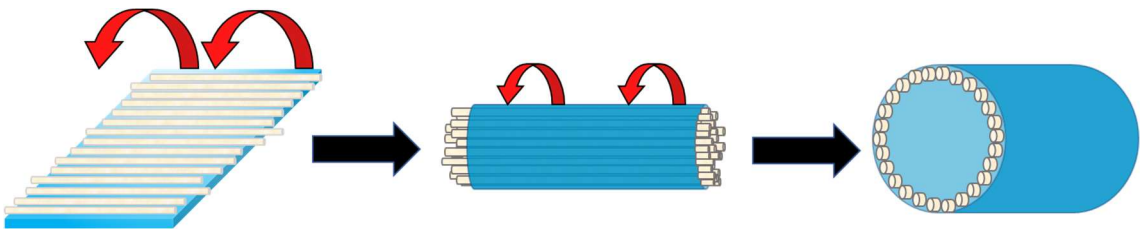

Figure 2.1*:* Process of manufacturing 3D scaffold using blend PHA and Ce-PGFs by rolling the composite mat to a tubular structure (adapted from (Kim *et al.*, 2015)).

2.10.3 Manufacture of aligned PHA microfibers by electrospinning

Electrospinning was performed using a high voltage power supply with a syringe pump and a rotating cylindrical collector (Figure 2.2) (custom made in house, Bochum, Germany). A plastic 2 mL syringe with a blunt needle (20 G) connected to the power supply was used to fabricate the fibres. The fibres were collected on aluminium foil sheet, which was used to wrap the electrically grounded collector.

Several electrospinning conditions were applied in order to fabricate fibres of different diameters and alignments. A polymer solution of 15 wt% concentration of 75/25 P(3HB)/P(3HO-co-3HD) was used under different conditions of collector speed (400, 600 and 800 rpm), syringe step (1 and 3 ml/h) and total duration of electrospinning (1, 3 and 5 min). All the fibres were electrospuned at a 10 cm distance of the syringe needle from the target collector and the voltage was constantly set at 12 kV.

The electrospun fibres will be used to confer guidance in the hollow tubes made vis the dip moulding technique.

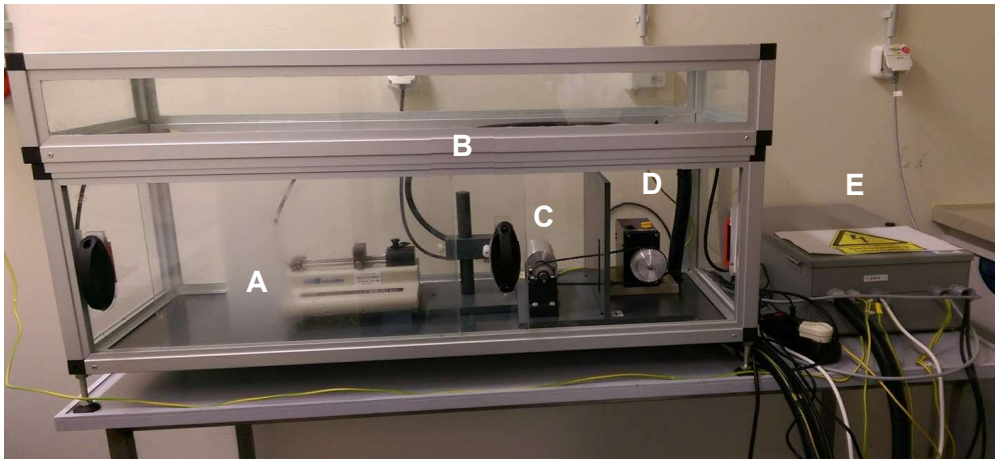

Figure 2.2: Electrospinning setup used for fabrication of aligned 75/25 P(3HB)/P(3HO-co-3HD) electrospun fibres (A) Syringe pump, (B) blunt needle connected to an electrode, (C) electrically grounded cylindrical collector, (D) electric motor, (E) voltage generator (Bochum Germany).

2.11 Antibacterial evaluation

2.11.1 Agar well diffusion method using allicin and garlic powder

Agar plates were inoculated with *S. aureus* (ATCC® 6538P™) and *Escherichia coli* (ATCC® 25922™), using a microbial suspension adjusted to 0.5 McFarland scale, which was spread over the entire agar surface. A hole with a diameter of 6 mm was punched aseptically and different volumes of the test compounds were introduced into the wells. The petri dishes were incubated at 37ºC for 24 h and the inhibition zones were measured.

2.11.2 Broth dilution method: estimation of MIC and MBC

The determination of the Minimum Inhibitory Concentration (MIC) and the Minimum Bactericidal Concentration (MBC) was done following the ISO 20776-1:2006. The broth dilution procedure was performed using 6 different bacterial strains *Staphylococcus aureus* (ATCC® 29213™), *Staphylococcus epidermidis* (ATCC® 35984™), *Escherichia coli* (ATCC® 25922™), *Pseudomonas aeruginosa* (ATCC® 27853™) and clinical isolates of Methicillin-resistant *S. aureus* (MRSA) and Methicillin-resistant *S. epidermidis* (MRSE).

A stock solution of 140 mg/ml of garlic powder in distilled water was prepared and was further diluted in Mueller-Hinton-Broth (MHB). Bacterial strains were grown overnight on blood agar plates and incubated at 37°C for 16 h. A bacterial suspension of approx. 5×10^5 CFU/mL was prepared. 50 µL of the bacterial suspension was inoculated into the wells containing dissolved garlic powder resulting in a final volume of 100 µl per well.

The first column was inoculated with 100 µL of uninoculated media (negative control) and the second column was charged with 100 µL of inoculated media (positive control). Additionally, positive control wells were used to do a colony forming units (CFU) growth control by spreading its content onto a blood agar plate (1:100 dilution). The 96-well polystyrene microtiter plate was incubated at 37ºC for 24 h.

The MIC was determined as the lowest concentration of garlic powder that prevented the appearance of visible bacterial growth. Following the MIC determination, 100 µL from the well correspondent to the MIC and three

concentrations above were entirely removed from the wells and spread onto blood agar plates with the help of a sterile loop.

The plates were incubated at 37^{o}C for 24 h. The MBC was determined as the lowest concentration of compound where 99.9 % or more of the initial inoculum was killed.

2.11.3 Prevention of biofilm formation

To assess the anti-biofilm activity of the films containing GP *in vitro* biofilm assay was performed. An inoculum of 0.5 McFarland was prepared and further diluted 200 times. The obtained suspension was added into 96 well plates and samples of polymers containing the different loadings of GP were placed on the top and incubated at 37 ^{o}C for 24 h. After incubation the samples and supernatant were carefully removed. The wells were rinsed with PBS and then fixed with ethanol for 15min. Ethanol was removed and the wells were stained with 0.1 % safranin for 5 min. Twice wash with PBS followed and wells were finally washed with 1 % SDS.100 µL aliquots were used to measure the absorbance at 490 nm. The ability of the polymer composites to inhibit the biofilm was expressed in biofilm inhibition %.

2.11.4 PHAs loaded with Garlic powder, Ce-doped PGFs and graphene oxide assessed for their antibacterial properties

All the antibacterial tests described below were conducted using composite discs cut from the original solvent cast films with the help of a puncher. Non-modified PHA discs were used as negative controls. Before each study, all samples were sterilized for 15 min on each side under the UV light.

2.11.5 Disc diffusion assay

To evaluate the release of garlic powder from the polymer matrix disc diffusion was tested against *Staphylococcus aureus* (ATCC® 29213™), *Staphylococcus epidermidis* (ATCC® 35984™), *Escherichia coli* (ATCC® 25922™), *Pseudomonas aeruginosa* (ATCC® 27853™), MRSA and MRSE. Using a sterile cotton swab, the bacterial inoculum previously adjusted to McFarland (0.5 approx. 10^{8} CFU/mL) was spread evenly on the entire surface of the agar plates. Polymer discs were placed on the agar plates and incubated at 37°C for 24 h.

After the incubation period, the zones of inhibition were measured. Antibiotic standard discs containing streptomycin (300 μg/disc), oxacillin (1 μg/disc) and gentamicin (300 μg/disc) were used as a positive control.

2.11.6 Evaluation of free planktonic cells and adhered cells on the PHA composites

In order to evaluate the antibacterial activity of the composites against both planktonic and adhered bacteria, the following study was carried out. In a 96-well plate format garlic powder discs were incubated overnight at 37ºC with 100 μL of bacterial suspension (approx. 5x 10^5 CFU/mL). After 24 h of incubation the samples were collected and washed 3 times with PBS to remove the remaining free planktonic cells from the composite. Thereafter, the polymer discs were placed inside sterile Eppendorfs and sonicated for 7 min. Aliquots of the Eppendorfs were plated in agar plates and the results were assessed using CFU method. The OD_{600} of the supernatant that remained on the 96-well plate format was measured using a microplate spectrophotometer, Thermo Scientific Multiskan GO - Thermo Fisher in order to quantify the bacterial growth.

The supernatant of the wells was also used to determine the loss of bacterial cells in the suspension compared to the non-modified samples, neat P(3HB), P(3HO-co-HD) and 75/25 blend. The bacterial strains which were tested for this assay were: *Staphylococcus aureus* (ATCC® 29213™), *Staphylococcus epidermidis* (ATCC® 35984™), *Escherichia coli* (ATCC® 25922™), *Pseudomonas aeruginosa* (ATCC® 27853™) and clinical isolates of MRSA and MRSE.

2.11.7 *In vitro* antibacterial evaluation of Graphene oxide composites

Due to graphene oxide mechanism of action, it was not possible to perform the antibacterial characterisation of this agent with the above-mentioned methods. Instead, the ISO 22196 was employed to evaluate the antibacterial activity of graphene oxide composites against *Staphylococcus aureus* (ATCC® 29213™) and *Escherichia coli* (ATCC® 25922™) using non-modified PHAs as control

samples. The nanocomposites were tested in the form of discs and the tests performed in triplicates.

This test allowed the evaluation of the antibacterial properties of the nanocomposites when bacteria were in contact with the materials. The antibacterial activity was measured by calculating the reduction of the number of bacteria in direct contact with the samples after a 24 h period of incubation. The evaluation of the viable bacterial cells was done by counting the colony forming units and the antibacterial activity was expressed using the following formula:

$$R = log(a) \times [control] - log(a) \times [modified]$$

where a is the average of the viable bacterial cells recovered after 24 h expressed as CFU/(mL × cm^2).

2.12 Cell Culture

2.12.1 L929 murine fibroblasts cell culture

L929 murine fibroblasts were obtained from The European Collection of Cell Cultures (ECACC) and grown in RPMI Medium (Sigma–Aldrich, Dusseldorf, Germany) under a humidified atmosphere of 5 % CO_2 at 37°C.The RPMI media were supplemented with 10 % (v/v) fetal bovine serum (FBS) and 1 % (w/v) penicillin/streptomycin. Experiments were carried out only when confluency of 70-80 % was achieved. After trypsinaization an number of 3 x 10^4 cells was seeded per sample in 96 well plate format and 100 µL of media.

The experiments were carried out in triplicates for a time period up to 7 days and media were exchanged every two days. The L929 cells were used between passages 2-9. All the cell culture experiments were performed in Bochum University in Germany.

2.12.2 NG108-15 neuronal cell culture

NG108-15 neuronal cells were obtained from The European Collection of Cell Cultures (ECACC) and grown in Dulbecco's Modified Eagle Medium (DMEM) (Sigma–Aldrich, Dusseldorf, Germany) under a humidified atmosphere of 5 % CO2 at 37°C. The DMEM was supplemented with 10 % (v/v) fetal calf serum, 1 % (w/v) glutamine, 1 % (w/v) penicillin/streptomycin, and 0.5 % (w/v) amphotericin B. Cells were only used in the experiments once they were 80 % -

90 % confluent. Cells were trypsinised and 3 x 10^4 cells were seeded directly onto the PHA film samples within 12 well plates in 3 mL of DMEM. The experiments were carried out in triplicates for a time period up to 7 days and media were exchanged every two days. The NG108-15 cells were used between passages 2-9. All the cell culture experiments were performed in Bochum University in Germany and Sheffield University, UK

2.12.2.1 Live/ dead measurement of NG108-15 neuronal cells

After growing the cells for 7 days, the culture medium was removed and replaced with fresh serum-free DMEM (Sigma–Aldrich, Gillingham, UK) containing 0.0015 % (w/v) propidium iodide (Invitrogen, 55B Bridge Cl, Dartford DA2 6PT, UK) and 0.001 % (w/v) Syto-9 (Invitrogen, Dartford, UK) at 37°C/5 % CO_2 for 15 min. After washing with phosphate-buffered saline (PBS) (× 3) (Sigma–Aldrich, Gillingham, UK), the samples were removed from the wells and the cells were imaged with an upright Zeiss LSM 510 confocal microscope (Zeiss, Carl-Zeiss-Strasse 22, 73447 Oberkochen, Germany).

A helium neon laser was used for the detection of propidium iodide (λex= 536 nm/λem=617 nm) while an argon-ion laser was used for Syto 9 (λex= 494 nm/λem = 515 nm). Three fields-of-view were imaged in order to express the data as a percentage of live cells ± Standard Error of the Mean (SEM). Quantification of live cells was performed using Image J and the analysis conducted on z-stack images.

2.12.2.2 Immunolabelling of neuronal cells for neurite outgrowth assessment

Fields-of-view selected at random by confocal microscopy were analysed using Image J in order to trace and assess the percentage of neurite-bearing neurons and the maximum neurite length. The length of each neurite was taken from the tip of the neurite to the cell body. Samples containing cultures of NG108-15 neuronal cells were washed three times with PBS and fixed with 4 % (v/v) paraformaldehyde for 20 min, permeabilized with 0.1 % Triton X-100 for 40 min followed by washing with PBS (× 3).

Unreactive binding sites were blocked with 3 % bovine serum albumin (BSA) for 30 min and cells incubated for 48 h with a mouse anti-β III-tubulin antibody (neuronal cell marker for NG108-15 neuronal cell culture) (1:500) (Promega, UK)

diluted in 1 % BSA at 4ºC. Cells were then washed three times with PBS before being incubated with Texas red-conjugated anti-mouse IgG antibody (1:100 dilution in 1 % BSA) (Vector Labs, USA) for 90 min. After washing once with PBS, 4′,6-diamidino-2-phenylindole dihydrochloride (DAPI) (Sigma Aldrich) (300 nM) was added to stain for nuclei and cells immersed for 15 min at room temperature, washed again three times with PBS before imaging.

An upright Zeiss LSM 510 confocal microscope using a helium-neon laser (543 nm) for Texas Red excitation (λex = 589 nm / λ_{em} = 615 nm). Nuclei were visualized by two photon excitations using a Ti: sapphire laser (800 nm) for DAPI (λ_{ex}= 358 nm / λ_{em} = 461 nm). The analysis conducted on z-stack images across a z-depth range of 90 to 130 µm.

2.13 Statistical analysis

Obtained data were presented with their mean standard deviation (mean value± SD). Statistical analysis was conducted using Graph Pad Prism 6 software to analyse the difference between data, a one-way ANOVA test ($p<0.05$) was conducted followed by Turkey's – post-test ($p<0.05$).

The differences were considered significant when p value was below 0.05 ($p<0.05$).

Chapter 3

Production and characterisation of P(3HB) and P(3HO-co-3HD)

3 Production and characterisation of P(3HB) and P(3HO-co-3HD)

3.1 Introduction

PHAs are linear polyesters produced *via* bacterial fermentation. These bio polyesters accumulate in the cytoplasm of bacteria as polymer granules as a result of carbon and energy storage linked metabolic processes which occur under unbalanced fermentation conditions such as a limitation of nitrogen and an excess of carbon sources.

They are divided into two major categories depending on the number of carbon atoms in their polymer chain. PHAs consisting of monomers with 3-5 carbon atoms are referred to as short chain length (scl)-PHAs and are generally brittle with high crystallinity while PHAs containing monomers with 6-14 carbon atoms are referred to as medium chain length (mcl)-PHAs and they are generally more elastomeric with lower melting temperatures.

Some of the most well-known scl-PHAs include poly(3-hydroxybutyrate), P(3HB) and the poly(4-hydroxybutyrate), P(4HB) homopolymers. Some examples of mcl-PHAs are poly(3-hydroxyhexanoate), P(3HHx), poly(3-hydroxyoctanoate), P(3HO) and poly(3-hydroxydecanoate) P(3HD). More than 300 microorganisms, both Gram-negative and Gram-positive, are capable of PHA synthesis (Keshavarz and Roy, 2010; Amache *et al.*, 2013; Anjum *et al.*, 2016; Li, Yang and Loh, 2016) and there are more than 150 different PHAs (Rhee, 2007; Li, Yang and Loh, 2016). Their excellent biocompatibility, bioresorbability as well as the versatility in terms of mechanical properties and degradation rate makes them promising candidates for use in biomedical applications.

This Chapter describes the production of the scl- and mcl- PHAs, P(3HB) and P(3HO-co-3HD) using glucose as the carbon source. *Bacillus subtills* OK2 and *Pseudomonas mendocina* CH50 bacterial strains were used to produce P(3HB) and P(3HO-co-3HD), respectively.

To ensure the reproducibility of the produced biopolymers the fermentation conditions such as temperature, airflow, pH, optical density (OD), biomass and

dissolved oxygen tension (DOT) were monitored throughout the process. After the extraction and precipitation of the polymer from the bacterial cells, the polyesters were fully characterised to verify their purity.

3.2 PHA production

3.2.1 P(3HB) production by *B. subtilis* OK2 using glucose as the carbon source

A 10L batch fermentation of *B. subtilis* OK2 was performed using 35 g/L of glucose as the sole carbon source for 48 h. The temporal profile of the fermentation was measured and is depicted below in Figure 3.1. The optical density (OD) was observed to gradually increase during the fermentation process, reaching a maximum value of 8 after 42 h confirming the increase of the bacterial population.

After 5 h of fermentation, the % DOT reached a value of zero, indicating rapid oxygen consumption, thus confirming active growth of the bacterial culture reaching the exponential phase. The % DOT remained at zero throughout the rest of the fermentation process, indicating active bacterial growth during the cultivation process.

The glucose concentration decreased from its initial concentration of 35 g/L to 12.3 g/L at the end of the fermentation, confirming the utilisation of the carbon source.

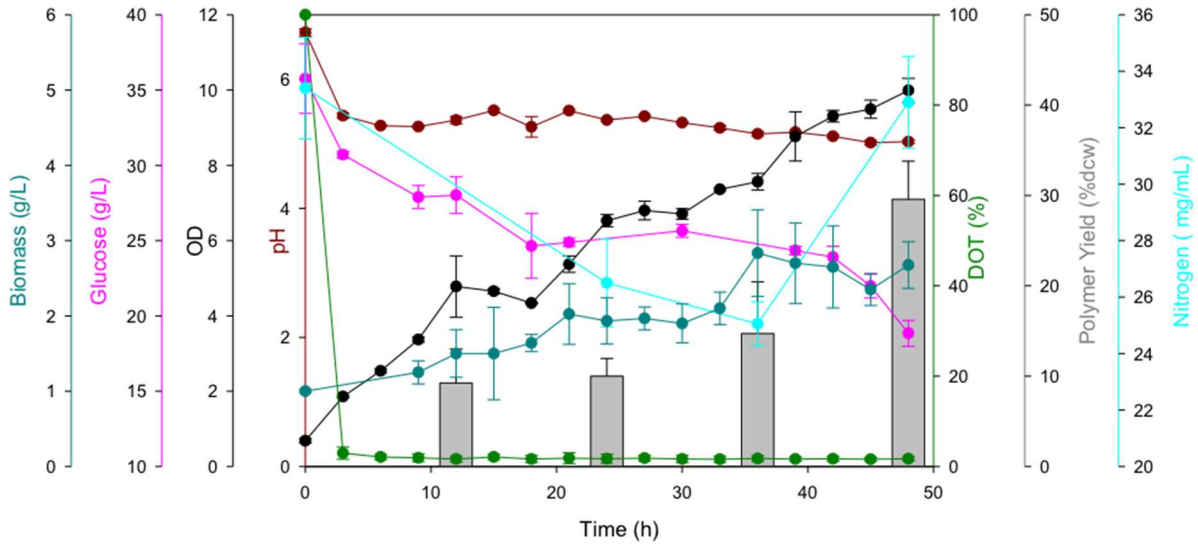

Figure 3.1: Temporal profiling of *B. subtilis* OK2 using glucose as the source of carbon.

The pH value of the production medium decreased from the starting value of 6.8 to 5.23 at 48 h. The rapid decrease of the pH at 3 h is attributed to the excess glucose in the carbon source, which was getting broken down to acetate resulting in a decrease in the pH. A slight fluctuation in pH values between 18 to 20 h is attributed to the addition of antifoaming agent which interfered with the pH value between these time points.

There was an initial decrease in the nitrogen concentration for the first 36 h of the fermentation due to the uptake of the nitrogen source by the bacteria. However, an unexpected increase in the nitrogen concentration was observed at 48 h. This increase in nitrogen could indicate the production of extracellular nitrogenous compounds by the bacteria at the end of the fermentation process. The maximum dry cell weight (DCW) obtained was 3.2 g/L after 48 h of cultivation. The synergy of the nitrogen limiting conditions coupled with the excess glucose resulted in the accumulation of the PHAs yielding 30 % dry cell weight (DCW) of polymer with a molecular weight (M_w) of 452 kDa. Figure 3.2 is a pictorial representation of the extracted and purified neat P(3HB) with a characteristic white colour.

Figure 3.2: Extracted and purified P(3HB) produced by *B. subtilis* OK2 using glucose as the source of carbon.

3.2.2 P(3HO-co-3HD) production by *P. mendocina* using glucose as the carbon source

A 20 L batch fermentation of *Pseudomonas mendocina* CH50 was carried out using 20 g/L of glucose as the sole carbon source for 48 h. A pictorial representation of the temporal profile of the fermentation is reproduced below in Figure 3.3.

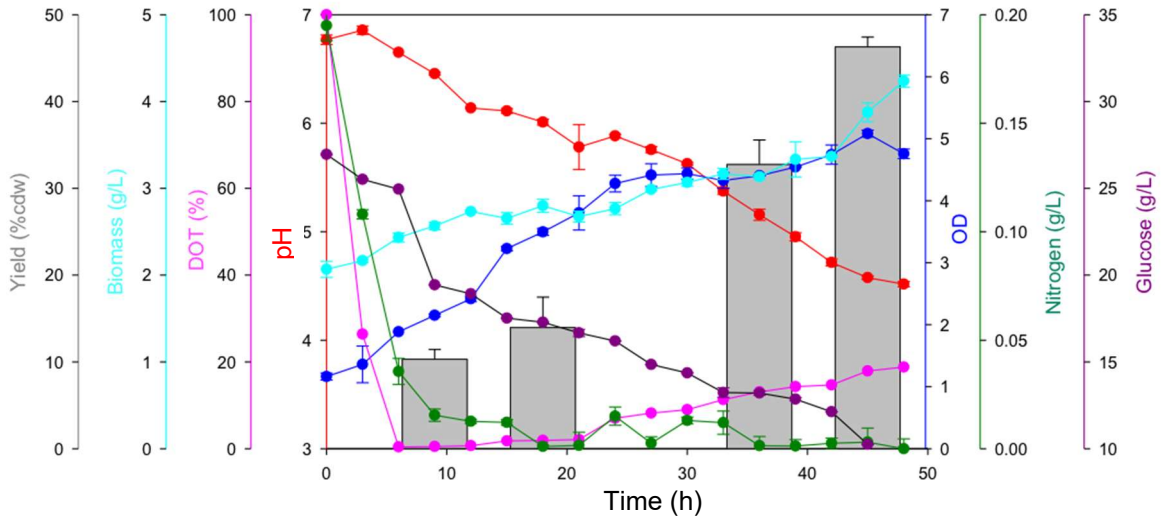

Figure 3.3: Temporal profiling of *P. mendocina* CH50 using glucose as the carbon source.

The OD_{450} value increased throughout the fermentation process, reaching a maximum value of 6. The nitrogen concentration was found to decrease drastically at around 9 h, creating a limiting condition for bacterial growth. As the fermentation progressed, it was observed that the glucose was slowly consumed throughout the fermentation process, indicated by a decrease from 20 g/L to 11 g/L. The pH of the culture medium decreased slightly from its initial value of 7 to approximately 5.5 at the end of the fermentation.

The maximum dry cell weight (DCW) obtained was 4.4 g/L after 48 h of cultivation. The synergy of the nitrogen limiting conditions and the excess of glucose resulted in the accumulation of PHAs, resulting in a polymer yield of 44.3 % DCW with a molecular weight (M_w) of 350 kDa. Figure 3.4 shows the extracted and purified neat P(3HO-co-3HD).

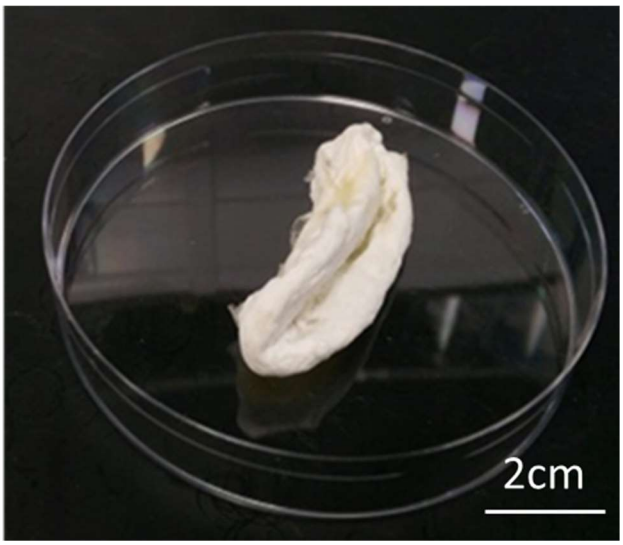

Figure 3.4: Extracted and purified P(3HO-co-3HD) produced by *P. mendocina* CH50 using glucose as the source of carbon.

3.3 PHA Characterization

3.3.1 Attenuated Total Reflectance Fourier Transform Infrared Spectroscopy (ATR/FTIR) of P(3HB) and P(3HO-co-3HD)

Preliminary confirmation of the chemical structure of the polymers produced by the batch fermentation of both *B. subtilis* OK2 (P(3HB)) and *P. mendocina* CH50 P(3HO-co-3HD)) using glucose as the sole carbon source in each case was carried out using ATR/FTIR (Figure 3.5 and Figure 3.6). Samples from the neat crude polymers produced were subjected to ATR/FTIR analysis every time a new batch of material was produced. In both cases, the ATR/FTIR spectrum revealed two bands, located between 1720 -1740 cm^{-1} and 1150-1300 cm^{-1}, corresponding to the ester carbonyl group (C=O) and the–CH group, respectively. These are characteristic bands for scl-PHAs, (Sun et al., 2007), and confirms the production of P(3HB) as shown in Figure 3.5 (Misra *et al.*, 2010).

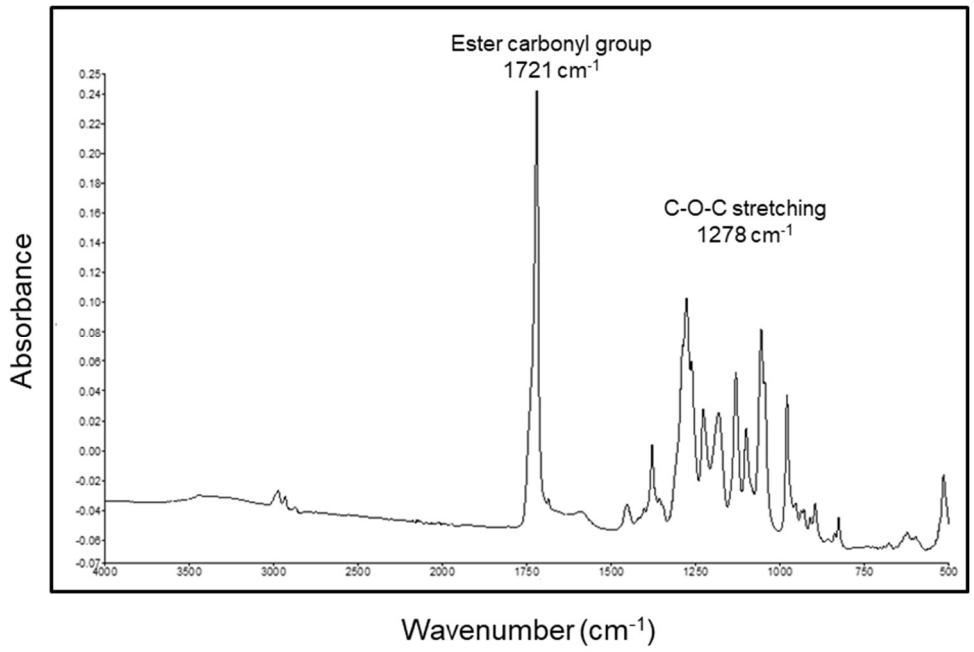

Figure 3.5: ATR/FTIR spectrum of P(3HB) produced by *B. subtilis* OK2 using glucose as the carbon source.

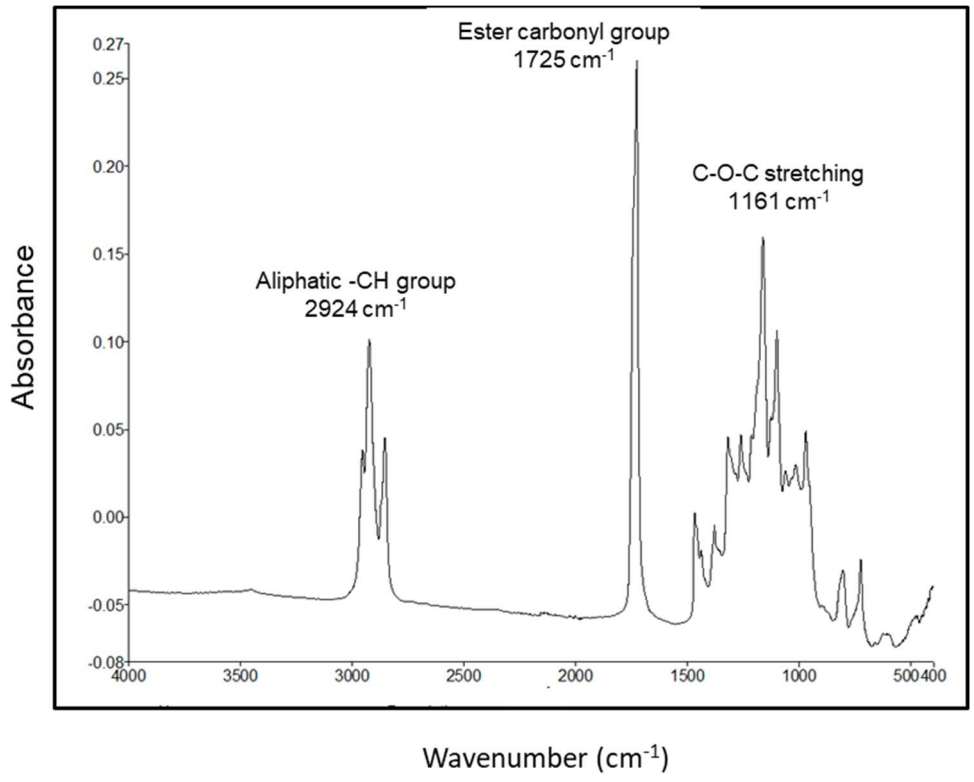

Figure 3.6: ATR/FTIR spectrum of P(3HO-co-3HD) produced by *P. mendocina* CH50 using glucose as the carbon source.

For the P(3HO-co-3HD) polymer derived from *P. mendocina* CH50, the ATR/FTIR spectrum revealed the characteristic peaks for the carbonyl and acyl groups present in mcl-PHAs which are found at approximately 1725 cm^{-1} and 1161 cm^{-1}. An additional intense peak at 2924 cm^{-1} corresponding to the stretching vibration of methylene (CH_2) groups was also found. More specifically, the triplet peak located at approximately 2924 cm^{-1} consists of the peak at approximately 2955 cm^{-1}, the main and more intense peak at approximately 2924 cm^{-1} and the peak at approximately 2855 cm^{-1} which correlate with the vibrations for CH_3, CH_2-CH_2 and CH_3-CH_2 groups respectively.

From the results of the FTIR analysis, it can be concluded that the polymer produced was an mcl-PHA (Rai *et al.*, 2011; Sharma *et al.*, 2017b). As can be seen from the ATR/FTIR spectra above, even though both polymers contain the same functional groups, the spectra obtained for each polymer contain some noticeable differences. The peaks located in the region of 3000 cm^{-1} are attributed to the vibration of the methylene group and are more prominent in the case of the P(3HO-co-3HD) compared with the weak band observed for P(3HB) which is a characteristic often used to distinguish between the mcl and the scl-PHAs (Hong *et al.*, 1999; Sharma *et al.*, 2017a). Besides, the C=O band located in the region between 1720-1740 cm^{-1} which represents the stretching mode of the ester carbonyl groups was found at lower frequencies for the P(3HB), which serves as an indication of the superior crystallinity of these polymers compared with P(3HO-co-3HD).

The changes in the spectra peaks attributed to C-O-C stretching are located at 1278 cm^{-1} in the case of the P(3HB) while they are located at 1161 cm^{-1} for P(3HO-co-3HD) and have been shown to relate to the crystalline and mobile-amorphous phases of the polymers (Kann, Shurgalin and Krishnaswamy, 2014; Sharma *et al.*, 2017b).

3.3.2 Gas Chromatography-Mass Spectrometry (GC-MS) of P(3HB) and P(3HO-co-3HD)

For further chemical characterisation, the produced polymers were subjected to methanolysis before GC-MS analysis as described in chapter 2.6.2.

The identity of the monomers highlighted during this analysis are depicted in the GC-MS spectra (Figure 3.7 and Figure 3.8). The system was calibrated using methyl benzoate as the internal standard, which gave a retention time peak at R_t=6.4 min. The peak observed at 4.1 min (Figure 3.7) was confirmed to be the methyl ester of 3-hydroxybutyric acid, 3HB, (using the NIST library), indicating that the polymer produced was poly(3-hydroxybutyrate) P(3HB).

For the mcl-PHAs, the mass spectrum resulted in two peaks identified as the methyl ester of 3-hydroxyoctanoic observed at a retention time (R_t) of 7.6 min and a methyl ester of 3-hydroxydecanoic acid observed at a retention time (R_t) of 9.6 min, indicating that the polymer produced was poly(3-hydroxyoctanoate-co-3-hydroxydecanoate) (Figure 3.8).

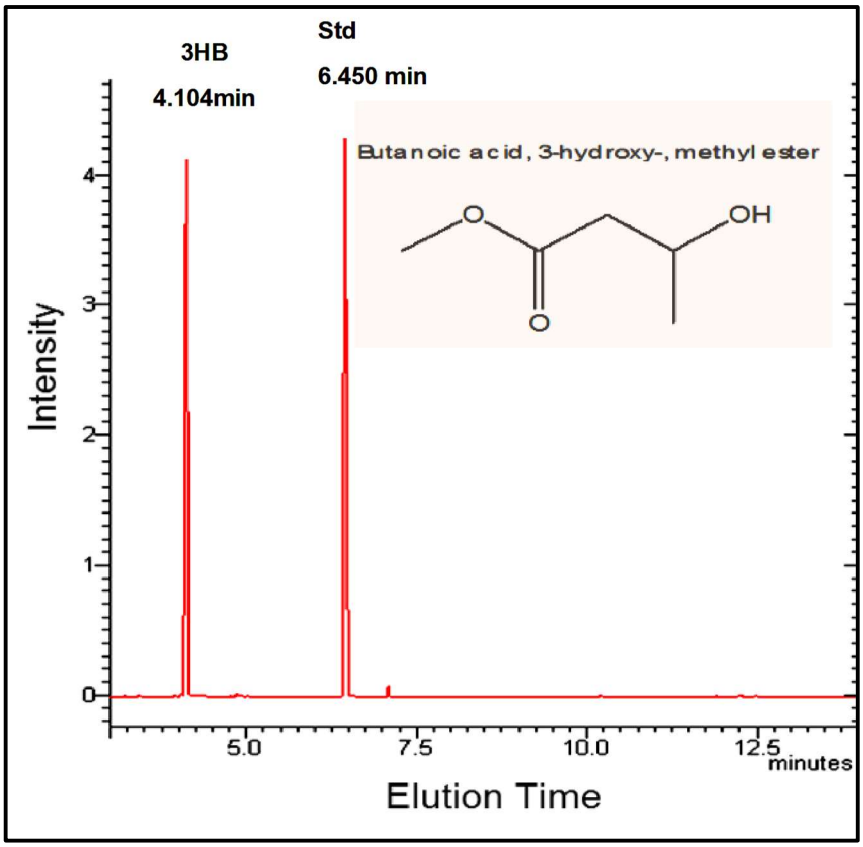

Figure 3.7:GC-MS analysis of the polymer produced by *B. subtilis* OK2 using glucose as the carbon source.

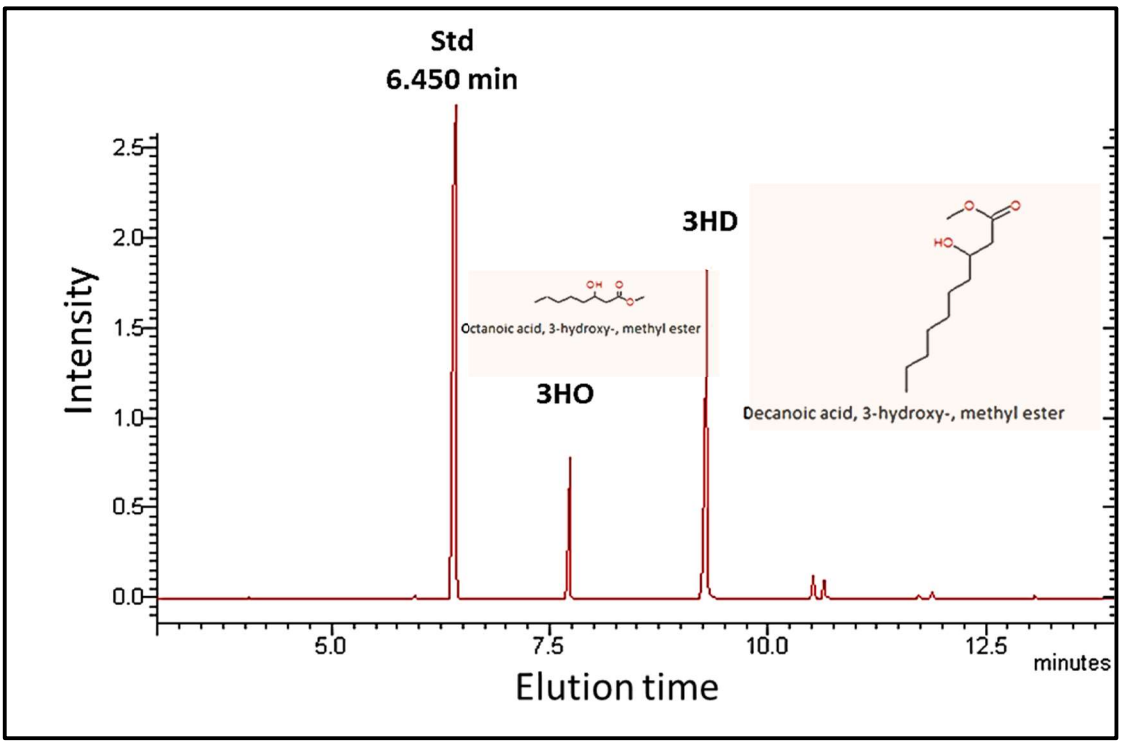

Figure 3.8: GC-MS analysis of the polymer produced by *P. mendocina* CH50 using glucose as the carbon source.

3.3.3 Nuclear Magnetic Resonance (NMR) of P(3HB) and P(3HO-co-3HD)

Proton (^{1}H) and carbon (^{13}C) NMR analysis were carried out to confirm the chemical structure of the polymers produced. For the scl-PHA produced by *B. subtilis* OK2, using glucose as the sole carbon source, the ^{1}H NMR revealed four peaks which were indicative of four different proton environments (Figure 3.9). The first peak at 1.27 ppm corresponds to hydrogens bonded within a methyl group ($-CH_3$) while the multiplet peak at 2.5 ppm and the peak at 5.26 ppm are attributed to methylene ($-CH_2$) and methine (-CH) protons bonded to carbons respectively. The ^{13}C NMR spectrum revealed four peaks associated to the different environments of the carbon atoms (Figure 3.10).

The chemical shift at 77 ppm was attributed to the carbon from the solvent $CDCl_3$. The chemical shifts observed at 169 ppm, 69 ppm, 40 ppm and 19 ppm correspond to the C_1 (C=O, carbonyl group), C_3 (-CH-, methine group), C_2 ($-CH_2$, methylene group) and C_4 ($-CH_3$, methyl group), which is the terminal carbon atom of P(3HB). Both ^{1}H NMR and ^{13}C NMR analysis were found to agree with existing literature (Doi *et al*., 1986).

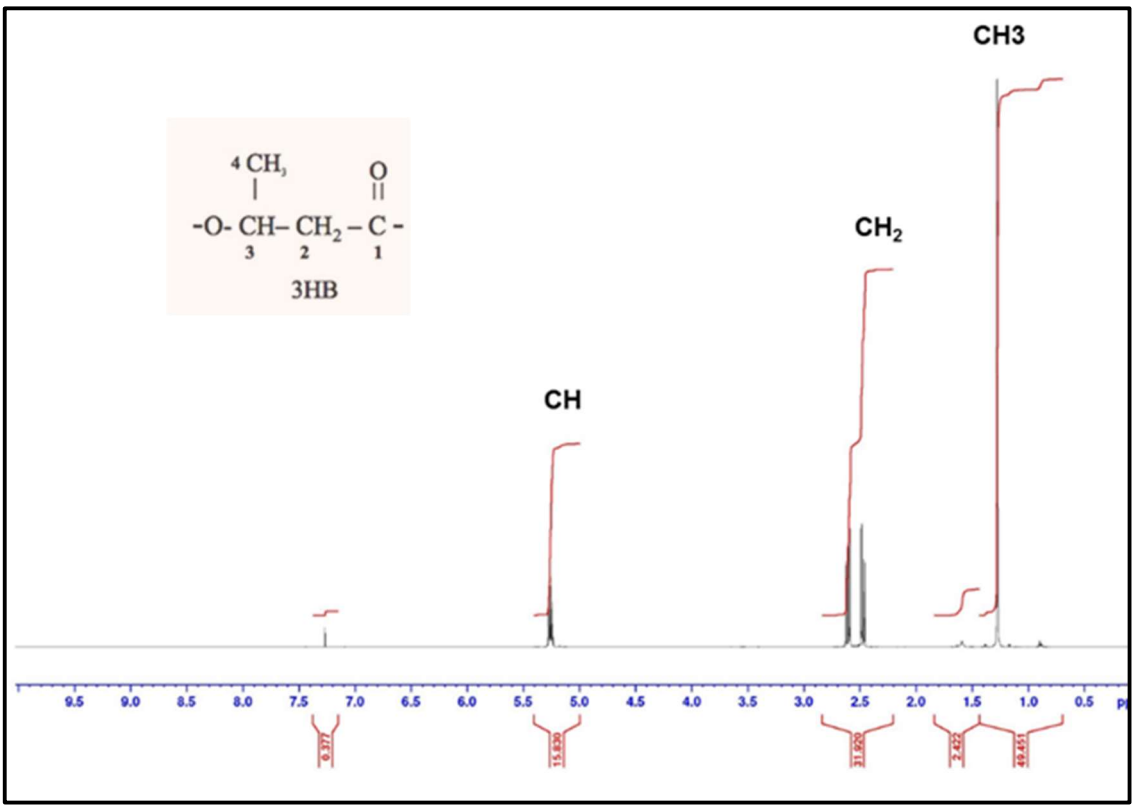

Figure 3.9: ^{1}H NMR spectrum of P(3HB).

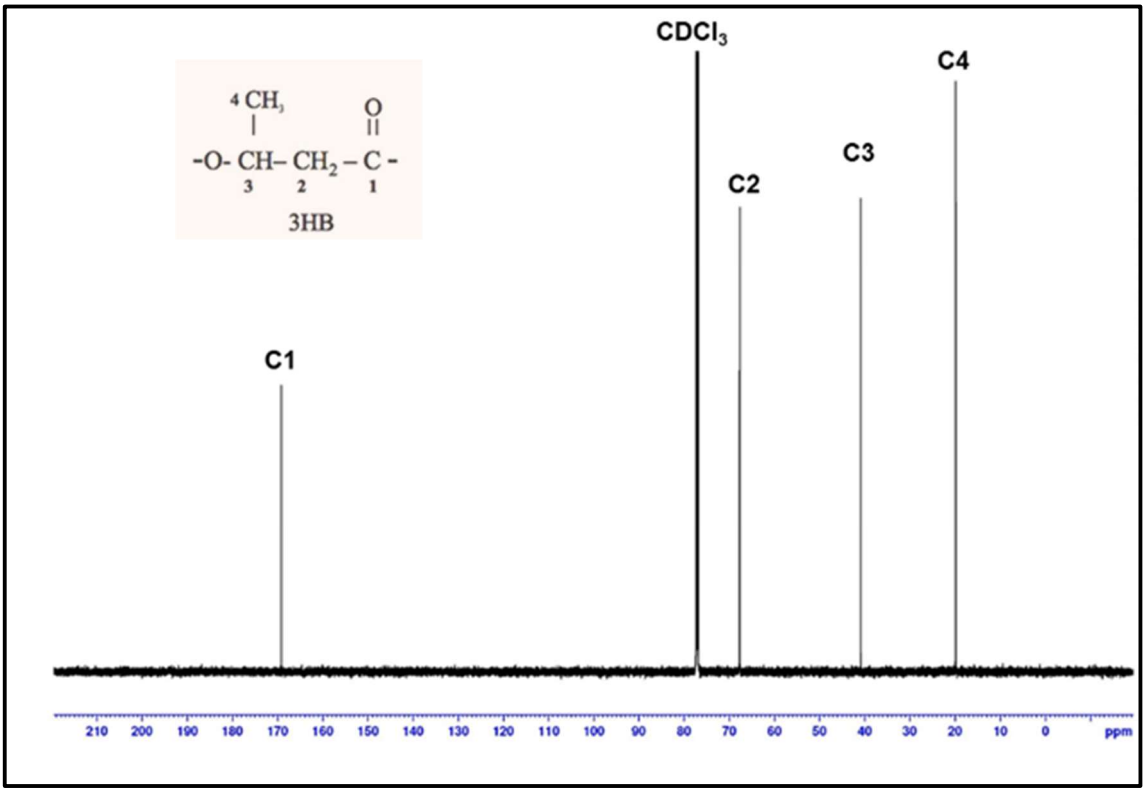

Figure 3.10: ^{13}C NMR spectrum of P(3HB).

Similarly, the ^{1}H and ^{13}C NMR spectra shown in Figure 3.11 and Figure 3.12 confirmed the molecular structure of the P(3HO-co-3HD) polymer produced by *P. mendocina* CH50 using glucose as the sole carbon source.

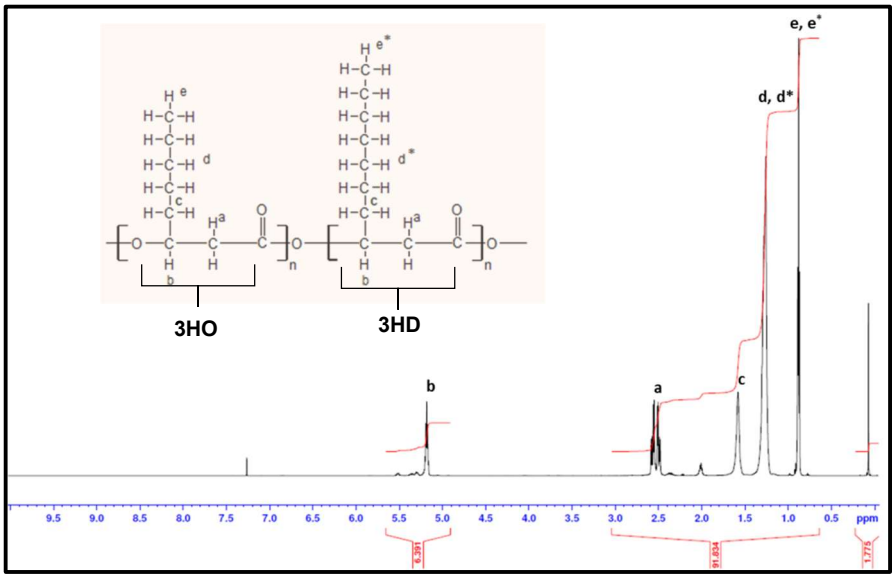

Figure 3.11: ^{1}H NMR spectrum of P(3HO-co-3HD).

The ^{1}H NMR spectrum showed five peaks associated with the five different environments for the protons expected for the target molecule. The chemical shifts located at 2.5 ppm and 5.2 ppm, correspond to the hydrogen atoms bonded to the $C_2(-CH_2)$ and $C_3(-CH)$ carbon atoms in the polymer backbone whereas the shifts located at 1.5 ppm and 1.3 ppm were attributed to hydrogens bonded to the first carbon atom of the alkyl chain $C_4(-CH_2)$ and the hydrogen atoms bonded to the main alkyl chain respectively.

Finally, the peak at 1ppm was envisaged to correspond to the hydrogens in the terminal methyl group ($-CH_3$), C_8 of 3-hydroxyoctanoate (3HO) and C_{10} of 3-hydroxydecanoate (3HD).

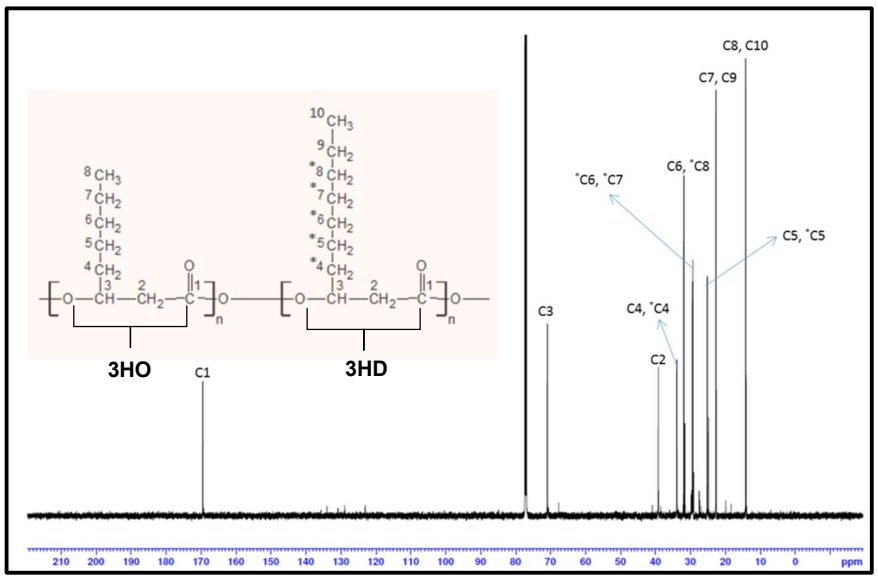

Figure 3.12: ^{13}C NMR spectrum of P(3HO-co-3HD).

The ^{13}C NMR revealed eleven peaks related to the different environments of the carbon atoms as expected. The chemical shift located at 77 ppm was attributed to the carbon from the solvent $CDCl_3$. The peaks at 169 ppm, 70 ppm, 40 ppm, 23-34 ppm and 14 ppm were envisioned to correspond to the C_1 (C=O, carbonyl group), C_3 (-CH-, methine group), C_2 (-CH_2-, methylene group), C_4, C_5, C_6, C_7 (CH_2-, methylene groups) and the C_8 (-CH_3 methyl group) respectively.

For both polymers, ^1H and ^{13}C NMR analysis further confirmed the findings from GC-MS results verifying the production of P(3HB) produced from *B. subtilis* OK2 and P(3HO-co-HD) from *P. medocina* CH50 using glucose as carbon source. Using both NMR and GC-MS it was shown that the polymers obtained were of very high purity (>90 %) due to the absence other peaks in both the ^1H and ^{13}C NMR in both cases and the absence of non- PHA peaks in GC-MS.

3.3.4 Thermal analysis – Differential Scanning Calorimetry (DSC) of P(3HB) and P(3HO-co-3HD)

The evaluation of the thermal properties of the raw materials was conducted utilising Differential Scanning Calorimetry (DSC). As described earlier in section 2.6.4. 6 mg of the polymers were exposed to cooling and heating ramps.

The thermogram obtained comprises the first (blue) and the second heating cycle (red). The first heating is applied to erase the thermal history of the material while the second provides the actual values for the thermal properties. The DSC thermogram of the P(3HB) is shown in Figure 3.13.

The analysis of the peaks highlighted on the thermograms provided the T_g, T_m and enthalpy of fusion (ΔH_f) which were found to be -3.4ºC, 173.9ºC and 80.44 J/g respectively. Also, the typical crystallisation peak for P(3HB) was identified at 49ºC.

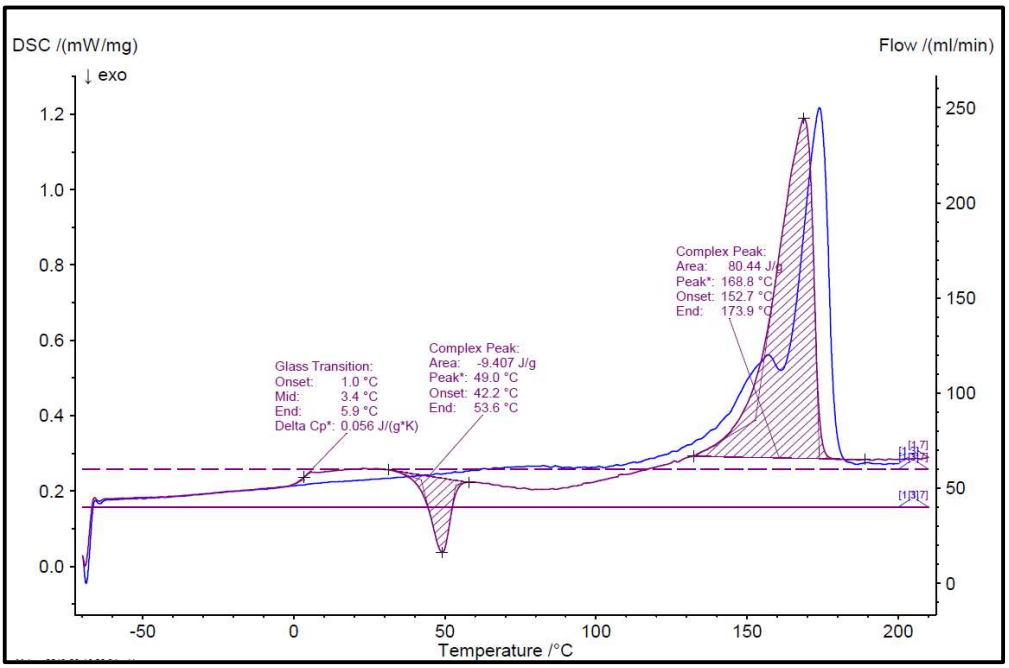

Figure 3.13: DSC Thermogram of P(3HB) derived from *B. subtilis* OK2.

The thermal values are shown in Figure 3.14. The melting temperature and enthalpy of fusion (ΔH_f) of the P(3HO-co-3HD) were found to be -47.6ºC, 58.7ºC and 17.76 J/g respectively.

No crystallisation peak was observed for the mcl-PHAs due to the amorphous nature of biopolymer. Table 3.1 summarises the thermal values for both polymers.

The degree of crystallinity (X_c) of neat P(3HB) was calculated using the following equation:

* X_C, the crystallinity degree of P(3HB) was calculated using the formula:

$$\chi_C = \frac{\Delta H_m}{\Delta H_0} \times 100\%$$

where ΔH_0 is the melting enthalpy of 100% crystalline P(3HB) (146.6 J/g) and ΔH_m is the melting enthalpy of P(3HB).

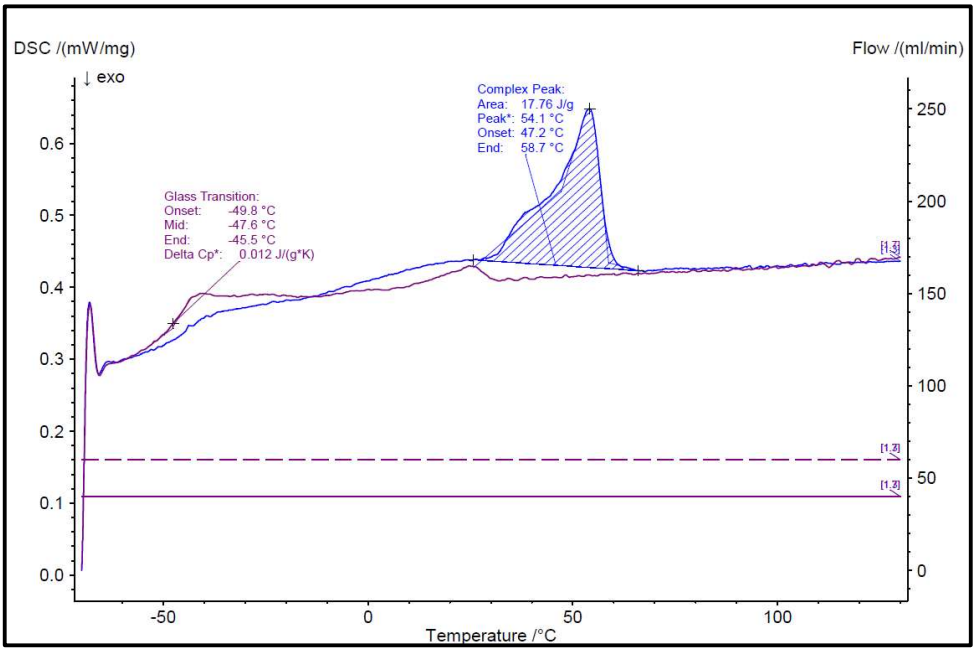

Figure 3.14: DSC Thermogram of P(3HO-co-3HD) derived from *P. mendocina* CH50.

Table 3.1: Thermal properties of P(3HO-co-3HD) and P(3HB) polymers as determined by DSC.

Sample	Glass transition temperature (T_g)	Melting temperature (T_m)	X_C, %*
P(3HB)	**-3.4 ± 0.5**	**173.9 ± 1.7**	**55.5**
P(3HO-co-3HD)	**-47.6 ± 0.9**	**58.7 ± 2.3**	**-**

3.3.5 Mechanical properties

To assess the mechanical properties of the polymers that were produced, an Instron tensile testing machine was used. Films of the polymers prepared as described above in section 2.6.5, were cut into strips of 5 mm width and 35 mm length and an average of the obtained results was used with the corresponding standard deviation.

Table 3.2 summarises the mechanical properties obtained for the produced polymers. P(3HB) was stiffer; therefore, its Young's modulus was found to be much higher (1091 MPa) than for P(3HO-co-3HD) (8.7 MPa).

Additionally, the tensile stress which P(3HB) can withstand before failure was calculated to be 21.5 MPa while in the case of P(3HO-co-3HD), the tensile strength was 14.3 MPa.

The tensile strength and the elongation at break were found to be inversely proportional values for P(3HB) which possessed a higher tensile strength. It also showed a lower elasticity, only 13.9 %, while the P(3HO-co-3HD) showed a much higher value of 609 % indicating that the mcl has a superior elasticity over the scl-PHA.

Table 3.2: Mechanical properties of P(3HB) and P(3HO-co-3HD) polymers.

Sample	Tensile strength (σ, MPa)	Young's Modulus (E, MPa)	Extension at break (ε_b, %)
P(3HB)	**21.5 ± 1.4**	**1091.5 ± 3.7**	**13.9 ± 1.9**
P(3HO-co-3HD)	**14.3 ± 1.8**	**8.7 ± 0.9**	**609 ± 2.7**

3.4 Discussion

The value of PHAs is as exciting, innovative new materials are highlighted by the number of companies that are engaged in the development and production of PHAs and the amount of interest they have generated over the last few years. China and the USA are the main countries where companies are actively producing and distributing PHAs on the market.

More specifically, Tepha, a company based in the USA, are using PHAs for medical implants (Chen, 2009). *Alcaligenes latus* is one of the most popular strains of bacteria utilised in the industry for the production of P(3HB). This wild type Gram-negative bacteria can grow in a variety of substrates such as in glucose, sucrose and molasses resulting in up to a 90 % accumulation of P(3HB) (Hänggi, 1990; Chen, 2009). Two other well-known bacterial strains that produce PHAs and are used by Tianjin Northern Food, a Chinese company, are *Ralstonia eutropha* and recombinant *Escherichia coli.* The use of *Ralstonia eutropha* and glucose as carbon source resulted in a cell density of 160 g/L from which a polymer yield of 80 % P(3HB) was achieved (Yu *et al.*, 2003).

There are several factors which can be exploited when planning a process for the scale-up of PHA production including, pH, the carbon source and the choice of bacterial strains. *Bacillus sp.* have been thoroughly investigated for their ability to produce PHAs. They can utilise a variety of carbon sources and depending on the substrate, they can produce a wide range of compositions from P(3HB) homopolymer and copolymers such as P(3HB-co-3HV), P(3HB-co-3HHx) and P(3HB-co-4HB-co-3HHx) (Łabuzek and Radecka, 2001; Valappil *et al.*, 2007, 2008; Kulpreecha *et al.*, 2009).

Bacillus sp. are one of the preferred bacterial strains for PHA production because they are a Gram-positive bacteria and lack lipopolysaccharides (LPS), which can cause immunogenic responses which have implications for the use of the PHAs in biomedical applications (Valappil *et al.*, 2006). In this study, *Bacillus subtilis* OK2, a wild-type bacteria classified as a GRAS organism by the Food and Drug Administration (FDA) was used as a P(3HB) producer (Harwood and Wipat, 1996; Sanders, Morelli and Tompkins, 2003). P(3HB) was produced from *Bacillus subtilis* OK2 using glucose as the sole carbon source. Studies reporting the yields of produced P(3HB) vary depending on the carbon source, the bacterial strains,

the mode of fermentation, the carbon/nitrogen ratio (C/N) and the limitation of the selected nutrient (Khanna and Srivastava, 2005; Verlinden *et al.*, 2007). In a previous study by Lukasiewicz, it was reported that the largest amount of P(3HB) was produced from *Bacillus subtilis* OK2 when using glucose as the carbon source. The study compared *Bacillus subtilis* OK2 with *Pseudomonas mendocina* CH50*, Cupriavidus necator* and *Bacillus cereus* SPV using a diverse range of carbon sources (Lukasiewicz, 2017). The amount of accumulated P(3HB) was 30.8 % of DCW.

The yield from the fermentation was 30 % of DCW which was similar to the 30.8 % of DCW reported in a previous study using *Bacillus subtilis* OK2 and glucose as carbon source in a batch mode of fermentation (Lukasiewicz, 2017).

On the other hand, mcl-PHAs are frequently produced from *Pseudomonas sp.* such as *Pseudomonas oleovorans, Pseudomonas putida*, *Pseudomonas aeruginosa* and *Pseudomonas mendocina* (Chan *et al.*, 2006; Kabilan *et al.*, 2012; Poblete-Castro *et al.*, 2012). The yield of the mcl-PHAs is dependent on nutrients such as nitrogen, magnesium, oxygen or phosphorus, which are the limiting factor along with an excess of the carbon source.

In this study, *Pseudomonas mendocina* CH50 was used for the production of P(3HO-co-3HD) with glucose as the sole carbon source resulting in a yield of 44.3 % of DCW of P(3HO-co-3HD) which was similar to the yield obtained by Odugbemi, who reported a yield of 43 % of DCW using the same fermentation conditions and bacteria strain (Odugbemi, 2018). The use of the same carbon source and extraction method utilised in this established fermentation and downstream process resulted in pure raw materials with minimal or no loss of product at the end of the procedure.

Complete characterisation of both types of the produced PHAs was carried out to confirm their chemical and structural identity, purity, thermal and mechanical properties. The FTIR spectrum revealed the characteristic peaks of PHAs between 1200-1300 cm^{-1} and 1700-1760 cm^{-1} which were attributed to asymmetric stretching of C-O-C and C=O groups respectively (Wu *et al.*, 2001; Kansiz *et al.*, 2007; Valappil *et al.*, 2008).

The characteristic peak from the mcl-PHA observed at 2924 cm^{-1} is consistent with literature reports and is attributed to the asymmetric vibration of the

methylene groups (-CH_2) (Hong *et al.*, 1999; Randriamahefa *et al.*, 2003). To discover what the basic monomer units were for each of the synthesised polymers, GC-MS analysis was performed. The monomer units were identified and confirmed for the produced PHAs utilising the NIST library. Different factors were found to be responsible for the thermal properties of the polymers, one of which is the length of the side chains.

As stated previously, two types of bio-polyesters: short-chain length and medium-chain length were produced. As their names imply, the short-chain length polymer consists of fewer carbon atoms than the medium-chain length polymer. For P(3HO-co-3HD), the medium-chain length polyester with long and flexible side chains provides a higher degree of freedom for rotation along the polymer chain backbone increasing their segmental mobility therefore, their melting temperature, T_m will be reduced when compared with the P(3HB) polymers (Jadhav *et al.*, 2009).

The thermal property analysis of the P(3HB) polymer found the T_g: -3.4^{o}C and T_m: 173.9^{o}C to be largely in agreement with the values reported in the literature ranging for T_g from -8.4 – 4^{o}C and for T_m 157-175^{o}C (Hu *et al.*, 2011; Bugnicourt *et al.*, 2014; Ramachandran and Amirul, 2014; Ishii-Hyakutake, Mizuno and Tsuge, 2018). As expected, the thermal properties of the mcl-PHA were completely different from the scl-PHA.

The physical properties of the P(3HO-co-3HD) polymer showed an elastomeric behaviour with T_g and T_m temperatures at -47.6^{o}C and 58.7^{o}C which are typical thermal properties for mcl-PHAs as reported in the literature (Simon-Colin *et al.*, 2007; Rai *et al.*, 2011; Rigouin *et al.*, 2019).

The mechanical properties of the P(3HB) polymer are similar to that of thermoplastics, and they show the high stiffness and crystallinity that this biopolymer exerts. Thermoplastics are polymers consisting of linear chains which gain the flexibility to move when they are heated to temperatures above their softening temperature. This change is reversible. Above this temperature, the intermolecular forces are overridden from the thermal motions yielding a viscous liquid which solidifies upon cooling (Teoh, Tang and Hastings, 2016).

The most well-known thermoplastics which are used in biomedical applications are PP (polypropylene) and PET (polyethene) both of these thermoplastics are extensively used as suture materials, surgical meshes, oxygenator membranes,

vascular grafts and scaffolds for ligaments and tendon repair (Maitz, 2015). P(3HB) has mechanical properties similar to those of isotactic polypropylene such as the Young modulus (3.5 GPa) and the tensile strength (43 MPa).
The most notable difference between the two materials is the elongation to break which is 5 % for PHB and 400 % for PP. This results in the P(3HB) polymer having a greater rigidity and brittleness than polypropylene (Sudesh, Abe and Doi, 2000; Zakaria *et al.*, 2010).

The obtained mechanical values for the P(3HB) polymer in this study are Tensile strength: 21.5 MPa, Young's Modulus: 1091 MPa and extension at break: 28.9% which are within the range of mechanical values previously reported in the literature (Sudesh, Abe and Doi, 2000; Valappil *et al.*, 2008; Singh *et al.*, 2015). The deviation in the mechanical values can be attributed to different factors such as the initial bacterial strain and the parameters of the fermentation (pH, temperature, carbon source and etch.).
For the mcl-PHA polymer, the values reported in the literature are within the ranges of 4.8-22 MPa for the Tensile Strength, 4-12 MPa for the Young's Modulus and 250-755 % for the extension at break and agree with the values found in this study (Sudesh, Abe and Doi, 2000; Rai *et al.*, 2011; Rigouin *et al.*, 2019).

The very noticeable differences between the scl and mcl-PHAs are attributed to the increasing length of side chains on the mcl-PHAs resulting in the decrease of glass transition and hence the different mechanical values (Haba *et al.*, 2007).
The short-chain of the P(3HB) consists of monomer units which confer a dense and ordered configuration on the polymer chains resulting in high crystallinity. This energetically stable conformation contributes to the formation of a stiffer and less ductile polymer. The different monomer units present in the P(3HO-co-3HD) and the long side chains on the polymer backbone allow for higher mobility of the side chains resulting in a more disordered configuration.

The mechanical and thermal values are affected by these movements and result in lower T_g and T_m values than for the scl-PHA. As shown by both the thermal and mechanical values P(3HB) is a thermoplastic with high crystallinity and stiffness while P(3HO-co-3HD) is a more malleable polymer able to withstand large deformations.

In conclusion, both P(3HB) and P(3HO-co-3HD) were successfully produced in this study using *B. subtilis* OK2 and *Pseudomonas mendocina* CH50 with glucose as the sole carbon source resulting in yields of 30 and 44.3 % DCW respectively.

A monitored process was carried out for the bacterial growth under sterile conditions, followed by the complete characterisation of the polymers produced to ascertain their identity, purity and physicochemical properties.

The obtained thermal and mechanical values meet the requirements of nerve conduits in small animal models with the range of tensile strength and Young's modulus found to be 1.4-5.7 MPa and 0.58-8.9 MPa respectively (Valappil *et al.*, 2006; Lizarraga-Valderrama *et al.*, 2015).

Chapter 4

Development of novel P(3HO-co-3HD)/P(3HB) blends, their chemical and biological characterisation

4 Development of novel P(3HO-co-3HD)/P(3HB) blends, their chemical and biological characterisation

4.1 Introduction

One of the key aspects in tissue engineering is the successful development of scaffolds which will be able to provide appropriate structural support and cell adhesion to affect the local environment to enable self-healing as an alternative to other reconstruction techniques and organ transplantation.

Over the years, biomaterials utilised as tissue engineering scaffolds have mainly consisted of biodegradable ceramics (e.g. bioglasses (BGs), metals (e.g. Mg), composites (e.g. BGs plus polymers) and polymers: synthetic, natural and hybrids (O'Brien 2011). The ideal bioartificial scaffold is one which can mimic the function of the original site of interest. The features which are desirable in materials for use as scaffolds have been specified and updated over the years.

An appropriate scaffold should possess biological, structural and chemical characteristics related to the biological requirements of the target site.
More specifically, it should be able to provide effective mechanical support, so the surrounding tissue does not undergo any compression, it should be thermally stable and remain *in situ* for an appropriate time before it's degradation and final absorption by the body. It should also be able to support cell adherence and proliferation (Eltom, Zhong and Muhammad, 2019).

Tissue engineering involves the use of a tremendously large number of polymers as starting materials, in an attempt to achieve the fabrication of the ultimate scaffold. More specific biodegradable polymers have attracted a lot of attention for their use in tissue engineering. The ideal material should have similar properties as those mentioned above but also other properties such as biocompatibility, porosity, for the exchange of nutrients, and a non-inflammatory response between the scaffold and the surrounding tissue (O'Brien 2011).

More specifically, in nerve regeneration, the most extensively used biopolymers include collagen, polyglycolic acid (PGA), poly(L-lactide-co-glycolic acid) (PLGA) polyvinyl alcohol (PVA) and poly DL-lactide-ε-caprolactone) (PLCL).

Amongst other polymers, PHAs have been investigated for their use as bio-mimetic scaffolds in tissue engineering. PHAs are naturally occurring polyesters with adjustable mechanical and thermal properties; therefore, they are promising candidates to be utilised in the fabrication of scaffolds for tissue engineering.

They are hitherto known to be biocompatible[1], biodegradable and easy to process. PHAs have been investigated for their use in many biomedical areas; both as tissue engineering scaffolds as well as medical devices class III (sutures, patches, orthopaedic pins, adhesion barriers, stents, guided tissue repair/regeneration devices, articular cartilage repair devices, nerve guides, tendon repair devices, bone marrow scaffolds, and wound dressings) (Chen and Wu 2005; Valappil *et al.*, 2006; Lim *et al.*, 2017; Ray and Kalia, 2017)).

P(3HB) is the most well studied and established antimicrobial biopolymer from the family of PHAs. Due to its mechanical properties, it is suitable mostly for hard tissue engineering. For soft tissue engineering, a more flexible and elastomeric polymer is required. Blends of scl and mcl-PHAs have previously been reported to possess the required material properties for nerve conduits.

To achieve polymers with properties, intermediate between mcl-PHAs and scl-PHAs Basnett *et al.* developed Poly(3-hydroxybutyrate)/Poly(3-hydroxyoctanoate) blended films of different ratios *via* solvent casting techniques to evaluate for their use in medical applications (Basnett *et al.*, 2013).
In another study, Lizarraga-Valderrama *et al.*, fabricated and investigated P(3HO)/P(3HB) blended films of 25:75, 50:50 and 75:25 ratios respectively for their use in nerve tissue engineering (Lizarraga-Valderrama *et al.*, 2015).

The aim of this chapter was the fabrication of a flexible PHA blend consisting of P(3HB) and P(3HO-co-3HD) for the fabrication of biodegradable and bioresorbable nerve conduits as post-traumatic peripheral nerve guidance and also their use in peripheral nerve tissue engineering. This was achieved by

[1] So far as currently known.

blending the known “biocompatible” P(3HB) with a novel mcl-PHA (P(3HO-co-3HD)) selected to provide the desired physical and biological features in the final film for the development of a nerve conduit in future.

The desired plasticising effect based on the increase of polymer-free volume was achieved by blending different ratios of the scl and mcl PHAs to obtain the required properties. Mechanical, physicochemical as well as cytocompatibility evaluation were conducted for the developed P(3HB) and P(3HO-co-3HD) films and their new biodegradable blends.

4.2 Results

4.2.1 Fabrication of films made of P(3HO-co-3HD)/P(3HB) blends

Four types of blends were prepared *via* the solvent casting technique, as previously described in section 2.8 to obtain different properties for the final films. P(3HB) and P(3HO-co-3HD) polymers (in the ratios: 80/20, 75/25, 25/75 and 20/80) were developed and characterised to evaluate their thermal and mechanical properties.

Several blends were initially developed and tested as films and finally processed to form tubes to achieve the mechanical properties required for the development of a nerve conduit. The different blends of the two PHAs are shown in Figure 4.1. Neat P(3HB) and P(3HO-co-3HD) solvent cast films were also fabricated as controls and investigated visually, physiochemically and mechanically.

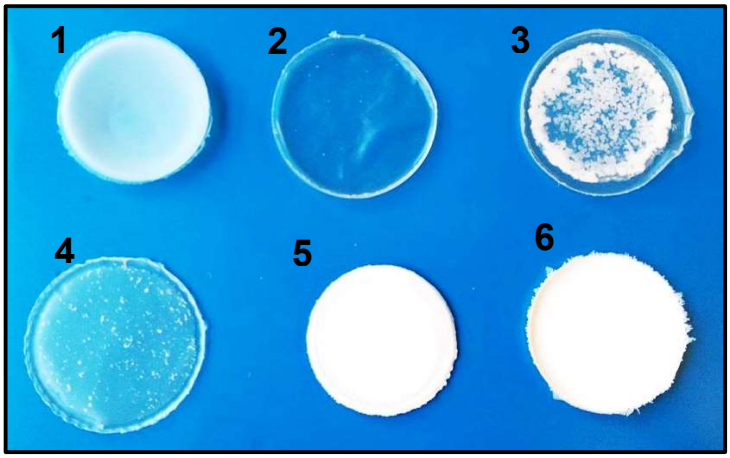

Figure 4.1: Films prepared by solvent casting technique; (1) neat P(3HB), (2) neat P(3HO-co-3HD); Blends (3) 80/20, (4) 75/25, (5) 25/75, (6) 20/80 (w/w) P(3HO-co-3HD)/P(3HB).

4.2.2 Attenuated Total Reflectance Fourier Transform Infrared Spectroscopy (ATR/FTIR) of the new PHA blends

The overlaid ATR/FTIR spectra in Figure 4.2 revealed the characteristic peaks corresponding to P(3HB), P(3HO-co-3HD) and their blends. Multiple bands were observed in the region of 1100-1320 cm^{-1} which represent the C-O-C vibrational modes both for the amorphous and crystalline regions of the polymers and polymer blends respectively.

More specifically, the C-O-C stretching bands which were observed at 1130 cm^{-1} and 1180 cm^{-1} are the most well-studied regions in the FTIR analyses of PHAs and are known as their fingerprint peaks.

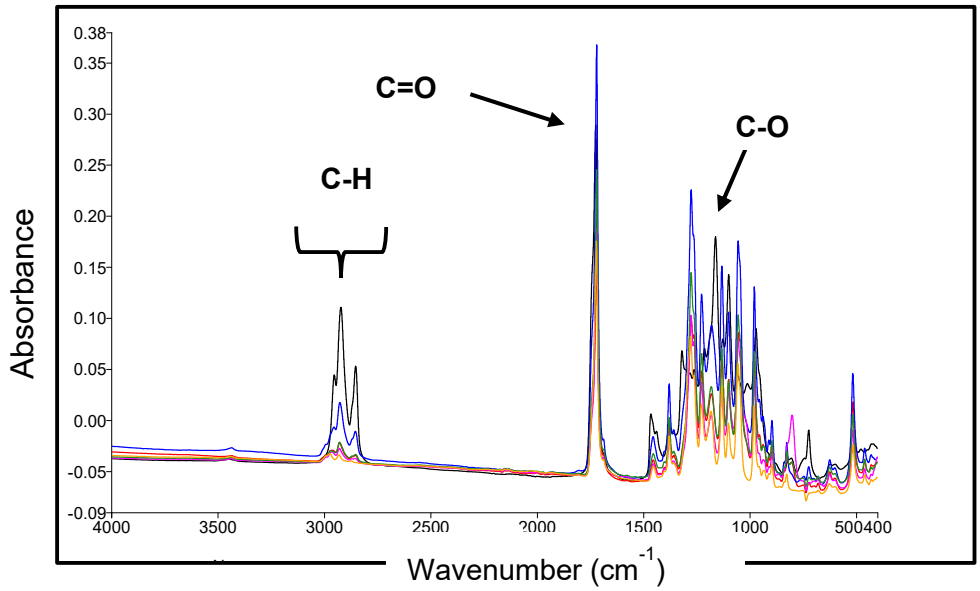

Figure 4.2: ATR-FTIR spectra of P(3HO-co-3HD)/P(3HB) films showing the characteristic peaks of P(3HO-co-3HD) and P(3HB). The FTIR spectra of the ---- P(3HO-co-3HD), ---- 80/20 P(3HO-co-3HD)/P(3HB), ---- 75/25 P(3HO-co-3HD)/P(3HB), ---- 25/75 P(3HO-co-3HD)/P(3HB), ---- 20/80 P(3HO-co-3HD)/P(3HB) and ---- P(3HB).

The band observed around 1182 cm^{-1} is attributed to the asymmetric stretching vibration of the C-O-C groups of the P(3HB). The new blends, (80/20, 75/25, 25/75 and 20/280 of P(3HO-co-3HD)/P(3HB), revealed a slight shift of this peak and was observed around 1180, 1179,1181 and 1181cm^{-1} respectively.

Table 4.1: Assignments of the peaks in the FTIR spectra of the controls and blends of P(3HO-co-3HD)/P(3HB).

P(3HO-co-3HD)/P(3HB) Films	100/0	80/20	75/25	25/75	20/80	0/100
Assignment	**Wavenumbers (cm^{-1}) of P(3HO-co-3HD)/P(3HB) films**					
C-O stretching mode, ether	1057.2	1051.4	1053.6	1055.5	1054.9	1055.4
C-O-C stretching mode	1099.1	1099.2	1099.5	1099.1	1099.6	1110.3
C-O-C stretching mode, crystalline state	ND	1130.5	1131.3	1131.9	1131.5	1131.0
C-O-C stretching mode	1161.2	1180.7	1179.8	1181.6	1181.3	1182.8
C-O-C stretching mode, amorphous state	ND	1225.8	1226.2	1226.7	1226.4	ND
C-O-C stretching mode, crystalline state	ND	1276.1	1275.6	1275.9	1275.7	1227.2 1279.0
C-O-C stretching mode, amorphous state	1318.7	ND	ND	ND	ND	ND
CH_3 symmetric deformation	1378.5	1378.9	1379.1	1379.0	1378.9	1379.3
CH_3 symmetric deformation, crystalline state	ND	1454.1	1454.9	1453.8	1453.9	1453.4
C=O stretching mode, crystalline	1725.4	1720.2	1720.4	1720.7	1720.6	1719.1
CH_2 stretching mode	2854.8	2850.7	2856.0	2866.0	2850.8	2857.8
CH_2 asymmetric stretching mode	2924.3	2930.1	2928.4	2930.8	2929.9	2936.0
CH_3 asymmetric stretching mode	2955.0	2962.7	2952.0	2968.0	2968.0	2973.3

ND, band not detected in the FTIR spectrum.

The characteristic peak for the carbonyl group corresponding to the crystalline phase in mcl-PHAs was observed at 1725 cm^{-1}, whereas for scl-PHAs this peak was observed at 1719 cm^{-1}. In the 80/20, 75/25, 25/75 and 20/280 (w/w) P(3HO-co-3HD)/P(3HB) blends the characteristic peaks assigned to the carbonyl group were located at around 1720 cm^{-1} and are attributed to the crystalline phase of the scl-PHA blend component.

The stretching vibration peaks of C-H aliphatic groups of the polymer backbones were located at 2900 cm^{-1}. Due to the longer polymer chains present in the material, these bands are stronger for mcl rather scl-PHAs. All the revealed peaks of the polymers and their blends are summarised in Table 4.1. These findings are in agreement with previous studies (Wu *et al.*, 2001; Furukawa *et al.*, 2005).

4.2.3 Thermal characterisation of the new PHA blends

Thermal characterisation of the biomaterials was carried out using Differential Scanning Calorimetry (DSC), to determine the glass transition temperature (T_g) and the melting temperature (T_m) of the neat P(3HB) and P(3HO-co-3HD) films and of the different blends.

Figure 4.3 shows the DSC thermograms of the first and second heating cycle of the obtained materials. After the first heating cycle, which is used to erase the thermal history of the polymer, samples were cooled at a controlled rate (20°C/min), and the second heating cycle is the one that provides the thermal properties of the developed blends at comparable thermal history.

A

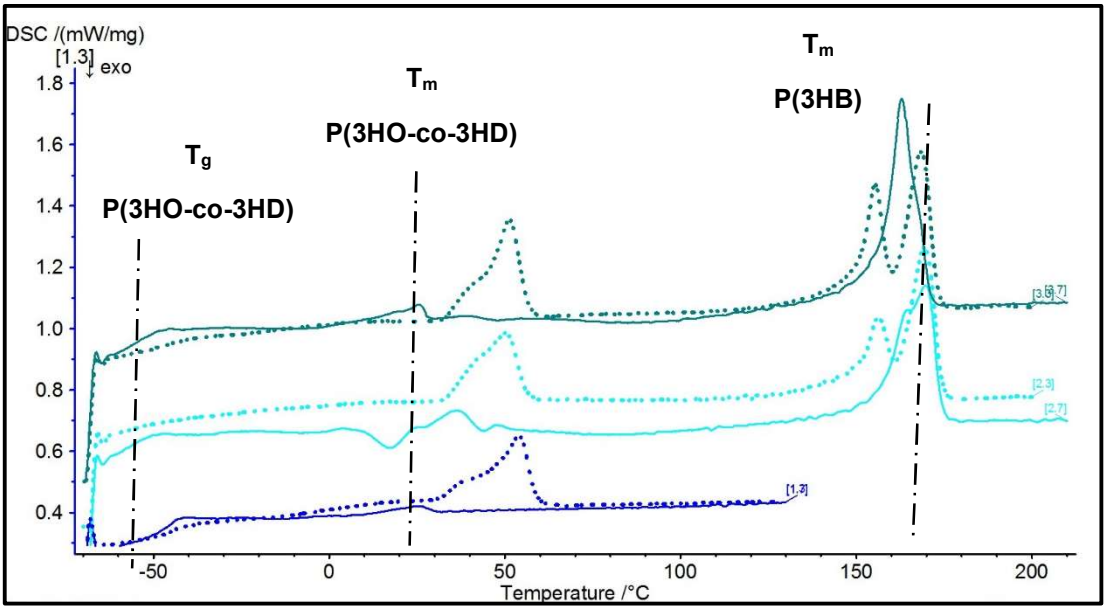

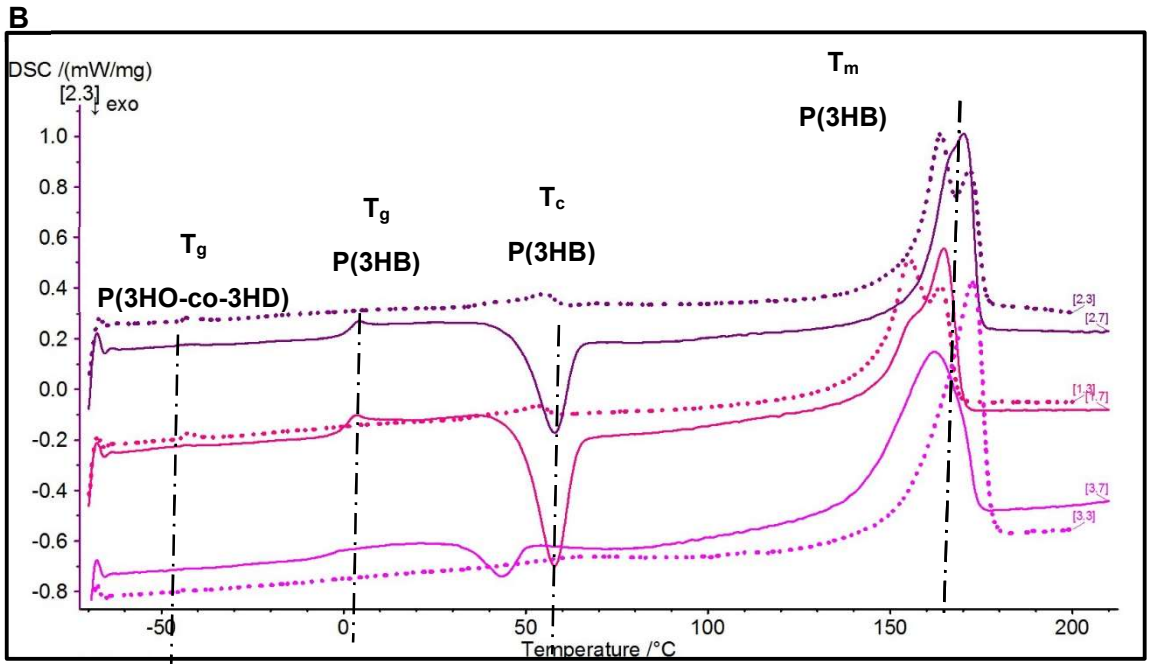

Figure 4.3: DSC thermograms of the (A): ---- P(3HO-co-3HD), ---- 80/20 P(3HO-co-3HD)/P(3HB), ---- 75/25 P(3HO-co-3HD)/P(3HB) AND (B): ---- 25/75 P(3HO-co-3HD)/P(3HB), ---- 20/80 P(3HO-co-3HD)/P(3HB) and ---- P(3HB). Dotted lines: representative thermograms of the first heating scan of the materials. Solid lines: thermograms of the second heating run.

During the second cycle of the blends containing 75 and 80 wt% P(3HB) did not show any melting event attributed to the presence of the P(3HO-co-3HD), indicating that such cooling conditions do not allow crystallisation of P(3HO-co-3HD).

Table 4.2 contains both T_g and T_m values for all the produced samples. Below the glass transition temperature, the amorphous fraction of polymer is in a glassy condition resulting in a brittle and stiff state, while at temperatures above the T_g value it becomes malleable and rubbery. P(3HB) and P(3HO-co-3HD) exhibit distinctive glass transition temperatures (T_g) and melting temperatures (T_m), at -3.4°C, -48°C and 52.8°C and 173.9°C respectively. Interestingly, the cold crystallisation temperature, which is an exothermic process observed in the second heating cycle and is a characteristic peak of P(3HB), is only present in the blends with high P(3HB) content (25/75 and 20/80 P(3HO-co-3HD)/ P(3HB)).

As the concentration of P(3HO-co-3HD) increased the melting temperature corresponding to the presence of P(3HO-co-3HD) showed proportional behaviour.

The second melting temperature observed in the blends is the melting temperature of the P(3HB) present in the films, in this case, the addition of higher amounts of P(3HB) contributed to the increase of the T_m. The addition of 20 wt% and 25 wt% of P(3HO-co-3HD) to P(3HB) showed an increase of the glass transition temperature compared to neat P(3HB), whereas the addition of 80 wt% and 75 wt% of P(3HO-co-3HD) resulted in a further reduction of the T_g compared to the neat P(3HO-co-3HD).

The thermograms of the blends illustrated the presence of two endothermic events, (T_m), characteristic for individual components, indicating the immiscible nature of the blend. The thermal values are summarised in Table 4.2.

Table 4.2: Thermal properties of P(3HO-co-3HD), P(3HB) and their blends obtained from the second heating cycle.

P(3HO-co-3HD)/P(3HB) Films	Glass transition temperature (T_g)	Melting temperature (T_m)
100/0	**-48±1.8**	**52.8±2.3**
80/20	**-49.5±0.7**	**52.3±0.2** **163.1±1.3**
75/25	**-47.4±0.9**	**51.1±0.4** **163.8±0.7**
25/75	**-2.1±1.3**	**169.8±0.9**
20/80	**-1.3±0.7**	**169.9±1.1**
0/100	**-3.4±1.5**	**173.9±1.1**

4.2.4 Mechanical characterisation of the new PHA blends

All the films made from the neat P(3HB), P(3HO-co-3HD) and the newly developed P(3HO-co-3HD)/P(3HB) blends were characterised to determine their mechanical properties. A summary of the mechanical properties for the neat polymers and their blends are shown in Table 4.3.

The addition of low weight percentage (20 and 25 wt%) of P(3HB) to the P(3HO-co-3HD) matrix, resulted in much stiffer materials compared to the neat P(3HO-

co-3HD) with the maximum Young's modulus of around 26 and 68 MPa for the developed 80/20 P(3HO-co-3HD)/P(3HB) and 75/25 P(3HO-co-3HD)/P(3HB) blends respectively, where the value of the neat P(3HO-co-3HD) was only 7.75 MPa.

The higher the content of the scl-PHA in the P(3HO-co-3HD) matrix the lower the elongation at break was, 128 and 96 % for the 80/20 P(3HO-co-3HD)/P(3HB) and 75/25 P(3HO-co-3HD)/P(3HB) respectively, compared with the initial value of 720 % of the neat P(3HO-co-3HD).

Table 4.3: Summary of the mechanical properties of P(3HO-co-3HD) produced by *P. mendocina* CH50 and P(3HB) produced by *B. subtilis* OK2 and their blends.

P(3HO-co-3HD)/P(3HB) Films	Tensile strength (σ, MPa)	Young's Modulus (E, MPa)	Extension at break (ε_b, %)
100/0	**12.2±2.1**	**7.7±0.9**	**720±5.2**
80/20	**7.5±0.5**	**26 ±2.1**	**128±1.4**
75/25	**10.2±0.0**	**68±3.9**	**96±1.6**
25/75	**5±0.0**	**177±1.9**	**48.2±6.5**
20/80	**18±0.9**	**230±3.5**	**23.5±0.6**
0/100	**20±2.3**	**776±17.1**	**13±2.3**

The addition of a low weight percentage (20 and 25 wt%) of the more elastomeric polymer P(3HO-co-3HD) to the P(3HB) matrix resulted in blend films with reduced values of Young's modulus and tensile strength than the initial neat polymer, while the elongation at break increased compared to neat P(3HB).

In the case of the P(3HB) and the blends containing a high ratio of the P(3HB), the presence of this semi-crystalline polymer have conferred higher values of the Young's modulus. P(3HB) consists of crystalline lamellae separated by a thin amorphous region. In the crystalline phase, the polymer chains are arranged in specific spatial patterns.

The P(3HO-co-3HD) and the blends fabricated with a high content of the mcl-PHA showed lower values of the tensile strength and the Young's modulus and higher values of the elongation at break, compared with the P(3HB) and the blends containing a high ratio of the P(3HB). P(3HO-co-3HD) is an amorphous polymer with highly entangled chains.

The randomly arranged molecular chains are bonded with intermolecular Van der Walls forces allowing more free movements. When a tensile load is applied, the crystalline lamellae slide past each other and begin to separate as chains unfold and become stretched. The folds in this lamellae tilt and become aligned in the load direction at this stage the ultimate strength is reached.

4.2.5 The water contact angle of the new PHA blends

To evaluate the wettability of the neat PHA films as well as the blends which were made from them, the static water contact angle was used. All the measurements were carried out in triplicate. It is generally accepted that surfaces that present a water contact angle higher than 90° are considered to be hydrophobic or water-repellent and they have a low wettability while the substances with contact angles lower than 90° are considered hydrophilic with a high wettability (Law, 2014; Almohammadi and Amirfazli, 2017; Tsai *et al.*, 2019).

As shown in Figure 4.4**,** the P(3HO-co-3HD) has a higher hydrophobicity from the P(3HB). When looking at the blended films, the water contact angles of the P(3HO-co-3HD)/P(3HB) films increased as the amount of P(3HO-co-3HD) increased (0/100 P(3HO-co-3HD)/P(3HB): 72.42±0.66°, 25/75 P(3HO-co-3HD)/P(3HB): 86.14±0.57°, 20/80 P(3HO-co-3HD)/P(3HB): 88.46±0.19°, 75/25 P(3HO-co-3HD)/P(3HB): 91.33±1.52°, 80/20 P(3HO-co-3HD)/P(3HB): 95.66±1.07° and 100/0 P(3HO-co-3HD)/P(3HB): 102.39±1.21°).

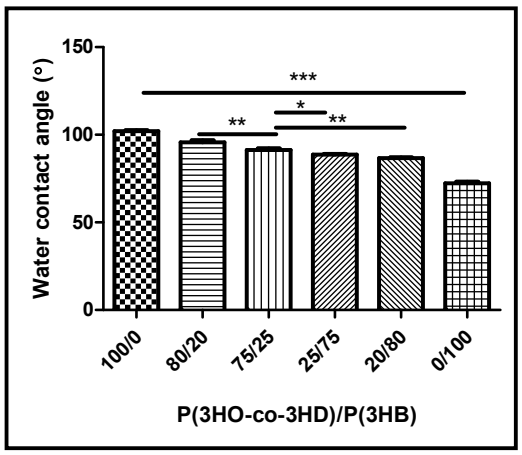

Figure 4.4: Static WCA values of the neat P(3HB) and P(3HO-co-3HD) films and their blends (n=3; error bars=±SD).

The long hydrophobic aliphatic chains of the P(3HO-co-3HD) contribute to the increase of hydrophobic behaviour of the blends. The statistical analysis showed that the difference between P(3HB) and all the other films was significant (p-value < 0.05).

The water contact angles of the blended films containing the higher amounts of P(3HO-co-3HD) were greater than 90° and hence they were considered to be hydrophobic. In contrast, the 25/75 P(3HO-co-3HD)/P(3HB) and 20/80 P(3HO-co-3HD)/P(3HB) showed water contact angles lower than 90° and therefore considered to be hydrophilic.

4.2.6 Scanning Electron Microscopy of the new PHA blends

SEM was used to examine the surface morphology of polymer films. As shown in Figure 4.5**,** both in the lower and higher magnifications when in the blend, the P(3HO-co-3HD) is the dominant polymer with the surfaces of the samples being very smooth and homogenous.

The higher the amount of the P(3HB) in the binary system of the polymers, the higher the number of changes observed in the morphology creating voids on the surface of the samples.

As shown in Figure 4.5 e, f, g and h which are the SEM pictures for the 25/75 P(3HO-co-3HD)/ P(3HB) and 20/80 P(3HO-co-3HD)/ P(3HB) respectively the increase of P(3HB) amount from 75 to 80 % resulted in bigger and less homogenous holes on the surface of the film.

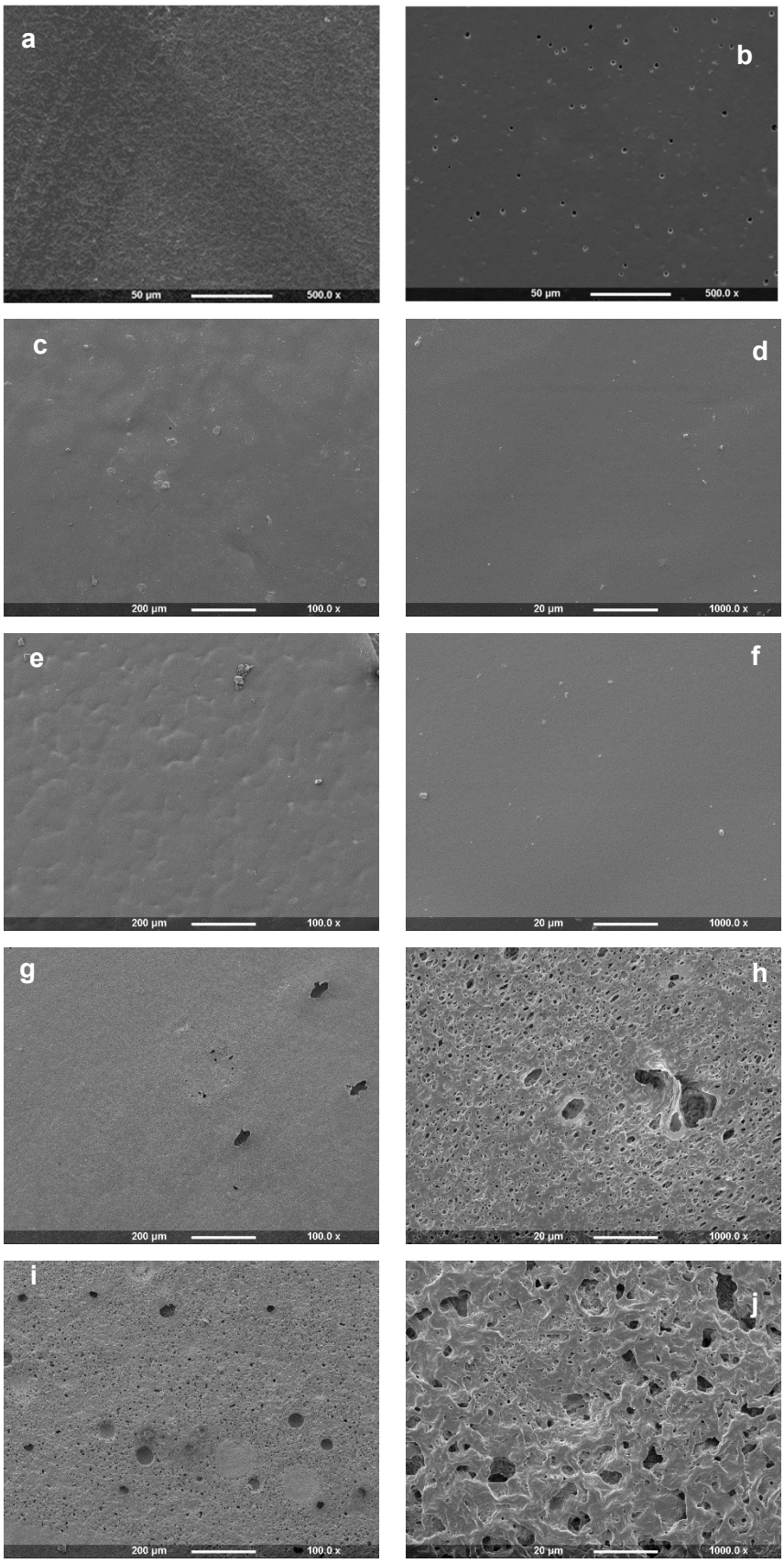

Figure 4.5: SEM images of (a) P(3HB), (b) P(3HO-co-3HD) (c), (d) 80/20 P(3HO-co-3HD)/P(3HB), (e), (f) 75/25 P(3HO-co-3HD)/P(3HB), (g), (h) 25/75 P(3HO-co-3HD)/P(3HB) and (i), (j) 20/80 P(3HO-co-3HD)/P(3HB) with high and low magnification.

4.2.7 XRD analysis of the new PHA blends

As shown in Figure 4.6, the addition of the P(3HB) to the P(3HO-co-3HD) resulted in a XRD spectra containing the characteristic peaks attributed to both the scl and mcl-PHAs. For the P(3HB), the observed peaks were sharp and narrow consistent with the high crystallinity of the polymer.

The peaks observed for the neat P(3HB) situated at 13.8°, 16.9°, 21–23°, 25.5°, 27.2° and 44° can be attributed to the (020), (110), (101)/(111) (121), (040) and (222) orthorhombic crystal planes respectively. These values are in agreement with findings from previous studies (Yokouchi *et al.*, 1973; Galego *et al.*, 2000; Anbukarasu, Sauvageau and Elias, 2016).

In contrast with the peaks mentioned above, attributed to the α-form crystals of P(3HB), the peak revealed at 2θ of 20° is related to the β-form crystal with a planar zigzag conformation which results from the amorphous domains between helix α-form lamellae (Wang and Hsiue, 2017).

The amorphous state of P(3HO-co-3HD) was represented in the diffractogram by diffraction peaks situated at around 18° and 21°. The diffractograms of all the blends with a higher percentage of P(3HO-co-3HD) revealed that the diffraction peaks corresponding mostly to P(3HB) since it has higher crystallinity and hence results in more intensive and sharp peaks in comparison to P(3HO-co-3HD). The contributions of the diffraction peaks from the mcl-PHA were noticeable only in the region of 18-21°, where the characteristic peak of P(3HO-co-3HD) is normally situated.
Additionally, the diffractograms for the blends with ratios containing 75/25 and 80/20 of P(3HO-co-3HD)/P(3HB) displayed the intensive peaks for P(3HB) (020), (110), (101)/(111) planes suggesting that even in the presence of 80 % of P(3HO-co-3HD), P(3HB) was able to crystallise; accentuating the α-form crystal formation attributed to the peaks at 2θ = 13.8 and 16.9 which appear to be as sharp as the neat P(3HB).

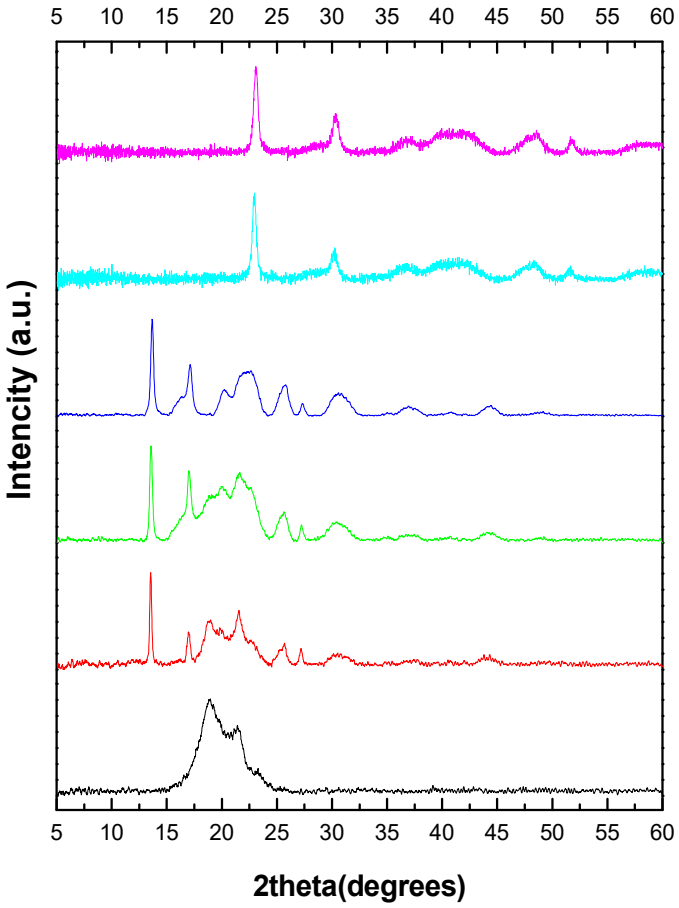

Figure 4.6: XRD spectra of: **----** P(3HO-co-3HD), **----** 80/20 P(3HO-co-3HD)/P(3HB), **----** 75/25 P(3HO-co-3HD)/P(3HB), **----** P(3HB), **----** 25/75 P(3HO-co-3HD)/P(3HB) and **----** 20/80 P(3HO-co-3HD)/P(3HB).

However, peaks corresponding to P(3HO-co-3HD) were not detected in the diffractograms of the blends with 25/75 and 20/80 of P(3HO-co-3HD)/P(3HB). Comparing the spectrum of the 25/75 and 20/80 of P(3HO-co-3HD)/P(3HB) blends with the neat P(3HB), showed that the peak positions corresponding to P(3HB) were shifted indicating that the P(3HB) unit cell changed due to the addition of the P(3HO-co-3HD) .

4.2.8 Cell Viability Studies on new PHA blends

Preliminary cell viability studies were conducted to determine the suitability of the developed polymer blend films for the fabrication of a nerve conduit. The evaluation of the neat polymers and their blends for their cytocompatibility and cytotoxicity against a well-studied L929 murine fibroblast cell line was conducted utilising both CellTiterBlue and CytotoxOne assays respectively.

The cytocompatibility was expressed as a percentage of cell viability relative to the positive control tissue culture polystyrene (TCPS) (Figure 4.7). Polyethene (PE) and TCPS were used as positive controls while a polyurethane film containing 0.1 % zinc diethyldithiocarbamate (ZDEC), supplied by Hatano Research Centre (Japan), reference material for biological tests of medical devices was used as the negative control.

The results showed that by day seven, all the polymers and the developed blends showed behaviour similar to the positive controls. All the samples exhibited cell viability higher than 80 % hence they are considered, according to ISO 10993-5, as cytocompatible materials. For all samples, the cell viability increased throughout the 168 h of cell culture, indicating high cytocompatibility for all the novel biomaterial surfaces in their direct interaction with L929.
Statistical analysis showed no significant difference ($p > 0.05$) in the percentage of the live cells for the samples of the blends and the neat polymers when compared with the positive controls by day seven. On the other hand, all the substrates showed significant differences when compared with the negative control, ZDEC ($p < 0.05$).

When tested for cytotoxicity, it was shown that the P(3HO-co-3HD), P(3HB) and P(3HO-co-3HD)/P(3HB) blends, as well as the positive controls for all the time points, did not exhibit cytotoxicity higher than 5 % as shown in Figure 4.8, verifying the non-cytotoxic nature of the new cytocompatible blends. The low percentages of cytotoxicity observed in all cases in the presence of the biopolymers (Figure 4.8) can be attributed to the overpopulation of the cells on the specific surface area provided. Since there was no space for more cells to proliferate, they remained “swimming” but alive in the culture media.

The CytotoxOne assay was used in this study as a proliferation assay protocol; hence the cells that did not manage to adhere due to the space confinement were considered as dead cells.

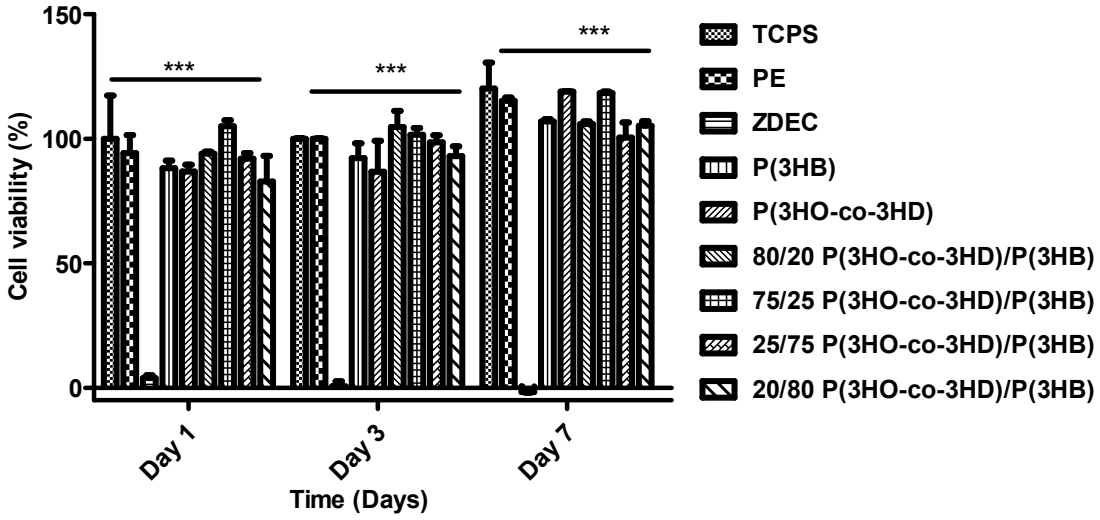

Figure 4.7: Cell viability (% TCPS) of L929 cells seeded on P(3HO-co-3HD), P(3HB) and P(3HO-co-3HD)/P(3HB) blends, PE and TCPS (positive control). (Mean± SEM, n = 9 independent experiments). Statistical significance determination is represented as *p ≤ 0.05, **p ≤ 0.01, and ***p ≤ 0.001 for cells on TCPS vs. all materials.

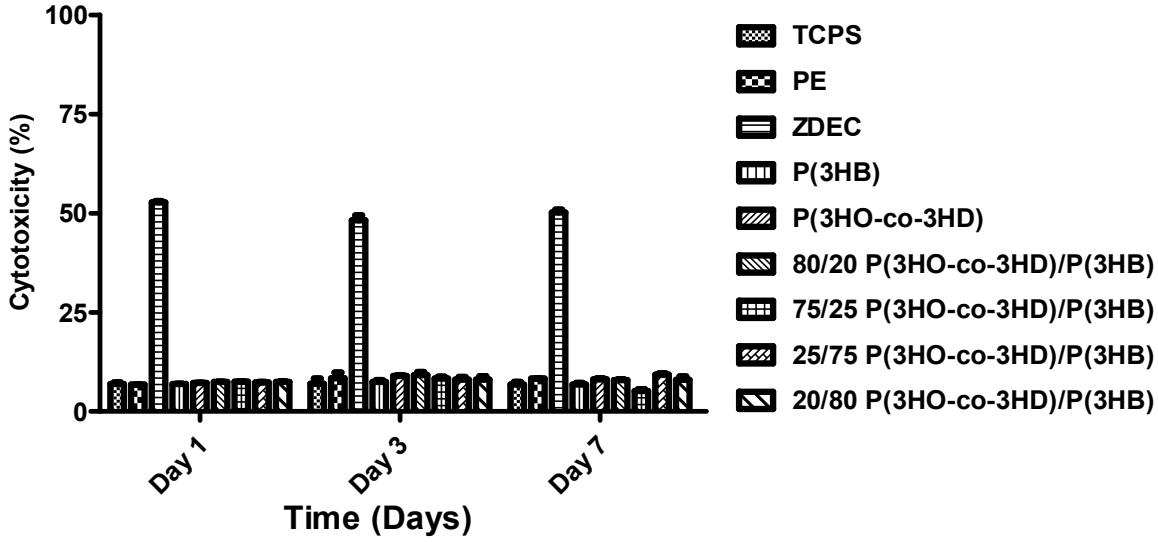

Figure 4.8: Cytotoxicity of L929 cells seeded on P(3HO-co-3HD), P(3HB) and P(3HO-co-3HD)/P(3HB) blends, PE and TCPS (positive control). (Mean± SEM, n = 9 independent experiments).

4.2.9 Cell Viability Studies on the new PHA blends using NG108-15 neuronal cells

After the cytocompatibility of the developed blends had been confirmed with the well-studied L929 cell line, cell viability studies were also carried out using a similar protocol but with the more suitable NG108-15 neuronal cells for the final assessments. Samples were seeded and evaluated for their cytocompatibility for 24, 72 and 168 h.

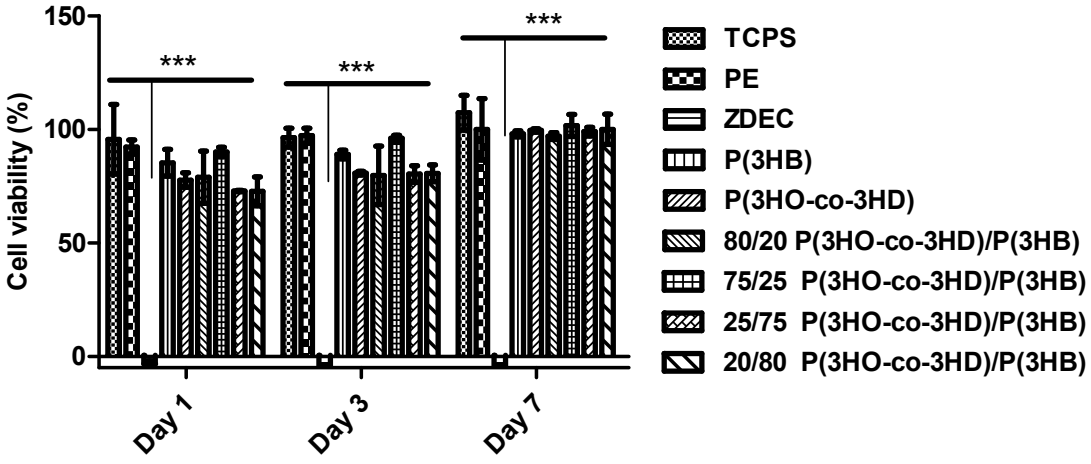

Figure 4.9: Cell viability of NG108-15 cells seeded on P(3HO-co-3HD), P(3HB) and P(3HO-co-3HD)/P(3HB) blends, PE and TCPS (positive control). Mean± SEM, n = 9 independent experiments). Statistical significance determination is represented as *p ≤ 0.05, **p ≤ 0.01, and ***p ≤ 0.001 for cells on TCPS vs. all materials.

The percentage of live cells grown on the P(3HO-co-3HD), 80/20 P(3HO-co-3HD)/P(3HB) blend, the 75/25 P(3HO-co-3HD)/P(3HB) blend, the 25/75 P(3HO-co-3HD)/P(3HB) blend, the 20/80 P(3HO-co-3HD)/P(3HB) blend and P(3HB) was found to be above 96 % in all cases by day seven with no significant differences observed from the statistical analysis for each of the substrates and the positive controls or between the substrates for all the time points.

The only significant difference that was observed was between the substrates and the positive controls with the ZDEC sample which was the negative control ($p > 0.05$) as shown in Figure 4.9.

According to ISO 10993-5, all the developed biopolymer blends are considered to be cytocompatible since they all present cell viabilities higher than 70 % throughout the experimental period. Hence, they are considered safe for their future utilisation in biomedical applications.

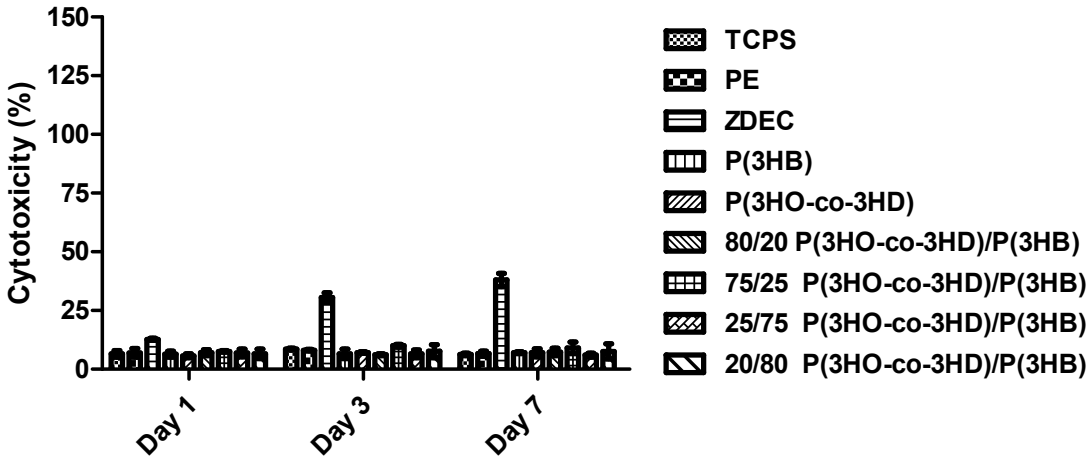

Figure 4.10: Cytotoxicity of NG108-15 cells seeded on P(3HO-co-3HD), P(3HB) and P(3HO-co-3HD)/P(3HB) blends, PE and TCPS (positive control). (Mean± SEM, n = 9 independent experiments).

The cytotoxicity of the samples was assessed using the CytotoxOne assay. Only in the case of the negative control was cytotoxicity observed, as shown in Figure 4.10. There were no cytotoxic effects observed for the substrates on the NG108-15 neuronal cells for any of the investigated time points (24, 72 and 168 h).

4.3 Discussion

The mechanical features of P(3HB) are not suitable for a range of applications and processes. Therefore, modification and tailoring of these properties are essential. Blends of P(3HO-co-3HD) and P(3HB) were developed in an attempt to alter these limiting properties.

The incorporation of P(3HO-co-3HD), as co-polymer from 20 to 80 wt%, acted as a plasticiser when added to the homopolymer, P(3HB) matrix.

The solvent casting technique was utilised to achieve the development of these blends with films fabricated in ratios of 80/20, 75/25, 20/80 and 75/25 of P(3HO-

co-3HD)/P(3HB). The synthesised blends were then physiochemically characterised and evaluated for their miscibility.

The ATR/FTIR spectra of the developed polymer blends revealed the presence of the characteristic functional group peaks attributed to both P(3HB) and P(3HO-co-3HD) bio-polyesters from which they were made. Shifts in the positions of the characteristic peaks for the P(3HB) functional groups were observed in the fabricated blends where the stretching vibration peaks of the C-H aliphatic groups of the polymer backbones located at 2900 cm^{-1} were stronger for the P(3HO-co-3HD) rather the P(3HB) dominant blends due to the longer polymer chains present in the films.

Both melting temperatures corresponding to the polymers of the binary system were observed in all blends indicating the immiscibility of the polymers in both the amorphous and crystalline phase. These phase separation problems are visually supported, exemplified the samples depicted in Figure 4.1. Similar problems with miscibility have also been reported with these types of biopolymers in previous studies (Basnett *et al.*, 2013; Lizarraga-Valderrama *et al.*, 2015).

The addition of the crystalline P(3HB) into the amorphous P(3HO-co-3HD) results in the mobility reduction of the amorphous region increasing the glass transition temperature compared with the neat P(3HO-co-3HD) sample. The addition of the amorphous nature of the P(3HO-co-3HD) bio-polyester, into the P(3HB) can reduce the formation of large spherulite crystals and secondary nucleation, which has a significant impact on the shift of the glass transition temperature to lower values and hence the effect on the mechanical properties of the final specimens.

The crystallisation peak (T_c) which is characteristic for the P(3HB) polyester was observed only for the blends with a high proportion of P(3HB), (80/20 and 25/75 of P(3HO-co-3HD)/P(3HB)) indicating that as a result of the high ratio of P(3HB) content in the blends the P(3HB) can form crystals.

The increase in the glass transition with the increase in crystallisation and the amount of P(3HB) in the blends is due to the presence of a higher amount of crystalline polymer in the amorphous matrix of P(3HO-co-3HD). The addition of P(3HB) led to the increase of the Young's modulus (E) and the reduction of the

elongation at break (ε_b %) when compared with the mechanical values of the neat P(3HO-co-3HD), which indicates that the crystallinity of the blends increased with the higher amounts of P(3HB) in the blends hence stiffer and less ductile samples were obtained as a result. Similar trends have been reported by other studies where mcl and scl-PHAs were blended (Basnett *et al.*, 2013; Lizarraga-Valderrama *et al.*, 2015; Odugbemi, 2018).

The mechanical values of the obtained blends make them suitable for use to fabricate nerve conduits since the tensile strength and Young's modulus of the obtained blends are in the range required for the support of peripheral nerve regeneration in different species such as rats and rabbits (Kwan *et al.*, 1992; Borschel *et al.*, 2003).

The XRD diffractograms confirmed the crystallisation of P(3HB) revealing well defined sharp and narrow peaks. There was no noticeable shift in the peaks corresponding to the P(3HB) polymer even with the addition of 80 wt% of P(3HO-co-3HD) in the binary system. The characteristic peaks of the P(3HO-co-3HD) were less sharp and broader than the P(3HB) peaks; however, because they were detectable, it implies that P(3HO-co-3HD) is not completely amorphous. The addition of higher amounts of P(3HO-co-3HD) to the blends, (80/20 and 75/25 P(3HO-co-3HD)/P(3HB)) altered the observed peaks of P(3HB) confirming the findings from the DSC thermograms which indicated that the blends had two melting temperatures, implying that the polymers would not be able to co-crystallize.

The SEM images showed that the P(3HB) film had a very smooth surface, whereas the P(3HO-co-3HD) films were porous. The surface topography of the 80/20 and 75/25 P(3HO-co-3HD)/P(3HB) blend samples had very smooth surfaces even under the higher magnification. On the other hand, samples of the blends with higher amounts of P(3HB) (20/80 and 25/27 of P(3HO-co-3HD)/P(3HB)) possessed voids on the surfaces of the samples. Increasing the amount of the P(3HB) from 75 to 80 wt% led to an increase in the number of holes whose distribution and size varied which was shown by the high magnifications of the SEM images. This might be attributed to the immiscibility of the two polymers, which resulted in the creation of these voids throughout the surface.

The wettability of a surface is a result of the three surface tensions: the interfacial surface tension between the solid surface and the liquid, the interfacial surface between the vapour and the solid substrate and the interface surface between the liquid and the vapour phase. The hydrophobicity of the fabricated blends here is a result of the different arrangements of the surface polymer molecules when in contact with air, during the solvent evaporation. Hence, the polymers can re-orient their hydrophobic groups towards the surface of the blend resulting in a more hydrophobic film with poor wettability. P(3HO-co-3HD) is more hydrophobic than P(3HB) and hence possesses higher contact angle values.

The methyl groups of P(3HO-co-3HD) may have rotated *via* chain rotation towards the hydrophobic interphase which is a favourable energetic orientation decreasing the surface free energy (Sabbatini, 2014; Wang *et al.*, 2017). The increase in the amount of P(3HO-co-3HD) present in the blends, therefore, resulted in a higher number of hydrophobic chains and led to poorer wettability of the surface of the films.

All blends are suitable for use as nerve conduits. The cytocompatibility of the fabricated specimens showed comparable behaviour with the positive controls. The P(3HO-co-3HD) film showed higher cell viability than the P(3HB) probably due to their different mechanical properties. Nevertheless, between the developed blends the highest number of live cells compared to the amount of neat P(3HO-co-3HD) was observed for 75/25 P(3HO-co-3HD)/P(3HB) with (118 ± 1.23 %) and (116 ± 0.78 %) of live cells by day 7. The tensile strength and the elongation at break of the 75/25 P(3HO-co-3HD)/P(3HB) could provide the appropriate elasticity and strength for its use in NGCs for the human ulnar nerve (Ma *et al.*, 2013).

In summary, in this chapter, different P(3HO-co-3HD)/P(3HB) blends were developed and fully characterised to assess their physicochemical properties. The effects of their mechanical, thermal and surface properties after the inclusion of various amounts of P(3HB) on the binary system were also investigated. Although all the fabricated blends were able to support the proliferation of L929 murine fibroblasts successfully as well as NG108-15 neuronal cells, the 75/25 P(3HO-co-3HD)/P(3HB) blend had the most suitable mechanical properties to warrant its application in peripheral nerve repair.

Chapter 5

Development of PHAs composites containing garlic powder

5 Development of PHAs composites containing garlic powder

5.1 Introduction

The efficiency and efficacy of surgical procedures such as implantation of any medical device such as: orthopaedic implants, are compromised often due to bacteria which are resistant to antibiotics. Patients that undergo surgical procedures are, in most cases, immunocompromised. They are therefore exposed to the harmful microorganisms that hospitals harbour, which places them at potentially high risk of surgical site infections (Li and Webster, 2018).

Numerous studies have revealed that nosocomial infections can have fatal outcomes for patients (McFarland *et al.*, 1989; Clabots *et al.*, 1992).
In many instances, patients have been admitted to hospital to undergo generally successful procedures; however, complications due to HAI have resulted in an increased mortality, (Centers for Disease Control and Prevention, 2016). The extensive use of antibiotics and the emergence of antimicrobial resistance have catalysed the need to explore other approaches to prevent biofilm formation on sensitive surfaces such as medical implants (Wang and Vermerris, 2016).

As an alternative, natural compounds that are inherently antibacterial are constantly being discovered and used in various medical applications (Rossiter, Fletcher and Wuest, 2017). A new area of research explores the development of biomaterials with antimicrobial properties as parts of medical devices with the potential to reduce microbial infections. The use of a combination of antimicrobial substances in conjunction with biopolymers is one of the main strategies being exploited in this line of research to address the current situation of bacterial resistance to antibiotics to prevent it worsening.

Traditionally, garlic has been renowned for millennia for its unique medical properties. Amongst other compounds that are responsible for the marvellous effects of garlic (Alliin, Ajoene, vinyldithiins, S-allylcysteine, and non-sulfur containing compounds like different enzymes, saponins, flavonoids, and maillard are the high concentration of sulphur-containing polysulfanes, consisting from hydrogen disulfide (H_2S), easing the treatment of cardiovascular disease, the reduction of high blood pressure/hypertension, its use as a natural immunity

booster, an anticancer agent, an antioxidant, an antiparasitic, an antiviral, an antibacterial, an antifungal and as an active agent against microorganisms that are resistant to antibiotics (Gebreselema Gebreyohannes and Mebrahtu Gebreyohannes, 2013). Amongst other bio-polymers, PHAs have been of heightened interest, particularly regarding their use for biomedical applications due to their biodegradability, biocompatibility and their ability not to cause any cytotoxicity (Muhammadi *et al.*, 2015).

In this chapter, PHAs containing garlic powder (GP) were evaluated for their cytocompatibility, physicochemical properties and antibacterial ability. P(3HB), P(3HO-co-3HD) and 75/25 (w/w) P(3HO-co-3HD)/P(3HB) blends were the polymer matrices chosen for this study to which different amounts of garlic powder (23, 45 and 90 wt%) sufficient to confer antibacterial activity on the final specimens were added. The different loadings of the GP were selected after preliminary broth dilution tests of the compound itself.

All neat PHA-based materials and the GP modified ones were investigated as novel biomaterials comprehensively in order to characterise their thermal and mechanical bulk properties and furthermore the physico-chemical surface properties (wettability, topomorphology and topochemistry) of film-type specimen. Finally, all novel biomaterial candidates were analysed in order to characterise their antibacterial properties and cytocompatibility with mammalian eukaryotes *in vitro*.

5.2 Results

5.2.1 Development of PHAs films and blends containing garlic powder

Scl-and mcl-PHA films, as well as 75/25 blends of scl/mcl PHAs, were impregnated with garlic powder (GP). These films were synthesised using the solvent casting technique. The PHAs were dissolved in chloroform to obtain a polymer concentration of approximately 4 wt% and then mixed overnight. The resulting polymer solution was then decanted into individual containers (i.e., snap cover glass). Different amounts of GP were then added to the respective polymer solutions (23 wt%, 45 wt% and 90 wt%) and stirred overnight until it resulted in a

homogenous solution in each situation. Finally, each mixture was poured into individual glass Petri dishes and allowed to dry for 2-7 days at room temperature. Garlic powder was chosen to be incorporated in the polymer matrixes due to its being a natural complex mixture with antibacterial capabilities.

Allicin, mentioned in the introduction, section 1.5.1, is one of the most well-known organosulphur compounds with excellent antibacterial activity. Pictures of the PHA films containing different amounts of GP appear in Figure 5.1. The non-modified polymers pose a white and opacue color in the form of films for P(3HB) and P(3HO-co-3HD) respectively. The addition of the yellowish GP in the polymers matrixes resulted in a light-yellow colour on the final specimens. Where further increase in the amount of GP resulted in a gradual change to a richer yellow shade in colour of the developed samples.

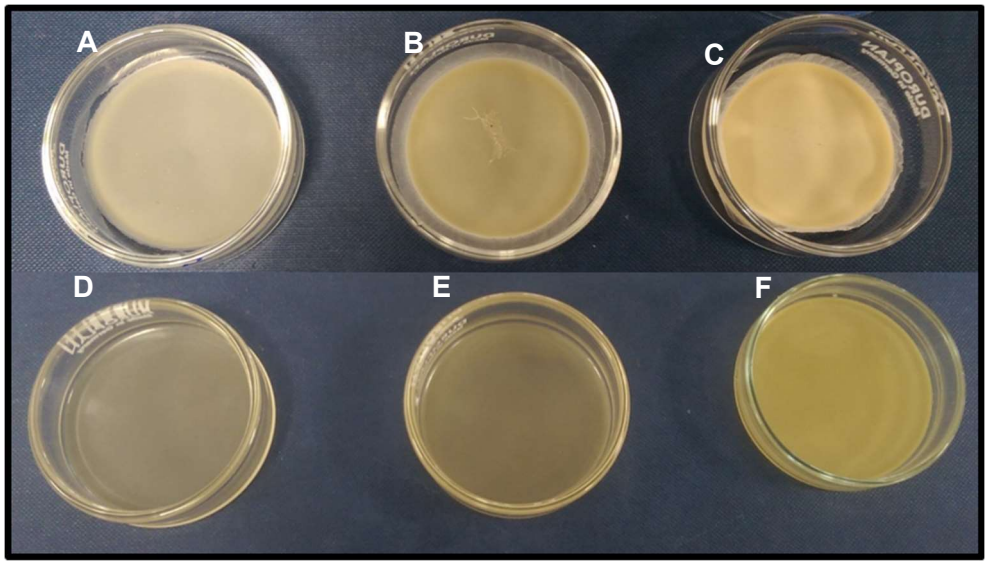

Figure 5.1: Composites of P(3HB) and P(3HO-co-3HD) containing different concentrations of garlic powder. (A) P(3HB)/ 23 wt% GP, (B) P(3HB)/ 45 wt% GP, C) P(3HB)/ 90 wt% GP, (D) P(3HO-co-3HD)/ 23 wt% GP, (E) P(3HO-co-3HD)/ 45 wt% GP and (F) P(3HO-co-3HD)/ 90 wt% GP.

5.2.2 ATR/FTIR of PHAs films and blends containing garlic powder

Preliminary investigations to examine the presence of GP on the different polymers were conducted by ATR/FTIR. The FTIR spectra of the polymer matrices reproduced in Figure 5.2, revealed the same characteristic peaks attributed to P(3HB) as described previously in section 3.3.1. Additional peaks were observed at 822 cm^{-1}, 934 cm^{-1}, 1024 cm^{-1}, 1124 cm^{-1}, 1402 cm^{-1}, 1639 cm^{-1}, 2924 cm^{-1} and 3299 cm^{-1} which correspond to the primary amine N-H of alliin, the C-H deformation of CH_2, vibrations of the primary amines C-N attributed to sulphur compounds, S=O sulfoxide absorption, OH groups of the carboxylate group, C=C allyl group, asymmetric stretching of the C-H bonds and the asymmetric C-H stretching of CH=CH group which is in close agreement with data from the literature (Figueroa-López *et al.*, 2015; Tasci, Kutuk and Koca, 2016; Barreto *et al.*, 2017).

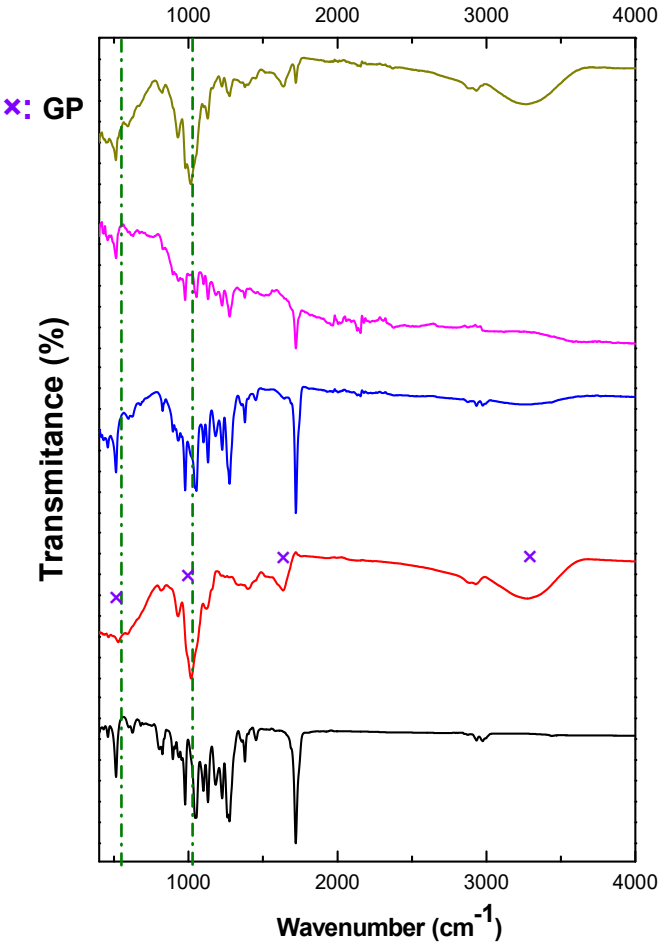

Figure 5.2: ATR-FTIR spectrum of the: ---- P(3HB), ---- GP, ---- P(3HB)/23 wt%GP, ---- P(3HB)/45 wt%GP P(3HB), ---- P(3HB)/90 wt%GP.

The higher the amount of garlic powder, the lower the intensity of the characteristic peaks of P(3HB). This reduction in intensity is exemplified by the peaks observed for the P(3HB)/90 wt% GP composite, attributed to the presence of the GP.

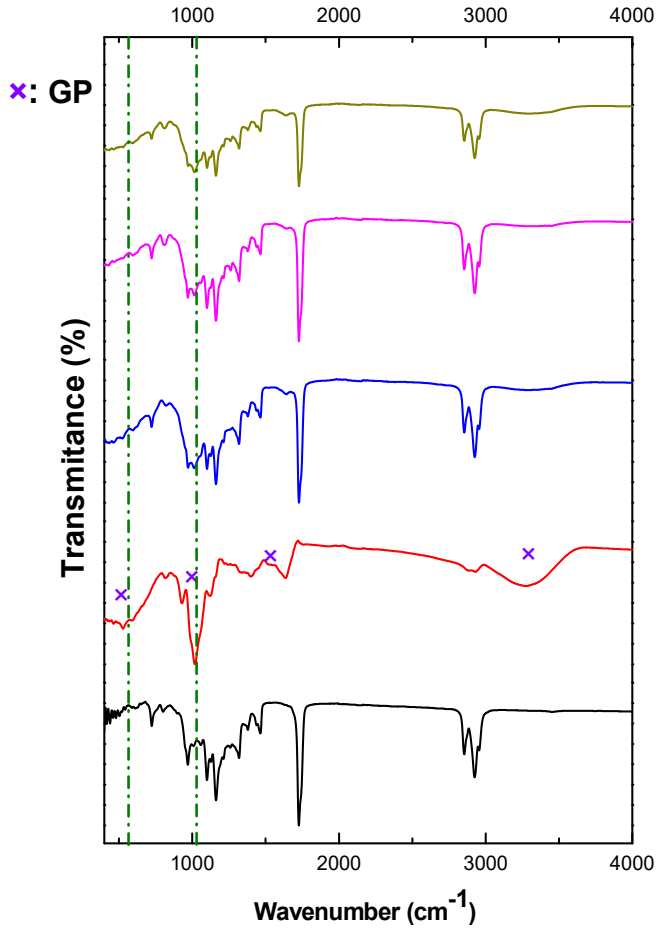

Figure 5.3: ATR-FTIR spectrum of the: ---- P(3HO-co-3HD), ---- GP, ---- P(3HO-co-3HD)/23 wt%GP, ---- P(3HO-co-3HD)/45 wt%GP P(3HB), ---- P(3HO-co-3HD)/90 wt%GP.

In order to verify the successful surface modification of the mcl-PHA with the inclusion of GP ATR/FTIR was carried out on the P(3HO-co-3HD) polymers containing three different GP loadings. As shown in Figure 5.3, the addition of GP into the P(3HO-co-3HD) matrix did not affect the peaks observed in the FTIR spectra. Interestingly, even with the higher amount of garlic powder (90 wt%), the observed characteristic peaks are attributed to the mcl-PHA as described in

section 3.3.1. Only the contribution of the stretching vibration of the primary amine groups C-N attributed to the presence of the sulphur compounds could be detected slightly at 1024 cm^{-1}.

Finally, the developed blend composites containing 23 wt%, 45 wt% and 90 wt% GP, were characterised using ATR-FTIR, as shown in Figure 5.4. The characteristic peaks of the non-modified blends have been described previously in section 4.2.2. In this case, the effect of the addition of GP is evident even at the lower concentration of 23 wt%. Characteristic ATR-FTIR peaks for GP typically found at: 822 cm^{-1}, 1024 cm^{-1}, 1638 cm^{-1}, 2932 cm^{-1} and 3286 cm^{-1} attributed to N-H primary amine groups of the alliin, stretching vibrations of primary C-N, C=C allyl group, stretching of C-H bonds and the stretching of hydroxyl groups respectively were observed in all blend composites.

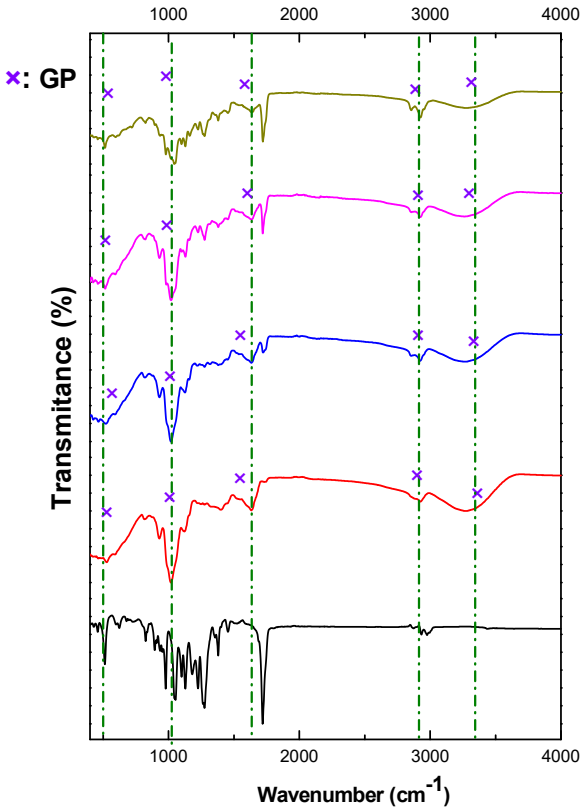

Figure 5.4: ATR-FTIR spectrum of the: ---- 75/25 P(3HO-co-3HD)/P(3HB), ---- GP and 75/25 P(3HO-co-3HD)/P(3HB) blends containing: ---- 23 wt%GP, ---- 45 wt%GP P(3HB) and ---- 90 wt%GP.

The ATR/FTIR spectra revealed the successful incorporation of GP into the three different polymer hosts showing the characteristic peaks attributed to GP. These

findings were the same for both sides of the samples indicating a homogenous final specimen.

5.2.3 Thermal characterisation of PHAs films and blends containing garlic powder

The thermal properties of the composites were evaluated by DSC to investigate the effect of the addition of GP into the composite blends. An examination of the thermal properties of the composites containing GP in comparison to the neat polymers highlighted that for the scl-PHA based composites, the addition of garlic powder increased the T_g value. Minor changes in the melting temperatures of the composites, when compared to neat P(3HB), were also observed.

The melting temperature of GP was around 140^{o}C, lower than the melting temperature of the polymer matrix. Hence, the synthesised composites were recorded with lower T_m than the P(3HB) polymer, as shown in Table 5.1.

Table 5.1: Thermal properties of P(3HB) and P(3HB) containing different amounts of garlic powder.

P(3HB) film	Glass transition temperature (T_g)	Melting temperature (T_m)
0 wt% GP	**-2±0.9**	**174±1.3**
23 wt% GP	**3.1±0.3**	**165.4±3.3**
45 wt% GP	**3.7±0.5**	**168.2±1.4**
90 wt% GP	**3.9±0.1**	**172.7±0.2**

In the case of the mcl-PHA based composites, the addition of GP resulted in a decrease in the T_g value, whereas the T_m values were very similar. In only one case, P(3HO-co-3HD) containing 90 wt% GP, a significant increase (59^{o}C) of the melting temperature was observed compared with the 54^{o}C of the neat polymer, as shown in Table 5.2.

Table 5.2: Thermal properties of P(3HO-co-3HD) and P(3HO-co-3HD) containing different amounts of garlic powder.

P(3HO-co-3HD) film	Glass transition temperature (T_g)	Melting temperature (T_m)
0 wt% GP	**-44±2.8**	**54±1.4**
23 wt% GP	**-46.5±1.1**	**54.9±0.5**
45 wt% GP	**-52±0.8**	**52.6±1.3**
90 wt% GP	**-48.5±1.4**	**59±0.4**

Additionally, composites based on the 75/25 P(3HO-co-3HD)/P(3HB) containing the three different loadings of GP were synthesized. The results are reproduced below in Table 5.3**.**

Table 5.3: Thermal properties of 75/25 blends of P(3HO-co-3HD) and P(3HB) containing garlic powder.

75/25 /P(3HO-co-3HD)/P(3HB) blend	Glass transition temperature (T_g)	Melting temperature (T_m)
0 wt% GP	**-42±0.2**	**56.5±0.1**
23 wt% GP	**-42.2±0.6**	**57.6±0.8**
45 wt% GP	**-42.8±1.4**	**56.6±2.1**
90 wt% GP	**-42.9±0.9**	**56.5±0.8**

The glass transition temperature of the composite blends containing the garlic powder decreased with the addition of GP. No significant change was observed to the melting temperatures of the final blend composites when compared to the neat polymer.

5.2.4 Mechanical characterisation of PHAs films and blends containing garlic powder

Mechanical characterisation of all the developed novel biomaterials containing GP was carried out in order to investigate their mechanical properties. The use of GP was mainly to confer antibacterial activity to the polymeric hosts. However, GP is a solid powder and its features such as the particle size could influence both the thermal and mechanical properties of the neat PHAs candidates and their blends.

Additionally, these studies highlighted other valuable information regarding the effect of the filler (GP) on the polymer matrix. A summary of the mechanical properties of the neat polymers and their composites are summarised below in Table 5.4, 5.5 and 5.6, respectively.

The addition of GP into the P(3HB) polymer matrix resulted in a decrease of the tensile strength compared with the neat polymer. Addition of GP to 45 wt% within the P(3HB) polymer matrix resulted in a decrease in the value of the Young' s modulus, whereas an observed increase in elongation at break. Further increases of the filler concentration led to a stiffer and less elastomeric material increasing the Young's modulus and tensile strength values.

Table 5.4: Mechanical properties of P(3HB) and P(3HB) containing garlic powder (GP).

P(3HB) film	Tensile strength (σ) (MPa)	Young's Modulus (E) (MPa)	Elongation at break (ε_b%)
0 wt% GP	**20±2.3**	**776±17.1**	**13±2.3**
23 wt% GP	**2.7±0.8**	**176±51**	**2.2±0.7**
45 wt% GP	**2.07±0.2**	**103±19**	**12.2±4.1**
90 wt% GP	**2.7±1.5**	**231±128**	**1.2±0.4**

Table 5.5: Mechanical properties of P(3HO-co-3HD) and P(3HO-co-3HD) containing garlic powder (GP).

P(3HO-co-3HD) film	Tensile strength (σ) (MPa)	Young's Modulus (E) (MPa)	Elongation at break (ε_b%)
0 wt% GP	**12.2±2.1**	**7.8±0.9**	**720±5.2**
23 wt% GP	**3.6±0.6**	**18.3±4.5**	**403±42**
45 wt% GP	**3.4±0.5**	**12.5±3.2**	**267±46**
90 wt% GP	**2.3±0.5**	**13.5±2.7**	**250±70**

The P(3HO-co-3HD) composites containing the GP showed a decrease in the elongation at break and increase of Young's modulus compared with the neat P(3HO-co-3HD). An increase in the amount of GP in the polymer matrix led to an increase in the tensile strength, Young's modulus.

Additionally, the elongation at break decreased, lowering the ductility in proportion to the amount of the filler added. The results from the mechanical characterisation are summarised in Table 5.5.

For the synthesised composites, the addition of GP to the blend binary system led to a reduction in both the tensile strength and Young's modulus when compared to the neat blends of 75/25 /P(3HO-co-3HD)/P(3HB) as shown in Table 5.6.

The inclusion of 23 wt% and 90 wt% of GP to the blend led to an increase in the elongation at break, resulting in relatively more elastomeric polymers in comparison with the neat blend at room temperature.

Table 5.6: Mechanical properties of 75/25 P(3HO-co-3HD)/ P(3HB) blends and blends containing garlic powder (GP).

75/25 /P(3HO-co-3HD)/P(3HB) blend	Tensile strength (σ) (MPa)	Young's Modulus (E) (MPa)	Elongation at break (ε_b%)
0 wt% GP	**10.2±0.0**	**68±3.9**	**96±1.6**
23 wt% GP	**2.7±0.8**	**2.2±0.7**	**176±51**
45 wt% GP	**2.07±0.2**	**12.2±4.1**	**103±19**
90 wt% GP	**2.7±1.5**	**1.24±0.4**	**231±128**

5.2.5 Water contact angle tests of PHAs films and blends containing garlic powder

Static water contact angle tests to evaluate the wettability of the developed composite blends containing GP, as well as the neat control samples, were performed. The tests were carried out in triplicate using different batches of solvent cast films and the tests conducted on both the air and the glass sides of each sample. The films were all cast in glass Petri dishes and allowed to dry naturally exposed to air.

The portion of the films exposed to the air was referred to as the air side of the specimens while the opposite side, which was in contract with the Petri dish, was referred to as the glass side.

The water contact angle of the P(3HB)/GP composites (Figure 5.5) increased as the content of GP increased, indicating a proportional relationship for both the air and glass sides. A comparison of the air side samples revealed a difference which was statistically significant between the 0 wt% GP and 90 wt% GP samples. No significant differences existed between the rest of the P(3HB) composites.

For the glass side samples of the P(3HB)/GP composites, the samples with lower percentages of the GP did not have any statistically significant change in the water contact angle, but higher percentages of GP increased the hydrophobicity of the composites. Further statistical analysis revealed significant differences

between the three P(3HB)/GP composites (glass side) when compared with the non-modified samples. Representative samples of the respective composites containing the same amount of GP (air and glass sides) showed no statistically significant change.

For the P(3HO-co-3HD)/GP composites, the addition of GP reduced the hydrophobicity of the final samples for both air side and glass side samples. For both sides, air and glass, the difference between the non-modified and the P(3HO-co-3HD)/GP composites was statistically significant, as shown in Figure 5.6. A significant difference was only observed for the 23 wt% composite when looking at samples of the air and glass sides of the same composite.

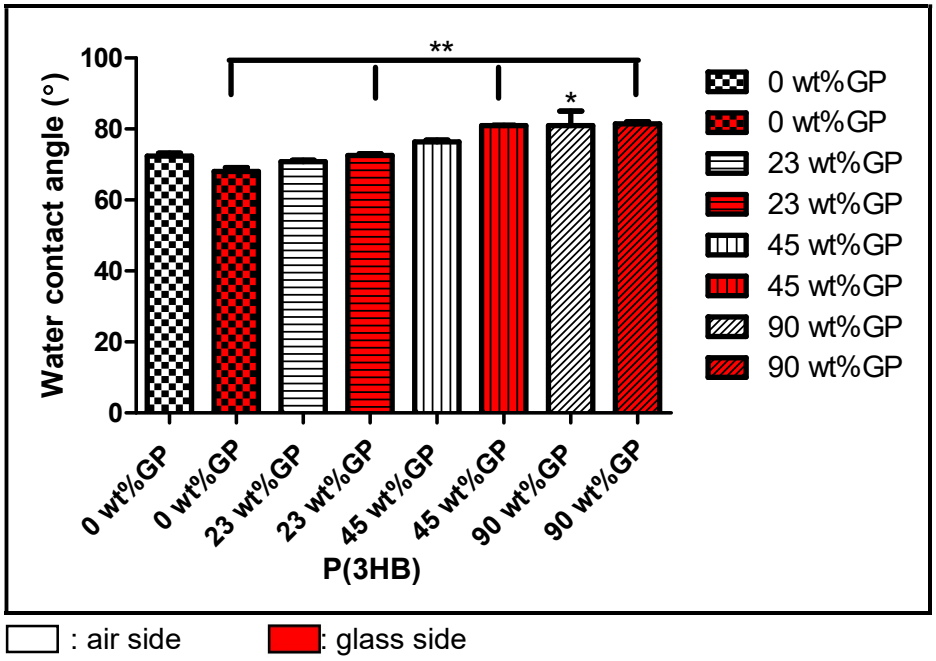

Figure 5.5: Static water contact angle measurements for P(3HB)/GP composites and control (Mean± SEM, n = 3 independent experiments, p statistical significance values (*p ≤ 0.05, **p ≤ 0.01, and ***p ≤ 0.001) were determined for air vs. respective glass side samples and neat matrix vs composites for both air and glass side).

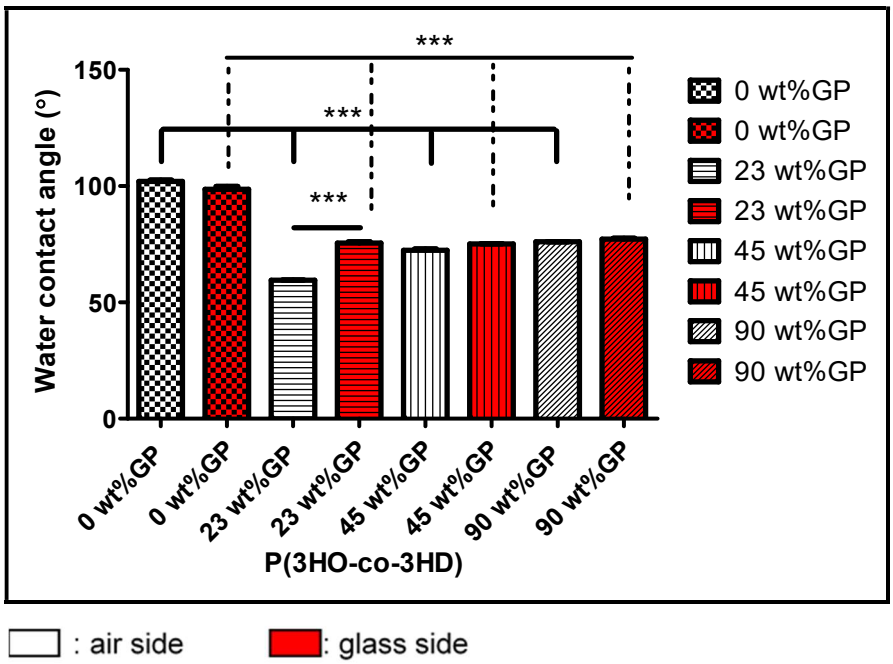

Figure 5.6: Static water contact angle measurements for P(3HO-co-3HD)/GP composites and control Mean± SEM, n = 3 independent experiments, p statistical significance values (*p ≤ 0.05, **p ≤ 0.01, and ***p ≤ 0.001) were determined for air vs. respective glass side samples and neat matrix vs composites for both air and glass side).

The water contact angle of the PHA blend/GP composites (Figure 5.7) decreased inversely to the content of GP up to 45 wt%. Further addition of GP up to 90 wt% led to an increase in the water contact angle for both the air and glass side samples. Detailed statistical analysis revealed significant differences between the three blend/GP composites and the non-modified PHA blend.

A significant difference was observed for the 23 wt% GP composites when compared with the non-modified blend for the glass side samples only. When samples with the same amount of GP were compared, significant differences were observed between the glass and the air side samples for the samples with higher concentrations of the GP in the composite blends (45 wt% and 90 wt%).

The P(3HB) and P(3HB)/GP composites displayed water contact angles lower than 90^{o,} which implies that they are hydrophilic for both the air and glass side samples. In contrast, the P(3HO-co-3HD) composite is hydrophobic with a water contact angle of 91^{o}. However, the addition of GP resulted in the P(3HO-co-3HD)/GP composites with water contact angles lower than 90^{o}.

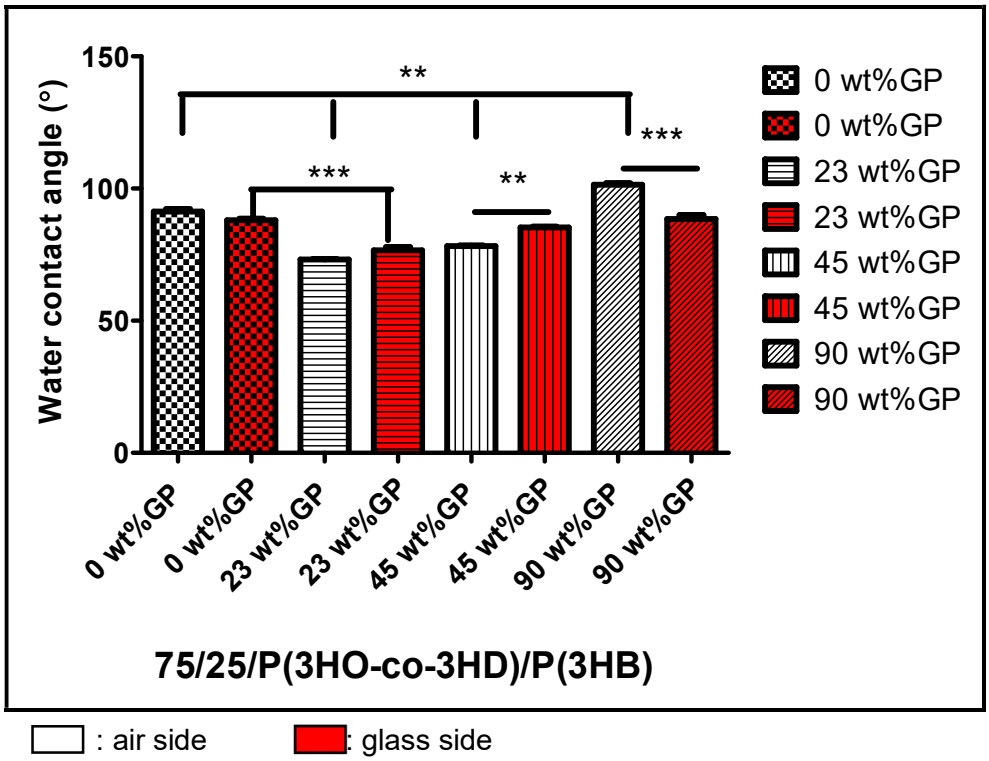

Figure 5.7: Static water contact angle measurements for 75/25/P(3HO-co-3HD)/ P(3HB)/GP composites and control Mean± SEM, n = 3 independent experiments, p statistical significance values (*p ≤ 0.05, **p ≤ 0.01, and ***p ≤ 0.001) were determined for air vs. respective glass side samples and neat matrix vs composites for both air and glass side).

Finally, the blend/GP composites showed water contact angles which corresponded to those expected for hydrophilic substrates except for the air side samples of the non-modified PHA blend and the 90 wt% GP blend composites.

5.2.6 Scanning Electron Microscopy of the PHAs films and blends containing garlic powder

The surface topography of the neat polymer, as well as the composite films containing GP, were studied using Scanning Electron Microscopy (SEM). The effect of the garlic powder on the surface properties of the composite films prepared using P(3HB), P(3HO-co-3HD) and 75/25/ P(3HO-co-3HD)/ P(3HB) are depicted below Figure 5.8. The polymers were loaded with different concentrations of garlic powder and their surface morphology compared to that of the neat P(3HB), P(3HO-co-3HD) and 75/25/ P(3HO-co-3HD)/ P(3HB) films.

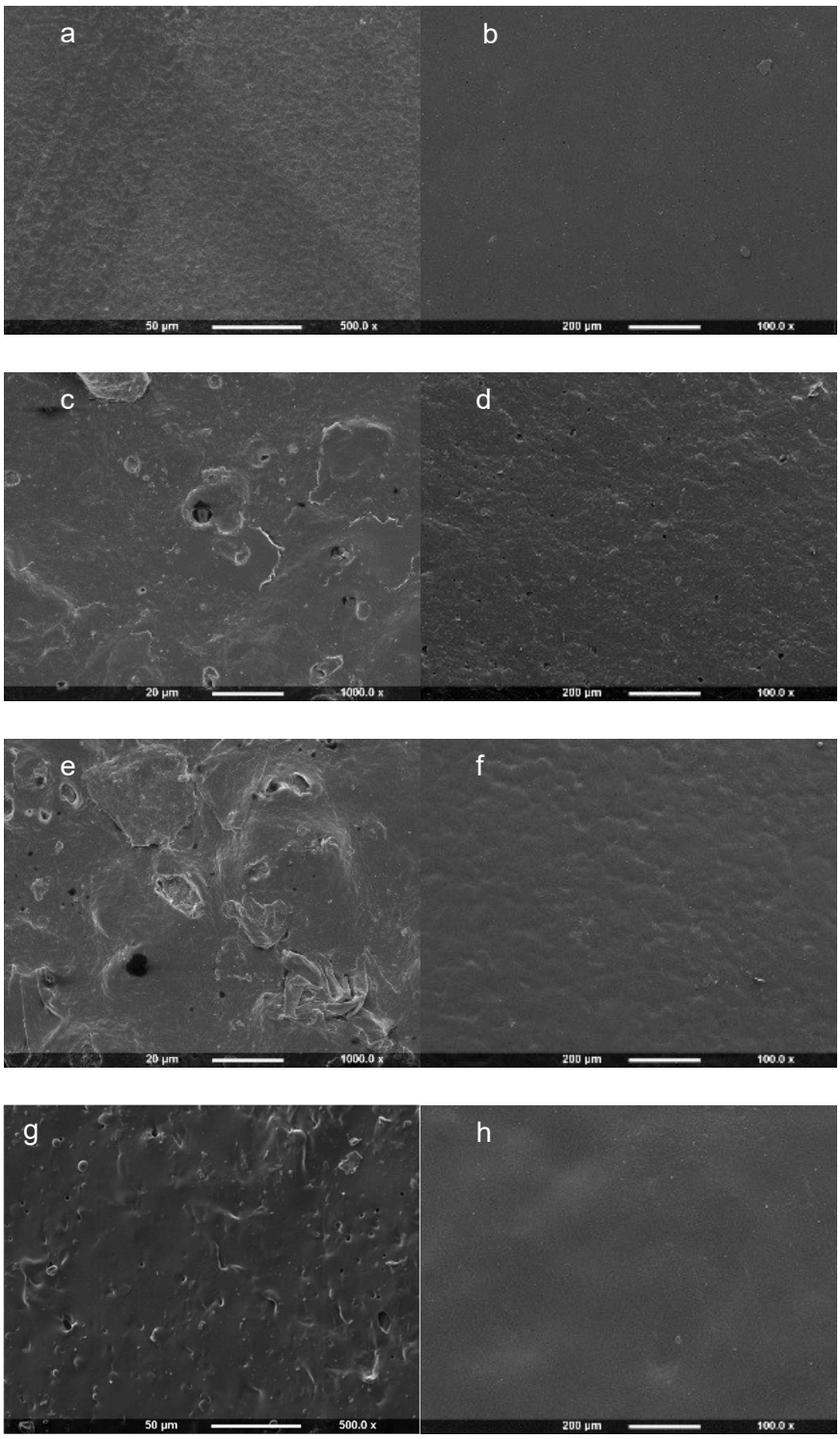

Figure 5.8: SEM images of (a) neat P(3HB), (b) neat P(3HO-co-3HD), (c) P(3HB)/23 wt% GP, (d) P(3HO-co-3HD)/23 wt% GP, (e) P(3HB)/45 wt% GP, (f) P(3HO-co-3HD)/45 wt% GP, (g) P(3HB)/90 wt% GP and (h) P(3HO-co-3HD)/90 wt% GP.

A different topography was observed for the composites with GP added within the P(3HB) matrix whereas in the case of the P(3HO-co-3HD) composites the surface topography observed was similar to that of the neat films. In the P(3HO-

co-3HD)/GP composites the surface of the sample containing 23 wt% GP reveals some small pores which disappear with the addition of higher loadings of GP (45 and 90 wt%) resulting in a more homogenous surface.

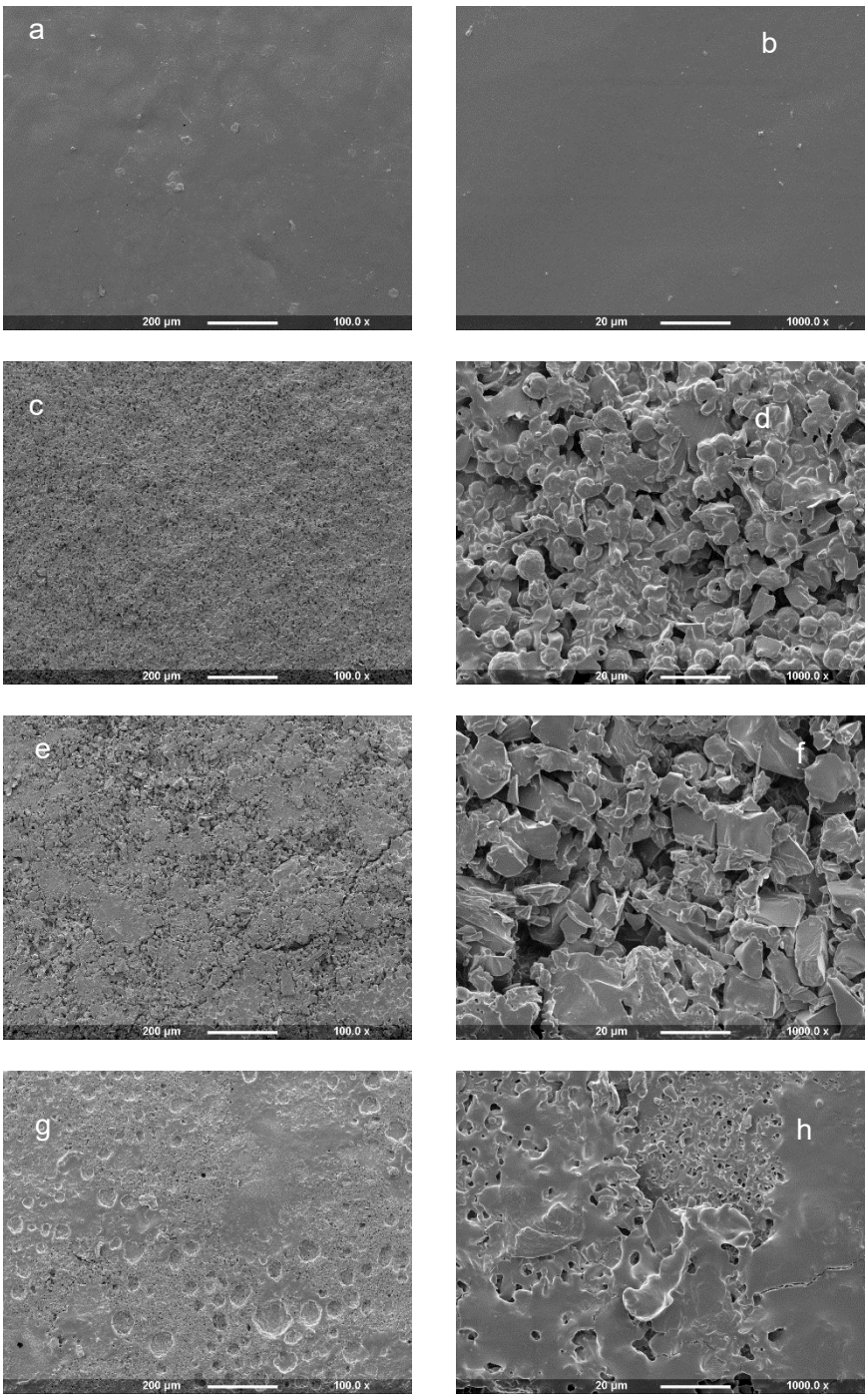

Figure 5.9: SEM images of (a), (b) neat 75/25 P(3HO-co-3HD)/P(3HB), (c), (d) 75/25 P(3HO-co-3HD)/P(3HB)/23 wt% GP (e), (f) 75/25 P(3HO-co-3HD)/P(3HB)/45 wt% GP (g), (h) 75/25 P(3HO-co-3HD)/P(3HB)/90 wt% GP of × 100 and × 1000 magnification.

After the addition of GP to the binary system of the 75/25 P(3HO-co-3HD)/P(3HB), a different morphology was detected, compared to the neat blend sample under magnification (× 100). Higher levels of magnification revealed a rock-like topography interspaced with gaps. This morphology appeared to become smoother when the highest amount of the garlic powder was added to the blend, as shown in Figure 5.9.

5.2.7 Antibacterial evaluation of garlic powder and films containing garlic powder

5.2.7.1 Agar well diffusion method using allicin and garlic powder

Preliminary screening for the antibacterial activity of both allicin-containing substrates, allicin powder and dehydrated garlic powder, was conducted against *S. aureus* (ATCC® 29213™) and *E. coli* (ATCC® 25922™) using the agar well diffusion method (Figure 5.10, Figure 5.11).

Garlic powder and allicin solutions of same concentrations were used for the formation of inhibition zones. Bacterial growth was inhibited only for GP against *S. aureus* (ATCC® 29213™), forming a halo around the inoculated wells (Figure 5.10). This showed that the GP was more active than the allicin using the same amount of the active agent. The sizes of the inhibition zones observed using garlic powder are shown in Table 5.7.

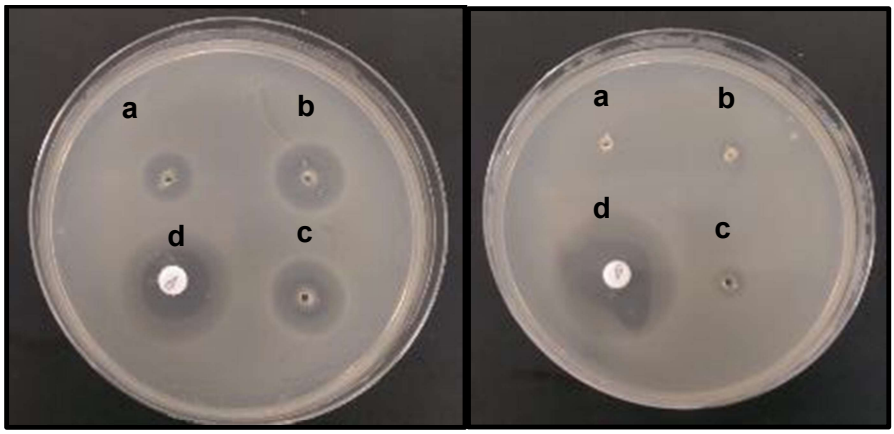

Figure 5.10: Antibacterial activity of Garlic Powder (left) and Allicin (right) against *S. aureus* (ATCC® 29213™) for different concentrations: (a) 3 mg, (b) 5 mg, (c) 7 mg and (d) positive control (antibiotic disc containing 1 µg of oxaccilin).

Table 5.7: Inhibition zone of Garlic Powder and Allicin against *S. aureus* (ATCC® 29213™).

Concentration of agents (mg/ml)	Garlic Powder/ Inhibition zone (cm)	Allicin/Inhibition zone (cm)
3	**1.1**	**No Halo**
5	**1.5**	**No Halo**
7	**1.7**	**No Halo**

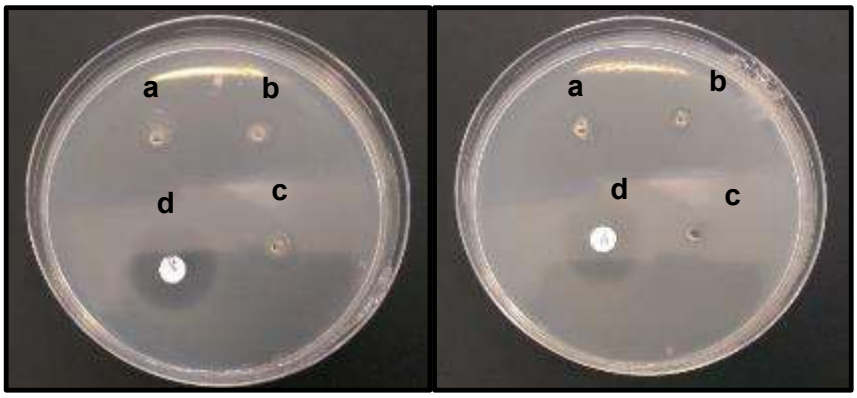

Figure 5.11: Antibacterial activity of Garlic Powder (left) and Allicin (right) against *E. coli* (ATCC® 25922™) for different concentrations: (a) 3 mg, (b) 5 mg, (c) 7 mg and (d) positive control (antibiotic disc containing 300 µg of streptomycin) .

There was also no antibacterial activity observed for either GP or allicin against *E. coli* (ATCC® 25922™) (Figure 5.11). Most probably the concentration of the GP and allicin solutions was not in the range to have an antibacterial effect against the *E. coli* (ATCC® 25922™) bacterial strain.

5.2.7.2 Minimum Inhibitory concentration of Garlic powder

In order to further investigate the efficacy of GP as an antimicrobial agent, the minimum inhibitory concentration was determined utilising the broth dilution method. GP dissolved in distilled water was used to prepare a stock solution of 140 mg/ml in line with the ISO 20776-1:2006 protocol.

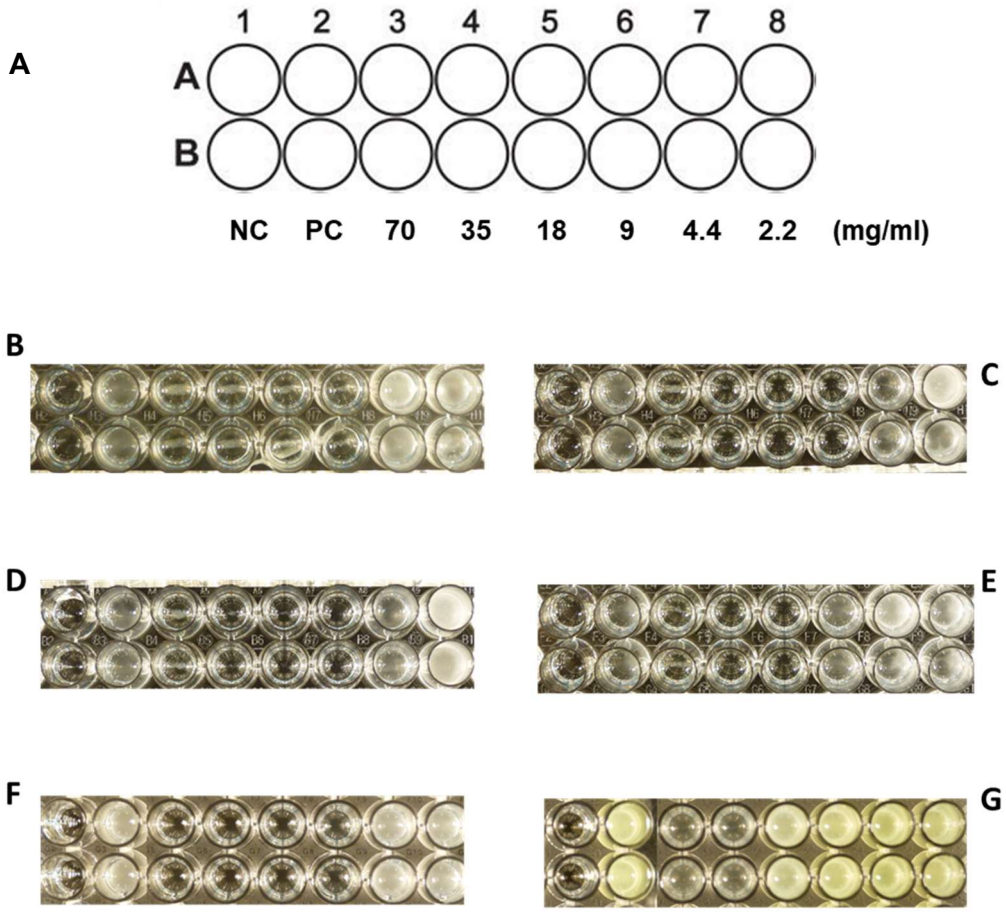

Figure 5.12: (A) Schematic demonstration of negative (NC) and positive (PC) controls and different concentrations of garlic powder solutions in the representative wells of the 96 well plate. Visual growth of (B) *Staphylococcus aureus* (ATCC® 29213™) (C) *Staphylococcus epidermidis* (ATCC® 12228™), (D) Methicillin-resistant *S. aureus* (MRSA), (E) Methicillin-resistant *S. epidermidis* (MRSE), (F) *Escherichia coli* (ATCC® 25922™), (G) *Pseudomonas aeruginosa* (ATCC® 27853™) using different concentrations of garlic powder.

Six of the most common nosocomial bacterial strains *Staphylococcus aureus* (ATCC® 29213™), *Staphylococcus epidermidis* (ATCC® 12228™), *Escherichia coli* (ATCC® 25922™), *Pseudomonas aeruginosa* (ATCC® 27853™), as well as clinical isolates of MRSA and MRSE were selected and tested against GP.

The MICs against the six above-mentioned bacterial strains are shown above Figure 5.12. The growth was interpreted not only at the lowest concentration that inhibits the visual growth of bacteria but also using a spectrometer measuring the OD_{600} to quantify the amount of bacterial growth in each well is shown below in Figure 5.13. As negative control was used broth without bacterial suspension were as positive broth containing bacteria.

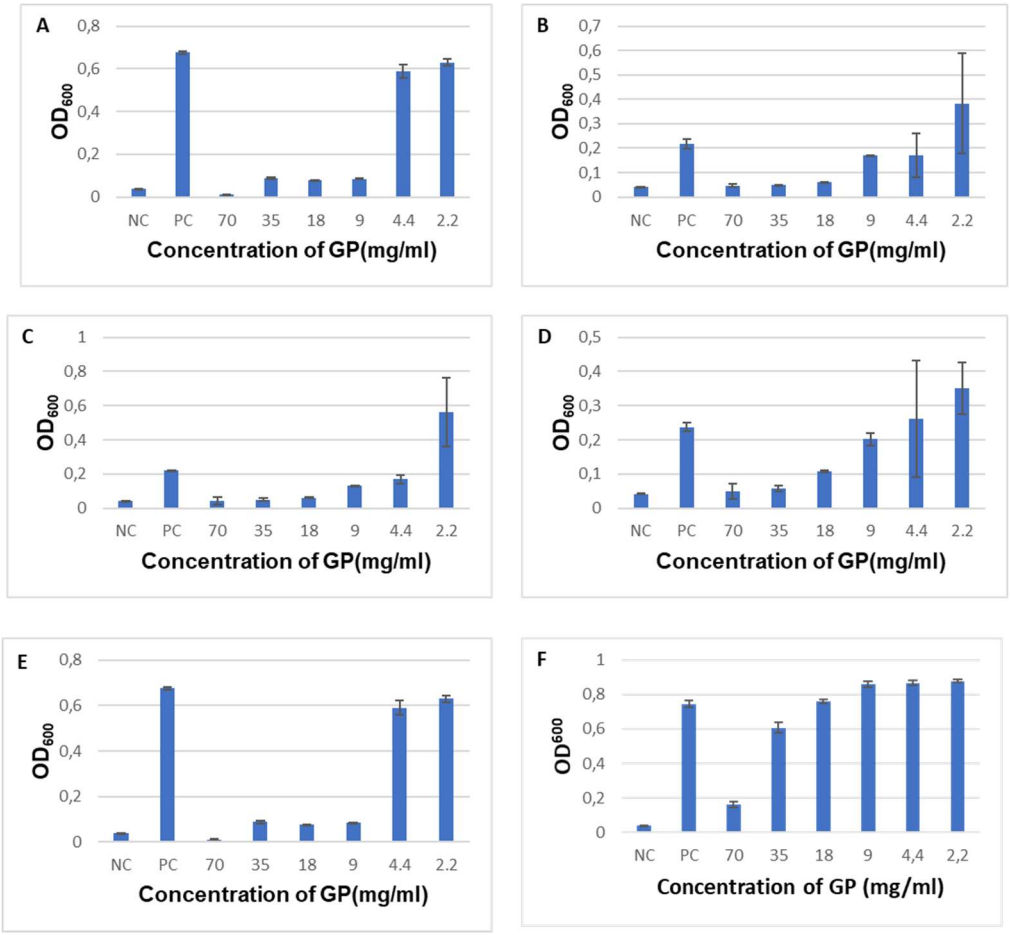

Figure 5.13: The optical density (600 nm) of the supernatants from (A) *Staphylococcus aureus* (ATCC® 29213™) (B) *Staphylococcus epidermidis* (ATCC® 12228™) (C) Methicillin-resistant *S. aureus* (MRSA), (D) Methicillin-resistant *S. epidermidis* (MRSE), (E) *Escherichia coli* (ATCC® 25922™), (F) *Pseudomonas aeruginosa* (ATCC® 27853™) after treatment with different concentrations of garlic powder solutions for 24h.

The high turbidity of the wells corresponds to the higher OD_{600} values and simultaneously, higher bacterial growth. For example, the MIC values against *Staphylococcus epidermidis*, *Staphylococcus aureus* and clinically isolated MRSA were 4.4 mg/ml while for *Escherichia coli,* the MIC obtained was 9 mg/ml. Finally, for *Pseudomonas aeruginosa* (ATCC® 27853™), the inhibition of bacteria were observed only for higher concentrations of the agent, which was 70 mg/ml.

The Minimum Bactericidal Concentration (MBC) of GP against the six bacteria, as mentioned above, were determined as described in paragraph 2.11.2 since

the MBC values are the concentrations required to kill the test bacteria and show no bacterial growth on the blood agar plates (Appendix section I).

Table 5.8 summarises both the MIC and the MBC values for all six bacterial strains. From the results obtained, it is apparent that is required higher GP concentrations for the MBC than the MIC tests with respect to the same bacterial strain.

Table 5.8: MIC and MBC values of selected bacterial strains.

Bacterial Strains	**MIC (mg/ml)**	**MBC (mg/ml)**
***Staphylococcus aureus* ATCC 29213**	**4.4**	**35**
***Staphylococcus epidermidis* ATCC 12228**	**4.4**	**18**
MRSA	**4.4**	**18**
MRSE	**9**	**18**
***Escherichia coli* ATCC 25922**	**9**	**35**
***Pseudomonas aeruginosa* ATCC 27853**	**35**	**70**

5.2.7.3 Prevention of biofilm formation

The disruption of the formed biofilm formation was assessed by safranin staining to quantify the biofilm biomass as described in section 2.11.3. The formed biofilm was resulted from a 24 h incubation of films containing different amounts of the GP in the presence of the bacterial inoculum. The developed biofilm was washed, fixed and stained prior to the measurement on a plate reader at 490 nm.

Figure 5.14: Absorbance of the stained biofilm formed in the 96 well plates after incubation with the different substrates (from left to right) of : NC, PC, 70, 35, 18, 9, 4.4, 2.2 mg/ml of garlic powder.

As shown in Figure 5.14, the lower the concentration of the agent, the higher the biofilm-forming capacity; therefore, the higher the intensity of the colour. The growth of the biofilm for all six bacterial strains was evaluated by measuring the OD_{490} and is represented graphically in Figure 5.15.

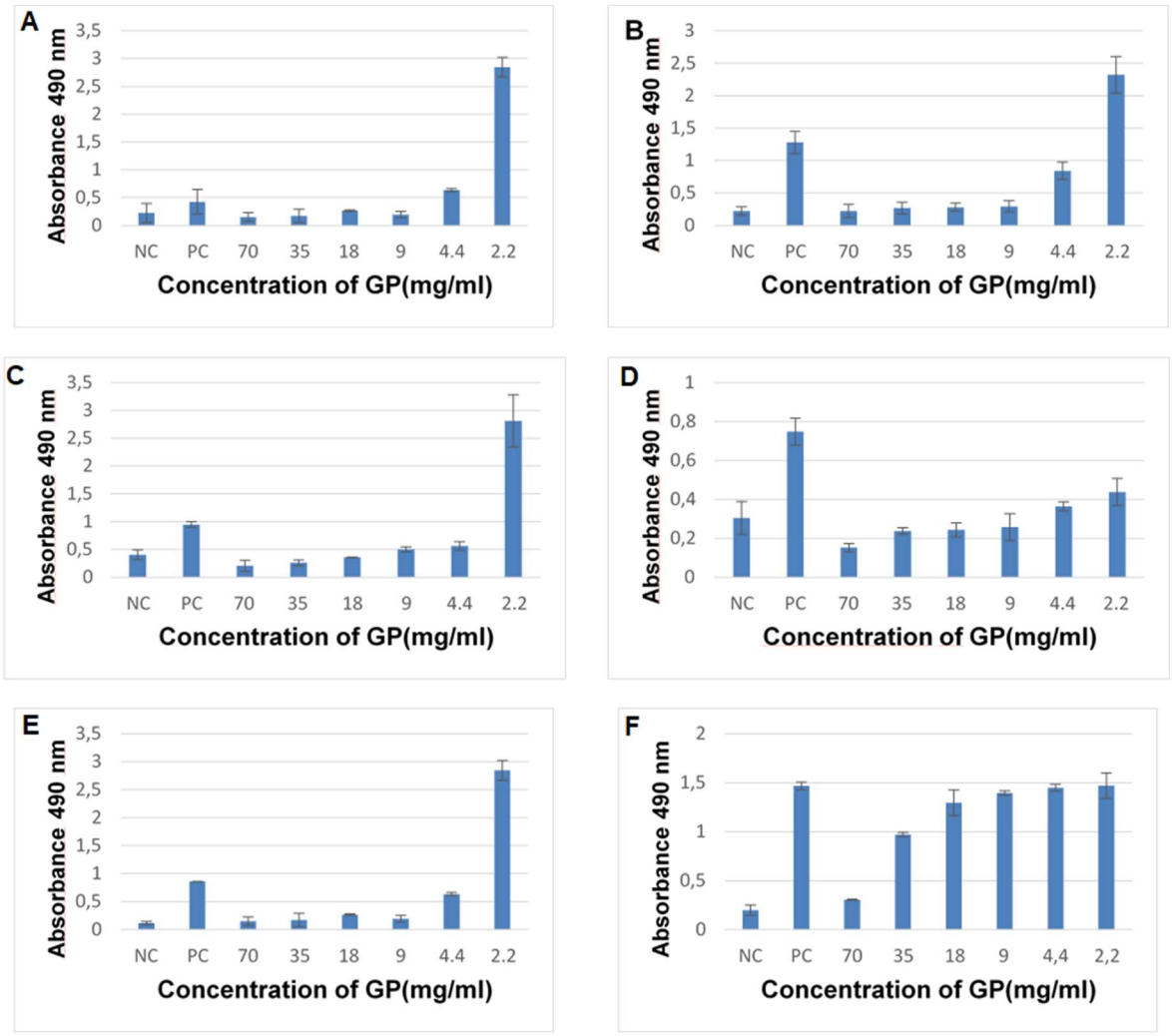

Figure 5.15: Biofilm-forming capacity of (A) *Staphylococcus aureus* (ATCC® 29213™), (B) *Staphylococcus epidermidis* (ATCC® 12228™), (C) Methicillin-resistant *S. aureus* (MRSA), (D) Methicillin-resistant *S. epidermidis* (MRSE), (E) *Escherichia coli* (ATCC® 25922™) and (F) *Pseudomonas aeruginosa* (ATCC® 27853™).

The values of the absorbance at 490 nm revealed that the biofilm-forming capacity was greater in the presence of the lower concentrations of the garlic powder. The high concentrations of the agent resulted in higher inhibition of the biofilm formation, as shown in Figure 5.15. In contrast, almost no ability to prevent

biofilm formation was observed for *Pseudomonas aeruginosa* (ATCC® 27853™) even at the higher concentrations of the GP.

Based on the information from the MIC values, different amounts of GP were incorporated into the P(3HB) and P(3HO-co-3HD) matrices and tested against Gram-positive and Gram-negative bacteria. Films were loaded with GP based on the MIC value of the Methicillin-resistant *Staphylococcus epidermidis* strain; since it was the Gram-positive bacteria that had the higher MIC value. The final composite films produced were loaded with final concentrations of 23 wt%, 45 wt% and the 90 wt% of garlic powder.

5.2.7.4 Disc diffusion of PHAs films and blends containing garlic powder against Gram-positive and Gram-negative bacterial strains

In order to assess the release efficiency of the GP filler agent from the polymer matrices, disc diffusion assays were performed on samples with the three different loadings of GP 23 wt%, 45 wt% and 90 wt% against the six bacterial strains mentioned above. The layout for the disc diffusion tests is depicted below, Figure 5.16. The controls used on the agar plates for MRSA, MRSE, *Escherichia coli* (ATCC® 25922™) and *Pseudomonas aeruginosa* (ATCC® 27853™) was an antibiotic disc containing 300 µg of streptomycin while for *Staphylococcus aureus* (ATCC® 29213™) a similar disc with 1 µg of oxacillin was used. The last control for *Staphylococcus epidermidis* (ATCC® 12228™) was an antibiotic disc containing 300 µg of gentamicin.

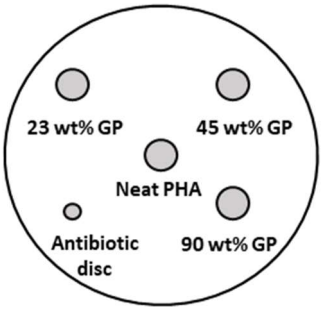

Figure 5.16: Schematic demonstration of samples and controls used for the disc diffusion tests.

The results from the disc diffusion assays (Figure 5.17) indicated that the GP was released from the matrix of the scl-PHA even at the lower concentration (23 wt%) (in the case of *Staphylococcus aureus* (ATCC® 29213™)). There was, however, no impact on the *Pseudomonas aeruginosa* (ATCC® 27853™) strain even with the composite with the highest concentration of GP. The results from the formed inhibition zones in cm for the composites containing the different loadings of garlic powder against the six strains are reproduced below, Figure 5.18 and Table 5.9.

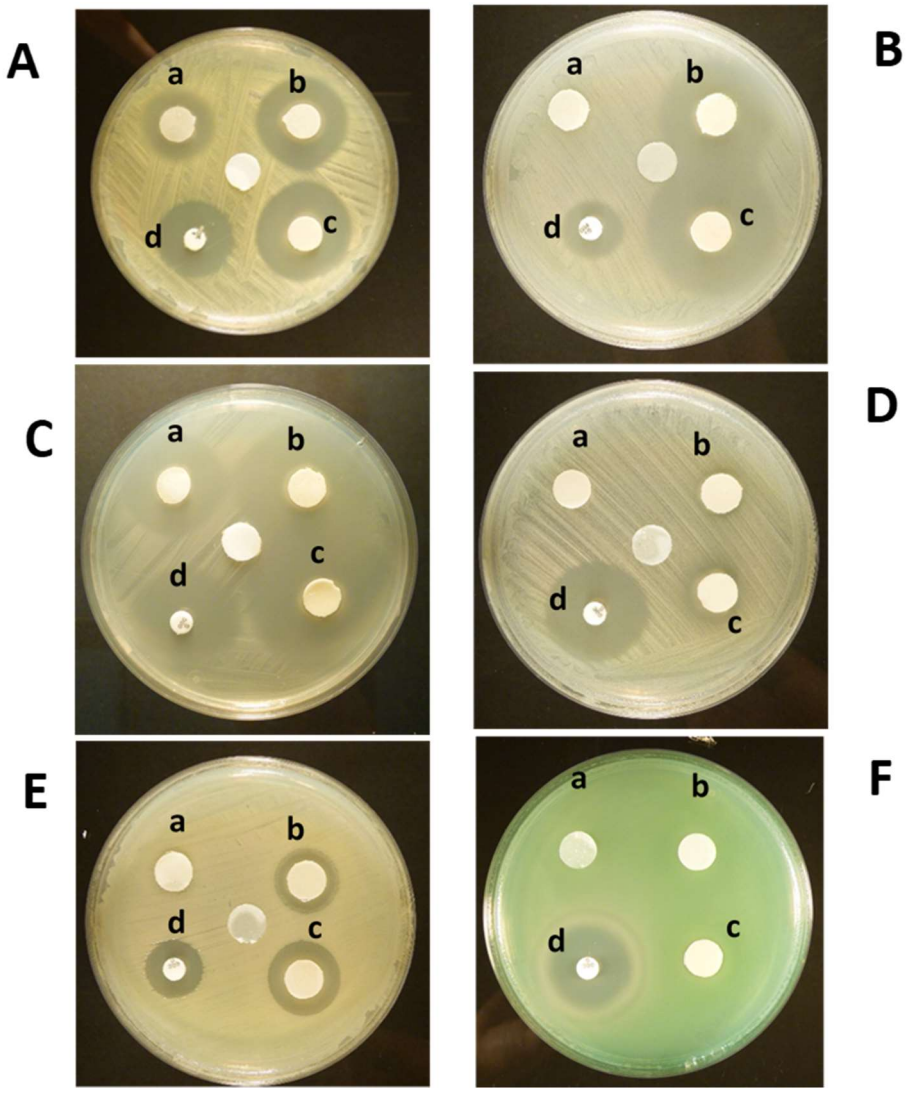

Figure 5.17: Antibacterial activity of P(3HB) films incorporated with different concentrations of Garlic Powder (a) 23 wt%, (b) 45 wt%, (c) 90 wt% and (d) positive control against (A) *Staphylococcus aureus* (ATCC® 29213™), (B) *Staphylococcus epidermidis* (ATCC® 12228™), (C) Methicillin-resistant S. *aureus* (MRSA), (D) Methicillin-resistant S. *epidermidis* (MRSE), (E) *Escherichia coli* (ATCC® 25922™), and (F) *Pseudomonas aeruginosa* (ATCC® 27853™) using the agar disc diffusion method.

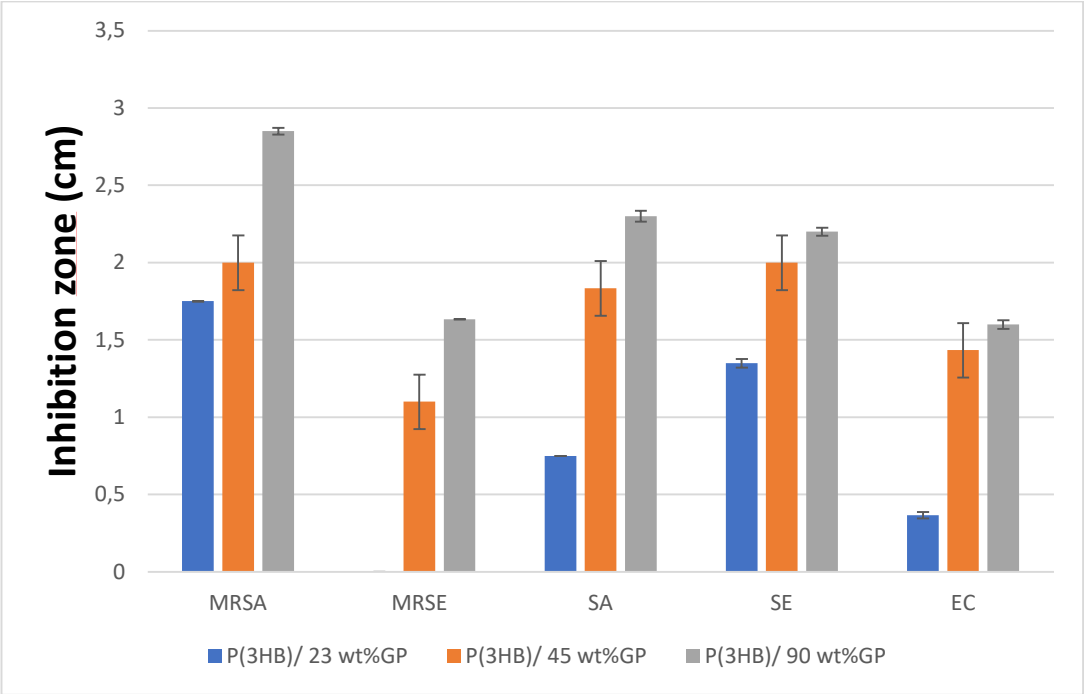

Figure 5.18: *In vitro* antibacterial inhibition zones of different P(3HB) composites against different bacterial strains.

Table 5.9: Inhibition zones of P(3HB)/GP composite samples against different bacterial strains.[2]

Samples	P(3HB)/ 23 wt%GP	P(3HB)/ 45 wt%GP	P(3HB)/ 90 wt%GP	Control
Inhibition zone (cm)				
SA	1.1±0.1	2.1±0.4	2.3±0.4	2.3±0.1
SE	1.0±0.1	2.8±0.6	3.2±0.3	1.7±0.2
MRSA	2.6±0.1	2.8±0.1	2.9±0.1	2.1±0.2
MRSE	1±0.1	1.2±0.1	1.6±0.1	2.8±0.1
EC	1.1±0.1	1.7±0.1	2.1±0.2	1.6±0.3
PA	0	0	0	2±0.02

[2] SA: *Staphylococcus aureus* (ATCC® 29213™)
SE: *Staphylococcus epidermidis* (ATCC® 35984™)
MRSA: Methicillin-resistant *S. aureus*
MRSE: Methicillin-resistant *S. epidermidis*
EC: *Escherichia coli* (ATCC® 25922™)
PA: *Pseudomonas aeruginosa* (ATCC® 27853™)

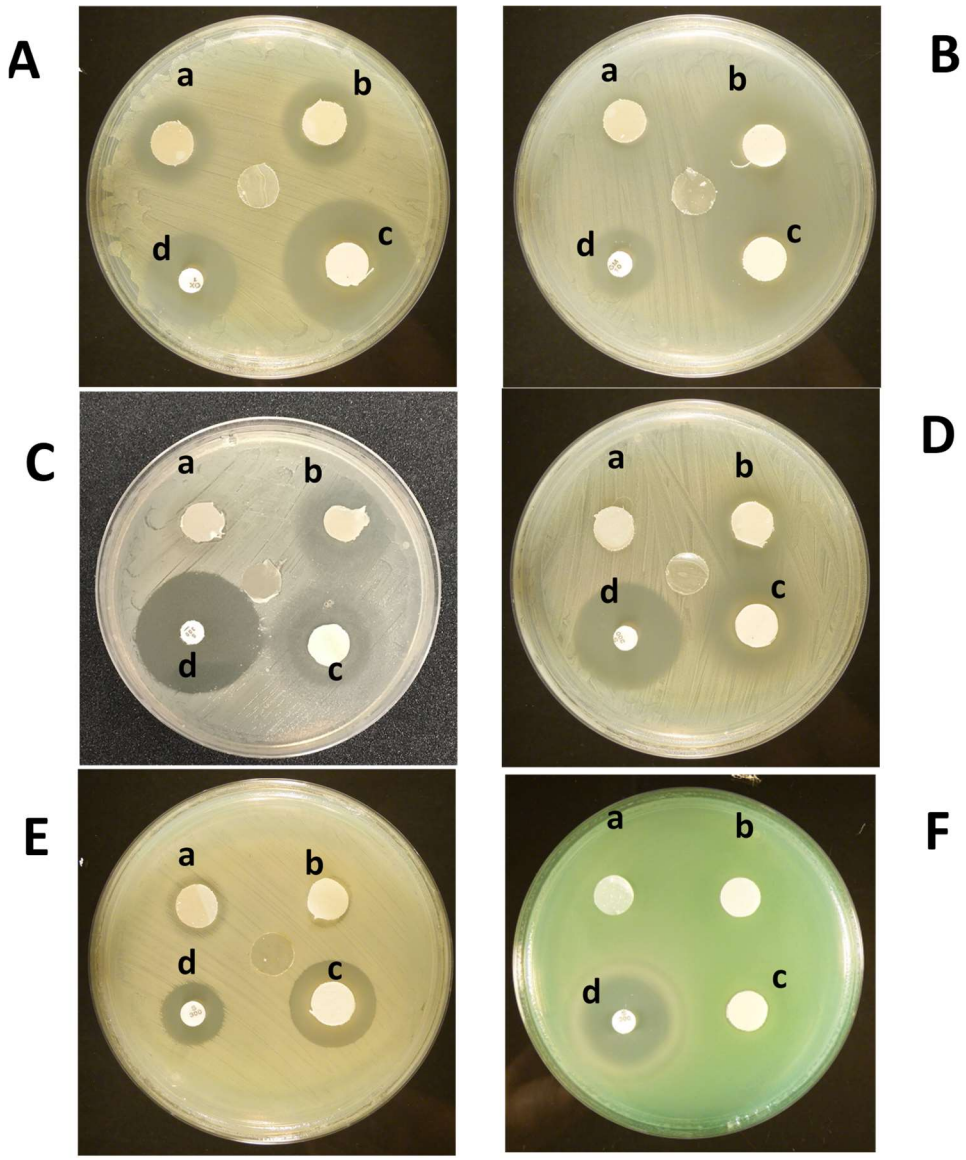

Figure 5.19: Antibacterial activity of P(3HO-co-3HD) films incorporated with different concentrations of Garlic Powder (a) 23 wt%, (b) 45 wt%, (c) 90 wt% and (d) positive control against (A) *Staphylococcus aureus* (ATCC® 29213™), (B) *Staphylococcus epidermidis* (ATCC® 12228™), (C) Methicillin-resistant *S. aureus* (MRSA), (D) Methicillin-resistant *S. epidermidis* (MRSE), (E) *Escherichia coli* (ATCC® 25922™) and (F) *Pseudomonas aeruginosa* (ATCC® 27853™) using the agar disc diffusion method.

For the various samples of mcl-PHA containing different loadings of GP, the results showed that the bacteria were susceptible to the GP filling agent even at the lower concentrations as shown in Figure 5.19. No inhibition was detected only for MRSE with the lowest, 23 wt%, loading GP

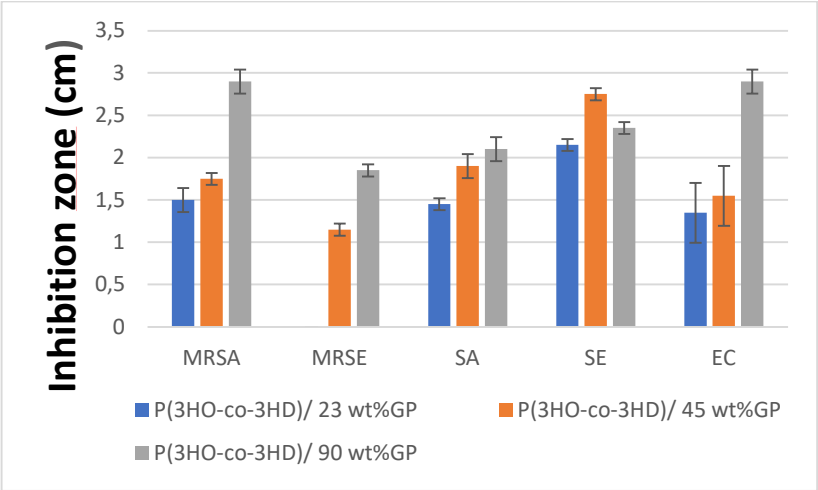

Figure 5.20: *In vitro* antibacterial inhibition zones of different P(3HO-co-3HD) composites against different bacterial strains.

Additionally, there was no effect from the samples on the growth of *Pseudomonas aeruginosa* (ATCC® 27853™). Figure 5.20 and Table 5.10 are displaying the values of the inhibition zones formed from the different loadings of GP in the P(3HO-co-3HD) matrix.

Table 5.10: Inhibition zones of P(3HO-co-3HD)/GP samples against different bacterial strains[3].

Samples	P(3HO-co-3HD)/23 wt%GP	P(3HO-co-3HD)/45 wt%GP	P(3HO-co-3HD)/90 wt%GP	Control
		Inhibition zone (cm)		
SA	1.7±0.2	2±0.3	3.3±0.1	2.3±0.1
SE	1±0.1	2.8±0.4	3.4±0.3	1.9±0.2
MRSA	1±0.1	2.6±0.3	2.9±0.7	2±0.2
MRSE	1±0.1	1.7±0.1	2.1±0.1	2.8±0.1
EC	1.3±0.2	1.4±0.1	2.15±0.1	1.8±0.2
PA	0	0	0	2±0.1

[3] SA: *Staphylococcus aureus* (ATCC® 29213™)
SE: *Staphylococcus epidermidis* (ATCC® 35984™)
MRSA: Methicillin-resistant *S. aureus*
MRSE: Methicillin-resistant *S. epidermidis*
EC: *Escherichia coli* (ATCC® 25922™)
PA: *Pseudomonas aeruginosa* (ATCC® 27853™)

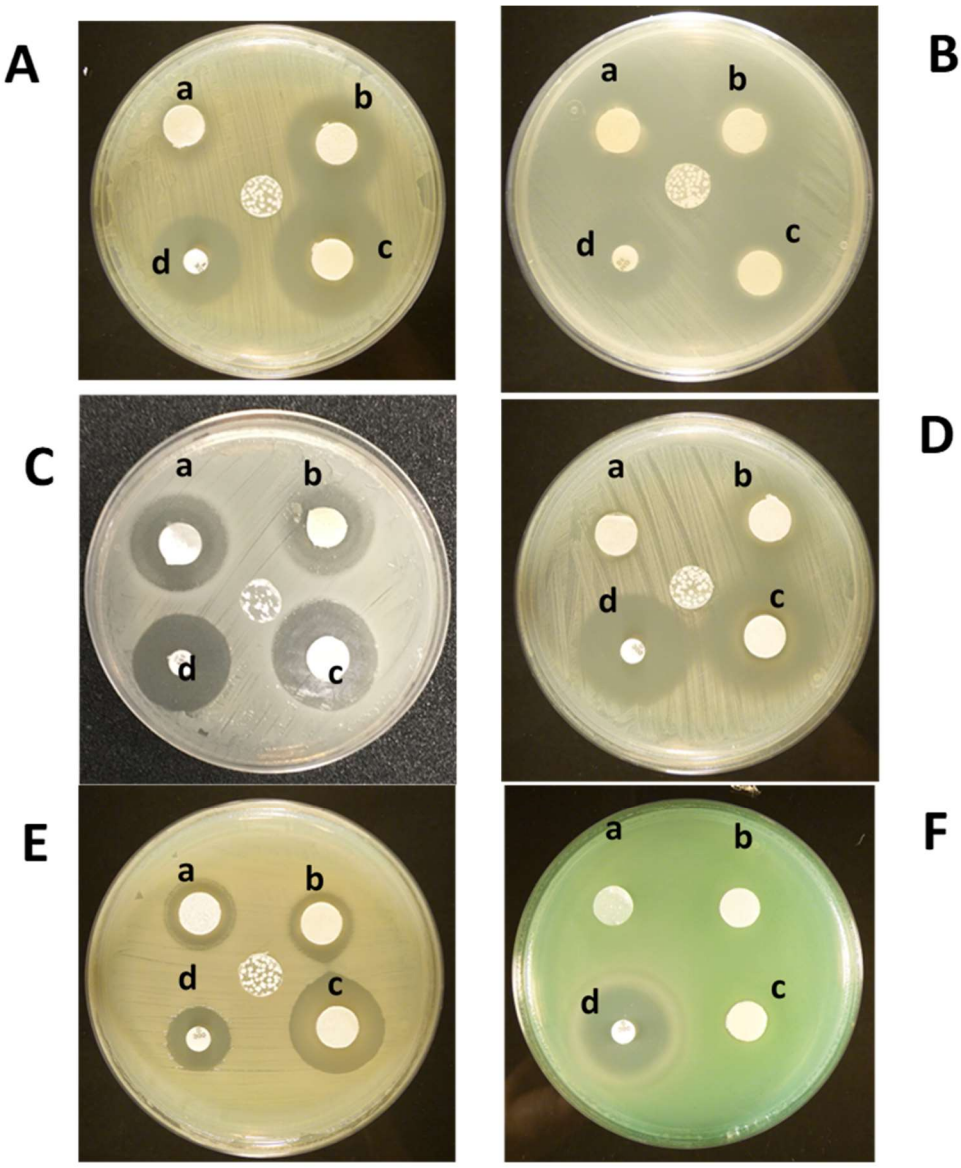

Figure 5.21: Antibacterial activity of blend films incorporated with different concentrations of GP (a) 23 wt%, (b) 45 wt%, (c) 90 wt% and (d) positive control against (A) *Staphylococcus aureus* (ATCC® 29213™), (B) *Staphylococcus epidermidis* (ATCC® 12228™), (C) Methicillin-resistant *S. aureus* (MRSA), (D) Methicillin-resistant *S. epidermidis* (MRSE), (E) *Escherichia coli* (ATCC® 25922™) and (F) *Pseudomonas aeruginosa* (ATCC® 27853™) using the agar disc diffusion method.

In the case of the 75/25 blends the neat polymers placed in the middle of the agar plates revealed their immiscibility with the presence of two different sides. The white dots are the attributed to the presence of the P(3HB) where the rest is the P(3HO-co-3HD). The inhibition zones formed from the release of GP from the 75/25 blend was in some cases superior even from the control samples. For

example, in the case of *Staphylococcus aureus* (ATCC® 29213™), *Staphylococcus epidermidis* (ATCC® 12228™), MRSA and *Escherichia coli* (ATCC® 25922™) the composite blends containing 45 and 90 wt% of the GP showed bigger inhibition zones than the antibiotic discs (Figure 5.21 and Table 5.11).

Table 5.11: Inhibition zones of blends containing GP samples against different bacterial strains[4].

Samples	PHA blend/23 wt%GP	PHA blend/45 wt%GP	PHA blend/90 wt%GP	Control
Inhibition zone (cm)				
SA	**1.1±0.1**	**2.5±0.1**	**3.3±0.1**	**2.3±0.7**
SE	**2.1±0.1**	**2.3±0.1**	**2.6±0.1**	**2.2±0.6**
MRSA	**2.2±0.4**	**2.6±0.1**	**2.9±0.7**	**2±0.1**
MRSE	**1.2±0.1**	**1.7±0.1**	**2.4±0.1**	**2.8±0.1**
EC	**1.6±0.2**	**1.8±0.1**	**2.5±0.1**	**1.6±0.1**
PA	**0**	**0**	**0**	**2±0.1**

All samples containing the various amounts of GP incorporated into their matrices conferred antibacterial activity on the final composites. The inhibition zones formed around the polymer discs are dose-dependent because the higher the amount of GP in the polymer the bigger the inhibition zone that formed. The same resistance of *Pseudomonas aeruginosa* (ATCC® 27853™) to the GP composites, even with the highest concentrations of GP was observed for all composites.

[4] SA: *Staphylococcus aureus* (ATCC® 29213™)
SE: *Staphylococcus epidermidis* (ATCC® 35984™)
MRSA: Methicillin-resistant *S. aureus*
MRSE: Methicillin-resistant *S. epidermidis*
EC: *Escherichia coli* (ATCC® 25922™)
PA: *Pseudomonas aeruginosa* (ATCC® 27853™)

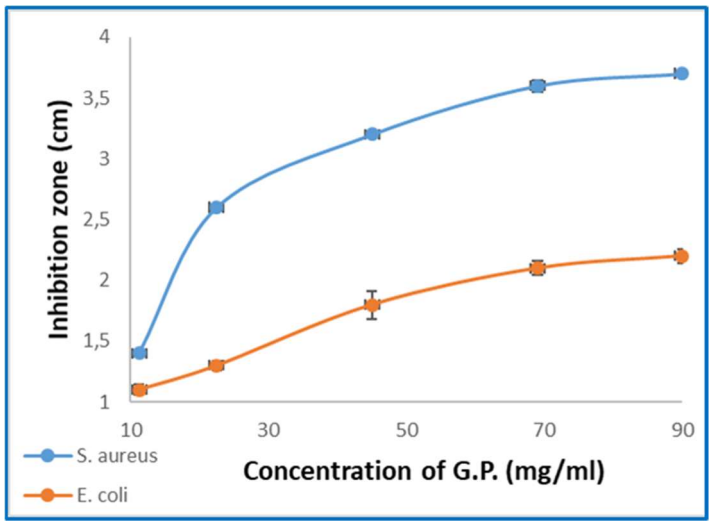

Figure 5.22: Dependence of concentration of Garlic powder incorporated into P(3HB) matrix against *S. aureus* (ATCC® 29213™) and *E. coli* (ATCC® 25922™).

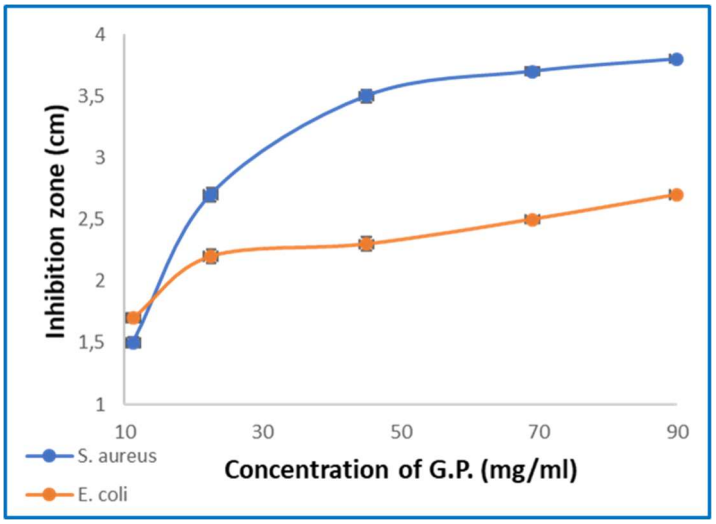

Figure 5.23: Dependence of the concentration of GP incorporated into P(3HO-co-3HD) matrix against *S. aureus* (ATCC® 29213™) and *E. coli* (ATCC® 25922™).

To further investigate the dose-dependent behaviour of the composite specimens; films of both types of PHAs, P(3HB) and P(3HO-co-3HD), containing a range of concentrations of GP from 11, 25, 45, 70 to 90 mg/ml were prepared and assessed against *S. aureus* and *E. coli*. The P(3HB) composites containing the same amount of GP showed a higher inhibition zone against *S. aureus* (ATCC® 29213™) rather *E. coli* (ATCC® 25922™) inhibition zones for both composites. Similarly, the P(3HO-co-3HD) composites formed bigger halo in the case of *S. aureus* (ATCC® 29213™). Both types of composites revealed a dose-dependent antibacterial effect against both strains as shown in Figure 5.22 and 5.23.

5.2.7.5 Evaluation of free planktonic cells and adhered cells on the garlic powder composites of PHAs films and blends

To evaluate the antibacterial efficiency of the garlic composites against both free planktonic and sessile cells, the assay described above in paragraph 2.11.6 was performed. Using the GP discs and aliquots from the suspension of the incubated bacteria, it was possible to evaluate the free cells, while the discs were used to evaluate the adhered cells on the top of the sample as shown in Figure 5.24.

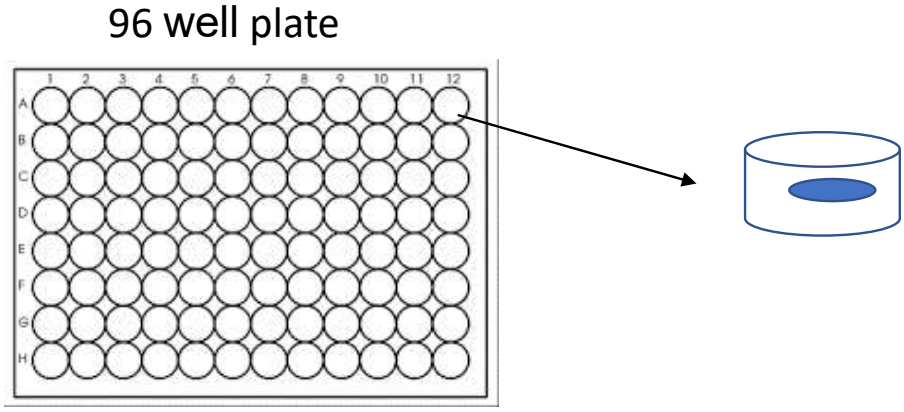

Figure 5.24: 96 well plate containing bacterial suspension and the polymer disc loaded with the antibacterial agent.

Figure 5.25 illustrates the % of bacterial loss of the adhere cells on the composite discs containing different loading of GP. For the evaluation of the adhered cells the conducted test included the following steps.

After 24 h of incubation of the samples with the bacterial suspension the samples were collected and washed with PBS three times. Then the discs were sonicated with PBS for 7 min to in order to detach any adhered bacterial cells. Aliquots of this suspension were plated on agar plates and the results were assessed using CFU method.

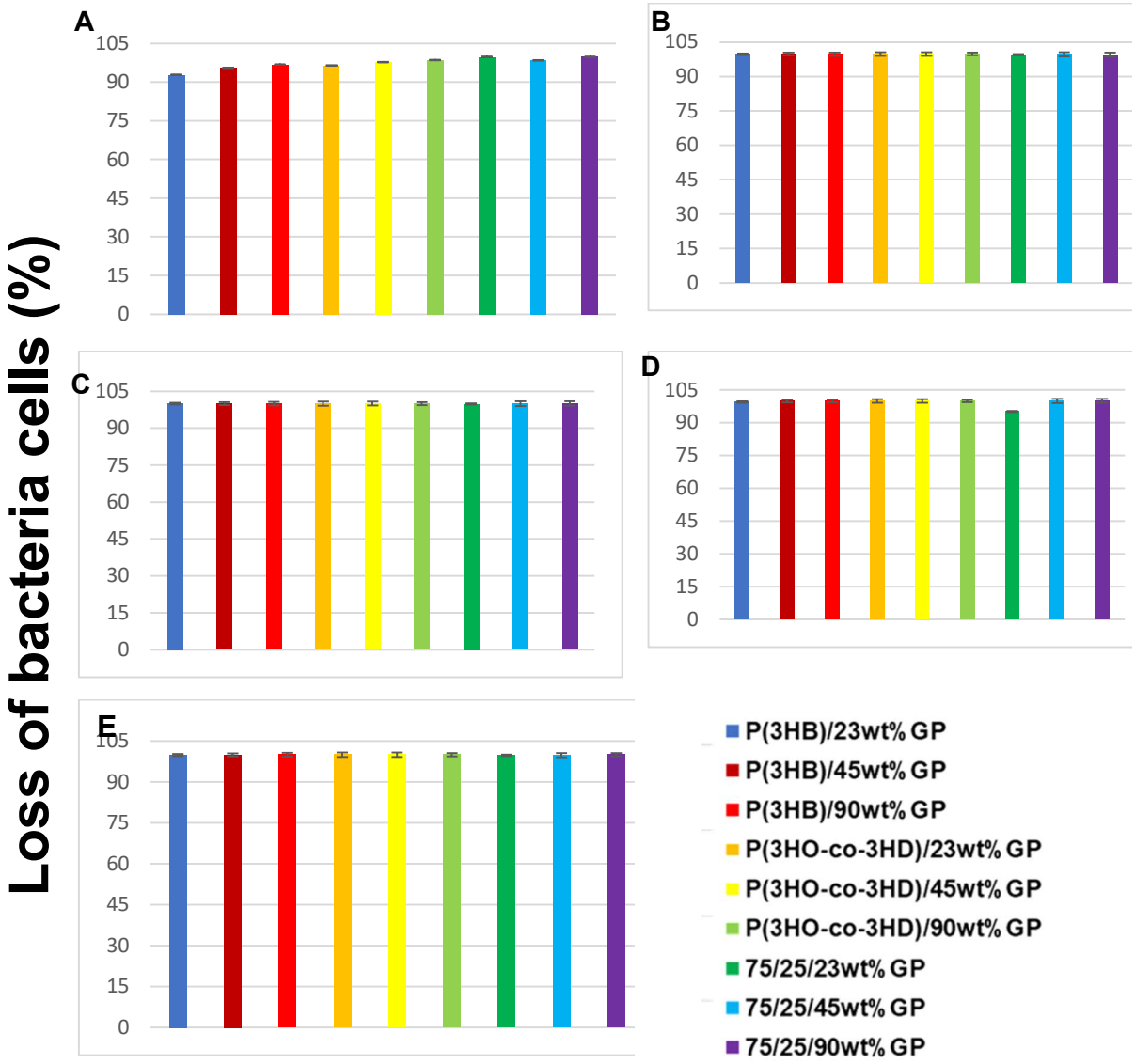

Figure 5.25: Loss of the adhered bacteria on the P(3HB), P(3HO-co-3HD) and 75/25 P(3HO-co-3HD)/ P(3HB) blend films incorporated with different concentrations of Garlic Powder: 23 wt%, 45 wt% and 90 wt% against (A) *Staphylococcus aureus* (ATCC® 29213™), (B) *Staphylococcus epidermidis* (ATCC® 12228™), (C) Methicillin-resistant S. aureus MRSA, (D) Methicillin-resistant S. epidermidis (MRSE) and (E) *Escherichia coli* (ATCC® 25922™).

The results in Figure 5.25 show that the composites containing the different amounts of GP resulted in a loss of greater than 90 % of all the adhered bacteria in all cases.

All the bacteria that managed to adhere to the surface of the composites were killed off as a result of the presence of the GP filler agent. Figure 5.25 shows that the GP modified composite materials showed a significant reduction in the

amount of *Staphylococcus aureus* (ATCC® 29213™) adhered bacteria in comparison with the non-modified composite material after incubation for 24 h. Further evaluation of the composite discs showed that there were no adhered MRSA bacterial cells on the composite discs for any of the concentrations in the case of P(3HB) and P(3HO-co-HD).Only the lower concentrations of GP in the composite blends contained some bacteria which were able to adhere. Also, for both P(3HB) and P(3HO-co-HD), the lowest concentration of GP was sufficient to prevent *Escherichia coli* (ATCC® 25922™) cells from adhering to the composites.

In contrast, the *P. aeruginosa* (ATCC® 27853™) bacterial cells were able to adhere on the polymer composites in all cases except when the highest concentration of GP was incorporated into the blended polymer matrix.

The results for the free planktonic cells were evaluated first by measuring the OD_{600} using the microplate reader, and the supernatant was used on agar plates to confirm the OD_{600} values visually. The results are summarised in the Appendix section I Figure 2-7 and show that the higher the OD_{600} was the more bacteria were obtained after 24 h of incubation on agar plates at 37^{o}C.

5.2.8 *In vitro* Cytocompatibility of films and blends containing garlic powder

The cytocompatibility of the films containing different amounts of GP was tested against L929 murine fibroblasts. Initially, indirect tests were performed as described in paragraphs 2.12.1 and 2.12.2. Briefly, the samples were incubated in specific media for the L929 cell line for 24 h and simultaneously, in another TCPS plate cells were seeded for 24 h as well.
The media from the seeded L929 cells was then removed and replaced with media in which the GP samples had been incubated, according to ISO 10993-5. As a positive control polyethylenene (PE) was used from Goodfellow while as a negative control Polyurethane film containing 0.1 % zinc diethyldithiocarbamate (ZDEC) was used from Hatano Research Institute.

The viability of the L929 murine fibroblasts after their incubation in media in which neat PE, P(3HB), P(3HO-co-3HD) and the 75/25 blend had previously been incubated respectively are shown in Figure 5.26.

The 75/25 blend was around 100 % of cell viability with very small variation of the standard deviation values as shown in Figure 5.26. For the P(3HB) samples containing 23 wt%, 45 wt% and 90 wt% GP the increase in the antibacterial agent, GP, resulted in the decrease of the cell viability to 50 %.
The samples showed statistical significance when compared with the non-modified polymer. The highest viability of the cells was achieved with the lower concentrations of GP. The P(3HO-co-3HD) films containing the different loadings of GP showed similar behaviour to the P(3HB) films containing GP.

As shown in Figure 5.26 B the lower loading of the GP into the P(3HO-co-3HD) resulted in the higher cell viability where further increase of the GP reduced the viability. Additionally, in Figure 5.26.C is shown that the blend composites presented a similar behaviour with the other two polymer composites. The higher the amount of the GP content the lower was the resulted cell viability.

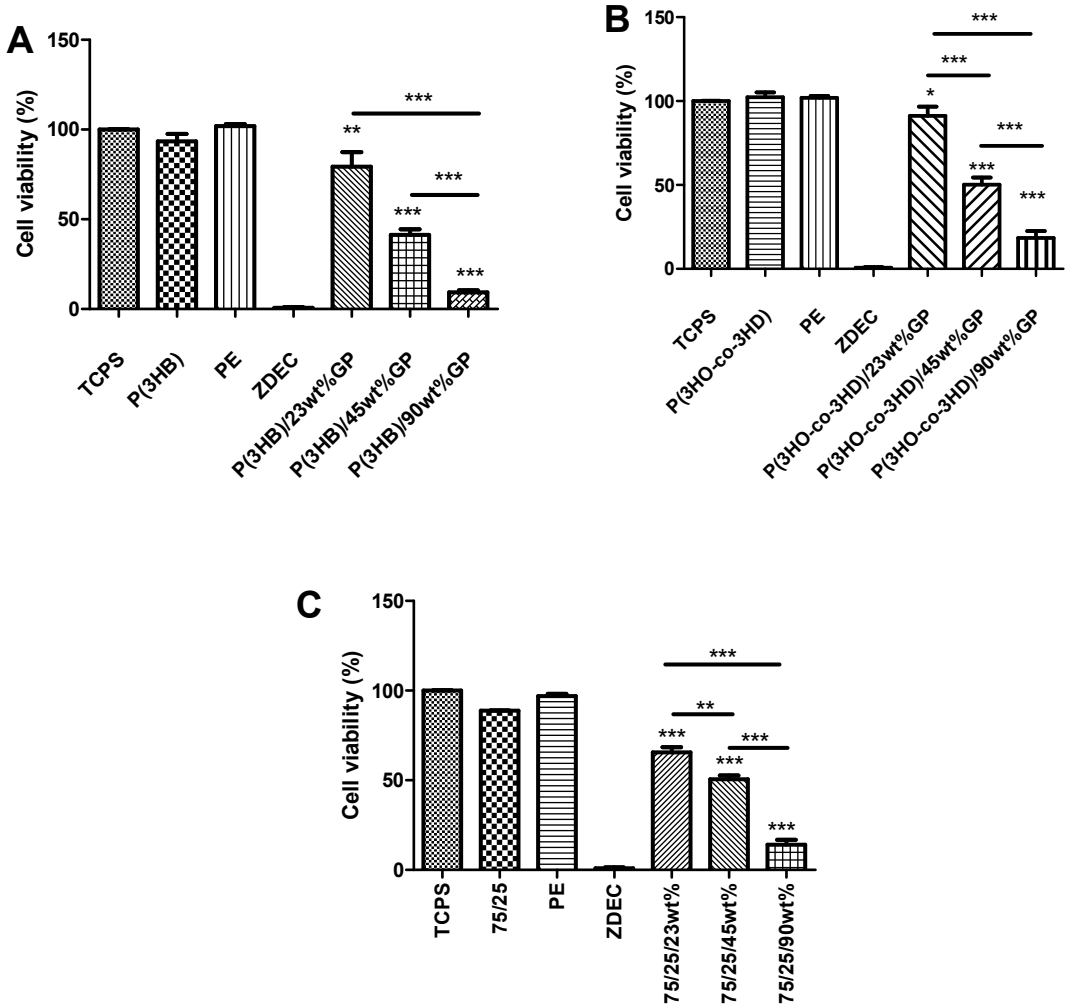

Figure 5.26: Indirect cytocompatibility evaluation of the (A) P(3HB), (B) P(3HO-co-3HD) and (C) 75/25 P(3HO-co-3HD)/ P(3HB) composites containing different loadings of GP with respect to L929 cells (Mean± SEM, n = 9 independent experiments). Statistical significance determination is represented as *p ≤ 0.05, **p ≤ 0.01, and ***p ≤ 0.001 for cells on TCPS vs. all materials, and non-modified polymer blend vs. GP composites

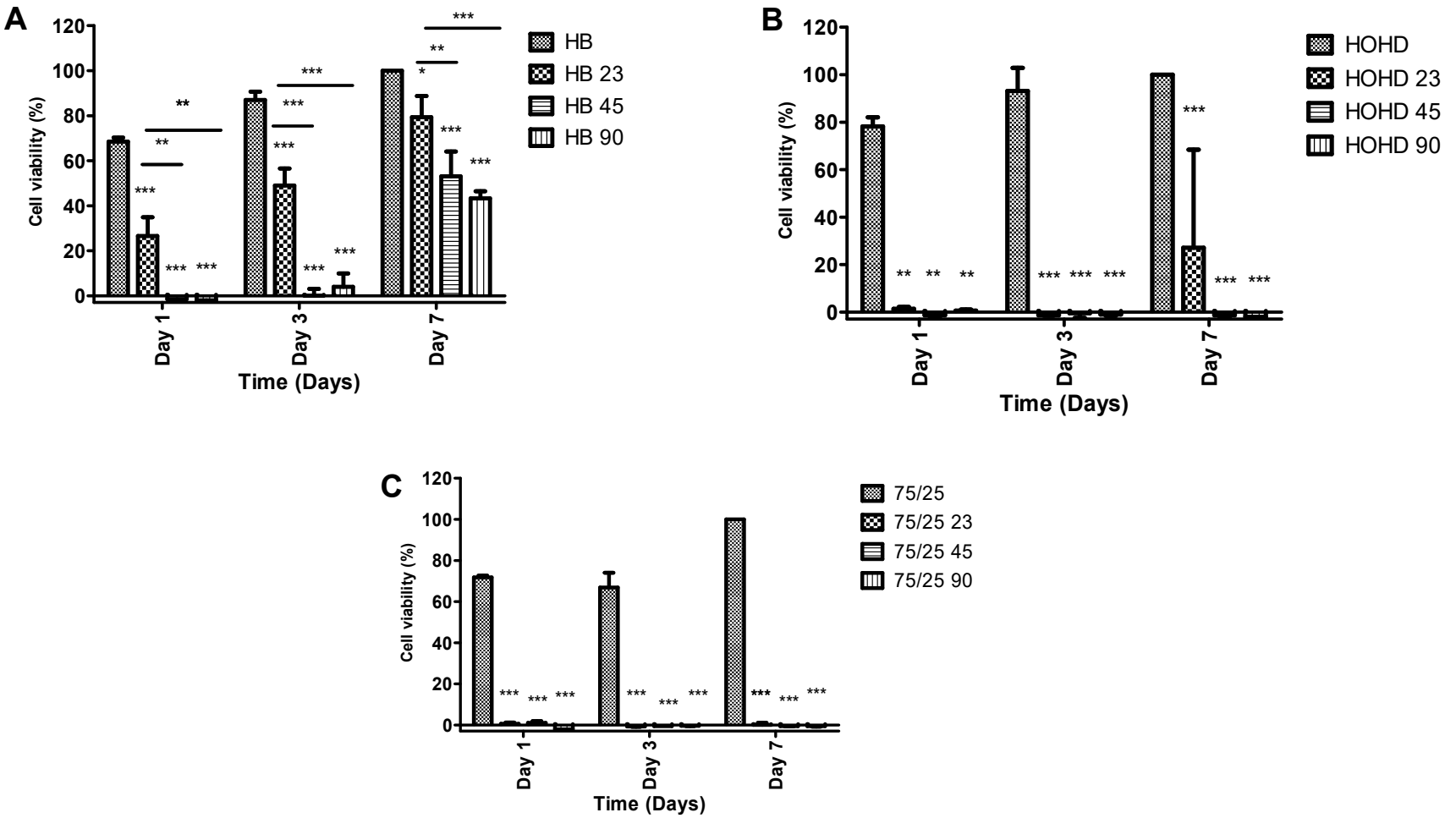

Figure 5.27: Direct cytocompatibility evaluation of the (A) P(3HB), (B) P(3HO-co-3HD) and (C) 75/25 P(3HO-co-3HD)/ P(3HB) composites containing different loadings of GP with respect to L929 cells (Mean± SEM, n = 9 independent experiments). Statistical significance determination is represented as *p ≤ 0.05, **p ≤ 0.01, and ***p ≤ 0.001 for cells on TCPS vs. all materials, and non-modified polymer blend vs. GP composites.

For the direct contact tests, the cells were seeded directly on the surface of the specimens, and their cytocompatibility was assessed using the cell viability assay Cell Titer-Blue® (Promega). The time points used for this investigation were Day 1, 3 and 7 after the seeding of the samples with the cells.

Cell proliferation of the L929 fibroblasts was found to increase from day 1 to day 7 for all non-modified PHA samples. For the P(3HB) samples containing the GP only the lowest concentration, 23 wt%, did not kill all the cells resulting in a cell viability of around 30 %.

The statistical analysis revealed significant differences (***$p<0.001$) between the composites and the neat P(3HB) film for day 1 and 3. After, 72 h (3 days) of direct seeding the P(3HB) composite containing the lower GP loading (23 wt%) revealed a cell viability of 49 %; showing an enhancement compared with day 1 viability of the same composite.

By day 7, all P(3HB)/GP samples showed an increase in cell proliferation. From the lower to the higher loading the cell viability was 79 %, 53 % and 43 %. The statistical analysis showed significant difference of the 45 and 90 wt% composites (***$p<0.001$) compared with the neat P(3HB). The mcl-PHA composites resulted a very low cell viability for all three investigated time points. The statistical analysis revealed significant difference between the composites and their positive control (neat P(3HO-co-3HD) (***$p<0.001$).

Only the composite containing the lower amount of GP, 23 wt%, showed an increase in the cell viability of 27 %. All the composites, for all the three different time points did not show any significant difference ($p>0.005$) upon statistical analysis. Finally, the composite blends containing the different content of GP did not show any cell viability for the three time points of investigation.

All composites showed significant differences (***$p<0.001$) after the statistical analysis compared with the neat blend for all days. Amongst the blend composites it was shown no significant differences ($p>0.05$) upon statistical analysis.

5.3 Discussion

Despite the advances in green technologies and their utilisation of in other industries such as in the manufacture of consumables, its use in biomaterials is still in its infancy. The multidisciplinary era of modern tissue engineering requires versatile, tuneable materials which are easily processed and will be suitable to improve or replace biological tissues.

The limitations of conventional techniques for successful nerve regeneration have led researchers to seek out alternative solutions. In spite of the significant revolution in the field since the first reports of silicone tubular NGCs up to the current tissue-engineered nerve NGCs, nerve tissue engineering can still be considered to be in its infancy. In this chapter, linear bio-polyesters were combined with the natural antibacterial compound GP and fully characterised for their potential use in nerve tissue engineering.

P(3HB), P(3HO-co-3HD) and the selected composite blend, (75/25 P(3HO-co-3HD)/ P(3HB)), were used as polymer matrices to which different ratios of GP was added to give final concentrations of (23 wt%, 45 wt% and 90 wt%). The developed composites were investigated for changes to their physicochemical, surface, antibacterial and cytocompatibility properties upon the addition of the natural compound in comparison with the neat samples.

The ATR/FTIR spectra of the samples contained the characteristic peaks indicative of the presence of GP in the matrixes. For samples derived from P(3HB), the peaks were observed only in the composite containing the highest, (90 wt%) concentration of GP. For the composite samples derived from P(3HO-co-3HD) and GP, the characteristic peaks were not detected in any of the samples. Finally, the composite blends loaded with the different concentrations of GP all possessed the characteristic peaks expected for GP even at the lowest concentration (23 wt%). The incorporation of GP appears to differ between the scl, mcl and binary system of PHA.

In the thermal analysis, the addition of GP into the P(3HB) matrix resulted in higher glass transition temperature (T_g) while there was no significant change in the melting temperature (T_m) observed when compared with the neat P(3HB). The addition of 45 wt% GP in the P(3HB) matrix reduced the Young's modulus and enhanced the elongation at break; indicating a poor filler-matrix adhesion at

the interface as the garlic powder might not behave as a reinforcement but as a defect in the matrix, yielding a more ductile composite. For P(3HO-co-3HD), the addition of GP reduced the glass transition temperatures resulting in a less crystalline composite with lower tensile strength obtained from the mechanical evaluation. Addition of GP into the binary system of the PHA blend did not affect the thermal values. In the mechanical evaluation, it was shown that the Young's modulus decreased inversely to the elongation at break, which indicates that GP reinforced the binary polymer matrix. However, the incorporation of 23 wt% and 90 wt% GP in the binary system resulted in a more elastomeric blend composite, with respect to the neat blend, indicating a plasticisation effect of the GP filler was attributed to the interaction of the particles with the polymer chains, resulting in greater mobility of the chains (or free volume).
The plasticising effect of the filler in both the P(3HO-co-3HD) and 75/25 P(3HO-co-3HD)/P(3HB) polymeric networks was attributed to the formation of hydrogen bonds with the hydroxyl and amino functional groups present in GP, (Thakur and Thakur, 2015). These findings are in agreement with the literature were the entrapment of the filler is responsible for this effect (Fama *et al.,* 2010).

Surface hydrophobicity is a key factor which affects cell attachment and proliferation. Water contact angle measurements were utilised to evaluate the developed composites for their hydrophobicity. The lower the value of the water contact angle, the more hydrophilic the surface is. To ensure the homogeneity of the developed composites both sides, air and glass sides, of the films were assessed.

A correlation between the concentration of GP and the water contact angle was observed in all the developed PHA composites. Increases in the amount of GP in the matrix of P(3HB) resulted in more hydrophobic specimens. A proportional relationship was observed between the increase in GP content and the hydrophobicity of the P(3HB) composites for both the air and glass sides of the samples. Additionally, for the same concentrations of GP, both sides resulted in similar values indicating a uniform formation of the composites even with the higher concentration (90 wt%).

With the P(3HO-co-3HD) samples a rapid decrease of the water contact angle was observed with increased addition of GP. Even with the lower concentrations

of GP added to P(3HO-co-3HD) resulted in more hydrophilic composites when compared to the neat P(3HO-co-3HD). This phenomenon was observed for both the air and glass sides of the samples. When compared, air and glass side samples from the same composites had similar hydrophobicity values, confirming a good dispersion of the GP into the polymeric suspension.

The addition of the GP into the binary system of the blend PHA resulted initially in a reduction of the hydrophobicity while further addition of GP afforded more hydrophobic composites. The highest amount of GP (90 wt%) resulted in a more hydrophobic sample than the non-modified blend (air side). Similarly, the glass side of the composite containing 23 wt% of GP in the polymer binary system resulted in a more hydrophilic composite than the non-modified blend and while further addition of GP produced more hydrophobic composites, their water contact angles did not exceed that of the non-modified blend.

The addition of GP into the P(3HB) polymers resulted in changes to the surface topography. Addition of the lowest concentration of GP, (23 wt%), to the polymer matrix resulted in a surface with irregularities and asymmetric pores. With the further addition of GP, (45 wt%), the number of irregularities and asymmetric pores increases. The P(3HB)/90 wt% sample, however, showed the least amount of irregularities when compared with the other two composites.

On the contrary, the addition of 90 wt% of GP to the polymer matrix of P(3HO-co-3HD) did not show any significant effect on the surface morphology. It seems that garlic powder precipitates on the P(3HO-co-3HD) surface creating a smooth cover which contains small pores in the case of the lowest concentration, 23 wt% GP, and as the amount of the agent increases it results in a more homogenous surface. For the 75/25 P(3HO-co-3HD)/ P(3HB) blend, the addition of 23 wt% and 45 wt% of GP respectively resulted in irregular topographies with rock-like features creating asymmetric pores as shown in Figure 5.9.
Further additions of GP resulted in a more even and smooth surface compared with the two other composites.

Garlic is a well-known spice for its long list of anecdotal therapeutic properties. A lot of attention has been focused on this plant recently due to its potent antibacterial and antifungal effects (Borlinghaus *et al.*, 2014; Marchese *et al.*,

2016; Leontiev *et al.*, 2018). Garlic powder (GP), garlic oil and garlic extract have been explored for their antibacterial abilities (O'Gara, Hill and Maslin, 2000).

The plethora of organosulfur compounds in garlic makes it a very powerful antibacterial agent with efficacy comparable to conventional antibiotics. The main identified antibacterial bioactivity of GP is due to its interaction with important thiol-containing enzymes (Ankri and Mirelman, 1999). The antibacterial activity of GP is mainly attributed to allicin, a reactive sulphur species (RSS) able to inhibit thiol-containing enzymes (Feldberg et al., 1988; Nostro, 2006; Borlinghaus *et al*., 2014).

When aliquots of GP in different concentrations were tested against both Gram-positive and Gram-negative bacteria, it was highlighted that the amount needed to induce bacteriostatic and bactericidal effects on the microorganisms was lower for the Gram-positive bacteria. This can most probably be attributed to the fact that Gram-positive bacteria lack a second phospholipid membrane which Gram-negative bacteria poses.
These findings are in agreement with other studies which have shown that Gram-negative bacteria needed higher doses of GP to be treated (O'Gara, Hill and Maslin, 2000; Bakri and Douglas, 2005).
Additionally, it was possible to treat both methicillin-resistant *Staphylococcus sp*. with GP aliquots while *Pseudomonas aeruginosa* (ATCC® 27853™) required much higher concentrations of the GP filling agent to inhibit bacterial growth. This might be attributed to the fact that mucoid strains, such as *Pseudomonas aeruginosa*, prevent allicin penetration due to their hydrophilic capsular and mucoid layers (Ankri and Mirelman, 1999). In all cases, an inversely proportional relationship between the concentration of GP and bacterial growth was observed. The higher the concentration of GP the lower the OD_{600} hence, lower bacterial growth as shown in Figure 5.12. Similarly, during the quantification of the biomass, the higher concentration of GP gave rise to less formation of biofilm.

The preliminary screening tests in section 5.2.7.1 showed that the *S. aureus* strain is more susceptible than the *E. coli* in the presence of GP. Abiy and co-workers previously reported this phenomenon and also observed that *E. coli* requires a higher concentration of garlic than *S. aureus* to inhibit bacterial growth (Abiy and Berhe, 2016).

Mozaffari Nejad *et al.*, (2014) showed that the minimum inhibition concentration of GP for Gram-positive bacteria such as *S. aureus* was between 15.6 - 48.3 mg/ml. In contrast, for gram-negative bacteria, the range is higher between 22.9 - 37.2 mg/ml (Mozaffari Nejad *et al.,* 2014). Saha *et al.* had also previously reported that aqueous garlic extract exhibited a MIC value of 400 µg/ml and 700 µg/ml against *S. aureus* and *E. coli* respectively (Saha *et al.,* 2016). The broth dilution assay used to obtain the MIC values of the GP solution (stock solution of 140 mg/ml), according to ISO 20776-1:2006 protocol, against the six different bacterial strains namely: *Staphylococcus aureus* (ATCC® 29213™), *Staphylococcus epidermidis* (ATCC® 12228™), *Escherichia coli* (ATCC® 25922™), *Pseudomonas aeruginosa* (ATCC® 27853™), as well as clinical isolates of MRSA and MRSE were selected and tested against GP. Results showed that GP exhibited very good inhibitory properties with MIC values ranging from 4.4 to 35 mg/ml against a variety of bacterial strains.
Additionally, by measuring the OD_{600} in a microplate reader, a dose-dependent growth inhibition effect at 37ºC was revealed for *Staphylococcus epidermidis* (ATCC® 12228™), MRSA and MRSE. Moreover, tests showed that the Gram-positive bacteria were more susceptible to the agent than the Gram-negative.

The results from MIC and MBC tests showed that GP acts more efficiently against Gram-positive bacteria than Gram-negative bacteria. Also, it is of significant interest that the concentrations of GP required to induce an inhibitory or bactericidal effect are the same against both non-resistant and Methicillin-resistant clinical isolates MRSA and MRSE.

From the biofilm assay it was highlighted that the efficiency of GP to inhibit the biofilm formation was similar for both the non-resistant and Methicillin-resistant *Staphylococcus aureus* bacteria. However, in the case of *Escherichia coli* (ATCC® 25922™) bacterial strain the lower loadings of GP were not sufficient to inhibit the adherence of the bacterial on the composite films. In addition, it was observed that the GP showed almost no effect on the biofilm formed from the *Pseudomonas aeruginosa* (ATCC® 27853™) bacterial strain. These findings are in agreement with literature where Methicillin-resistant *Staphylococcus aureus*, as well as other MDR strains, are reported to be more sensitive to GP compounds

such as allicin. It has also been reported previously that some bacterial strains are resistant to the action of allicin such as mucoid strains of *Pseudomonas aeruginosa*, which prevent allicin penetration due to the hydrophilic capsular or mucoid layers they possess (Ankri and Mirelman, 1999). In addition, these results are supported from the findings in the previous performed assays verifying the resistance of *P. aeruginosa* (ATCC® 27853™) strain to GP.

Standard antibiotic discs containing streptomycin (300 μg/disc), oxacillin (1 μg/disc) and gentamicin (300 μg/disc) were used as positive controls. The antibiotic used as a positive control in the experiments against *Staphylococcus aureus* (ATCC® 29213™) was oxacillin (1 μg/disc). According to EUCAST Clinical Breakpoint Tables *Staphylococcus aureus* (ATCC® 29213™) is susceptible when tested with the antibiotic oxacillin and if the inhibition zone is ≥ 2 cm and resistant for inhibition zones which are < 2 cm. The observed inhibition zones from the PHAs samples containing GP were compared with those obtained from oxacillin and revealed in some cases inhibition zones less than 2 cm. More specifically, *Staphylococcus aureus* (ATCC® 29213™) was resistant to all the samples containing 23 wt% of GP, (P(3HB)/ 23 wt% GP, P(3HO-co-3HD)/ 23 wt% GP and 75/25 P(3HO-co-3HD)/ P(3HB)/ 23 wt% GP) because their inhibitory zones were much lower than 2 cm. All the other test samples exhibited inhibition zones which were greater than 2 cm, and hence the microorganism was considered to be susceptible for those samples.

For *Staphylococcus epidermidis* (ATCC® 12228™), the antibiotic used was gentamicin (300 μg/disc). The EUCAST Clinical Breakpoint Tables defines the microorganism resistant to this agent when the inhibition zones formed are less than 2.2 cm and susceptible when ≥ 2.2 cm. According to the findings from the paragraph 5.2.7.5 *Staphylococcus epidermidis* (ATCC® 12228™) is resistant to the P(3HB) polymers containing 23 and 45 wt% as well as P(3HO-co-3HD)/23 wt% GP and 75/25P(3HO-co-3HD)/P(3HB)/23 wt% GP specimens since the inhibition zones in these cases were less than 2.2 cm.

The microorganism was found to be susceptible to all other samples. MRSA and MRSE were both investigated for their resistance to the PHAs containing different amounts of GP compared with antibiotic disks which contained 5 μg t of ceftobiprole.

The results showed that for MRSA, all samples except for P(3HO-co-3HD)/ 23 wt% GP showed inhibition zones greater than 1.7 cm hence MRSA was considered to be susceptible in the presence of these samples. P(3HO-co-3HD)/ 23 wt% GP formed an inhibition zone of only 1 cm and therefore the microorganism is considered to be resistant to this sample. MRSE also showed resistance to all samples containing GP except the 90 wt% specimens of the P(3HO-co-3HD) and the PHA blend. Finally, the polymers containing GP were tested against *Escherichia coli* (ATCC® 25922™) in comparison to the aminoglycoside antibiotic, gentamicin. The antibiotic disc used for the susceptibility evaluation of *Escherichia coli* (ATCC® 25922™) contained 10 μg of gentamicin. From the results obtained the microorganism was found to be resistant to the following specimens: all the samples containing 23 wt% GP and the P(3HO-co-3HD)/ 45 wt% sample. The interpretation of the results was conducted following the guidelines described in EUCAST (E. Matuschek and D. F. J. Brown and G. Kahlmeter, 2014).

From the tests evaluating the bacterial cells that managed to adhere to the GP composites, it was shown that there was no significant difference between the efficacies of the different composites against all the tested pathogens. In all cases, the loss of bacterial viability was higher than 90 % even in the composites containing only 23 wt% GP, indicating that the bacteria which managed to adhere onto the surfaces did not survive and the recovered bacterial cells were much less in number compared to the respective controls.

For the planktonic cells, it was shown from the OD_{600} measurements that the high values of the optical density resulted in a high number of recovered bacterial colonies after the incubation of the respective aliquots on agar plates for 24 h. It was shown that there was an inversely proportional relationship between the concentration of the GP on the composites and the OD_{600} and hence the number of the recovered bacteria. The higher the amount of the GP in the composite, the lower the respective value of the OD_{600} measured, the less the number of the bacterial colonies recovered. Only in the case of *Pseudomonas aeruginosa* (ATCC® 27853™), the only composites able to fight these pathogens were lower OD_{600} values observed for the P(3HB) and 75/25/P(3HO-co-3HD) composites containing 90 wt% of GP. From all the antibacterial tests conducted, the most significant finding is that GP can kill or inhibit Gram-positive, Gram-negative and

methicillin-resistant bacteria in a dose-dependent manner. Similar findings have been reported in other studies (Borlinghaus *et al.*, 2014).

The *in vitro* indirect cytocompatibility test highlighted that in all cases, the statistical analysis showed significant differences between the composites and the positive controls, TCPS. Similarly, when the composites were compared amongst themselves, significant differences were also observed. In all cases, an inversely proportional relationship between the amount of GP contained in the composite and the viability of the cells was observed. When the GP composites were tested directly for their cytocompatibility over seven days, it was observed that the cells were not able to survive in the presence of these composites.

As shown in Figure 5.27 A, B and C, the release of the agent interferes with the proliferation of the cells resulting in a low viability percentage. Only in the case of the P(3HB), garlic composites were some cells able to recover by day 7. This is most probably because of the short chain of the polymers in the matrices of these samples. The release of the GP filler agent appears to be more rapid, compared to the P(3HO-co-3HD) and the blended composites. Hence with the repeated exchange of the media, by day 7, some of the cells which managed to survive were able to recover because the newly provided nutrient contained lower amounts of the released GP compounds. The redox-dependant mechanism of allicin has been reported previously in other studies. It was proven that concentrations which were able to kill bacterial cells did not harm mammalian cells due to the affinity of allicin for bacterial cells (Yamada and Azuma, 1977; Ankri *et al.*, 1997).

Recent studies conducted on different cell lines for their reaction to the presence of different concentrations of allicin showed that mammalian cell lines differ in their sensitivity and responses to allicin (Gruhlke *et al.*, 2016).

In this study, eco-friendly polymers were successfully developed and fully characterised for their physicochemical, antibacterial and cytocompatibility properties. Different composites containing various ratios of GP were produced with a range of different thermal and mechanical properties which were able to be tailored. It was shown that the antibacterial activity conferred on the polymer matrices was dose dependent.

The addition of GP altered the surface morphology in some of the composites. The addition of the antibacterial agent, GP filler, caused changes in the hydrophobicity of the developed samples. Unfortunately, the sensitivity of the L929 murine fibroblasts in the presence of these composites was very high. Allicin induced cell-death and inhibited cell proliferation.

The use of such composites could blossom not only in the food packaging industry but could also be of use for anti-cancer and cardiovascular devices.

Chapter 6

Development of PHA- based composites containing cerium doped phosphate fibres

6 Development of PHA- based composites containing cerium doped phosphate fibres

6.1 Introduction

Biomaterials science is moving forward to an era where implant removal will not demand a revision surgery after the completion of their functional role. As an alternative, bioactive and biodegradable materials have been investigated in order to evaluate their applicability in different biomedical devices and implants (Knowles, 2003a).

A class of inorganic biomaterials with temporary and bioactive properties are the phosphate-based glasses (PBGs) which have been explored for hard and soft tissue engineering and regeneration purposes (Knowles, 2003b; Islam *et al.*, 2017). Glasses had their quantum leap in biomaterials sciences in the late 1960s when Larry Hench discovered Bioglass®, also known as 45S5, and the interest in PBGs is still continuously increasing (Hench, 1970). This is due to the unique properties of PBGs. Firstly, is their ability to completely degrade in aqueous solutions within specific periods of time. Their solubility can be modified and tuned by changing their chemical composition to meet the requirements of specific applications. The addition of ions to the PBGs can alter their physicochemical properties (degradation and dissolution rate) and furthermore, confer specific biologically interesting properties to them such as support of cell attachment, migration, differentiation, and proliferation (Ahmed, Ren and Booth, 2019; Lapa *et al.*, 2019). The development of composites of PBGs containing silver, copper, gallium and other metal ions have shown potent antibacterial activity against both, Gram-positive and Gram-negative pathogens (Ahmed *et al.*, 2006; Valappil *et al.*, 2008).

The versatile geometries and designs that are possible with the PBGs make them highly attractive for their application in the production of scaffolds for tissue engineering, coatings of invasive medical devices and long-term implants. Among all the different forms of PBGs, the phosphate glass fibres (PGFs) have attracted much attention due to their excellent cytocompatibility and interesting mechanical properties. This makes PGFs a promising candidate as cell guidance structure in e.g. peripheral nerve conduits and as a reinforcement additive in e.g.

load bearing implants (Sharmin *et al.*, 2014). In this context, fibre-reinforced composites (FRC) led to a range of bioresorbable materials with suitable mechanical properties.

Both unidirectional and randomly oriented reinforcements of the PBG-based composites have been reported, and the obtained mechanical properties differ depending on the direction of measurement (Ahmed *et al.*, 2011; Zakir Hossain *et al.*, 2016). Most of the composites fabricated with PBGs are used in bone fixation devices. Other medical applications of such composites are found in dental implants, drug delivery systems and scaffolds for nerve and vascular tissue engineering (Bitar *et al.*, 2004; Vitale-Brovarone *et al.*, 2012). Yang *et al.* reported that the reinforcement of gelatin with tri-calcium phosphate ceramic particles resulted in better results for nerve regeneration compared with the silicone nerve conduits (Yang *et al.*, 2011).

In another study, it was shown that $TiPS_{2.5}$ glass fibres promoted the polarisation of neurons but also assisted with the directionality for the axon growth (Vitale-Brovarone *et al.*, 2012). In another study, a collagen matrix was reinforced with aligned phosphate glass fibres (PGFs). The developed composite mats were rolled into a tubular form to obtain nerve conduits. The specimens were subjected to both *in vitro* and *in vivo* experiments, and they successfully supported the directional axonal growth providing sufficient guidance for the transacted sciatic nerves of rats (Kim *et al.*, 2015). Previous findings combining PHA blend composites containing (0.5, 1.0 and 2.5 wt%) fibrous bioactive glasses (BGs) showed superior support of proliferation and dendritic outgrowth of NG108-15 compared to PHA blend and PCL controls (Lizarraga Valderrama, 2017).

Taking advantage of the synergy of the scaffold architecture and suitable fillers, leading to more suitable structures and additional biological advantages, fibre-reinforced composites were fabricated using polyhydroxyalkanoates (PHAs) as the polymer matrix and PGFs doped with cerium (Ce). The Ce-doped PGFs were produced and delivered by Agata Lapa, from Professor Boccaccini's group at University of Erlangen (Lapa *et al.*, 2019). The applied blend based on two PHAs, P(3HO-co-3HD)/P(3HB) in the mass ratio 75/25 (w/w), was reinforced using different amounts of PGFs (37, 74 and 90 wt%).

The fabricated composites were comprehensively analysed to assess their physicochemical properties, antibacterial capabilities and cytocompatibility with the aim to be applied for peripheral nerve reconstruction and tissue engineering, respectively. In detail, thermal properties were investigated by the application of DSC, surface characteristics by ATR-FTIR and SEM, crystallinity by XRD, and biological activity by agar diffusion assay or broth dilution method (antibacterial) and cytocompatibility by multiplex assay.

6.2 Results

6.2.1 Development of PHA composites containing cerium-doped phosphate glass fibres

The main aim of this part of the project was the development and characterisation of novel PHA/Ce-doped PGF composite biomaterials for the purpose of peripheral nerve reconstruction and regeneration, particularly the improvement of neuronal guidance. Thus, phosphate glass fibres (PGFs) were added into the polymer blend matrix of defined P(3HO-co-3HD)/P(3HB) compositions. Figure 6.1 shows the picture of a bundle of PGFs (left) and a magnified image of a single PGF by scanning electron microscopy (SEM; Right).

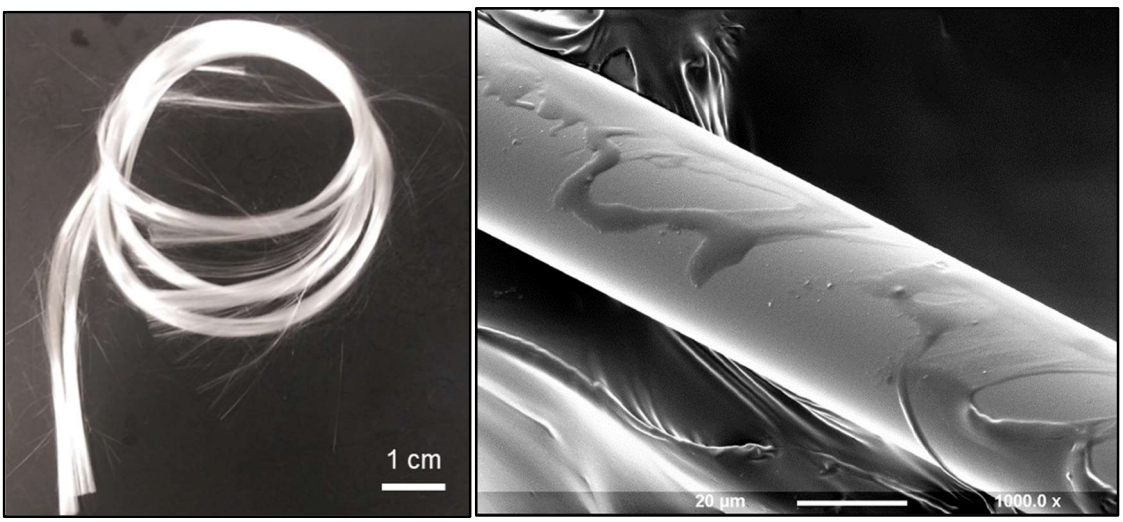

Figure 6.1: Bundles of phosphate glass fibres (PGFs) (left) and SEM image of a melt-drawn spinning fibre made of phosphate glass (right).

The PGFs were produced by a continuously working melt-draw spinning process (Muñoz-Senovilla *et al.*, 2017) and had a diameter of approximately 10 – 25 μm. The chemical composition of the fabricated cerium-doped fibres were **18-**MgO-**10**CaO-**25**Na_2O-**42**P_2O_5-**3**SiO_2-**2**CeO_2**.** Composites were developed by the incorporation of these novel inorganic microfibres into the blend polymer matrix.

The preparation of the 75/25 (w/w) P(3HO-co-3HD)/P(3HB)/Ce-doped PGF composite is described in detail in section 2.9, but briefly the blend of 75/25 (w/w) P(3HO-co-3HD)/P(3HB) was dissolved in chloroform and poured into a glass petri dish. Once the polymer blend solution reached a certain viscosity while the organic solvents were evaporating Ce-doped PGFs were added in an aligned fashion.

Figure 6.2 shows images of the 75/25 (w/w) P(3HO-co-3HD)/P(3HB)/ Ce-doped PGF composites containing different weight percentage of three Ce-PGFs: 37, 74 and 90 wt%. All composites are reinforced by unidirectional Ce-PGFs mats as it was demonstrated by the aligned orientation of the fibres within the polymer blend matrix.

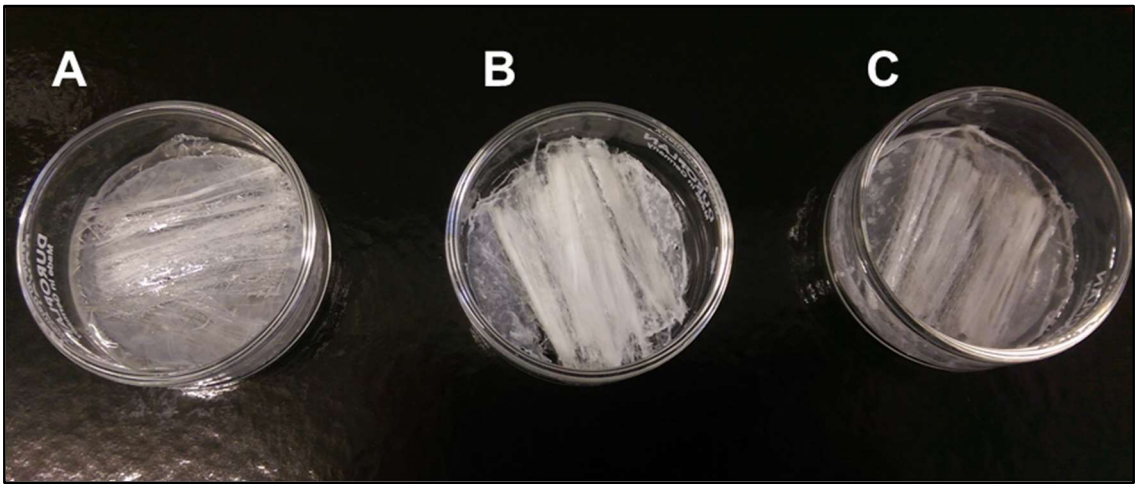

Figure 6.2: 75/25 (w/w) P(3HO-co-3HD)/P(3HB)/ Ce-doped PGF composites processed by the solvent casting method containing (A) 37 wt% Ce-PGFs, (B) 74 wt% Ce-PGFs and (C) 90 wt% Ce-PGFs.

6.2.2 Attenuated Total Reflectance Fourier Transform Infrared Spectroscopy (ATR/FTIR) of PHA/PGF composites

In order to verify the chemical composition of the different composite film surfaces ATR/FTIR was applied. Characteristic peaks of the 75/25 (w/w) P(3HO-co-3HD)/P(3HB) blend are a result of the combination of peaks from both the scl and mcl-PHAs located at 1720-1740 cm^{-1} and 1150-1300 cm^{-1} corresponding to the ester carbonyl group (C=O) and the CH group, respectively. The peak located at 2924 cm^{-1} corresponds to the stretching vibrations of C-H bonds of methyl (CH_3), and methylene (CH_2) groups and is characteristic for the mcl-PHA (and have been described in detail in section 4.2.2) (Reis *et al.*, 2008).

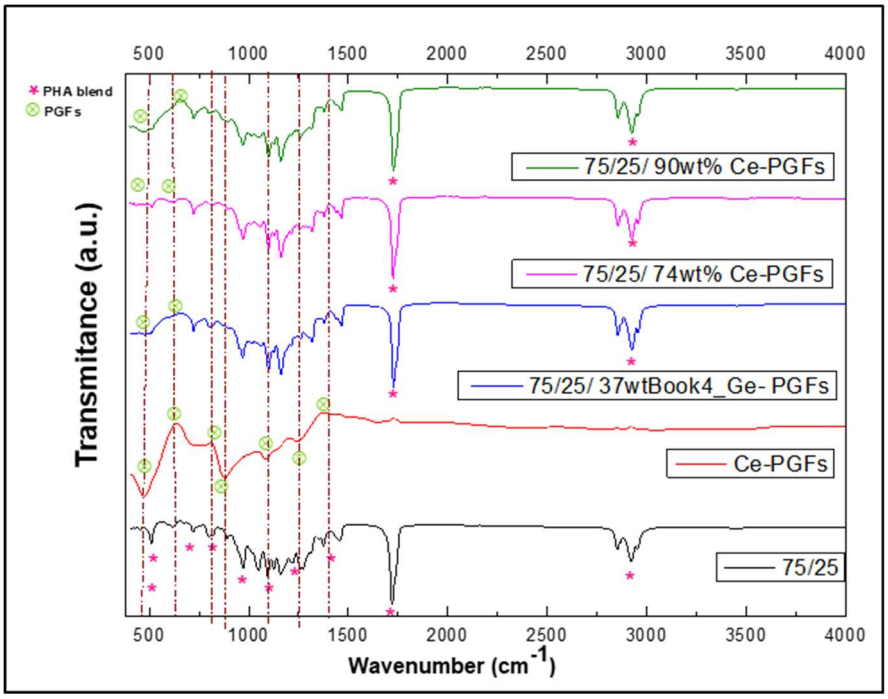

Figure 6.3: ATR/FTIR spectra of**: ----** 75/25 P(3HO-co-3HD)/P(3HB), **----** Ce-PGFs and 75/25 P(3HO-co-3HD)/P(3HB) composites with **----** 37 wt%, **----** 74 wt% and **----** 90 wt% Ce-PGFs.

The FTIR peaks that characterises the Ce-doped PGFs are located at 472 cm^{-1} and are attributed to the vibration of cation-oxygen polyhedron and the deformation mode of the tetrahedral phosphate group. The symmetric stretching of the non-bridging oxygen is responsible for the peak at 730 cm^{-1}, whereas the peak at 812-882 cm^{-1} is attributed to the symmetric stretching vibration of P–O–P linkages.

The asymmetric stretching of the non-bridging oxygen is responsible for the peaks located between 1050-1092 cm^{-1} while the asymmetric stretching vibration of P–O–P linkages are responsible for the peaks located between 1204-1252 cm^{-1} (Lai *et al.*, 2011; Łapa *et al.*, 2019).

It was possible to distinguish two characteristic peaks of PGFs in all specimens that are located at lower wavenumbers (472 and 730 cm^{-1}) as shown in Figure 6.3. Further characteristic peaks attributed to the Ce-PGFs were not illustratable due to overlaps with the peaks corresponding to the 75/25 P(3HO-co-3HD)/P(3HB) blend matrix. As shown in Figure 6.3, in all the composites, the characteristic peaks of the PHA blend were detected.

6.2.3 Thermal characterisation of PHA/PGF composites

The thermal properties of the 75/25 P(3HO-co-3HD)/P(3HB)/Ce-doped PGF composites containing Ce-PGFs in different ratios were compared with the neat 75/25 P(3HO-co-3HD)/P(3HB) blend polymer and the Ce-doped PGFs. Figure 6.4 A shows the thermograms ranging from -60 to 200^{o}C. Figures 6.4 B, C, D and E depict specific regions of the obtained thermograms attributed to the glass transition temperature (T_g) of P(3HO-co-3HD) and P(3HB), crystallisation temperature (T_c) and melting temperature (T_m) respectively. The brown lines in the thermograms represent the first heating cycle which is conducted to erase the thermal history of the composites, whereas the lines shown in different colours represent the second heating cycle of the samples to analyse the thermal properties of the composites.

All composites showed a T_g approximately at -48.3^{o}C that correspond to the T_g of P(3HO-co-3HD), with 75 wt% the main component in the polymer blend (Figure 6.4 B).

The second glass transition temperature at -1^{o}C is attributed to the presence of P(3HB) in the blends as shown in Figure 6.4 C. Figure 6.4 D reveals the presence of the crystallisation peak that characterises P(3HB). The blend, as well as the composites, presented the T_c. The crystallisation peak of the 75/25 P(3HO-co-3HD)/P(3HB) blend was at 42^{o}C. The addition of 34 wt% Ce-PGFs led to an increase in the temperature of the crystallisation to 52^{o}C. Further addition of the Ce-PGFs shifted the crystallisation temperature to 56.8^{o}C.

The highest amount (90 wt%) of Ce-PGFs within the polymer matrix led to a slightly lower T_c value of 55.2ºC as shown in Figure 6.4 D. Finally, the melting temperature was found in the last region of the thermogram, Figure 6.4 E. The melting temperature peak observed at 169.3ºC is attributed to the presence of the P(3HB) in the composites. The addition of the different ratios of the Ce-PGFs (37, 74 and 90 wt%) did not significantly shift the melting point of the samples.

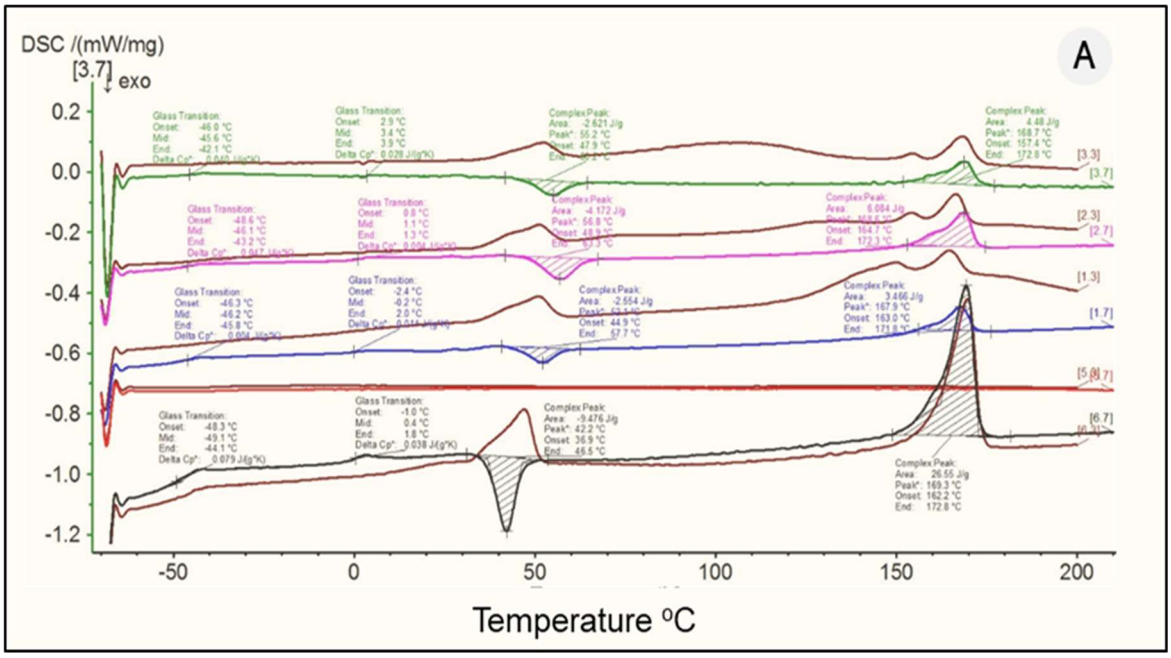

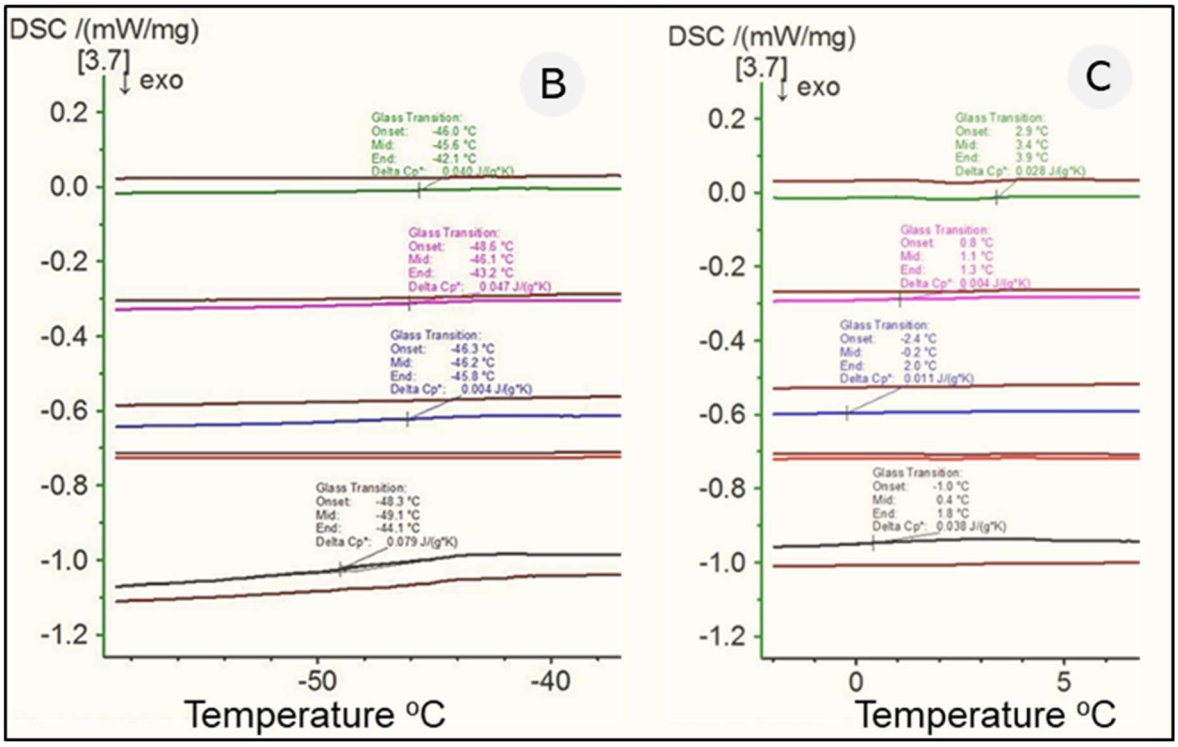

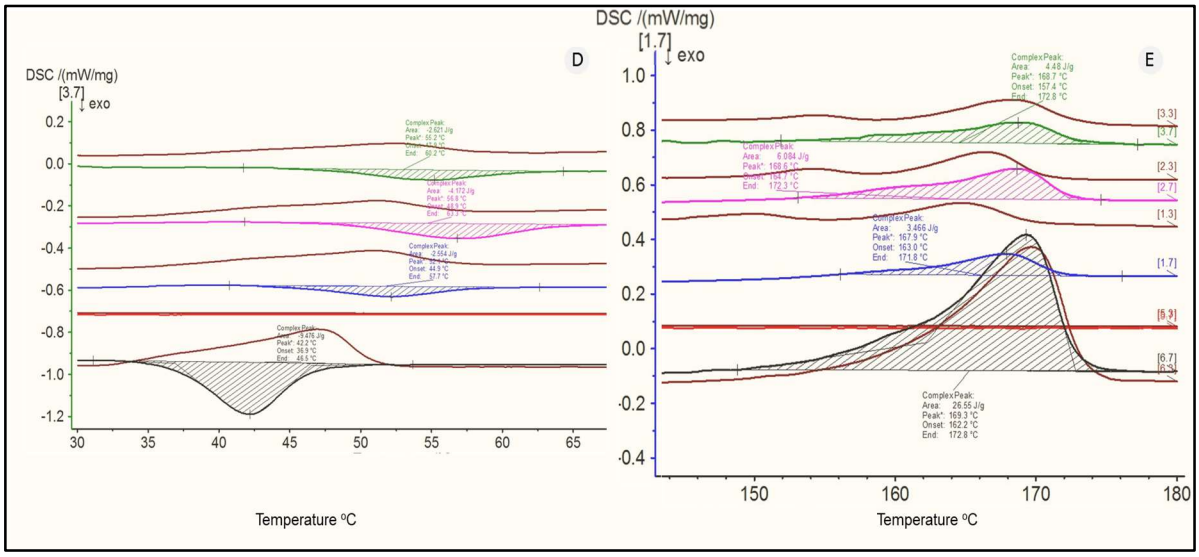

Figure 6.4: DSC thermograms: **----** 75/25 P(3HO-co-3HD)/P(3HB), **----** Ce-PGFs and 75/25 P(3HO-co-3HD)/P(3HB) composites with **----** 37 wt%, **----** 74 wt% and **----** 90 wt% Ce-PGFs (A) whole thermograms, (B) thermograms from -60°C to -40°C, (C) thermograms from -2°C to 5°C, (D) thermograms from 30°C to 65°C, (E) thermograms from 140°C to 180°C.

6.2.4 SEM analysis of PHA/PGF composites

SEM was used to analyse the different 75/25 (w/w) P(3HO-co-3HD)/P(3HB)/ Ce-doped PGF composites processed by the solvent casting modified with either 37 wt%, 74 wt% or 90 wt% Ce-PGFs. Both surfaces, air side and glass side, of each specimen were analysed. “Glass” side means the side of the composite film that is in contact with the bottom of the petri dish during the film casting process. SEM of the 37 wt% composite showed more or less unidirectional aligned glass fibres surrounded the polymer blend matrix (Figure 6.5 a-c). Interestingly, the surface of the glass side showed glass fibres covered randomly with the polymer blend material and not fully embedded as expected. In case of 74 and 90 wt% composite the samples exhibited a more homogenous distribution of densely packed and aligned PGFs (figure 6.5 d-f and g-i).

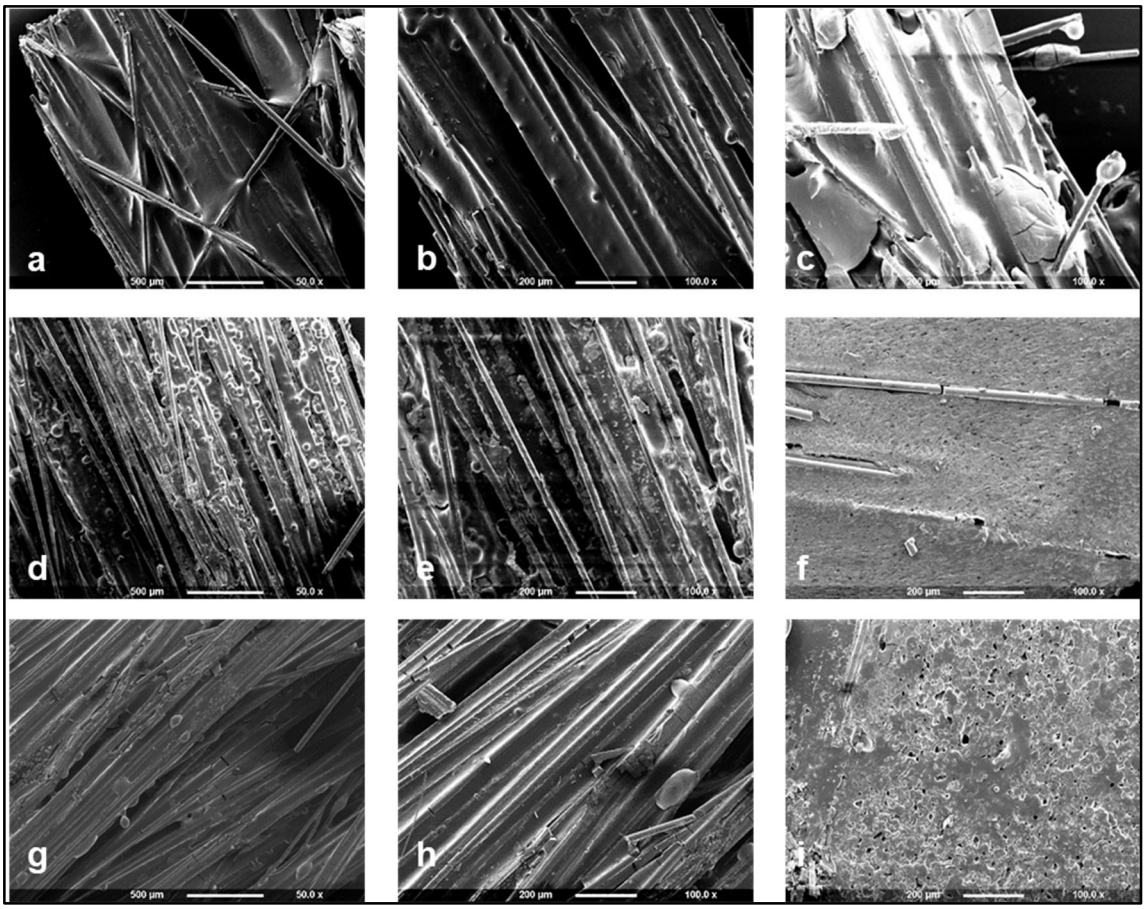

Figure 6.5: SEM micrographs of 75/25 (w/w) P(3HO-co-3HD)/P(3HB)/ Ce-doped PGF composites processed by the film casting method modified with either 37 wt% (a-c), 74 wt% (d-f) or 90 wt% (g-i) Ce-PGFs at different magnifications. Images a, d and g were taken with a magnification of × 50 and b, c, e, f, h and i were taken with a magnification of × 100.

The glass side of the developed specimens revealed that in the case of the lower amount of the PGFs the fibres were able to penetrate the polymer matrix and were exposed on both sides of the developed sample. Further addition of PGFs retained the fibres to penetrate the polymer matrix.

The micrographs of the glass side of 74 wt% and 90 wt% revealed very few fibres and also showed the formation of pores within the composite (Figure 6.5 f and i).

6.2.5 XRD analysis of the PHA/PGF composites

As shown in 4.2.7 the 75/25 P(3HO-co-3HD)/P(3HB) blend is a semi-crystalline material. In order to analyse the influence of amorphous Ce-PGFs added in different weight percentages to the blend polymer matrix on the semi-crystallinity of the novel composites XRD was performed. The corresponding XRD spectra of 75/25 P(3HO-co-3HD)/P(3HB) blend and Ce-PGFs only and modified with 37, 74 and 90 wt% Ce-PGFs are shown in Figure 6.6. The 75/25 P(3HO-co-3HD)/P(3HB) blend showed the characteristic XRD peaks already described in Figure 4.6 (4.2.7, green dashed line). The Ce-PGFs showed no peaks as expected for a glass, an amorphous inorganic solid.

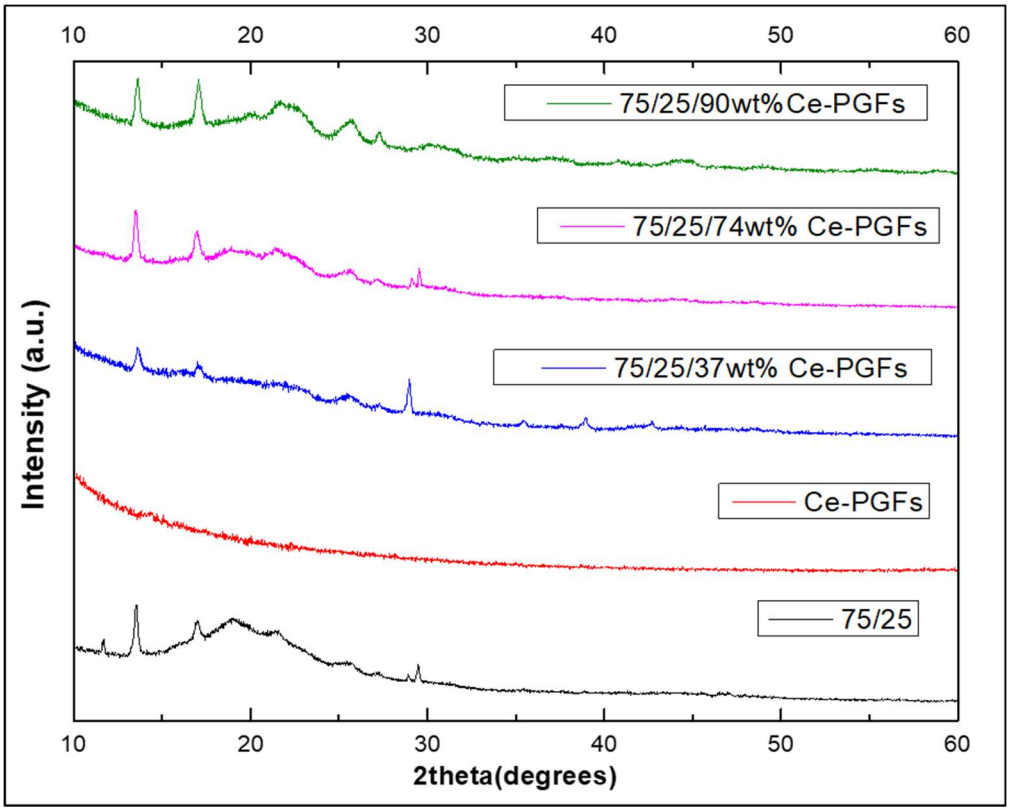

Figure 6.6: XRD spectra of: **----** 75/25 P(3HO-co-3HD)/P(3HB), **----** Ce-PGFs and 75/25 P(3HO-co-3HD)/P(3HB) composites with **----** 37 wt%, **----** 74 wt% and **----** 90 wt% Ce-PGFs.

The addition of any compound into the polymeric base can possibly have an impact on the molecular arrangement of the macromolecules within the material and this could possibly affect specific crystalline regions leading to a slight peak

shift or reducing the intensity or the full width at half maximum (FWHM) of a specific peak.

In comparison to the neat materials the composites showed only slight changes in the XRD spectra. The characteristic peaks attributed to the neat 75/25 polymer blend are located at 13.5°, 16.9°, 19°, 21.45°, 25.46° and 29.5° as explained in detail in section 4.2.7. The addition of 37 wt% Ce-PGFs resulted in the reduction of the peaks intensity and reduced significantly the full width at half maximum (FWHM) of the peak in the region between 17-25°. Further addition of the Ce-PGFs increased the intensity of the peaks located at around 13 and 16°. The higher content of Ce-PGFs showed even higher intensities of the peaks and significantly reduced the intensity of the peak located at 29°.

6.2.6 *In vitro* antibacterial evaluation of PHA/PGF composites

The antibacterial activity of the composites containing the cerium-doped phosphate fibres was evaluated for their ability to inhibit free planktonic bacterial cells (swarming phenotype), the adhered bacterial cells (sessile phenotype) and their capability to inhibit biofilm formation. The samples were cut into small discs of 6mm diameter and immersed in bacterial suspension adjusted to 0.5 McFarland. After 24 h of incubation aliquots from the wells were collected and the OD_{600} was measured using a spectrometer to evaluate the growth of the bacteria. Additionally, the obtained aliquots were plated on blood agar plates to count the CFU to investigate the inhibition of the free planktonic cells caused by the presence of the composites in the bacterial suspension.

To assess the effect of the composites on the adhered cells, samples which had been immersed in the bacterial suspension for 24 h were recovered and washed with PBS and sonicated to remove any bacterial cells which had managed to adhere to the surface of the composites. The samples were tested against six different bacterial strains, known to be responsible for many nosocomial infections: *Staphylococcus aureus* (ATCC® 29213™), *Staphylococcus epidermidis* (ATCC® 12228™), Methicillin-resistant *S. aureus* (MRSA), Methicillin-resistant *S. epidermidis* (MRSE), *Escherichia coli* (ATCC® 25922™), *Pseudomonas aeruginosa* (ATCC® 27853™) as shown in Figures 6.7-6.11.

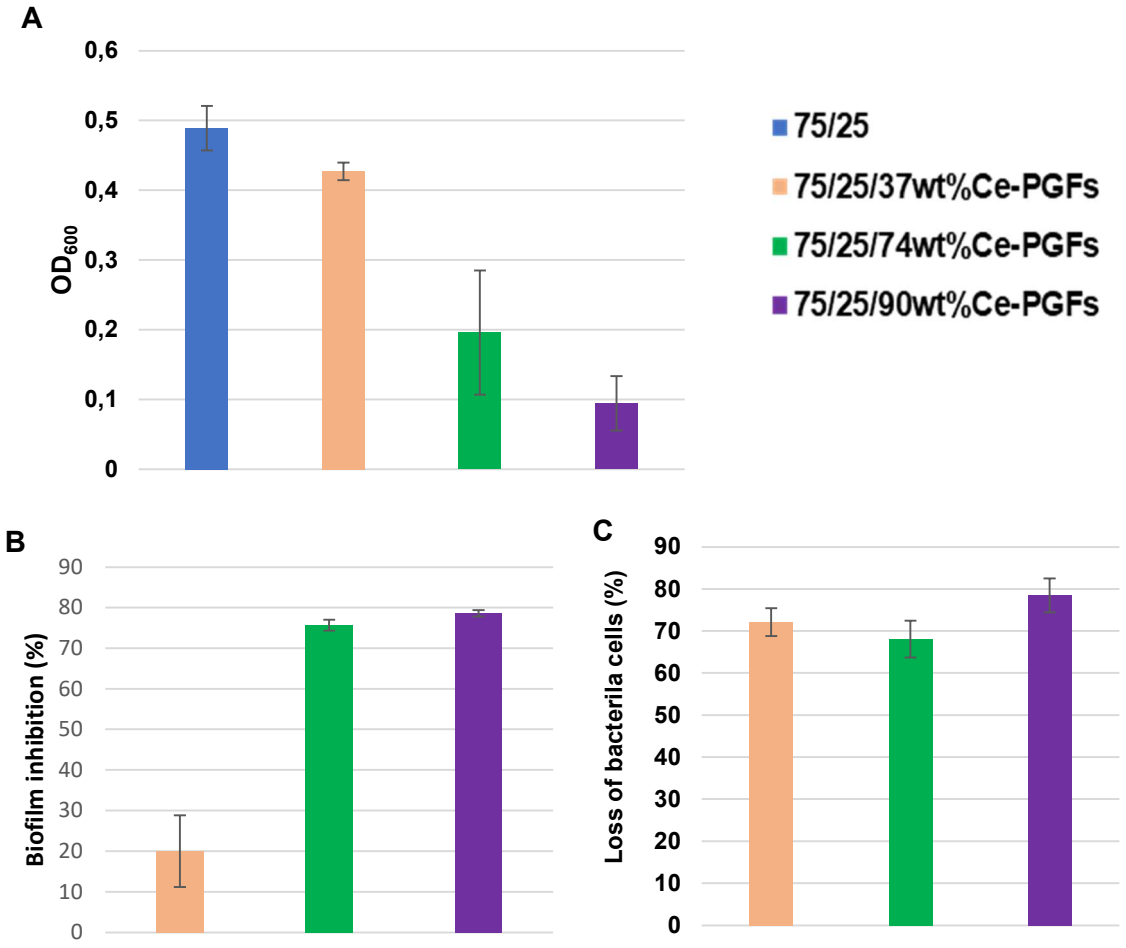

Figure 6.7: Antibacterial evaluation of the samples against *Staphylococcus aureus* (ATCC® 29213™): (A) Optical density of the supernatants at 600 nm, (B) Biofilm inhibition in % and (C) Reduction of the adhered bacterial cells on the samples, labelled as “Loss of bacterial cells” in %.

The graphs in Figure 6.7 depict the inverse proportional correlation of the optical density and the increase in the ratio of the Ce-PGFs (the optical density decreases with the addition of the Ce-doped PGFs compared to the non-modified blend). The addition of higher amounts of the inorganic compound led to lower values for the optical density showing that the number of bacteria decreases; in the presence of the modified samples.

The highest observed inhibition of *Staphylococcus aureus* was 98 % for the blend containing 90 wt% of Ce-PGFs while the blend containing the lower amount of Ce-PGFs (37 wt%) showed an inhibition of 80 %. The results from the assessment of the biofilm formation, depicted in Figure 6.7 B, highlighted that higher the amount of the inorganic compound, the higher the inhibition of biofilm formation.

The inhibition of biofilm formation by applying the composites with the two higher amounts (74, 90 wt%) of Ce-PGFs reached values of around 80 %, while the composite with the lower loading (37 wt%) of Ce-PGFs displayed only a 20 % inhibition.

The ability of the bacterial cells to adhere to the surface of the samples was reduced by the addition of the inorganic compounds, that reached a maximum reduction of 80 % compared to the non-modified blend.

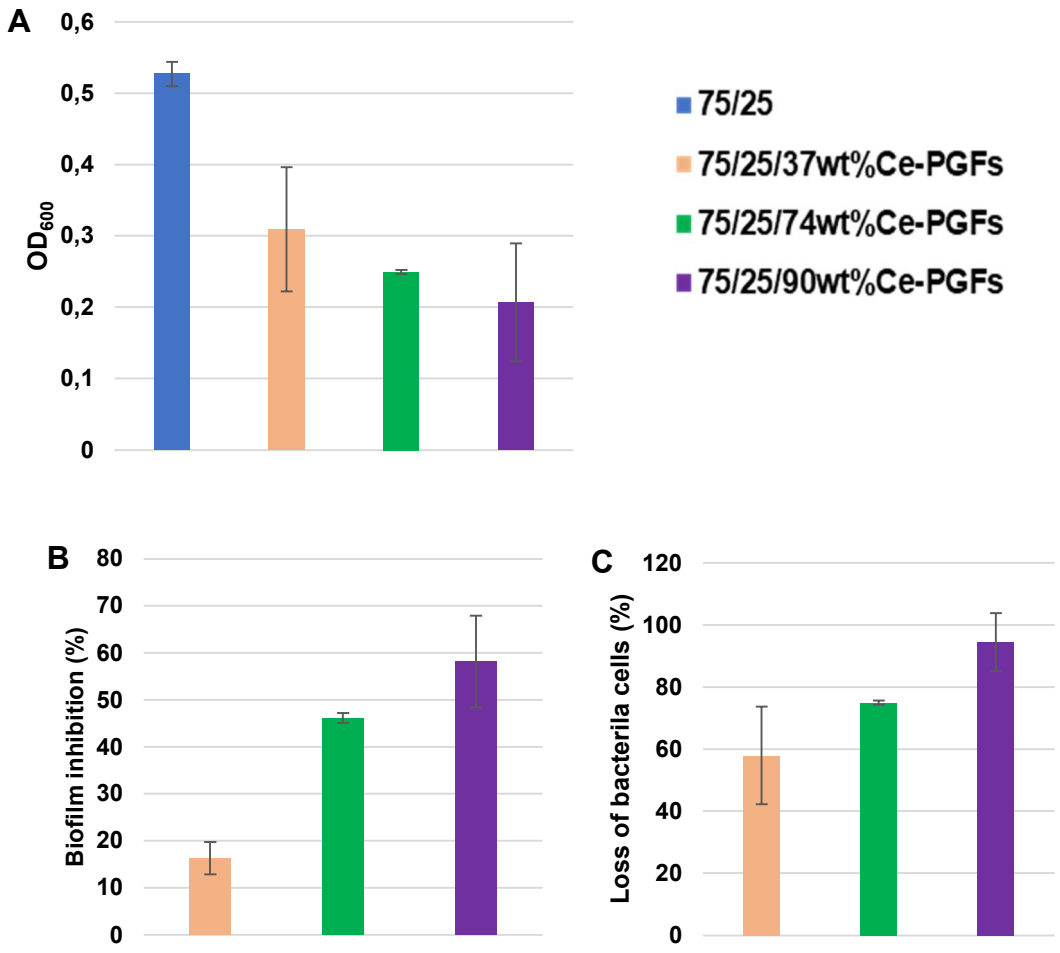

Figure 6.8: Antibacterial evaluation of the samples against Methicillin-resistant *Staphylococcus aureus*: (A) Optical density of the supernatants at 600 nm, (B) Biofilm inhibition in % and (C) Reduction of the adhered bacterial cells on the samples in %.

Antibacterial evaluation of the Ce-PGFs containing composites against MRSA**,** a clinical isolate, are summarised in Figure 6.8. The optical density decreased with the addition of Ce-PGFs as shown in Figure 6.8 A.

Furthermore, the biofilm formed by the MRSA could be inhibited and the higher the amount of Ce-PGFs in the composite specimen was the more effective the inhibition was. In case of the 75/25 P(3HO-co-3HD)/P(3HB)/90 wt% Ce-PGFs composite a biofilm inhibition of approx. 60 % could be achieved. Interestingly, this value around 20 % lower than that for the sensitive strain.

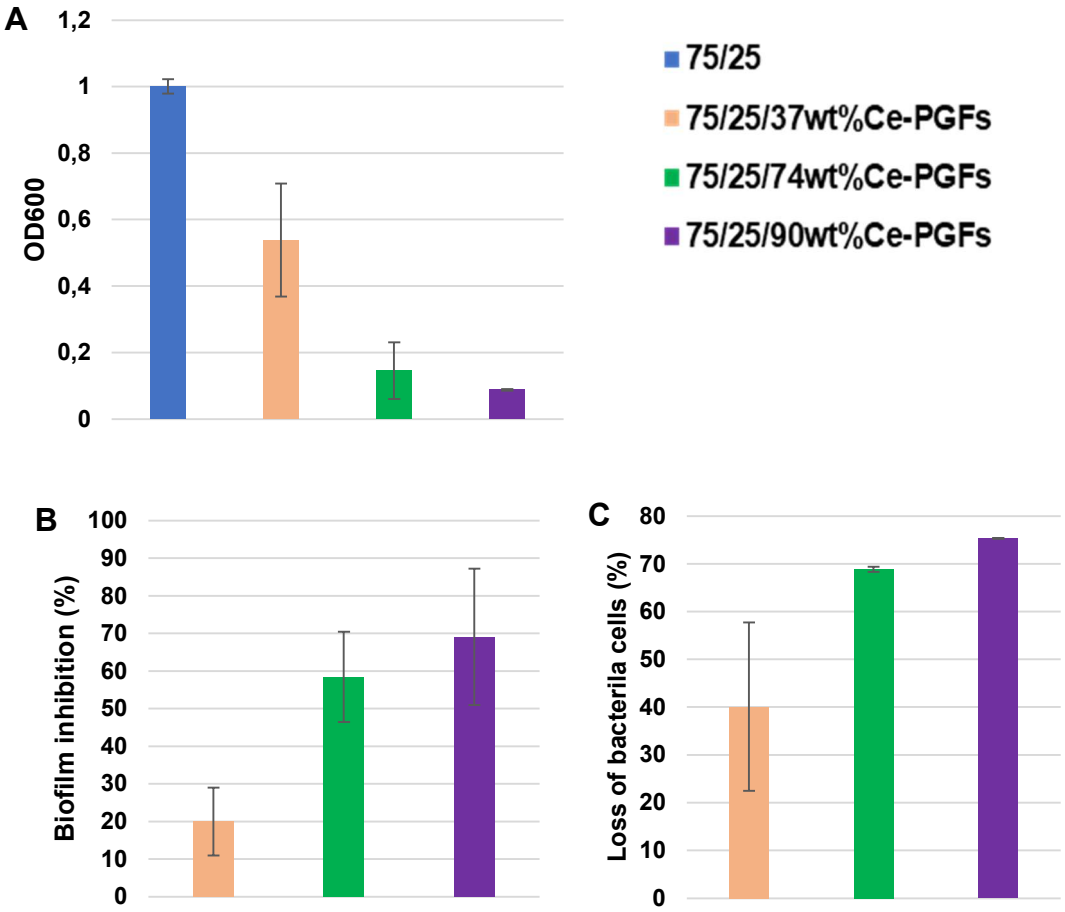

Figure 6.9: Antibacterial evaluation of the samples against *Escherichia coli* (ATCC® 25922™): (A) Optical density of the supernatants at 600 nm, (B) Biofilm inhibition in % and (C) Reduction of the adhered bacterial cells on the samples in %.

For the Gram-negative bacteria, *Escherichia coli* (ATCC® 25922™) the samples containing the Ce-PGFs showed superior antibacterial activity compared to the non-modified control sample as shown in Figure 6.9 A. Inhibition of biofilm formation reached 70 % for the composite containing 90 wt% of the inorganic compound (Figure 6.9 B). The effect on the adhered bacteria increased with the increase of the added wt% of Ce-PGFs as shown in Figure 6.9 C.

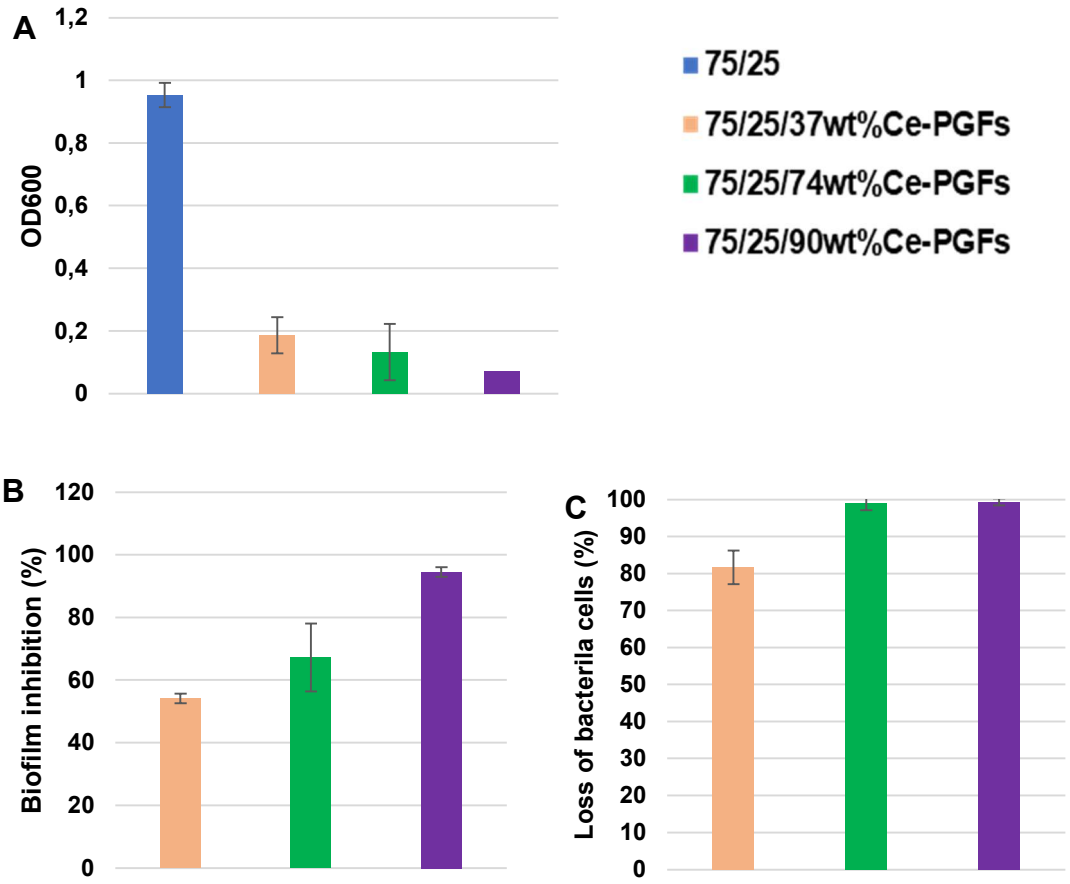

Figure 6.10: Antibacterial evaluation of the samples against *Staphylococcus epidermidis* (ATCC® 12228™): (A) Optical density of the supernatants at 600 nm, (B) Biofilm inhibition in % and (C) Reduction of the adhered bacterial cells on the samples in %.

Testing of the newly developed composites against *Staphylococcus epidermidis* (ATCC® 12228™) showed, that the growth of the free planktonic cells was inhibited in the presence of the Ce-PGFs compared to the non-modified blend (Figure 6.10 A). The addition of the inorganic compound from 37 to 90 wt% enhanced the biofilm inhibition as shown in Figure 6.10 B.

Furthermore, it could be shown that the number of attached bacteria reduced by 80 % with 74 wt% of Ce-PGFs (Figure 6.10 C).

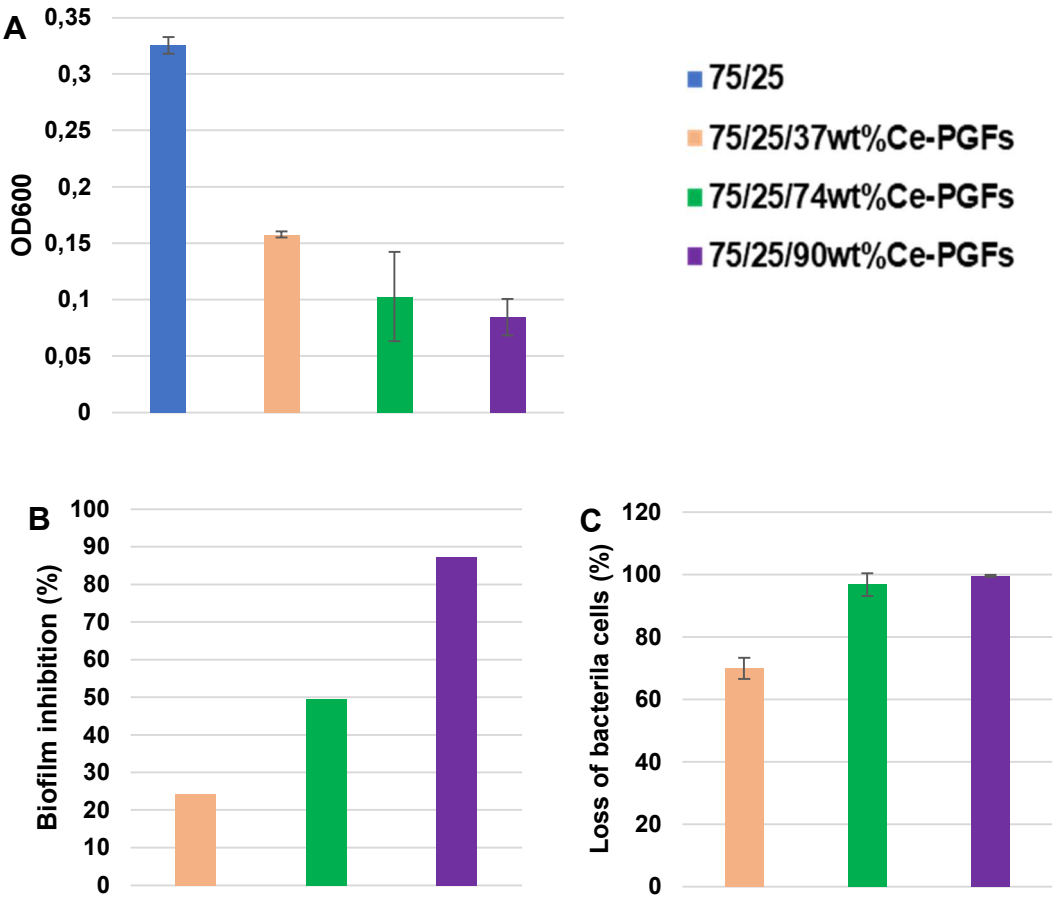

Figure 6.11: Antibacterial evaluation of the samples against Methicillin-resistant *Staphylococcus epidermidis* (A) Optical density of the supernatants at 600 nm, (B) Biofilm inhibition in % and (C) Reduction of the adhered bacterial cells on the samples in %.

In order to compare the results of the non-clinical isolate *Staphylococcus epidermidis* (ATCC® 12228™), the same experiments were performed with the clinical isolate Methicillin-resistant *Staphylococcus epidermidis* (MRSE). As shown in Figure 6.11A, the addition of Ce-PGFs led to the inhibition of the bacterial cells as expected. It could be observed that with increased amount of the novel, inorganic and antimicrobial compound, the biofilm inhibition could be enhanced (Figure 6.11 B).

Finally, the number of adhered bacterial cells could be reduced with the addition of the Ce-PGFs as shown in Figure 6.11 C. Compared with the sensitive *Staphylococcus epidermidis* biofilm inhibition, as well as loss of bacterial cells, showed no significant differences to the MRSE.

When tested against *Pseudomonas aeruginosa* (ATCC® 27853™) there was no effect on the inhibition of this bacterial strain.

The novel class of PHA/PGF composites showed no antibacterial effect against the Gram-negative *Pseudomonas aeruginosa* (ATCC® 27853™) according to the applied panel of test parameters.

6.2.7 *In vitro* cytocompatibility of PHA/PGF composites

The cytocompatibility of the composite films containing different amounts of Ce-PGFs was investigated by applying L929 murine fibroblasts as recommended by the ISO 10993-5:2009 (Biological evaluation of medical devices- Part5: Tests for in vitro cytotoxicity) and NG108-15, thus the novel biomaterials could be applied for nerve conduit fabrication. Indirect contact tests performed as described in sections 2.12.1 and 2.12.3 were conducted. As a positive control, LDPE (low density polyethylene) and as negative control ZDEC (Polyurethane film containing 0.1 % zinc diethyldithiocarbamate) were used.

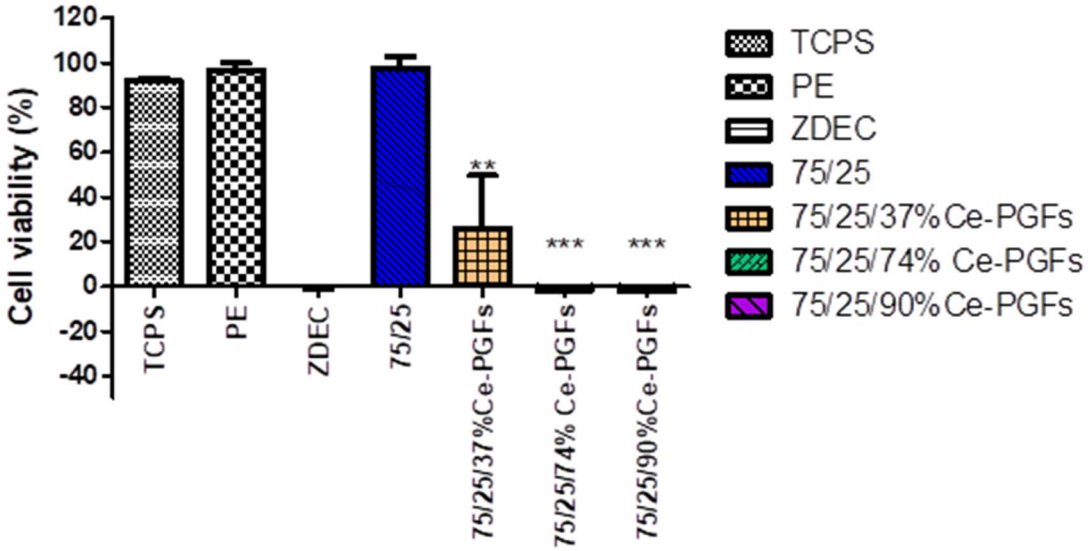

Figure 6.12: Indirect cytocompatibility evaluation of the non-modified 75/25 P(3HO-*co*-3HD)/ P(3HB) blend polymer and 75/25 P(3HO-co-3HD)/P(3HB)/Ce-PGFs composites containing 37 wt%, 74 wt% and 90 wt% Ce-PGFs with respect to L929 cells (mean ± SEM, n = 9 independent experiments). Statistical significance determination is represented as *p ≤ 0.05, **p ≤ 0.01, and ***p ≤ 0.001 for cells on TCPS vs. all materials, and non-modified polymer blend vs. Ce-PGFs composites.

After 24 h incubation of samples with cell culture medium the supernatant was added to L929 cells that were already cultured to sub-confluence for 24 h on TCPS. The supernatant was the cell culture medium usually used for L929 and could possibly contain extractable substances eluted from the samples to be tested. After the incubation of sub confluent L929 with the extraction solution of the controls TCPS and LDPE and all novel composites, the viability of the cells were analysed.

After 24 h of incubation, it was shown that the cell viability of cells cultured on TCPS, PE and the 75/25 PHA blends was around 100 % with a very small variation of the standard deviation values as shown in Figure 6.12. The addition of the Ce-PGFs (37 %) to the polymer matrix resulted in a cell viability reduction of 60 % compared to the non-modified PHA blend. Further addition of Ce-PGFs resulted in a significant reduction of L929 viability, as shown in Figure 6.12.

Additionally, direct contact tests were performed to evaluate the behaviour of the same cells in direct contact with the samples. As expected, the results showed that the Ce-PGFs modified PHA blend samples were toxic to the L929 murine fibroblasts, as shown in Figure 6.13. Samples of TCPS, PE and 75/25 P(3HO-co-3HD)/P(3HB) resulted in viability values of 100, 96.5 and 90.6 % respectively. Statistical analysis showed that the 75/25 P(3HO-co-3HD)/P(3HB) samples were significantly different from both TCPS ($^{***}p<0.05$) and PE specimens ($^{**}p<0.05$).

The fabricated composites showed statistically insignificant differences with the negative control, ZDEC. No significant differences were found between the composites containing different wt% of Ce-PGFs. There was a significant difference (***$p<0.05$) in the cell viability after direct contact with the composites as compared to the polymer blend of 75/25 P(3HO-co-3HD)/P(3HB).The L929 cells showed a high cell viability after 24 h on 75/25 P(3HO-co-3HD)/P(3HB), whereas all composites led to a 100 % decrease of cell viability.

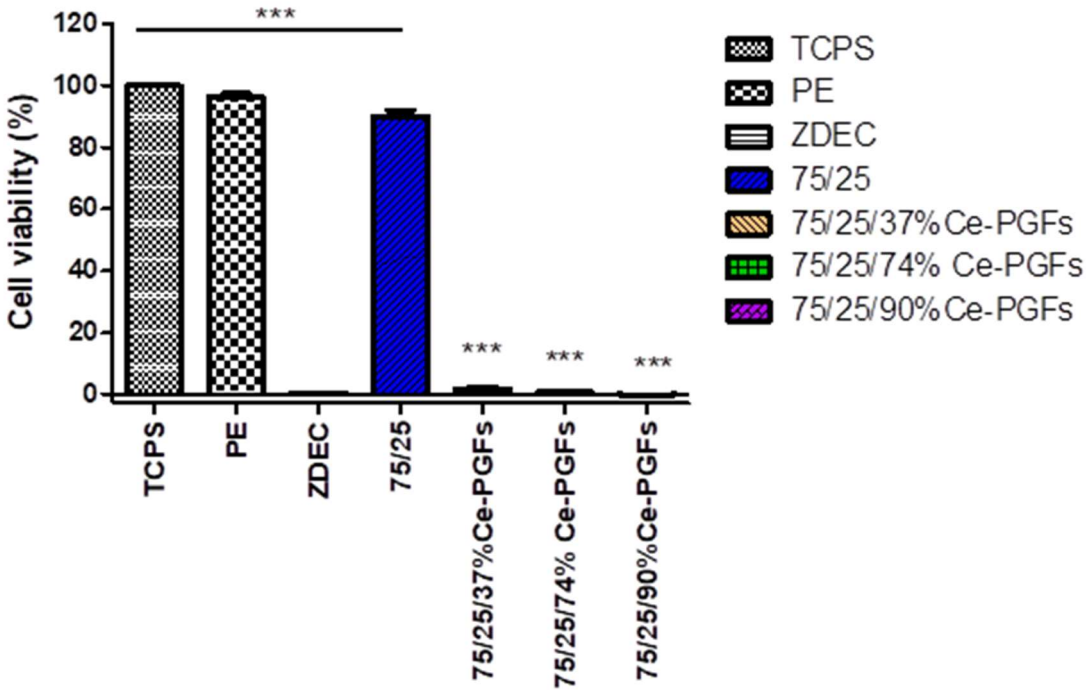

Figure 6.13: Direct cytocompatibility evaluation of the non-modified 75/25 P(3HO-co-3HD)/P(3HB) polymer blend and 75/25 P(3HO-co-3HD)/P(3HB) composites with 37 wt%, 74 wt% and 90 wt% Ce-PGFs with respect to L929 cells (mean ± SEM, n = 9 independent experiments). Statistical significance determination is represented as *p ≤ 0.05, **p ≤ 0.01, and ***p ≤ 0.001 for cells on TCPS vs. all materials, and non-modified polymer blend vs. Ce-PGFs composites.

In order to understand the strong cytotoxic effect of the three PHA/PGF composites on the usually robust L929 murine fibroblasts, further investigations were necessary.

The used RPMI 1640 medium contained the indicator dye phenol red. Enhanced metabolism of a eukaryotic cell or bacteria could lead to acidic products the microorganisms secrete into the media leading to an acidic pH shift and yellowish colour shift. All the additional indirect and direct tests showed that neither L929 murine fibroblasts showed an increased metabolism when cultured on the composites nor were any bacterial contaminations responsible for this. But the composites incubated alone in the medium showed in all cases an immediate colour shift from pink (phenol red) to yellow (Figure 6.14).

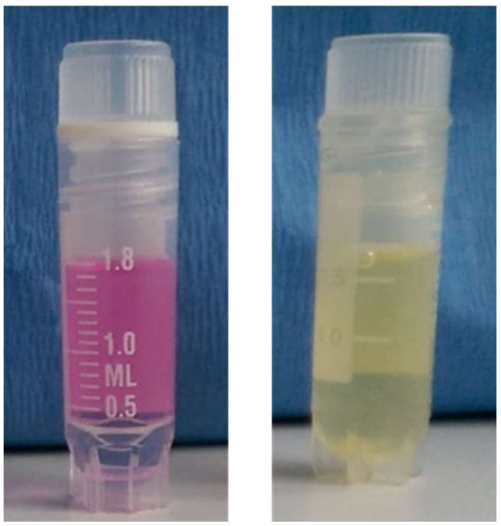

Figure 6.14: Normal pink colour of cell culture media coming from the indicator phenol red (left) and colour shift to yellow of the media in the presence of the composite materials (right) indicating an acidification of the applied RPMI 1640 medium.

In this study, further *in vitro,* direct tests were conducted after pre-conditioning of the samples, by immersing them in RPMI 1640 medium until no change of colour was observed. After the conditioning of the samples, direct tests were performed using L929 murine fibroblasts for seven days. The evaluation of cytocompatibility was conducted at time points of day one, day three and day seven, as shown in Figure 6.15.

The viability of the cells cultured on the composite specimen at day 1 were higher when compared with the results shown in Figure 6.13. After the complete removal of all leachable acidic products of the Ce-PGFs, the L929 cell viability on 75/25 P(3HO-co-3HD)/P(3HB)/34 wt%PGFs showed a value of 79 % compared to 1.69 % previous to extraction. A cell viability of 77 % (74 wt% Ce-PGFs) and 64 % (90 wt%) was observed for the composites after 24 h of culturing on the pre-conditioned specimen (Figure 6.15).

The comparison between the controls, blend and the Ce-PGFs containing composites among each other after a culture time of 24 h revealed a continuous decrease of viability with increase of wt% of Ce-PGFs, but a significant difference in cell viability could only be found between the blend and the 90 wt% composite.

On the third day of the experiment the composites containing 37 wt%, 74 wt% and 90 wt% PGFs showed cell viabilities of 67, 77 and 65 % respectively. All the composites showed significant statistical difference when compared with the TCPS (***$p<0.05$).

The statistical analysis between the non-modified polymer blend and the Ce-PGFs composites (37 wt% and 90 wt%) revealed significant differences (**p<0.01).

By day seven the composites of 75/25 P(3HO-co-3HD)/P(3HB) with 37 wt%, 74 wt% and 90 wt% PGFs showed a cell viability of 36 %, 29 % and 10 % respectively. These values were much lower compared with day 1 and day 3 of the same samples (Figure 6.15). The statistical analysis showed significant differences (***p<0.05) between the controls, TCPS and non-modified blend, and the Ce-PGFs composites

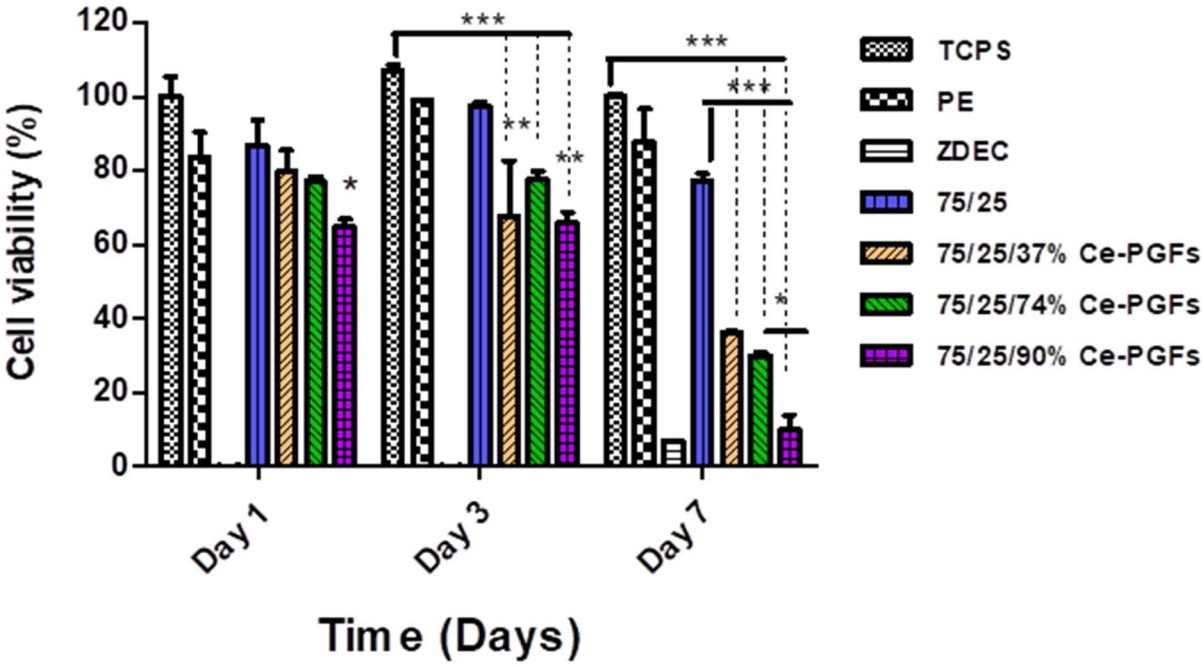

Figure 6.15: Direct cytocompatibility evaluation of the non-modified 75/25 P(3HO-co-3HD)/ P(3HB) and 75/25 P(3HO-co-3HD)/P(3HB) composites with 37 wt%, 74 wt% and 90 wt% Ce-PGFs with respect to L929 cells for a time period of 7 days (mean ± SEM, n = 9 independent experiments). Statistical significance was represented as *p≤ 0.05, **p ≤ 0.01, and ***p ≤ 0.001 for cells on TCPS vs. all materials, non-modified polymer blend vs. Ce-PGFs composites and between Ce-PGFs composites.

The cytocompatibility of the composites was also tested by using the hybrid NG108-15 cell line (Figure 6.16).

Cell viability results of the direct cytocompatibility testing of the previously described composites in comparison to different control materials previously used as well over a time course of 7 days is summarised in Figure 6.16.

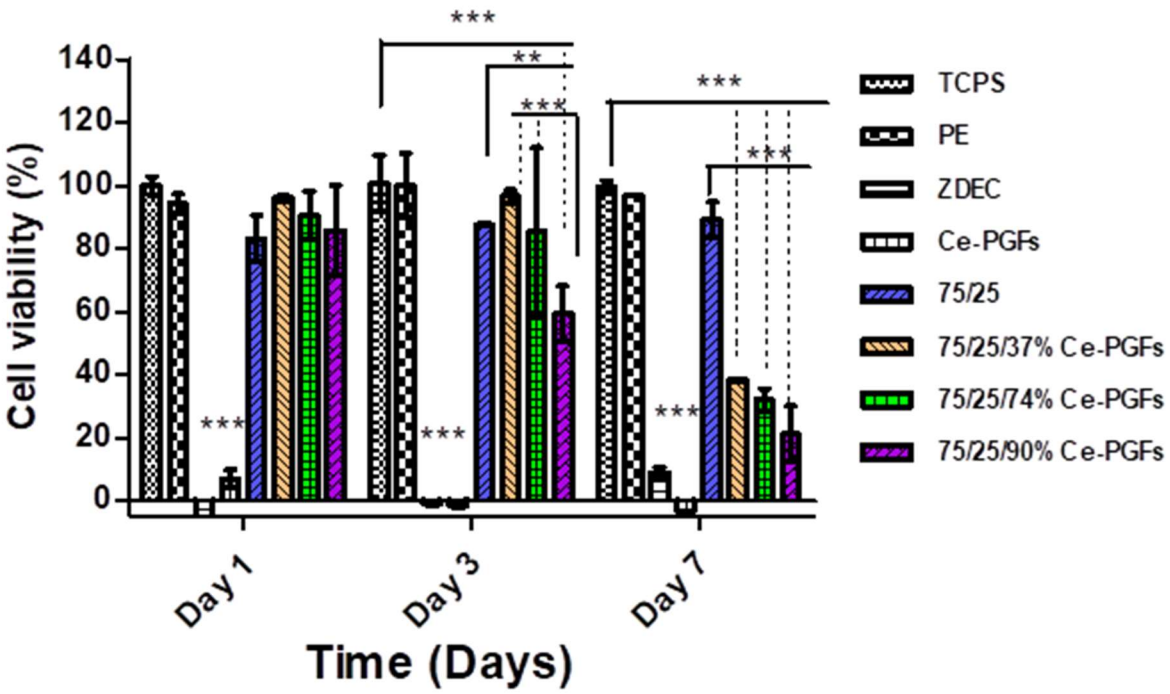

Figure 6.16: Direct cytocompatibility evaluation of the non-modified 75/25 P(3HO-co-3HD)/ P(3HB) and 75/25 P(3HO-co-3HD)/P(3HB) composites with 37 wt%, 74 wt% and 90 wt% PGFs with respect to NG108-15 (mouse neuroblastoma/ rat glioblastoma) hybrid cells for a time period of 7 days (mean ± SEM, n = 9 independent experiments). Statistical significance determination is represented as *p ≤ 0.05, **p ≤ 0.01, and ***p ≤ 0.001 for cells on TCPS vs. all materials, non-modified polymer blend vs. Ce-PGFs composites and between Ce-PGFs composites.

In this experiment, the neat Ce-PGFs were used without any embedding in the PHA matrix. The motivation to do this was to understand if the hybrid cells would survive the direct interaction with the Ce-doped Phosphate Glass fibres, that were intended as guiding architectures.

The viability of the neuronal cells cultured with the Ce-PGFs composites on day 1 was 95 %, 90 % and 85 % for the 37 wt%, 74 wt% and 90 wt% composites respectively, where the free-standing Ce-PGFs showed a cell viability of 6.9 %. The statistical analysis showed significant differences (***p<0.001) between the

free-standing Ce-PGFs and all other samples both controls and composites. No statistical differences revealed between the Ce-PGFs composites and the controls, TCPS and the non-modified polymer blend.

A continous decrease in the cell viability with increase of wt% of Ce-PGFs was observed on day three with significant differences (***$p<0.001$), upon statistical analysis, only in the case of 90 wt% composite with respect to TCPS. Significant differences (***$p<0.001$) were observed between the 90 wt% composite and the non-modified polymer blend as well as the 37 wt% composite. The cell viability of the free-standing Ce-PGFs used as control decreased significantly from day one to day three, when compared with the other controls.

By day seven, the Ce-PGFs composites, as well as the free-standing Ce-PGFs, showed sizable reductions of cell viability compared to the positive control as shown in Figure 6.16. The resulting cell viability of the composites was 38 %, 32 % and 21 % for the 37 wt%, 74 wt% and 90 wt% Ce-PGFs composites respectively. The statistical analysis showed no significant differences between the composites containing different amounts of the Ce-PGFs but all the Ce-PGFs revealed significant statistical (***$p<0.001$) differences compared to the un-modified polymer blend and the TCPS.

6.3 Discussion

Bioactive glasses have attracted a lot of attention since their development by Hench *et al.* in 1969. These reactive materials have been applied in different medical applications such as bone and soft tissue engineering, dental applications, wound healing and drug delivery (Bunting *et al.*, 2005; Fernandes *et al.*, 2018). More specific phosphate glasses containing oxide modifiers such as CaO and Na_2O have been extensively used in the biomedical field (Franks *et al.*, 2000; Salih *et al.*, 2000; Ahmed *et al.*, 2004a; Ahmed *et al.*, 2004b). Lately, a lot of interest has stimulated for the use of bioglasses in soft tissue engineering and more particularly in nerve regeneration.

A Silastic conduit was filled with Bioglass 45S5 fibres and was used *in vivo* (in the sciatic nerves of adult rats across an interstump gap of 0.5 cm). The resultant axonal regrowth was comparable with that seen using an autograft while the bioresorbability of the fibres were sufficient for the completion of the successful

regeneration (Bunting *et al.*, 2005). In another study, Koudehi *et al.* fabricated a bioglass/gelatin conduit which was implanted into the right sciatic nerve of 10 male Wistar rats to repair a 10 mm gap. The results showed no cytotoxicity effect and high regeneration of the nerves and the myelinated axons after three months (Koudehi *et al.*, 2014). Borate-based bioactive glass (BBG) has shown no cytotoxicity under both static and transient cell culture conditions when tested with chick dorsal root ganglia (DRG).

Moreover, BBG/fibrin scaffolds afforded greater neurite extension when compared with sole fibrin indicating that the addition of BBG enhanced the nerve outgrowth (Marquardt *et al.*, 2014). In an attempt to treat peripheral nerve injuries, PGFs were developed and tested *in vitro* on thoracic, and lumbar DRGs dissected from 6-week-old Sprague–Dawley rats. These fabricated PGFs were also used for the development of a composite of collagen-containing longitudinally aligned PGFs to confer guidance for the neuron outgrowth.

The *in vivo* test showed that the presence of the PGFs resulted in superior directionality of the neurite outgrowth when compared with the control samples which lacked PGFs. The tested 3D scaffolds of collagen and PGFs revealed a better rate of the axonal extension compared with the control conduits (Kim *et al.*, 2015). The presence of the PGFs in a composite scaffold could provide aligned intraluminal guidance for the axonal outgrowth of the neurons facilitating and accelerating regeneration and functional recovery (Bunting *et al.*, 2005; Koudehi *et al.*, 2014; AM, 2018).

To develop a fibre reinforced composite (FRC) Ce-PGFs fibres were added in the polymer matrix of the 75/25 P(3HO-*co*-3HD)/P(3HB). These composites provided sufficient guidance for the nerve reconstruction supporting neuronal outgrowth where the presence of the cerium cations conferred antibacterial activity to the final specimen.

The ATR/FTIR analysis revealed the presence of peaks corresponding to the 75/25 P(3HO-co-3HD)/P(3HB) blend in all the fabricated composites. Only two of the characteristic peaks attributed to the Ce-PGFs were observed in the final samples due to their overlapping with the peaks attributed to the polymer matrix. The ATR/FTR technique was able to detect peaks attributed to the cerium doped

PGFs (in all the developed composites) and hence confirmed the presence of the inorganic compound in the PHA blend.

To investigate the change of the thermal properties of the Ce-PGFs composites loaded with different amounts of the inorganic fibres DSC was used. The thermograms obtained from DSC didn't reveal any peaks for the PGF samples since the T_g of the bioglasses is around 500^{o}C while the obtained thermograms were only run up to 200^{o}C.

The thermograms of the fabricated composites possessed two glass transition temperatures attributed to the two polymers combined to create the 75/25 P(3HO-co-3HD)/P(3HB) blend (P(3HO-co-3HD) and P(3HB)). The crystallisation peak was observed in the 75/25 P(3HO-co-3HD)/P(3HB) blend and also in all the fabricated composites. As described above, in section 6.2.3 the T_c is a characteristic peak of P(3HB). Addition of the inorganic compound shifted the T_c to a higher temperature when compared with the 75/25 P(3HO-co-3HD)/P(3HB) blend. The melting event of the composites was observed to be a single peak in the region of 170^{o}C and did not change significantly with the addition of different amounts of cerium doped PGFs. The melting temperature in this region is attributed mainly to the presence of the P(3HB) in the composites.

In all composites uniaxial mats were formed, the SEM micrographs showed that good alignment of the fibres occurred within the polymer matrix. The composites were also found to be porous on the glass side of the composites. The lower concentration of the cerium doped PGFs (37 wt%) did not reveal any voids where further addition of the PGFs (74 and 90 wt%) increased the size and number of pores. Moreover, in the 75/25 P(3HO-co-3HD)/P(3HB)/90 wt% PGFs were interconnected. It was also found that the aligned fibres were able to penetrate and get through from the air side of the polymer matrix into the glass side. More specifically the lower loading of the PGFs (37 wt%) showed a lower ability to retain the fibres on one side of the composite.

The XRD spectra confirmed the amorphous nature of the PGFs (were no peak was detected). The addition of the compound into the polymer matrix did not reveal any new peaks attributed to the presence of the inorganic compound but affect the intensity of the revealed peaks of the composites attributed to the 75/25

P(3HO-co-3HD)/P(3HB) matrix. Unfortunately, XRD was not able to confirm the presence of the cerium doped PGFs in the composites.

The higher the amount of the filler in the polymer matrix, the lower the OD_{600} indicating the inhibition of bacterial growth. Additionally, an inverse correlation emerged between the amount of cerium doped PGFs and biofilm formation as well as bacterial loss. The higher the ratio of the agent, the lower was the biofilm formation and the ability of the cells to adhere to the fabricated composites after incubation in the bacterial suspension. Also, the antibacterial activity was found to be superior against Gram-positive rather than Gram-negative bacteria (*Escherichia coli* (ATCC® 25922™), *Pseudomonas aeruginosa* (ATCC® 27853™)) most probably due to the lack of the outer cell membrane as is the case for Gram-positive bacterial strains. Similar observations for cerium doped Phosphate fibres were reported by the creator of this compound Lapa *et al.* (Lapa *et al.*, 2019). Finally, the composite containing 90 wt% of PGFs reduced the amount of adhered bacterial cells by almost 100 %, as shown in Figure 6.8 C. The PHA/PGF composites showed good antibacterial activity against both the clinical and non-clinical *Staphylococcus aureus* strains.

The efficient antibacterial activity of the composites results from the presence of cerium, known to exhibit antibacterial activity most probably due to its ability to dissociate the outer membrane of bacterial cells from the cytoplasmic membrane (Lin *et al.*, 2007; Zeyons *et al.*, 2009; Chen *et al.*, 2010; Cai *et al.*, 2012; Goh *et al.*, 2014).

The rapid change of the colour of the culture media is a result of the significant change in localised pH due to high rate of ion exchange which leads to burst release. This spontaneous shift of the pH is correlated to cytotoxic effects over the cells. Several studies also report the cytotoxicity of bioactive glasses in the absence of pre-treatment of the samples (Hasan *et al.*, 2012; Ciraldo *et al.*, 2018). Immersion of the samples in aqueous solutions such as (a) TRIS buffer (Pryce and Hench, 2003; Rohanová *et al.*, 2011), (b) simulated body fluid (SBF) (Kokubo and Takadama, 2006; Bellucci *et al.*, 2011), as well as (c) Dulbecco's Modified Eagle's Medium (DMEM) are some of the reported methods used for preconditioning of the samples to overcome the cytotoxicity (Pryce and Hench, 2003).

The rapid change in colour and hence pH of the unconditioned samples reduced following the treatment of the composites with the media in which the respective cell lines were grown. As a result, the cell viability of the PGFs composites was significantly enhanced after their pre-treatment process when tested directly with the L929 cells. The composites with 37 wt% PGFs after the pre-treatment showed a 79 % higher cell viability than the unconditioned sample. Similarly, the 74 and 90 wt% composites after pre-conditioning resulted in 77 % and 64 % higher cell viability than the unconditioned samples when tested against L929 murine fibroblasts.

When the samples were tested for a period of seven days against both L929 and NG108-15 cell lines, the cell viability reduced drastically from day one to day seven. The reduction in cell viability might be attributed to the shift of the pH in the cell culture media over time due to the release of the ions in the liquid. The longer the period the composites remain in the cell culture media, the higher the glass dissolution and hence the higher the release of ions; which significantly changes the localised pH influencing cell function and activity.

A similar phenomenon has been reported previously in other studies were the ions released into the cell culture media shifted the pH creating an acidic environment which influences cell respiration mechanisms causing enzyme alteration and modification of the diffusion of nutrients and gases to cells and hence pre-condition of the samples was required (El-Ghannam, Ducheyne and Shapiro, 1995; Pryce and Hench, 2003; Bellucci *et al.*, 2011; Hoppe, Güldal and Boccaccini, 2011).

These results were obtained from transient cell culture conditions but localised in well plates when the kinetics driven in the body might result in different observations for the same nanocomposites when tested *in vivo*.

Further studies are required to assess the mechanical and hydrophobic properties of the developed composites. In addition, XPS would be a great tool to investigate the oxidation state of the rare earth element before and after its incorporation into the polymer matrix. Further *in vitro* studies under dynamic cell culture conditions are required to mimic the body circulation conditions and prove the efficiency of the 75/25 P(3HO-co-3HD)/P(3HB) composites with 37 wt%, 74 wt% and 90 wt% PGFs in supporting peripheral nerve regeneration.

Also, Live/dead cell tests, co-cultures of NG108-15/Schwann cell neurite outgrowth assessment on NG108-15 neuronal cells need to be performed and compared with the efficacy of the autografts.

Chapter 7

Development of PHA composites containing graphene oxide

7 Development of PHAs composites containing graphene oxide

7.1 Introduction

In recent times both the scientific and academic societies have moved towards understanding nerve physiology and regeneration, however, the ability to reconstruct damaged nerves surgically and successfully regenerate their motor, and sensory function is still not satisfactory (D Grinsell and Keating, 2014a). Despite technological advancements, peripheral nerve injuries remain a severe and difficult condition for surgeons to treat.

Successful and complete recovery from nerve damage is very rare and requires long periods of post-surgery recovery. Such nerve injuries are mostly associated with upper or lower-limb trauma resulting in the loss of communication between the brain (CNS) and the motor and sensory function with the peripheral organs (PNS), a fact that has a great impact on the quality of the patient's life (Arslantunali *et al.*, 2014). For small gaps and nerve injuries which are not too severe, the peripheral nerves have the capacity to self-repair, but this regeneration is associated with several parameters such as the length of the nerve gap, the age of the patient as well as the time it takes for the repair which often is unable to achieve complete motor and functional recovery (Mohanna P.-N. *et al.*, 2003; Arslantunali *et al.*, 2014; Pateman *et al.*, 2015).
Conventional treatments, when complete lesions occur, include tension-free, end-to-end repair by suturing of the nerve stump, the gold-standard technique, nerve grafts which include autografts, allografts and xenografts, but their limitations are related to donor site morbidity as well as immunogenic reactions leading to rejection of the implant (Evans, 2001; Arslantunali *et al.*, 2014; Gaudin *et al.*, 2016a; Kornfeld, Vogt and Radtke, 2019).

As an alternative, nerve conduits are becoming extremely popular for their use in the treatment of peripheral nerve injuries. The existence of many different types of conduits of various sizes is making the proper utilisation of these reconstructive tools difficult (Rebowe *et al.*, 2018).

Nowadays, modern biomedical engineering targets the development of a nerve conduit, which will provide surface related structural and biological assistance to ensure complete and satisfactory nerve regeneration (Chrząszcz *et al.*, 2018).

Due to their good physicochemical and biological properties, PHAs are promising candidates, when compared with other polymers, for use in nerve tissue engineering. P(3HB) was the first of the PHA tested as a nerve conduit biomaterial which successfully bridged a nerve gap of 2–3 mm in cat and 10 mm in rat animal models producing results comparable with an autologous graft (Valappil *et al.*, 2006; Chen, 2009; Rai *et al.*, 2011; Masood, Yasin, and Hameed, 2016).

More recently, various blends of mcl and scl PHAs were utilised for the fabrication of nerve conduits. The study showed that the developed blends were able to support the proliferation of NG108-15 neuronal cells sufficiently, and in most cases, neurite growth as well, due to their unique mechanical properties (Lizarraga-Valderrama *et al.*, 2015).

Lately, graphene and graphene-based materials (GBMs) have been generating a great deal of interest for their use in biomedical applications. More specifically, graphene oxide (GO), a carbon allotrope with remarkable properties, is generating a lot of attention due to the fabrication of graphene oxide-based polymer nanocomposites and their potential use in medical applications (Das and Prusty, 2013). Drug and gene delivery, cancer treatment, development of biosensors, fabrication of nanocomposites with antibacterial properties and the development of beneficial biological scaffolds for cell proliferation and differentiation are some of the areas in which GO is under investigation for potential use (Chung *et al.*, 2013; Ege, Kamali and Boccaccini, 2017; Paik and Pradip Paik, 2017; Tadyszak, Wychowaniec and Litowczenko, 2018; Wu *et al.*, 2018).

The cytocompatibility of GO was studied using L929 fibroblasts, and the results showed that there was a direct correlation between the amount of GO and the cytotoxicity towards cells. The cytocompatibility levels were higher for a concentration range between 3125 g/mL and 25 g/mL of GO (Wojtoniszak *et al.*, 2012). Other studies also reported that graphene and GBMs successfully supported the proliferation and differentiation of neural stem cells and other non-

neuronal cells with no detectable adverse effects pointing to cell stress (Akhavan *et al.*, 2014; Guo *et al.*, 2017; Rastogi *et al.*, 2017). Finally, when graphene-based substrates were tested against neuronal cells, the fabricated substrates were found to have the ability to interface neuronal circuit regrowth without altering the cells and synapses. They are therefore suitable candidates for nerve regeneration (Park *et al.*, 2011; Fabbro *et al.*, 2016).

The antibacterial activity of graphene and its derivatives against both Gram-positive and Gram-negative bacteria have also been reported. However, conflicting results were reported due to the different culture media and assays used in these studies. The main mechanisms of action which confers the antibacterial activity of graphene-based materials are reported to be the physical disruption of the cell membrane caused by direct contact with sharp nanosheets and oxidative stress, induced to the cell membrane *via* ROS (reactive oxygen species) (Hegab *et al.*, 2016; Ji, Sun and Qu, 2016; Zhang *et al.*, 2016; Gao *et al.*, 2017; Hofmann *et al.*, 2017; Youse *et al.*, 2017; Wu *et al.*, 2018).
The conjugation of GO in the polymeric matrix of PVK (polyvinyl-N-carbazole) was also shown to enhance the antimicrobial properties of the nanocomposite compared to GO alone due to the increased dispersion caused by the polymer matrix. It was noticed, that GO/PVK composites exhibited excellent antibacterial properties while the toxicity levels on the fibroblast cells were insignificant, indicating that there is a selective cytotoxicity towards prokaryotic cells (Meji'as Carpio *et al.*, 2012).

The main aim of this chapter is the development of novel bioresorbable nanocomposites, combining the PHAs produced and characterized in Chapter 3 with the inorganic filler of GO. The aim is to develop novel, antibacterial and cytocompatible substrates. Various nanocomposites were fabricated using P(3HB), P(3HO-co-3HD), and the 75/25 P(3HB)/P(3HO-co-3HD) blend as the polymer matrix with GO as the inorganic filler intended to enhance the physicochemical and biological properties compared to the neat PHAs.

Different proportions of GO (0.5, 2 and 5 wt%) were used to determine which GO concentration would result in superior mechanical features, antibacterial properties and cytocompatibility. All the composites that were developed were

assessed for their thermal, mechanical, morphological and physicochemical properties. Two cell lines L929 murine fibroblasts, and NG108-15 neuronal analogue cells were used to evaluate their cytocompatibility. Indirect and direct *in vitro* tests were carried out. Additionally, the 75/25 blends containing different amounts of GO were assessed for their ability to support the differentiation and expression of neurite growth.

Direct contact test (DCT) analysis according to ISO 22196 was used to evaluate the antimicrobial properties of the composites against both Gram-positive and Gram-negative bacterial strains.

7.2 Results

7.2.1 Production of PHA/GO composites

PHA-based composites were developed using graphene oxide as the filler in an attempt to develop materials with biocompatible and antibacterial properties suitable for nerve tissue engineering. GO was a gift from the group of Professor Costa Galiotis at the Foundation of Research and Technology Hellas/Institute of Chemical Engineering Sciences FORTH/(ICE-HT) Patras, Greece, synthesised using natural graphite flakes (NGS Naturgraphit GmbH, Germany). (method of synthesis shown in Appendix II).

Various amounts of graphene oxide particles (0.5, 2 and 5 wt%) were blended with the mcl-polyhydroxyalkanoate P(3HO-co-3HD), the scl-polyhydroxyalkanoate P(3HB), as well as the 75/25 P(3HO-co-3HD)/P(3HB) blend. The films were produced *via* the solvent casting technique (section 2.9) and analysed to assess their physicochemical properties. The images of the samples obtained after the drying period of the composites are shown in Figure 7.1 and 7.2.

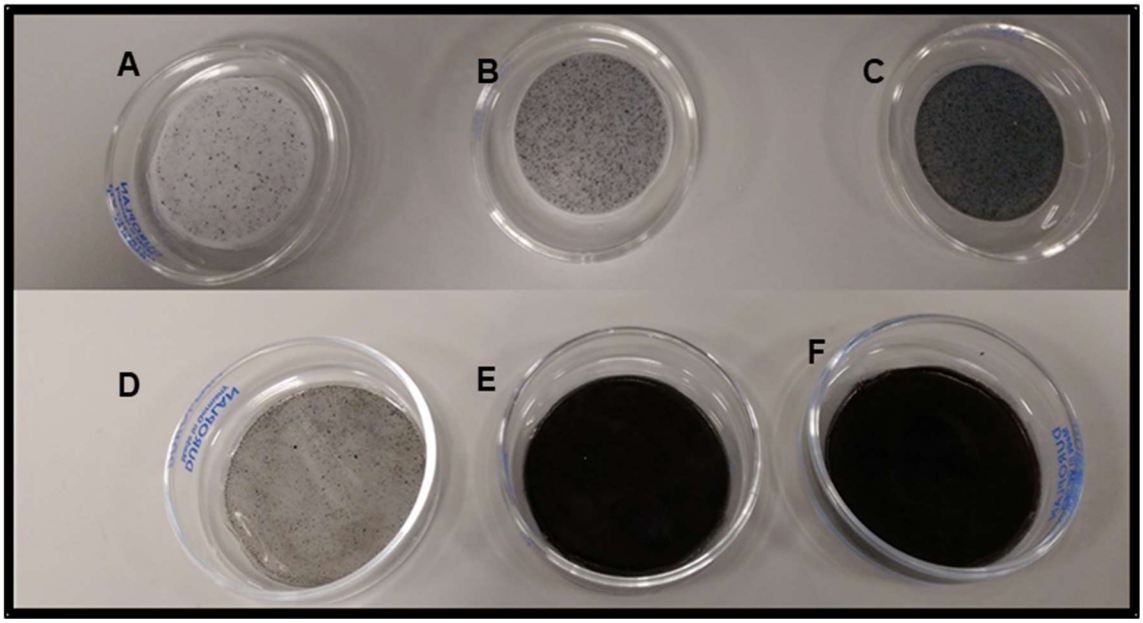

Figure 7.1: Composites of P(3HB) and P(3HO-co-3HD) containing different concentrations of graphene oxide. (A) P(3HB)/0.5 wt% GO, (B) P(3HB)/2 wt% GO, (C) P(3HB)/5 wt% GO, (D) P(3HO-co-3HD)/0.5 wt% GO, (E) P (3HO-co- 3HD)/2 wt% GO and (F) P(3HO-co-3HD)/5 wt% GO.

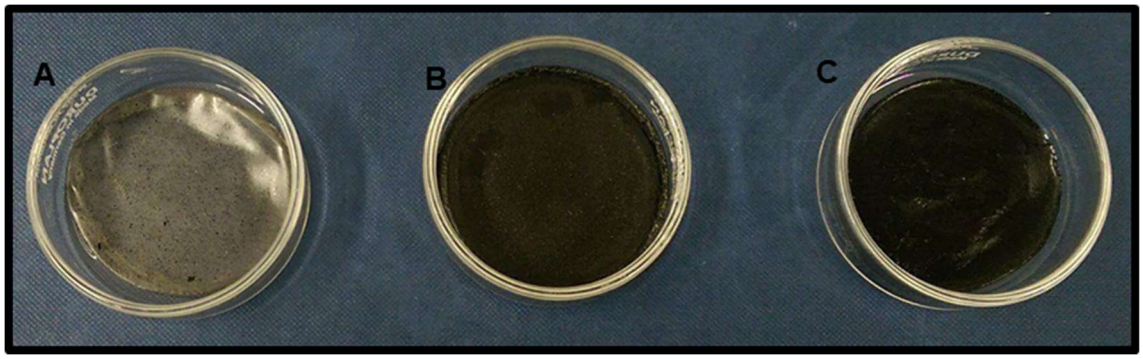

Figure 7.2: Composites of (75/25) P(3HO-co-3HD)/P(3HB) blend, containing different concentrations of graphene oxide. (A) 75/25 blend /0.5 wt% GO, (B) 75/25 blend /2 wt% GO and (C) 75/25 blend /5 wt% GO.

7.2.2 Attenuated Total Reflectance Fourier Transform Infrared Spectroscopy (ATR/FTIR) of PHA/GO composites

ATR/FTIR spectroscopy was used to characterise the topochemical differences between the neat polymers P(3HB) and P(3HO-co-3HD) and the neat blend 75/25 P(3HO-co-3HD)/P(3HB) with their GO composites containing different amounts of GO.

The ATR/FTIR spectra are shown in Figures 7.3, 7.4 and 7.5. The PHA polymers and the blend were used as the polymer matrix in which the inorganic compound (GO) was dispersed in different ratios, resulting in the final composite specimens. Various oxygen configurations such as the hydroxyl group (-OH), carbonyl (-CO), carboxyl (-COOH) and epoxy (C-O-C) groups, are known to be present on the hexagonal plane and at the edge of GO (Guo *et al.*, 2009; Sudesh *et al.*, 2013).

ATR/FTIR spectroscopy is a very useful technique capable of determining the presence of these different functional groups. The characteristic peaks from the scl-PHAs are found between 1720–1740 cm^{-1} and 1150 - 1300 cm^{-1} corresponding to the ester carbonyl group (C=O) and the (>C-H) methanetriyl group, respectively. For the mcl-PHAs, the presence of the aliphatic groups of the polymer backbone was revealed by the additional intense peaks at 2924 cm^{-1} which correspond to the stretching vibration of the C-H bonds of methyl groups (CH_3), and methylene groups (CH_2) and have been described in details in section 4.2.2 (Reis *et al.*, 2008).

The characteristic peaks of the different non-modified polymer matrices and their graphene oxide composites are shown in Figure 7.3, 7.4 and 7.5.

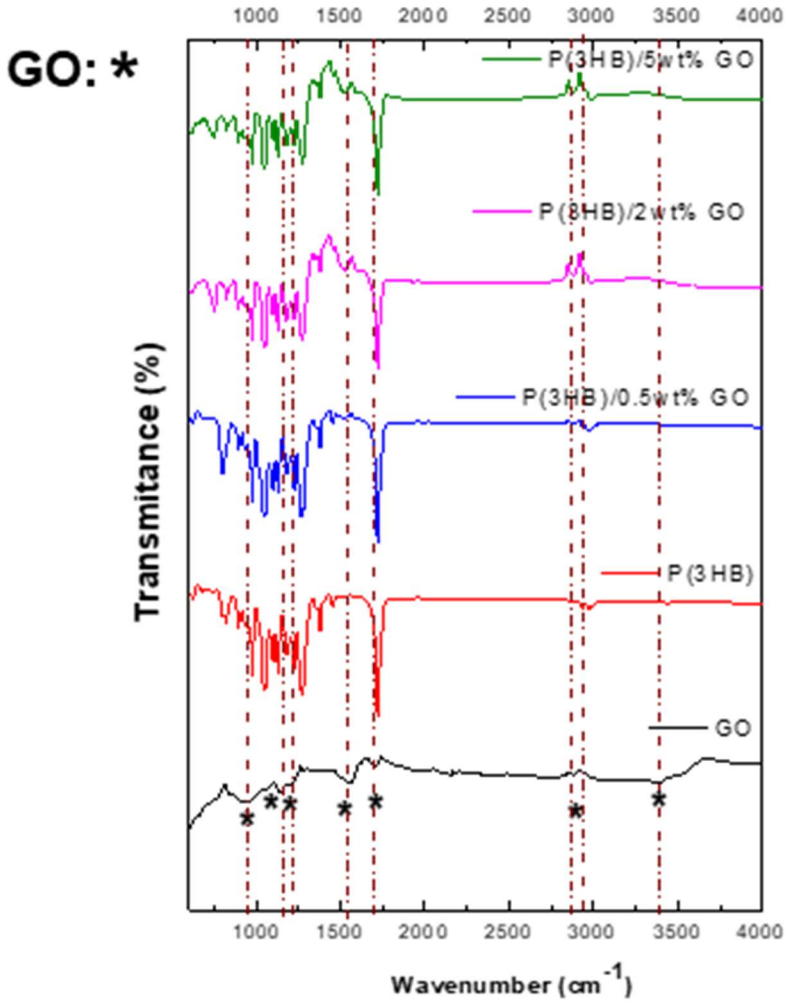

Figure 7.3: ATR/FTIR spectra of: --- GO , ---P(3HB) and P(3HB) composites containing :---0.5 wt%, ---2 wt% and ---5 wt% GO

A very broad peak centred at 3396 cm^{-1} is attributed to the stretching vibration peak for hydroxyl group (-OH) of carboxylic acids or intercalated water molecules (Mo *et al.*, 2005; Shahriary and Athawale, 2014). The peaks located around 2800-2900 cm^{-1} are assigned to both, asymmetric and symmetric CH_2 stretching (Mo *et al.*, 2005; Ciszewski *et al.*, 2015; Emiru and Ayele, 2017; Kumar *et al.*, 2018; Tang, Tang and Liu, 2018). The peak located at 1744 cm^{-1} was attributed to the (C=O) stretching vibration of carboxylic acids and carbonyl moieties (Sudesh *et al.*, 2013; Ciszewski *et al.*, 2015; Emiru and Ayele, 2017; Kumar *et al.*, 2018). The peak at 1652 cm^{-1} is assigned to the C=C stretching vibration of an un-oxidized graphitic domain or a contribution from the stretching deformation vibration of intercalated water (Guo *et al.*, 2009; Emiru and Ayele, 2017; Kumar *et al.*, 2018; Tang, Tang and Liu, 2018).

The peaks at around 1264 cm^{-1} correspond to the C-OH deformation of alcohol groups, while the peak observed at 1174 cm^{-1} is attributed to the alkoxy (C-O) stretching vibrations of C-O-C (Ciszewski *et al.*, 2015; Emiru and Ayele, 2017; Kumar *et al.*, 2018). Additionally, the prominent peak at around 987 cm^{-1} is assigned to the presence of epoxy groups. (Shahriary and Athawale, 2014; Roy *et al.*, 2016).

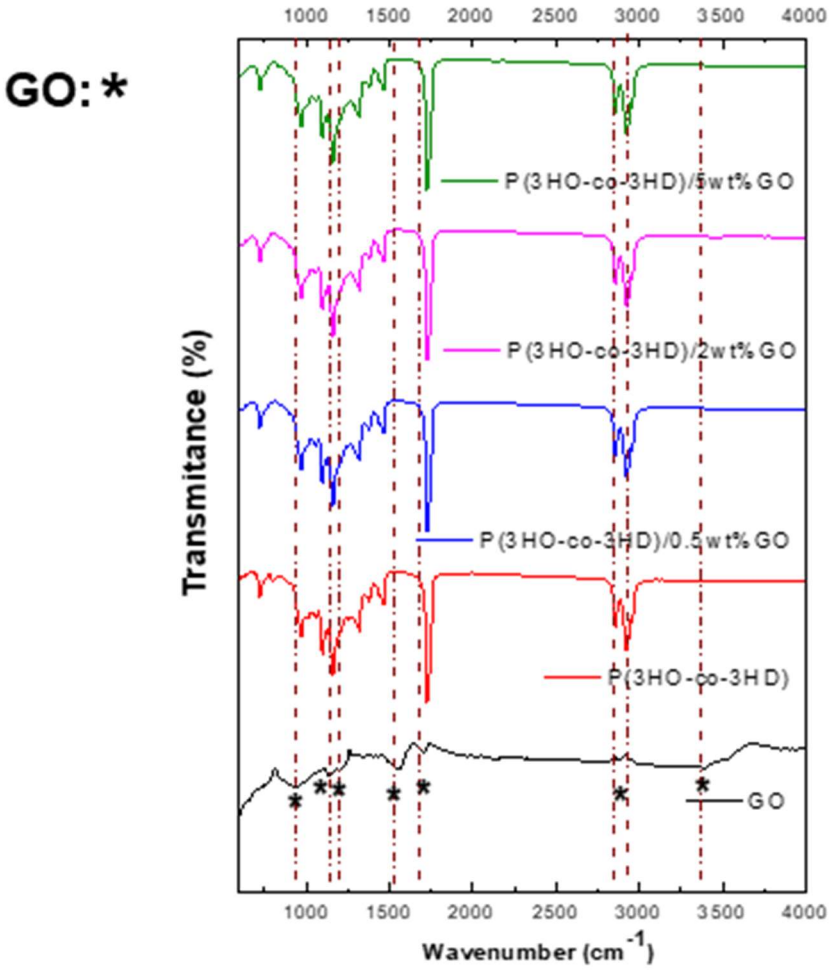

Figure 7.4: ATR/FTIR spectra of: --- GO , ---P(3HO-co-3HD) and P(3HO-co-3HD) composites containing :---0.5 wt%, ---2 wt% and ---5 wt% GO.

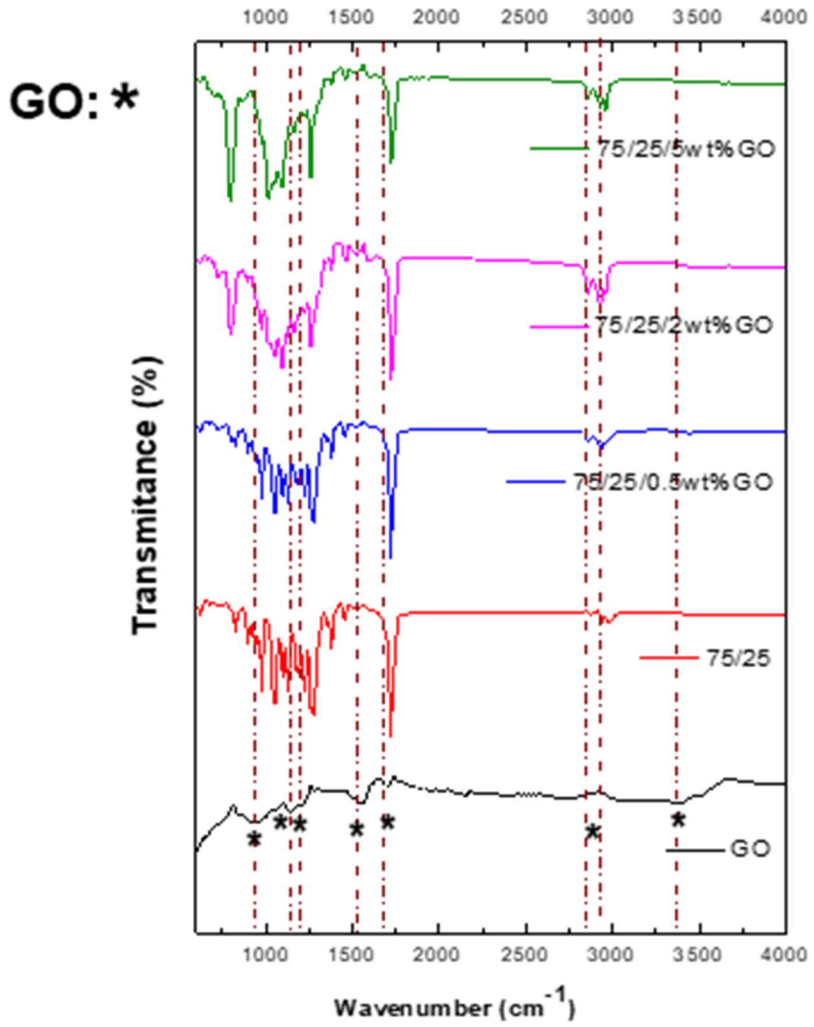

Figure 7.5: ATR/FTIR spectra of: --- GO, ---75/25 P(3HO-co-3HD)/P(3HB) and 75/25 P(3HO-co-3HD)/P(3HB) composites containing :---0.5 %, ---2 % and ---5 wt% GO.

As it can be seen in Figures 7.3, 7.4 and 7.5 the peaks observed for all the composite materials were attributed to the neat matrices. In addition, it was shown that the position of the peaks, in the FTIR spectrum, did not change with the addition of GO.

7.2.3 Thermal characterisation of PHA/GO composites

Differential scanning calorimetry (DSC) was used to evaluate the effect of the addition of different amounts (0.5, 2 and 5 wt%) of GO on the thermal properties of the different PHAs. Glass transition temperature (T_g) and the melting temperature (T_m) for the neat polymers and the developed composites are shown in Table 7.1.

The T_g values obtained from the second heating cycle of DSC revealed no significant differences between the composites and their matrix. The addition of GO, therefore, appeared not to affect the T_g values, as shown in Table 7.1

Table 7.1: Thermal properties of P(3HB), P(3HO-co-3HD) and 75/25 composite which contain different amounts of graphene oxide.

Sample	T_g (^OC)	T_m (^OC)
P(3HB)	-4	174
P(3HB)/0.5 wt% GO	-1.8	172.6
P(3HB)/2 wt% GO	0.5	172.3
P(3HB)/5 wt% GO	-0.1	172.7
P(3HO-co-3HD)	-45	54
P(3HO-co-3HD)/0.5 wt% GO	-49.3	61.3
P(3HO-co-3HD)/2 wt% GO	-51.3	60
P(3HO-co-3HD)/5 wt% GO	-48.6	59
75/25 blend	-47.8 0.7	56.5 163.8
75/25 blend /0.5 wt% GO	-48.6 n/a	55.2 170
75/25 blend/2 wt% GO	-43.5 2.1	56.6 171.3
75/25 blend /5 wt% GO	-44.7 1.6	57.9 174.5

Since there are no reported values in the literature for the heat of fusion for the theoretical value of 100 % crystalline samples of P(3HO-co-3HD), the values for the degree of crystallinity cannot be calculated from the DSC results. However, the degree of crystallinity is proportional to the enthalpy of fusion. Therefore, the effect of the GO on the crystallinity of the polymers was considered in terms of the enthalpy of fusion (ΔH_f) or the melting enthalpy (ΔH_m), determined from the area under the melting endotherm.

The higher the values of ΔH_m obtained, the higher the crystallinity of the sample would be. The melting enthalpies of the specimens for both cycles as well as the normalised values based on a mass fraction of the corresponding polymer are shown in Table 7.2.

Table 7.2: Normalized values of ΔH_m of P(3HB), P(3HO-*co*-3HD), and 75/25 blend containing different amounts of graphene oxide.

Sample		ΔH_{obs}^{PHOHD}, J/g	ΔH_{norm}^{PHOHD}, J/g	ΔH_{obs}^{PHB}, J/g	ΔH_{norm}^{PHB}, J/g
P(3HB)	First heating	n/a	n/a	89.4	89.4
	Second heating	n/a	n/a	67.4	67.4
P(3HB)/0.5 wt% GO	First heating	n/a	n/a	63.8	64.1
	Second heating	n/a	n/a	61.3	61.6
P P(3HB)/2 wt% GO	First heating	n/a	n/a	84.5	86.2
	Second heating	n/a	n/a	79.9	81.5
P(3HB)/5 wt% GO	First heating	n/a	n/a	69.8	73.4
	Second heating	n/a	n/a	68.3	71.9
P(3HO-co-3HD)	First heating	16.5	16.5	n/a	n/a
	Second heating	1.1	1.1	n/a	n/a
P(3HO-co-3HD)/0.5 wt% GO	First heating	17.6	17.7	n/a	n/a
	Second heating	0.3	0.3	n/a	n/a
P(3HO-co-3HD)/2 wt% GO	First heating	19.9	20.3	n/a	n/a
	Second heating	1.3	1.3	n/a	n/a
P(3HO-co-3HD)/5 wt% GO	First heating	20.5	21.5	n/a	n/a
	Second heating	1.6	1.7	n/a	n/a
75/25 blend	First heating	17.6	23.5	43.5	174.2
	Second heating	3.4	4.5	27.4	109.7
75/25 blend /0.5 wt% GO	First heating	23.3	31.0	34.6	138.4
	Second heating	6.4	8.5	43.3	173.9
75/25 blend/2 wt% GO	First heating	10.5	14.0	50.1	200.6
	Second heating	0.9	1.2	45.6	186.0
75/25 blend /5 wt% GO	First heating	16.0	21.4	37.3	149.3
	Second heating	10.1	14.2	34.4	144.5

For the bio-polyester P(3HB), the addition of 0.5 wt% of the filler into the polymer reduced the ΔH_m to 61.6 compared with 67.4 J/g for pure P(3HB).

However, higher loadings of 2 and 5 wt% of GO enhanced the crystallinity of the composites, resulting in enthalpies of melting of 81.5 and 71.9 J/g. The composite containing the higher amount of GO (5 wt%) showed an approximately 12 % lower ΔH_m value compared to the 2 wt% composite.

For the P(3HO-co-3HD), the addition of the lower loading of the filler decreased the ΔH_m value of the composite by 68.57 % compared to the neat polymer matrix. Further addition of the nanofiller, 2 and 5 wt%, increased the melting enthalpy of the fabricated composites by 27 and 58 % respectively.

The fabrication of the 75/25 blend increased the T_g value compared with the P(3HO-co-3HD) and decreased when compared with the P(3HB) (Table 7.1). Since the proportion of the P(3HO-co-3HD) was higher than for the scl-PHA, the values of the T_g and T_m were slightly higher than that compared to the neat P(3HO-co-3HD).

The addition of 0.5 wt% of the filler GO to the binary polymeric matrix 75/25 P(3HO-co-3HD)/ P(3HB) led to an increase of the melting enthalpies ΔH_m of both polymers P(3HB) and P(3HO-co-3HD) by 89.7 % in case of P(3HB) and by 58.6 % in that of P(3HO-co-3HD), respectively, when compared with the neat polymer blend. The addition of 2 wt% GO filler resulted in a decrease in crystallinity, evidenced by a decrease in ΔH_m of 74.4 % for P(3HB). While the same amount of the filler increased the crystallinity manifested as the increase of ΔH_m to 69.6 % compared to the pure P(3HO-co-3HD) matrix.

Further addition of the filler (5 wt%) resulted in a higher enthalpy of melting in the P(3HB) of 14.2 J/g, while the neat P(3HB) was only 4.5 J/g. The same amount of the filler (5 wt%) resulted in a decrease of 22 % of melting enthalpy of the P(3HO-co-3HD) compared with the 2 wt% composite.

The crystallinity improved most for the 2 wt% P(3HB) polymer while for the P(3HO-co-3HD) and the 75/25 blend higher crystallinity was achieved with the addition of 5 wt% of GO into the polymer systems. (All the represented thermograms are included in the appendix section III).

7.2.4 Mechanical characterisation of PHA/GO composites

The PHAs/GO nanocomposites were analysed to reveal their mechanical properties. Films of the composites and their neat matrices were cut into strips as described in section 2.6.5 and subjected to tensile testing's. A summary of the observed mechanical properties, Young's modulus, tensile strength and elongation at break, for both the neat polymers and their composites are summarized in Table 7.3.

Table 7.3: Mechanical properties of PHA/GO composites.

Sample	Tensile strength (σ) (MPa)	Elongation at break (ε_b %)	Young's modulus (E) (MPa)
P(3HB)	20±3.3	21.3±1.8	776±15.2
P(3HB)/0.5 wt% GO	15.7±4.8	1.8±0.3	968±26.7
P(3HB)/2 wt% GO	18.4±2.9	1.7±0.3	1055±28
P(3HB)/5 wt% GO	13±2.0	2.3±0.1	839±.14.4
P(3HO-co-3HD)	9.8±2.4	543±69	7±2.3
P(3HO-co-3HD)/0.5 wt% GO	7±1.2	370±42	9.1±1
P(3HO-co-3HD)/2 wt% GO	4.5±0.3	332±60	10.1±1.5
P(3HO-co-3HD)/5 wt% GO	3.8±0.6	287±34	12±2.3
75/25 blend	10.2±0.9	161±17	193±38.5
75/25 blend/0.5 wt% GO	3.5±0.7	87.7±6	96.7±18
75/25 blend/2 wt% GO	2.9±0.3	91±10	76.6±7
75/25 blend/5 wt% GO	8.2±1	65±11	136.7±50

P(3HB)/GO composites showed an enhancement of the Young's modulus upon the addition of the GO filler, which reached a maximum for the 2 wt% loading (1055 MPa). The highest tensile strength values that were obtained for the 2 wt% GO P(3HB) composites, were 18 MPa (2 MPa less than the neat polymer).

As compared to the 2 wt% composites versus the 5 wt%, the Young's modulus and tensile strength values decreased from 1055 MPa to 839 MPa and 18.4 MPa to 13 MPa, respectively.

Incorporation of GO nanoparticles into the P(3HO-co-3HD) copolymer matrix resulted in a decrease in the elongation at break and an increase in Young's modulus values when compared to neat P(3HO-co-3HD). There was a proportional correlation observed between the GO content and Young's modulus; the higher the loading of the GO into the P(3HO-co-3HD) matrix the higher were Young's modulus values. Conversely, the elongation at break decreased with the increase of the GO content within the polymer.

The neat 75/25 blend showed a tensile strength of 10.2±0.9 MPa, elongation at break of 161±17 % and a Young's modulus of 193±38.5 MPa. The 0.5 wt% GO composite showed a tensile strength of 3.5±0.7, around 6.7 MPa less than the neat blend polymer. This is a reduction in tensile strength of about 65 %. Further addition of GO (2 wt%) resulted in a further decrease in the tensile strength and the Young's modulus when compared with the other composites and the neat blend. Finally, the 5 wt% GO composite revealed the highest values of tensile strength and Young's modulus amongst the composites.

7.2.5 The water contact angle of the PHA/GO nanocomposites

The wettability of a biomaterial surface has a large impact on the initial interaction of the biomaterial surface with the cell surface at the bio interface. In order to characterise the wettability of the different GO modified PHAs, their static water contact angle (WCA) measurements using the sessile drop method were carried out.

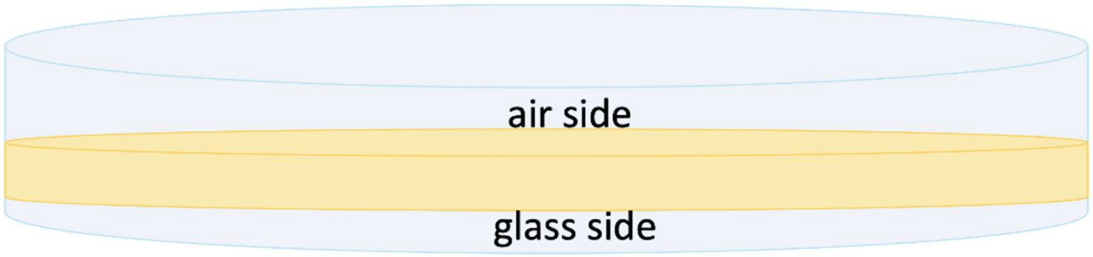

Figure 7.6: Air and glass sides of solvent casted film.

The tests were carried out in triplicate and the tests conducted on both the air and the glass sides of each sample. The films were all cast in glass Petri dishes and allowed to dry naturally, exposed to air. The portion of the films exposed to the air was referred to as the air side of the specimens while the opposite side, which was in contact with the Petri dish, was referred to as the glass side (as shown in Figure 7.6).

Both air and glass sides were studied in order to investigate whether there are any differences in the wettability between the two sides of the same film.

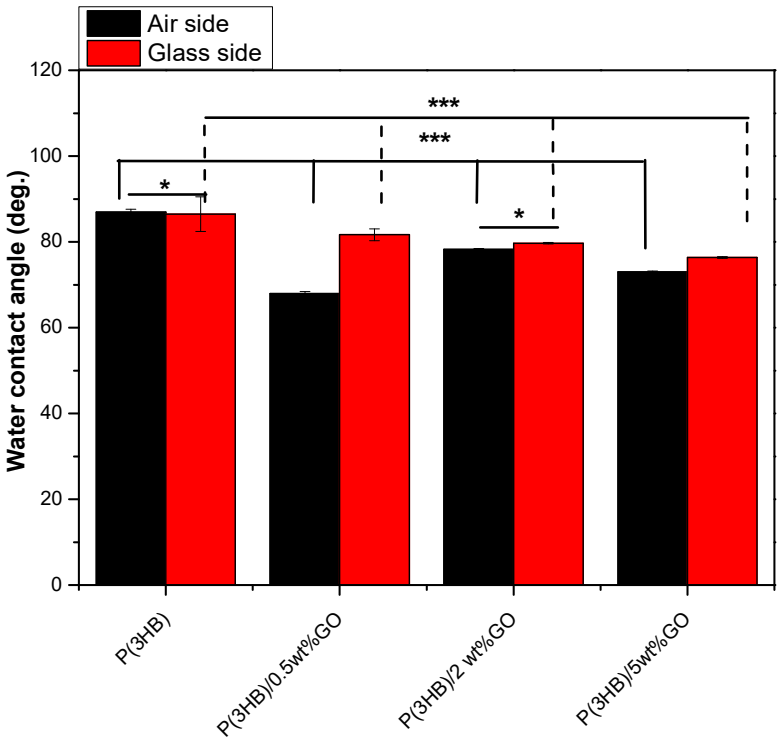

Figure 7.7: WCA (sessile drop) of neat P(3HB) and P(3HB)/GO composite films (GO contents: 0.5, 2 and 5wt%) (n=3). (p statistical significance values (*p ≤ 0.05, **p ≤ 0.01, and ***p ≤ 0.001) were determined for air vs. respective glass side samples and neat matrix vs composites for both air and glass side).

P(3HB) is a hydrophobic polymer and its film surface exhibited a water contact angle of 86.9º ± 0.6 (Figure 7.7, Table 7.4). All composite films had slightly lower contact angle values in comparison to that of neat P(3HB). The incorporation of GO into the homopolymer resulted in lower water contact angles for both air and glass side. A trend was observed by increasing the ratio of the GO filler so that the water contact values were reduced.

For example, the air side of the P(3HB) upon 5 wt% GO exhibited a water contact value of 67.9º, 21.9 % lower than the neat matrix. While the glass side of the same composite revealed a water contact angle of 81.7º similar to the glass side of the neat matrix that showed a value of 84.4º.

The statistical analysis showed significant differences, (***p ≤ 0.001) between neat P(3HB) and the developed composites for both the air and glass sides of the films.

When compared, the air and the glass sides of the same composites exhibited a noticeable difference as shown in Table 7.4.

Table 7.4: WCA values of the neat P(3HB) and its GO composites.

Sample	θ (°)
P(3HB) Air side	86.9±0.6
P(3HB) Glass side	84.4±4.0
P(3HB)/0.5 wt% GO Air side	78.3±0.2
P(3HB)/0.5 wt% GO Glass side	84.7±0.2
P(3HB)/2 wt% GO Air side	73.0±0.2
P(3HB)/2 wt% GO Glass side	78.4±0.2
P(3HB)/5 wt% GO Air side	67.9±0.4
P(3HB)/5 wt% GO Glass side	81.7±1.3

The WCA values obtained for the P(3HO-co-3HD) sample and composites are shown in Figure 7.8 and Table 7.5.

The addition of GO led to a decrease in the hydrophobicity of the final samples compared with the neat P(3HO-co-3HD) film for both sides. The WCA value of the air side of the neat matrix was 104º whereas the addition of 0.5, 2 and 5 wt% of GO resulted in a decrease of the WCA values of about 14.8 %, 17.5 % and 27.9 %, respectively. Almost no difference was detected between the air and the glass side of the neat copolymer.

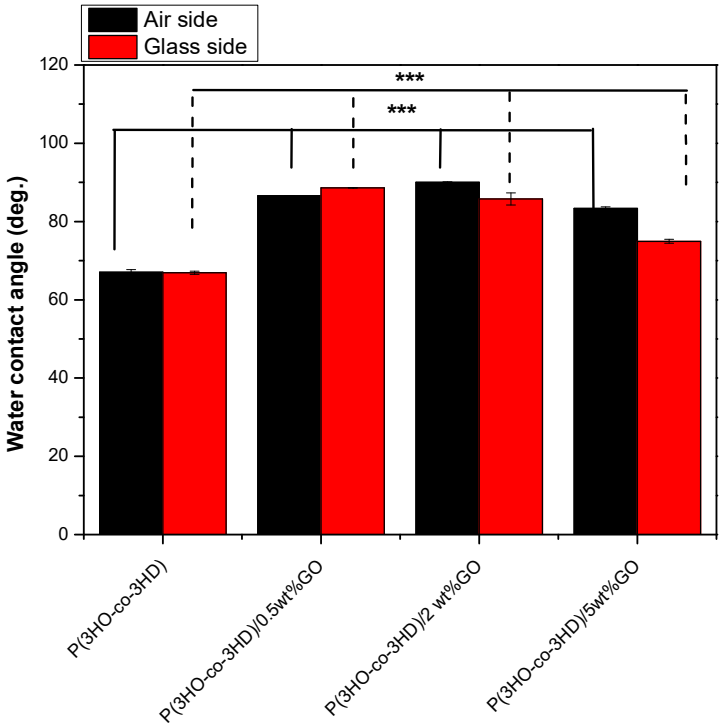

Figure 7.8: Static water contact angle measurements for the neat P(3HO-co-3HD) film and its GO composites (n=3). (p statistical significance values (*p ≤ 0.05, **p ≤ 0.01, and ***p ≤ 0.001) were determined for air vs. respective glass side samples and neat matrix vs composites for both air and glass side).

The Glass side of the composites revealed a similar behaviour, in terms of WCA values. The addition of GO resulted in values of 90º, 83º and 67º for the 0.5, 2 and 5 wt% composites. All the WCA values of the composites were significantly lower from the glass side values of the P(3HO-co-3HD) sample, 102º.

The statistical analysis of the P(3HO-co-3HD)/GO composites showed significant differences compared to the neat P(3HO-co-3HD) for both the air and glass sides of the films (***p≤0.001), as well as between the different sides of the same composite.

Table 7.5: Water contact angle values of the neat P(3HO-co-3HD) film and its GO composites.

Sample	θ (^{o})
P(3HO-co-3HD) Air side	104±0.7
P(3HO-co-3HD) Glass side	102±0.1
P(3HO-co-3HD)/0.5 wt% GO Air side	88.6±0.02
P(3HO-co-3HD)/0.5 wt% GO Glass side	90.1±0.07
P(3HO-co-3HD)/2 wt% GO Air side	85.8±1.5
P(3HO-co-3HD)/2 wt% GO Glass side	83.4±0.4
P(3HO-co-3HD)/5 wt% GO Air side	74.9±0.5
P(3HO-co-3HD)/5 wt% GO Glass side	67.1±0.7

The addition of 0.5 and 2 wt% of the GO as filler material to the 75/25 PHAs blend resulted in an increase in the WCA values, of the air side of the composites, 4 % and 13.2 % respectively. Further addition of 5 wt% GO decreased the water contact angle compared to the neat blend and the other related composites (Figure 7.9 and Table 7.6).

The statistical analysis of the 75/25 P(3HO-co-3HD)/P(3HB) composites showed significant differences (***$p \leq 0.001$) compared to the neat 75/25 blend for both air and glass side (Figure 7.9). The statistical difference was found to be significant for both air and glass sides amongst the composites containing the different amounts of GO (0.5, 2 and 5 wt%).

The glass side of the 75/25 P(3HO-co-3HD)/P(3HB) blend showed a water contact angle of 86.8^{o}, the addition of 0.5, 2 and 5 wt% GO resulted in a reduction of 14.3 %, 8.2 % and 15.3 % respectively.

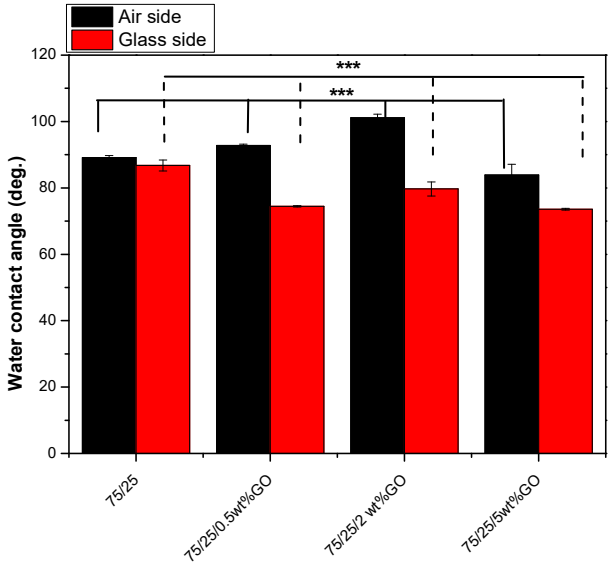

Figure 7.9: Static water contact angle measurements for the neat blend film and its GO composites (n=3). (p statistical significance values (*p ≤ 0.05, **p ≤ 0.01 and ***p ≤ 0.001) were determined for air vs. respective glass side samples and neat matrix vs composites for both air and glass side).

Table 7.6: Water contact angle values of neat 75/25 P(3HO-co-3HD)/P(3HB) film and its GO composites.

Sample	θ (^{O})
75/25P(3HO-co-3HD)/P(3HB) Air side	89.2±0.6
75/25P(3HO-co-3HD)/P(3HB) Glass side	86.8±1.7
75/25P(3HO-co-3HD)/ P(3HB)/0.5 wt% GO Air side	92.8±0.5
75/25P(3HO-co-3HD)/P(3HB)/0.5 wt% GO Glass side	74.4±0.2
75/25P(3HO-co-3HD)/P(3HB)/2 wt% GO Air side	101±1.1
75/25P(3HO-co-3HD)/P(3HB)/2 wt% GO Glass side	79.7±2.1
75/25P(3HO-co-3HD)/P(3HB)/5 wt% GO Air side	83.8±3.2
75/25P(3HO-co-3HD)/P(3HB)/5 wt% GO Glass side	73.5±0.2

The addition of the hydrophilic filler into the polymer matrix of P(3HB) and P(3HO-co-3HD) resulted in a decrease in hydrophobicity of the composites compared with the neat polymers, whereas the incorporation of GO into the matrix of 75/25P(3HO-co-3HD)/P(3HB) increased the hydrophobicity of the composites containing 0.5 and 2 wt% of GO, and a significant reduction of hydrophobicity was observed for the composite containing 5 wt% of the hydrophilic filler.

7.2.6 Scanning Electron Microscopy of PHA/GO composites

The surface topography of the neat polymer and the composites films were studied using SEM**.** Figures 7.10 and 7.11 show the effect of the addition of GO (0.5, 2 and 5 wt%) to the surface of the composite films prepared using P(3HB), P(3HO-co-3HD) and 75/25P(3HO-co-3HD)/P(3HB) compared with the neat films.

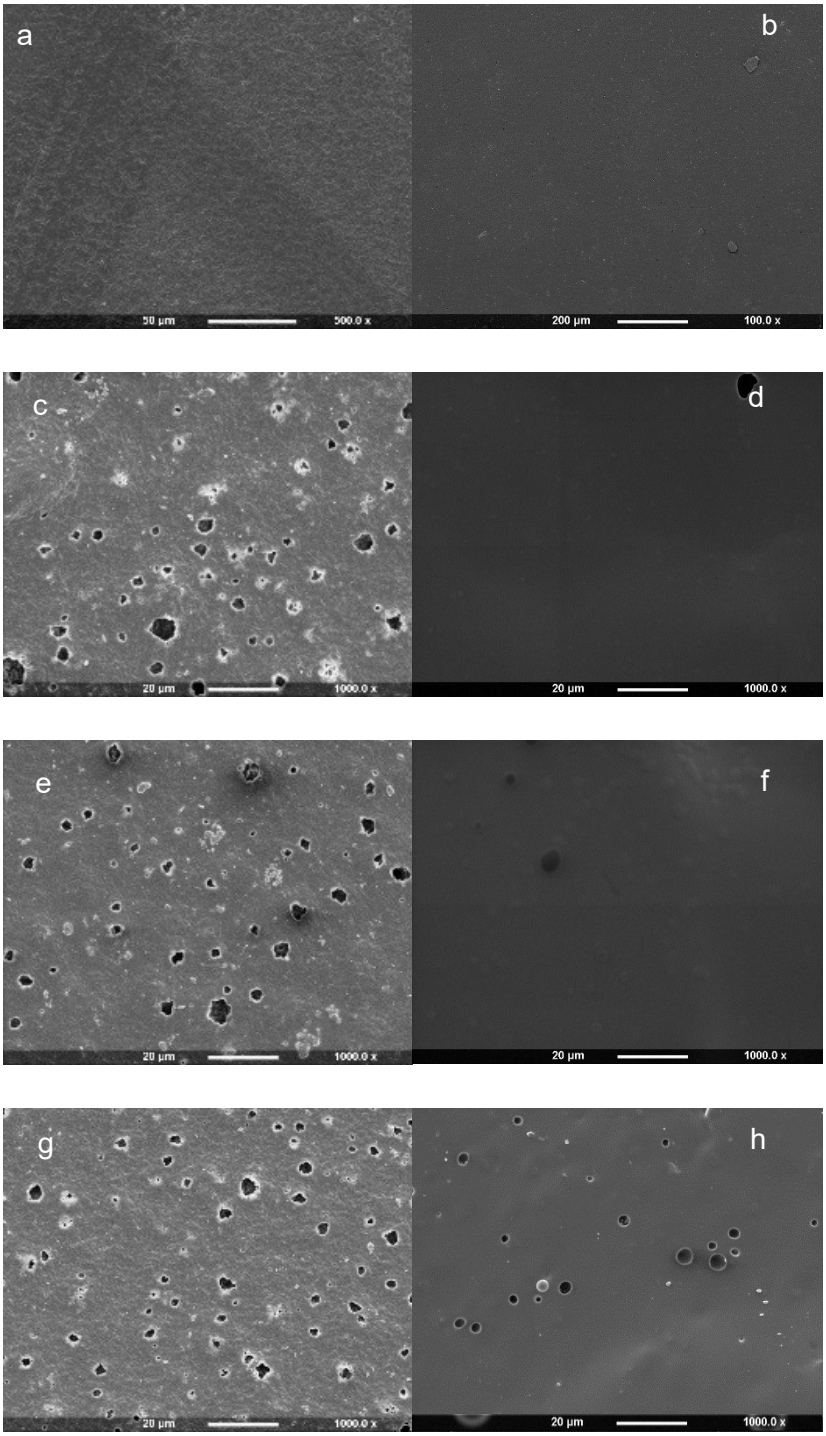

Figure 7.10: SEM images of (a) neat P(3HB), (b) neat P(3HO-co-3HD), (c) P(3HB)/0.5 wt% GO, (d) P(3HO-co-3HD)/0.5 wt% GO, (e) P(3HB)/2 wt% GO, (f) P(3HO-co-3HD)/2 wt% GO, (g) P(3HB)/5 wt% GO and (h) P(3HO-co-3HD)/5 wt% GO.

All the prepared films were intact, smooth-surfaced without any apparent defects. Most of the lower magnifications of the samples revealed no significant changes in the surface morphology. However, higher magnifications of the composites revealed the presence of the dispersed nanoparticles and the effect on the polymer surface, as shown in Figure 7.10 and 7.11.

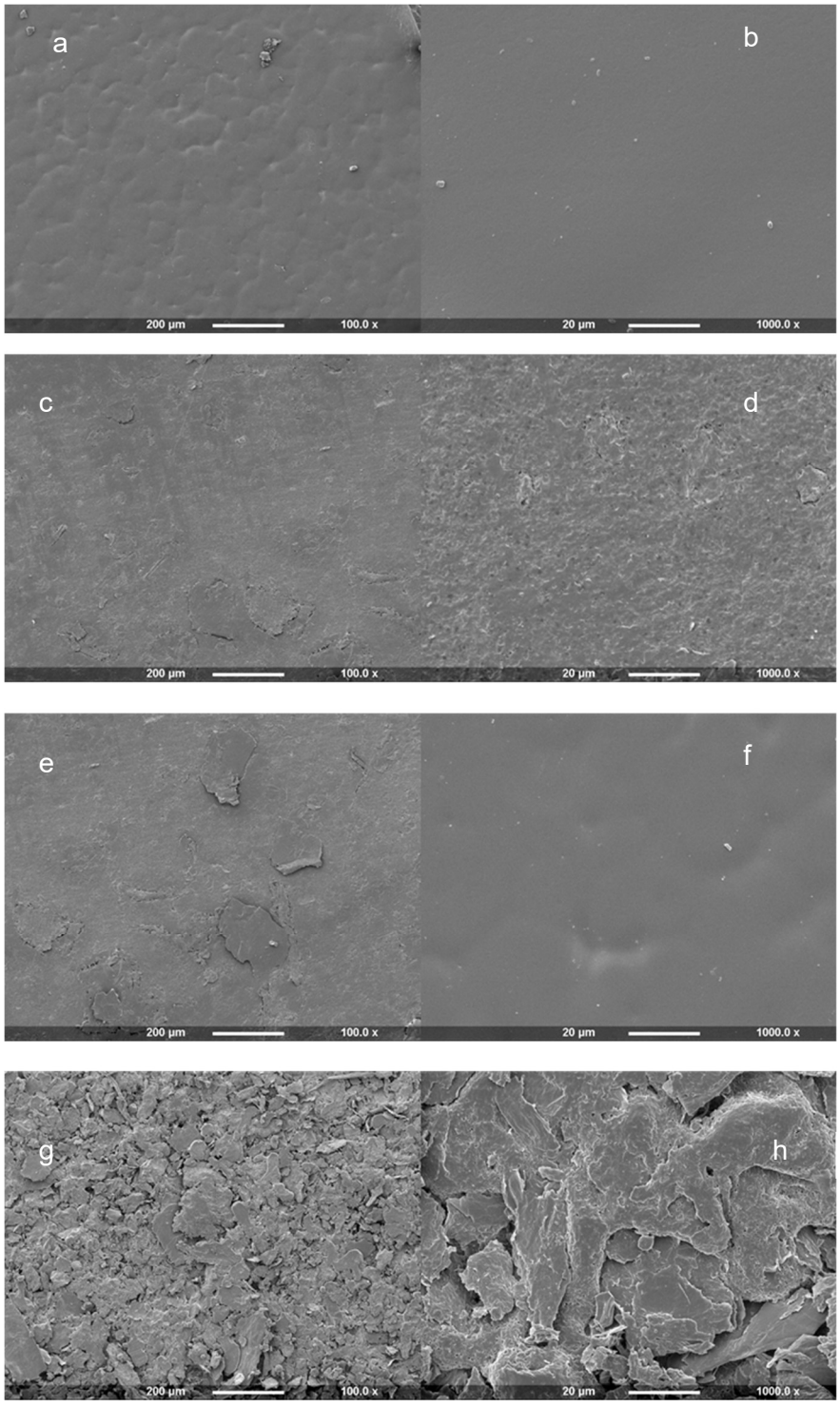

Figure 7.11: SEM images of: (a), (b) neat 75/25P(3HO-co-3HD)/P(3HB) (c), (d) 75/25 blend containing 0.5 wt%GO, (e), (f) 75/25 blend containing 2 wt%GO and (g), (h) 75/25 blend containing 5 wt%GO (low and high magnification × 100 and × 1000).

The P(3HB) composites were observed to have more significant differences compared to the neat polymers than with the P(3HO-co-3HD) composites revealing a rougher surface and the presence of irregular GO particles on the whole surface of the P(3HB) composites.

At the lower concentration (0.5 wt%) of GO, the surface of the P(3HO-co-3HD) composites seemed smooth and compact without irregularities. As the concentration of GO increased within the polymer matrix of P(3HO-co-3HD), more GO particles were observed on the surface of the composite.

7.2.7 XRD of PHA/GO composites

The effect of the addition of GO on the crystallinity of the materials as well as the identification of phases present in GO was studied using X-ray diffraction. The diffractograms for the composites of P(3HB), P(3HO-co-3HD) and 75/25 P(3HO-co-3HD)/P(3HB) polymer matrices containing 0.5, 2 and 5 wt% GO are shown in Figure 7.12, 7.13 and 7.14.

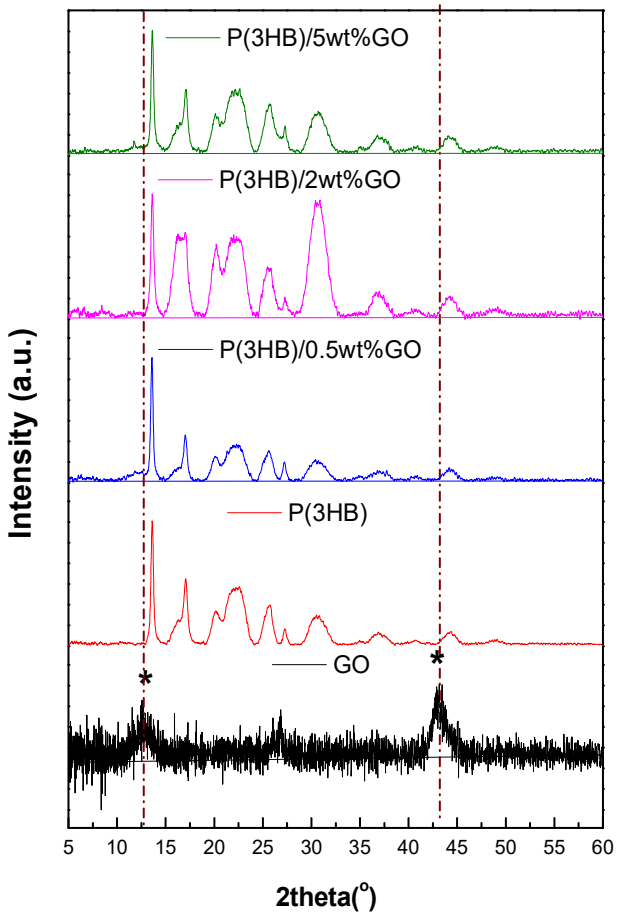

Figure 7.12: XRD patterns of GO and P(3HB)/GO composites with 0.5 wt%, 2 wt% and 5 wt% GO.

The high-intensity peaks that reflect the crystalline lattice of P(3HB) are shown in Figure 7.12. These characteristic peaks correspond to orthorhombic crystal planes (020), (110), (021), (111), (121), (040) and (222) at 2θ values of 13.6°, 17°, 20°, 22°, 25°, 27° and 44°, respectively, were found to be similar for all samples and agree with existing literature (Mohapatra *et al.*, 2017, Anbukarasu *et al.*, 2016). The diffraction pattern of GO consists of two characteristic peaks located at 2θ = 12° and 44° corresponding to (001) and (100) planes with d-spacing of 7.3 Å and 2.1 Å respectively confirming the successful synthesis of GO (Johra, Lee and Jung, 2014; Ameer and Gul, 2016; Ain *et al.*, 2019).

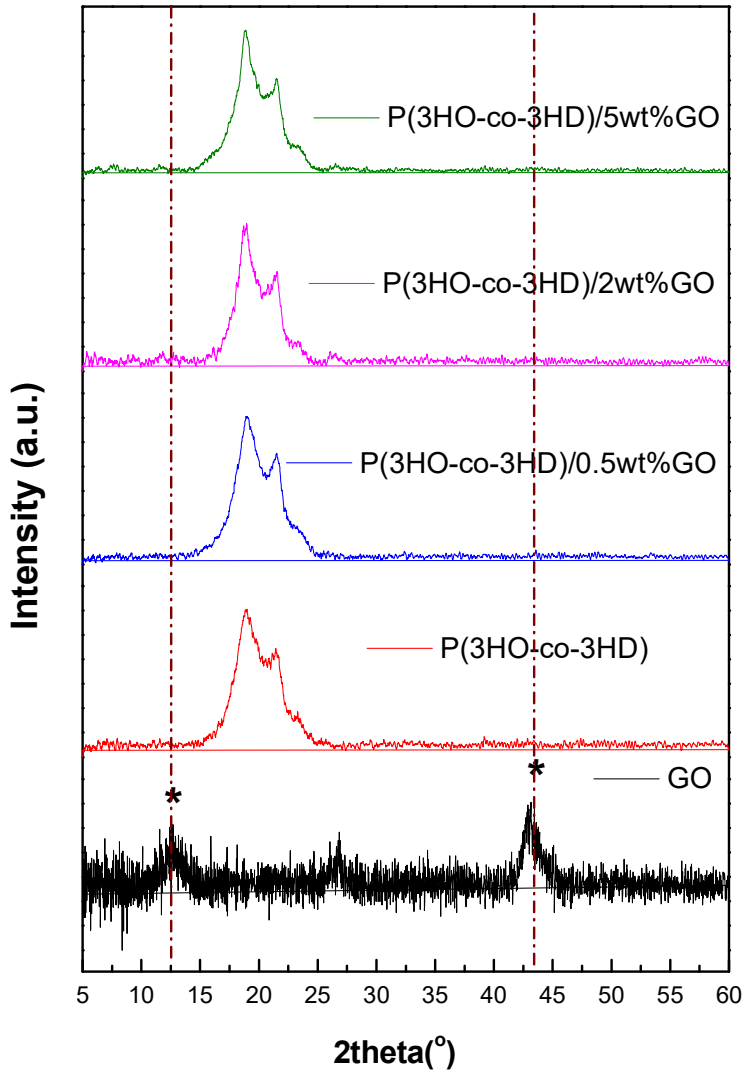

Figure 7.13: XRD patterns of GO and P(3HO-co-3HD)/GO composites with 0.5 wt%, 2 wt% and 5 wt% GO.

The XRD pattern of the P(3HB) composites loaded with 0.5, 2 and 5 wt% GO were almost the same as the neat P(3HB) showing only diffraction peaks

characteristic of the biopolymer. The peaks of the P(3HB) polymer were detected in the 2 and 5 wt% composites with a broadened shape.

For the P(3HO-co-3HD) composites containing 0.5, 2 and 5 wt% GO there were no diffraction peaks which could be attributed to GO. All the observed peaks were characteristic peaks of P(3HO-co-3HD) (Figure 7.13), even for the higher loading of GO (5 wt%).

When GO was added into the binary system of 75/25 of P(3HO-co-3HD)/ P(3HB), the obtained composites did not reveal the characteristic 2θ=12° of GO. Instead, a broader peak emerged at lower values relative to 2θ=12°. Additionally, it is noticeable that the intensity of the characteristic peaks attributed to the polymer matrix is reduced with the addition of GO, as shown in Figure 7.14.

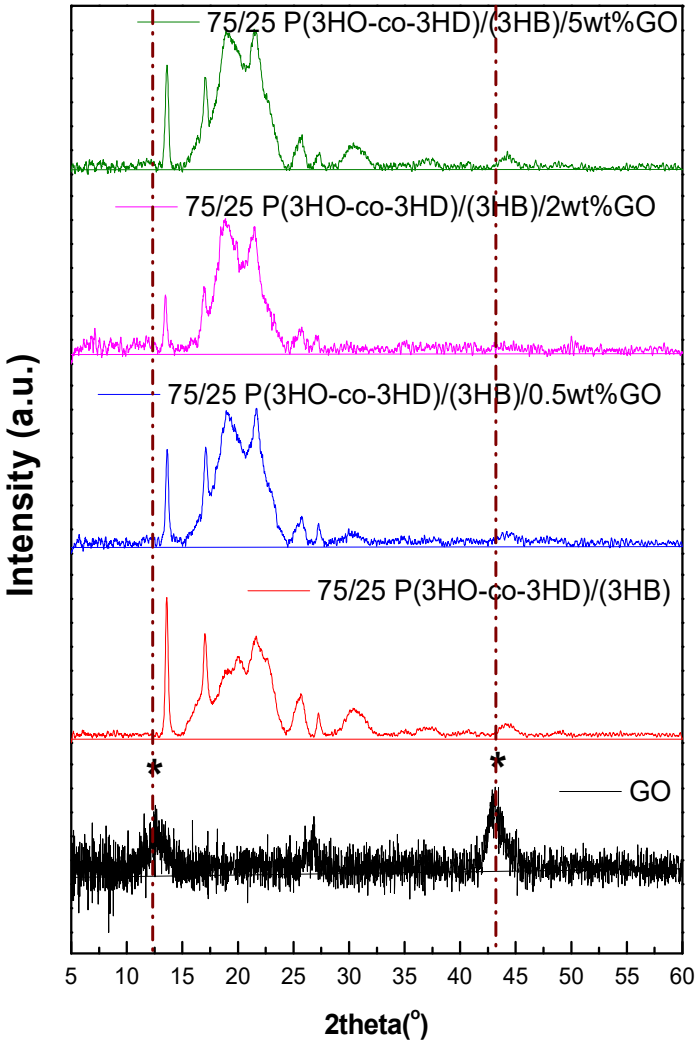

Figure 7.14: XRD patterns of GO and 75/25 of P(3HO-co-3HD)/ P(3HB) /GO composites with 0.5 wt%, 2 wt% and 5 wt% GO.

7.2.8 Raman of PHA/GO composites

Raman spectroscopy was used to investigate the structural fingerprints of the polymer matrix, composites and GO. The most prominent peaks for GO are the G and D bands attributed to in-plane vibrations of bonded carbon atoms and the out of plane vibrations (disorder) which arise from the presence of structural defects such as vacancies, grain boundaries and amorphous carbon species, respectively.

The intensity ratio of these two peaks (I_D/I_G) shows the quality of the GO. In this study, the characteristic peaks of GO, D and G were located at 1318 and 1588 cm^{-1} respectively, verifying the successful synthesis of GO. These values were in agreement with existing literature (Sasaki, Tokura and Sogawa, 2012).

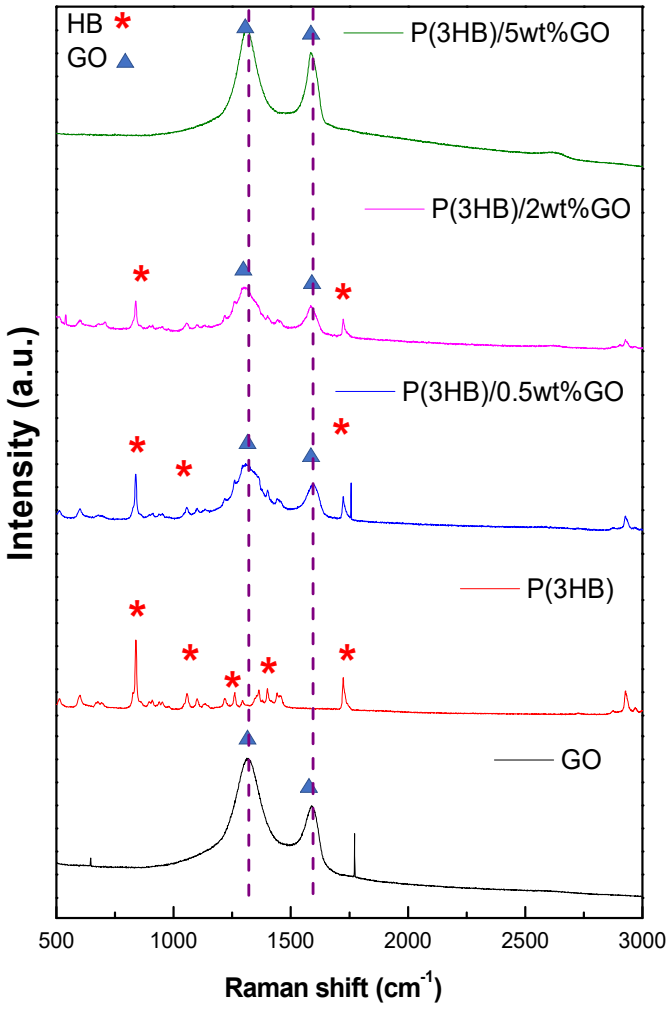

Figure 7.15: Raman spectra of GO and P(3HB)/GO composites with 0.5 wt%, 2 wt% and 5 wt% GO.

For the scl-PHA composites containing different amounts of GO, it was clear that the Raman spectra of the P(3HB) had no peaks in the regions similar to the D and G characteristic peaks of GO. It was quite obvious that the addition of GO to the polymer resulted in the detection of the characteristic peaks of GO, as shown in Figure 7.15. The peaks of the biopolymer located at 837, 1065, and 1725 cm^{-1}, are characteristics peaks of the helical structure of crystalline P(3HB) attributed to C-C, CH bending (Izumi and Temperini, 2010).

The characteristic peaks for the GO, D and G, were observed in all composites containing (0.5, 2 and 5 wt% GO); even with the lower amount of GO (0.5 wt%) added into the P(3HB) matrix, the characteristic peaks for GO, D and G, were observed at 1315 and 1597 cm^{-1} respectively as shown in Table 7.7. The Raman spectra of the 0.5 and 2 wt% P(3HB)/GO composites showed broader peaks for D and G bands. Despite the presence of the characteristic bands for GO in all the composites, their intensity was much lower for the 0.5, and 2 wt% GO concentrations compared with neat GO. The values of the intensity ratio (I_D/I_G) of the P(3HB)/GO composites was close to the values of pristine GO as shown in Table 7.7.

Table 7.7: D and G band position and ratio of I_D/I_G for different composites containing GO.

Sample	D peak (cm^{-1})	G peak (cm^{-1})	I_D/I_G ratio
GO	1318	1588	1.2
P(3HB)	-	-	-
P(3HB)/0.5 wt% GO	1315	1597	1.2
P(3HB)/2 wt% GO	1300	1589	1.2
P(3HB)/5 wt% GO	1311	1585	1.2
P(3HO-co-3HD)	-	-	-
P(3HO-co-3HD)/0.5 wt% GO	-	-	0
P(3HO-co-3HD)/2 wt% GO	1306	1603	1.2
P(3HO-co-3HD)/5 wt% GO	1320	1588	1.2
75/25 blend	-	-	-
75/25 blend/0.5 wt% GO	-	-	0
75/25 blend/2 wt% GO	1303	1597	1.2
75/25 blend /5 wt% GO	1306	1596	1.2

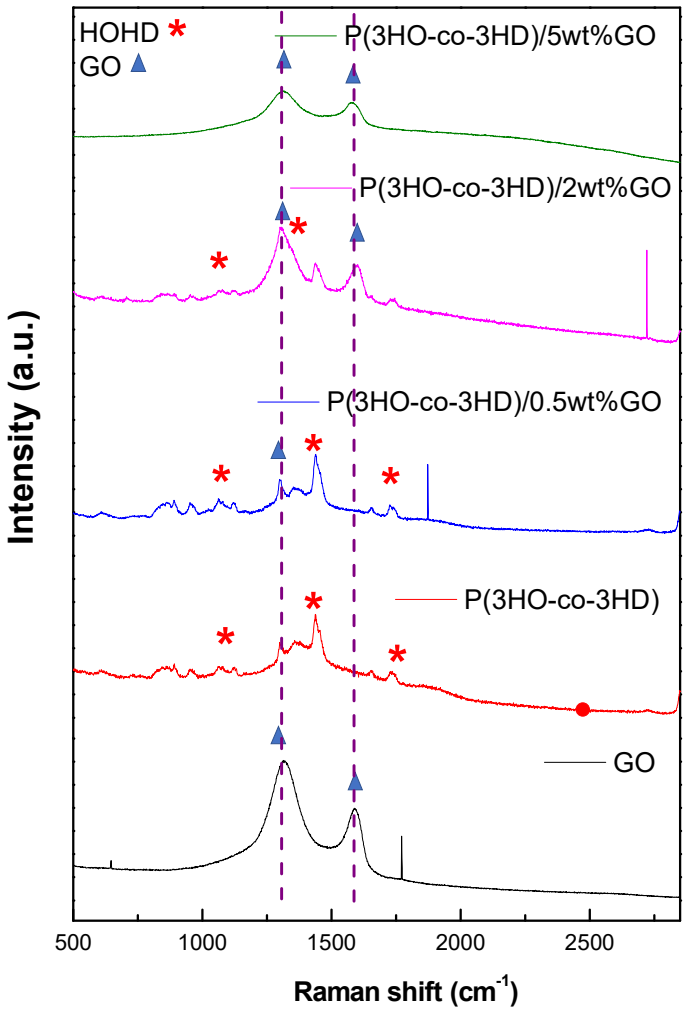

Figure 7.16: Raman spectra of GO and of P(3HO-co-3HD)/GO composites with 0.5 wt%, 2 wt% and 5 wt% GO.

With the addition of a range of amounts of GO (0.5, 2 and 5 wt%) to the polymer matrix of P(3HO-co-3HD) no peaks which could be attributed to GO were observed for the lower concentration of 0.5 wt%. The addition of 2 and 5 wt% GO, however, revealed the characteristic peaks for GO in the Raman spectra, as shown in Figure 7.16. For both of these composites, the G and D bands were broader compared to the pristine GO. The intensity ratio of (I_D/I_G) of 2 wt% is increased compared to the pristine GO and the (3HO-co-3HD) composites.

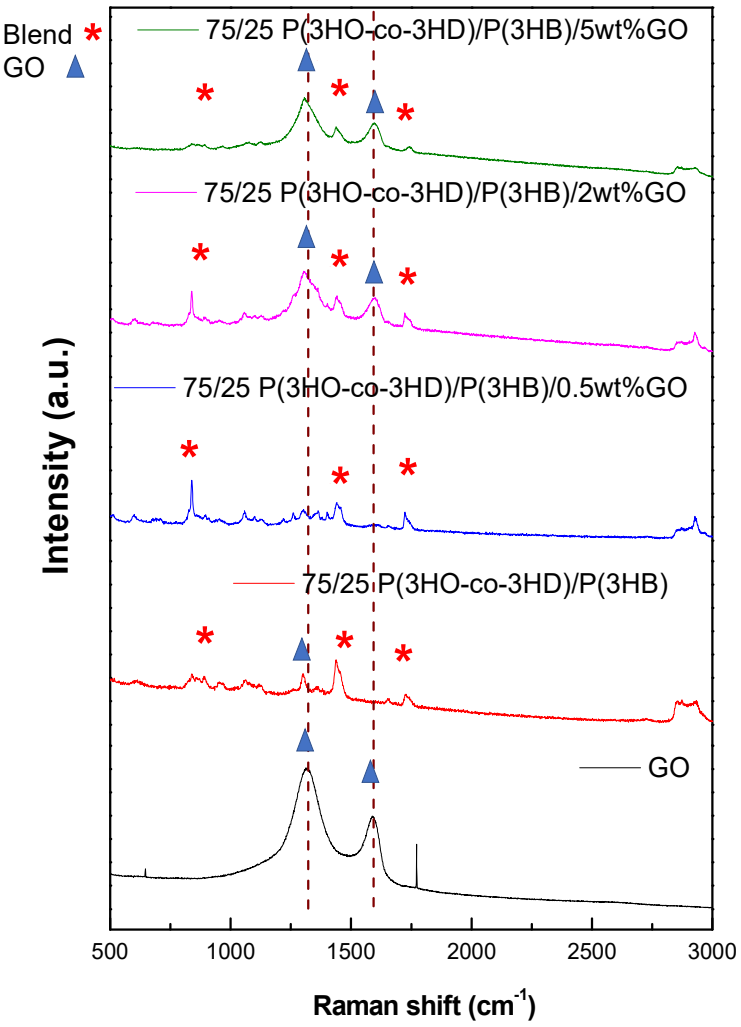

Figure 7.17: Raman spectra of GO and of P(3HO-co-3HD)/ P(3HB) /GO composites with 0.5%, 2% and 5%wt GO.

The 75/25 composites displayed the characteristic G and D bands of GO only in case of the 2 and 5 wt% samples (Figure 7.17).

As shown in Table 7.7 the G band was broader and shifted to lower wavenumbers compared to the pure GO. The values of the intensity ratio of (I_D/I_G) were 1.23 and 1.22 respectively for the 2 and 5 wt% composites, which were higher than the pure GO.

7.2.9 XPS of PHA/GO composites

XPS was used to investigate quantitatively the functional groups and the electron transition states of the various elements present on the PHAs/GO composite surfaces. The XPS spectra revealed the presence of carbon and oxygen moieties. The detailed C1s and O1s XPS peaks were deconvoluted to calculate the carbon/oxygen ratio of the composites. The electron transition from carbon-oxygen atoms from different functional groups depends on the atomic densities. First, a Shirley type background was subtracted, and then the XPS peak was fitted utilising a mixed Gaussian-Lorentzian asymmetric function and selecting the relevant binding energy values from literature.

The calibration of the analyser's kinetic energy scale was performed according to ASTM-E 902-88. Wide Scans were recorded for all samples. However, the core level peaks which were recorded in detail and presented here were: O1s and C1s. Errors in the quantitative data were found to be in the region of ~10 %, (peak areas) while the accuracy for binding energies (BEs) assignments was ~0.1 eV. (These experiments were carried out by Dr. Lambrini Sygellou at the Institute of Chemical Engineering and High-Temperature Chemical Processes, Foundation of Research and Technology Hellas).

For comparison reasons, neat matrices were investigated alongside the composites containing the highest amount of the GO (5 wt%). All the C1s spectra shown in Figure 7.8, revealed a prominent peak at 284.5 eV attributed to sp^2 carbons.

The deconvolution of the C1s and O1s peaks for all samples were grouped into four peaks: (1) carbon in graphitic type (C-C), (2) carbon bonded to oxygen as (C-O) or (C-OH), (3) carbon doubly bonded to oxygen (C=O) and (4) carbon bonded to two oxygens (-COOH) in the form of carboxylic group as shown in Figure 7.18 and Table 7.8.

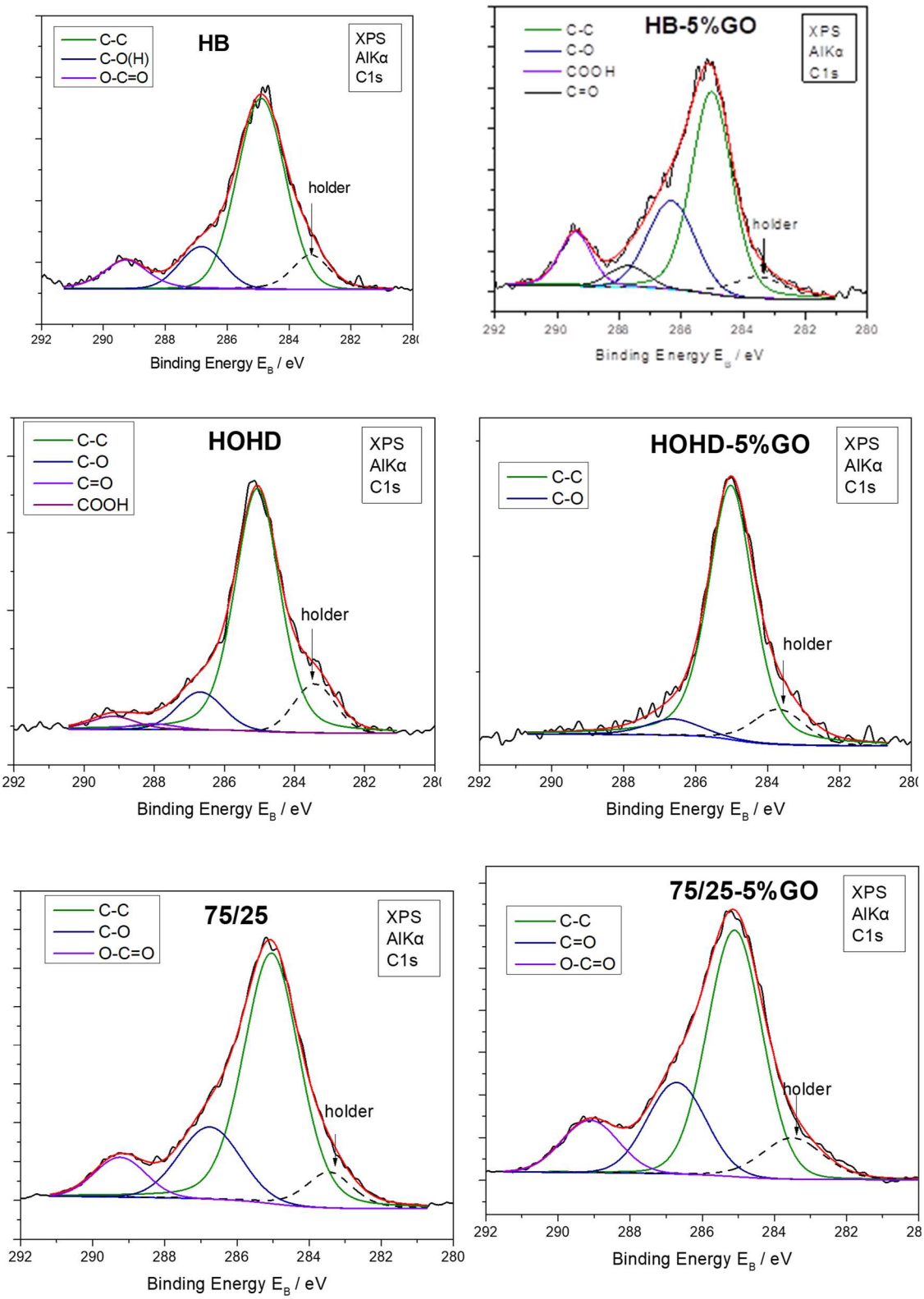

Figure 7.18: Deconvoluted C1s XPS spectra of samples: P(3HB) neat, P(3HO-co-3HD) neat, 75/25 neat, P(3HB)/5 wt% GO, P(3HO-co-3HD)/5 wt% GO, 75/25 /5 wt% GO.

Table 7.8: Assignment of C1s and O1s XPS peaks.

C1s		O1s	
Binding energy (±0.1) eV	Assignment	Binding energy (±0.1) eV	Assignment
284.5	C-C	532.5	C-O
286.4	C-O-C, C-O(H)	531.0	C=O
287.9	C=O	~534	ads. water
289.3	O=C-O(H)		

Using the total peak area of the O1s and C1s peaks in each sample and the appropriate sensitivity factors (based on Wagner's collection and adjusted to the transmission characteristics of the analyser EA10) and equations, the percentage of the average relative atomic concentration in the analysed region can be determined (within experimental error ~10%). The results are summarised in Table 7.9.

Table 7.9: Percentage of atomic oxygen and carbon in the carbon samples.

Sample	% atomic O	% atomic C
P(3HB) neat	36	64
P(3HB) 5 wt%GO	36	64
P(3HO-co-3HD) neat	37	63
P(3HO-co-3HD)/5 wt%GO	40	60
75/25 neat	32	68
75/25/5 wt%GO	33	67

From the deconvolution of the C1s, the percentages of C-C, epoxides-hydroxides (C-O-C, C-O(H)), carbonyl (C=O) and carboxyls (O-C=OH) can be derived. The results for each sample are presented inTable 7.10. In sample P(3HB), the carbonyl (C=O) and carboxyl (O-C=OH) peaks increased relative to the neat sample indicating the presence of GO.

Table 7.10: Percentages of sp2, sp3, epoxides-hydroxides (C-O-C, C-O(H)), carbonyl and carboxyl groups as derived from C1s XPS spectrum deconvolution.

Sample	% C-C	% C-O-C, C-O(H))	C=O	O-C=OH
P(3HB) neat	**73**	**15**	**0**	**12**
P(3HB) 5wt%GO	**56**	**26**	**5**	**12**
P(3HO-co-3HD) neat	**82**	**12**	**1**	**4**
P(3HO-co-3HD)/5 wt%GO	**90**	**10**	**0**	**0**
75/25 neat	**71**	**20**	**0**	**9**
75/25/5 wt%GO	**64**	**25**	**0**	**11**

From the results shown in Table 7.10, it is obvious that only in the P(3HB) sample containing 5 wt% of GO, a contribution from carbonyl groups (existent in the GO sheet) was presented. Additionally, the concentration of epoxides increased from the presence of GO in the polymers.

7.2.10 *In vitro* antibacterial evaluation of Graphene oxide composites

Direct contact test (DCT) – ISO 22196

To evaluate the antibacterial activity of the composite films containing graphene oxide nanoparticles, the direct contact test (DCT) according to ISO 22196 was performed as described in Section 2.11.7. Specimens containing graphene oxide were incubated with a bacterial culture for 24 h. After 10-fold serial dilutions, it was possible to count the CFU of the samples incubated with *S. aureus* (ATCC® 29213™) and *E. coli* (ATCC® 25922™).

A dependency was observed between the concentration of GO and the recovered CFU, as shown in Figure 7.19. Increasing the amount of the graphene oxide resulted in higher antibacterial activity, so less colony forming units were recovered.

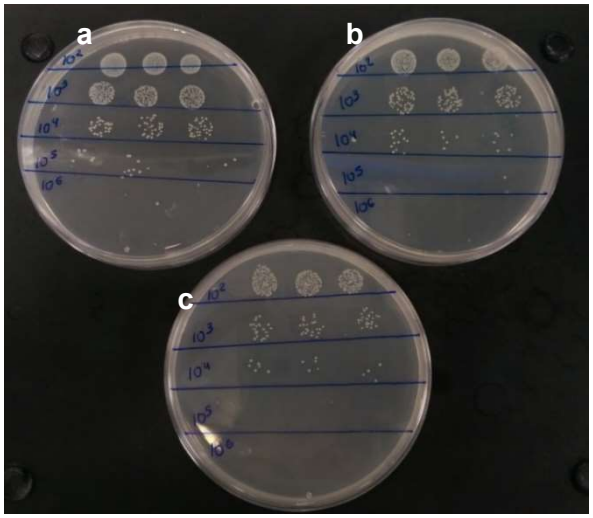

Figure 7.19: Recovered colonies after incubation with *S. aureus* (ATCC® 29213™): (a) P(3HB)/0.5 wt% GO (b) P(3HB)/2 wt% GO and (c) P(3HB)/5 wt% GO.

After the 24 hour incubation of the samples with the bacterial culture, the specimens were collected and assessed for changes to the number of bacterial colonies. The samples were washed with PBS and sonicated to evaluate the amount of the bacteria which adhered to the surface of the composite samples.

All the tests were performed in triplicate using fresh samples for each of the experiments. Both the antibacterial activity and the bacterial loss were expressed using the non-modified representative polymer sample as control.

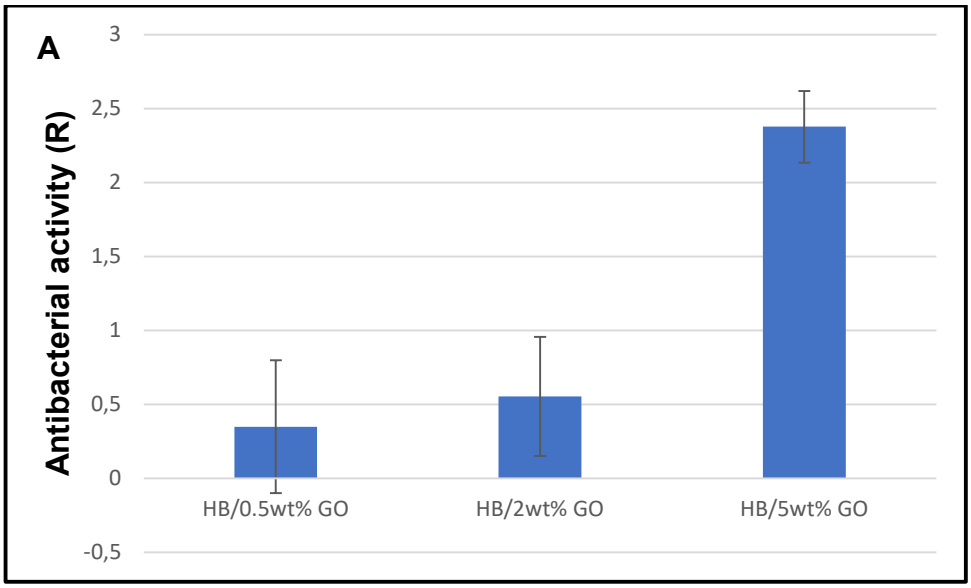

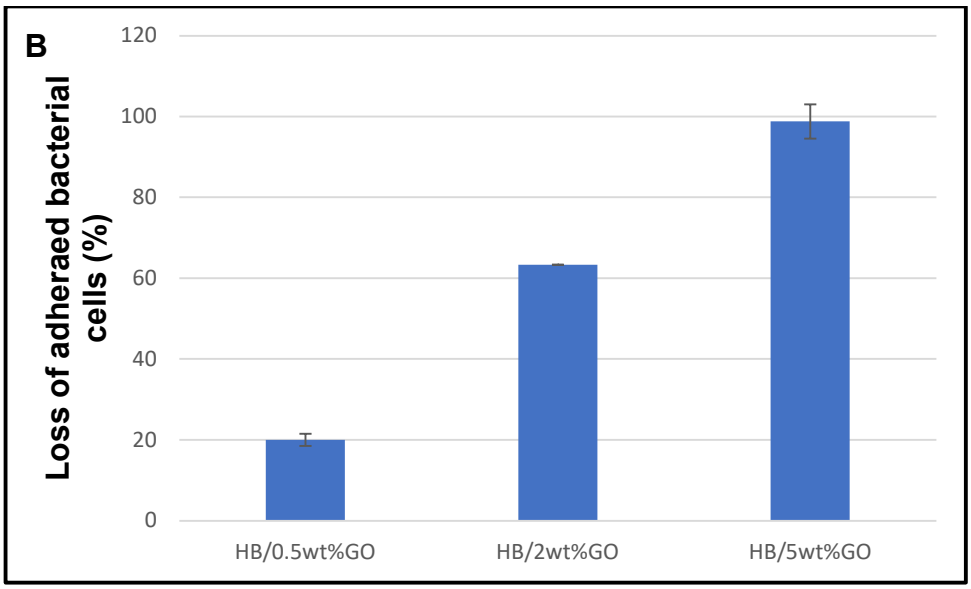

Figure 7.20: 7(A) Antibacterial activity against free planktonic bacterial cells and (B) loss of adhered bacteria of P(3HB)/0.5 wt% GO, P(3HB)/2 wt% GO and P(3HB)/5 wt% GO against *S. aureus* (ATCC® 29213™).

The increase in the amount of GO led to the increase of the antibacterial activity of the P(3HB)/GO samples for both the free planktonic and adhered bacterial cells of *S. aureus* (ATCC® 29213™) as shown in Figure 7.20 A and B. The effect of the P(3HB) composite containing the higher amount of GO (5 wt%) showed a loss of the number of adhered bacteria of 98 % compared with the neat matrix.

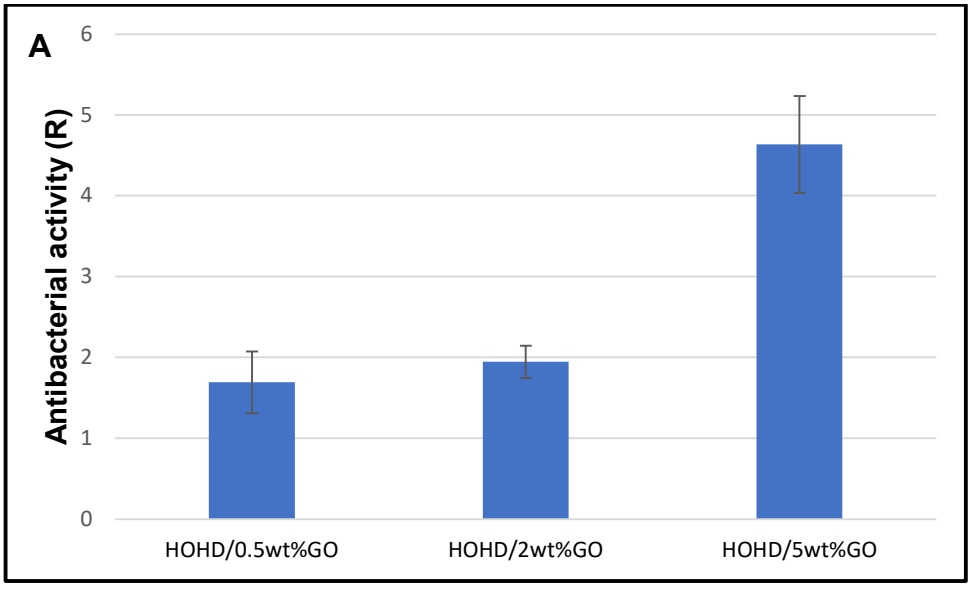

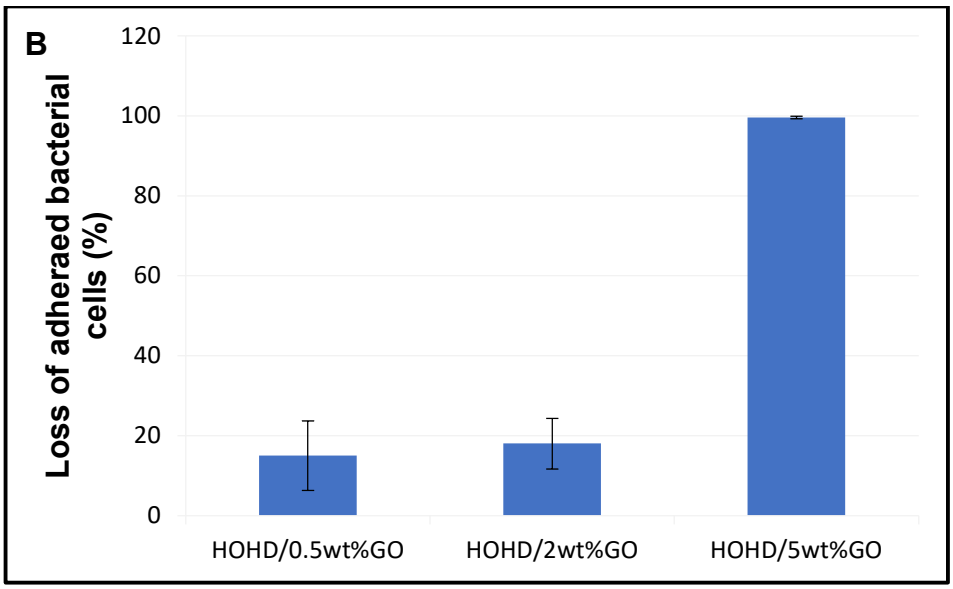

Figure 7.21: (A) Antibacterial activity against free planktonic bacterial cells and (B) loss of adhered bacteria of P(3HO-co-3HD)/0.5 wt% GO, P(3HO-co-3HD)/2 wt% GO and P(3HO-co-3HD)/5 wt% GO against *S. aureus* (ATCC® 29213™).

Similar to the P(3HB) composites, the P(3HO-co-3HD) composites demonstrated the same correlation between the increase of the amount of GO in the polymer matrix and the efficacy of their antibacterial activity against *S. aureus* (ATCC® 29213™). The higher the amount of the inorganic compound, the greater the antibacterial activity against bacterial cells from both the sessile and planktonic forms (Figure 7.21 A and B). The P(3HO-co-3HD) composite revealed the higher loss of adhered bacterial cells almost 100% compared with the non-modified matrix.

For the blend of 75/25 P(3HO-co-3HD)/P(3HB) containing GO, it was observed that the specimen containing 2 wt% GO displayed a superior antibacterial activity over the 0.5 and 5 wt% composites. While the inhibition of adhered bacterial cells was almost the same for the 2 and 5 wt% composites; resulting in 100 and 97 % reduction of the adhered cells respectively (Figure 7.22).

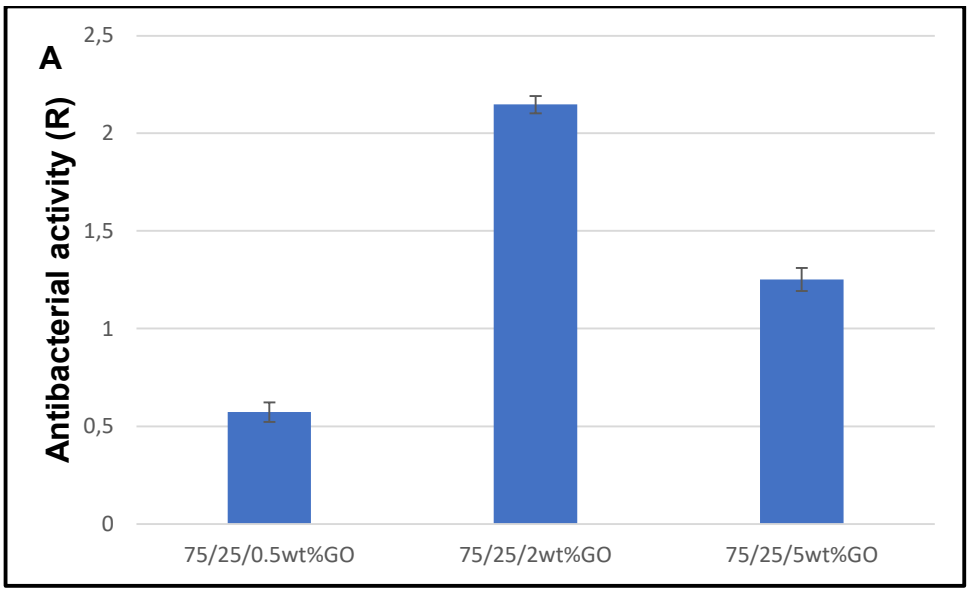

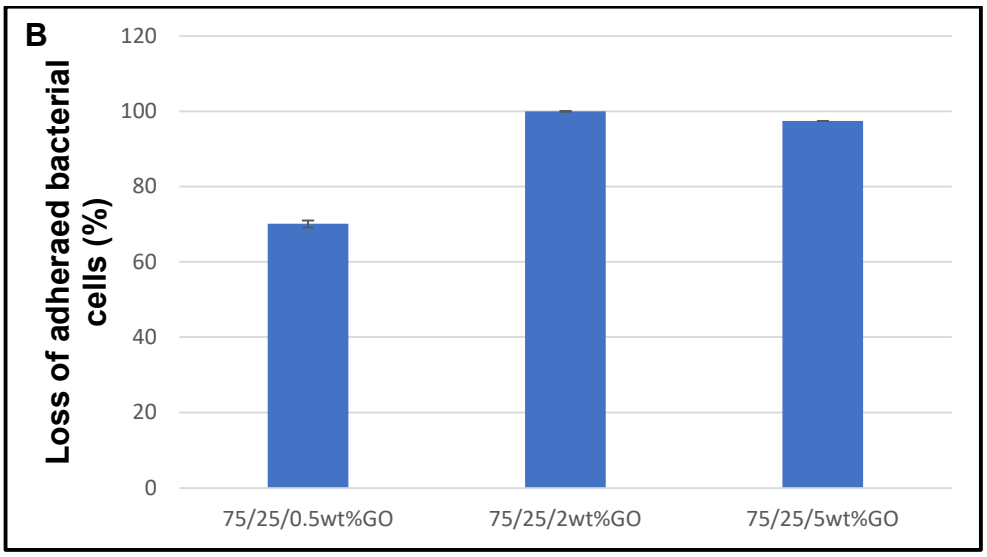

Figure 7.22: (A) Antibacterial activity against free planktonic bacterial cells and (B) loss of adhered bacteria of 75/25 P(3HO-co-3HD)P(3HB)/0.5 wt% GO, 75/25 P(3HO-co-3HD)P(3HB)/2 wt% GO and 75/25 P(3HO-co-3HD)P(3HB)/5 wt% GO against *S. aureus* (ATCC® 29213™).

The developed specimens were also tested against Gram-negative bacterial strain and more specifically, against *E. coli* (ATCC® 25922™).

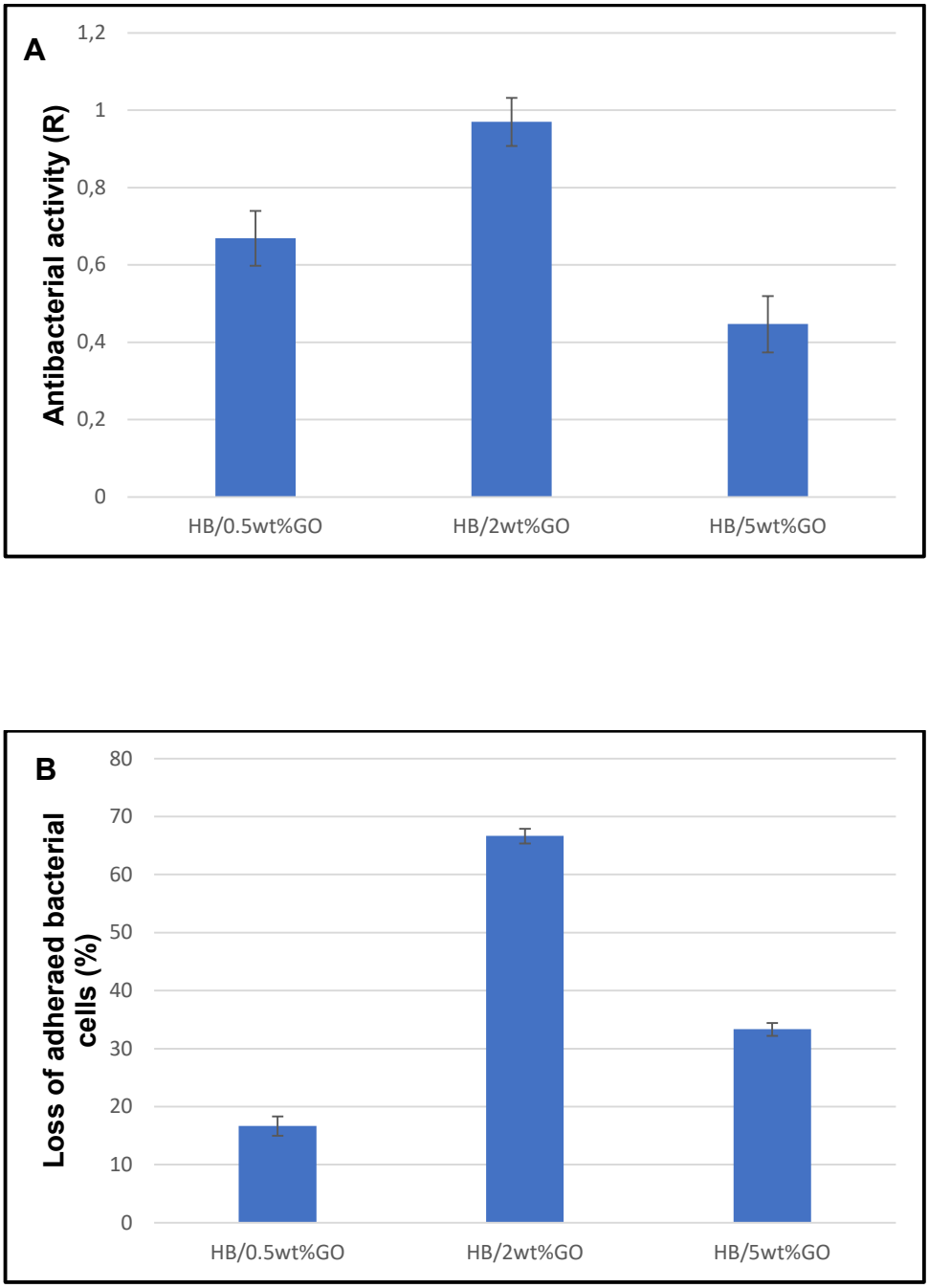

Figure 7.23: (A) Antibacterial activity against free planktonic bacterial cells and (B) loss of adhered bacteria of P(3HB)/0.5 wt% GO, P(3HB)/2 wt% GO and P(3HB)/5 wt% GO against *E. coli (ATCC® 25922™).*

As shown in Figure 7.23, the addition of 2 wt% GO to scl-PHA conferred higher antibacterial activity than the 0.5 and 5 wt% P(3HB) composites. The higher bacterial loss was detected for the higher concentration of GO 2 and 5 wt% revealing reductions of 66 % and 33 % respectively.

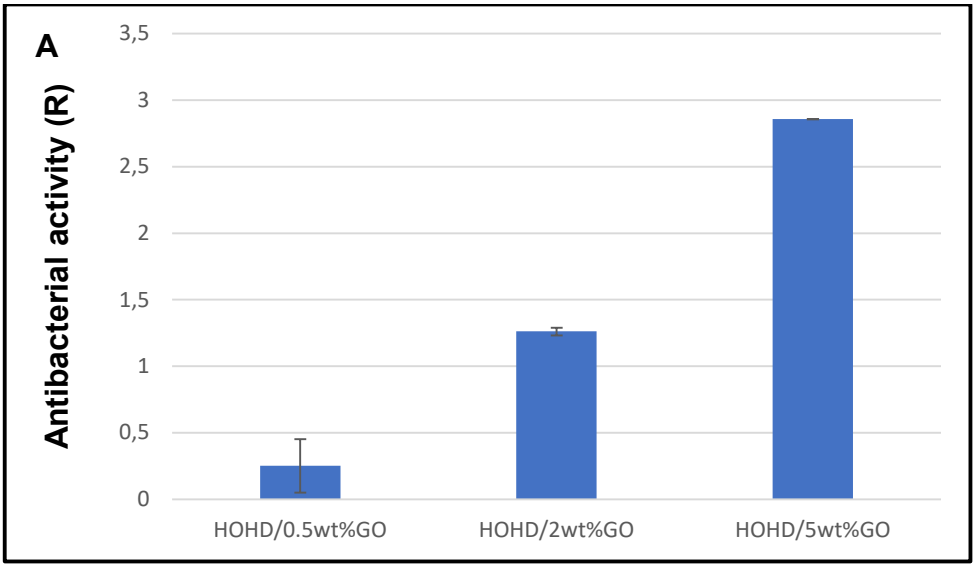

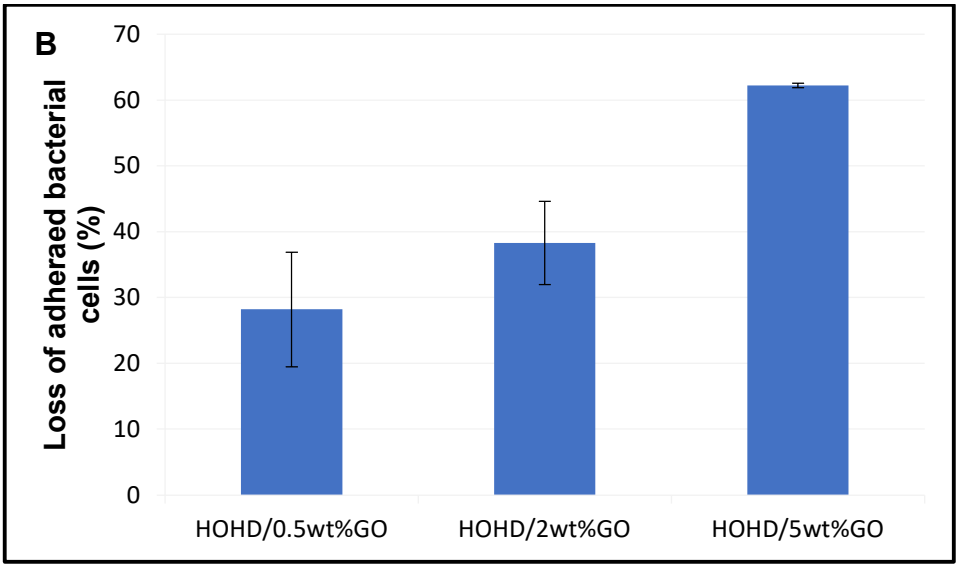

Figure 7.24: (A) Antibacterial activity against free planktonic bacterial cells and (B) loss of adhered bacteria of P(3HO-co-3HD)/0.5 wt% GO, P(3HO-co-3HD)/2 wt% GO and P(3HO-co-3HD)/5 wt% GO against *E. coli (ATCC® 25922™).*

When the P(3HO-co-3HD) composites containing, 0.5, 2 and 5 wt% GO, tested against *E. coli* (ATCC® 25922™) they showed a reduction of the number of bacterial cells by 28 %, 38 % and 62 % respectively. The addition of different ratios of GO to the P(3HO-co-3HD) revealed a concentration-dependent correlation with the antibacterial activity. The higher the amount of GO in the polymer matrix, the higher the antibacterial activity was for both planktonic and adhered bacteria, as shown in Figure 7.24 A and B.

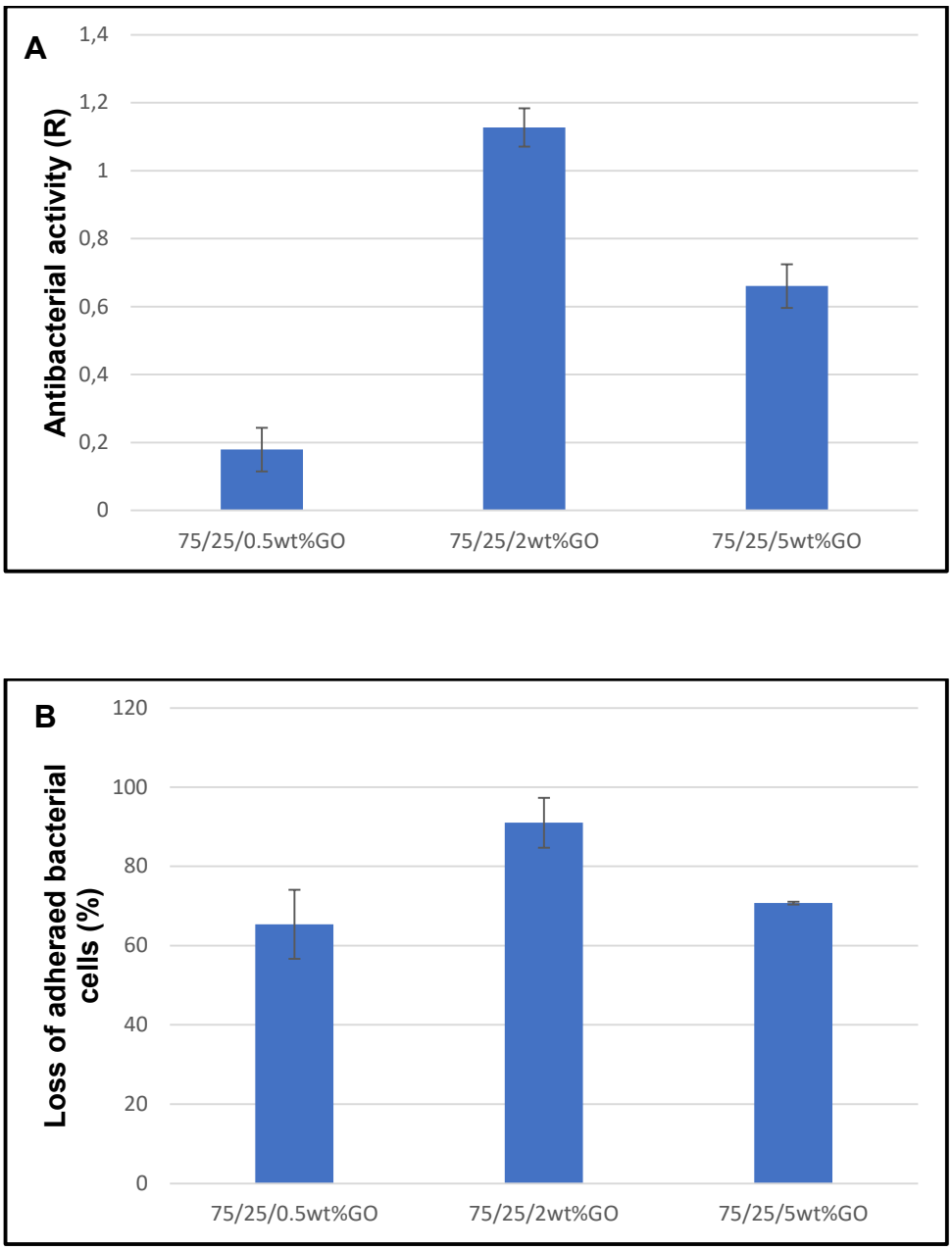

Figure 7.25: (A) Antibacterial activity against free planktonic bacterial cells and (B) loss of adhered bacteria of 75/25 P(3HO-co-3HD)P(3HB)/0.5 wt% GO, 75/25 P(3HO-co-3HD)P(3HB)/2 wt% GO and 75/25 P(3HO-co-3HD)P(3HB)/5 wt% GO against *E. coli* (ATCC® 25922™).

The results in Figure 7.25 A and B show that the composites containing different amounts of GO resulted in bacterial loss of the *E. coli* cells higher than 65 % in all cases. The higher loss was achieved for the 2 wt% composite where the 0.5 and 5 wt% samples revealed similar bacterial loss against *E. coli* (ATCC® 25922™).

7.2.11 Indirect and direct cytocompatibility tests

The cytocompatibility of the graphene oxide composites was assessed against two cell lines, L929 murine fibroblasts and NG108-15 neuronal cells. First, indirect contact test was performed as described previously in section 2.12. The cell viability, expressed as a percentage of the positive control tissue culture polystyrene (TCPS), was a result from the application of CellTiterBlue assay (Figure 7.26). Polyethylene (PE) and TCPS were used as positive controls while a polyurethane film containing 0.1 % zinc diethyldithiocarbamate (ZDEC), (Materials and methods) was used as the negative control.

Figure 7.26 shows that the media which had been pre-incubated with the GO samples did not show the presence of any substances harmful to the cells. All the composites showed a cytocompatibility higher than 90 %, even the specimens containing 5 wt% of GO which was the highest loading of the agent in the polymer matrices. These results show that all the developed composites are cytocompatible according to ISO 10993-5.

The statistical analysis showed significant differences (***$p \leq 0.05$) between the negative control (ZDEC), all the neat polymers and the developed composites. Only for the 75/25 P(3HO-co-3HD)/P(3HB) composites did the statistical analysis show significant differences between the neat 75/25 polymer matrix and the composites containing 0.5 and 2 wt% of the GO.

In addition, to further support these findings, fluorescence microscopy was used. The cells were stained with the Live/Dead staining Kit from Promocell containing Calcein AM and Ethidium homodimer-III. The images obtained are shown in Figure 7.27 and revealed high cell adhesion and growth compared to the negative control (provoked cell lysis) and the positive control (TCPS).

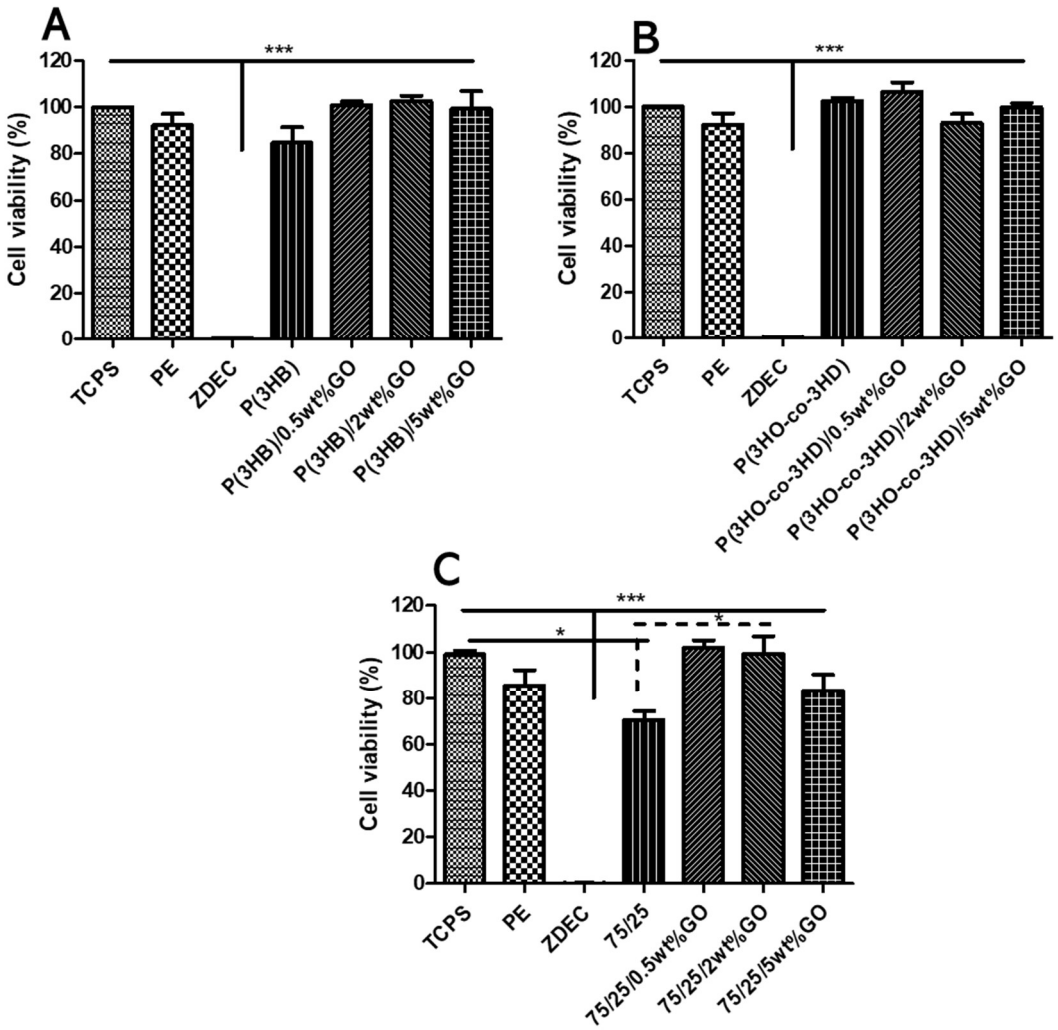

Figure 7.26: Cell viability (% TCPS) of L929 cells seeded on (A) P(3HB), (B) P(3HO co-3HD) and (C) 75/25 P(3HO-co-3HD)/ P(3HB) composites containing different loadings of graphene oxide (Mean± SEM, n = 9 independent experiments). Statistical significance determination is represented as *p ≤ 0.05, **p ≤ 0.01, and ***p ≤ 0.001 for cells on TCPS vs. all materials, and non-modified polymer blend vs. GO composites

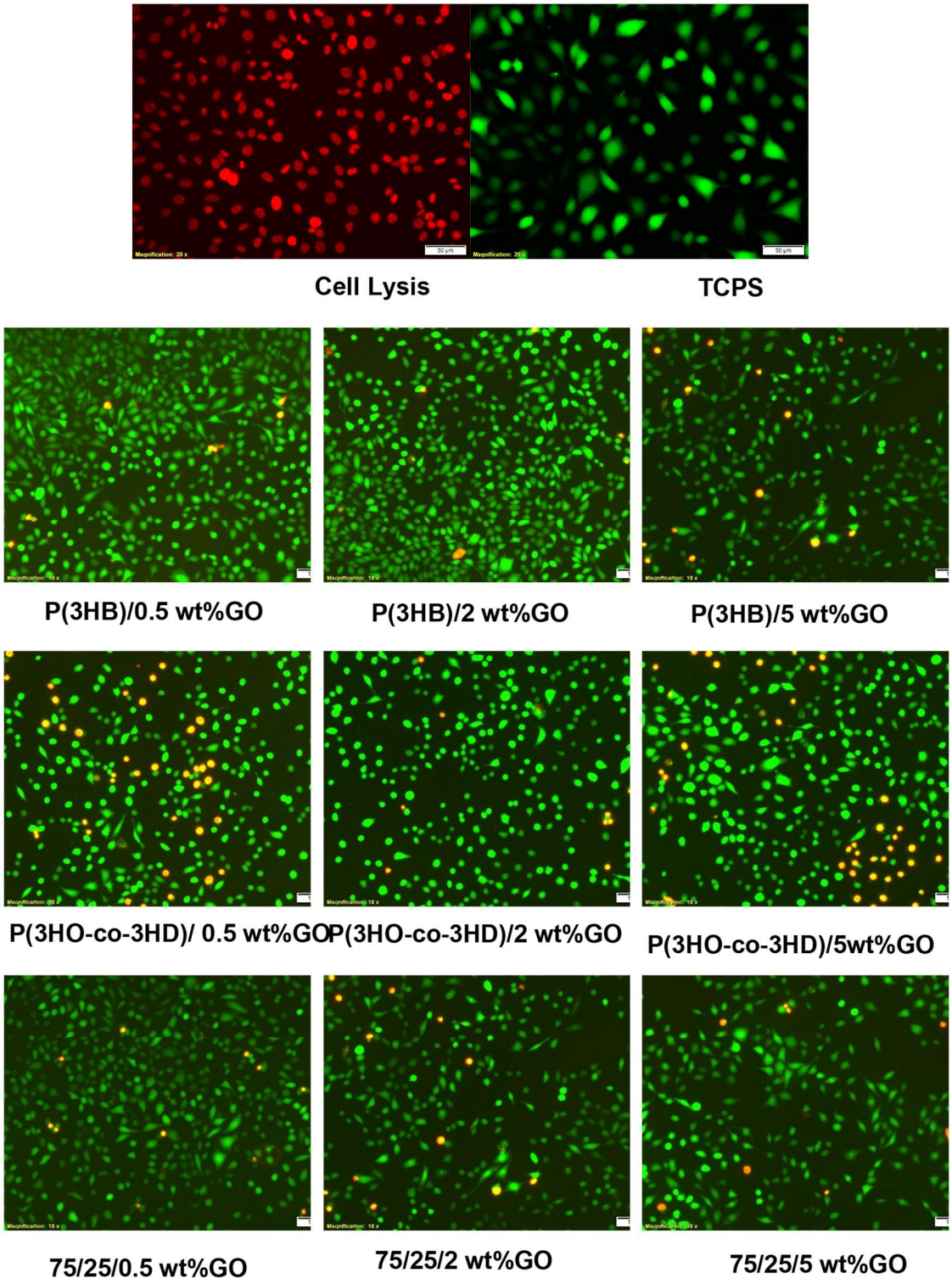

Figure 7.27: Fluorescence micrographs of L929 cells stained with Ethidium homodimer-III (red) and Calcein AM (green) after 24 h in culture with the aliquots of the respective samples (indirect test).

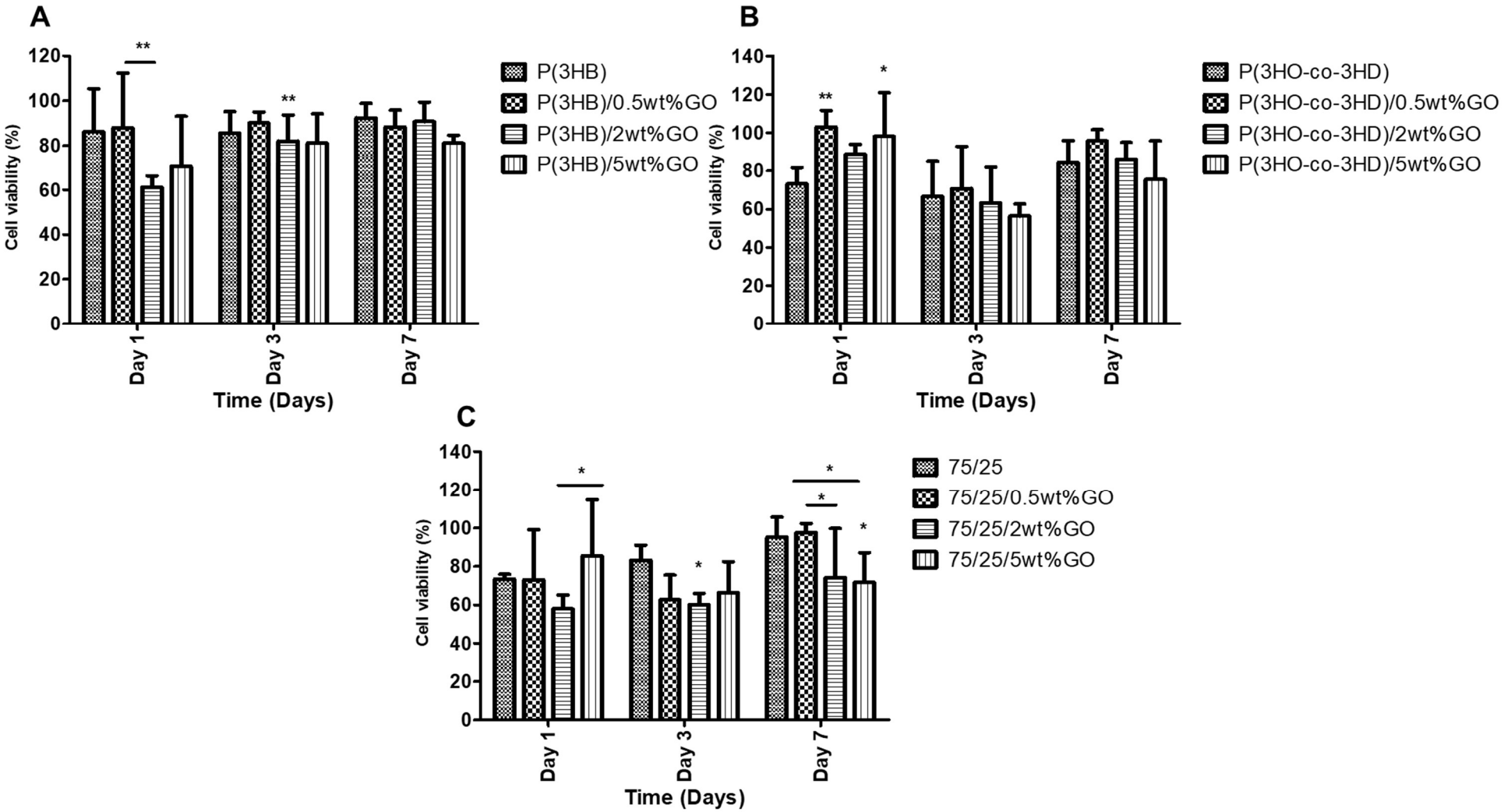

Figure 7.28: Direct cytocompatibility evaluation of the (A) P(3HB), (B) P(3HO-co-3HD) and (C) 75/25 P(3HO-co-3HD)/P(3HB) composites containing different loadings of graphene oxide with respect to L929 cells (Mean± SEM, n = 9 independent experiments). Statistical significance determination is represented as *p ≤ 0.05, **p ≤ 0.01, and ***p ≤ 0.001 for cells on TCPS vs. all materials, and non-modified polymer blend vs. GO composites.

To further investigate the cytocompatibility of these samples, direct contact tests were performed utilising the well-established L929 cells. The cells were seeded directly on the surface of the specimens, and their cytocompatibility was assessed using the cell viability assay Cell Titer-Blue® (Promega). The time points which were investigated were Day 1, 3 and 7 after the seeding of the samples with the cells.

For the P(3HB) composites containing different quantities of GO, when tested directly against the L929 murine fibroblasts, the statistical analysis showed significant differences between the P(3HB)/0.5 wt% GO sample and the P(3HB)/2 wt% GO sample after 24 h of incubation. Significant differences (***$p \leq 0.001$) were also highlighted after the statistical analysis between P(3HB)/2 wt% GO samples and the neat polymer matrix P(3HB) after 72 h of incubation as shown in Figure 7.28 A. The addition of the different amounts of the GO resulted in cell viability similar to the neat P(3HB) for all three time points.

The statistical analysis of the composites of P(3HO-co-3HD) containing GO showed significant differences only between the neat polymer (P(3HO-co-3HD)) and the samples of P(3HO-co-3HD)/0.5 wt% and P(3HO-co-3HD)/5 wt% for the first 24 h of incubation as shown in Figure 7.28 B. The addition of the 0.5, 2 and 5 wt% GO to the polymer matrix resulted in 40 %, 20 % and 34 % higher cell viability compared with the corresponding neat matrix.

The statistical analysis of the 75/25 hybrid specimens showed significant differences after 24 h between the 75/25 sample containing 2 wt% GO and the 75/25 sample containing 5 wt% GO. After 72 h of incubation of the GO hybrids with the L929 murine fibroblasts, the statistical analysis showed significant changes between the 75/25 sample containing 2 wt% GO and the neat polymer matrix.

After 7 days the 0.5 wt% composite showed the higher viability 95 % followed by the 2 wt% which exibited a cell viability of 85 %, similar with the neat matrix. The 75/25 sample containing 5 wt% GO showed significant differences with the neat polymer matrix revealing the lower cell viability. Also, the 75/25 sample containing 0.5 wt% GO showed significant difference with both 75/25 samples containing 2

and 5 wt% GO, revealing 20 % and 23 % higher cell viability as shown in Figure 7.28 C.

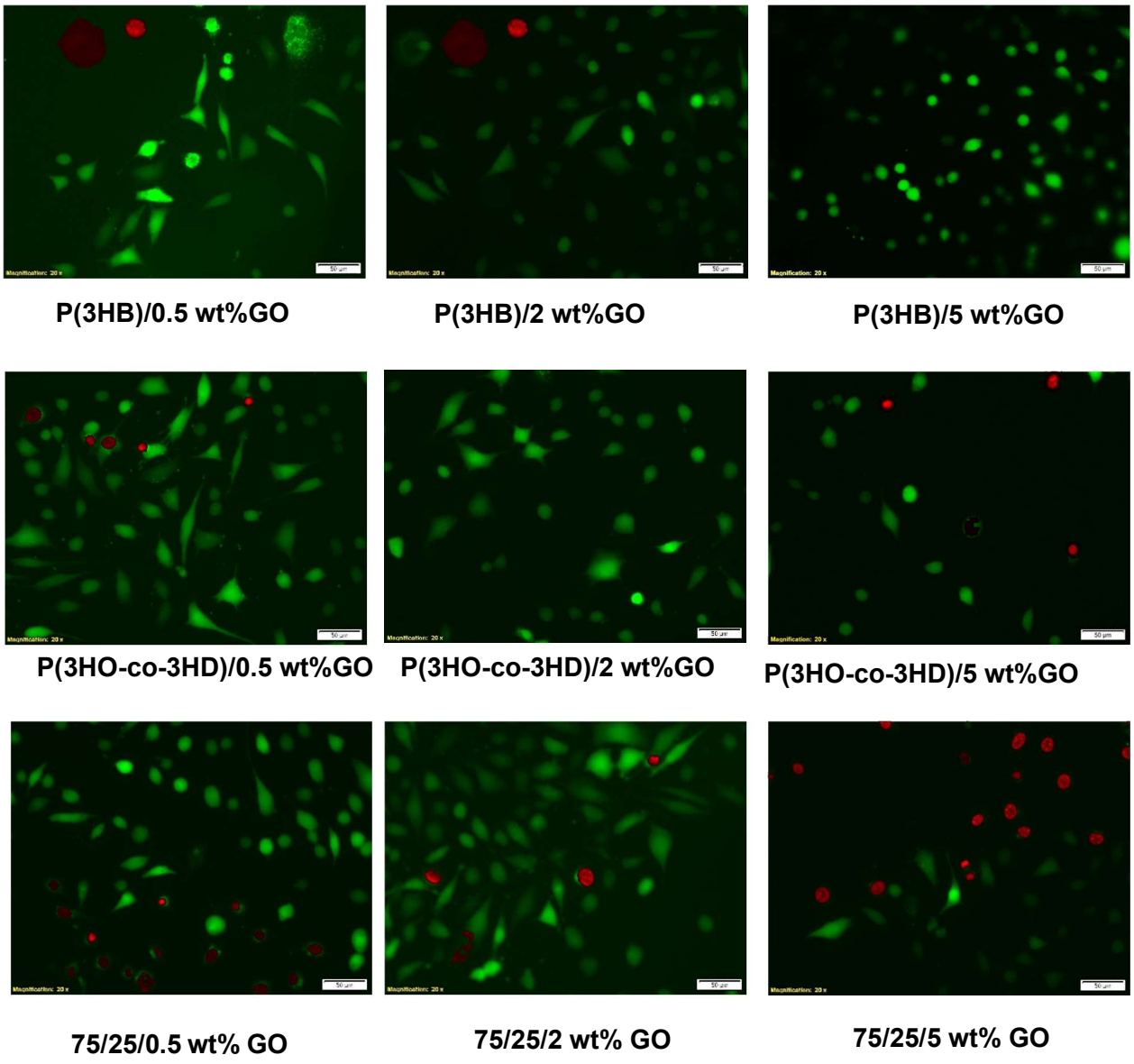

Figure 7.29: Fluorescence micrographs of L929 cells stained with Ethidium homodimer-III (red) and Calcein AM (green) after 3 days in culture on the respective samples (direct test).

When the developed hybrids were tested directly with the L929 murine fibroblasts, they didn't display any cytotoxic effects even after 7 days of incubation.

The cell viability remained higher than 80 % during the experiment, and even the higher loading of GO was not harmful for the viability of the cells, as shown in

Figure 7.28. These findings are in agreement with the findings from the fluorescence micrographs shown in Figure 7.29. Figure 7.29 demonstrates that when cells are in direct contact with the composite samples low or no toxicity is triggered with respect to L929 murine fibroblasts.

Utilising the CellTiterBlue assay, the cytocompatibility of the composites were investigated. As shown in Figure 7.30, no cytotoxicity was induced to the already proliferated neuronal cell when incubated with media which were in contact with the GO composites for 24 h. When the composites containing different quantities of GO were tested indirectly against the NG108-15 neuronal cell line, it was shown that for both P(3HB) and P(3HO-co-3HD) composites no significant differences were observed after the statistical analysis (Figure 7.30 A and B).

Only for the 75/25 composites containing GO, the statistical analysis showed significant differences ($*p \leq 0.05$) between the 75/25 sample containing 0.5 wt% GO and the 75/25 neat polymer with the 0.5 wt% composite revelling 16 % lower proliferation. Additionally, significant differences were observed between the 75/25 sample containing 0.5 wt% GO and the 75/25 sample containing 5 wt% GO as shown in Figure 7.30 C. In all cases; the cell viability remained higher than 87 %. To further investigate the behaviour of this particular cell line in the presence of GO, direct contact tests were performed, and the results are displayed in Figure 7.31. The direct assessment of the developed composites for 7 days was conducted with live/dead analysis of neuronal cells on the composites for three different time points day 1, 3 and 7.

The fluorescence micrographs were collected, and the surviving cells counted in order to compare them with the proliferated NG108-15 cells on the surface of the composite films using TCPS as controls. Figure 7.32 shows representative confocal images of the cells grown on the different substrates. The displayed micrographs are showing only the 75/25 composites since these were selected to be used for the preparation of tubes due to their physicochemical suitability compared with the rest of the composites. The analysis of the live/dead cell measurements were expressed in percentages of live cells grown on the substrates utilising TCPS as control.

After 24 h of direct incubation of the GO composites with the NG108-15 neuronal cells, the statistical analysis showed significant differences (***p≤0.001) between most of the composites compared to the TCPS control. A trend of increase in live cells number with the increase in the amount of GO added into the polymer matrices was observed, as shown in Figure 7.33.

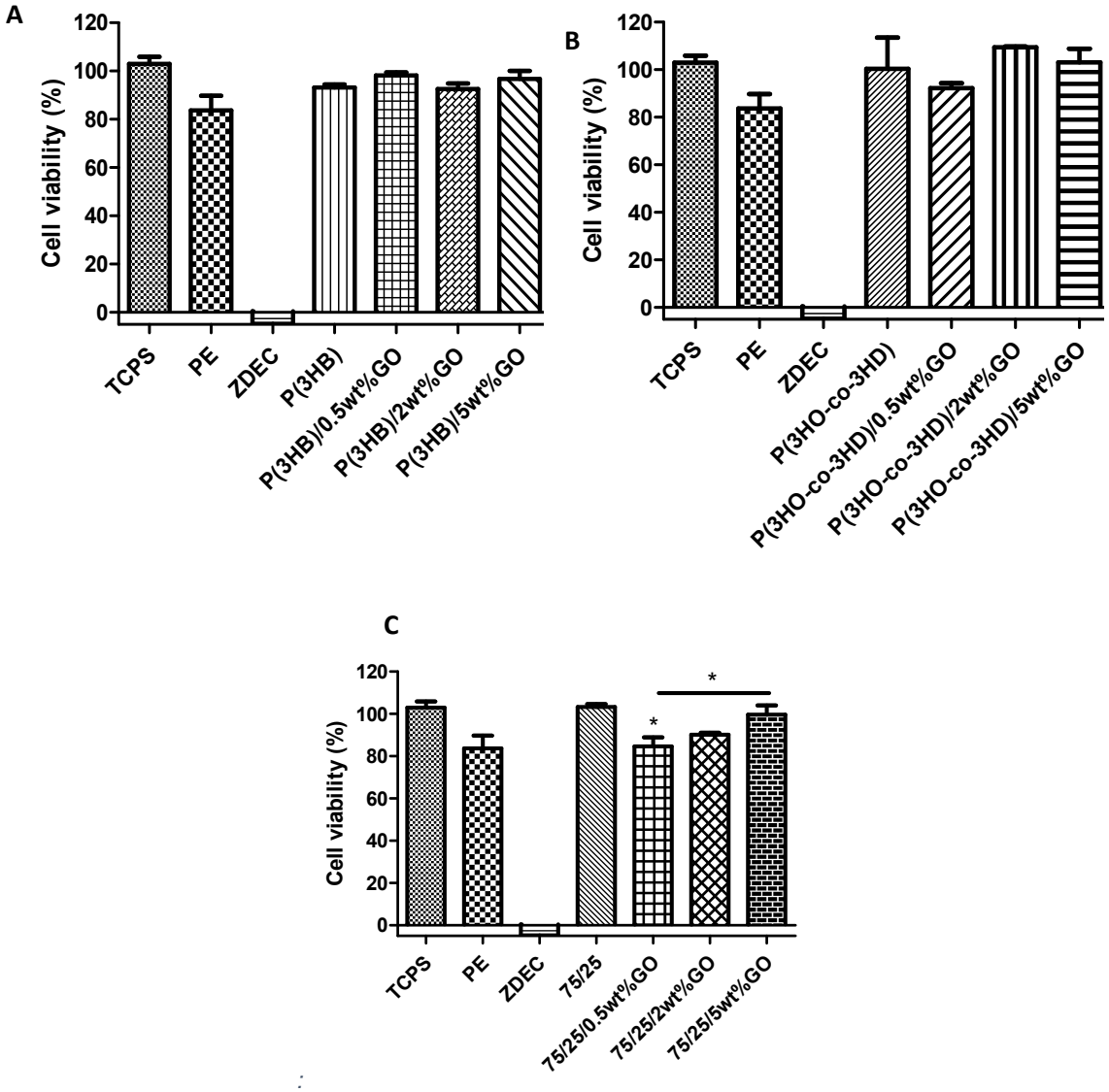

Figure 7.30: Indirect cytocompatibility evaluation of the (A) P(3HB), (B) P(3HO-co-3HD) and (C) 75/25 P(3HO-co-3HD)/ P(3HB) composites containing different loadings of graphene oxide with respect to NG108-15 neuronal cell line (Mean± SEM, n = 9 independent experiments). Statistical significance determination is represented as *p ≤ 0.05, **p ≤ 0.01, and ***p ≤ 0.001 for cells on TCPS vs. all materials, and non-modified polymer blend vs. GO composites

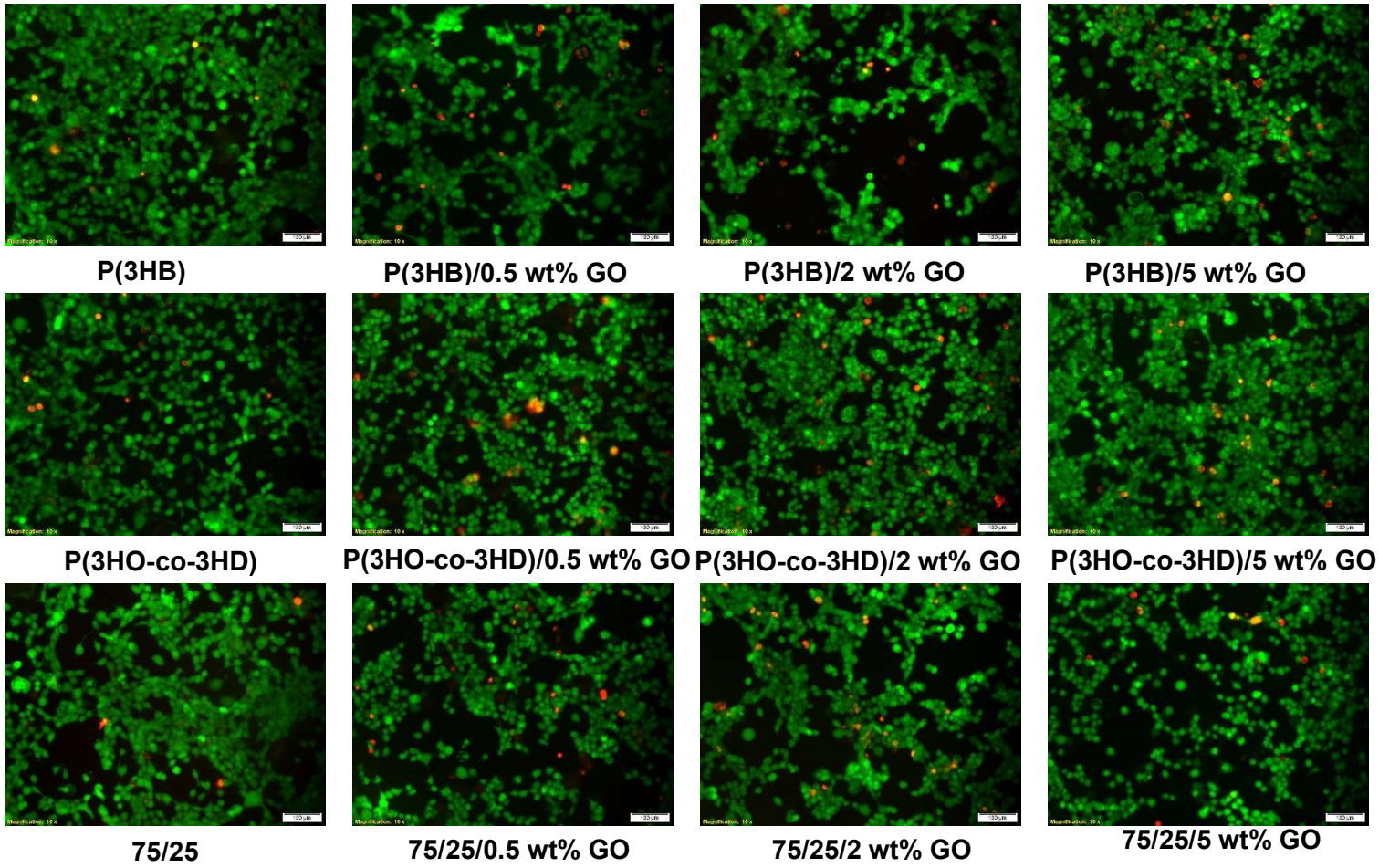

Figure 7.31: Fluorescence micrographs of NG108-15 neuronal cells stained with Ethidium homodimer-III (red) and Calcein AM (green) after 24 h in culture with the aliquots on the respective samples (indirect test).

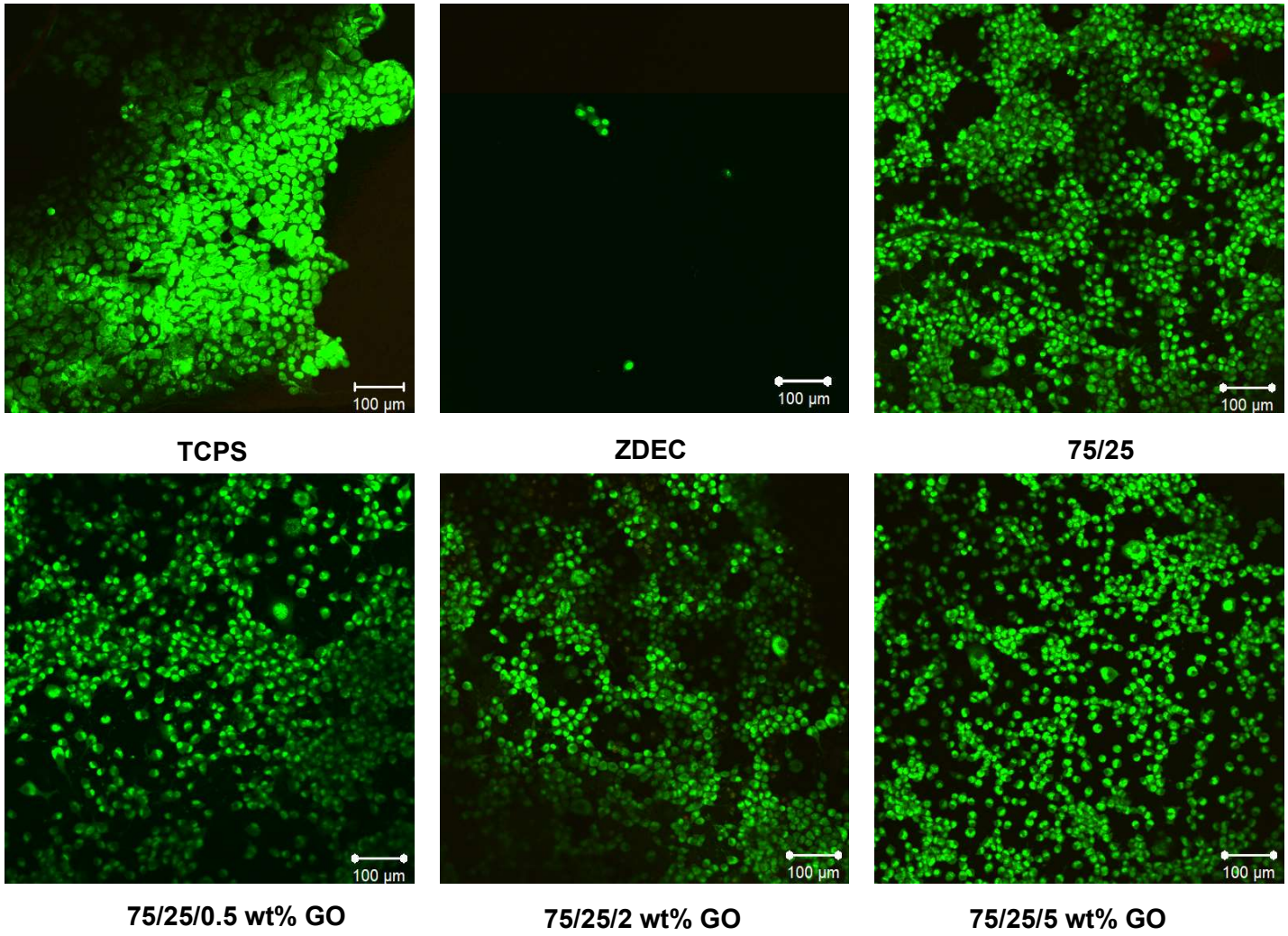

Figure 7.32: Fluorescence micrographs of NG108-15 neuronal cells stained with Ethidium homodimer-III (red) and Calcein AM (green) after 7 days in culture on the respective samples (direct test).

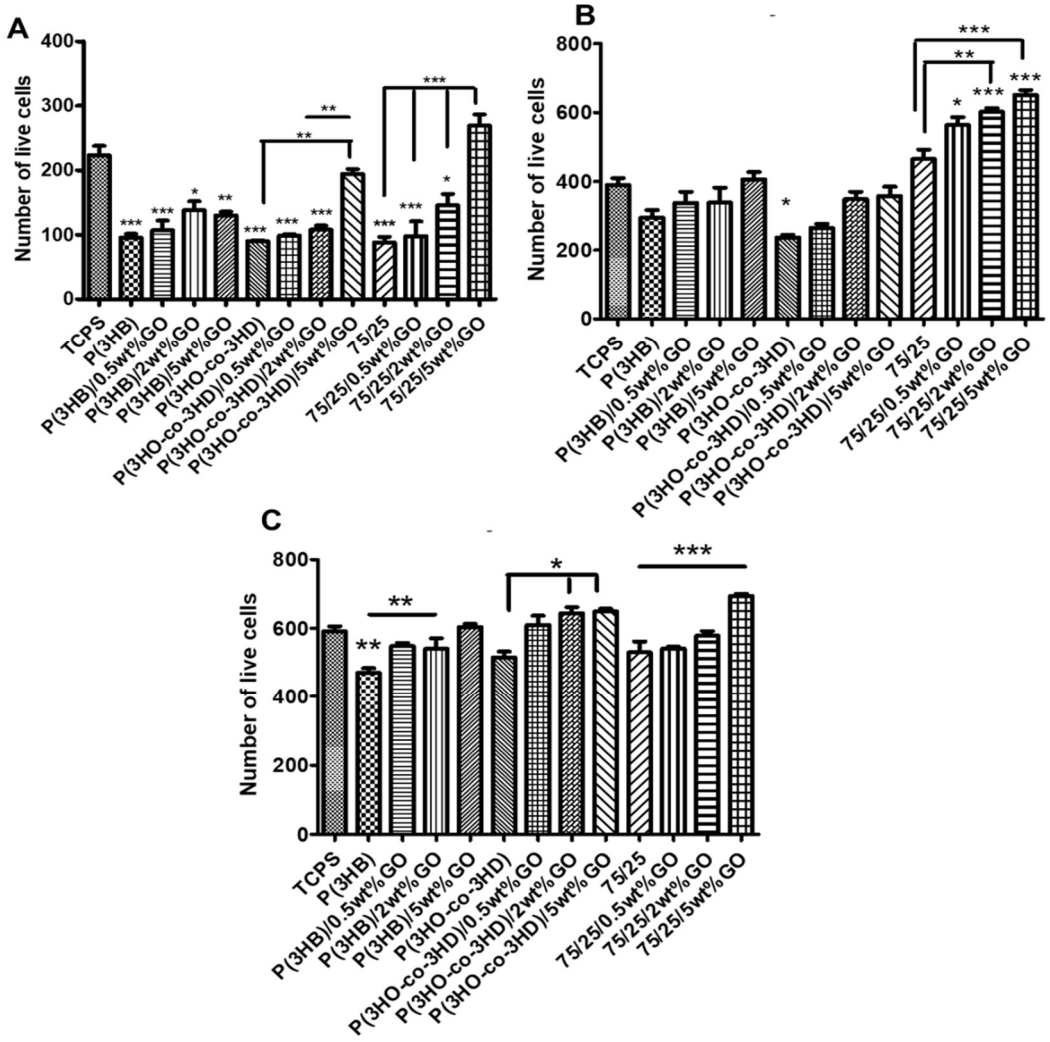

Figure 7.33: Number of live cells from live/dead analysis of neuronal cells on P(3HB), P(3HO-co-3HD) and 75/25 P(3HO-co-3HD)/ P(3HB) composites containing different loadings of graphene oxide for time periods of (A) 1 day (B) 3 days and (C) 7 days using TCPS as control (Mean± SEM, n = 9 independent experiments). Statistical significance determination is represented as *p ≤ 0.05, **p ≤ 0.01, and ***p ≤ 0.001 for cells on TCPS vs. all materials, and non-modified polymer blend vs. GO composites (direct test).

After the first 24 h, the P(3HB) composites reached a higher number of adhered neuronal cells of 138.3±23.6 for the composite containing 5 wt% GO while the P(3HO-co3HD)/5 wt% GO composites had a cell density of 194.3±49.9 neuronal cells per view.

Finally, the 75/25 blend containing 5 wt% GO had superior cytocompatibility, compared with the 5 wt% composites from P(3HB) and P(3HO-co-3HD) respectively as well as the positive control (TCPS), revealing significantly higher number of neuronal cells 269.2±39.2. Of the 75/25 composites, the statistical analysis showed significant differences (***p≤0.001) between the 75/25 blend containing 5 wt% GO and all the other blend composites as well as the respective neat matrix.

After 72 h (3 days) direct contact of the neuronal cells with the composites it was evident that the 75/25 hybrids had the best cytocompatibility compared with the respective P(3HB) and P(3HO-co-3HD) exhibiting cell densities which were equal but higher than the positive control (TCPS). The positive control had an average around 390±28.3 cells per view while the non-modified 75/25 blend had on average 464.8±61.6 viable cells and the blend composites containing 0.5, 2 and 5 wt% GO, 564.3±38.9, 602.4±23.3 and 651.6±31.9 respectively.

The statistical analysis highlighted significant differences (***p≤0.001) between the 75/25/5 wt% GO and the rest of the composite blends as well as the non-modified blends. Finally, after 168 h (7 days) of direct incubation of the samples with the NG108-15 neuronal cells, the average number of cells adhered to the positive control (TCPS) was 591±25.5 while the average number of cells on the 75/25 blend was 529.5±64.0. The number of the proliferated neuronal cells on the 75/25 composites were 541±63.1, 578±30.3, and 694.7±23.6 for the 0.5, 2 and 5 wt% samples respectively.

No statistically significant differences (p>0.05) were found between the 75/25 blend and its 0.5 and 2 wt% composites whereas the comparison with the 75/25 composite with 5 wt% GO sample revealed significant differences (***p≤0.001) with the neat 75/25 blend and the other two blend composites.

7.2.12 Neurite outgrowth assessment on NG108-15 cells cultured on 75/25 blend and composite surfaces

The 75/25 blend and its composites were further evaluated for their ability to support the neurite outgrowth of NG108-15 neuronal analogue cells. The NG108-15 cells were grown on the film surfaces and immunolabelled with the anti-β III-tubulin antibody to assess neurite outgrowth and thus indirectly their differentiation. Figure 7.34 shows the fluorescent images of immunolabelled NG108-15 cells cultured on all the substrates. It was observed that the addition of the GO improved the expression of the neurites.

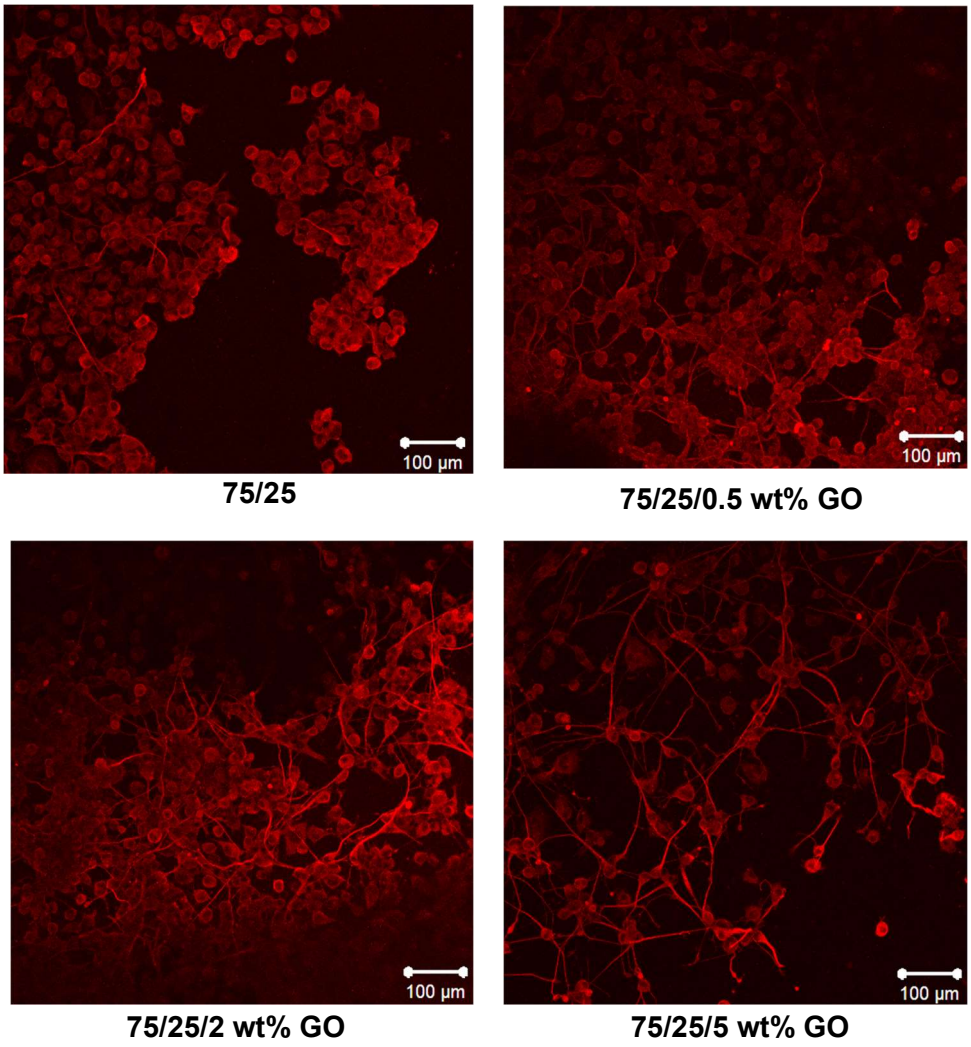

Figure 7.34: Micrographs of NG108-15 neuronal analogue cells immune-cytochemically- labelled for beta-III tubulin after 7 days culture on PHA blend composites.

The percentage of the NG108-15 cells of the composites expressing neurites did not show any statistical difference (p≥0.05). More specifically, the composite containing the lower amount of GO (0.5 wt%) resulted in 5.4 % higher number of cells expressing neurites where the 2 wt% showed 9.3 % more than the neat 75/25 blend. Finally, the blend containing 5 wt% of GO resulted in 9.7 % more cells expressing neurites compared with the control polymer matrix, as shown in Figure 7.35.

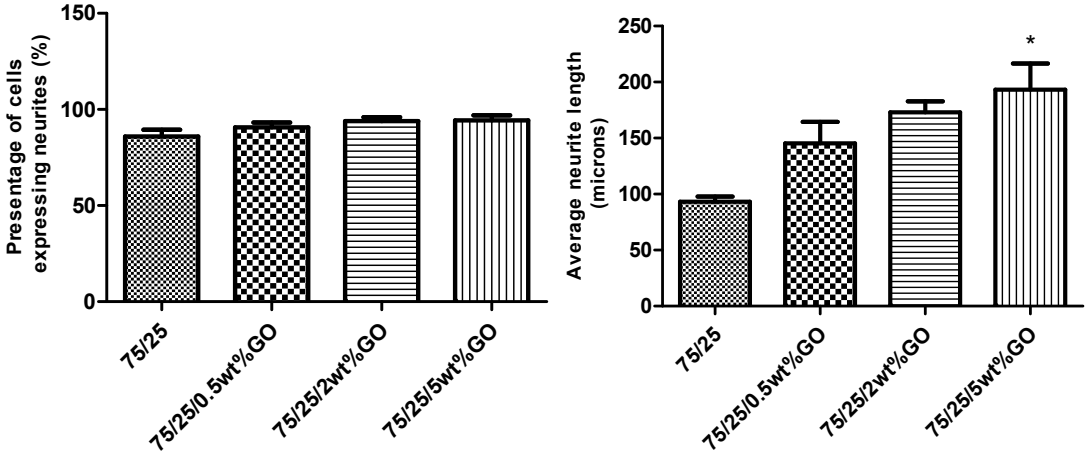

Figure 7.35: Percentage of NG108-15 neuronal cells expressing neurites (left) and average length o neurites(right) (mean ± SEM, n = 9 independent experiments). Statistical significance determination is represented as *p ≤ 0.05, **p ≤ 0.01, and ***p ≤ 0.001 for cells on TCPS vs. all materials, and non-modified polymer blend vs. GO composites.

The average length of these neurites were determined using Image J, and it was established that the longer neurites were expressed for the composite containing the higher content of GO (5 wt%). The statistical analysis showed a significant difference (p≤0.05) from the control blend.

The addition of 0.5 wt% and 2 wt% of GO into the binary system resulted in 56 % and 86 % longer neurites respectively compared with the control blend (Figure 7.35). This difference tends to suggest that the addition of GO has beneficial bioactivity, which promotes and enhances cell proliferation and differentiation.

7.3 Discussion

In the search for suitable materials for biomedical applications, a lot of attention has been focused on biopolymers combined with inorganic molecules in order to enhance the biological features and physicochemical properties. Surface modification, tuneable thermal and mechanical properties, as well as enhanced cell proliferation and viability, are some of the most important requirements for successful regeneration in tissue engineering.

More recently, graphene and GBMs have generated a lot of interest as inorganic molecules which can be used as a suspension or loaded in polymeric matrices to provide beneficial biological responses to the cells of interest. Additionally, these materials have been reported to be antibacterial and confer electroconductive properties to the final composites. With this in mind, this study set out to investigate the physicochemical and biological properties of PHA based composites including GO as the filler. The two polyhydroxyalkanoates P(3HB) and P(3HO-co-3HD) and one of their possible blends 75/25 P(3HO-co-3HD)/ P(3HB) were loaded with three different ratios of GO (0.5, 2 and 5 wt%) and fabricated into films by the solvent-casting method. The fabricated film composites were analysed to determine their properties, and the results are presented below.

From the FTIR spectra obtained, the GO composites showed multiple signs of oxygen-derived species and functional groups which are present in the host polymeric matrices of P(3HB), P(3HO-co-3HD) and 75/25 P(3HO-co-3HD)/P(3HB) blend. Most of apparent bands in unmodified PHA matrices also occured in the modified GO composites. The incorporation of the GO filler into the polymer hosts did not change the FTIR spectra, indicating that the addition of the filler did not exert a significant influence on the molecular structure of the polymer matrices. Considering that similar functional groups are present in all the polymer matrices and the GO and the fact that the polymer amount is larger than the filler the generated signal from the GO is not strong enough to form a distinguishable fingerprint.

The DSC analysis provided information on both the effect of the GO on the thermal properties of the developed composites and their crystallinity. The addition of the filler into the polymer matrix of P(3HB) led to an overall increase

in the T_g while there was no significant change observed for the T_m. The lower amount of GO (0.5 wt%) reduced the crystallinity compared with the neat P(3HB) indicating a lower crystallinity for the polymer matrix in the composite. In this case, the addition of the filler acted as a plasticiser and induced lower crystallization of the fabricated sample, hence reducing its crystallinity.

The addition of 2 and 5 wt% GO into the P(3HB) enhanced the crystallinity of the composites; indicating that the GO particles acted as nucleation sites. The lower crystallinity observed for the 5 wt% composite, when compared with the 2 wt% sample, is attributed to the barrier effect of the GO particles obstructing the nucleation and growth of the crystals.

The insignificant change in the baselines surrounding the T_g area, for the P(3HO-co-3HD) specimens, indicates that the change of the heat capacity of these composites is much lower than the blends. This phenomenon might be attributed to the decrease of free volume in the amorphous phase due to the presence of GO sheets. This suggests an affinity between the filler and the P(3HO-co-3HD) matrix in the amorphous state. The addition of the GO filler in the P(3HO-co-3HD) increased the T_g and the T_m compared with the neat polymer. Only the 2 and 5 wt% amounts of GO increased the crystallinity of the composites compared with the neat matrix, achieving the highest crystallinity with the 5 wt% loading indicating that the addition of GO increases the number of nucleation centres within the polymer. The crystallinity was improved most for the 5 wt% composite indicating that GO was localised at the interphase improving its dispersion.

Finally, the binary system of 75/25 P(3HO-co-3HD)/P(3HB) blend showed a reduction of the T_g with the addition of the GO while no significant changes were observed in the T_m. The highest crystallinity of this polymer composite was recorded for the addition of 2 wt% GO. These findings indicate that there is a different intercalation of the GO depending on the choice of polymer and the amount of the filler.

The addition of GO to the P(3HB) polymer matrix enhanced the Young's modulus, resulting in stiffer materials. This indicates a good matrix-filler interphase due to the high degree of hydrogen bonding between the ester groups of the P(3HB) chains with the hydroxyl and carboxyl moieties of the GO surface. These findings

are in agreement with other studies (Abdala, Barrett and Srienc, 2013; Layek and Nandi, 2013; Ervina, Mariatti and Hamdan, 2016; Mahendran *et al.*, 2016; Smith *et al.*, 2019). All P(3HB) composites exhibited greater Young's moduli values compared with the neat polymer, indicating that the addition of GO acted as a reinforcing filler promoting more entanglements between the filler and the polymer matrix of the composite enabling load transfer to the interphase.

The composite containing the higher loading of GO, 5 wt%, showed lower tensile strength and Young's modulus values compared with the 2 wt% composite, most likely due to restacking of GO which diminished the reinforcement capability of the filler. The agglomeration of the filler limits the load transfer from the matrix to GO particles causing cracks that are easy to propagate. These cracks are reported to be responsible for the reduction of the strength of the developed composites (Ervina *et al.*, 2016).

The P(3HO-co-3HD) composites revealed lower elongation at break when compared with the neat matrix, indicating the development of less ductile composites. The developed composites seemed to maintain a homogeneous dispersion of the filler in the polymer matrix allowing the GO to act as a reinforced material and hence, improve the mechanical values.

The lower amount of GO (0.5 wt%) in the blend resulted in a decrease of all mechanical values compared with the neat blend. The long aliphatic chains present in the polymer matrix can shield the oxygen atoms along the polyester backbone and thus reduce the interaction between the polymer and the GO surface. This phenomenon can also lead to GO restacking, which diminishes the mechanical properties and the ability of GO to reinforce the composite. Further increase of filler from 0.5 to 2 wt% led to diminished tensile strength and Young's moduli values, compared with the neat blend and the other composites indicating particle aggregation and poor dispersion of the filler. The addition of 5 wt% of GO led to a decrease in the elongation at break and an increase in Young's modulus, indicating the development of a stiffer and less ductile composite.

For the P(3HO-co-3HD) and 75/25 P(3HO-co-3HD)/P(3HB), the highest Young's modulus was obtained for the composites containing the highest amount of GO (5 wt%). This indicates a good dispersion of the filler into the polymer matrix,

hence resulting in good polymer-matrix interphase capable of transferring the load from the surface to the matrix-filler interface (due to the high degree of hydrogen bonding between the GO and PHA).
These findings are in agreement with the literature. Barrett *et al.*, also mentioned that the addition of GO particles promoted additional entanglements between the polymer chain and the particles enhancing the stiffness of the polymer matrix compared to the neat PHO and PHD (Barrett, Abdala and Srienc, 2014; Mahendran *et al.*, 2016; Smith *et al.*, 2019).

The Neat P(3HB) and 75/25 P(3HO-co-3HD)/P(3HB) showed similar hydrophobicity while the neat P(3HO-co-3HD) had a higher hydrophobicity compared to the other polymer matrices, due to the presence of long hydrophobic chains. For the P(3HB) composites, the addition of a hydrophilic filler (GO) reduced the hydrophobicity of the composites by increasing GO content, indicating strong molecular interaction between the GO and the P(3HB) polymer matrix.
These findings are in agreement with the results of thermal and mechanical tests, where higher crystallinity and Young's moduli values are achieved by incorporation of GO due to good polymer matrix and the GO interphase. The P(3HO-co-3HD) composites showed an inverse relationship between hydrophobicity values and the content of the filler (GO), with an increase in filler leading to lower hydrophobic behaviour, due to the homogeneity and good dispersion of the filler in the polymeric host.

The mechanical and thermal values support these findings as the addition of the GO filler resulted in an increase in crystallinity and Young's modulus for the 2 and 5 wt% composites, indicating the creation of additional entanglements between the polymer chain and the GO filler due to good dispersion and strong interfacial interaction.

The glass side of the 75/25 /GO composites of 0.5 and 2 wt%, were found to be much less hydrophobic than the air side, due to the setting of GO towards the glass bottom. This finding is in agreement with the reduced crystallinity and mechanical properties of these composites due to their weak attractive forces between the blend polymer matrix and the GO filler. The blend composite containing 5 wt% of GO had the lowest hydrophobicity due to the additional

entanglements between the polymer matrix and the filler, improving the dispersion of the GO in the interphase.

SEM micrographs reveals the effect of GO on the surface topography. The addition of different amounts of GO filler resulted in different effects on the polymer matrix of neat P(3HB), P(3HO-co-3HD) and 75/25 P(3HO-co-3HD)/P(3HB) films. The least affected topography compared with the corresponding neat films was observed for the P(3HO-co-3HD) composites.
The P(3HB) composites exhibited various sized pin-holes and GO particles on the composites' surfaces, which were visible even with the lowest GO (0.5 wt%) loading. These results are supported by the Raman and XPS finding as described below. The addition of the inorganic compound had a greater effect on the 75/25 P(3HO-co-3HD)/P(3HB) blend composites, where flakings and irregularly shapes were observed. These visible inequalities were attributed to the differential intercalation of the GO in the binary matrix, causing an extensive agglomeration of the GO sheets, compared to the other polymer composites.

The absence of the characteristic XRD peak of GO at $2\theta=12^{o}$, in all the P(3HB) and P(3HO-co-3HD) composites, indicates that the GO formed a good network with the PHA matrices. Additionally, variations in the XRD characteristic peaks of the polymer indicated that the filler affected the crystallinity of the final composites. For the P(3HB)/GO composites, the characteristic peaks corresponding to the polymer matrix deceased in intensity compared with the pure P(3HB) indicating a more disordered structure. Higher loading of the filler (5 wt%) resulted in a higher peak intensity compared to the other composites implying stacking of the graphene oxide layers within P(3HB) matrix. Whereas the low-intensity peaks of 0.5 and 2 wt% composites show a more amorphous structure and additional defects of the composites (Larsson *et al.*, 2017a).

When GO was incorporated into the 75/25 blend it resulted in a reduction of the peaks attributed to the polymer matrices. In addition, the composites revealed broader peaks relatively lower to the characteristic GO peak at $2\theta=12^{o}$ indicating successful intergration of the filler into the blend and the fabrication of a more amorphous and disordered composite. Of all the composites, the lower concentrations of 0.5 and 2 wt% did not show the characteristic hump of GO located at around $2\theta=12^{o}$, but by increasing the loading of GO to 5 wt%, the

characteristic peak intensity (001) became prominent and also shifted to lower 2θ values (10-12.2).

These findings are in agreement with other studies, when high molecular weight polyurethanes, and ethylene methyl acrylate hybrid nanocomposites were developed with the addition of GO (Bhawal *et al.*, 2016; Strankowski *et al.*, 2016; Larsson *et al.*, 2017).

Raman spectroscopy was used to investigate the presence of GO in the polymer, revealing the characteristic peaks of D and G. The G and D bands of GO were observed in all P(3HB) composites, even for the lowest content of filler (0.5 wt%), indicating that the short aliphatic chains did not disrupt the hydrogen bonds and other non-covalent interactions of the polymer with the oxygen molecules of GO (Bhawal *et al.*, 2016; Keyte, Pancholi and Njuguna, 2019). In addition, the close values for the ratio I_D/I_G of the composites compared with the value of GO indicated the well-preserved structure of GO.

Only by the addition of 2 and 5 wt% of GO into the P(3HO-co-3HD) the characteristic peaks of GO were detected. Both D and G peaks showed a broader shape compared with pristine GO, indicating the incorporation of GO into the polymer host forming a much higher disordered and defected structure than pure GO (Strankowski *et al.,* 2016). For the 2 wt% composite, the upshift of the G band at 1603 cm^{-1} is attributed to the GO dispersion in the polymer matrix, reducing the GO-GO interactions. The intensity ratio (I_D/I_G) of the 2 wt% composite was higher compared to the pristine GO, indicating a higher degree of defects in the composite material.

The addition of 2 and 5 wt% revealed a broadening and downshift of the G peak, indicating the incorporation of the GO into the polymer matrix. In addition, the higher intensity ratio (I_D/I_G) for these composites, compared with the GO leads to an increase in structure disorder due to the good dispersion of the filler in the polymer hosts.

In most of the composites, any interaction of the polymer host with the GO filler had a small effect on the frequency of the GO's G band. In the P(3HO-co-3HD) and the blend composites containing GO, the long aliphatic chains also competed for bonding with GO making them observable from 2 wt% and above. Broader G

and D band peaks in the composites compared to the pristine GO indicated good dispersion in the polymer host. The broader the peaks, the better the dispersion.

The deconvolution of the C1s and O1s peaks obtained from the XPS spectra allowed the calculation of the percentage of the average relative atomic concentration for the neat polymers and their composites containing the highest amount of the filler (5 wt% GO). The analysis showed that only in the case of the P(3HB)/5 wt% composite the carbonyl (C=O) and carboxyls (O-C=OH) numbers increase indicating that the increased numbers of these functional groups was due to the presence of GO. The rest of the P(3HO-co-3HD) and the 75/25 composites did not show any enrichment of functional groups assigned to GO. The different entanglements of the P(3HB) and the rest of the polymeric matrices are responsible for intergrating the different amounts of GO.

The investigation of the antibacterial properties of the developed composites containing different amounts of the inorganic filler (GO) was conducted using the direct contact test (DCT) – ISO 22196 (established for measuring antibacterial activity on plastics). The addition of the filler into the different polymer matrices (P(3HB), P(3HO-co-3HD) and 75/25 blend) resulted in different antibacterial efficacy.

When tested against the Gram-positive *S. aureus* (ATCC® 29213™), composites of P(3HB) and P(3HO-co-3HD) showed greater antibacterial activity against both free and planktonic bacteria for the composites which contained the highest amount of GO (5 wt%). While the 75/25 blend showed better antibacterial performance when the composite contained 2 wt% of GO. The different entanglements of the polymer chains and the changes in the final composite materials upon the addition of the GO, led to different antibacterial activities.

When the same composites were tested against Gram-negative *E. coli* (ATCC® 25922™) the antibacterial efficacy of the P(3HB) and 75/25 blends was more significant for the 2 wt% composites, while the P(3HO-co-3HD) showed better antibacterial activity for the composite containing 5 wt% GO. A comparison of the antibacterial activity of the composites against both Gram-positive and negative bacterial strains, indicated that overall, the composite results were better against Gram-positive bacteria. These findings are in agreement with the literature, since having previously been reported that GO suspensions are toxic

to bacteria and have good antibacterial activity, with stronger effect against Gram-positive
S. aureus than Gram-negative *E. coli* bacteria (Akhavan and Ghaderi, 2010; Perreault *et al.*, 2015). Akhavan *et al*. investigated the antibacterial effect of graphene nanosheets against both *Escherichia coli* and *Staphylococcus aureus* bacteria and reported that *E. coli* was more resistant to GO than *S. aureus* (Akhavan and Ghaderi, 2010).
Moreover, Gao and co-workers observed that for the same exposure time, 40 mg/L of GO displayed higher antibacterial activity against *S. aureus* than *E. coli*. For *S. aureus;* 12 h was sufficient to completely kill the bacteria, whereas, for *E. coli,* took 168 h. This phenomenon is attributed to the different size of *S. aureus* and *E. coli* strains. Since *E. coli* is bigger than *S. aureus,* the damage caused by GO will affect *S. aureus* strains relatively more easily than *E. coli*. This difference in damage, was evaluated by measuring the concentration of RNA from the supernatant of the bacterial strain samples and the concentration of RNA released from the *S. aureus* samples was greater than that of *E. coli* samples (Gao *et al.*, 2017). The size and shape of *E. coli* and *S. aureus* are: rhabdoid in shape (about 1230 – 3538 nm) and spherical in shape (840 nm), hence GO can wrap around the surface of *S. aureus* more easily than *E. coli,* leading to higher toxicity towards the *S. aureus* strain.

Another reason was the presence of the outer membrane in the Gram-negative *Escherichia coli* that could act as protection against GO damage while Gram-positive *Staphylococcus aureus* lacks outer membrane, thereby increasing the chances of cell death (Akhavan and Ghaderi, 2010). Additionally, different sizes and distribution patterns of the GO particles could potentially influence the intercalation of the inorganic compound within the respective polymer matrices and thus the topography of the specimens, resulting in higher or lower antibacterial activity.

Both indirect and direct tests were conducted utilising the well-studied L929 murine fibroblasts and the NG108-15 neuronal cell lines. For both experiments, no evidence of induced cytotoxicity originating from the composites was observed. The CellTiterBlue assay, as well as fluorescence micrographs,

revealed good cytocompatibility for the developed composites, according to ISO 10993-5.

The cell viability and proliferation increased throughout the incubation period. Similarly, in other studies, chitosan composites containing different GO loads were tested, both indirect and direct evaluation, using VERO from the African green monkey cell line and murine preosteoblasts MC3T3-E1, respectively. The results revealed that the extracts of the composites exhibited no cytotoxic effects, whereas the addition of GO into the composites enhanced the bioactivity of the scaffold material. This behaviour appeared to be proportional to the GO concentration (Dinescu *et al.*, 2014). Moreover, the incubation of GO/sodium alginate composites for 5 days with MC3T3-E1 mouse preosteoblasts, enhanced the metabolic activity and viability by promoting cell adhesion and proliferation (Huang *et al.*, 2018).

The live/dead analysis for the direct assessment of the samples for 7 days with NG108-15 neuronal cells showed that there is a proportional correlation between the amount of GO and the cell viability. The higher the ratio of the inorganic compound, the higher the neuronal cells viability. As shown in Figures 7.32 and 7.33**,** the 75/25 blend of composites, showed higher cell densities than the corresponding P(3HB) and P(3HO-co-3HD) composites, indicating that the different intercalation of the inorganic filler into the respective matrices and hence the different morphology plays a crucial role in the proliferation of the neuronal cells. In addition, the neurite outgrowth assessment showed that the addition of GO within the blend matrices enhanced the proliferation and the neurite expression as well as their length proportional to the amount of the GO.

In conclusion, P(3HB), P(3HO-co-3HD) and 75/25 blend composites containing different amounts of GO were successfully produced and characterised. The presence, as well as the amount and the intercalation of GO into the polymeric hosts, effected the physicochemical properties of the final composites differently. The obtained results confirmed the antibacterial activity of the composites against both Gram-positive and negative bacterial strains. The indirect and direct contact tests of the GO containing samples were not found to be harmful to the L929 and NG108-15 cells, maintaining high cell viability even for the specimens with the highest concentration of GO.

GO composites have been shown to be selective towards bacteria as they do not induce indirect and/or direct cytotoxicity to either L929 fibroblasts and NG108-15 neuronal cells.

Chapter 8

Development of P(3HO-co-3HD)/P(3HB) blend tubes and composites

8 Development of hollow P(3HO-co-3HD)/P(3HB) blend tubes and composites and incorporation of electro-spun PHA fibres

8.1 Introduction

The ideal material for fabricating a nerve conduit must have several properties. In order to achieve successful nerve regeneration, the nerve conduit should provide guidance of axonal regrowth, biocompatibility, porosity for nutrient/metabolite exchange, biodegradability to avoid a second operation, no/minimized swelling (avoiding internal compression), regeneration-adapted degradation rate, and at least suitable mechanical stability (avoiding external compression) and tube flexibility (preventing tension on regenerating axons) (Kehoe, X.F. Zhang and Boyd, 2012; Nectow, Marra and Kaplan, 2012; Muheremu and Ao, 2015; Chrz, Derbisz and Suszy, 2018; Rebowe *et al.*, 2018). The current available FDA approved nerve conduits are made from collagen, polyglycolic acid (PGA), polycaprolactone (PCL) and polyvinyl alcohol (PVA). They only possess some of the aforementioned properties, while some of these market products have been discontinued due to inflammatory responses (Kehoe, X.F. Zhang and Boyd, 2012; Arslantunali *et al.*, 2014; Duncan *et al.*, 2015; Alberti *et al.*, 2016; Gaudin *et al.*, 2016a; Means *et al.*, 2016; Chrz, Derbisz and Suszy, 2018; Kornfeld, Vogt and Radtke, 2018).

It has been reported since 1985 that a large number of patients undergoing neurosurgery (CNS) were prone to infections caused by surgery and therefore antibiotic prophylaxis was suggested as a solution (Blomstedt, 1985). One of the studies revealed, currently available NGCs are insufficient as removal of a collagen implant was required, possibly due to super-infection, poor tissue coverage, or persistent neuroma pain (Means *et al.*, 2009).

In addition, it has been reported that post-operative infections after neurosurgical procedures have a high potential to lead to life-threatening condition and eventually to morbidity. Surgical site infections also have a major impact on the economy and the environment, as prolonged hospitalization and prescription of antibiotics are required (Abu Hamdeh, Lytsy and Ronne-Engström, 2014).

A study (Means *et al.*, 2016) comparing the use of allografts and hollow tubes for distal nerve repair of the hand had shown that the hollow NGCs used, caused a series of problems such as: osteomyelitis and fungal infection. The infections required hospitalization and amputation of the affected area was considered necessary. Since then, treating bacterial resistance to antibiotics has been a key factor in any implantation procedure.

As an alternative to the already developed NGCs, polyhydroxyalkanoates have been exploited for their use in tissue engineering (Williams *et al.*, 1999) and more specifically in nerve regeneration. Both short and medium chain-length PHAs have been investigated for their use in nerve regeneration (HAZARI, 1999; Young, Wiberg and Terenghi, 2000, 2002; Novikov *et al.*, 2002; Kalbermatten *et al.*, 2008). PHAs have properties that make them superior to available NGCs, such as long-lasting stability, low degradation acidity and adequate mechanical support. Here the aim was to develop NGCs based on PHA biopolymers that will provide the appropriate support and time for successful nerve regeneration. Moreover, the addition of inorganic compounds (GO and PGFs, as single additives) will confer antibacterial activity to the site of interest after the implantation of the conduit.

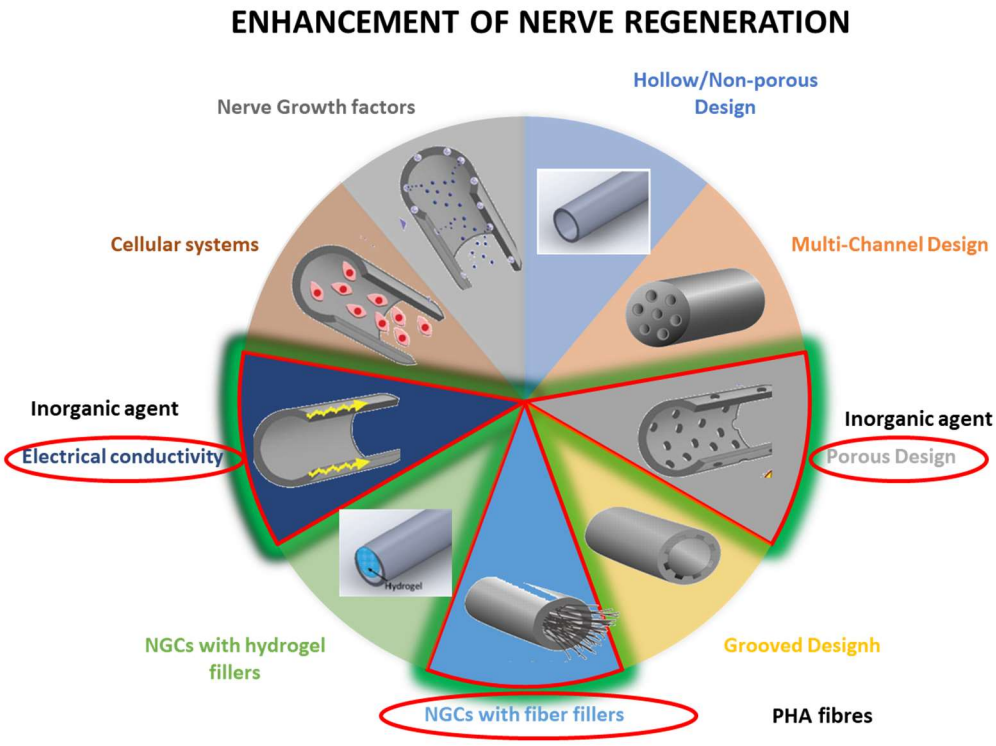

Figure 8.1: A range of designs for effective NGCs.

With regard to different parameters (e.g. porous channel wall, etc.) and strategies, that have been used to reinforce existing hollow nerve guidance conduits; this study combines some of these parameters with two different strategies for NGC development (de Ruiter *et al.*, 2009; Farrukh, Zhao and del Campo, 2018; Sarker *et al.*, 2018). The fabrication techniques and the use of specific inorganic compounds can be used to confer porosity, electroconductivity and intraluminal guidance structures to support cell migration and axonal growth to the final design (Figure 8.1).

This chapter provides information about the analysed properties of new biomaterials after they have been processed into tubes. The properties of the unprocessed 75/25 P(3HO-co-3HD)/P(3HB) polymer blend and its composites with either different wt% of nanoparticulated GO or different wt% of Ce-PGFs have already been described in the previous chapter. Additionally, the PHA blend was used to form electrospun fibres as filler material for the novel tubes.

Tubes made of neat 75/25 P(3HO-co-3HD)/P(3HB) were developed by optimizing the parameters of a dip coating process, already described in section 2.10. The composite tubes with different amounts of GO were prepared by applying these optimized conditions for the formation of tubes based on 75/25 P(3HO-co-3HD)/P(3HB) blend. These tube prototypes were used to design implants with enhanced intraluminal alignment and directional growth of neuronal cells by incorporation of electrospun fibres of 25/75 P(3HO-co-3HD)/P(3HB) blend. The other 75/25 P(3HO-co-3HD)/P(3HB)-based NGCs were produced by film casting, adding aligned Ce-PGFs (37, 74 and 90 wt%) to the binary blend matrix. This composite mat was then folded to form tubes that were fixed by gluing the ends together with P(3HO-co-3HD) polymer. All different types of NGCs based on innovative composite biomaterials were analysed comprehensively.

8.2 Results

8.2.1 Tube formation by dip moulding technique using a 75/25 P(3HO-co-3HD)/P(3HB) polymer blend mixture

A 75/25 P(3HO-co-3HD)/P(3HB) blend mixture was used for the fabrication of tubular structures applying the dip moulding technique as described in section 2.10.1. Briefly, the 75/25 P(3HO-co-3HD)/P(3HB) blend was dissolved in a mixture of chloroform and 1,1,2,2-tetrachloroethane at room temperature. The preparation of the GO-functionalized tubes was carried out by dispersing GO in the same solvent system at a specific concentration and sonication time. The stainless-steel needles were dipped into the polymer solution several times. After drying the tubes were fully characterized.

Both, neat and composite tubes based on the 75/25 P(3HO-co-3HD)/P(3HB) blend are shown in Figure 8.2.

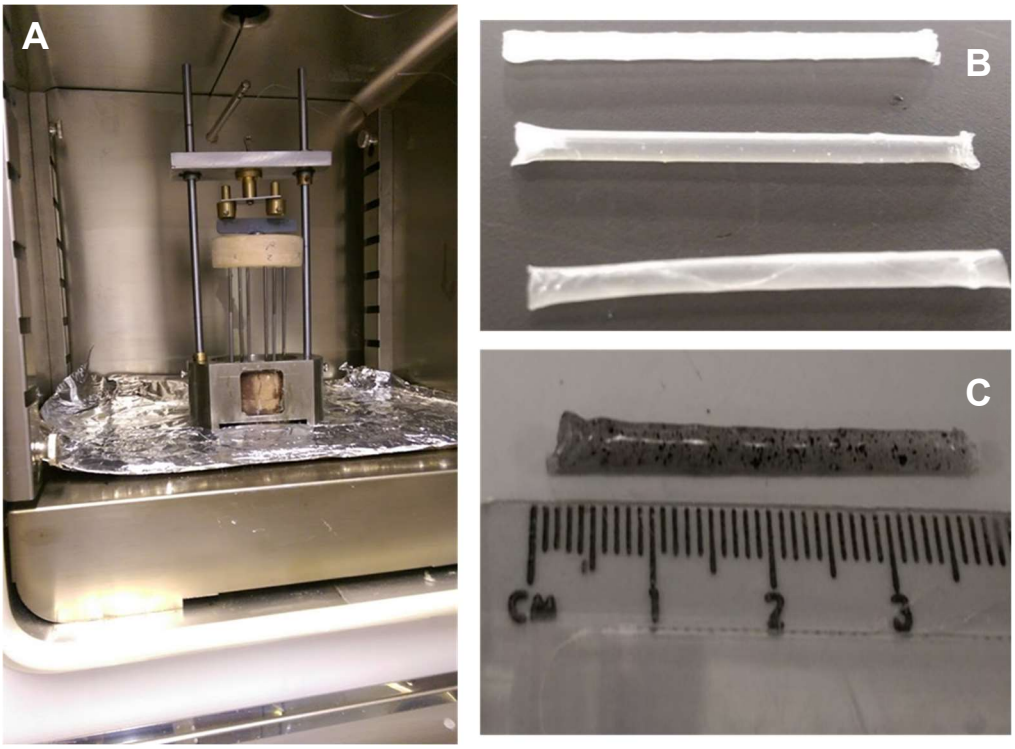

Figure 8.2: Manufacturing of tubes by dip-moulding. A) Dip-moulding apparatus, B) dried hollow tubes of 75/25 P(3HO-co-3HD)/P(3HB) blend and C) 75/25 blend/0.5 wt% GO.

Table 8.1 summarizes the values of inner, outer diameter and the wall thickness of the tube. The obtained tubes were measured at three different points and the average value was recorded as the outer diameter. The difference between outer diameter and the size of the mould was calculated as wall thickness.

The inner diameter was 1.8 mm for all the tubes where the outer diameter was in a range of 2.2 to 2.8 mm. The wall thickness of the final tubes 0.3, 0.2, 0.5 and 0.25 mm for the non-modified, 0.5 wt%, 2 wt% and 5 wt% GO tube respectively.

Table 8.1: Summary of the dimensions of the tube manufactured by the dip moulding technique.

Material	Inner diameter (mm)	Outer diameter (mm)	Wall thickness (mm)
75/25 P(3HO-co-3HD)/ P(3HB)	1.8	2.4	0.3
0.5 wt% GO	1.8	2.2	0.2
2 wt% GO	1.8	2.8	0.5
5 wt% GO	1.8	2.3	0.3

8.2.1.1 Thermal characterization of P(3HO-co-3HD)/P(3HB)/ GO composites post-processing into tubes

The blend composites were characterised by DSC post-processing. The two obtained values of T_g and T_m, attributed to the existence of the two types of PHAs as presented in Table 8.2.

Figure 8.3 shows the thermograms obtained for the non-modified and GO composite tubes. Thermogram (A) reveals the thermal values of the non-modified tube with T_g values of -46.8 and 0.8^{o}C and the T_m of 172.8^{o}C. The thermogram (B) represents the 0.5 wt% GO tube having T_g values of -44.7 and 3.2^{o}C (for the P(3HO-co-3HD) and P(3HB) respectively) and T_m of 172.1^{o}C, which is similar to the non-modified tube T_m. Thermogram (C) represents the 2 wt% GO tube, with T_g of -47.7 and 3.8^{o}C and T_m of 52.1 and 172.1^{o}C. Finally, (D) curve reveals the 5 wt% GO tube thermal values with T_g of -45.9 and 3.3^{o}C and T_m of 53.7 and 170^{o}C.

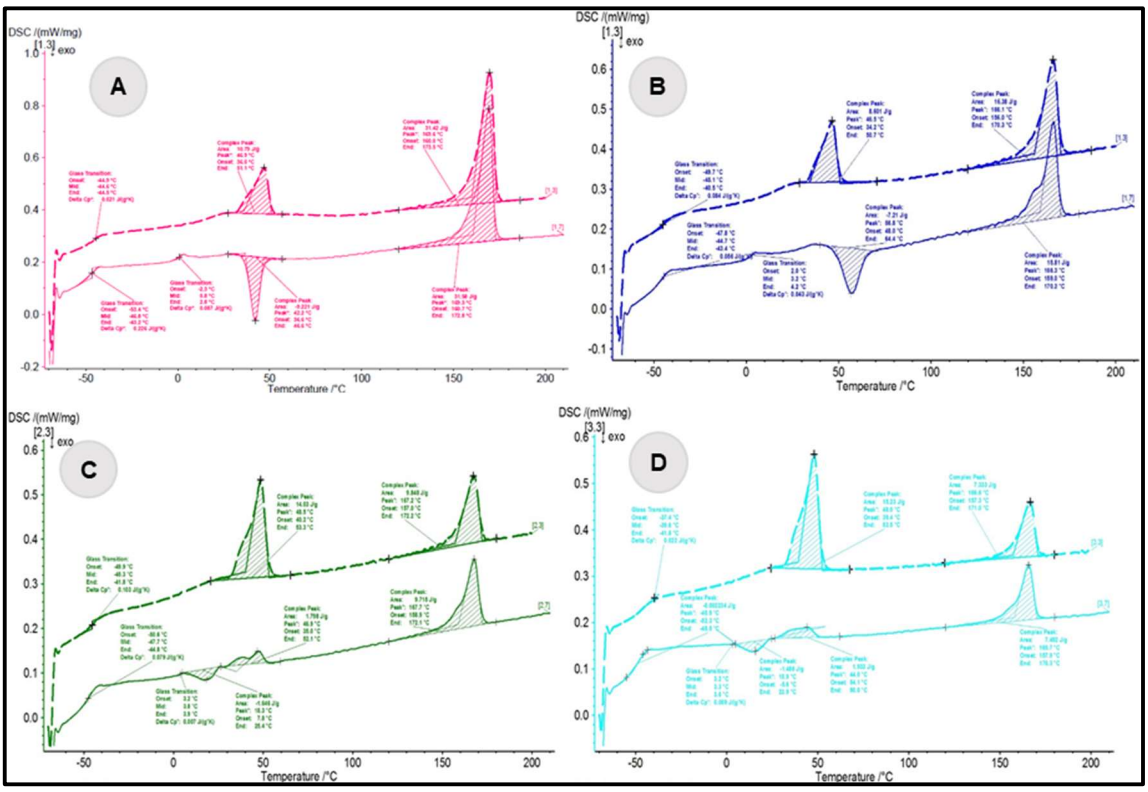

Figure 8.3: DSC thermograms of the: (A) ---- 75/25 P(3HO-co-3HD)/P(3HB) neat tube, 75/25 P(3HO-co-3HD)/P(3HB) tube composites with (B) ---- 0.5 wt%,(C) ---- 2 wt% and (D) ---- 5 wt% GO content.

All composite tubes showed insignificant differences in T_g and T_m values compared to the neat tube (Table 8.2).

Table 8.2: Thermal properties of 75/25 P(3HO-co-3HD)/P(3HB) and GO composite tubes.

Tubes based on 75/25 P(3HO-co-3HD)/P(3HB)	T_g (°C)	T_c (°C)	T_m (°C)
Neat tube	-46.8 0.8	46.6	N/D 172.8
0.5 wt% GO	-44.7 3.2	64.4	N/D 170.2
2 wt% GO	-47.7 3.8	25.4	52.1 172.1
5 wt% GO	-45.9 3.3	22.9	53.7 170

The following Table 8.3 shows the observed melting enthalpies of polymers for both heating cycles as well as the normalized values based on the mass fraction of the respective polymer. The higher the melting enthalpy, the higher the crystallinity of the sample.

Table 8.3: Normalized and observed values of ΔH_m of P(3HB), P(3HO-co-3HD) and 75/25 P(3HO-co-3HD)/P(3HB) blend containing different amounts of graphene oxide.

Sample		ΔH_{obs}^{PHOHD}, J/g	ΔH_{norm}^{PHOHD}, J/g	ΔH_{obs}^{PHB}, J/g	ΔH_{norm}^{PHB}, J/g
75/25 blend	First heating	10.9	14.4	31.4	125.7
	Second heating	n/a	n/a	31.6	126.3
75/25 blend /0.5 wt% GO	First heating	8.6	11.5	16.4	65.5
	Second heating	n/a	n/a	15.8	63.6
75/25 blend/2 wt% GO	First heating	14.0	18.7	9.9	39.4
	Second heating	1.8	2.4	9.7	39.6
75/25 blend /5 wt% GO	First heating	15.2	20.3	7.3	29.3
	Second heating	1.9	2.7	7.5	31.5

The presence of GO in the polymer host, can either act as a nucleation centre or inhibit the growth of crystals due to spatial constraints and thus lead to an increase or decrease in the degree of crystallinity. The lower amount of filler (0.5 wt%) reduced the ΔH_m of both polymers present in the blend matrix from 126.3 to 63.6 J/g and from 14.3 to 11.5 J/g for P(3HB) and P(3HO-co-3HD) respectively. Further addition of GO filler (2 wt%) caused a further decrease of the crystallinity of the P(3HB) by 68.7 % and 19 %, lower than the neat tube and 0.5 wt% sample respectively. Finally, the composite tubes containing 5 wt% GO revealed the highest crystallinity obtained for P(3HO-co-3HD) compared to all other samples. Whereas, for the same composite material, the crystallinity of P(3HB) had the lowest value with the melting enthalpy at 31.5 J/g.

The highest crystallinity of the biopolymer P(3HB), was detected in the non-modified tube with a melting enthalpy at 126.3 J/g, whereas the P(3HO-co-3HD) showed the highest crystallinity in the composite containing the highest amount of the filler (5 wt%).

8.2.1.2 Mechanical characterization of P(3HO-co-3HD)/P(3HB)/ GO composites post-processing into tubes

In order to achieve the required mechanical properties, for the development of a nerve conduit, the blends (chapter 4) were developed and tested as films and then processed to form 3D structures. The selected blend of 75/25 P(3HO-co-3HD)/P(3HB) was chosen and further used for the formation of tubes.

The neat tube showed tensile strength, Young's modulus and elongation at break of 7.8 MPa, 11.5 MPa and 220 % respectively. The addition of 0.5 wt% GO to the polymer matrix, resulted in a reduction in the mechanical values of the final composite material, compared to the neat polymer matrix as shown in Table 8.4. Further addition of filler (2 wt%) revealed a more ductile and soft composite compared with the other fabricated composites with 134 % elongation at break. 0.5 and 2wt% composite tubes, showed the lowest tensile strength (3.6 and 3.4 MPa) and Young's modulus (9 and 6.4 MPa) values. The composite tube containing the highest amount of GO (5 wt%) exhibited the highest tensile strength value (10.4 MPa) and Young's modulus (13 MPa) amongst the fabricated composites and the neat blend tube.

Table 8.4: Mechanical properties of 75/25 tubes of P(3HO-co-3HD) and P(3HB) containing graphene oxide.

Specimens	Tensile strength (σ) (MPa)	Elongation at break (ε_b%)	Young's modulus (E) (MPa)
75/25 P(3HO-co-3HD)/P(3HB) tube	**7.8±1.8**	**220±40**	**11±5.8**
Tubes 0.5 wt% GO	**3.6±0.1**	**110±20**	**9±2**
Tubes 2 wt% GO	**3.4±1.4**	**130±60**	**6.4±4**
Tubes 5 wt% GO	**10.4±0.3**	**120±20**	**13±1.2**

8.2.1.3 Scanning Electron Microscopy of P(3HO-co-3HD)/P(3HB)/ GO composites post-processing into tubes

The cross-section of the fabricated tube developed using 75/25 P(3HO-co-3HD)/P(3HB) blend confirmed the uniform optical observation. There was no visible disparity and porosity of the material on the outer and inner surface of the tube (Figure 8.4 b and c). In addition, the morphology of tubes loaded with different amounts of GO was also studied using SEM. As shown in Figure 8.5 an increase in the GO load on the developed tubes did not result in a visible porosity, neither on the outer nor the inner surface of the specimens, even with higher magnifications.

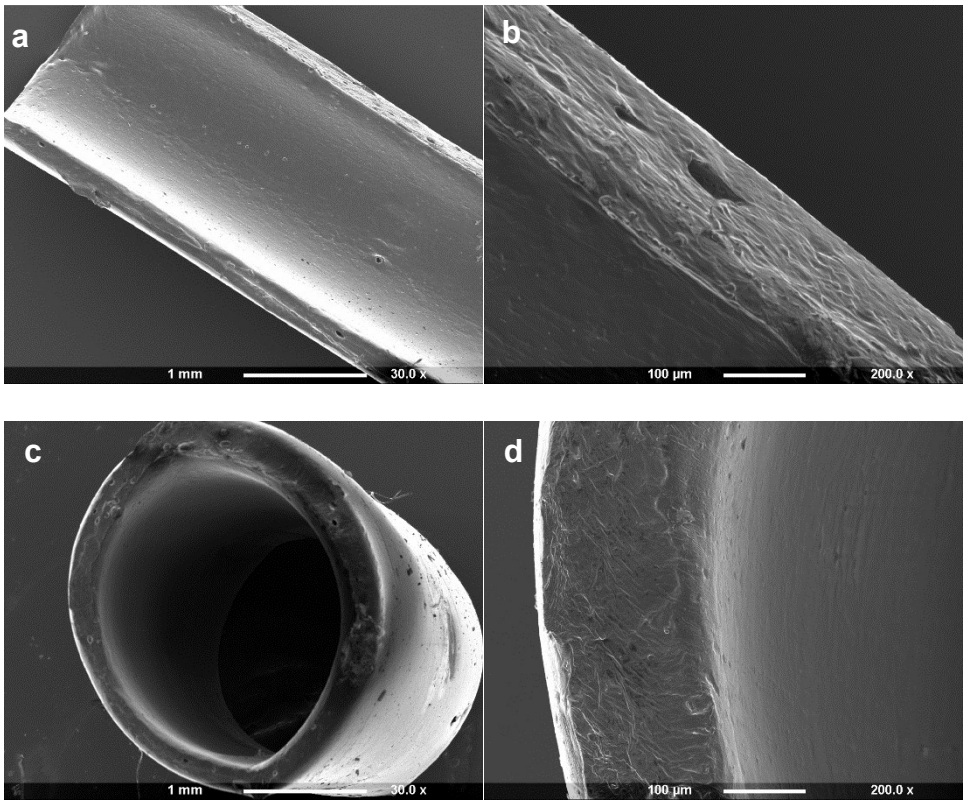

Figure 8.4: SEM micrographs of the (75/25) P(3HO-co-3HD)/P(3HB) tubes: (a) and (b) intralaminar and (c) and (d) cross section views .

The inner surfaces of the (75/25) P(3HO-co-3HD)/P(3HB) tubes containing different amounts of GO were smooth and homogenous even when the concentration of the GO compound increased, Figure 8.5 a, b and c. Moreover, the outer part of the tubes showed no abnormalities or deformations by further addition of GO (Figure 8.5 d, e and f). In Figure 8.5 g, h and i, it is observed that the tubes retain their shape after being removed from the mandrels, used for tube formation. In addition, the dip coating conditions were optimal, thus delamination or redundancy channels were formed. The inner diameter of the tubes was fixed at 1.8 mm. However, the thickness of the tube perimeter (and more

pronounced at the end of the tubular structure) varied; e.g. in the case of 0.5 wt% GO tube (Figure 8.3 g) the wall thickness was less than 500 µm whereas in the case of 5 wt% GO the walls were not homogenous and measured at 650 µm (Figure 8.3 i).

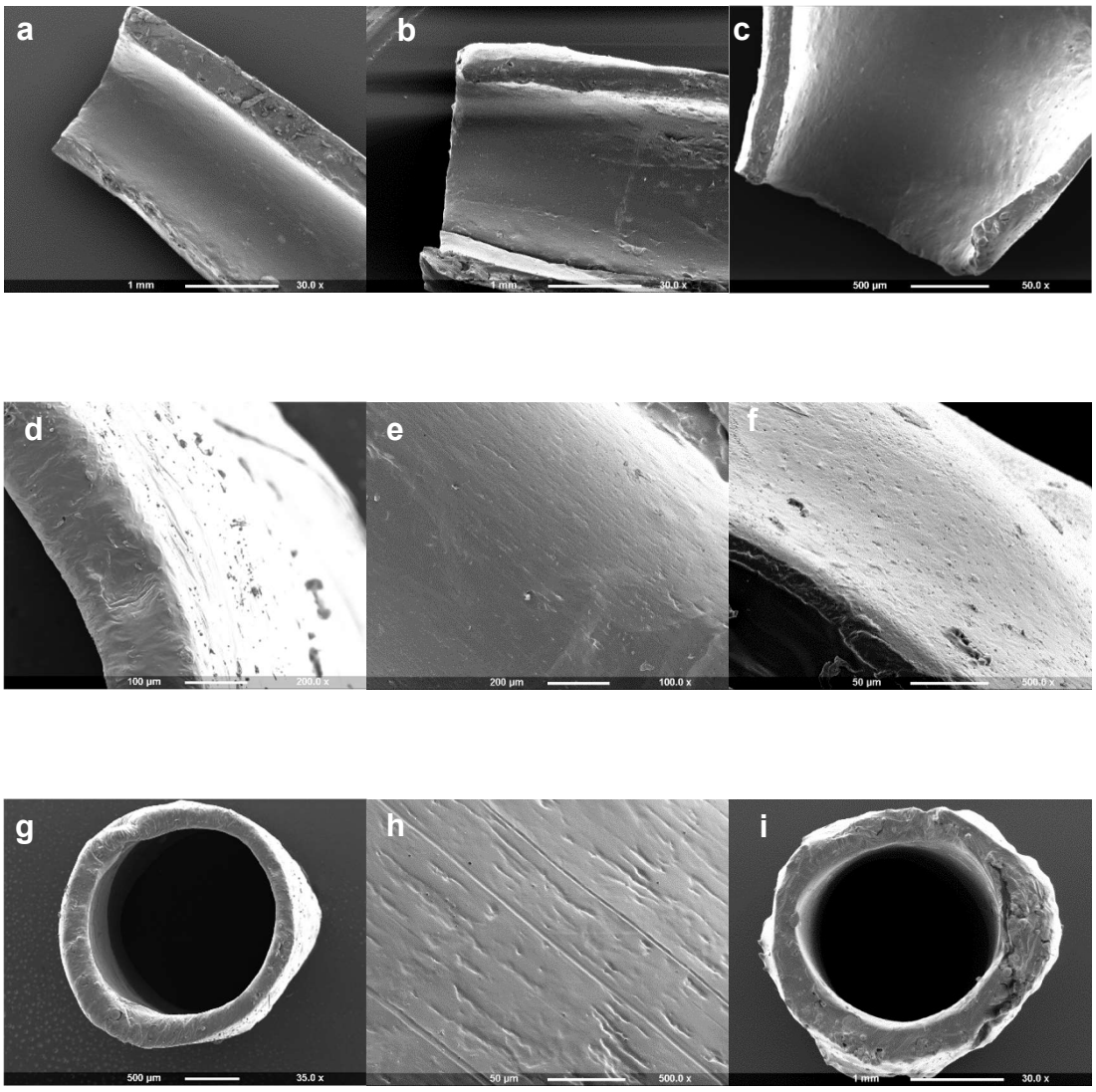

Figure 8.5: SEM micrographs of (75/25) blends of P(3HO-co-3HD) and P(3HB) containing (a), (d), (g) 0.5 wt% GO, (b), (e), (h) 2 wt% GO and (c), (f), (i) 5 wt% GO.

8.2.1.4 *In vitro* cytocompatibility of P(3HO-co-3HD)/P(3HB)/ GO composites post-processing into tubes with respect to NG108-15 neuronal cells

The cytocompatibility of the developed nerve conduits was investigated by directly seeding the neuronal cells on the specimens and incubating them for a period of 7 days. Cell viability assay CellTiter-Blue® (Promega) was used to determine cell viability in contact with the samples. Day 1, 3 and 7 were the investigated time points after seeding the neuronal cells samples.

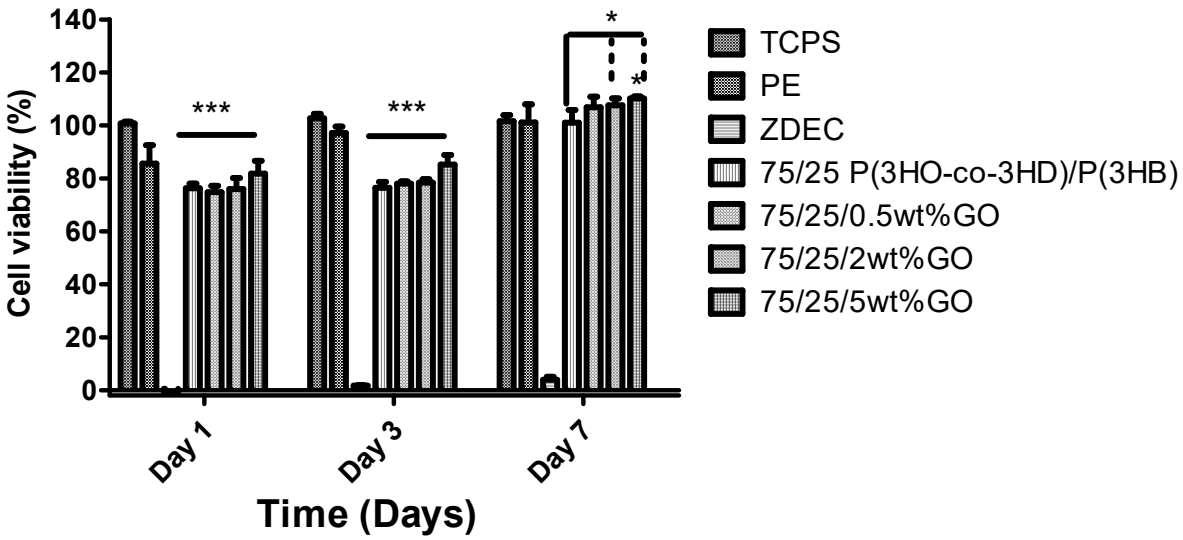

Figure 8.6: Direct cytocompatibility evaluation of NG108-15 cells seeded on 3D PHA composites containing different graphene oxide loadings (mean ± SEM, n = 9 independent experiments). Statistical significance determination is represented as *p ≤ 0.05, **p ≤ 0.01, and ***p ≤ 0.001 for cells on TCPS vs. all materials, non-modified polymer blend vs. GO composites and between GO composites.

The CellTiter-Blue® assay demonstrated the viability of the NG108-15 cells after contact with the tubes. As shown in Figure 8.6 the cytocompatibility of all fabricated composite tubes remained above 70 % throughout the experimental period which according to ISO 10993-5 confirmed that all the composites are cytocompatible materials. After 24 h of direct incubation of the hollow composite tubes with the NG108-15 neuronal cells, there was a significant statistical difference (***p<0.001) between the fabricated composites and the positive control (TCPS). The highest cell viability was observed for the composite containing 5 wt% GO with 81 % cell viability, whereas the other two composites

containing 0.5 and 2 wt% GO showed cell viability around 75 %. No significant statistical analysis ($p>0.05$) was observed between the composite tubes. After 72 h of direct incubation (day 3) of the composite tubes with the neuronal cells, it was shown that the only significant statistical difference (***$p<0.001$) was observed between the composites and the positive control (TCPS).

The control tube fabricated from the blend, revealed 76% cell viability followed by 77% and 78% viability of 0.5 and 2 wt% composite tubes, respectively. The composite tube containing the highest amount of GO (5 wt%) showed the highest cell viability compared to the neat and the rest of the composite tubes (85 %). Finally, after 7 days of incubation, only the 5 wt% composite showed a significant statistical difference (*$p<0.05$) with the positive control (TCPS).

All samples showed superior cell viability, approximately 100 %, compared to the other two investigated time points of the incubation process. Statistical difference (*$p<0.05$) between the fabricated tubes was revealed only for the 2 and 5 wt% composite tubes with the control tube (neat blend tube).

To confirm these findings, a live/dead assay was performed by staining of the neuronal cells when in contact with the tubes, using Ethidium homodimer-III and Calcein AM after 7 days of incubation. Figure 8.7 shows the representative tube area in bright field and fluorescence micrographs. The micrographs revealed that hollow tubes allowed the adhesion and proliferation of neuronal cells, with no cytotoxic effect caused by their presence. The green colour in the micrographs represents the existing live cells whereas the red ones are the dead cells.

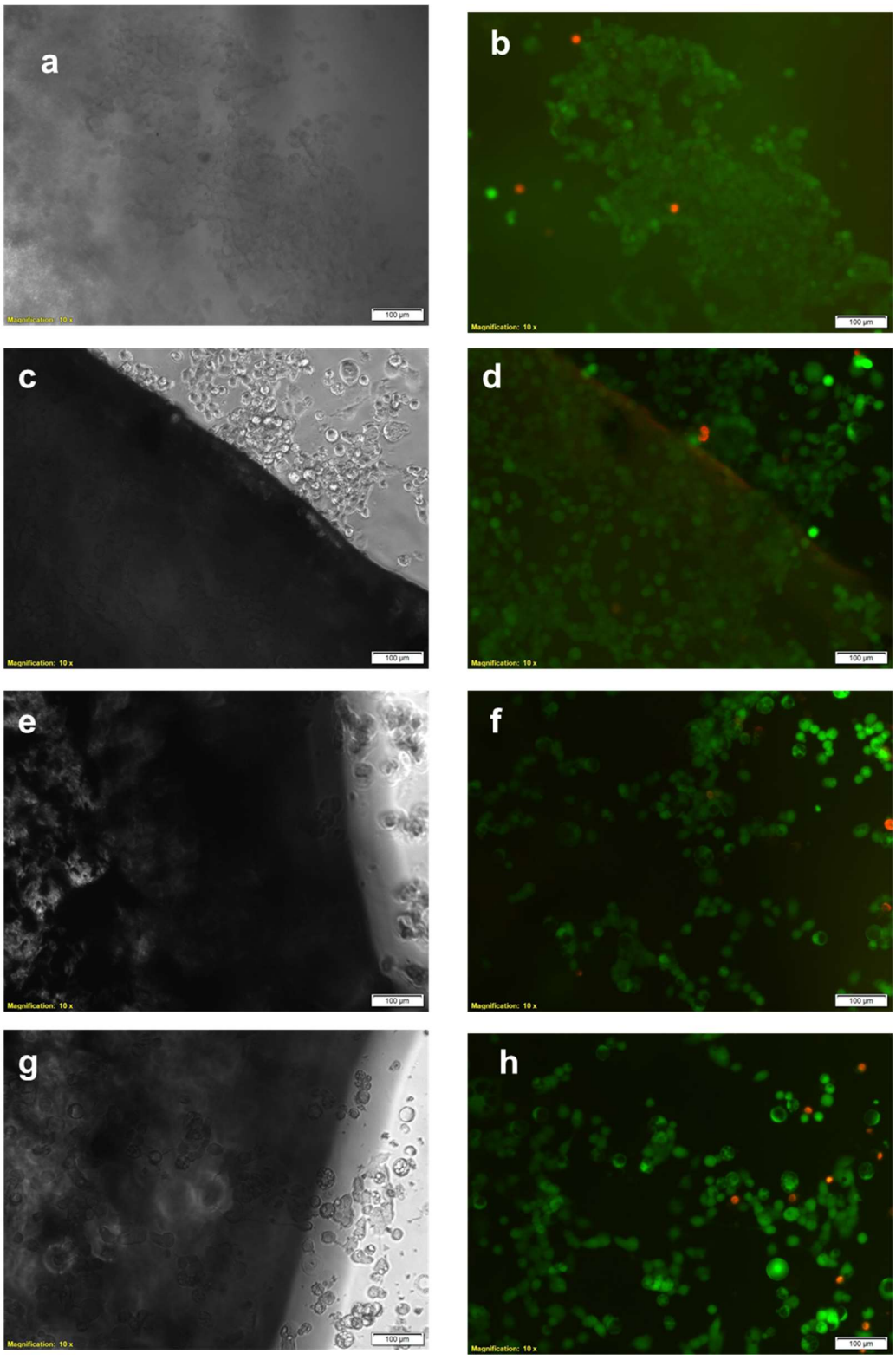

Figure 8.7: Micrographs of brightfield and fluorescence microscopy images: (a), (b) 75/25 blend tube, (c), (d) 75/25 0.5 wt% GO tube, (e), (f) 75/25 2 wt% GO tube and (g), (h) 75/25 5 wt% GO tube.

8.2.2 Development of P(3HO-co-HD)/P(3HB) blend tubes and PGFs composites

As stated at the beginning of this chapter, the developed films with the embedded cerium doped PGFs were rolled as shown in Figure 8.8 into a tube. The actual dimensions and specifications of the tubes are shown in Figure 8.9 and Table 8.4.

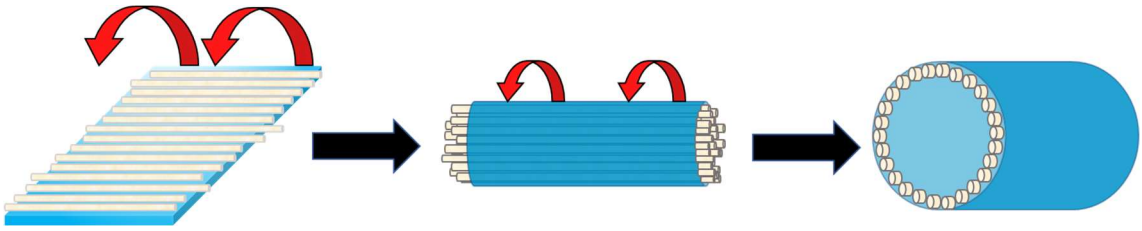

Figure 8.8: Process of manufacturing 3D scaffold using blend PHA and Ce-PGFs by rolling the composite mat to a tubular structure (adapted from (Kim *et al.*, 2015)).

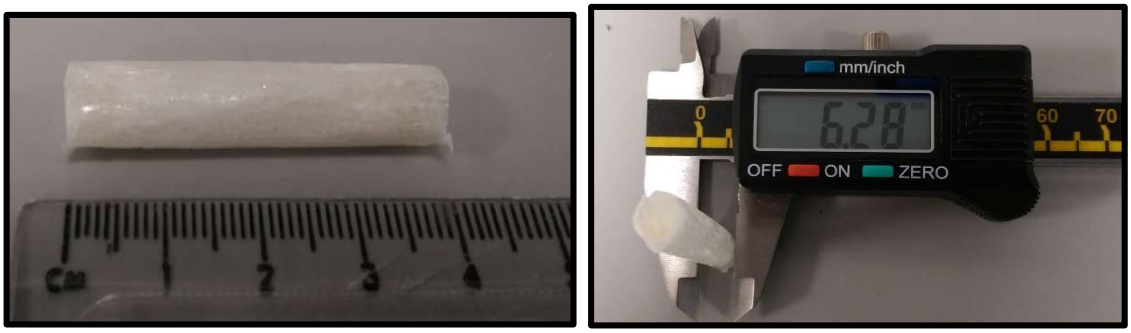

Figure 8.9: PHA composite mat with aligned PGFs fibres blend rolled into a NGC.

The length of the developed tubes was 4 cm as shown in Figure 8.9. The inner diameter of the developed tubes was between 5.2 to 7.5 mm and the wall thickness was from 0.55 to 2.25 mm as shown in Table 8.5.

Table 8.5: Summary of the dimensions of the tubes manufactured by rolling a composite mat.

Specimens	Inner diameter (mm)	Outer diameter (mm)	Thickness (mm)
37 wt% PGFs	7.5	12	2.3
74 wt% PGFs	5.2	6.3	0.6
90 wt% PGFs	7.2	9.2	1

The size of the final diameter mentioned above was not intentional but developed according to how, the polymer mat containing the cerium doped PGFs, was able to roll without breaking the fibres or tearing the hole mat.

8.2.2.1 SEM analysis of PHA/PGFs composite tubes

The cross-section of the developed tubes was investigated by scanning electron microscopy. At × 50 magnification, it was not possible to detect the presence of the PGFs in the case of the 37 wt% sample (Figure 8.10 a). Only at magnification × 500 it was possible to detect the incorporated PGFs in the polymer matrix (Figure 8.10 c). While, in the cases of 74 wt% and 90 wt% PGFs, the fibres were noticeable even at the lower magnifications (Figure 8.10 d and g). Higher magnification of × 500 revealed the fibres alignment within the polymer matrix (Figure 8.10 f and h). The addition of the fibres created some voids as well as loose fibres.

The walls of the tubes remained intact after applying force to the tube to cut the cross-sections for imaging. The rolling technique provided a stable 3D structure as shown in Figure 8.10.

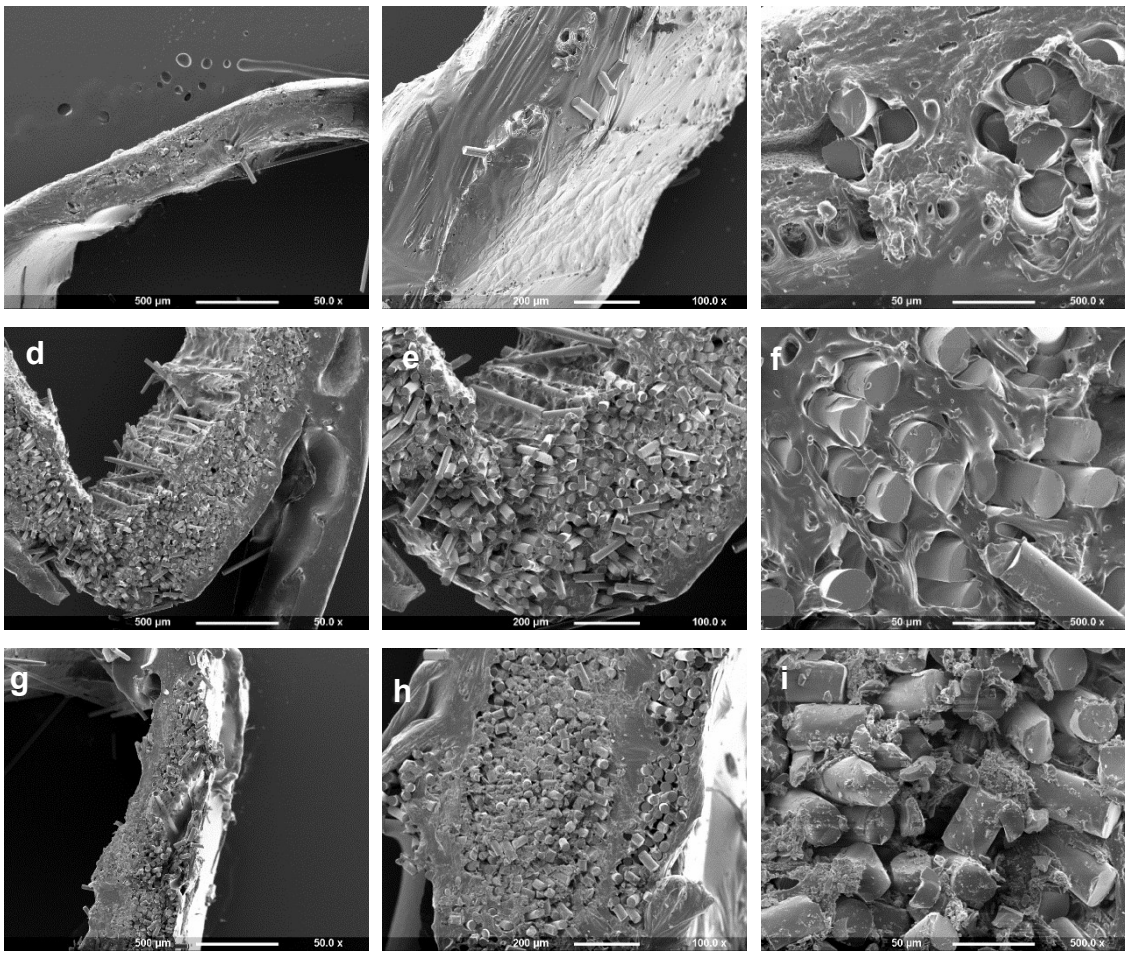

Figure 8.10: SEM micrographs of the (75/25) P(3HO-co-3HD)/P(3HB)/PGFs composite tubes of (a), (b), (c) 37 wt% PGFs (d), (e), (f) 74 wt% PGFs and (g), (h), (i) 90 wt% PGFs.

8.2.3 Development of electrospun fibres of PHA blends

In order to create aligned channels in the developed hollow nerve conduits containing GO, PHAs fibres were developed via electrospinning. Briefly, a solution of a concentration of 15 wt% of 75/25 P(3HB)/P(3HO-co-3HD) was produced using chloroform the solvent. Different parameters (shown in Table 8.6) of the electrospinning process were used to achieve the desired fibres. The dominant polymer for the development of the PHA fibres is the short chain length polymer, P(3HB), which conferred a more stable and easier to handle property to the final fibres. The produced fibres were in the range of 2.4 to 7.1 µm.

Table 8.6: Different conditions to develop electrospun PHA fibres formed from 15 wt% solution of 75/25 P(3HB)/P(3HO-co-3HD) blend.

Condition Samples	Speed of target (rpm)	Syringe pump (ml/h)	Voltage (kV)	Time of e-spinning (min)
1	**600**	**1**	**12**	**5**
2	**600**	**1**	**12**	**3**
3	**600**	**1**	**12**	**1**
4	**600**	**3**	**12**	**5**
5	**400**	**1**	**12**	**5**
6	**800**	**1**	**12**	**5**

8.2.3.1 Scanning Electron Microscopy of electrospun PHAs

To evaluate the morphology of the developed fibres, micrographs of the samples were taken using SEM. In Figure 8.11 the first, second and third columns represent a magnification of × 100, × 1000 and × 10000 of the 6 aforementioned PHA fibres. As all the × 10000 magnification micrographs reveal in all conditions the surface of the developed fibres remains smooth without any defects. For samples 1 to 3, the only variable parameter was the duration of the electrospinning. The decrease of time resulted in lower fibre alignment (micrographs a, d and g) and also a slightly smaller diameter of the fibres as shown in b, e and h.

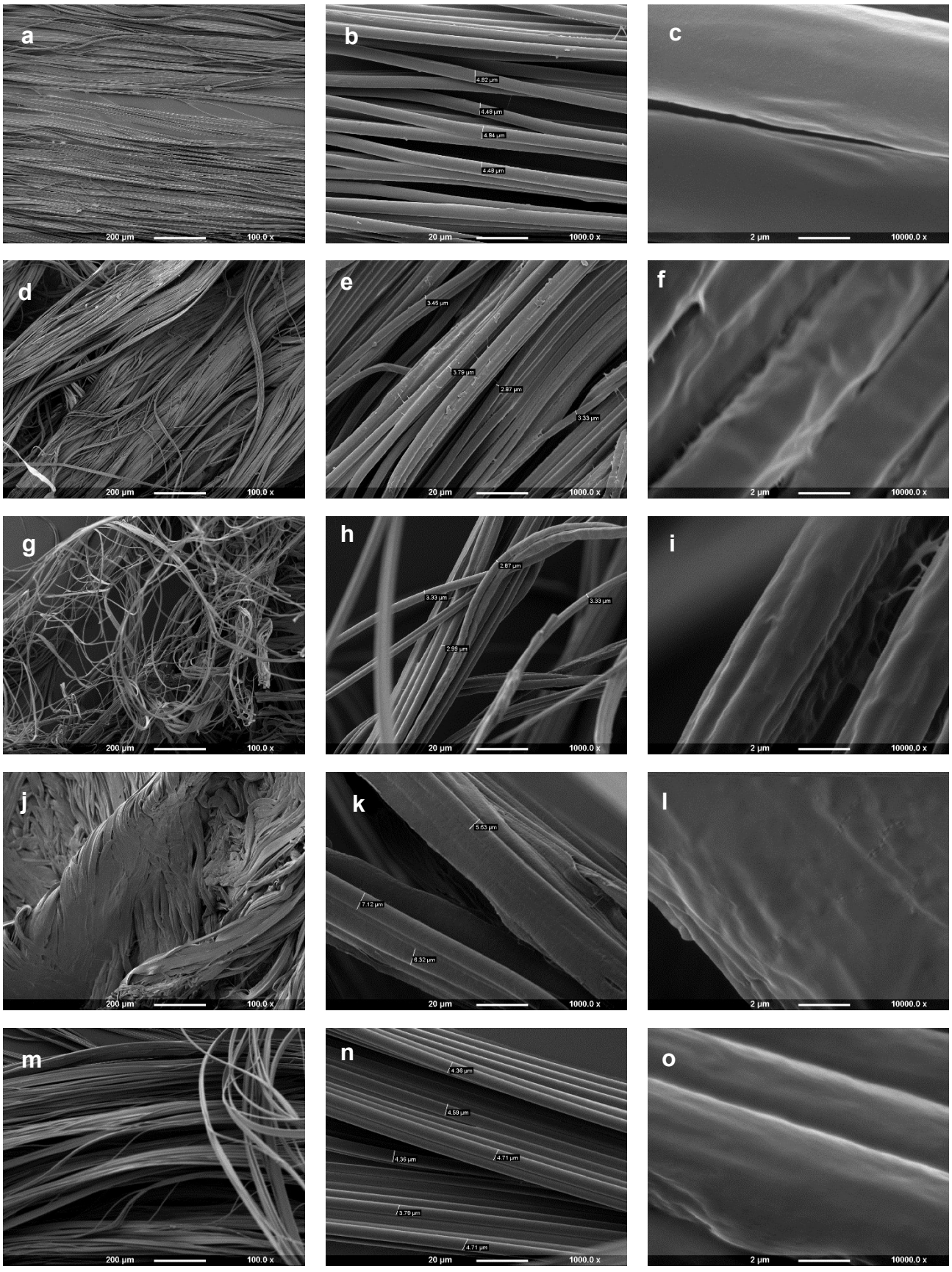
a
200 µm
100.0 x
b
4.82 µm
4.48 µm
4.94 µm
4.48 µm
20 µm
1000.0 x
c
2 µm
10000.0 x
d
200 µm
100.0 x
e
3.45 µm
3.79 µm
2.87 µm
3.33 µm
20 µm
1000.0 x
f
2 µm
10000.0 x
g
200 µm
100.0 x
h
2.87 µm
3.33 µm
3.33 µm
2.99 µm
20 µm
1000.0 x
i
2 µm
10000.0 x
j
200 µm
100.0 x
k
5.53 µm
7.12 µm
6.32 µm
20 µm
1000.0 x
l
2 µm
10000.0 x
m
200 µm
100.0 x
n
4.36 µm
4.59 µm
4.36 µm
4.71 µm
3.79 µm
4.71 µm
20 µm
1000.0 x
o
2 µm
10000.0 x

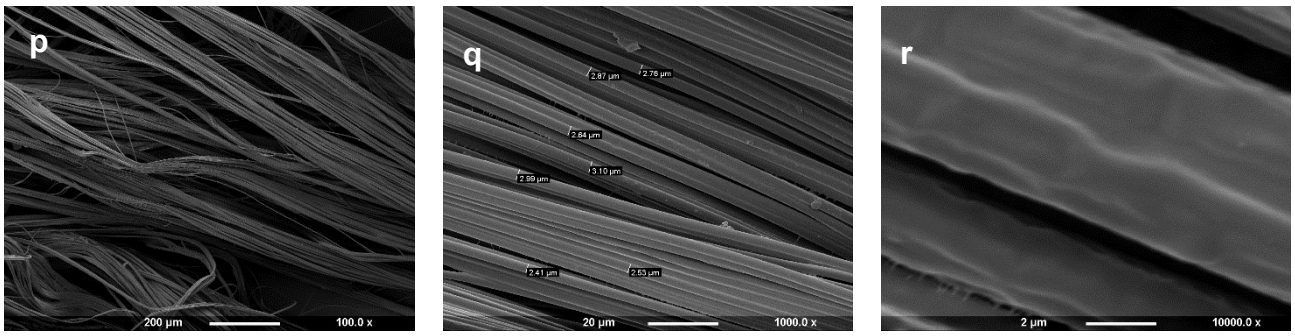

Figure 8.11: Micrographs of the developed PHA fibres using: (a)-(c): condition 1, (d)-(f): condition 2, (g)-(i): condition 3, (j)-(l): condition 4, (m)-(o): condition 5 and (p)-(r): condition 6 .

The increase in the flow rate of the syringe pump resulted in bundles of fibres in which the fibres appeared to be fused together (j). These conditions also resulted in a distortion of their round shape; the formed fibres were more flattened (k). Despite the morphology change, the surface of these individual fibres was kept intact, providing a very smooth and homogenous morphology (l).

Table 8.7: Average diameter of the developed electrospun fibres under different conditions of electrospinning.

Condition	Fiber diameter (µm)
1	**4.7±0.2**
2	**3.4±0.5**
3	**3.1±0.2**
4	**6.4±0.8**
5	**4.4±0.4**
6	**2.7±0.2**

Sample 1 resulted in fibre diameter of 4.7 µm. By reducing the electrospinning period to 3 and 1 min (sample 2 and 3) the fibres produced showed a decrease in fibre size of 3.4 and 3.1 µm in diameter. Sample 4 showed the highest fibre diameter, when conditions were the same as sample 1, apart from the syringe pump step (3 ml/h).

In the case of samples 5 and 6 the parameter which was different was the target speed (400 and 800 rpm respectively). For sample 5, there was a notable increase of the fibre diameter (4.4 μm) compared to sample 6 (2.7 μm) (n and q).

Table 8.7 summarizes the fibre diameters obtained from the different electrospun conditions.

8.2.3.2 *In vitro* cytocompatibility of electrospun PHAs

To evaluate the cytocompatibility of the PHA electrospun fibres, the developed samples were tested directly with respect to NG108-15 neuronal cells at three time points: day 1, 3 and 7. As a positive control PE (polyethylene) was used from Goodfellow whereas negative control ZDEC (Polyurethane film containing 0.1% zinc diethyldithiocarbamate) was used from Hatano Research Institute.

As shown in Figure 8.12, cell viability for all conditions of the developed fibres was comparable to the positive control and the tissue culture plastic. At day 7, in all samples it was observed that the cell viability was greater than 80 % confirming that the fibres were suitable substrates for the proliferation of the NG108-15 neuronal cells. According to ISO 10993-5 all the electrospun PHAs fibres were considered as cytocompatible substrates.

After 24 h of seeding with NG108-15 neuronal cells only the fibres made with the 4^{th} condition revealed a significant difference after statistical analysis (**$p<0.01$) compared to the positive control (TCPS). The highest neuronal cell viability was detected in the case of the fibres made under condition 1 and 4 resulting in 98.5 % and 97.3 % of cell viability, respectively. Also, close to these values were the fibres fabricated according to condition 2 revealing 96.75 % cell viability. After 72 h of direct seeding with NG108-15 cells, statistical analysis revealed significant differences between the positive control and the fibres developed according to condition 3, 4 and 5 (*$p<0.05$, **$p<0.01$ and ***$p<0.001$ respectively). Significant differences were detected between the developed fibres, made according to condition 2 and 4 (*$p<0.05$).

On day 3, greater cell viability was observed for fibres made following the condition 1 and 2 resulting in 94.6 % and 93.7 % cell viability, respectively. After

168 h of incubation with the neuronal cells, the statistical analysis showed a significant difference only between the fibres made according to condition 1 and 4 (*$p<0.05$). The highest cell viability was detected for the fibres made according to condition 1. As shown in Figure 8.12 all the electrospun fibres prepared with different electrospinning conditions were capable of facilitating the proliferation and growth of NG108-15 neuronal cells.

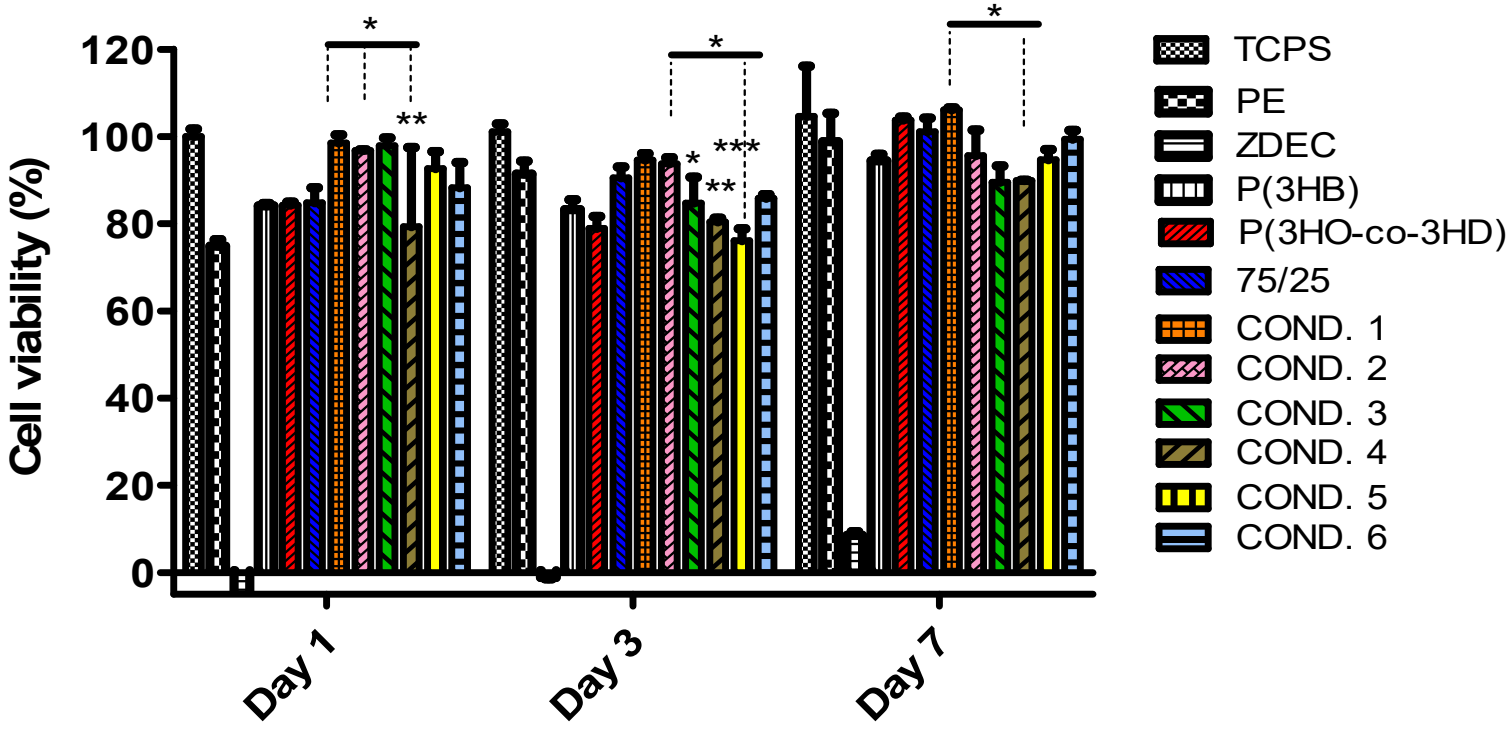

Figure 8.12: Direct cytocompatibility evaluation of electrospun75/25 P(3HB)/P(3HO-co-3HD) with respect toNG108-15 cell line for a time period of 7 days.

8.3 Incorporation of the electrospun fibres in the hollow PHA/GO composite tubes

The developed hollow tubes described in section 8.2.1 were cut in 1 cm length and threaded with the 10 cm long electrospun fibres developed in accordance with condition 1 as described in section 8.2.3. As shown in Figure 8.13, the long-threaded fibres containing the hollow tubes were then cut to the same size of the tube surrounding the electrospun fibres (1 cm). The final structure showed flexibility and stability as a structure where it was easy to handle and process. These samples in future will be further used for preliminary *ex-vivo* experiments by culturing Embryonic Chick Dorsal Root Ganglion Neurons (DRGs).

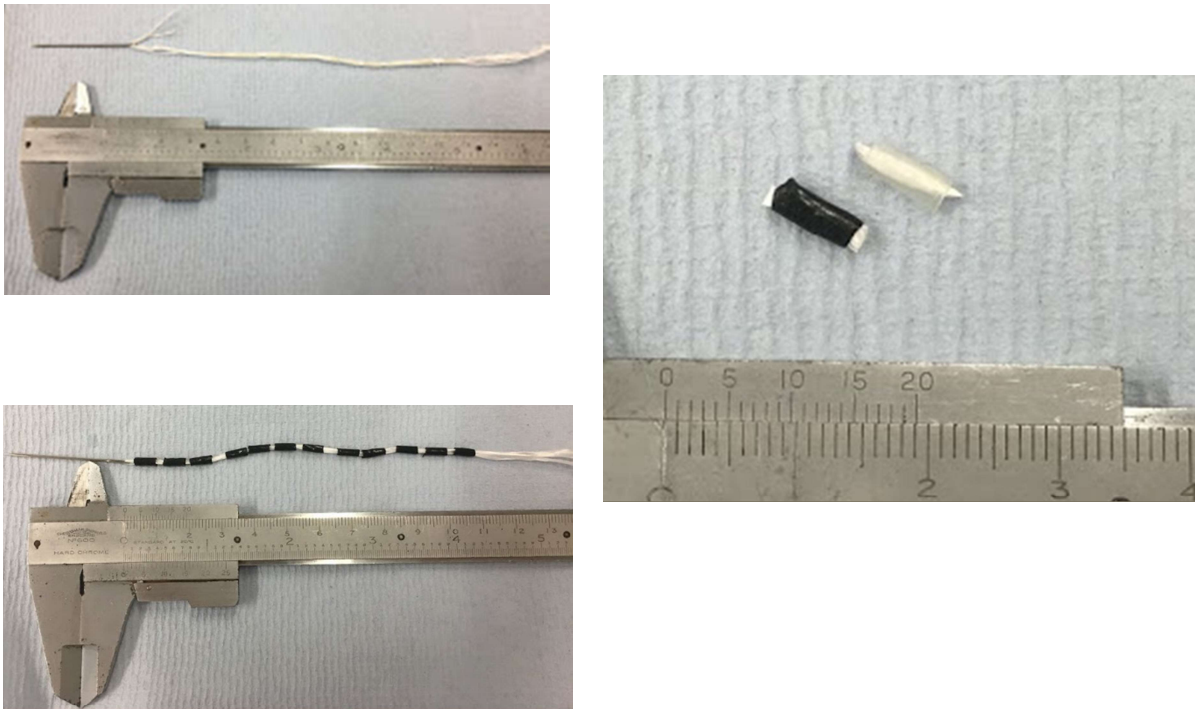

Figure 8.13: Threading electrospun fibres into the hollow tubes. The transparent tube is the control neat tube of 75/25 P(3HO-co-3HD)/P(3HB) and the black tube is the tube containing 5 wt% GO.

8.4 Discussion

There are a large number of cases where peripheral nerve injuries are responsible for serious and challenging health issues. Inadequacies and limitations (scarring, neuroma formation, sensory and/or motor loss etc.) of tension free repair and autografts have pushed for other solutions. The use of artificial Nerve Guide Conduits (NGCs) is gaining more attention as an effective alternative to the aforementioned conventional treatments. Although, hollow NGC designs have been clinically proven to be an excellent alternative to autograft repair, their application is insufficient for critical nerve gaps greater than 4 cm (D Grinsell and Keating, 2014b; Gaudin *et al.*, 2016b; Vijayavenkataraman *et al.*, 2018; Cavanaugh *et al.*, 2019).

Different strategies and designs have been utilized to achieve effective artificial nerve grafts. The convenience, simplicity and repeatability of hollow NGCs make them a promising design for nerve regeneration. The porosity for sufficient permeability of the nutrients and the structural guidance cues in the tube to facilitate neuronal growth from proximal to distal stump are the two key properties for a successful NGC (Daly *et al.*, 2012).

Regardless of the variety of natural and synthetic materials, approved by FDA when applied in clinical use, the regeneration of these commercially available NGCs have limitations due to scar formation, inflammation and poor mechanical properties.

In an attempt to address these problems, a mixture of 75/25 P(3HO-co-3HD)/P(3HB) blend of PHAs was used in this study as a polymer matrix for the fabrication of NGCs. Previous studies have demonstrated the feasibility of NGCs based on PHAs. Thus, the tailoring properties of PHAs could be a solution to the limitations of the available NGCs. The strategies used to fabricate the aligned fibrous designs were dip moulding and the roll of composite mats. In both cases the evaporation of the solvents would create pores conferring permeability to the final scaffolds.

To address the topographical cues to improve migration, proliferation and intraluminal guidance of axonal regrowth cerium doped PGFs and electrospun PHA fibres were used. One of the developed designs was the 2D PHA

composite mat containing PGFs which was rolled to form a 3D tubular structure. The second design was the PHA hollow composite tubes containing GO in which elctrospun fibres of PHAs were threaded as described in section 8.3. Both inorganic compounds (PGFs and GO), as presented in Chapters 6 and 7 respectively, will impart antibacterial properties to the final tubular structure, minimizing the chances of implant rejection due to infection.

The 75/25 P(3HO-co-3HD)/P(3HB) blend was selected due to its properties and was further modified and translated into 3D structures. Solvent casting technique combined with fibre alignment and rolling, as well as dip moulding in conjunction with electrospun fibres were the methods employed to successfully fabricate NGCs.

The presence of two melting peaks detected in all samples indicates a heterogeneous material resulting from the immiscibility of the two polymers used in this blend. In addition, all composite tubes as well as the non-modified tube possess two T_g peaks attributed to the presence of P(3HB) and P(3HO-co-3HD). The 2 wt% GO tube revealed slightly lower glass transition temperature compared to the other composites, indicating lower spatial restrictions due to the presence of GO in the polymer matrix. The melting temperatures for both polymers consisting of the blend polymer matrix showed insignificant changes.

The addition of 0.5 wt% of GO to the polymer blend, resulted in a decrease in crystallinity. In this case the addition of the filler acted as plasticizer causing deformation in the final composite material and hence resulted in decrease, in its degree of crystallinity. A further increase in the GO content (2 wt%) enhanced the crystallinity of the P(3HO-co-3HD) bio-polyester indicating that the addition of GO promoted the crystallization of this polymer.

The addition of the filler supressed the crystallinity of P(3HB) due to the increase in crowding within the polymer host. In the case of the P(3HB) the system is overcrowded, and the addition of the filler inhibits crystallization due to the space constraint, so in this case it lacks formation of large, well-defined crystals. Whereas due to the slow crystallization rate of P(3HO-co-3HD), the addition of the GO filler acts as a nucleation point and enhances the rate of crystal formation.

The addition of the lower quantity of GO (0.5 wt%) reduced the mechanical properties of the final composite compared with the neat blend. Similarly, this effect was previously observed in Chapter 7, section 7.2.4 where composites films with the same GO concentration were fabricated.

The addition of 0.5 and 2 wt% GO decreased the mechanical properties of the final composites, compared to the neat blend tube due to the competition of the filler with the different lengths adjacent polymers chains to form a bond. Hence, this could probably lead to agglomeration of the filler that restricted the load transferred from the matrix to the GO causing easily propagating cracks under external load.

Further addition of the filler (5 wt%) increased both the tensile strength and Young's modulus compared to all other composites and neat blend, resulting in reinforced composite material with higher stiffness.

SEM micrographs were taken to investigate the effect of GO loading on the surface topography of the blend tube. A uniform and the smooth surface was observed for the composite tubes containing the different GO loading proportional to the neat tubes made from the 75/25 P(3HO-co3HD)/P(3HB) blend. Both the neat and the composites tubes retained their shape when removed from the mandrels with a homogenous surface on the inner and outer part of the tubes.

In the case of the composite tubes containing cerium doped fibres, SEM micrographs revealed that the presence of cerium doped PGFs in the 3D structures was detectable at lower magnification only for the 74 and 90 wt% loading. In all cases the fibres were fully aligned whereas in some areas, due to the high amount of the fibres, the composite exhibited voids and poor impregnation of the incorporated PGFs. In addition, the developed electrospun fibres based on the 75/25 P(3HB)/P(3HO-co-3HD) blend were characterised for their fibre alignment and diameter.

As shown in section 8.2.3.1, the different conditions used to fabricate these electrospun fibres, played a crucial role in the alignment and the fibre diameter. Condition 1 and 6 resulted in the best aligned fibres with a fibre diameter of 4.7 and 2.7 μm respectively.

Many biodegradable polymers, both synthetic and natural, have been used to develop electrospun fibres for peripheral nerve reconstruction. Some of the features of electrospun fibres that effects the response of neuronal cells are the fibre density, the alignment, the diameter and the surface topography. The fibres can vary in diameter, from nano to micro, and their alignment can be random, highly aligned or partially aligned. The surface topography can also be tailored having smooth, and pitted fibres. There are many studies referring to electrospun fibres as a means of enhancement of nerve regeneration. However, the intense investigation of this matter is not entirely clear whether nano or microfibres support better nerve regeneration.

The different materials used and tested with different cell lines *in vitro* and *in vivo* cannot be directly compared. Conversely, there are studies arguing that either nano- or microfibres supports better the neurite outgrowth and Schwann cell migration. Wen and Tresco showed that between polypropylene fibres fabricated in a wide range of size from 5 to 500 μm, the 5 μm filaments were characterised by a superb directional and evenly distributed neuronal growth (Wen and Tresco, 2006). In another study (Jiang *et al.*, 2014), PCL fibres were fabricated on a nano and micro scale of 250 nm and 980 nm respectively. These fibres were tested *in vivo* and after 3 months of post implantation, the axons regenerated across the defect gap in all treated animals.

However, the nanofibre substrates revealed a higher total number of myelinated axons and thicker myelin sheaths as well as a significant increase in the number of regenerated dorsal root ganglion compared to microfibre substrates. Three groups of highly aligned electrospun poly-L-lactic acid (PLLA) fibres were created and tested to evaluate neurite and Schwann cell (SC) behaviour from dorsal root ganglia (DRG) explants. Large, intermediate and small diameter fibres of 1325, 759 and 293 nm were investigated using chick DRG. After 5 days of culturing chick dorsal root ganglion, the small fibres showed lower neurite growth, 42 % and 36 %, less than the intermediate and large fibres (Wang *et al.*, 2010).

Additionally, PLGA nanofibers were produced in an aligned and random structure with 5 and 2 μm fibre diameters, respectively. After 5 days of culture

with PC12 and S42 cells the *in vitro* biocompatibility results showed that the aligned fibres have better guidance for the neuronal cells and hence achieve higher cell proliferation and migration compared to randomly oriented nanofibers (Kim *et al.*, 2016). Lately, Lizarraga *et al.*, evaluated different diameter PHA fibres compared to neuronal and Schwann cells. This *in vitro* study showed that all the constructed fibres were well aligned with a diameter distribution of 2.4, 3.7 and 13.5 μm and were able to facilitate neuronal cell growth, proliferation, and differentiation. However, the aligned long fibres are the most promising candidates as they revealed the greatest number of neuronal cells when grown individually and in co-culture conditions (Lizarraga-Valderrama *et al.*, 2019).

The cytocompatibility of the composite tubes was assessed by performing the CellTiter-Blue® assay for a time period of 168 h (7 days). The results showed that there is a direct correlation between the amount of the GO incorporated into the polymer and the cell viability. Higher GO content, resulted in higher number of viable cells, capable of adhering and proliferating in these hollow composite tubes. The bright field as well as the fluorescence micrographs supported the finding from the cytocompatibility assay. According to ISO 10993-5, all the fabricated tubes are declared as cytocompatible materials. The tube containing 5 wt% GO showed superior cytocompatibility compared to the other neat and composites tubes.

The cytocompatibility results showed that the fabricated electrospun fibres were able to successfully facilitate neuronal proliferation and growth. The high percentage of the cell viability considers them as cytocompatible substrates according to ISO 10933-5.

There is a correlation observed between the diameter of the fibres and the resulting cell viability. The fibres obtained using condition 1, had an intermediate fibre diameter of 4.7 μm and high alignment and density, exhibited the higher cell viability among the PHA fibres produced.

Since 75/25 P(3HO-co-3HD)/P(3HB) blend films have been shown in previous studies that possess the required flexibility for implantation in peripheral nerves, this material was selected for the fabrication of NGCs. As shown in

section 8.2.1.2 the mechanical properties obtained from the GO composite tubes meet both Young's modulus and tensile strength required for their use in peripheral nerves of different animal models; rat sciatic nerve and rabbit with ultimate tensile strength of 2.72 ± 0.97 MPa and 2.5 MPa respectively (Ballantyne, 1980; Borschel *et al.*, 2003)

In conclusion, composite tubes based on a 75/25 P(3HO-co-3HD)/P(3HB) polymer blend with GO and cerium doped PGFs were successfully fabricated and characterised. The *in vitro* cell viability of the GO composite tubes and the PHA electrospun fibres, revealed high cytocompatibility of the materials with respect to NG108-15 neuronal cells. In addition, the composite tubes containing cerium doped PGFs showed a very promising structure with high alignment. These composites tubes are suitable for use in nerve regeneration.

Further studies are required to fully characterized the physicochemical properties of both GO and cerium doped PGFs tubes. In addition, neuronal growth assessment and co-culture with Schwann cells and NG108-15 neuronal cells are required to investigate the efficacy of the composites NGCs in supporting peripheral nerve regeneration. Samples in several replicates should be evaluated for their ability to support the proliferation and outgrowth of DRGs prior to any *in vivo* experiments.

Chapter 9

Conclusions and future perspectives

9 Conclusions and future perspectives

9.1 Conclusions

Polyhydroxyalkanoates are biological polyesters that have attracted a lot of attention for their use in medical field (Hazer, 2010) due to their biodegradability and biocompatibility (Philip, Keshavarz and Roy, 2007). They possess a wide range of properties and are easy to be processed into 2D and 3D structures. Their properties can be tailored to the requirements of a particular application with a variety of strategies such as blend development and/or composites. Therefore, there is a great interest in the production and commercialization of these materials on a large scale. The main constraint for the commercialization of these materials is their high cost of production. Cheaper carbon sources, genetically modified strains and solvent - free polymer extraction is some of the ways used to reduce costs. (Koller *et al.*, 2016; Anjum *et al.*,2016; Choi and Lee, 1999).

One of the promising biomedical application of PHA is peripheral nerve regeneration. Currently, the availability of nerve conduits on the market faces several drawbacks and is a challenge in terms of immune response reactions that can lead to implant rejection. In addition, the often-required post-surgery as well as the lack of antibacterial properties of the implants themselves, increase the risk of infections. Infections prolong both hospitalization and antibiotic prescription, leading to excessive costs. With respect to these problems, this study aims to develop a novel PHA-based antibacterial nerve conduit.

Initially, two different types of PHAs were produced: a short chain length PHA, P(3HB) and a medium chain length PHA, P(3HO-co-HD). Both polymers were produced using glucose as a carbon source while the bacterial strain used during the fermentation process was *Bacillus subtilis* OK2 and *Pseudomonas mendocina* CH50 respectively. Although, the laboratory-scale production is successful for both polymers, further studies are required to maximize polymer yields and reduce production costs. Optimization of the fermentation conditions as well as alternative cheap carbon sources could be investigated to produce more cost-effective PHAs.

Both produced biopolymers were characterized by a variety of physicochemical techniques and identified as the P(3HB) homopolymer and novel P(3HO-co-3HD)

co-polymer. The cytocompatibility of these materials was investigated and showed high cell viability using two representative cell lines: the well-studied and established L929 murine fibroblasts and the NG108-15 neuronal cells.

Since the P(3HB) homopolymer is a brittle and rigid material and the P(3HO-co-3HD) co-polymer is very elastomeric blends of these two biopolymers were developed in a variety of compositions in order to achieve a range of mechanical properties. The fabricated blends were obtained via solvent casting technique and evaluated for their physicochemical properties with emphasis on their mechanical properties. Thermal analysis confirmed the immiscibility of the blends especially at the ratios of 20/80 and 75/25 of P(3HO-co-3HD)/P(3HB) revealing two melting events corresponding to individual PHA polymers. The water wettability measurements showed a direct correlation between the content of the P(3HO-co-3HD) indicating an increase in hydrophobicity for blends with higher P(3HO-co-3HD) content.

Cell proliferation studies showed that all the developed blends, 80/20, 75/25, 20/80 and 25/75 of P(3HO-co-3HD)/P(3HB), showed good cell viability when seeded directly with L929 and NG108-15 cells for a period of 7 days. Since the 75/25 P(3HO-co-3HD)/P(3HB) blend presented adequate elasticity and durability, it was considered as a promising composition for use in nerve reconstruction. Also, this composition was characterised by a higher cell viability compared with the other blends.

To impart antibacterial properties to these biopolymers and the selected blend of 75/25 P(3HO-co-3HD)/P(3HB), inorganic and organic additives were incorporated into these materials. Garlic powder (GP), cerium doped phosphate fibres (PGFs) and graphene oxide (GO) were selected as antimicrobial additives. The addition of the antibacterial agents was carried out on the selected 75/25 P(3HO-co-3HD)/P(3HB) blend, P(3HB) homopolymer and P(3HO-co-3HD) co-polymer, to investigate the effect of incorporation of these compounds on the physicochemical properties and antimicrobial activity.

Three different amounts of GP were incorporated into the polymeric matrix of the aforementioned samples 23, 45 and 90 wt%. The selected amounts of the incorporated garlic powder were defined by the antibacterial activity estimated by the MIC and MBC assays for GP. The physicochemical characterization of the

final specimens showed that the thermal properties of the polymer matrices did not change significantly with the addition of different GP ratios. However, the mechanical properties changed on incorporation of GP due to plasticization, reducing the mechanical properties compared to the neat polymer.

The plasticizing effect caused by the presence of GP is attributed to the hydrogen bonds formed between the hydroxyl and amino groups (Thakur and Thakur, 2015). In addition, Kirby–Bauer test was used to evaluate the ability of polymer containing different amounts of garlic powder to impart antibacterial effect. The release of the GP from the polymer matrices resulted in the formation of halo on incubation with bacterial agar plates. The antibacterial tests were conducted against 6 bacterial strains frequently present in nosocomial environment: namely *Staphylococcus aureus* (ATCC® 29213™), *Staphylococcus epidermidis* (ATCC® 12228™), *Escherichia coli* (ATCC® 25922™), *Pseudomonas aeruginosa* (ATCC® 27853™), clinical isolates of MRSA and MRSE. The GP composites showed good antibacterial activity although in some cases the microorganism was found to be resistant. Finally, the cell culture data obtained from this study revealed, in both direct and indirect trials, that GP release interferes with the proliferation of the L929 murine fibroblasts. The induced cell-death due to the release of GP from the polymer makes it a possible candidate in other applications, such as anti-cancer and cardiovascular diseases.

Epidemiologic studies have shown a inverse correlation between garlic and progression of cardiovascular disease as well as decreased risk of cancer (Khalid Rahman and Gordon M. Lowe 2006; Nicastro, Ross and Milner, 2015; Petrovic *et al.*, 2018). PHAs could be used as carrier of the active ingredients of garlic and result a prolonged and controlled release of them on the target sites.

Much research has been conducted on the effect of phosphate fibres on nerve tissue engineering, resulting in promising findings. In this work, cerium doped PGFs were selected and incorporated into 75/25 P(3HO-co-3HD)/P(3HB) blend in different PGFs contents. The developed composites have been tested for their thermal, morphological and crystallization properties. In addition, they were characterized for their bioactivity as antibacterial agents against both Gram-positive and Gram-negative bacterial strains.

These composites were tested for their cytocompatibility with respect to L929 murine fibroblasts and NG108-15 neuronal cells. It was shown that the addition of the PGFs to the polymers did not change the melting temperature of the obtained composites. SEM micrographs showed that all the composites exhibit good fibre alignment within the polymer matrix resulting in uniaxial composite mats. Higher amounts of the PGFs content were found to cause a greater number and size of pores formed within the composite substrate. The crystallinity of the composites was investigated using XRD and it was shown that the PGFs fibres are completely amorphous. Their antibacterial evaluation showed that there was an inversely proportional correlation between the amount of the cerium doped PGFs and to the biofilm formation as well as the viability of the cells.

These composites were found to be more efficient against Gram-positive rather than Gram-negative bacteria. The conditioning step implemented to the composite samples prior to their cell compatibility evaluation seemed to improve the cytocompatibility of the composites. When the direct incubation of the samples with NG108-15 the cell viability decreased drastically from day 1 to day 7. Most probably due to the high glass dissolution rate and hence the rapid release of ions; which significantly changes the localised pH influencing cell function and activity.

The physicochemical properties of the PHA matrixes (P(3HB), P(3HO-co-3HD) and 75/25 P(3HO-co-3HD)/P(3HB)), were affected differently by the GO in the composites of the various filler content (0.5, 2 and 5 wt%). The SEM micrographs revealed the presence of various size pinholes and flake-like, irregular shapes in some of the composites. Indicating, the different interference of the GO filler in the different polymer hosts. The presence of GO in the polymer matrices was detected by XRD only in the case of the P(3HB) composites, likely due to the poorer filler matrix interphase. Also, according to the DSC results, the addition of GO filler gave higher crystallinity to the polymeric matrix of the final composites. Moreover, the mechanical evaluation has shown that the addition of GO in the polymer matrices has in most cases acted as reinforced filler.

The presence of two polymers in the polymer blend, which the P(3HO-co-3HD) has longer aliphatic chains, created competition between the polymer chains and the GO, protecting the oxygen atoms along the polyester backbone and hence

diminishing the mechanical properties of the blend composite films. The overall hydrophilicity of the composites improved with the addition of the GO filler.
The surface with augmented content of the carbonyl (C=O) and carboxyl (O-C=OH) groups, ascribed to the presence of GO, was detected by XPS only in the case of the P(3HB)/5 wt% composite.

The antibacterial efficacy of these composites was assessed by direct contact test (DCT) – ISO 22196. In most cases, the number of free and planktonic bacteria decreased with the increase of the GO content for both Gram-positive and Gram-negative bacteria. No cytotoxicity was observed when the composites were tested indirectly and directly with L929 murine fibroblasts and NG108-15 neuronal cells. All composite samples showed good growth and proliferation for both cell lines.

The fluorescence micrographs confirmed the good cytocompatibility of the fabricated composites which was quantified by CellTiter Blue® assay. In all the experiments, the presence of GO at all concentrations (0.5, 1 and 5 wt%) increased the number of neuronal cells compared to the PHA controls. Moreover, the 75/25 composites containing (0.5, 2 and 5 wt%) GO revealed very good growth and differentiation of NG108-15 cells. The cell viability in these composite films was higher compared to the neat films when tested directly with the NG108-15 neuronal cells.
The neurite outgrowth evaluation on the composite blend films revealed that the addition of GO had a significant effect on neuronal expression and neurite length. The higher the GO content of 75/25 P(3HO-co-3HD)/P(3HB), the greater the number of neuronal cells expressing neurites. Overall, the addition of GO has shown to have a significant impact on the compatibility of the PHA films.

Finally, the 75/25 blend was used to fabricate 3D tubular structures. Here two strategies were utilized. First, hollow composite tubes containing (0.5, 2 and 5 wt%) GO were fabricated by dip moulding process. The addition of 0.5 and 2 wt% GO in the 75/25 blend resulted in softer composite tubes compared to the neat blend tube. While further increase of GO to 5 wt% enhanced the mechanical stability of the final conduit. The SEM micrographs showed smooth and homogenous surfaces intra and extraluminal of the composite tubes even with

the highest GO content. The cell viability after their direct incubation with tubes for a period of 7 days showed that there was a direct correlation between the GO content and the number of proliferated neuronal cells.
These hollow composite tubes were threaded with electrospun PHAs fibres. Different conditions were used to obtain the electrospun PHAs fibres produced from a 75/25 P(3HB)/P(3HO-co-3HD) blend. Various alignments, densities and fibre diameters were obtained. All the fibres were tested for their cytocompatibility with respect to the NG108-15 neuronal cells. All the produced fibres revealed good cytocompatibility allowing the proliferation and growth of the neuronal cells. The fibres produced in the first condition, where the target speed was 600 rpm, the syringe pump was set at 1 ml/h and the total time of electrospinning was 5 min, revealed greater cell viability than the rest fibres. The threaded hollow tubes were cut in 1 cm length for future *ex-vivo* experiments, by culturing Embryonic Chick Dorsal Root Ganglion Neurons (DRGs).

The second strategy was to develop a 2D mat based on the 75/25 P(3HB)/P(3HO-co-3HD) blend containing different amounts (37, 74 and 90 wt%) of aligned PGFs fibres. The films were allowed to dry and then rolled into a nerve conduit and adhered with the PHA polymer. The 4 cm long PGF composites showed different outer diameter depending on the amount of the incorporated PGFs. The SEM micrographs showed high alignment of the fibres in the polymer matrix however with uneven voids. In composites with the highest loading of the PGFs, loose fibres could be detected.
The incorporation of PGFs conferred intraluminal guidance and hence no further modification is required for these composites. Overall, the final structure showed flexibility and stability. The final composites were easy to handle and process. These tubes were cut into 1 cm long specimens, similar to the GO composite tubes, for their *ex-vivo* assessment by culturing Embryonic Chick Dorsal Root Ganglion Neurons (DRGs).

In summary, the solvent-casting method, dip moulding and the electrospinning technique, allowed the fabrication of nerve conduits with intraluminal guidance delivered either by the incorporated electropun fibres or the PGFs. From the preliminary cytocompatibility evaluation it can be conclude that the fabricated composite tubes are promising candidates for their use in nerve regeneration.

9.2 Future perspectives

The results obtained in this study demonstrated the possibility of using different types of PHAs and their blends for medical devices such as NGCs. The addition of compounds to impart antibacterial properties, has also led to changes in the physicochemical properties of the final composites. The results of this work indicate the ground research to be carried out in the following areas.

Starting from raw materials, optimisation studies of P(3HB) and P(3HO-co-3HD) production is required to enhance polymer yield and reduce production cost. The composition of the media and a cheap alternative source of carbon are two of the parameters that are needed to be investigated in addition to the fermentation process. Experimental design could be used as a valuable tool to achieve a more sustainable and cost-effective PHA production.

The solvent casting technique is an easy and fast process commonly used for film development. Since the solvent evaporation rate plays an important role in surface topography, a more controlled evaporation of the solvent should be considered. A temperature and humidity chamber could be used to resolve this issue or a solvent system with lower solvent-s volatility rate.

The fabrication of the blend polymers could be optimized by design experiments where the threshold of immiscibility could be predicted as closely as possible. An important parameter in this strategy is the molecular weight of the polymers used. Hence the reproducibility of the polymer properties obtained from the fermentation process is crucial.

With respect to the composite films, a deeper understanding of the intercalation / incorporation of the different fillers into various polymer matrices is required.

The 3D tubular structures developed in this study showed homogenous and reproducible specimens. However, this was a time consuming and long process. As an alternative, melt extrusion process could be used. In addition, a more sophisticated internal microstructure could be achieved using laser micropatterning.

Concerning the antibacterial tests, the antibacterial properties of the composite samples could be extended over longer periods, such as 14, 21 days evaluating

interval time points. In addition, the composites could be evaluated against already formed biofilm, obtained from different bacterial strains and investigated their ability to disrupt this mature biofilm. SEM images could also be utilized to visually support the findings from the various antibacterial tests. On another note, co-cultures of Gram-positive and Gram-negative bacteria could be treated with a known concentration that is effective against both strains and the efficacy of the samples evaluated when in the presence of both bacterial strains.

In addition to preliminary cytocompatibility studies using NG108-15 neuronal cells, further studies on their ability to support cell proliferation using a co-culture of NG108-15/RN22 Schwann cells, NG108-15/primary Schwann cells and/or dorsal root ganglion/Schwann cells, could be performed. Moreover, experiments could be conducted for longer time period rather only for 7 days.

Additionally, the use of a 3D bioreactor could provide a better perspective of the response of the cells to the samples transitioning from static to perfusion fluid flow culture, performing co-culture experiments.

In this study, one organic and two inorganic compounds were selected in order to confer antibacterial properties to the final specimens and to allow cell viability of the cell lines simultaneously. It will be worth exploring more GBMs as other potential agents, and phosphate glass fibres as possible antibacterial compounds with minimal reduction in the biocompatibility of the final specimens. Additionally, other molecules derived from nature, could be investigated for their potential antibacterial and cytocompatibility properties. Moreover, it would be of great value to evaluate 2D and 3D samples under static and dynamic *in vitro* degradation studies, to investigate the change of the composite material itself and also the effect of degradation and/or release of the compounds on the surrounding media. In addition, *in vivo* studies of the nerve conduit in small and large animals would provide valuable information about its actual biological functionality and any side effects of degradation of these biodegradable NGCs.

References

Abdala, A., Barrett, J. and Srienc, F. (2013). Synthesis of Poly-(R)-3 Hydroxyoctanoate (PHO) and Its Graphene Nanocomposites. *Green Polymer Chemistry: Biocatalysis and Materials II*, pp.199–209. doi: 10.1021/bk-2013-1144.ch014.

Abiy, E. and Berhe, A. (2016). Anti-Bacterial Effect of Garlic (Allium sativum) against Clinical Isolates of Staphylococcus aureus and Escherichia coli from Patients Attending Hawassa Referral Hospital, Ethiopia, *Journal of Infectious Diseases and Treatment*. doi: 10.21767/2472-1093.100023.

Abou Neel, E.A., Pickup, D.M., Valappil, S.P., Newport, R.J. and Knowles, J.C. (2009). Bioactive functional materials: a perspective on phosphate-based glasses. *J. Mater. Chem*., 19(6), pp.690–701. doi: 10.1039/B810675D.

Abu Hamdeh, S., Lytsy, B. and Ronne-Engström, E. (2014). Surgical site infections in standard neurosurgery procedures– a study of incidence, impact and potential risk factors. *British Journal of Neurosurgery*, 28(2), pp. 270–275. doi: 10.3109/02688697.2013.835376.

Ahmed, A. E. I. Hay, J.N., Bushell, M.E., Wardell, J.N. and Cavalli, G. (2008). Biocidal polymers (I): Preparation and biological activity of some novel biocidal polymers based on uramil and its azo-dyes. *Reactive and Functional Polymers*, 68(1), pp. 248–260. doi: 10.1016/j.reactfunctpolym.2007.09.004.

Ahmed, I., Jones, I.A., Parsons, A.J., Bernard, J., Farmer, J., Scotchford, C.A., Walker, G.S. and Rudd, C.D. (2011). Composites for bone repair: phosphate glass fibre reinforced PLA with varying fibre architecture. *Journal of Materials Science: Materials in Medicine*, 22(8), pp. 1825–1834. doi: 10.1007/s10856-011-4361-0.

Ahmed, I., Lewis, M., Olsen, I. and Knowles, J.C. (2004). Phosphate glasses for tissue engineering: Part 1. Processing and characterisation of a ternary-based P2O5-CaO-Na2O glass system. *Biomaterials,* 25(3), pp. 491–507. doi: 10.1016/s0142-9612(03)00546-5.

Ahmed, I., Ready, D., Wilson, M. and Knowles, J.C. (2006). Antimicrobial effect of silver-doped phosphate-based glasses. *Journal of Biomedical Materials Research Part A*., 79A (3), pp. 618–626. doi: 10.1002/jbm.a.30808.

Ahmed, I., Ren, H. and Booth, J. (2019). Developing unique geometries of phosphate-based glasses and their prospective biomedical applications. *Johnson*

Matthey Technology Review, pp. 34–42. doi: 10.1595/205651319X15426460058863.

Ahmed, N. A. A. M. (2011). Bacterial Resistance and Challenges of Biocide Plastics. *Antimicrobial Polymers,* pp. 23–49. doi: 10.1002/9781118150887.ch2.

Ain, Q. T., Haq, S.H., Alshammari, A., Al-Mutlaq, M.A. and Anjum, M.N. (2019). The systemic effect of PEG-nGO-induced oxidative stress in vivo in a rodent model. *Beilstein Journal of Nanotechnology*, *Beilstein-Institut Zur Forderung der Chemischen Wissenschaften*, 10, pp. 901–911. doi: 10.3762/BJNANO.10.91.

Ajibade, P.A. and Kolawole, G.A., (2008). Synthesis, characterization, antiplasmodial and antitrypanosomal activity of some metal (III) complexes of sulfadiazine. *Bulletin of the Chemical Society of Ethiopia*, pp. 261-268.

Akhavan, O. and Ghaderi, E. (2010). Toxicity of Graphene and Graphene Oxide Nanowalls Against Bacteria. *ACS Nano,* 4(10), pp. 5731–5736.

Akhavan, O., Ghaderi, E., Abouei, E., Hatamie, S. and Ghasemi, E. (2014). Accelerated differentiation of neural stem cells into neurons on ginseng-reduced graphene oxide sheets. *Carbon*, *66*, pp. 395–406. doi: 10.1016/j.carbon.2013.09.015.

Alarfaj, A. A., Lee, H. H., Munusamy, M. A., Ling, Q., Kumar, S., Chang, Y., Chen, Y., Lin, H., Lu, Y., Wu, G. and Higuchi, (2016) Development of biomaterial surfaces with and without microbial nanosegments, *Journal of Polymer Engineering*. Walter de Gruyter GmbH, pp. 1–12. doi: 10.1515/polyeng-2015-0046.

Alberti, K. A., Neufeld, C.I., Wang, J. and Xu, Q. (2016). In Vivo Peripheral Nerve Repair Using Tendon-Derived Nerve Guidance Conduits. *ACS Biomaterials Science and Engineering,* 2(6), pp. 937–945. doi: 10.1021/acsbiomaterials.6b00034.

Alsharabasy AM, A. (2018). A Mini-Review on the Bioactive Glass-Based Composites in Soft Tissue Repair. *Bioceramics Development and Applications*. OMICS Publishing Group, 08(01). doi: 10.4172/2090-5025.1000105.

Amache, R. A., Safari, M., Roy, I. and Keshavarz, T. (2013). Advances in PHAs production. *Chemical Engineering Transactions*, 32, pp. 931–936. doi: 10.3303/CET1332156.

Ameer, S. and Gul, I. H. (2016). Influence of Reduced Graphene Oxide on Effective Absorption Bandwidth Shift of Hybrid Absorbers. *PLOS ONE*, 11(6). doi: 10.1371/journal.pone.0153544.

Anbukarasu, P., Sauvageau, D. and Elias, A. (2016). Tuning the properties of polyhydroxybutyrate films using acetic acid via solvent casting. *Scientific Reports*, Nature Publishing Group, 5(1), p. 17884. doi: 10.1038/srep17884.

Anderson, R. L. (1989). Lodophor Antiseptics: Intrinsic Microbial Contamination with Resistant Bacteria. *Infection Control and Hospital Epidemiology,* 10(10), pp. 443–446. doi: 10.1086/645918

Anjum, A., Zuber, M., Zia, K.M., Noreen, A., Anjum, M.N. and Tabasum, S. (2016). Microbial production of polyhydroxyalkanoates (PHAs) and its copolymers: A review of recent advancements. *International Journal of Biological Macromolecules*, 89, pp. 161–174. doi: 10.1016/j.ijbiomac.2016.04.069.

Ankri, S. and Mirelman, D. (1999). Antimicrobial properties of allicin from garlic. *Microbes and Infection*, pp. 125–129. doi: 10.1016/S1286-4579(99)80003-3.

Ankri, S., Miron, T., Rabinkov, A., Wilchek, M. and Mirelman, D. (1997). Allicin from garlic strongly inhibits cysteine proteinases and cytopathic effects of Entamoeba histolytica. *Antimicrobial agents and chemotherapy*, American Society for Microbiology (ASM), 41(10), pp. 2286–8. Available at: http://www.ncbi.nlm.nih.gov/pubmed/9333064 (Accessed: 7 October 2019).

Antibiotic resistance—the need for global solutions. (2014). *British Dental Journal,* 216(3), pp.133–133. doi: 10.1038/sj.bdj.2014.77.

Arslantunali, D., D., Dursun, T., Yucel, D. and Hasirci, N. (2014). Peripheral nerve conduits: Technology update. *Medical Devices: Evidence and Research,* 7, pp. 405–424. doi: 10.2147/MDER.S59124.

Artini, M., Papa, R., Barbato, G., Scoarughi, G.L., Cellini, A., Morazzoni, P., Bombardelli, E. and Selan, L. (2012). Bacterial biofilm formation inhibitory activity revealed for plant derived natural compounds. *Bioorganic and Medicinal Chemistry,* 20(2), pp. 920–926. doi: 10.1016/j.bmc.2011.11.052.

Bachmann, B. M. and Seebach, D. (1999). Investigation of the enzymatic cleavage of diastereomeric oligo(3-hydroxybutanoates) containing two to eight HB units. A model for the stereoselectivity of PHB depolymerase from Alcaligenes faecalis T1. *Macromolecules,* 32(6), pp. 1777–1784. doi: 10.1021/ma981496w.

Bae, B.-S. and Weinberg, M. C. (1991). Oxidation-Reduction Equilibrium in Copper Phosphate Glass Melted in Air. *Journal of the American Ceramic Society,* 74(12), pp. 3039–3045. doi: 10.1111/j.1151-2916.1991.tb04299.x.

Bakri, I. M. and Douglas, C. W. I. (2005). Inhibitory effect of garlic extract on oral bacteria. *Archives of Oral Biology*, 50(7), pp. 645–651. doi: 10.1016/j.archoralbio.2004.12.002.

Ballantyne, J. P. (1980). Critical Resection Length and Gap Distance in Peripheral Nerves. *Journal of Neurology, Neurosurgery & Psychiatry,* 43(1), pp. 96–96. doi: 10.1136/jnnp.43.1.96.

Baptist, J. N. (1960). Process for preparing poly-beta-hydroxybutyric acid. US Patent No. 3.182.036,. Available at: https://patents.google.com/patent/US3044942A/en (Accessed: 28 March 2018).

Barreto, L. S., Tokumoto, M.S., Guedes, I.C., Melo, H.G. de, Amado, F.D.R. and Capelossi, V.R. (2017). Evaluation of the anticorrosion performance of peel garlic extract as corrosion inhibitor for ASTM 1020 carbon steel in acidic solution. *Matéria* (Rio de Janeiro). Revista Matéria, 22(3). doi: 10.1590/s1517-707620170003.0186.

Barrett, J. S. F., Abdala, A. A. and Srienc, F. (2014). Poly(hydroxyalkanoate) elastomers and their graphene nanocomposites. *Macromolecules,* 47(12), pp. 3926–3941. doi: 10.1021/ma500022x.

Barzic, A. I. and Ioan, S. (2015). Antibacterial Drugs — From Basic Concepts to Complex Therapeutic Mechanisms of Polymer Systems. *Concepts, Compounds and the Alternatives of Antibacterials.* Available at: http://www.intechopen.com/books/concepts-compounds-and-the-alternatives-of-antibacterials.

Basnett, P. and Roy, I. (2010). Microbial Production of Biodegradable Polymers and their Role in Cardiac Stent Development. Current Research, Technology and Education Topics in Applied Microbiology and Microbial *Biotechnology*, pp. 1405–1415.

Basnett, P., Ching, K.Y., Stolz, M., Knowles, J.C., Boccaccini, A.R., Smith, C., Locke, I.C., Keshavarz, T. and Roy, I. (2013). Novel Poly(3-hydroxyoctanoate)/Poly(3-hydroxybutyrate) blends for medical applications. *Reactive and Functional Polymers*, 73(10), pp. 1340–1348. doi: 10.1016/j.reactfunctpolym.2013.03.019.

Batakliev, T., Petrova-Doycheva, I., Angelov, V., Georgiev, V., Ivanov, E., Kotsilkova, R., Casa, M., Cirillo, C., Adami, R., Sarno, M. and Ciambelli, P. (2019). Effects of graphene nanoplatelets and multiwall carbon nanotubes on the structure and mechanical properties of Poly(lactic acid) composites: A comparative study. *Applied Sciences* 9(3), p.469. doi: 10.3390/app9030469.

Belkas, J. S., Shoichet, M. S. and Midha, R. (2004). Peripheral nerve regeneration through guidance tubes. *Neurological Research,* 26(2), pp. 151–160. doi: 10.1179/016164104225013798.

Bellucci, D., Cannillo, V., Sola, A., Chiellini, F., Gazzarri, M. and Migone, C. (2011). Macroporous Bioglass®-derived scaffolds for bone tissue regeneration. *Ceramics International,* 37(5), pp. 1575–1585. doi: 10.1016/j.ceramint.2011.01.023.

Bhawal, P., Ganguly, S., Chaki, T.K. and Das, N.C. (2016). Synthesis and characterization of graphene oxide filled ethylene methyl acrylate hybrid nanocomposites. *RSC Advances*, 6(25), pp. 20781–20790. doi: 10.1039/c5ra24914g.

Biot, C., Delhaes, L.A., N'Daiye, C.M., Maciejewski,L., Camus, D., Dive, D and Brocard, J.S. (2000). Synthesis and potential metabolites of ferrochloroquine and related compounds. Biorg. *Med. Chem,* 7, 2843-2846.

Bitar, M., Salih, V., Knowles, J.C. and Lewis, M.P. (2008). Iron-phosphate glass fiber scaffolds for the hard-soft interface regeneration: The effect of fiber diameter and flow culture condition on cell survival and differentiation. *Journal of Biomedical Materials Research - Part A,* 87(4), pp. 1017–1026. doi: 10.1002/jbm.a.31855.

Bitar, M., Salih, V., Mudera, V., Knowles, J.C. and Lewis, M.P. (2004). Soluble phosphate glasses: in vitro studies using human cells of hard and soft tissue origin. *Biomaterials,* 25(12), pp. 2283–2292. doi: 10.1016/J.BIOMATERIALS.2003.08.054.

Blomstedt, G. C. (1985). Infections in neurosurgery: a retrospective study of 1143 patients and 1517 operations., *Acta Neurochirurgica*, 78(3–4), pp. 81–90. Available at: http://www.ncbi.nlm.nih.gov/pubmed/3911746 (Accessed: 27 November 2018).

Bobbarala, V. (2012). *A Search for Antibacterial Agents*. InTech. doi: 10.5772/1085.

Borlinghaus, J., Albrecht, F., Gruhlke, M., Nwachukwu, I. and Slusarenko, A. (2014). Allicin: Chemistry and Biological Properties. *Molecules,* 19(8), pp. 12591–12618. doi: 10.3390/molecules190812591.

Borschel, G. H., Kia, K.F., Kuzon, W.M. and Dennis, R.G. (2003). Mechanical properties of acellular peripheral nerve. *Journal of Surgical Research,* 114(2), pp. 133–139. doi: 10.1016/S0022-4804(03)00255-5.

Bozkurt, A., Brook, G.A., Moellers, S., Lassner, F., Sellhaus, B., Weis, J., Woeltje, M., Tank, J., Beckmann, C., Fuchs, P., Damink, L.O., Schügner, F., Heschel, I. and Pallua, N. (2007) In vitro assessment of axonal growth using dorsal root ganglia

explants in a novel three-dimensional collagen matrix. *Tissue engineering*, 13(12), pp. 2971–9. doi: 10.1089/ten.2007.0116.

Braunegg, G., Lefebvre, G. and Genser, K. F. (1998). Polyhydroxyalkanoates, biopolyesters from renewable resources: physiological and engineering aspects. *Journal of Biotechnology*, 65(2–3), pp. 127–61. Available at: http://www.ncbi.nlm.nih.gov/pubmed/9828458 (Accessed: 28 March 2018).

Bryers, J. D. (2008). Medical biofilms. *Biotechnology and Bioengineering,* pp. 1–18. doi: 10.1002/bit.21838.

Bunting, S., DI SILVIO, L., DEB, S. and HALL, S. (2005). Bioresorbable glass fibres facilitate peripheral nerve regeneration. *Journal of Hand Surgery,* 30(3), pp. 242–247. doi: 10.1016/j.jhsb.2004.11.003.

C Tella, A. and A Obaleye, J., (2009). Copper (II) Complexes of 4, 4-diaminodiphenylsulphone: synthesis, characterization and biological studies. *Journal of Chemistry,* 6(S1), pp. S311-S323.

Cai, X., Dai, G.-J., Tan, S.-Z., Ouyang, Y., Ouyang, Y.-S. and Shi, Q.-S. (2012). Synergistic antibacterial zinc ions and cerium ions loaded α-zirconium phosphate. *Materials Letters,* 67(1), pp. 199–201. doi: 10.1016/j.matlet.2011.09.041.

Cavanaugh, M., Silantyeva, E., Pylypiv Koh, G., Malekzadeh, E., Lanzinger, W.D., Willits, R.K. and Becker, M.L. (2019). RGD-modified nanofibers enhance outcomes in rats after sciatic nerve injury. *Journal of Functional Biomaterials,* 10(2), p. 24. doi: 10.3390/jfb10020024.

Centers for Disease Control and Prevention (2019). *Biggest Threats and Data* | Antibiotic/Antimicrobial Resistance | CDC. Available at: https://www.cdc.gov/drugresistance/biggesthreats.html?CDC_AA_refVal=https%3A%2F%2Fwww.cdc.gov%2Fdrugresistance%2Fbiggest_threats.html (Accessed: 14 October 2018).

Chen, A., Shi, Q., Feng, J., Ouyang, Y., Chen, Y. and Tan, S. (2010). Dissociation of outer membrane for Escherichia coli cell caused by cerium nitrate. *Journal of Rare Earths,* 28(2), pp. 312–315. doi: 10.1016/S1002-0721(09)60103-4.

Chen, G.-Q. (2009). A microbial polyhydroxyalkanoates (PHA) based bio- and materials industry. *Chemical Society Reviews,* 38(8), p. 2434. doi: 10.1039/b812677c.

Chrząszcz, P., Derbisz, K., Suszyński, K., Miodoński, J., Trybulski, R., Lewin-Kowalik, J. and Marcol, W. (2018). Application of peripheral nerve conduits in clinical

practice: A literature review. Polish Journal of *Neurology and Neurosurgery*, 52, pp. 427–435. doi: 10.1016/j.pjnns.2018.06.003.

Chung, C., Kim, Y.-K., Shin, D., Ryoo, S.-R., Hong, B.H. and Min, D.-H. (2013). Biomedical Applications of Graphene and Graphene Oxide. *Accounts of Chemical Research,* 46(10), pp. 2211–2224. doi: 10.1021/ar300159f.

Ciraldo, F. E., Boccardi, E., Melli, V., Westhauser, F. and Boccaccini, A.R. (2018). Tackling bioactive glass excessive in vitro bioreactivity: Preconditioning approaches for cell culture tests. *Acta Biomaterialia*, 75, pp. 3–10. doi: 10.1016/J.ACTBIO.2018.05.019.

Ciszewski, M., Mianowski, A., Szatkowski, P., Nawrat, G. and Adamek, J. (2015). Reduced graphene oxide–bismuth oxide composite as electrode material for supercapacitors. *Ionics,* 21(2), pp. 557–563. doi: 10.1007/s11581-014-1182-4.

Clabots, C. R., Johnson, S., Olson, M.M., Peterson, L.R. and Gerding, D.N. (1992). Acquisition of Clostridium difficile by Hospitalized Patients: Evidence for Colonized New Admissions as a Source of Infection. *Journal of Infectious Diseases,* 166(3), pp. 561–567. doi: 10.1093/infdis/166.3.561.

Collection, S. (2016). The discovery of artemisinin and Nobel Prize in Physiology or Medicine. *Sci China Life Sci.,* 8(5), pp. 583–592.

Cowan, M. M. (1999). Plant products as antimicrobial agents. *Clinical microbiology reviews,* 12(4), pp. 564–82. doi: 10.1128/CMR.12.4.564

Daly, W., Yao, L., Zeugolis, D., Windebank, A. and Pandit, A. (2012). A biomaterials approach to peripheral nerve regeneration: Bridging the peripheral nerve gap and enhancing functional recovery. *Journal of the Royal Society Interface,* 9(67), pp.202–221. doi: 10.1098/rsif.2011.0438.

Das, S.S., Baranwal, B.P., Gupta, C.P. and Singh, P. (2003). Characteristics of solid-state batteries with zinc/cadmium halide-doped silver phosphate glasses as electrolytes. *Journal of Power Sources,* 114(2), pp. 346–351. doi: 10.1016/S0378-7753(02)00604-3.

Das, T. K. and Prusty, S. (2013). Graphene-Based Polymer Composites and Their Applications. *Polymer-Plastics Technology and Engineering,* 52(4), pp. 319–331. doi: 10.1080/03602559.2012.751410.

de Ruiter, G.C.W., Malessy, M.J.A., Yaszemski, M.J., Windebank, A.J. and Spinner, R.J. (2009). Designing ideal conduits for peripheral nerve repair. *Neurosurgical Focus*, 26(2), p.E5. doi: 10.3171/FOC.2009.26.2.E5.

Dettenkofer, M. and Spencer, R. C. (2007). Importance of environmental decontamination--a critical view. *Journal of Hospital infection,* 65, pp. 55–57. doi: 10.1016/S0195-6701(07)60016-4.

Dinescu, S., Ionita, M., Pandele, A.M., Galateanu, B., Iovu, H., Ardelean, A., Costache, M. and Hermenean, A. (2014). In vitro cytocompatibility evaluation of chitosan/graphene oxide 3D scaffold composites designed for bone tissue engineering. *Bio-Medical Materials and Engineering*, 24(6), pp. 2249–2256. doi: 10.3233/BME-141037.

Dizaj, S. M., Lotfipour, F., Barzegar-Jalali, M., Zarrintan, M.H. and Adibkia, K. (2014). Antimicrobial activity of the metals and metal oxide nanoparticles. *Materials Science and Engineering C.* Elsevier B.V., 44, pp. 278–284. doi: 10.1016/j.msec.2014.08.031.

Doyle C, Tanner ET, B. W. (1991). In vitro and in vivo evaluation of polyhydroxybutyrate and of polyhydroxybutyrate reinforced with hydroxyapatite. *Biomaterials,* 12(9), pp. 841–847.

Dubey, N., Bentini, R., Islam, I., Cao, T., Castro Neto, A.H. and Rosa, V. (2015). Graphene: A Versatile Carbon-Based Material for Bone Tissue Engineering. *Stem Cells International,* doi: 10.1155/2015/804213.

Duncan, Duncan, S.F., Kakinoki, R., Rizzo, M. and Kang, W. (2015). Extrusion of a neurotube: a case report. *Ochsner Journal,* 15(2), pp.191-192.

E. Matuschek and D. F. J. Brown and G. Kahlmeter (2014). Development of the EUCAST disk diffusion antimicrobial susceptibility testing method and its implementation in routine microbiology laboratories. *Clinical Microbiology and Infection,* 20(4), pp. 255–266. doi: 10.1111/1469-0691.12373.

Ege, D., Kamali, A. R. and Boccaccini, A. R. (2017). Graphene Oxide/Polymer-Based Biomaterials. *Advanced Engineering Materials,* 19, pp. 1–22. doi: 10.1002/adem.201700627.

El-Ghannam, A., Ducheyne, P. and Shapiro, I. M. (1995). Bioactive material template forin vitro, synthesis of bone. *Journal of Biomedical Materials Research,* 29(3), pp. 359–370. doi: 10.1002/jbm.820290311.

El-Refaie Kenawy, S. D. Worley, and Broughton, R. (2007). The Chemistry and Applications of Antimicrobial Polymers: A State-of-the-Art Review. *Biomacromolecules,* 8(5), pp.1359–1384. Available at:

http://pubs.acs.org/doi/abs/10.1021/bm061150q#.WAzyOb03KSE.mendeley (Accessed: 23 October 2016).

Emil, S.E. and Albert, P.R., Wyeth Holdings LLC, 1967. *Surgical sutures.* U.S. Patent 3,297,033. Available at: https://patents.google.com/patent/US3297033A/en (Accessed: 28 March 2018).

Emiru, T. F. and Ayele, D. W. (2017). Controlled synthesis, characterization and reduction of graphene oxide: A convenient method for large scale production. *Egyptian Journal of Basic and Applied Sciences,* 4(1), pp. 74–79. doi: 10.1016/j.ejbas.2016.11.002.

Ervina, J., Mariatti, M. and Hamdan, S. (2016). ScienceDirect Effect of Filler Loading on the Tensile Properties of Multi-walled Carbon Nanotube and Graphene Nanopowder filled Epoxy Composites. *Procedia Chemistry,* 19(19), pp. 897–905. doi: 10.1016/j.proche.2016.03.132.

Evans, G. R. (2001). Peripheral nerve injury: a review and approach to tissue engineered constructs. *The Anatomical record,* 263(4), pp. 396–404. doi: 10.1002/ar.1120.

Fabbro, A., Scaini, D., León, V., Vázquez, E., Cellot, G., Privitera, G., Lombardi, L., Torrisi, F., Tomarchio, F., Bonaccorso, F., Bosi, S., Ferrari, A.C., Ballerini, L. and Prato, M. (2016). Graphene-Based interfaces do not alter target nerve cells. *ACS Nano,* 10(1), pp. 615–623. doi: 10.1021/acsnano.5b05647.

Fama, L., Bittante, A.M.B.Q., Sobral, P.J.A., Goyanes, S. and Gerschenson, L.N. (2010). Garlic powder and wheat bran as fillers: Their effect on the physicochemical properties of edible biocomposites. *Materials Science & Engineering C,* 30(6), pp. 853–859. doi: 10.1016/j.msec.2010.03.022.

Farias, I. A. P., Dos Santos, C. C. L. and Sampaio, F. C. (2018). Antimicrobial activity of cerium oxide nanoparticles on opportunistic microorganisms: A systematic review. *BioMed Research International,* pp. 1–14. doi: 10.1155/2018/1923606.

Farrukh, A., Zhao, S. and del Campo, A. (2018). Microenvironments Designed to Support Growth and Function of Neuronal cells. *Frontiers in Materials,*5. doi: 10.3389/fmats.2018.00062.

Feldberg, R. S., Chang, S.C., Kotik, A.N., Nadler, M., Neuwirth, Z., Sundstrom, D.C. and Thompson, N.H. (1988). In vitro mechanism of inhibition of bacterial cell growth by allicin. *Antimicrobial agents and chemotherapy,* 32(12), pp. 1763–1768. doi: 10.1128/AAC.32.12.1763.

Fernandes, H.R., Gaddam, A., Rebelo, A., Brazete, D., Stan, G.E. and Ferreira, J.M.F. (2018). Bioactive Glasses and Glass-Ceramics for Healthcare Applications in Bone Regeneration and Tissue Engineering. *Materials*, 11(12), p.2530. : 10.3390/ma11122530.

Figueroa López, K.J., Torres Vargas, O.L., Prías Barrgán, J.J. and Ariza Calderón, H. (2014). Caracterización óptica y estructural de nanopartículas de Allium sativum L. impregnadas en lomo de bovino. *Acta Agronómica,* 64(1), pp.54–60. doi: 10.15446/acag.v64n1.43651.

Fradkin, J.E. and Rodgers, G.P. (2013). Diabetes Research: A Perspective From the National Institute of Diabetes and Digestive and Kidney Diseases. *Diabetes,* [online] 62(2), pp.320–326. Available at: https://www.ncbi.nlm.nih.gov/pmc/articles/PMC3554357/ [Accessed 22 Nov. 2019].

Francis, L., Meng, D., Knowles, J., Keshavarz, T., Boccaccini, A. and Roy, I. (2011). Controlled Delivery of Gentamicin Using Poly(3-hydroxybutyrate) Microspheres. I*nternational Journal of Molecular Sciences,* 12(7), pp.4294–4314.

Franks, K., Abrahams, I. and Knowles, J. C. (2000). Development of soluble glasses for biomedical use part I: In vitro solubility measurement. *Journal of Materials Science: Materials in Medicine,* 11(10), pp. 609–614. doi: 10.1023/A:1008949527695.

Gao, Y., Wu, J., Ren, X., Tan, X., Hayat, T., Alsaedi, A., Cheng, C. and Chen, C. (2017). Impact of graphene oxide on the antibacterial activity of antibiotics against bacteria. *Environmental Science: Nano,* 4(5), pp.1016–1024. doi: 10.1039/C7EN00052A.

Gaudin, R., Knipfer, C., Henningsen, A., Smeets, R., Heiland, M. and Hadlock, T. (2016). Approaches to Peripheral Nerve Repair: Generations of Biomaterial Conduits Yielding to Replacing Autologous Nerve Grafts in Craniomaxillofacial Surgery. *BioMed Research International,* 2016, pp.1–18. doi: 10.1155/2016/3856262.

Gebreselema Gebreyohannes and and Mebrahtu Gebreyohannes (2013). Medicinal values of garlic: A review. *International Journal of Medicine and Medical Sciences,* 5(9), pp. 401–408. doi: 10.5897/IJMMS2013.0960.

Gilchrist, T., Glasby, M.A., Healy, D.M., Kelly, G., Lenihan, D.V., McDowall, K.L., Miller, I.A. and Myles, L.M., (1998). In vitro nerve repair in vivo. The reconstruction of peripheral nerves by enturbulation with biodegradable glass tubes—a preliminary report. *British journal of plastic surgery*, *51*(3), pp.231-237.

Gilchrist, T., Healy, D. M. and Drake, C. (1991). Controlled silver-releasing polymers and their potential for urinary tract infection control. *Biomaterials,* 12(1), pp. 76–80. doi: 10.1016/0142-9612(91)90136-x.

Gironi, F. and Piemonte, V. (2011). Bioplastics and Petroleum-based Plastics: Strengths and Weaknesses. *Energy Sources, Part A: Recovery, Utilization, and Environmental Effects,* 33(21), pp. 1949–1959. doi: 10.1080/15567030903436830.

Goh, Y.-F., Alshemary, A.Z., Akram, M., Abdul Kadir, M.R. and Hussain, R. (2014). In-vitro characterization of antibacterial bioactive glass containing ceria. *Ceramics International,* 40(1), pp.729–737. doi: 10.1016/j.ceramint.2013.06.062.

Grinsell, D. and Keating, C.P. (2014). Peripheral Nerve Reconstruction after Injury: A Review of Clinical and Experimental Therapies. *BioMed Research International,* [online] 2014, pp.1–13. Available at: https://www.hindawi.com/journals/bmri/2014/698256/ [Accessed 17 May 2019]. doi: 10.1155/2014/698256.

Gruhlke, M., Nicco, C., Batteux, F. and Slusarenko, A. (2016). The Effects of Allicin, a Reactive Sulfur Species from Garlic, on a Selection of Mammalian Cell Lines. *Antioxidants,* 6(1), p.1. doi: 10.3390/antiox6010001.

Guo, H.-L., Wang, X.-F., Qian, Q.-Y., Wang, F.-B. and Xia, X.-H. (2009). A Green Approach to the Synthesis of Graphene Nanosheets. *ACS Nano,* 3(9), pp.2653–2659. doi: 10.1021/nn900227d.

Guo, W., Qiu, J., Liu, J. and Liu, H. (2017). Graphene microfiber as a scaffold for regulation of neural stem cells differentiation. *Scientific Reports,* 7(1) pp. 1–8. doi: 10.1038/s41598-017-06051-z.

Han, N., Jiang, B.-G., Zhang, P.-X., Kou, Y.-H., Zhu, Q.-T., Liu, X.-L., Quan, D.-P. and Chen, J.-G. (2019). Tissue engineering for the repair of peripheral nerve injury. *Neural Regeneration Research. Wolters Kluwer Medknow Publications,* 14(1), pp. 51–58. doi: 10.4103/1673-5374.243701.

Han, Y., Luo, Z., Yuwen, L., Tian, J., Zhu, X. and Wang, L. (2013). Synthesis of silver nanoparticles on reduced graphene oxide under microwave irradiation with starch as an ideal reductant and stabilizer. *Applied Surface Science,* 266, pp.188–193doi: 10.1016/j.apsusc.2012.11.132.

Hasan, M., Ahmed, I., Parsons, A., Walker, G. and Scotchford, C. (2012). Cytocompatibility and Mechanical Properties of Short Phosphate Glass Fibre Reinforced Polylactic Acid (PLA) Composites: Effect of Coupling Agent Mediated

Interface. *Journal of Functional Biomaterials,* 3(4), pp.706–725. doi: 10.3390/jfb3040706.

Hazari, A., Johansson-Rudén, G., Junemo-Bostrom, K., Ljungberg, C., TerenghI, G., Green, C. and Wlberg, M. (1999). A New Resorbable Wrap-Around Implant as an Alternative Nerve Repair Technique. *Journal of Hand Surgery,* 24(3), pp.291–295. doi: 10.1054/jhsb.1998.0001.

Hazer, B. (2010). Amphiphilic Poly(3-hydroxy alkanoate)s: Potential Candidates for Medical Applications. *International Journal of Polymer Science,* 2010, pp.1–8. doi: 10.1155/2010/423460.

Hazer, B. and Steinbüchel, A. (2007). Increased diversification of polyhydroxyalkanoates by modification reactions for industrial and medical applications. *Applied Microbiology and Biotechnology,* pp. 1–12. doi: 10.1007/s00253-006-0732-8.

Hegab, H.M., ElMekawy, A., Zou, L., Mulcahy, D., Saint, C.P. and Ginic-Markovic, M. (2016). The controversial antibacterial activity of graphene-based materials. *Carbon,* 105, pp.362–376. doi: 10.1016/j.carbon.2016.04.046.

Hench, L. (1970). Semiconducting glass-ceramics. *Journal of Non-Crystalline Solids,* North-Holland, 2, pp. 250–277. doi: 10.1016/0022-3093(70)90143-2.

Hiromi Matsusaki, Hideki Abe, and Doi, Y. (2000). Biosynthesis and Properties of Poly(3-hydroxybutyrate-co-3-hydroxyalkanoates) by Recombinant Strains of Pseudomonas sp. 61-3. *Biomacromolecules,* 1(1), pp.17–22. doi: 10.1021/BM9900040.

Holm, R.H., Kennepohl, P. and Solomon, E.I. (1996). Structural and Functional Aspects of Metal Sites in Biology. *Chemical Reviews*, 96(7), pp.2239–2314. doi: 10.1021/cr9500390.

Holmes P.A., Wright L.F., Collins, S. H. (1982). Copolyesters and process for their production. European Patent No. 69.497. Available at: https://encrypted.google.com/patents/EP0069497A2?cl=fi (Accessed: 28 March 2018).

Hoppe, A., Güldal, N.S. and Boccaccini, A.R. (2011). A review of the biological response to ionic dissolution products from bioactive glasses and glass-ceramics. *Biomaterials,* 32(11), pp.2757–2774. doi: 10.1016/j.biomaterials.2011.01.004.

Hu, W., Peng, C., Luo, W., Lv, M., Li, X., Li, D., Huang, Q. and Fan, C. (2010). Graphene-Based Antibacterial Paper. *ACS Nano,* 4(7), pp.4317–4323. doi: 10.1021/nn101097v.

Huang, X., He, J., Sun, K., Chen, Y., Zha, Z. and Zhou, C. (2018). Liquid crystal behavior and cytocompatibility of graphene oxide dispersed in sodium alginate solutions. *Carbon,* 129, pp.258–269. doi: 10.1016/j.carbon.2017.12.006.

Huang, Y.-C., Huang, Y.-Y., Huang, C.-C. and Liu, H.-C. (2005). Manufacture of porous polymer nerve conduits through a lyophilizing and wire-heating process. *Journal of Biomedical Materials Research Part B: Applied Biomaterials,* 74B (1), pp.659–664. doi: 10.1002/jbm.b.30267.

Hummers, W. S. and Offeman, R. E. (1958). Preparation of Graphitic Oxide. *Journal of the American Chemical Society. American Chemical Society,* 80(6), pp. 1339–1339. doi: 10.1021/ja01539a017.

Islam, M.T., Felfel, R.M., Abou Neel, E.A., Grant, D.M., Ahmed, I. and Hossain, K.M.Z. (2017). Bioactive calcium phosphate–based glasses and ceramics and their biomedical applications: A review. *Journal of Tissue Engineering,* SAGE PublicationsSage UK: London, England, 8. doi: 10.1177/2041731417719170.

iu, S., Hu, M., Zeng, T.H., Wu, R., Jiang, R., Wei, J., Wang, L., Kong, J. and Chen, Y. (2012). Lateral Dimension-Dependent Antibacterial Activity of Graphene Oxide Sheets. *Langmuir,* 28(33), pp.12364–12372. doi: 10.1021/la3023908.

Izumi, C. M. S. and Temperini, M. L. A. (2010). FT-Raman investigation of biodegradable polymers: Poly(3-hydroxybutyrate) and poly(3-hydroxybutyrate-co-3-hydroxyvalerate). *Vibrational Spectroscopy,* 54(2), pp. 127–132. doi: 10.1016/j.vibspec.2010.07.011.

Jendrossek, D. (1998). Microbial degradation of polyesters: a review on extracellular poly(hydroxyalkanoic acid) depolymerases. *Polymer Degradation and Stability,* 59(1–3), pp. 317–325. doi: 10.1016/S0141-3910(97)00190-0.

Jendrossek, D., Schirmer, A. and Schlegel, H. G. (1996). Biodegradation of polyhydroxyalkanoic acids. *Applied Microbiology and Biotechnology,* 46(5–6), pp. 451–63. Available at: http://www.ncbi.nlm.nih.gov/pubmed/9008883 (Accessed: 3 April 2018).

Ji, H., Sun, H. and Qu, X. (2016). Antibacterial applications of graphene-based nanomaterials: Recent achievements and challenges. *Advanced Drug Delivery Reviews,* 105, pp. 176–189. doi: 10.1016/j.addr.2016.04.009.

Jiang, X., Mi, R., Hoke, A. and Chew, S.Y. (2012). Nanofibrous nerve conduit-enhanced peripheral nerve regeneration. *Journal of Tissue Engineering and Regenerative Medicine,* 8(5), pp.377–385. doi: 10.1002/term.1531

Johra, F. T., Lee, J. W. and Jung, W. G. (2014). Facile and safe graphene preparation on solution based platform. *Journal of Industrial and Engineering Chemistry,* 20(5), pp. 2883–2887. doi: 10.1016/j.jiec.2013.11.022.

Kalbermatten, D.F., Kingham, P.J., Mahay, D., Mantovani, C., Pettersson, J., Raffoul, W., Balcin, H., Pierer, G. and Terenghi, G. (2008). Fibrin matrix for suspension of regenerative cells in an artificial nerve conduit. *Journal of Plastic, Reconstructive & Aesthetic Surgery,* 61(6), pp.669–675. doi: 10.1016/j.bjps.2007.12.015.

Kato, M., Bao, H.J., Kang, C.-K., Fukui, T. and Doi, Y. (1996). Production of a novel copolyester of 3-hydroxybutyric acid and medium-chain-length 3-hydroxyalkanoic acids by Pseudomonas sp. 61-3 from sugars. *Applied Microbiology and Biotechnology,* 45(3), pp.363–370. doi: 10.1007/s002530050697.

Kehoe, S., Zhang, X. F. and Boyd, D. (2012). FDA approved guidance conduits and wraps for peripheral nerve injury: A review of materials and efficacy. *Injury,* 43(5), pp. 553–572. doi: 10.1016/j.injury.2010.12.030.

Kenawy, E. R., Worley, S. D. and Broughton, R. (2007). The chemistry and applications of antimicrobial polymers: A state-of-the-art review. *Biomacromolecules,* pp. 1359–1384. doi: 10.1021/bm061150q.

Keyte, J., Pancholi, K. and Njuguna, J. (2019). Recent Developments in Graphene Oxide/Epoxy Carbon Fiber-Reinforced Composites. *Frontiers in Materials,* 6. doi: 10.3389/fmats.2019.00224.

Kim, H.-W., Son, Y.-J., Knowles, J.C. and Hyun, J.K. (2012). Phosphate glass fibres promote neurite outgrowth and early regeneration in a peripheral nerve injury model. *Journal of Tissue Engineering and Regenerative Medicine,* 9(3), pp.236–246. doi: 10.1002/term.1626.

Kim, J.I., Hwang, T.I., Aguilar, L.E., Park, C.H. and Kim, C.S. (2016). A Controlled Design of Aligned and Random Nanofibers for 3D Bi-functionalized Nerve Conduits Fabricated via a Novel Electrospinning Set-up. *Scientific Reports*, 6(1), pp. 1–12. doi: 10.1038/srep23761.

Knight, M.A.F. and Evans, G.R.D. (2004). Tissue Engineering: Progress and Challenges. *Plastic and Reconstructive Surgery,* 114(2), pp.26e-37e.

Knowles, J.C. (2003). Phosphate based glasses for biomedical applications. *Journal of Materials Chemistry,* 13(10), p.2395. doi: 10.1039/b307119g.

Kokubo, T. and Takadama, H. (2006). How useful is SBF in predicting in vivo bone bioactivity?. *Biomaterials,* 27(15), pp. 2907–2915. doi: 10.1016/j.biomaterials.2006.01.017.

Kornfeld, T., Vogt, P.M. and Radtke, C. (2018). Nerve grafting for peripheral nerve injuries with extended defect sizes. *Wiener Medizinische Wochenschrift,* 169(9–10), pp.240–251. doi: 10.1007/s10354-018-0675-6.

Kostopoulos, L. and Karring, T. (1994). Guided bone regeneration in mandibular defects in rats using a bioresorbable polymer. *Clinical Oral Implants Research,* [online] 5(2), pp.66–74. Available at: http://www.ncbi.nlm.nih.gov/pubmed/7918911.

Koudehi, M.F., Fooladi, A.A.I., Mansoori, K., Jamalpoor, Z., Amiri, A. and Nourani, M.R. (2013). Preparation and evaluation of novel nano-bioglass/gelatin conduit for peripheral nerve regeneration. *Journal of Materials Science: Materials in Medicine,* 25(2), pp.363–373. doi: 10.1007/s10856-013-5076-1.

Kovtyukhova, N.I., Ollivier, P.J., Martin, B.R., Mallouk, T.E., Chizhik, S.A., Buzaneva, E.V. and Gorchinskiy, A.D. (1999). Layer-by-Layer Assembly of Ultrathin Composite Films from Micron-Sized Graphite Oxide Sheets and Polycations. *Chemistry of Materials,* 11(3), pp.771–778. doi: 10.1021/cm981085u.

Kuilla, T., Bhadra, S., Yao, D., Kim, N.H., Bose, S. and Lee, J.H. (2010). Recent advances in graphene based polymer composites. *Progress in Polymer Science,* 35(11), pp.1350–1375.doi: 10.1016/j.progpolymsci.2010.07.005.

Kumar, P., Som, S., Pandey, M.K., Das, S., Chanda, A. and Singh, J. (2018). Investigations on optical properties of ZnO decorated graphene oxide (ZnO@GO) and reduced graphene oxide (ZnO@r-GO). *Journal of Alloys and Compounds,* 744, pp.64–74. doi: 10.1016/j.jallcom.2018.02.057.

Lai, Y.M., Liang, X.F., Yang, S.Y., Wang, J.X., Cao, L.H. and Dai, B. (2011). Raman and FTIR spectra of iron phosphate glasses containing cerium. *Journal of Molecular Structure,* 992(1–3), pp.84–88. doi: 10.1016/j.molstruc.2011.02.049.

Langer, R. and Vacanti, J. (1993). Tissue engineering. *Science,* 260(5110), pp. 920–926. doi: 10.1126/science.8493529.

Łapa, A., Cresswell, M., Campbell, I., Jackson, P., Goldmann, W.H., Detsch, R., Parsons, A., Ahmed, I. and Boccaccini, A.R. (2019). Ga and Ce ion-doped phosphate glass fibres with antibacterial properties and their composite for wound healing

applications. *Journal of Materials Chemistry B,* 7(44), pp.6981–6993. doi: 10.1039/C9TB00820A.

Lapa, A., Cresswell, M., Jackson, P. and Boccaccini, A.R. (2019). Phosphate glass fibres with therapeutic ions release capability – a review. *Advances in Applied Ceramics,* 119(1), pp.1–14. doi: 10.1080/17436753.2018.1564413.

Larsson, M., Hetherington, C.J.D., Wallenberg, R. and Jannasch, P. (2017). Effect of hydrophobically modified graphene oxide on the properties of poly(3-hydroxybutyrate-co-4-hydroxybutyrate). *Polymer,* 108, pp.66–77. doi: 10.1016/J.POLYMER.2016.11.042.

Latia, A. and Vancea, C., (2003). Fast ion conduction in silver molybdenum phosphate glasses. *Journal of Optoelectronics and Advanced Materials,* 5(1), pp.185-190.

Layek, R.K. and Nandi, A.K. (2013). A review on synthesis and properties of polymer functionalized graphene. *Polymer,* 54(19), pp.5087–5103. doi: 10.1016/j.polymer.2013.06.027.

Lee, K.Y., Woo, C.J., Bae, K.S. and Heo, T.R., 2000. Development of the selection technique of entrapment materials for the viability improvement of entrapped bifidobacteria. *Kor. J. Biotechnol. Bioeng,* 15, pp.1-8. doi: 10.1002/(SICI)1097-0290(19960105)49:1<1:AID-BIT1>3.0.CO;2-P.

Lemire, J. a, Harrison, J. J. and Turner, R. J. (2013). Antimicrobial activity of metals: mechanisms, molecular targets and applications. *Nature reviews Microbiology,* 11(6), pp. 371–84. doi: 10.1038/nrmicro3028.

Lenz, R.W. and Marchessault, R.H. (2005). Bacterial Polyesters: Biosynthesis, Biodegradable Plastics and Biotechnology. *Biomacromolecules,* 6(1), pp.1–8. doi: 10.1021/bm049700c.

Leontiev, R., Hohaus, N., Jacob, C., Gruhlke, M.C.H. and Slusarenko, A.J. (2018). A Comparison of the Antibacterial and Antifungal Activities of Thiosulfinate Analogues of Allicin. *Scientific Reports,* 8(1). 1–19. doi: 10.1038/s41598-018-25154-9.

Lewis, K. (2013). Platforms for antibiotic discovery. *Nature Reviews Drug Discovery*, 12(5), pp.371–387. doi: 10.1038/nrd3975.

Li, B. and Webster, T. J. (2018). Bacteria antibiotic resistance: New challenges and opportunities for implant-associated orthopedic infections. *Journal of orthopaedic research: official publication of the Orthopaedic Research Society,* 36(1), pp. 22–32. doi: 10.1002/jor.23656.

Li, F., Li, Q., Wu, S. and Tan, Z. (2017). Salting-out extraction of allicin from garlic (Allium sativum L.) based on ethanol/ammonium sulfate in laboratory and pilot scale. *Food Chemistry,* 217, pp.91–97. doi: 10.1016/j.foodchem.2016.08.092.

Li, P., Gao, Y., Sun, Z., Chang, D., Gao, G. and Dong, A. (2016). Synthesis, Characterization, and Bactericidal Evaluation of Chitosan/Guanidine Functionalized Graphene Oxide Composites. *Molecules,* 22(1), p.12. doi: 10.3390/molecules22010012.

Liebergesell, M., Mayer, F. and Steinb�chel, A. (1993). Anaylsis of polyhydroxyalkanoic acid-biosynthesis genes of anoxygenic phototrophic bacteria reveals synthesis of a polyester exhibiting an unusal composition. *Applied Microbiology and Biotechnology,* 40(2–3). doi: 10.1007/BF00170383.

Lin, Y., Yang, Z. and Cheng, J. (2007). Preparation, Characterization and Antibacterial Property of Cerium Substituted Hydroxyapatite Nanoparticles. *Journal of Rare Earths. Chinese Society of Rare Earths,* 25(4), pp. 452–456. doi: 10.1016/S1002-0721(07)60455-4.

Liu, S., Zeng, T.H., Hofmann, M., Burcombe, E., Wei, J., Jiang, R., Kong, J. and Chen, Y. (2011). Antibacterial Activity of Graphite, Graphite Oxide, Graphene Oxide, and Reduced Graphene Oxide: Membrane and Oxidative Stress. *ACS Nano*, 5(9), pp.6971–6980. doi: 10.1021/nn202451x.

Liu, S., Zeng, T.H., Hofmann, M., Burcombe, E., Wei, J., Jiang, R., Kong, J. and Chen, Y. (2011). Antibacterial Activity of Graphite, Graphite Oxide, Graphene Oxide, and Reduced Graphene Oxide: Membrane and Oxidative Stress. *ACS Nano,* 5(9), pp.6971–6980. doi: 10.1021/nn202451x.

Lizarraga Valderrama, L. (2017). Nerve tissue engineering using blends of Polyhydroxyalkanoates. [online] westminsterresearch.westminster.ac.uk. Available at: https://westminsterresearch.westminster.ac.uk/item/q430w/nerve-tissue-engineering-using-blends-of-polyhydroxyalkanoates (Accessed: 16 October 2019).

Lizarraga-Valderrama, L.R., Nigmatullin, R., Taylor, C., Haycock, J.W., Claeyssens, F., Knowles, J.C. and Roy, I. (2015). Nerve tissue engineering using blends of poly(3-hydroxyalkanoates) for peripheral nerve regeneration. *Engineering in Life Sciences,* 15(6), pp.612–621. doi: 10.1002/elsc.201400151.

Lizarraga-Valderrama, L.R., Taylor, C.S., Claeyssens, F., Haycock, J.W., Knowles, J.C. and Roy, I. (2019). Unidirectional neuronal cell growth and differentiation on aligned polyhydroxyalkanoate blend microfibres with varying diameters.

Journal of Tissue Engineering and Regenerative Medicine, 13(9), pp.1581–1594. doi: 10.1002/term.2911.

Lloyd, A.W. (2002). Interfacial bioengineering to enhance surface biocompatibility. *Medical Device Technology,* [online] 13(1), pp.18–21. Available at: http://www.ncbi.nlm.nih.gov/pubmed/11921776 (Accessed: 28 March 2018).

Löbler, M., Saß, M., Kunze, C., Schmitz, K.P. and Hopt, U.T., 2002. Biomaterial implants induce the inflammation marker CRP at the site of implantation. *Journal of Biomedical Materials Research: An Official Journal of The Society for Biomaterials, The Japanese Society for Biomaterials, and The Australian Society for Biomaterials and the Korean Society for Biomaterials,* 61(1), pp.165-167.

Lu, X.-Y., Ciraolo, E., Stefenia, R., Chen, G.-Q., Zhang, Y. and Hirsch, E. (2011). Sustained release of PI3K inhibitor from PHA nanoparticles and in vitro growth inhibition of cancer cell lines. *Applied Microbiology and Biotechnology,* 89(5), pp.1423–1433. doi: 10.1007/s00253-011-3101-1.

Luklinska ZB, B. W. (1997). Morphology and ultrastructure of the interface between hydroxyapatite-polyhydroxybutyrate composite implant and bone. *Journal of Materials Science: Materials in Medicine,* 8(379–383).

Lundborg, G. (2003). Richard P. Bunge memorial lecture. Nerve injury and repair--a challenge to the plastic brain. *Journal of the peripheral nervous system: JPNS,* 8(4), pp. 209–226. doi: 10.1111/j.1085-9489.2003.03027.x.

Luzier, W. D. (1992). Materials derived from biomass/biodegradable materials. *Proceedings of the National Academy of Sciences of the United States of America,* 89(3), pp. 839–42. doi: 10.1073/PNAS.89.3.839.

Mahendran, R., Sridharan, D., Santhakumar, K. and Gnanasekaran, G., 2016. Green route fabrication of graphene oxide reinforced polymer composites with enhanced mechanical properties. *Journal of Nanoscience,* 2016.

Manavitehrani, I., Fathi, A., Badr, H., Daly, S., Negahi Shirazi, A. and Dehghani, F. (2016). Biomedical Applications of Biodegradable Polyesters. *Polymers,* 8(1), p.20. doi: 10.3390/polym8010020.

Marchese, A., Barbieri, R., Sanches-Silva, A., Daglia, M., Nabavi, S.F., Jafari, N.J., Izadi, M., Ajami, M. and Nabavi, S.M. (2016). Antifungal and antibacterial activities of allicin: A review. *Trends in Food Science & Technology,* 52, pp.49–56. doi: 10.1016/j.tifs.2016.03.010.

Marquardt, L.M., Day, D., Sakiyama-Elbert, S.E. and Harkins, A.B. (2013). Effects of borate-based bioactive glass on neuron viability and neurite extension. *Journal of Biomedical Materials Research Part A,* 102(8), pp.2767–2775. doi: 10.1002/jbm.a.34944.

Martinez, J. and Baquero, F., 2000. Mutation Frequencies and Antibiotic Resistance. *Antimicrobial Agents and Chemotherapy*, 44(7), pp.1771-1777.

Masood, F., Yasin, T. and Hameed, A. (2016). Critical Reviews in Biotechnology Polyhydroxyalkanoates – what are the uses? Current challenges and perspectives and perspectives. *Critical Reviews in Biotechnology,* 35(4), pp. 514–521. doi: 10.3109/07388551.2014.913548.

Mcdermott, P. F., Walker, R. D. and White, D. G. (2003). Antimicrobials: Mode of Action and Mechanisms of Resistance. *International Journal of Toxicology*, 22, pp. 135–143. doi: 10.1080/10915810390198410.

McFarland, L.V., Mulligan, M.E., Kwok, R.Y.Y. and Stamm, W.E. (1989). Nosocomial Acquisition ofClostridium difficileInfection. *New England Journal of Medicine,* 320(4), pp.204–210. Available at: https://www.nejm.org/doi/full/10.1056/NEJM198901263200402. doi: 10.1056/NEJM198901263200402.

Means, K.R., Rinker, B.D., Higgins, J.P., Payne, S.H., Merrell, G.A. and Wilgis, E.F.S. (2016). A Multicenter, Prospective, Randomized, Pilot Study of Outcomes for Digital Nerve Repair in the Hand Using Hollow Conduit Compared with Processed Allograft Nerve. *HAND,* 11(2), pp.144–151. doi: 10.1177/1558944715627233.

Mejías Carpio, I.E., Santos, C.M., Wei, X. and Rodrigues, D.F. (2012). Toxicity of a polymer–graphene oxide composite against bacterial planktonic cells, biofilms, and mammalian cells. *Nanoscale,* 4(15), p.4746. doi: 10.1039/c2nr30774j.

Menorca, R.M.G., Fussell, T.S. and Elfar, J.C. (2013). Nerve Physiology. Hand Clinics, 29(3), pp.317–330. doi: 10.1016/j.hcl.2013.04.002.Peripheral.

Miguez-Pacheco, V., Greenspan, D., Hench, L.L. and Boccaccini, A.R., 2015. Bioactive glasses in soft tissue repair. *American Ceramic Society Bulletin,* 94(6), pp.27-31. Available at: www.ceramics.org (Accessed: 19 November 2019).

Misra, S.K., Ansari, T., Mohn, D., Valappil, S.P., Brunner, T.J., Stark, W.J., Roy, I., Knowles, J.C., Sibbons, P.D., Jones, E.V., Boccaccini, A.R. and Salih, V. (2009). Effect of nanoparticulate bioactive glass particles on bioactivity and cytocompatibility

of poly(3-hydroxybutyrate) composites. *Journal of The Royal Society Interface,* 7(44), pp.453–465. doi: 10.1098/rsif.2009.0255.

Misra, S.K., Valappil, S.P., Roy, I. and Boccaccini, A.R. (2006). Polyhydroxyalkanoate (PHA)/Inorganic Phase Composites for Tissue Engineering Applications. *Biomacromolecules,* 7(8), pp.2249–2258. doi: 10.1021/bm060317c.

Mo, Z., Sun, Y., Chen, H., Zhang, P., Zuo, D., Liu, Y. and Li, H. (2005). Preparation and characterization of a PMMA/$Ce(OH)_3$, Pr_2O_3/graphite nanosheet composite. *Polymer,* 46(26), pp.12670–12676. doi: 10.1016/j.polymer.2005.10.117.

Mohanna, P.-N., Young, R.C., Wiberg, M. and Terenghi, G. (2003). A composite poly-hydroxybutyrate-glial growth factor conduit for long nerve gap repairs. *Journal of Anatomy,* 203(6), pp.553–565.. doi: 10.1046/j.1469-7580.2003.00243.x.

Mohapatra, S., Sarkar, B., Samantaray, D.P., Daware, A., Maity, S., Pattnaik, S. and Bhattacharjee, S. (2017). Bioconversion of fish solid waste into PHB using *Bacillus subtilis* based submerged fermentation process. *Environmental Technology,* 38(24), pp.3201–3208. doi: 10.1080/09593330.2017.1291759.

Moraes, A., Araujo Lima, B., Fonseca de Faria, A., Brocchi, M. and Luiz Alves, O., (2015). Graphene oxide-silver nanocomposite as a promising biocidal agent against methicillin-resistant Staphylococcus aureus. *International Journal of Nanomedicine*, p.6847.

Mosahebi, A., Fuller, P., Wiberg, M. and Terenghi, G. (2002). Effect of Allogeneic Schwann Cell Transplantation on Peripheral Nerve Regeneration. *Experimental Neurology,* 173(2), pp.213–223. doi: 10.1006/exnr.2001.7846.

Mozaffari Nejad, A.S., Shabani, S., Bayat, M. and Ebrahim Hosseini, S. (2014). Antibacterial Effect of Garlic Aqueous Extract on Staphylococcus aureus in Hamburger. *Jundishapur Journal of Microbiology,* [online] 7(9). doi: 10.5812/jjm.13134.

Muhammadi, Shabina, Afzal, M. and Hameed, S. (2015). Bacterial polyhydroxyalkanoates-eco-friendly next generation plastic: Production, biocompatibility, biodegradation, physical properties and applications. *Green Chemistry Letters and Reviews,* 8(3–4), pp.56–77. doi: 10.1080/17518253.2015.1109715.

Muheremu, A. and Ao, Q. (2015). Past, Present, and Future of Nerve Conduits in the Treatment of Peripheral Nerve Injury. *BioMed Research International,* [online] 2015, pp.1–6. doi: 10.1155/2015/237507.

Mulligan, A. M., Wilson, M. and Knowles, J. C. (2003). The effect of increasing copper content in phosphate-based glasses on biofilms of Streptococcus sanguis. *Biomaterials,* 24(10), pp. 1797–1807. doi: 10.1016/S0142-9612(02)00577-X.

Muñoz-Senovilla, L., Muñoz, F., Tricot, G., Ahmed, I. and Parsons, A.J., 2017. Structure–properties relationships in fibre drawing of bioactive phosphate glasses. *Journal of Materials Science*, 52(15), pp.9166-9178.

Nair, L.S. and Laurencin, C.T. (2007). Biodegradable polymers as biomaterials. *Progress in Polymer Science,* 32(8–9), pp.762–798. doi: 10.1016/j.progpolymsci.2007.05.017.

Nascimento, G.G.F., Locatelli, J., Freitas, P.C. and Silva, G.L. (2000). Antibacterial activity of plant extracts and phytochemicals on antibiotic-resistant bacteria. *Brazilian Journal of Microbiology*, 31(4). doi: 10.1590/S1517-83822000000400003.

Nectow, A. R., Marra, K. G. and Kaplan, D. L. (2012). Biomaterials for the Development of Peripheral Nerve Guidance Conduits. *Tissue Engineering Part B: Reviews,* 18(1), pp. 40–50. doi: 10.1089/ten.teb.2011.0240.

NHS Choices (2019). *Causes-Peripheral neuropathy.* [online] Available at: https://www.nhs.uk/conditions/peripheral-neuropathy/causes/.

Nicastro, H.L., Ross, S.A. and Milner, J.A., 2015. Garlic and onions: their cancer prevention properties. *Cancer prevention research*, 8(3), pp.181-189.

Nigmatullin, R., Thomas, P., Lukasiewicz, B., Puthussery, H. and Roy, I. (2015). Polyhydroxyalkanoates, a family of natural polymers, and their applications in drug delivery. *Journal of Chemical Technology & Biotechnology,* 90(7), pp.1209–1221. doi: 10.1002/jctb.4685.

Nih.gov. (2018). *Peripheral Neuropathy Fact Sheet | National Institute of Neurological Disorders and Stroke.* [online] Available at: https://www.ninds.nih.gov/Disorders/Patient-Caregiver-Education/Fact-Sheets/Peripheral-Neuropathy-Fact-Sheet.

Noble, J., Munro, C.A., Prasad, V.S.S.V. and Midha, R. (1998). Analysis of Upper and Lower Extremity Peripheral Nerve Injuries in a Population of Patients with Multiple Injuries. *The Journal of Trauma: Injury, Infection, and Critical Care,* 45(1), pp.116–122. doi: 10.1097/00005373-199807000-00025.

Nostro, A. (n.d.). Activity of Plant Extracts and Plant-Derived Compounds against Drug-Resistant Microorganisms. *Modern Phytomedicine,* pp.199–231. doi: 10.1002/9783527609987.ch10.

Novikov, L.N., Novikova, L.N., Mosahebi, A., Wiberg, M., Terenghi, G. and Kellerth, J.O., 2002. A novel biodegradable implant for neuronal rescue and regeneration after spinal cord injury. *Biomaterials,* 23(16), pp.3369-3376.

Numata, K., Abe, H. and Iwata, T. (2009). Biodegradability of poly(hydroxyalkanoate) materials. *Materials,* 2(3), pp. 1104–1126. doi: 10.3390/ma2031104.

O'Brien, F.J. (2011). Biomaterials & scaffolds for tissue engineering. *Materials Today,* [online] 14(3), pp.88–95. Available at: https://www.sciencedirect.com/science/article/pii/S136970211170058X [Accessed 29 Apr. 2019]. doi: 10.1016/S1369-7021(11)70058-X.

O'Gara, E. A., Hill, D. J. and Maslin, D. J. (2000). Activities of garlic oil, garlic powder, and their diallyl constituents against Helicobacter pylori. *Applied and Environmental Microbiology,* 66(5), pp. 2269–2273. doi: 10.1128/AEM.66.5.2269-2273.2000.

O'neill, J.I.M., 2014. Antimicrobial resistance: tackling a crisis for the health and wealth of nations. *Review on Antimicrobial Resistance,* 20, pp.1-16. The Available at: http://amr-review.org/sites/default/files/Report-52.15.pdf.

Obaleye, J.A., Tella, A.C. and Bamigboye, M.O., 2012. Metal complexes as prospective antibacterial agents. *In A Search for Antibacterial Agents.* IntechOpen.

Orvig, C. and Abrams, M. J. (1999). Medicinal Inorganic Chemistry: Introduction. *Chemical Reviews,* 99(9), pp. 2201–2204. doi: 10.1021/cr980419w.

Paik, P. and Pradip Paik (2017). Graphene Oxide for Biomedical Applications. *Journal of Nanomedicine Research,* 5(6), pp. 1–6. doi: 10.15406/jnmr.2017.05.00136.

Palza, H. (2015). Antimicrobial polymers with metal nanoparticles. *International Journal of Molecular Sciences,* 16(1), pp. 2099–2116. doi: 10.3390/ijms16012099.

Park, S.Y., Park, J., Sim, S.H., Sung, M.G., Kim, K.S., Hong, B.H. and Hong, S. (2011). Enhanced Differentiation of Human Neural Stem Cells into Neurons on Graphene. *Advanced Materials,* 23(36), pp.H263–H267. doi: 10.1002/adma.201101503.

Papkou, A., Hedge, J., Kapel, N., Young, B. and MacLean, R., (2020). Efflux pump activity potentiates the evolution of antibiotic resistance across S. aureus isolates. *Nature Communications*, 11(1), pp. 1–15. doi: 10.1038/s41467-020-17735-y.

Pateman, C.J., Harding, A.J., Glen, A., Taylor, C.S., Christmas, C.R., Robinson, P.P., Rimmer, S., Boissonade, F.M., Claeyssens, F. and Haycock, J.W. (2015).

Nerve guides manufactured from photocurable polymers to aid peripheral nerve repair. *Biomaterials,* 49, pp.77–89. doi: 10.1016/j.biomaterials.2015.01.055.

Perreault, F., de Faria, A.F., Nejati, S. and Elimelech, M. (2015). Antimicrobial Properties of Graphene Oxide Nanosheets: Why Size Matters. *ACS Nano,* 9(7), pp.7226–7236. doi: 10.1021/acsnano.5b02067.

Petrovic, V., Nepal, A., Olaisen, C., Bachke, S., Hira, J., Søgaard, C.K., Røst, L.M., Misund, K., Andreassen, T., Melø, T.M. and Bartsova, Z., 2018. Anti-cancer potential of homemade fresh garlic extract is related to increased endoplasmic reticulum stress. *Nutrients*,10(4), p.450.

Petrovska, B. (2012). Historical review of medicinal plants′ usage. *Pharmacognosy Reviews,* 6(11), pp. 1–6. doi: 10.4103/0973-7847.95849.

Philip, S., Keshavarz, T. and Roy, I. (2007). Polyhydroxyalkanoates: biodegradable polymers with a range of applications. *Journal of Chemical Technology & Biotechnology,* 82(3), pp. 233–247. doi: 10.1002/jctb.1667.

Piddock, L., (2006). Clinically Relevant Chromosomally Encoded Multidrug Resistance Efflux Pumps in Bacteria. *Clinical Microbiology Reviews*, 19(2), pp.382-402.

Pinto, A. M., Gonçalves, I. C. and Magalhães, F. D. (2013). Graphene-based materials biocompatibility: A review. *Colloids and Surfaces B: Biointerfaces,* 111, pp.188–202. doi: 10.1016/j.colsurfb.2013.05.022.

Potts, J.R., Dreyer, D.R., Bielawski, C.W. and Ruoff, R.S. (2011). Graphene-based polymer nanocomposites. Polymer, 52(1), pp.5–25. doi: 10.1016/j.polymer.2010.11.042.

Pouton, C.W. and Akhtar, S. (1996). Biosynthetic polyhydroxyalkanoates and their potential in drug delivery. *Advanced Drug Delivery Reviews,* 18(2), pp.133–162. doi: 10.1016/0169-409X(95)00092-L.

Pryce, R.S. and Hench, L.L. (2003). Dissolution Characteristics of Bioactive Glasses. *Key Engineering Materials,* 240–242, pp.201–204.. doi: 10.4028/www.scientific.net/kem.240-242.201.

Rajan K.P., Thomas S.P., Gopanna A., Chavali M. (2018) Polyhydroxybutyrate (PHB): A Standout Biopolymer for Environmental Sustainability. In: Martínez L., Kharissova O., Kharisov B. (eds) *Handbook of Ecomaterials*. Springer, Cham. https://doi.org/10.1007/978-3-319-48281-1_92-1.

Rahman, K. and Lowe, G.M., 2006. Garlic and cardiovascular disease: a critical review. *The Journal of nutrition*,136(3), pp.736S-740S.

Rai, R., Keshavarz, T., Roether, J.A., Boccaccini, A.R. and Roy, I. (2011). Medium chain length polyhydroxyalkanoates, promising new biomedical materials for the future. *Materials Science and Engineering: R: Reports,* 72(3), pp.29–47. doi: 10.1016/j.mser.2010.11.002.

Rasmussen, T. B. and Givskov, M. (2006). Quorum sensing inhibitors: A bargain of effects. *Microbiology,* 152(4), pp. 895–904. doi: 10.1099/mic.0.28601-0.

Rastogi, S. K., Raghavan, G., Yang, G. and Cohen-Karni, T. (2017). Effect of Graphene on Nonneuronal and Neuronal Cell Viability and Stress. *Nano Letters,* 17(5), pp. 3297–3301. doi: 10.1021/acs.nanolett.7b01215.

Rebowe, R., Rogers, A., Yang, X., Kundu, S., Smith, T. and Li, Z. (2018). Nerve Repair with Nerve Conduits: Problems, Solutions, and Future Directions. *Journal of Hand and Microsurgery,* 10(02), pp.61–65. doi: 10.1055/s-0038-1626687.

Reddy, C.S.., Ghai, R., Rashmi and Kalia, V.. (2003). Polyhydroxyalkanoates: an overview. *Bioresource Technology,* [online] 87(2), pp.137–146. Available at: https://www.sciencedirect.com/science/article/pii/S0960852402002122. doi: 10.1016/S0960-8524(02)00212-2.

Reis, K.C., Pereira, J., Smith, A.C., Carvalho, C.W.P., Wellner, N. and Yakimets, I. (2008). Characterization of polyhydroxybutyrate-hydroxyvalerate (PHB-HV)/maize starch blend films. *Journal of Food Engineering,* 89(4), pp.361–369. doi: 10.1016/j.jfoodeng.2008.04.022.

Rivard, C.H., Chaput, C., Rhalmi, S. and Selmani, A., 1996. Bio-absorbable synthetic polyesters and tissue regeneration. A study of three-dimensional proliferation of ovine chondrocytes and osteoblasts. *In Annales de chirurgie*, 50(8), pp. 651-658).

Rohanová, D., Boccaccini, A.R., Yunos, D.M., Horkavcová, D., Březovská, I. and Helebrant, A. (2011). TRIS buffer in simulated body fluid distorts the assessment of glass–ceramic scaffold bioactivity. *Acta Biomaterialia,* 7(6), pp.2623–2630. doi: 10.1016/j.actbio.2011.02.028.

Rosenberg, L.E., Carbone, A.L., Römling, U., Uhrich, K.E. and Chikindas, M.L. (2008). Salicylic acid-based poly(anhydride esters) for control of biofilm formation in Salmonella enterica serovar Typhimurium. *Letters in Applied Microbiology,* 46(5), pp.593–599. doi: 10.1111/j.1472-765X.2008.02356.x.

Roy, S., Das, T., Zhang, L. and Hu, X.M. (2016). Harnessing the maximum reinforcement of graphene oxide for poly(vinylidene fluoride) nanocomposites via polydopamine assisted novel surface modification. *RSC Advances,* 6(74), pp.69919–69929. doi: 10.1039/C6RA12997H.

Rudzinski, W.E., Aminabhavi, T.M., Biradar, N.S., and Patil, C.S. (1982). Biologically active sulfonamide Schiff base complexes of Selenium (IV) and Tellurium (IV). *Inorg Chim. Acta,* 67, 177-182.

Sabongi, R. G., Fernandes, M. and Dos Gomes Santos, J. B. (2015). Peripheral nerve regeneration with conduits: Use of vein tubes. *Neural Regeneration Research,* 10(4), pp. 529–533. doi: 10.4103/1673-5374.155428.

Saga, T. and Yamaguchi, K., 2009. History of antimicrobial agents and resistant bacteria. *Japan Medical Association Journal,* 52(2), pp.103-108.

Saha, S.K., Saha, S., Akhter, S.M., Khatun, S., Islam, M.M. and Roy, P. (2016). In Vitro Determination of Minimum Inhibitory Concentration of Aqueous Garlic Extract and Imipenem against Staphylococcus aureus and Escherichia coli. *Mymensingh medical journal: MMJ,* [online] 25(3), pp.477–484. Available at: http://www.ncbi.nlm.nih.gov/pubmed/27612894 [Accessed 16 Feb. 2020]. (Accessed: 21 May 2018).

Saito, T.E.R.U.M.I., Suzuki, K., Yamamoto, J., Fukui, T., Miwa, K., Tomita, K., Nakanishi, S., Odani, S., Suzuki, J.L. and Ishikawa, K., (1989). Cloning, nucleotide sequence, and expression in Escherichia coli of the gene for poly(3-hydroxybutyrate) depolymerase from Alcaligenes faecalis. *Journal of bacteriology*, 171(1), pp. 184–9. Available at: http://www.ncbi.nlm.nih.gov/pubmed/2644188 (Accessed: 3 April 2018).

Saito, Y. and Doi, Y. (1994). Microbial synthesis and properties of poly(3-hydroxybutyrate-co-4-hydroxybutyrate) in Comamonas acidovorans. *Journal of biological macromolecules*, 16(2), pp. 99–104. Available at: http://www.ncbi.nlm.nih.gov/pubmed/8011595 (Accessed: 28 March 2018).

Salih, V., Franks, K., James, M., Hastings, G.W., Knowles, J.C. and Olsen, I. (2000) Development of soluble glasses for biomedical use part II: The biological response of human osteoblast cell lines to phosphate-based soluble glasses. *Journal of Materials Science: Materials in Medicine*. Kluwer Academic Publishers, 11(10), pp. 615–620. doi: 10.1023/A:1008901612674.

Santos, M., Fonseca, A., Mendonça, P., Branco, R., Serra, A., Morais, P. and Coelho, J. (2016). Recent Developments in Antimicrobial Polymers: A Review. *Materials*, 9(7), p. 599. doi: 10.3390/ma9070599.

Sarker, M.D., Naghieh, S., McInnes, A.D., Schreyer, D.J. and Chen, X. (2018). Regeneration of peripheral nerves by nerve guidance conduits: Influence of design, biopolymers, cells, growth factors, and physical stimuli. *Progress in Neurobiology*. Elsevier Ltd, pp. 125–150. doi: 10.1016/j.pneurobio.2018.07.002.

Sasaki, K., Tokura, Y. and Sogawa, T. (2012). The origin of Raman D Band: Bonding and Antibonding Orbitals in Graphene. *Crystals,* 3(1), pp. 120–140. doi: 10.3390/cryst3010120.

Scott, G. (1999) Polymers and the Environment. Cambridge: Royal Society of Chemistry (RSC Paperbacks). doi: 10.1039/9781847551726.

Sedki, M., Mohamed, M.B., Fawzy, M., Abdelrehim, D.A. and Abdel-Mottaleb, M.M.S.A. (2015). Phytosynthesis of silver–reduced graphene oxide (Ag–RGO) nanocomposite with an enhanced antibacterial effect using Potamogeton pectinatus extract. *RSC Adv*., 5(22), pp. 17358–17365. doi: 10.1039/C4RA13117G.

Sekhon, B. S. and Gandhi, L. (2006). Medicinal uses of inorganic compounds. *Resonance,* 11(8), pp. 62–68. doi: 10.1007/BF02855781.

Shah, V., Shah, S., Shah, H., Rispoli, F.J., McDonnell, K.T., Workeneh, S., Karakoti, A., Kumar, A. and Seal, S. (2012). Antibacterial activity of polymer coated cerium oxide nanoparticles. *PloS one*. Public Library of Science, 7(10), p. e47827. doi: 10.1371/journal.pone.0047827.

Shahriary, L. and Athawale, A. a. (2014). Graphene Oxide Synthesized by using Modified Hummers Approach. *International Journal of Renewable Energy and Environmental Engineering*, 02(01), pp. 58–63.

Shao, W., Liu, X., Min, H., Dong, G., Feng, Q. and Zuo, S. (2015). Preparation, characterization, and antibacterial activity of silver nanoparticle-decorated graphene oxide nanocomposite. *ACS applied materials & interfaces*, 7, pp. 6966–73. doi: 10.1021/acsami.5b00937.

Sharmin, N., Parsons, A.J., Rudd, C.D. and Ahmed, I. (2014). Effect of boron oxide addition on fibre drawing, mechanical properties and dissolution behaviour of phosphate-based glass fibres with fixed 40, 45 and 50 mol% P2O5. *Journal of Biomaterials Applications,* SAGE Publications Sage UK: London, England, 29(5), pp. 639–653. doi: 10.1177/0885328214539824.

Shishatskaya EI, Volova TG, Puzyr AP, Mogilnaya OA, E. S. (2004). Tissue response to the implantation of biodegradable polyhydroxyalkanoate sutures. *Journal of Materials Science: Materials in Medicine*,15, pp. 719–728.

Shishatskaya, E.I., Goreva, A.V., Voinova, O.N., Inzhevatkin, E.V., Khlebopros, R.G. and Volova, T.G., (2008). Evaluation of Antitumor Activity of Rubomycin Deposited in Absorbable Polymeric Microparticles. *Bulletin of experimental biology and medicine,* 145(3), pp. 358–361.

Shishatskaya, E.I., Volova, T.G., Puzyr, A.P., Mogilnaya, O.A. and Efremov, S.N. (2004). Tissue response to the implantation of biodegradable polyhydroxyalkanoate sutures. *Journal of Materials Science: Materials in Medicine,* 15(2005), pp. 719–728. doi: 10.1023/B:JMSM.0000030215.49991.0d.

Shrivastav, A., Kim, H.-Y. and Kim, Y.-R. (2013). Advances in the Applications of Polyhydroxyalkanoate Nanoparticles for Novel Drug Delivery System. *BioMed Research International*, 2013(Mcl), pp. 1–12. doi: 10.1155/2013/581684.

Siedenbiedel, F. and Tiller, J. C. (2012). Antimicrobial polymers in solution and on surfaces: Overview and functional principles. *Polymers*, pp. 46–71. doi: 10.3390/polym4010046.

Smith, A.T., LaChance, A.M., Zeng, S., Liu, B. and Sun, L. (2019). Synthesis, properties, and applications of graphene oxide/reduced graphene oxide and their nanocomposites. *Nano Materials Science,* Elsevier BV, 1(1), pp. 31–47. doi: 10.1016/j.nanoms.2019.02.004.

Steinbüchel, A. (2001). Perspectives for Biotechnological Production and Utilization of Biopolymers: Metabolic Engineering of Polyhydroxyalkanoate Biosynthesis Pathways as a Successful Example. *Macromolecular Bioscience*. Wiley-Blackwell, 1(1), pp. 1–24. doi: 10.1002/1616-5195(200101)1:1<1::AID-MABI1>3.0.CO;2-B.

Stewart, P. S., Grab, L. and Diemer, J. A. (1998). Analysis of biocide transport limitation in an artificial biofilm system. *Journal of Applied Microbiology*, 85(3), pp. 495–500. doi: 10.1046/j.1365-2672.1998.853529.x.

Strankowski, M., Włodarczyk, D., Piszczyk, Ł. and Strankowska, J. (2016). Polyurethane Nanocomposites Containing Reduced Graphene Oxide, FTIR, Raman, and XRD Studies. *Journal of Spectroscopy*, 2016, pp.1–6. doi: 10.1155/2016/7520741.

Sudesh, K., Abe, H. and Doi, Y. (2000). Synthesis, structure and properties of polyhydroxyalkanoates: Biological polyesters. *Progress in Polymer Science (Oxford),* 25(10), pp. 1503–1555. doi: 10.1016/S0079-6700(00)00035-6.

Sudesh, Kumar, N., Das, S., Bernhard, C. and Varma, G.D. (2013). Effect of graphene oxide doping on superconducting properties of bulk MgB2. *Superconductor Science and Technology,* 26(9). doi: 10.1088/0953-2048/26/9/095008.

Tadyszak, K., Wychowaniec, J. K. and Litowczenko, J. (2018). Biomedical Applications of Graphene-Based Structures. *Nanomaterials* (Basel, Switzerland). Multidisciplinary Digital Publishing Institute (MDPI), 8(11). doi: 10.3390/nano8110944.

Tang, X., Tang, P. and Liu, L. (2018). Preparation of tetraethylenepentamine modified magnetic graphene oxide for adsorption of dyes from aqueous solution. *Journal of the Brazilian Chemical Society. Sociedade Brasileira de Quimica*, 29(2), pp. 334–342. doi: 10.21577/0103-5053.20170145.

Tasci, B., Kutuk, H. and Koca, I. (2016). Determination of alliin and allicin in the plant of Allium scorodoprasum L. subsp. rotundum by using the infrared spectroscopy technique. *Acta Horticulturae*, (1143), pp. 133–138. doi: 10.17660/ActaHortic.2016.1143.19.

Taylor, C.A., Braza, D., Rice, J.B. and Dillingham, T. (2008). The Incidence of Peripheral Nerve Injury in Extremity Trauma. *American Journal of Physical Medicine & Rehabilitation,* 87(5), pp. 381–385. doi: 10.1097/PHM.0b013e31815e6370.

Thakur, V. K. and Thakur, M. K. (2015). Eco-friendly Polymer Nanocomposites: Chemistry and Applications. *Advanced Structured Materials*. doi: 10.1007/978-81-322-2470-9.

Thomas, P. K. (1989). Focal nerve injury: Guidance factors during axonal regeneration. *Muscle & Nerve*, pp. 796–802. doi: 10.1002/mus.880121003.

Valappil, S.P., Misra, S.K., Boccaccini, A.R. and Roy, I. (2006). Biomedical applications of polyhydroxyalkanoates: an overview of animal testing and in vivo responses. *Expert review of medical devices*, 3(6), pp. 853–868. doi: 10.1586/17434440.3.6.853.

Valappil, S.P., Ready, D., Neel, E.A.A., Pickup, D.M., Chrzanowski, W., O'Dell, L.A., Newport, R.J., Smith, M.E., Wilson, M. and Knowles, J.C. (2008). Antimicrobial Gallium-Doped Phosphate-Based Glasses. *Advanced Functional Materials. John Wiley & Sons,* Ltd, 18(5), pp. 732–741. doi: 10.1002/adfm.200700931.

Van Duin, D. and Paterson, D., (2016) . Multidrug-Resistant Bacteria in the Community. *Infectious Disease Clinics of North America*, 30(2), pp.377-390.

Ventola, C. L. (2015). The antibiotic resistance crisis: part 1: causes and threats. P & T: A peer-reviewed journal for formulary management (2015), 40(4), pp. 277–83. doi: Article.

Vijayavenkataraman, S., Zhang, S., Thaharah, S., Sriram, G., Lu, W.F. and Fuh, J.Y.H. (2018). Electrohydrodynamic Jet 3D Printed Nerve Guide Conduits (NGCs) for peripheral Nerve Injury Repair. *Polymers,* MDPI AG, 10(7). doi: 10.3390/polym10070753.

Vitale-Brovarone, C., Novajra, G., Lousteau, J., Milanese, D., Raimondo, S. and Fornaro, M. (2012). Phosphate glass fibres and their role in neuronal polarization and axonal growth direction. *Acta Biomaterialia*. Elsevier, 8(3), pp. 1125–1136. doi: 10.1016/J.ACTBIO.2011.11.018.

Volova, T. G. (Tat'iana G. (2004). Polyhydroxyalkanoates--plastic materials of the 21st century: production, properties, applications. Nova Science Publishers. Available at: https://www.novapublishers.com/catalog/product_info.php?products_id=1628 (Accessed: 28 March 2018).

Wallen, L. L. and Rohwedder, W. K. (1974). Poly-B-hydroxyalkanoate from Activated Sludge. *Environmental Science & Technology,* 8(6), pp. 576–579. doi: \url{10.1021/es60091a007}.

Wang, H.B., Mullins, M.E., Cregg, J.M., McCarthy, C.W. and Gilbert, R.J., (2010). Varying the diameter of aligned electrospun fibers alters neurite outgrowth and Schwann cell migration. *Acta biomaterialia*, 6(8), pp.2970-2978. doi: 10.1016/j.actbio.2010.02.020.

Wang, J. and Vermerris, W. (2016). Antimicrobial nanomaterials derived from natural products-a review. *Materials*, 9(4), p.255. doi: 10.3390/ma9040255.

Wang, K., Ruan, J., Song, H., Zhang, J., Wo, Y., Guo, S. and Cui, D. (2011). Biocompatibility of Graphene Oxide. *Nanoscale Research Letters. Springer Open Ltd,* 6(1), pp. 1–8. doi: 10.1007/s11671-010-9751-6.

Wen, X. and Tresco, P. A. (2006). Effect of filament diameter and extracellular matrix molecule precoating on neurite outgrowth and Schwann cell behavior on multifilament entubulation bridging device *invitro*. *Journal of Biomedical Materials Research Part A*. John Wiley & Sons, Ltd, 76A(3), pp. 626–637. doi: 10.1002/jbm.a.30520.

Williams, S.F., Martin, D.P., Horowitz, D.M. and Peoples, O.P. (1999). PHA applications: Addressing the price performance issue. *International Journal of Biological Macromolecules,* 25(1999), pp. 111–121. doi: 10.1016/S0141-8130(99)00022-7.

Witholt, B. and Kessler, B. (1999). Perspectives of medium chain length poly(hydroxyalkanoates), a versatile set of bacterial bioplastics. *Current Opinion in Biotechnology,* 10(3), pp. 279–285. doi: 10.1016/S0958-1669(99)80049-4.

Wojtoniszak, M., Chen, X., Kalenczuk, R.J., Wajda, A., Łapczuk, J., Kurzewski, M., Drozdzik, M., Chu, P.K. and Borowiak-Palen, E. (2012). Synthesis, dispersion, and cytocompatibility of graphene oxide and reduced graphene oxide. *Colloids and Surfaces B: Biointerfaces*. Elsevier, 89, pp. 79–85. doi: 10.1016/J.COLSURFB.2011.08.026.

Wu, P.-C., Chen, H.-H., Chen, S.-Y., Wang, W.-L., Yang, K.-L., Huang, C.-H., Kao, H.-F., Chang, J.-C., Hsu, C.-L.L., Wang, J.-Y., Chou, T.-M. and Kuo, W.-S. (2018). Graphene oxide conjugated with polymers: a study of culture condition to determine whether a bacterial growth stimulant or an antimicrobial agent?. *Journal of nanobiotechnology BioMed Central*, 16(1), p. 1. doi: 10.1186/s12951-017-0328-8.

Xue, Y., Xiao, H. and Zhang, Y. (2015). Antimicrobial polymeric materials with quaternary ammonium and phosphonium salts. *International Journal of Molecular Sciences,* pp. 3626–3655. doi: 10.3390/ijms16023626.

Yagmurlu, M.F., Korkusuz, F., Gürsel, I., Korkusuz, P., Ors, U. and Hasirci, V. (1999). Sulbactam-cefoperazone polyhydroxybutyrate-co-hydroxyvalerate (PHBV) local antibiotic delivery system: in vivo effectiveness and biocompatibility in the treatment of implant-related experimental osteomyelitis. *Journal of biomedical materials research,* 46(4), pp. 494–503. Available at: http://www.ncbi.nlm.nih.gov/pubmed/10398010 (Accessed: 28 March 2018).

Yamada, Y. and Azuma, K. (1977). Evaluation of the in vitro antifungal activity of allicin. *Antimicrobial Agents and Chemotherapy*, 11(4), pp. 743–749. doi: 10.1128/AAC.11.4.743.

Yang, Y.-C., Shen, C.-C., Cheng, H.-C. and Liu, B.-S. (2011). Sciatic nerve repair by reinforced nerve conduits made of gelatin-tricalcium phosphate composites. *Journal of Biomedical Materials Research Part A*, 96A (2), pp. 288–300. doi: 10.1002/jbm.a.32973.

Young, R. C., Wiberg, M. and Terenghi, G. (2002). Poly-3-hydroxybutyrate (PHB): a resorbable conduit for long-gap repair in peripheral nerves. *British Journal of Plastic Surgery*, 55, pp. 235–240. doi: 10.1054/bjps.2002.3798.

Yousefi, M., Dadashpour, M., Hejazi, M., Hasanzadeh, M., Behnam, B., de la Guardia, M., Shadjou, N. and Mokhtarzadeh, A. (2017). Anti-bacterial activity of graphene oxide as a new weapon nanomaterial to combat multidrug-resistance bacteria. *Materials Science and Engineering: C*, 74, pp. 568–581. doi: 10.1016/j.msec.2016.12.125.

Zakir Hossain, K.M., Felfel, R.M., Grant, D.M. and Ahmed, I. (2016). Chapter 11. Phosphate Glass Fibres and Their Composites. *Bioactive Glasses*, pp. 257–285. doi: 10.1039/9781782622017-00257.

Zeyons, O., Thill, A., Chauvat, F., Menguy, N., Cassier-Chauvat, C., Oréar, C., Daraspe, J., Auffan, M., Rose, J. and Spalla, O. (2009). Direct and indirect CeO2 nanoparticles toxicity for Escherichia coli and Synechocystis. *Nanotoxicology,* 3(4), pp. 284–295. doi: 10.3109/17435390903305260.

Zhang, N., Hou, J., Chen, S., Xiong, C., Liu, H., Jin, Y., Wang, J., He, Q., Zhao, R. and Nie, Z. (2016). Rapidly Probing Antibacterial Activity of Graphene Oxide by Mass Spectrometry-based Metabolite Fingerprinting. *Scientific Reports. Nature Publishing Group,* 6(May), pp. 1–10. doi: 10.1038/srep28045.

Zhu, Y., Romain, C. and Williams, C. K. (2016). Sustainable polymers from renewable resources. *Nature*, 540(7633), pp. 354–362. doi: 10.1038/nature21001.

Zinn, M., Witholt, B. and Egli, T. (2001). Occurrence, synthesis and medical application of bacterial polyhydroxyalkanoate. *Advanced Drug Delivery Reviews,* pp. 5–21. doi: 10.1016/S0169-409X (01)00218-6.

Appendix:

I. MBC results from garlic powder composites

Figure 1: The minimum bactericidal concentration (MBC) of (A) *Staphylococcus aureus* (ATCC® 29213™), (B) *Staphylococcus epidermidis* (ATCC® 12228™), (C) Methicillin-resistant *S. aureus* MRSA, (D) Methicillin-resistant *S. epidermidis* (MRSE), (E) *Escherichia coli* (ATCC® 25922™) using different concentrations of garlic powder (decreasing from left to right) after 24h of incubation.

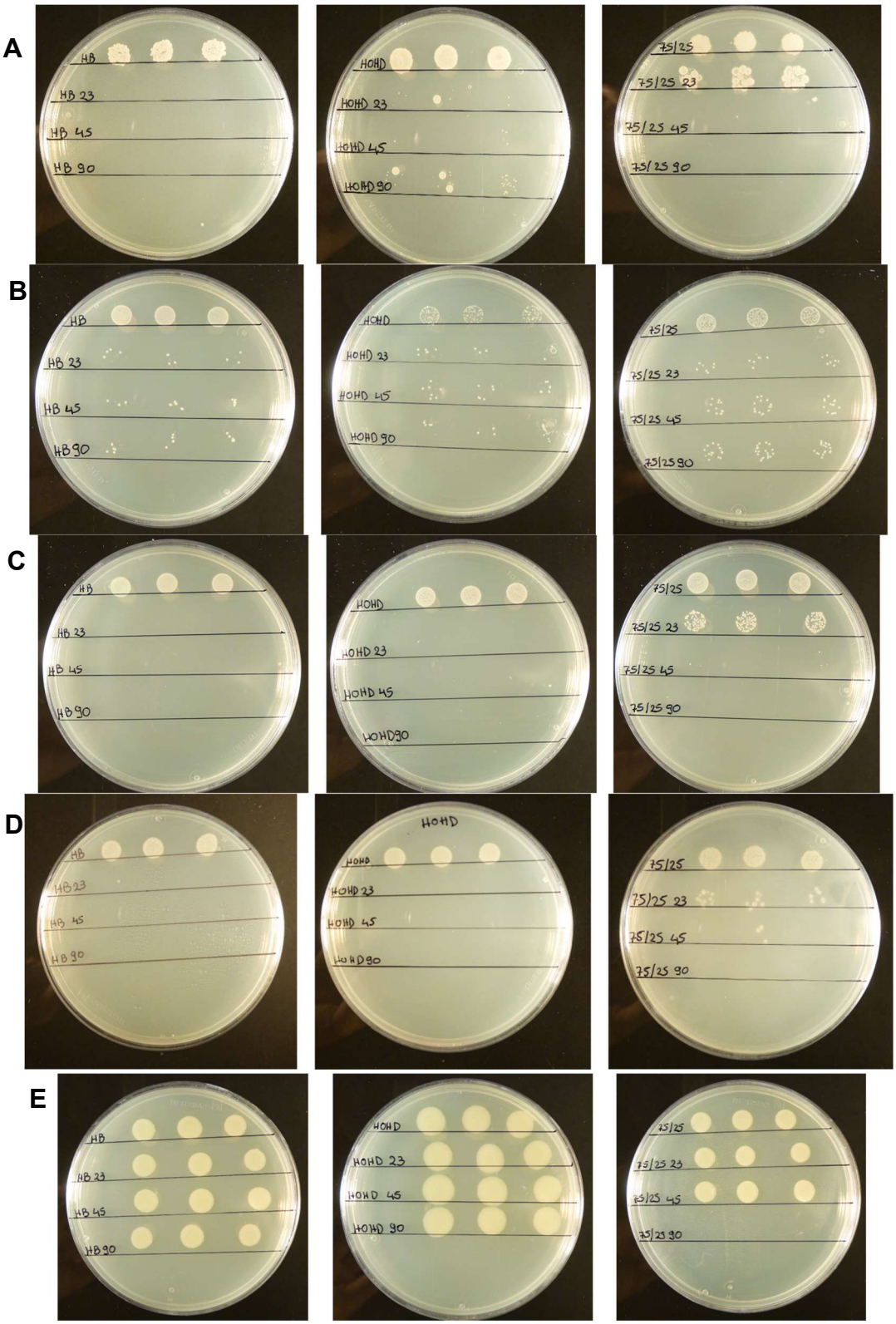

Figure 2: Effect of GP composites against (A) *S. aureus* (ATCC® 29213™), (B) *S. epidermidis* (ATCC® 12228™), (C) Methicillin-resistant *S. aureus* MRSA, (D) *E. coli* (ATCC® 25922™) and (E) *P. aeruginosa* (ATCC[6] 27853™) adhered cells.

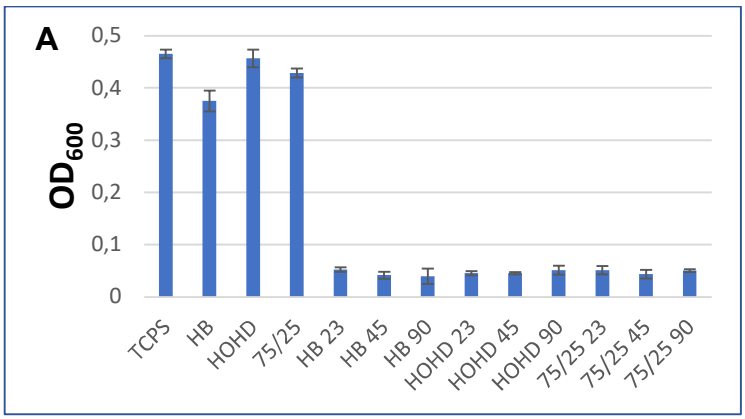

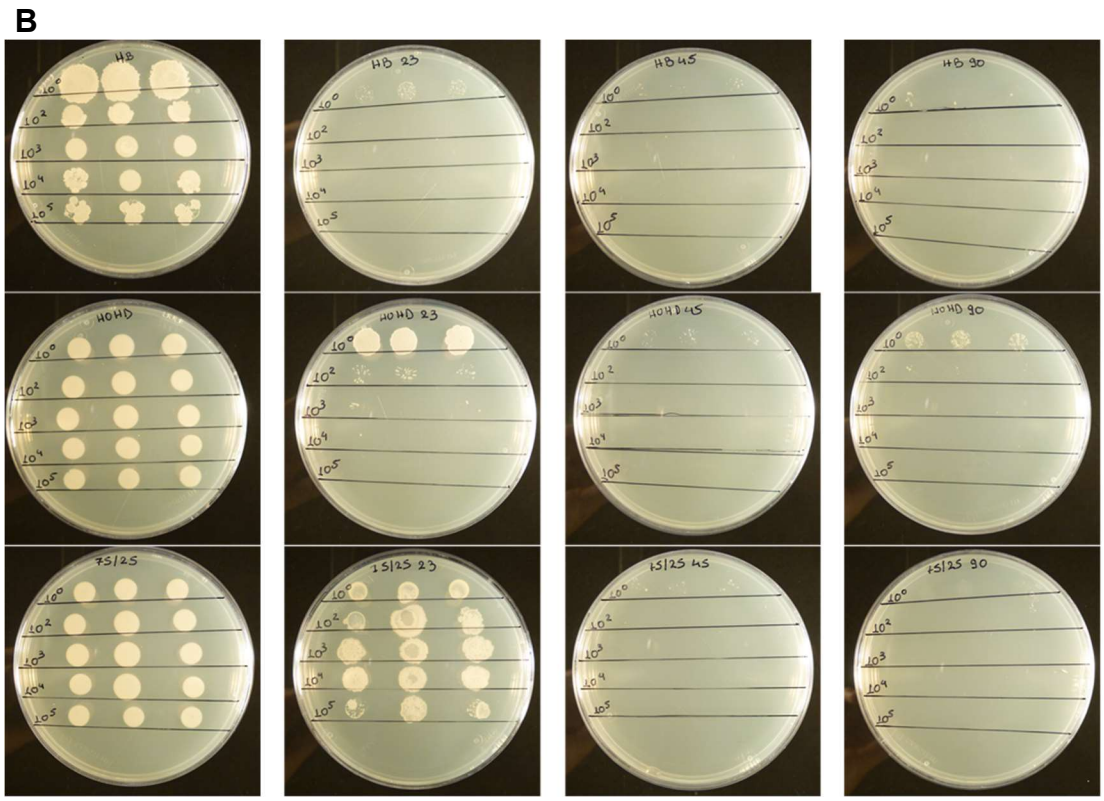

Figure 3: Antibacterial effect of GP composites against *S. aureus* (ATCC® 29213™) planktonic cells measuring (A) the optical density at 600 nm and (B) the cells that manage to recover after the contact with the composites for 24 h.

In Figure 3 are displayed the results of the bacterial inhibition of the garlic powder composites against the planktonic cells of *S. aureus* (ATCC® 29213™). First the OD_{600} was measured using the microplate reader and then the supernatant was used on agar plates to visually confirm the OD_{600} values. As shown in these two Figures the higher the OD_{600} is the more bacterial are obtained after 24h of incubation on agar plates at 37ºC. The 45 and 90 wt%

loading of garlic powder on the P(3HB), P(3HO-co-HD) and 75/25 (P(3HO-co-HD) / P(3HB)) blend induced bactericidal effect on the free cells of *S. aureus*.

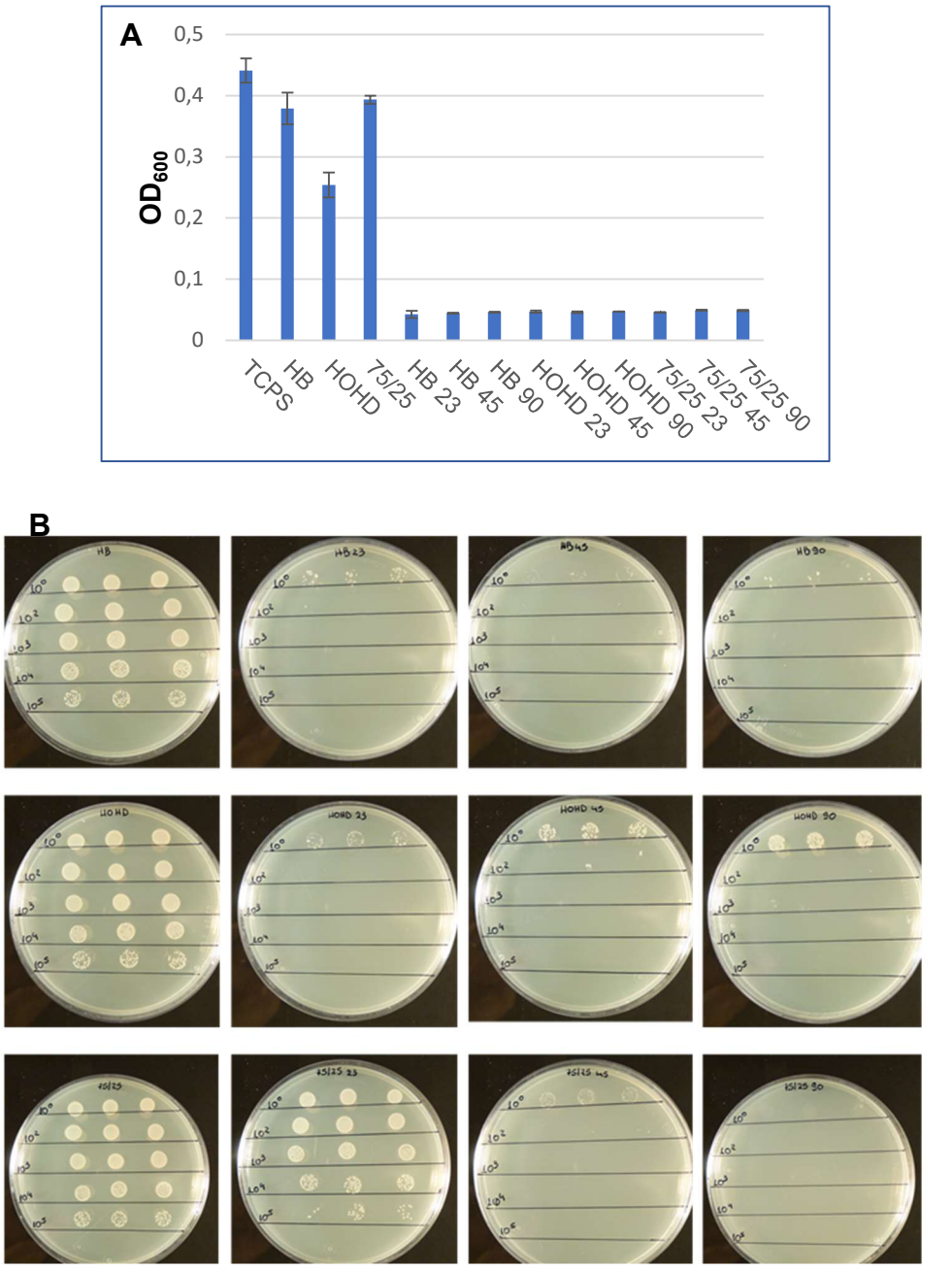

Figure 4: Antibacterial effect of GP composites against *S. epidermidis* (ATCC® 12228™) planktonic cells measuring (A) the optical density at 600 nm and (B) the cells that manage to recover after the contact with the composites for 24 h.

Figure 4 shows the effect of the composite discs of garlic powder against planktonic cells of *S. epidermidis* (ATCC® 12228™). Even the lower concentrations of garlic powder were able to prevent the bacterial growth compared to the respective non-modified samples.

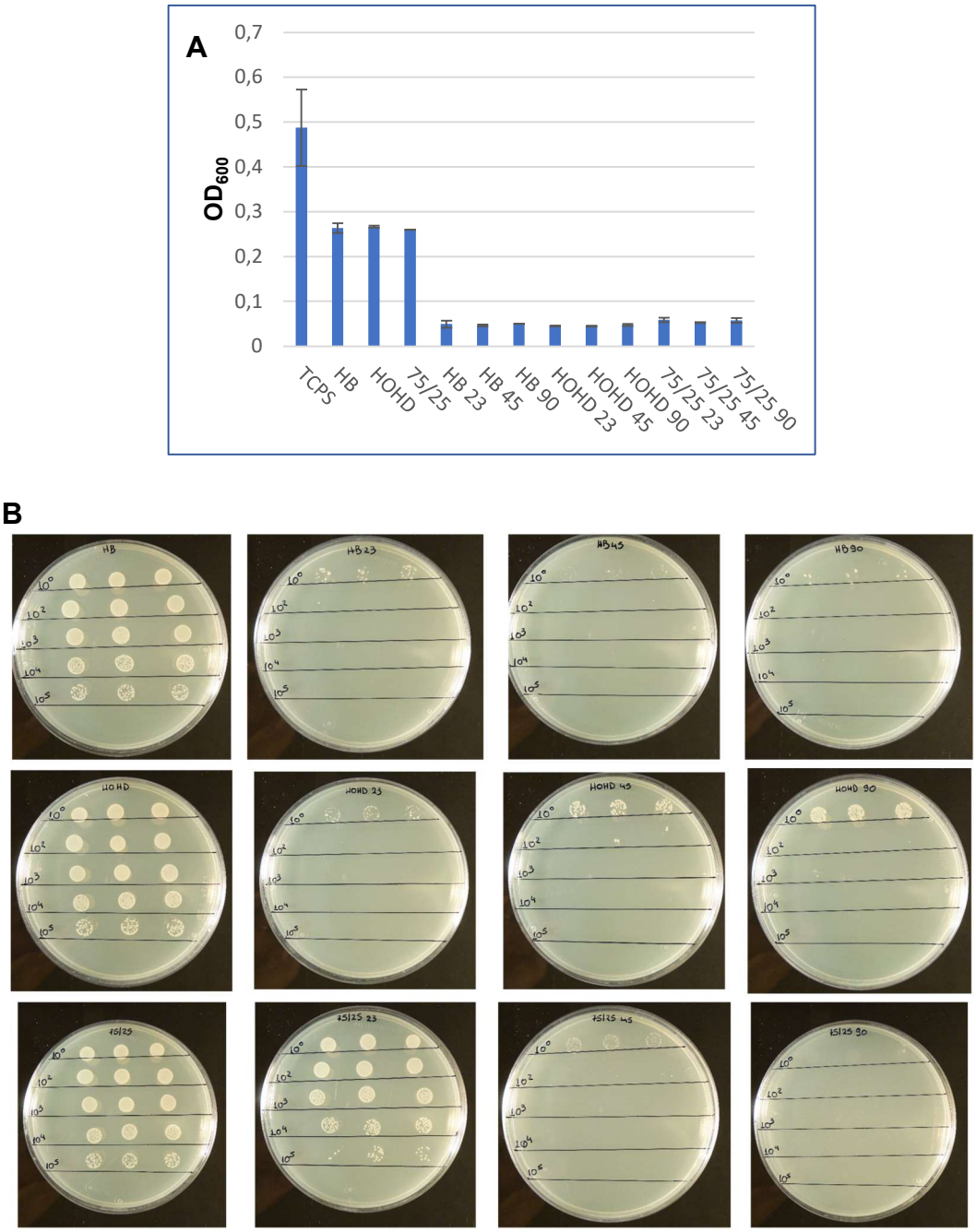

Figure 5: Antibacterial effect of GP composites against MRSA planktonic cells measuring (A) the optical density at 600 nm and (B) the cells that manage to recover after the contact with the composites for 24 h.

Figure 5 shows the drastically decrease of the planktonic cells of MRSA when in contact with the polymeric discs containing the garlic powder. Even the lower amount of 23 wt% of garlic powder was able to inhibit the bacterial growth after 24h of incubation.

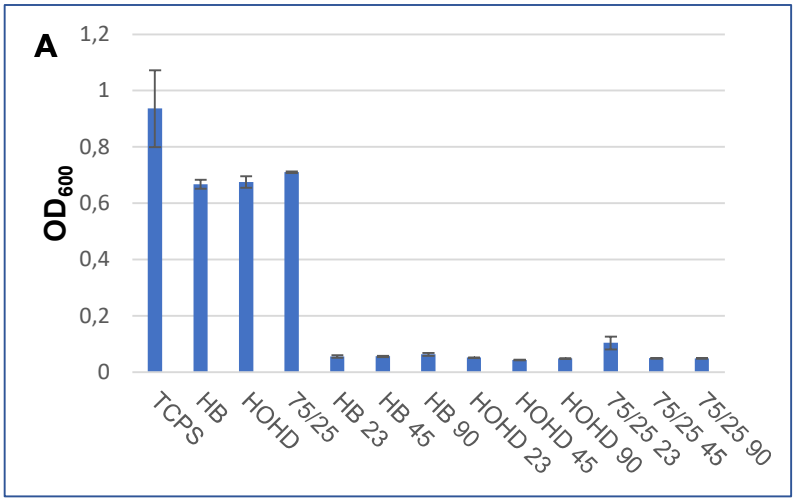

B

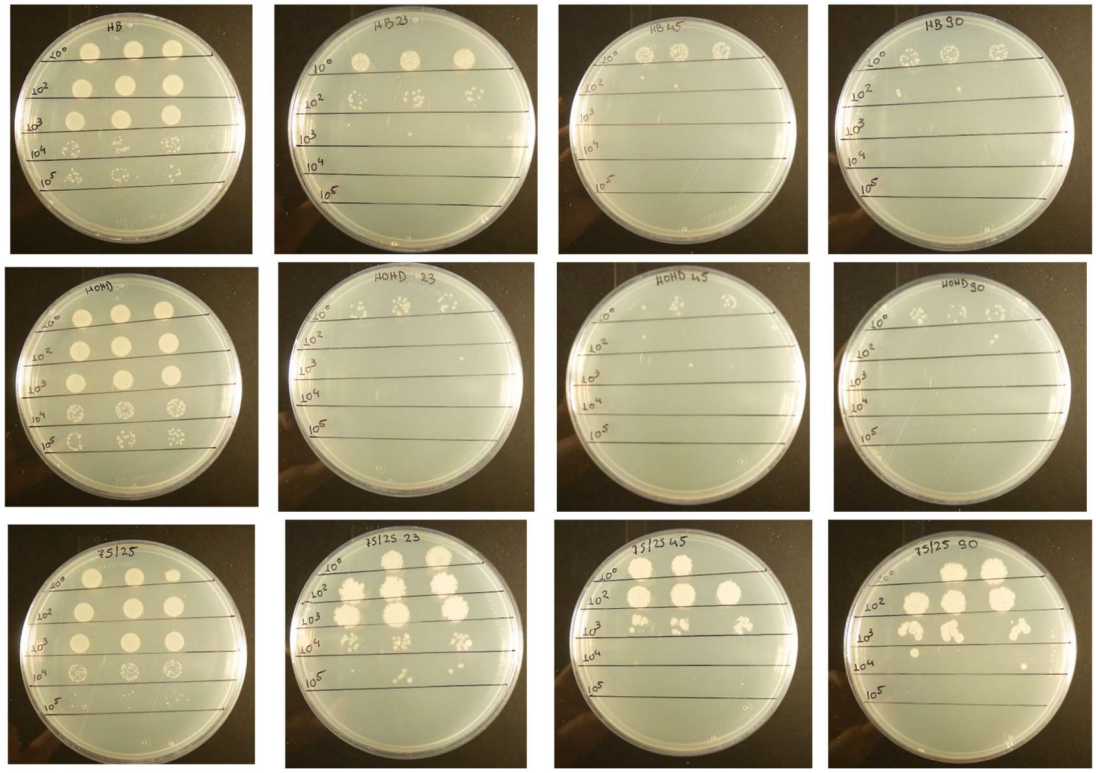

Figure 6: Antibacterial effect of GP composites against bacterial *E. coli* (ATCC® 25922™) planktonic cells measuring (A) the optical density at 600 nm and (B) the cells that manage to recover after the contact with the composites for 24 h.

Figure 6 shows the effectivity of garlic powder discs against the Gram-negative bacterial *E. coli* (ATCC® 25922™). Here also we can detect, the high inhibition of the composites to the free planktonic cells and the supportive pictures are confirming the high efficiency of the composites.

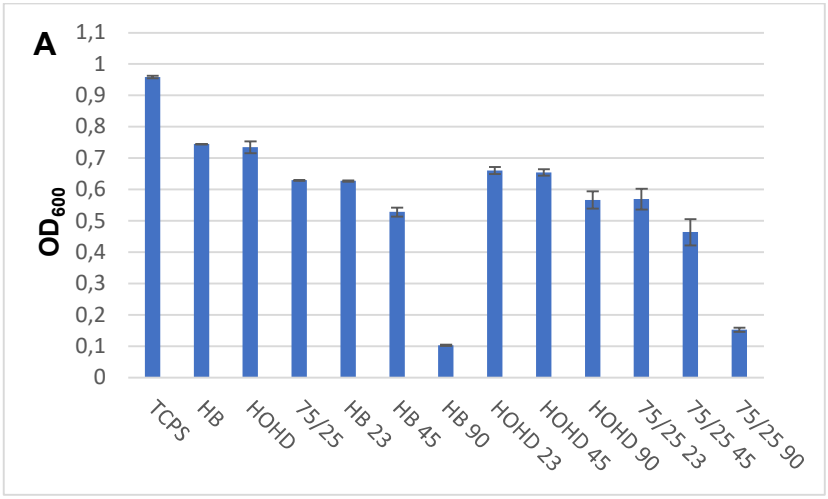

B

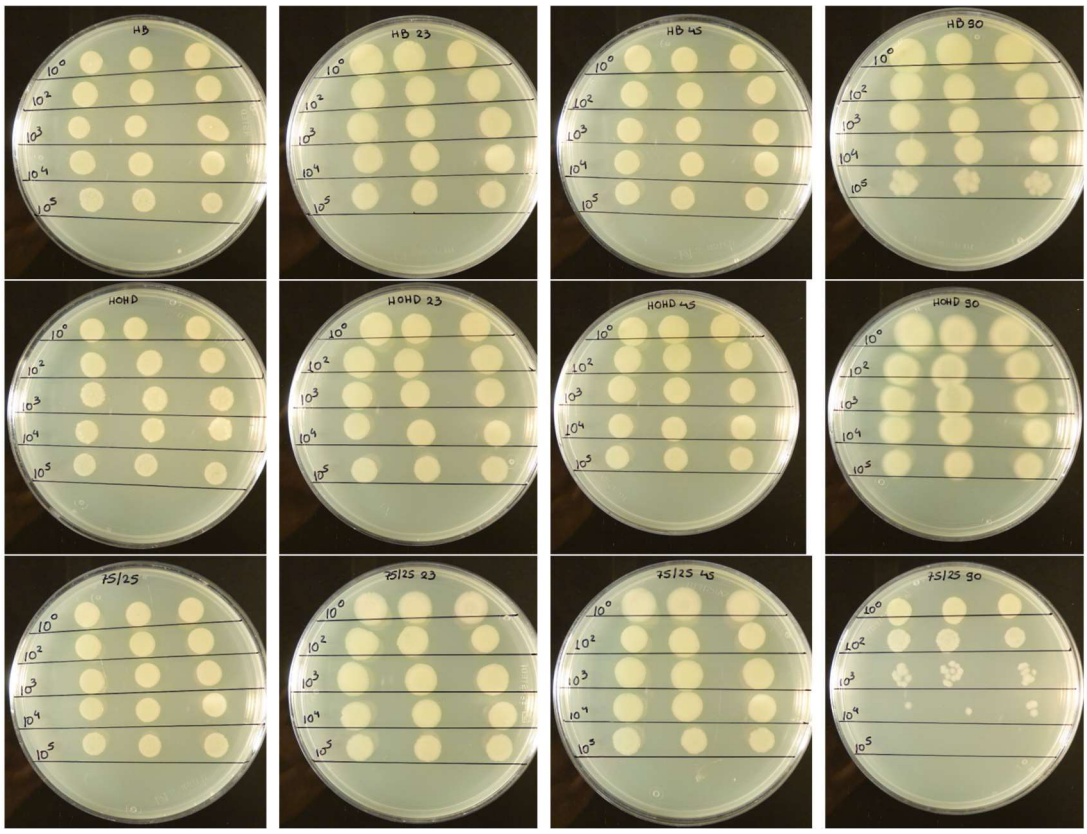

Figure 7: Antibacterial effect of GP composites against bacterial *Pseudomonas aeruginosa* (ATCC® 27853™) planktonic cells measuring (A) the optical density at 600 nm and (B) the cells that manage to recover after the contact with the composites for 24 h.

Figure 7 reveals that the garlic powder exhibit antibacterial effectivity against the free planktonic cells of only for case of P(3HB) and the blend of 75/25 (P(3HO-co-HD)/P(3HB)) containing 90 wt% of the agent. The representative pictures are supporting these findings.

II. Synthesis of Graphene oxide

GO was synthesised from natural graphite flakes (NGS Naturgraphit GmbH, Germany), according to the method of Kovtyukhova *et al.*, (Kovtyukhova *et al.*, 1999) which is itself a modification of Hummers method (Hummers and Offeman, 1958) with an extra pre-oxidation step of the graphite at the beginning, followed by the final oxidation step where small GO flakes were collected. The exact synthetic protocol used is as follows; 10 g natural graphite flakes were added to a solution of 6.5 g potassium persulfate ($K_2S_2O_8$) and 8.8 g phosphorus pentoxide (P_2O_5) in 37.5 mL concentrated sulfuric acid (H_2SO_4 96 %). The mixture was then placed in an oil bath and heated at 80 °C for one hour with constant stirring. After one hour, the mixture was stirred and allowed to cool to room temperature over a period of five h. Deionised water was carefully added into the mixture and then it was filtered and washed on the filter until the rinse water pH became the same as the deionised water's pH. Finally, the pre-oxidized graphite was air-dried at ambient conditions overnight. Subsequently, the pre-oxidized graphite powder was subjected to further oxidation utilising Hummer's method. The pre-oxidized graphite powder was added to an ice-cold flask, cooled in an ice bath, containing 230 mL of H_2SO_4 96 %, with constant stirring. Gradually, 32 g of potassium permanganate ($KMnO_4$) was added to the mixture, making sure that the temperature of the system was not allowed to reach 20 °C. The ice bath was removed 20 min after completion of the addition, and the mixture then stirred at 35 °C for 2 h, following the careful addition of 0.5 L deionized water. 1.5 L of deionised water and 25 mL of hydrogen peroxide (H_2O_2 30 %) was then added over 15 min to quench the reaction. The mixture was then filtered and washed with a 1:10 solution of HCl to remove most of the metal ions. The GO was dispersed into deionised water before being dried on a filter by vacuum filtration. The solution was subjected to dialysis until the pH became the same as the pH of deionised water. Mono-layers of the GO material was collected by a combination of sonication and centrifugation with an average size of 0.5 μm. The Graphene Oxide was provided by the Foundation of Research and Technology Hellas/Institute of Chemical Engineering Sciences FORTH/(ICE-HT) Patras, Greece from the group of Professor Costa Galiotis. Figure 8 demonstrates the steps used for GO nanopowder synthesis from

graphite resulting in an average particle size of 500 nm.

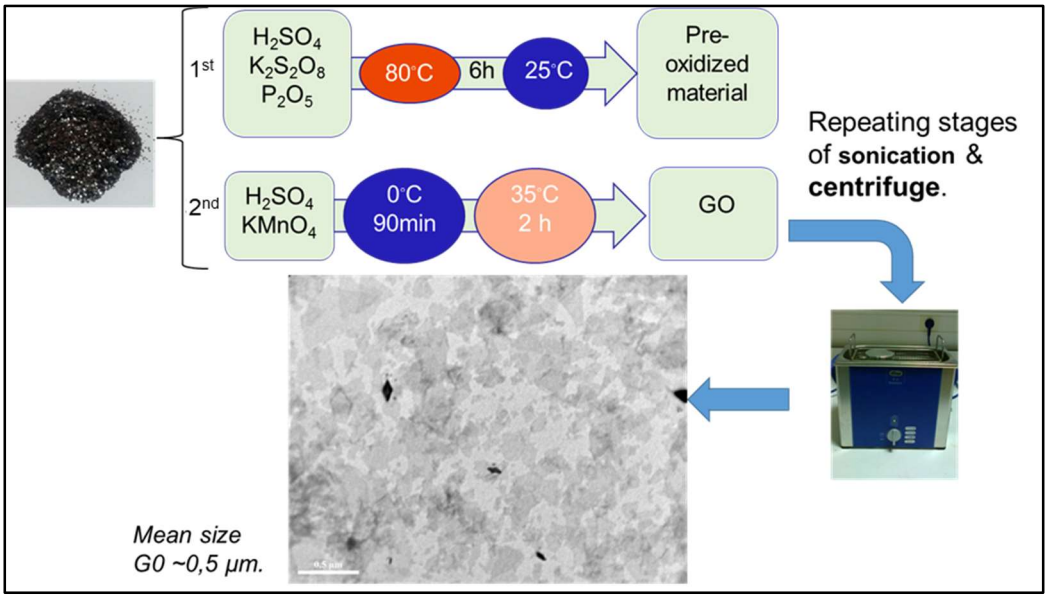

Figure 8: Steps of graphene oxide synthesis from graphite.

III. DSC thermographs of graphene oxide composites

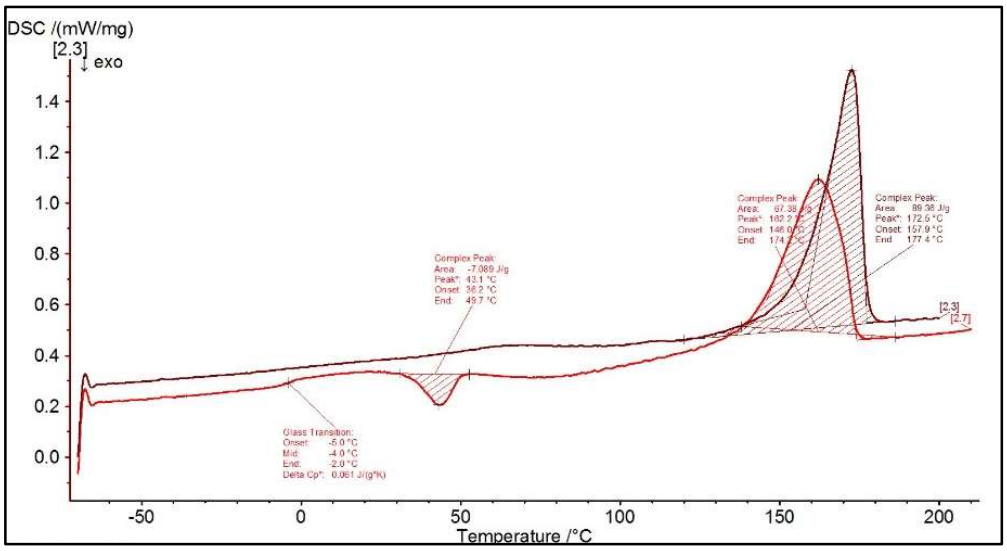

Figure 1.8: DSC thermograms of the P(3HB).

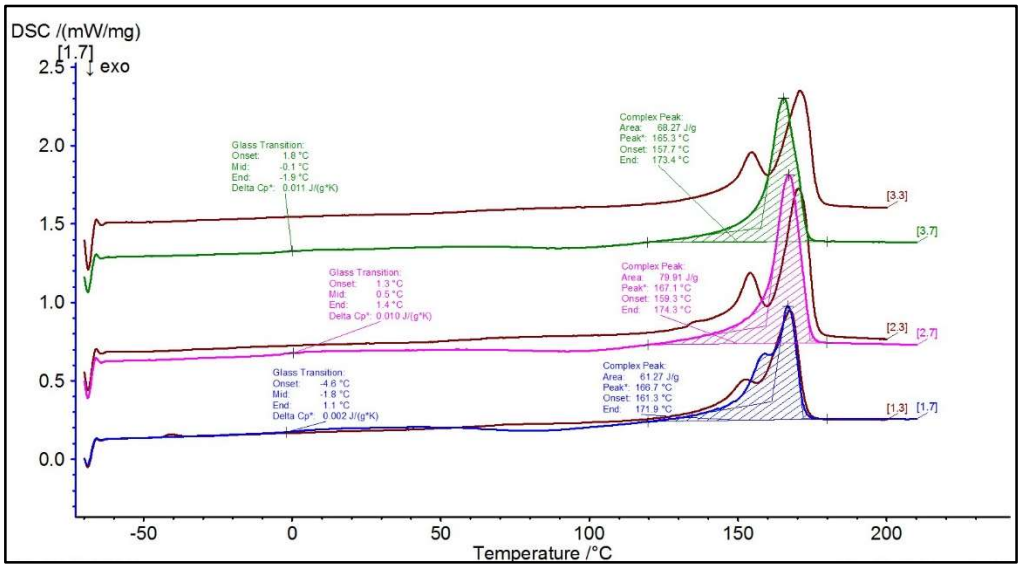

Figure 9: DSC thermograph of P(3HB) containing: ---0.5 wt%GO, ---2 wt%GO and ---5 wt%GO. (The first heating cycle of each composite is represented with the brown line (---)).

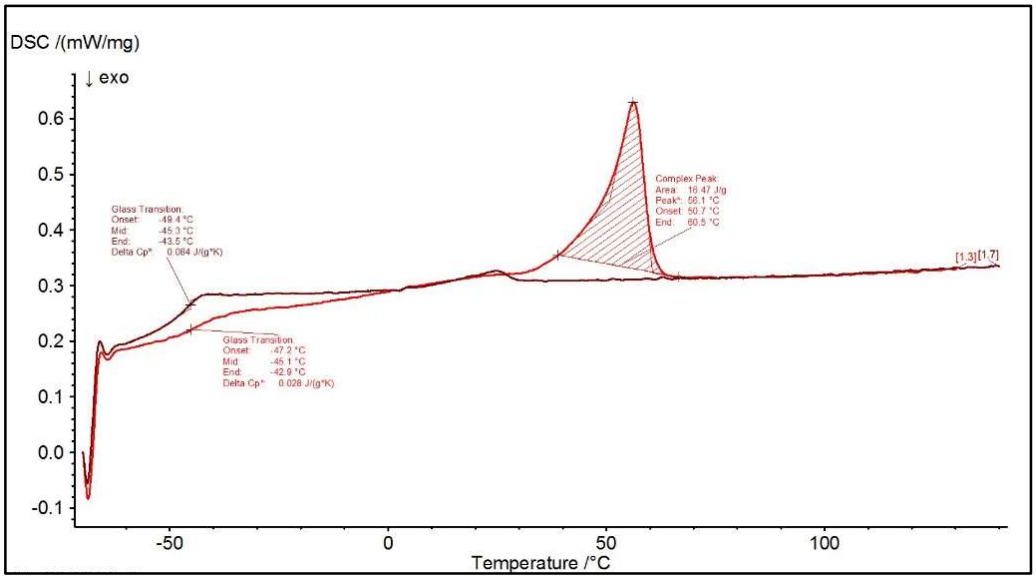

Figure 10: DSC thermograph of P(3HO-co-3HD).

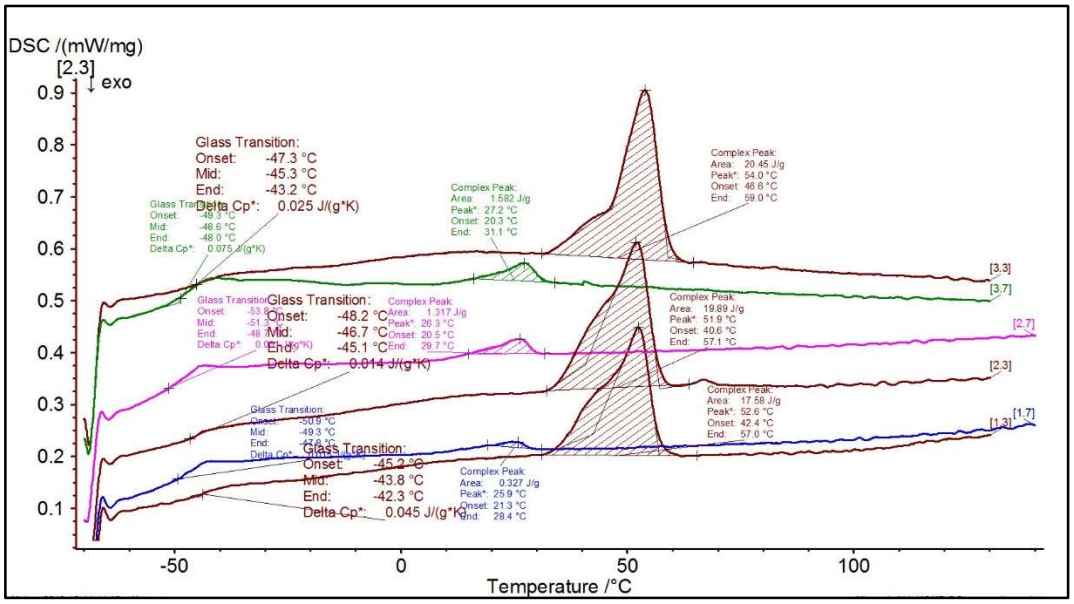

Figure 11: DSC thermograph of P(3HO-co-3HD) containing: ---0.5 wt%GO, ---2 wt%GO and ---5 wt%GO. (The first heating cycle of each composite is represented with the brown line (---)).

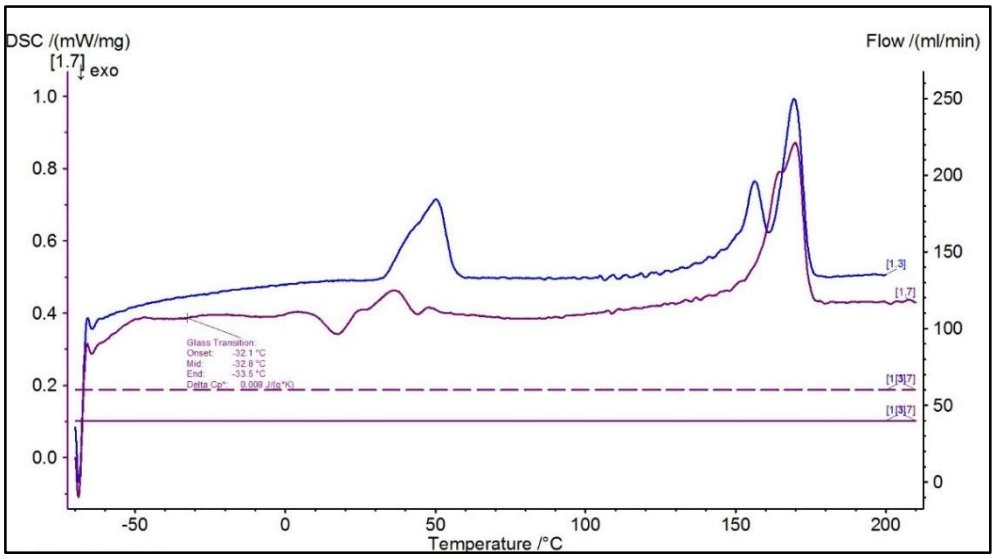

Figure 12: DSC thermograph of 75/25 P(3HO-co-3HD)/P(3HB).

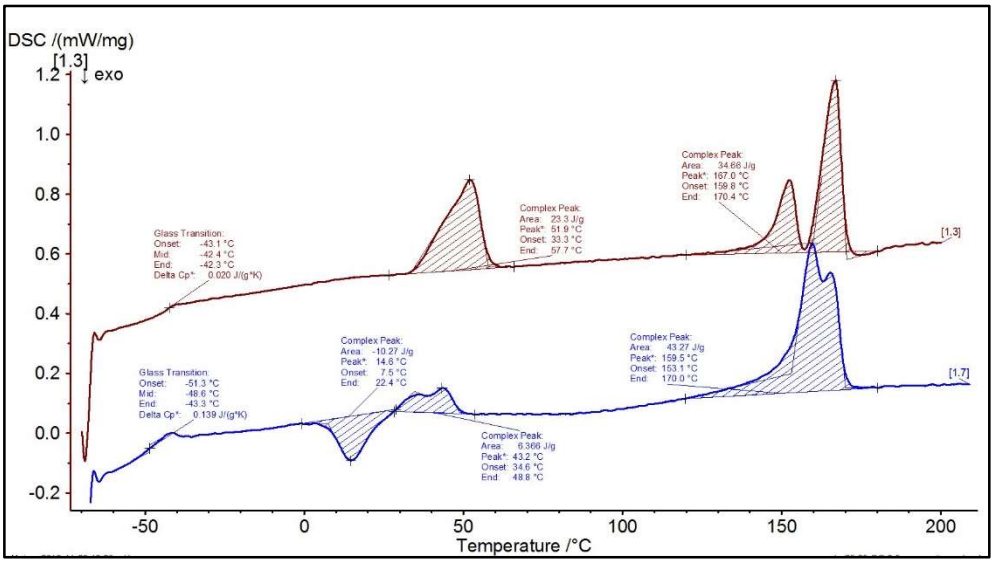

Figure 13: DSC thermograph of 75/25 P(3HO-co-3HD)/P(3HB)/0.5 wt%GO. (The first heating cycle of each composite is represented with the brown line (---)).

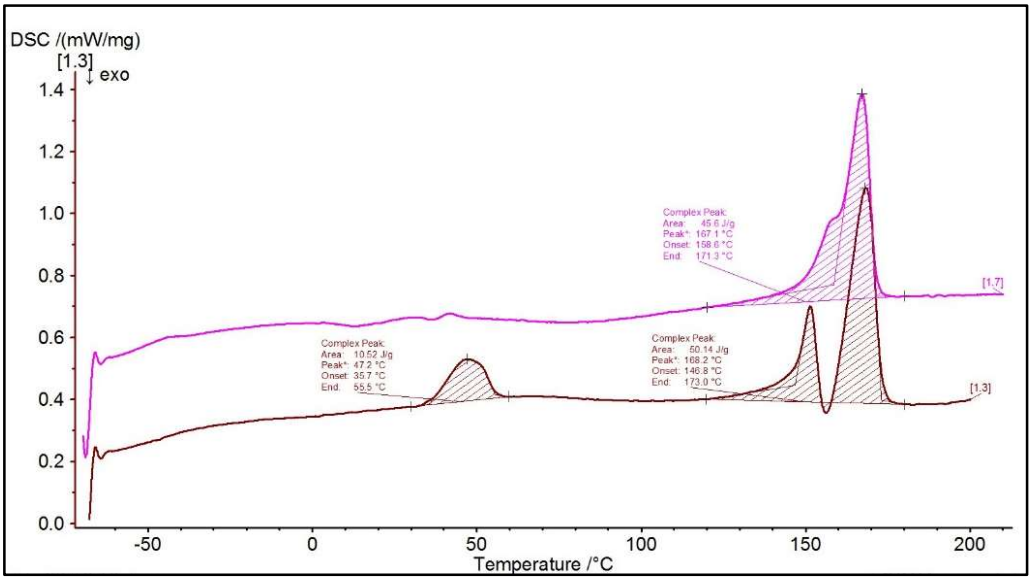

Figure 14: DSC thermograph of 75/25 P(3HO-co-3HD)/P(3HB)/2 wt%GO. (The first heating cycle of each composite is represented with the brown line (---)).

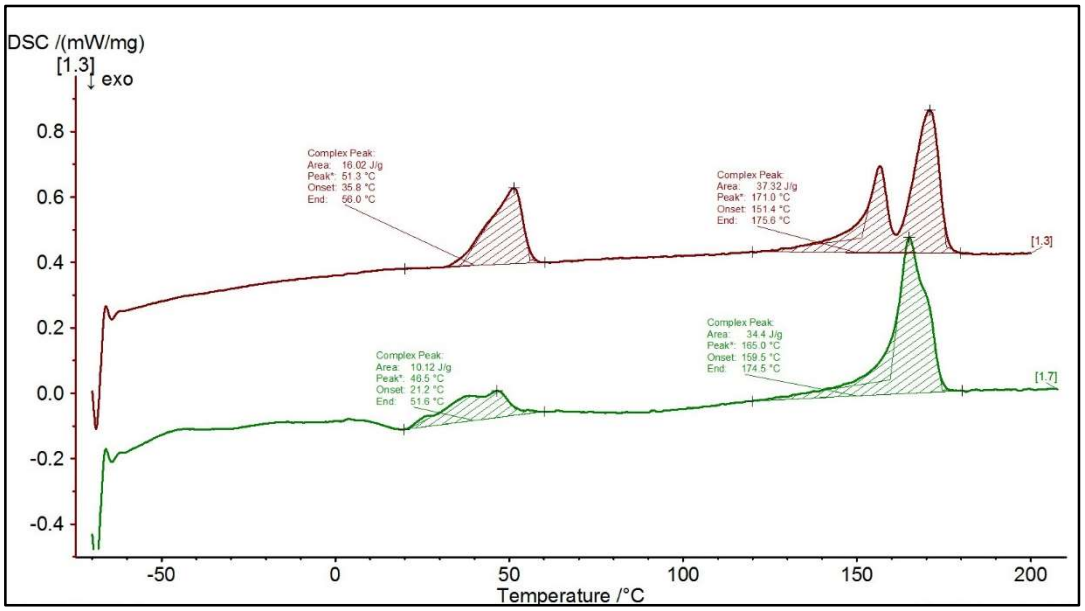

Figure 15: DSC thermograph of 75/25 P(3HO-co-3HD)/P(3HB)/5 wt%GO. (The first heating cycle of each composite is represented with the brown line (---)).